The Molecular Basis of Familial Danish Dementia

Nesgaard, Lise

Publication date:
2009

Document Version
Publisher's PDF, also known as Version of record

Aalborg University
Department of Life Sciences
Sohngaardsholmsvej 49
DK-9000 Aalborg, Denmark

Thesis title
The Molecular Basis of Familial Danish Dementia

Author
Lise Walther Nesgaard

Thesis period
September 2003-March 2009

Supervisor
Daniel E. Otzen

Number of pages
222

Issues printed
10

PhD school
The International Doctoral School of Technology and Science

PhD programme
Biotechnology, Chemistry, and Environmental Engineering

Lise Walther Nesgaard

Preface

The main focus of this thesis is the characterisation of the aggregation and membrane interaction of the 34-amino acid peptide SerADan, a modified variant of the ADan peptide, which is the primary component of protein deposits in Familial Danish dementia (FDD). The main bulk of the thesis work is presented in the two papers. Paper 1 focuses on biophysical characterisation by spectroscopic and microscopic methods of SerADan. Paper 2 describes development and documentation of a novel method for secondary structure characterisation of protein aggregates by vacuum-ultra violet circular dichroism spectroscopy. In chapter 1, I will summarise current knowledge of protein misfolding for the amyloid diseases, characteristics of the deposited polypeptides and the prevailing hypotheses of disease. Chapter 2 describes FDD, FBD and the deposited proteins in more detail while chapter 3 presents and discusses the two central papers. Additionally, chapter 4 (appendix) covers additional work on expression and purification of precursor proteins to ADan and ABri, which is deposited in Familial British dementia (FBD).

The majority of the PhD study time was devoted to characterisation of SerADan, ADan and the precursor proteins, for which the bulk of the work was carried out in the laboratories of Professor Daniel E. Otzen (Department of Molecular Biology, Interdisciplinary Nanoscience Centre, Aarhus University, Denmark, previously Department of Life Sciences, Aalborg University, Denmark). Electron microscopy was carried out at the Institute of Medical Microbiology and Immunology, Aarhus University, in collaboration with Professor Gunna Christiansen. Concentration-dependent calcein-release was performed by Brian Vad and X-ray fibre distraction was performed by Christian B. Andersen, Protein Structure and Biophysics group, Novo Nordisk A/S, Måløv, Denmark. The secondary project was development and description of dry-phase protein synchrotron radiation circular dichroism in collaboration with Dr Søren V. Hoffmann at the Institute for Storage Ring Facilities (ISA), Aarhus University, Denmark. With few exceptions, the work was performed at the ASTRID storage ring facility, Aarhus University.

The PhD project was funded by pre-doctoral grants from Aalborg University, the Danish Research Training Council and the BioNET research network, funded by the Villum Kann Rasmussen Foundation. In addition, I received a COST Short Term Scientific Mission grant for a visit to Structure and Function of Membrane Biology Laboratory, Université Libre, Bruxelles, Belgium in collaboration with Dr Erik Goormaghtigh. The purpose was characterisation of membrane proteins advanced infrared spectroscopy methods.

I would like to acknowledge the support I have received from my fellow members of the Protein Biophysics group, particularly my supervisor Daniel Otzen, and past and present staff and students at the Department of Life Sciences. I would especially like to thank Hanne K. Nielsen, Tony Ebdrup, Taru Deva, Rajiv V. Basaiawmoit, Lise Giehm, Jesper S. Pedersen, Peter A. Christensen and Brian Vad for many inspiring discussions and, more importantly, for being warm and wonderful human beings. I am thankful to Søren V. Hoffmann for an en exciting and inspiring collaboration. I am grateful to Brian Vad, Christian B. Andersen and Gunna Christensen for their help with calcein release, X-ray fibre diffraction and electron microscopy, respectively, and to Anders Malmendal for his work on PCA and a great introduction to it. Last, but not least, I would like to thank my parents, Inge and Hans, and my family and friends. In particular and in no particular order: Kurt, Lea, Ole and the rest of the Borup family, Hanne, Thorkil and the Hansen Clan, Helle, Freddy, Tony, Louise, Johanne, Jeppe, Rainer and the rest of the gang.

List of included papers

1. **Nesgaard, L.**, Vad, B., Christiansen, G. and Otzen, D.: Kinetic partitioning between aggregation and vesicle permeabilization by modified ADan. *Biochim Biophys Acta* (2009) 1794 p. 84-93.
2. **Nesgaard, L. W.**, Hoffmann, S. V., Andersen, C. B., Malmendal, A. and Otzen, D. E.: Characterization of dry globular proteins and protein fibrils by synchrotron radiation vacuum UV circular dichroism. *Biopolymers* (2008) 89 p. 779-95.

Additional aspects of interest can be found in papers 3-6, which fall outside the central scope of the thesis and therefore are not included for assesment. These papers deal with membrane protein aggregation in membrane-mimicking halogenated alcohols, antimicrobial peptide structure and solvent-tuning of aggregation of globular proteins S6 and cutinase.

3. Otzen, D. E., **Nesgaard, L. W.**, Andersen, K. K., Hansen, J. H., Christiansen, G., Doe, H. and Sehgal, P.: Aggregation of S6 in a quasi-native state by submicellar SDS. *Biochim Biophys Acta* (2008) 1784 p. 400-14.
4. Otzen, D. E., Sehgal, P. and **Nesgaard, L. W.**: Alternative membrane protein conformations in alcohols. *Biochemistry* (2007) 46 p. 4348-59.
5. Pedersen, S., **Nesgaard, L.**, Baptista, R. P., Melo, E. P., Kristensen, S. R. and Otzen, D. E.: pH-dependent aggregation of cutinase is efficiently suppressed by 1,8-ANS. *Biopolymers* (2006) 83 p. 619-29.
6. Wimmer, R., Andersen, K. K., Vad, B., Davidsen, M., Molgaard, S., **Nesgaard, L. W.**, Kristensen, H. H. and Otzen, D. E.: Versatile interactions of the antimicrobial peptide novispirin with detergents and lipids. *Biochemistry* (2006) 45 p. 481-97.

Resumé

Hovedemnet for denne afhandling er biofysisk karakterisering af et peptid knyttet til the neurodegenerative sygdom Arvelig Dansk Demens. Derudover blev anvendelsen af synkrotronstrålings cirkulær dikroism undersøgt med hensyn til karakterisering af protein aggregater.

Arvelig Dansk Demens er associeret med proteolytisk kløvning og aggregering af det 34-amino syre peptid ADan, der i lighed med andre amyloid-dannende polypeptider er i stand til at danne transmembrane kanaler og hvis celletoksicitet kan finde sted gennem vekselvirkning med cellemembranen. Peptidet indeholder to cysteiner og kan derfor forefindes i en lineær, reduceret eller cirkulær, oxideret form, blandt hvilke den reducerede form har den højeste celletoksicitet. Vi karakteriserede the afledte peptid SerADan i hvilket de to cysteiner er udskiftet med serin for at efterligne det reducerede peptid. Derudover er fenyl-aminosyrerester i position 15 udskiftet med tryptofan for at inkorporere en fluorescensmarkør. SerADan aggregerer hurtigt ved pH 5.0 og 7.5 gennem en serie af konformationelle stadier til en β-rig fibril-lignende struktur. Til trods for den generelle lighed med amyloid-lignende fibriller viser røntgen fiber diffraktion ikke det klassiske amyloide kryds-β mønster og SerADan fibre binder ikke amyloid-specifikke farvemarkører. Dette kan formentlig tilskrives en mangel på organiserede kontakter mellem β-plader og tilstedeværelse af bindingssteder. Aggregering forhindres af negativt ladede lipid vesikler ved neutral/sur pH og lav ionstyrke mens øget ionstyrke eliminerer effekten af liposomerne, hvilket tyder på at elektrostatiske vekselvirkninger spiller en vigtig rolle. Lipid/peptid-kontakten leder til dannelse af stabile β-rige strukturer, som er forskellige fra aggregater i opløsning, og permeabilisering af liposomerne, der her vises som frigivelse af den 623 Da fluorefor calcein. Ved ældning af SerADan i opløsning reduceres den permeabiliserende effekt i først omgang, hvorefter den elimineres. Det eksperimentelle arbejde, der præsenteres i denne afhandling, viser at aggregater, der ikke har klassiske amyloide egenskaber, kan samles gennem serie af trin og danne et hierarki af højere-orden strukturer i tilfælde, hvor hurtig dannelse af stabile, lokale β-strenge kunne forhindrer omdannelse til klassisk amyloid struktur. Det viser også at en snæver balance kan findes mellem aggregering og membran-interaktion med det deraf følgende potentiale for celletoksicitet. Konkurrencen mellem lipidbinding og aggregering kan tænkes at tilsvare en tvedeling af aggregeringsmekanismen for ADan *in vivo* mellem ophobning af inerte aggregater og dannelse af celletoksiske, permeabiliserende strukturer.

Som et sideprojekt til afhandlingens hovedemne undersøgte jeg anvendelsen af synkrotronstrålings cirkulær dikroisme til karakterisering af tørrede proteinaggregater og fibriller. Brugen af synkrotronstråling kan udvide det

tilgængelige bølgelængdeområde ned til ~130nm for tørrede proteiner, hvilket potentielt kan give ny strukturel information. For at muliggøre sammenligning og estimere den strukturelle effekt af tørring på ikke-aggregerede prøver benyttede vi et udvalg af modelproteiner i våd og tør fase. Der var tale om α-heliske, β-plade og blandende strukturer. Vi viste at tørringsprocessen ikke leder til store ændringer i den sekundære struktur og ikke inducerer orienteringseffekter. Vi observerede et lav-bølgelængde bånd ved 130-160nm hvis intensitet og topplacering er følsom overfor sekundær struktur og som potentielt kunne indeholde information om ændringer i super-sekundær struktur. Dette bånd er tidligere beskrevet for peptider, men ikke for globulære proteiner eller proteinaggregater, og det er kompatibelt med publicerede teoretiske beregninger af π-orbitalovergange. Sammen med principal komponent analyse tillader vores data os at differentiere mellem to typer proteinfibriller; de klassiske fibriller dannet af lysozym er strukturelt tættere forbundet med ikke-amyloide aggregater af SerADan end med de klassiske α-synuclein fibriller. Denne analyse tillader os også at beskrive ellers ukendte forskelle i sekundær struktur mellem SerADan fibre dannet ved pH 5.0 og 7.5. En mere detaljeret analyse er påkrævet før der er muligt at drage klare strukturelle konklusioner, men en omfangsrig SRCD-baseret database over spektre af tørrede proteiner kan måske bidrage til differentiering mellem forskellige typer super-sekundær struktur og typer af protein-aggregater.

Summary

The main topic of this thesis is the biophysical characterisation of a peptide associated with the neurodegenerative illness Familial Danish Dementia (FDD). Additionally, the use of synchrotron radiation circular dichroism on protein aggregates was investigated.

Familial Danish Dementia is linked to proteolytic formation and aggregation of the 34-residue ADan peptide, which is capable of forming transmembrane channels in a manner similar to other amyloidogenic polypeptides and whose cytotoxicity may be mediated by membrane interactions. The peptide contains two cysteines and can therefore exits in the linear, reduced and circular, oxidised form, of which the reduced form is the more cytotoxic in culture. We characterised the derived peptide SerADan, in which the two cysteines found in ADan were substituted with serines to emulate the reduced peptide. Additionally, the phenyl residue at position 15 was replaced with a tryptophan residue acting as a fluorescent marker. SerADan aggregates rapidly at pH 5.0 and 7.5 in a series of conformational transitions to form β-sheet rich fibril-like structures. Despite the overall morphological similarities with amyloid-like fibrils, X-ray fibre diffraction does not yield the classical amyloid cross-β pattern, nor do the SerADan fibres bind amyloid-specific dyes. This is probably due to the absence of organized β-sheet contacts and surface binding sites. Aggregation is prevented by anionic lipid vesicles at neutral/acidic pH and low ionic strength, while increased ionic strength abolishes the effect of the anionic liposomes suggesting an important role for electrostatic interaction. The lipid/peptide association leads to formation of stable β-sheet structures, which are different from the solution aggregates, and permeabilisation of the liposomes, here demonstrated as the release of the 623 Da fluorophore calcein. Solution ageing of SerADan first reduces and then abolishes the ability of the peptide assembly to alter membrane permeability. The work presented within this thesis demonstrates that non-fibrillar aggregates can assemble in a series of steps to form a hierarchy of higher-order assemblies, where rapid formation of stable local β-sheet structure may prevent rearrangement to amyloid proper. It also shows that a fine balance can exist between non-fibrillar aggregation and membrane interaction with associated potential cytotoxicity. The competition between lipid binding and aggregation may reflect bifurcating pathways for the ADan peptide *in vivo* between accumulation of inert aggregates and formation of cytotoxic permeabilising species.

As an offshoot of the main thesis subject, I investigated the use of synchrotron radiation circular dichroism (SRCD) for characterisation of dried protein aggregates and fibrils. The use of synchrotron radiation can extend the spectral range down to ~130nm for dry proteins and has the potential to provide new structural

information. To allow comparison and to estimate the structural effect of drying on non-aggregated samples, we used a selection of model proteins, including α-helical, β-sheet, and mixed-structure proteins, in the wet and dried phases. We showed that drying does not lead to large changes in the secondary structure and does not induce orientational artefacts. The access to the higher-energy regions allowed us to observe a low-wavelength band in the range 130-160nm, whose intensity and peak position is sensitive to secondary structure and may also reflect changes in super-secondary structure. This band has previously been observed for peptides but not for globular proteins, and is compatible with previously published theoretical calculations related to π-orbital transitions. In combination with principal component analysis, our SRCD data allow us to distinguish between two different types of protein fibrils, high-lighting that *bona fide* fibrils formed by lysozyme are structurally more similar to the nonclassical fibrillar aggregates formed by the SerADan peptide than with the amyloid formed by α-synuclein. The analysis also allows us to describe otherwise unidentified differences in secondary structure between SerADan fibres at pH 5.0 and 7.5. A more detailed study is required for any firm conclusions to be drawn, but a comprehensive SRCD-based database of dried protein spectra may provide a useful method to differentiate between various types of super-secondary structure and aggregated protein species.

Frequently used abbreviations

Ordered alphabetically

Aβ	Amyloid β-peptide of Alzheimer's disease
$(Aβ)_n$	Oligomeric form of Aβ
AβPP	Aβ precursor protein
ABri	Amyloid peptide of Familial British dementia
ABriPP	ABri precursor protein
ACBP	Acyl-CoA-binding protein
ACP	Acylphosphatase
AD	Alzheimer's disease
ADAM10	ADAM metallopeptidase domain 10
ADan	Amyloid peptide of Familial Danish dementia
ADan-pE	ADan with N-terminal pyroglutamate
ADanPP	ADan precursor protein
ADDLs	Aβ-derived diffusible ligands
AEC	Anion-exchange chromatography
AFM	Atomic force microscopy
ALS	Amyotrophic lateral sclerosis
APP	Gene encoding AβPP
ATR	Attenuated total reflection
β2m	$β_2$-microglobulin
Bri	C-terminal proteolytic fragment of BriPP, wildtype analogue of pathogenic ABri and ADan peptides
BriPP	Bri precursor protein
$BriPP_{EC}$	C-terminal, extra-cellular domain of BriPP
$BriPP_S$	Short form of BriPP beginning at position 57
CA	Carbonic anhydrase
CAA	Cerebral amyloid angiopathy
CD	Circular dichroism
CNS	Central nervous system
ConA	Concanavalin A
CR	Congo red
C_R	Critical concentration of fibrillation
CSF	Cerebrospinal fluid
DOPC	1,2-dioleoyl-*sn*-glycero-3-phosphocholine
DOPG	1,2-dioleoyl-*sn*-glycero-3-[phospho-*rac*-(1-glycerol)]
EM	Electron microscopy
FBD	Familial British dementia
FDD	Familial Danish dementia
FFI	Fatal familial insomnia
FTIR	Fourier-transform infrared spectroscopy

GAG	Glycosaminoglycan
HFIP	1,1,1,3,3,3-hexafluoropropan-2-ol
HSPGs	Heparan sulphate proteoglycans
HypF	Hydrogenase maturation factor of *Escherichia coli*
HypF-N	N-terminal domain of HypF
IAPP	Islet amyloid polypeptide
ITM2A-C	Gene encoding integral membrane protein 2 (ITM2) isoform A-C. ITM2B corresponds to BriPP.
ITM2-LG	*Integral membrane protein 2*-like gene
LTP	(Hippocampal) long-term potentiation
MPL	Fibril mass-per-length
MTT	3-(4,5-dimethylthiazol-2-yl)-2.5-diphenyltetrazolium bromide
n*	Critical fibrillation nucleus
NAC	Nickel-affinity chromatography
NFTs	Neurofibrillar tangles
NMR	Nuclear magnetic resonance spectroscopy
oxABri	Oxidised form of ABri by disulphide C5-C22
oxADan	Oxidised form of ADan by disulphide C5-C22
oxBri	Oxidised form of Bri by disulphide C5-C22
PCA	Principle component analysis
PD	Parkinson's disease
PSA	Porcine serum albumin
PSEN1, 2	Gene encoding presenilin 1 or 2
redABri	Reduced form of ABri
redADan	Reduced form of ADan
redBri	Reduced form of Bri
rm-III9	The ninth type III domain of fibronectin
ROS	Reactive oxygen species
SAP	Serum amyloid P-component
SCAA	Sporadic cerebral amyloid angiopathy
SDS	Sodium dodecylsulphate
SEC	Size-exclusion chromatography
SerADan	Variant of ADan (C5S, C22S, F15W)
SH3	SH3 domain of phosphatidylinositol-3'-kinase
SPPL2a,b	Signal peptidase-like protease 2a, b
SRCD	Synchrotron radiation circular dichroism
SSNFOS	SDS-stable non-fibrillar oligomeric species
STEM	Scanning transmission electron microscopy
TEM	Transmission electron microscopy
TFE	2,2,2-trifluoroethanol
ThS	Thioflavin S
ThT	Thioflavin T
TII27	Titin, Ig repeat 27
Tnfn3	Tenescin, third fibronectin type III repeat
TTR	Transthyretin

Table of contents

INTRODUCTION

1 Amyloid: Protein folding, misfolding and disease

The interest in protein misfolding has increased over the past decade, partly due to the importance of maintaining protein structure and function in pharmaceutical, enzymatic and other industrial protein preparations [1] and partly due to the emerging significance of protein misfolding in disease including cancer and dementia (table 1) [2]. The underlying mechanism of disease understandably depends on the relevant protein. Protein misfolding results in loss of biological activity and this loss-of function can have greatly damaging effects on cell and organ function. This is the case for cystic fibrosis and p53-deficient cancers [3]. Conversely, gain-of-function, or perhaps rather 'gain-of-cellular-toxicity', is believed to be at the basis of many of the protein deposition diseases including the two well-known neurodegenerative amyloidoses Alzheimer's disease and Parkinson's disease [4]. Familial Danish dementia (FDD) and the closely related Familial British dementia (FBD) belong to this latter group and are the focus of the present work.

Disease	Affected proteins
Inability to fold	
Cystic fibrosis	Cystic fibrosis transmembrane conductance regulator
Marfan syndrome	Fibrillin
Amyotrophic lateral sclerosis	Superoxide dismutase
Scurvy	Collagen
Maple syrup urine disease	α-ketoacid dehydrogenase complex
p53-deficient cancer	p53
Fabry's disease	α-Galactosidase A
Osteogenesis imperfecta	Type I procollagen pro α
Toxic, non-native folds	
Scrapie/kuru/Creutzfelt-Jacob/FFI [a]	Prion protein
Parkinson's disease	α-synuclein
Alzheimer's disease	Amyloid precursor protein
Huntington's disease	Huntingtin
Spinocerebellar ataxia	Ataxin
Cataracts	Crystalins
Mislocation owing to misfolding	
Familial hypercholesterolemia	LDL receptor
α-antitrypsin deficiency	α-antitrypsin
Tay-Sachs disease	β-hexosaminidase
Retinitis pigmentosa	Rhodopsin
Leprechaunism	Insulin receptor

Table 1. Examples of protein misfolding diseases. Adapted from [2, 3]. [a] Fatal familial insomnia.

Table 2 (opposite). A. Amyloidoses/diseases with amyloid-like deposits and associated proteins or peptides. B. Examples of inclusions with amyloid-like properties. Adapted from [4, 8, 10, 11]

1.1 Amyloidosis and amyloid characteristics

1.1.1 The protein misfolding disorders and amyloidoses

The amyloid diseases, or amyloidoses, are a diverse group of generally life-threatening protein misfolding disorders with one unifying characteristic: The presence of systemic or organ-specific extra-cellular deposits of insoluble amyloid [4, 5]. The first amyloidoses were described in the early 19th century as presence of abnormal tissues that appeared 'waxy' or 'lardaceous' upon gross inspection [6, 7]. Much controversy resulted from the subsequent attempts at characterisation of the amyloid material, particularly following observations by Virchow in 1853 of the cellulose-like staining properties of 'waxy' spleen tissue and of *corpora amylacea* from human brain tissue. 150 years later, it is commonly accepted that the deposits, or plaques, are predominantly proteinaceous with a single-species fibrous fibril[1] as the main component [8]. The iodine-sulphuric acid staining reaction of Virchow has been replaced by amyloid-specific dyes among which Congo red (CR) and thioflavin S (ThS) are most commonly used for staining of tissue while thioflavin T (ThT) is useful for *in vitro* characterisation [9].

The amyloidoses are a part of the larger group of protein misfolding disorders and more than 20 amyloid-forming proteins or peptides have been identified to date [8, 10] (table 2.A) including several associated with well-known diseases such as type II diabetes mellitus (IAPP) and Alzheimer's disease (Aβ). Some of these polypeptides are full-length proteins, e.g. β_2-microglobulin (β_2m), that lose their native structure and deposit in a misfolded, β-rich conformation [12]. Others are truncated, usually intrinsically unfolded, fragments of longer precursor proteins, e.g. Aβ, ABri and ADan. Under the definition of amyloid used by pathologists, intra-cellular deposits (table 2.B), as in the case of Lewy bodies of Parkinson's disease, are not considered amyloid, but rather amyloid-like [8] although the deposits appear structurally alike. Similarly, fibrils formed *in vitro* are more accurately referred to as amyloid-like. The fibril is the central component of amyloid, but additional non-fibrillar components are consistently present in biological amyloid, e.g. serum amyloid P-component (SAP), heparan sulphate proteoglycans (HSPGs) and apolipoprotein E [7]. The roles of these additional species are as yet unresolved although some studies suggest a role as enhancers of amyloid formation or protection of plaques from clearance mechanisms [13].

1.1.2 Functional amyloid

Amyloid has not been exclusively linked to disease. Numerous discoveries of functional amyloid have been made within the past decade highlighting its possible beneficial functions. Several prion types have been identified in fungi including the *S. cerevisiae* Sup35 [14, 15] which has become an important model system. Briefly, Sup35 is a normally soluble member of the yeast translation termi-

1 Derived from Latin *fibrilla* meaning 'small fibre'.

A. Proteins and peptides associated with amyloidoses or diseases with amyloid-like deposits in human

Disease	Aggregating protein or peptide
Neurodegenerative localised amyloidoses	
Alzheimer's disease [a]	Aβ, proteolytic fragment of Aβ protein precursor (AβPP)
Spongiform encephalopathies [a,b]	Prion protein and fragments thereof
Familial British dementia [c]	ABri, proteolytic fragment of ABri precursor protein (ABriPP)
Familial Danish dementia	ADan, proteolytic fragment of ADan precursor protein (ADanPP)
Neurodegenerative diseases with inclusion bodies with amyloid-like properties	
Parkinson's disease [a]	α-synuclein
Dementia with Lewy bodies [a]	α-synuclein
Frontotemporal dementia with Parkinsonism	Tau and fragments thereof
Huntington's disease	Huntingtin with polyQ expansion
Spinocerebellar ataxias [d]	Ataxins with polyQ expansion
Spinocerebellar ataxia 17 [d]	TATA box-binding protein with polyQ expansion
Spinal and bulbar muscular atophy [d]	Androgen receptor with polyQ expansion
Hereditary dentatorubral-pallidoluysian atrophy [d]	Atrophin with polyQ expansion
Nonneuropathic systemic amyloidoses	
AL amyloidosis [a]	Immunoglobulin light chains or fragments
AA amyloidosis [a]	Fragments of serum amyloid A protein (SAA)
Familial Meditteranean fever [a]	Fragments of serum amyloid A protein
Senile systemic amyloidosis [a]	Wild-type transthyretin (TTR)
Familial amyloidotic polyneuropathy [d]	Mutants of transthyretin
Haemodialysis-related amyloidosis [a]	β2-microglobulin (β2m)
ApoAI amyloidosis [d]	N-terminal fragments of apolipoprotein AI (ApoAI)
ApoAII amyloidosis [d]	N-terminal fragment of apolipoprotein AII (ApoAII)
ApoAIV amyloidosis	N-terminal fragment of apolipoprotein AIV (ApoAIV)
Finnish hereditary amyloidosis [d]	Fragments of gelsolin mutants
Lysozyme amyloidosis [d]	Mutants of lysozyme
Fibrinogen amyloidosis [d]	Variants of fibrinogen Aα-chain and fragments thereof
Icelandic hereditary cerebral amyloid angiopathy [d]	Mutant of cystatin C
Nonneuropathic localised diseases	
Type II diabetes [a]	Islet amyloid polypeptide (IAPP), also named amylin
Medullary carcinoma of the thyroid [a]	Calcitonin
Atrial amyloidosis [a]	Atrial natriuretic factor (ANF)
Hereditary cerebral haemorrhage with amyloidosis	Mutants of Aβ
Pituitary prolactinoma	Prolactin
Injection-localised amyloidosis [a]	Insulin
Aortic medial amyloidosis [a]	Medin, fragment of lactadherin
Hereditary lattice corneal dystrophy [d]	Mainly C-terminal fragments of kerato-epithelin
Corneal amyloidosis associated with trichiasis [a]	Lactoferrin
Cataract [a]	γ-Crystallins
Calcifying epithelial odontogenic tumour [a]	Unknown
Pulmonary alveolar proteinosis [d]	Lung surfactant protein C
Inclusion-body myositis [a]	Aβ
Cutaneous lichen amyloidosis [a]	Keratins
Senile seminal vesicle amyloidosis	Fragments of semenogelin I

[a] Predominantly sporadic, in some cases hereditary forms associated with specific mutations are documented. [b] Five percent of cases are transmitted (e.g. iatrogenic). [c] Systemic deposits are documented. [d] Predominantly hereditary, although in some cases sporadic forms are documented.

B. Examples of intracellular, amyloid-like inclusions in human and their primary protein component

Inclusion name	Main component	Site	Example of associated disease
Lewy bodies	α-synuclein	Neurons (intracytoplasmic)	Parkinson's disease Alzheimer's disease with Lewy bodies
Huntington bodies	polyQ expanded huntingtin	Neurons (intranuclear)	Huntington's disease
Neurofibrillary tangles	Hyperphosphorylated protein tau	Neurons (intracytoplasmic)	Alzheimer's disease Frontotemporal dementia
Hirano bodies	Actin	Neurons	Neurodegenerative disorders

nation complex [16]. Sequestration of Sup35 into insoluble amyloid form results in decreased concentration and in generation of the dominantly inherited [*PSI*$^+$] phenotype, which confers suppression of nonsense mutations by increasing the read-through rate of nonsense stop codons. The protein-only inherited [*PSI*$^+$] element is structurally self-perpetuating in a manner similar to the mammalian PrP prions [17]. Like prions, several [*PSI*$^+$] 'strains' have been described with differing morphological and kinetic characteristics [18]. Amyloid-like fibrils have also been isolated from bacterial biofilms [19, 20]. The fibril structure assist in adherence to surfaces and is biochemically resistant to degradation making it an excellent biofilm component. Protective, functional amyloid has also recently been described in phyla ranging from fungi to mammals [21-23]. The formation of melanin, the polymer that confers protection against small toxins, pathogens and UV-radiation in skin and eyes, is dependent on the generation of insoluble fibres consisting of the Pmel17 subunit that have strikingly similar properties to disease-related amyloid. Consequently, amyloid plays protective or functional roles in bacteria, fungi and higher eukaryotes.

1.1.3 Familial and sporadic, localised and systemic amyloidoses

Some amyloidoses occur sporadically while others are exclusively hereditary (e.g. British and Danish Familial dementias), transmissible (spongiform encephalopathies) or a result of external factors (e.g. haemodialysis-associated amyloidosis) [24]. Several amyloidoses, including Alzheimer's disease (AD) and Parkinson's disease (PD), arise sporadically as the body ages or as early-onset disease as a result of an inherited mutation. For AD, numerous variants have been identified of the AβPP-encoding *APP* gene and the presenilin genes (*PSEN1* and *PSEN2*) that are related to early-onset or particularly aggressive variants of the disease [25]. In contrast, possession of the ε4 allele of the gene encoding apolipoprotein E is associated with increased susceptibility to late-onset, sporadic AD.

For systemic amyloidoses, protein deposits can be found in several tissues e.g. heart, liver and kidneys in reactive serum AA amyloidosis and/or skeletal tissue and joints in haemodialysis-related amyloidosis [26]. In extreme situations, the deposited mass can reach several kilograms, which in itself can cause organ damage by physical disruption and compression of vasculature. Deposition of smaller amounts can also cause organ dysfunction, e.g. renal failure resulting from deposition of lysozyme, apolipoproteins AI and AII or fragments of fibrinogen Aα-chain in renal vasculature or glomeruli [26-28]. For the localised amyloidoses, the mass of deposited material can be very low and clinical symptoms are associated with cell death co-localised with protein deposits [29]. The predominant hypothesis holds that cell death is cause by the presence of toxic protein oligomers *via* a number of subtle mechanisms (covered in more detail in section 1.4). Deposits are restricted to one organ, but the localised amyloidoses have highly varied organ- and cellular specificities, e.g. islets of Langerhans in the pancreas in type II diabetes mellitus [30]. However, toxicity due to protein deposits rather than obstruction may also play a role in systemic disease [31].

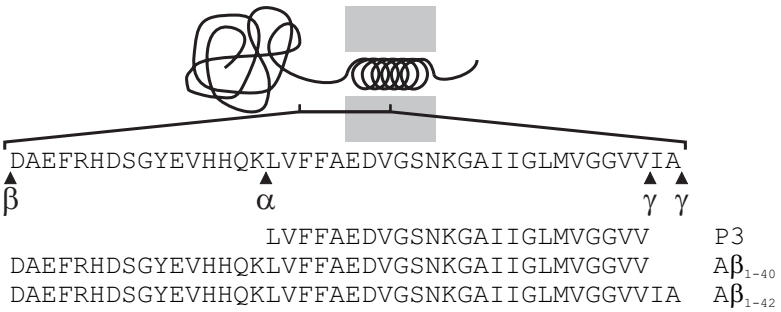

Figure 1. Proteolytic processing of AβPP by α-, β- and γ-secretase and the sequences of the resulting peptides. Adapted from [36]

1.1.4 Aspects of Alzheimer's disease

Alzheimer's disease (AD) is the most common neurodegenerative amyloidosis and arguably the most studied. It is characterised clinically by progressive dementia, loss of cognitive function and ultimately death. Histopathological examination shows neuronal loss and plaques composed of Aβ distributed throughout the central nervous system (CNS) but with particular intensity in the cerebral cortex [32-34] in addition to neurofibrillar tangles (NFTs) composed of paired helical filaments of hyperphophorylated microtubule-associated protein tau [35]. The Aβ peptide is proteolytic fragment of the Aβ precursor protein (AβPP), which contains a single transmembrane helix (figure 1). A small fraction of AβPP is processed sequentially by the membrane-bound β- and γ-secretases to yield Aβ [36-38] while the larger fraction is processed by α- and γ-secretases to give non-pathogenic P_3 peptide. Cleavage by γ-secretase results in fragments of variable length from 39 to 43 residues with $Aβ_{1-40}$ and $Aβ_{1-42}$ as the predominant species. These cleavage sites are positioned midway along the transmembrane helix leaving the soluble Aβ peptide with an exposed hydrophobic C-terminal region. Biophysical characterisation of $Aβ_{1-40}$ and $Aβ_{1-42}$ has shown that the longer peptides is the more amyloidogenic [39] and correlations have been observed between occurrence of disease and elevation of total serum Aβ and $Aβ_{1-42}$ [40, 41].

The classical amyloid plaque consists of a dense, fibrillar core surrounded by dystrophic neurites of axonal and dendritic origin, reactive microglia and fibrillar astrocytes [42] but Aβ immunostaining has revealed that diffuse CR-negative deposits is widespread in the cortex and cerebellum [43, 44]. These non-fibrillar or preamyloid plaques are rarely associated with cellular abnormalities of the surrounding tissue. Similar non-fibrillar deposits, termed cotton wool plaques from their distinct appearance, are observed in certain variants of AD with spastic paraparesis [45, 46]. These lack the dense core but have sharply defined boundaries and are primarily composed of $Aβ_{1-42}$. In addition to the presence of parenchymal plaques, AD is often accompanied by development of cerebral amyloid angiopathy (CAA) [47, 48]. Amyloid accumulates in the walls of cerebral and leptomeningeal arteries, arterioles and smaller vessels, resulting in severe cases in loss of smooth muscle cells and degenerative changes progressively weakening the vessel wall dramatically increasing the risk of haemorrhagic stroke. Perivascular amyloid deposits can often be observed surrounding affected vessels. Several hereditary forms of CAA exist associated with deposition of Aβ and AD-unrelated proteins or peptides of which several are associated with other

Table 3. Selected sporadic and hereditary cerebral amyloid angiopathies. Adapted from [48, 49].

	Gene	Chromosome	Precursor	Amyloid protein
Sporadic cerebral amyloid angiopathy (SCAA)				
SCAA in AD	AβPP	21	AβPP	Aβ
Hereditary cerebral angiopathies				
HCHWA-D	AβPP (E22Q)	21	AβPP	Aβ
FAD	AβPP, PS1, PS2	21, 14, 1	AβPP	Aβ
Flemish	AβPP (A21G)			
Italian 1	AβPP (E22K)			
Arctic	AβPP (E22G)			
Iowa	AβPP (D23N)			
Italian 2	AβPP (A42T)			
Austrian	AβPP (T43I)			
Iranian	AβPP (T43A)			
French	AβPP (V44M)			
Florida	AβPP (I45V)			
London	AβPP (V46I/F/G/L)			
HCHWA-I	CYST C	20	Cystatin C	ACys
FAP/MVA	TTR	18	Transthyretin	TTR
FAF	GEL	99	Gelsolin	AGel
PrP-CAA	PRNP	20	Prion protein	APrP
FBD	ITM2B	13	ABriPP	ABri
FDD	ITM2B	13	ADanPP	ADan

HCHWA-D: Hereditary cerebral haemorrhage with amyloidosis - Dutch type; FAD: Familial Alzheimer's disease; HCHWA-I: Hereditary cerebral haemorrhage with amyloidosis - Icelandic type; FAP/MVA: Familial amyloid polyneuropathy/meningo-vascular amyloidosis; FAF: Familial amyloidoses Finnish type; Prp-CAA: Prion disease with cerebral amyloid angiopathy.

neurodegenerative amyloidoses (table 3). However, CAA in the absence of AD or other amyloidoses appears to be an aspect of normal ageing [48, 49]. The incidence of sporadic CAA increases sharply after the age of 60 and may account for as many as 15% of cerebral haemorrhagic incidents in the elderly.

1.2 Amyloid and amyloid-like properties and structure

The next question that arises is what are the structural and mechanistic characteristics that define the fibril component of amyloid. For laboratory purposes and particularly for *in vitro* work, the following three detectable characteristics provide a useful definition of amyloid-like fibrils [7, 50]: *i*) Affinity for amyloid-specific stains such as CR and the thioflavin dyes ThS and ThT, *ii*) β-rich structure with organisation giving rise to a characteristic cross-β pattern observable by X-ray fibre diffraction and *iii*) ultrastructure composed of long fibres with variable periodicities, branching and curvature, as observed by electron microscopy (EM) or atomic force microscopy (AFM). Additionally, fibril-formation often proceeds *via* a characteristic nucleation-dependent mechanism which may be attenuated by addition of seeds of preformed fibrils [51] (covered in more detail in section 1.3).

1.2.1 Staining with amyloid-specific dyes

Binding of amyloid-specific dyes has long been central to identification of amyloid in post-mortem samples and thereby to the understanding of development and pathology of amyloidoses. Congo red (CR) is a sulfonated azo dye (figure 2.A) consisting of two negatively charged amine- and sulphonate-substituted naph-

thalene groups separated by a biphenyl group and binds to amyloid-like fibrils with a visual change in colour from red-orange to pale red [9]. The amyloid-characteristic apple-green birefringence is thought to arise from linear orientation of CR molecules along the fibril, but the exact nature of the binding is not well understood [53-56]. Nonetheless, the resulting spectral shift and increased absorbance intensity may be used for quantitative analysis of *in vitro* fibrillation in the visual range, although the light-scattering from insoluble fibrils and saturable binding demands that care must be taken in determining the appropriate concentrations and in data interpretation [57]. The binding specificity of CR is relatively high but whereas the characteristic birefringence appears to be specific for the continuous β-sheet structure of amyloid, CR also binds all-α, α+β, all-β and β-helical proteins [58, 59] as well as extended β-sheets of the short-chain polyamines polyglycine and poly-L-serine albeit with low affinity [60]. An alternative to CR for tissue staining is thioflavin S (ThS), which is a blend of several compounds with diverse properties [9].

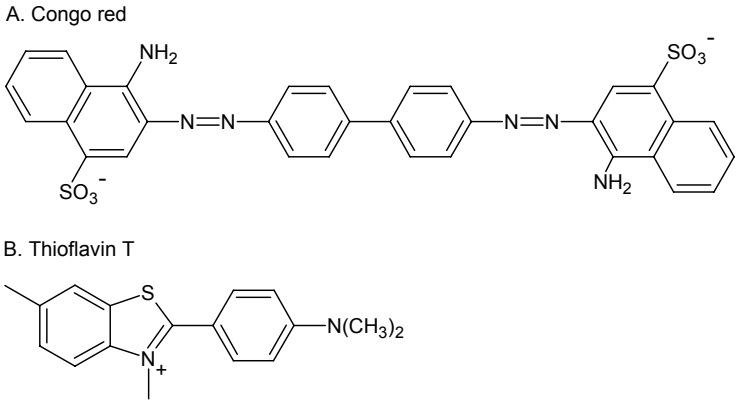

Figure 2. Structure of the amyloid-binding dyes Congo red (A) and thioflavin T (B). Adapted from [9] and [52], respectively.

Thioflavin T (ThT) is a good choice for studies of fibril formation *in vitro*. It is a fluorescent benzoethiazole dye that bind amyloid with higher sensitivity than CR but somewhat greater nonspecificity [9]. ThT binds poorly to natively folded proteins and non-fibrillar structures formed along the fibrillation pathway [52, 61] although non-amyloid conformations with ThT-affinity have been described [62, 63]. The ThT molecule has a well-defined structure (figure 2.B) and contains a single positive charge. Binding of ThT to fibrils elicits a dramatic red-shift in excitation maximum from ~350nm to ~450nm while the emission maximum is moderately shifted from ~440nm to ~480nm resulting in minimal background fluorescence allowing quantitative analysis [64, 65]. ThT is particularly useful for continuous detection of fibrils in solution, e.g. in assay application, because it does not interfere appreciably with the formation of fibril structure [66]. However, the affinity of the charged ThT molecule towards fibrils varies greatly depending on pH. Differential binding is also observed depending on the properties of the fibrillating polypeptide making direct quantitative comparison between fibril species challenging [52, 67]. Several fibril species that bind ThT poorly or do not bind the dye in detectable amounts have been identified including fibrillar structures of poly-L-serine or poly-L-lysine, fibrils formed of β_2m [61] or truncated amylin peptide [68] and ThT-negative, CR-positive fibrils of

$A\beta_{1-40}$ [69]. Several models have been suggested for the binding of ThT to amyloid fibrils, including association of ThT micelles [70]. However, recent studies suggest that ThT binds with its long axis parallel to the fibril within cavities [71, 72], e.g. between protofilaments (see section 1.2.3), and it has been suggested that CR binds in a similar manner [53]. Lockhart and co-workers [73, 74] identified three ThT binding site on Aβ fibrils including a high-affinity site with low binding stoichiometry (1 mole per 300 mole Aβ in fibril from). Groenning *et al.* [72] demonstrated two binding sites for insulin fibrils although the high-affinity site has somewhat higher capacity (1 mole ThT per mole fibrillar insulin). Interestingly, ThT bound to the high-affinity site was found to be responsible for the increase in ThT fluorescence upon binding.

1.2.2. Morphology of amyloid-like fibrils

The morphology of biological amyloid and amyloid-like fibrils formed *in vitro* has been examined comprehensively by AFM, EM and scanning transmission electron microscopy (STEM). The later method allows measurement of the mass-per-length (MPL) of fibrils [75]. Despite the seeming overall similarity in fibril structure, significant morphological differences exist between fibrils composed of different polypeptides as well as for fibrils of identical polypeptides formed under different experimental conditions [76-78]. An ensemble of morphologies within the same sample is also a common find. Fibrils may be found in bundles or alone, be straight, curled or branched and appear smooth, twisted or as ribbons. However, the overall morphology is of highly structured, long, thin fibres with well-defined dimensions ranging from 6 to 13nm in width [7, 79] and with varying lengths in the micron range. The mature fibril found in aged samples is often composed of thinner (2-5nm-wide), laterally associated protofilaments giving rise to a wide range of possible morphologies (table 4). As such, mature fibrils can be described based on their dimensions, number of protofilaments and MPL.

Table 4. Examples of fibril and protofilament dimensions. N.A.: Not available. Adapted from [80]. [a] from [68]. [b] from [81].

Amyloid protein	Mass(kDa)	Number of protofilaments	Cross-section dimensions (Å) Protofilaments	Fibril
TTR (V30M)	15	4	50	120
Immunoglobulin light chain λVI	13	4-6	~30	90
ApoAI (L60R)	~9	5/6	~32	100
AA	8.4	5	~30	100
Lysozyme (D67H)	15	5	~30	95
TTR_{10-19}	~1	6	~28	90
IAPP [a]	4	2-many	~50	80-higher
Insulin [b]	N.A.	2/4/6	~35	50-100

Fibril polymorphism and the variability of fibrils structure among closely related polypeptides sequences were illustrated by Goldsbury *et al*. [68, 82], who studied the fibril ensemble of the amyloidogenic hormone IAPP *in vitro* by EM and STEM. A common 5nm-wide protofilament (termed protofibril by the authors) was found with 2.5-3.0 IAPP monomers per nm measured along the filament axis by STEM. These protofilaments were rarely found in isolation but rather as constituents of twisted rope-like fibrils or arranged sidewise in flat ribbons (figure 3.A, C-F). A shorter fragment ($IAPP_{20-29}$) covering the amyloidogenic core did

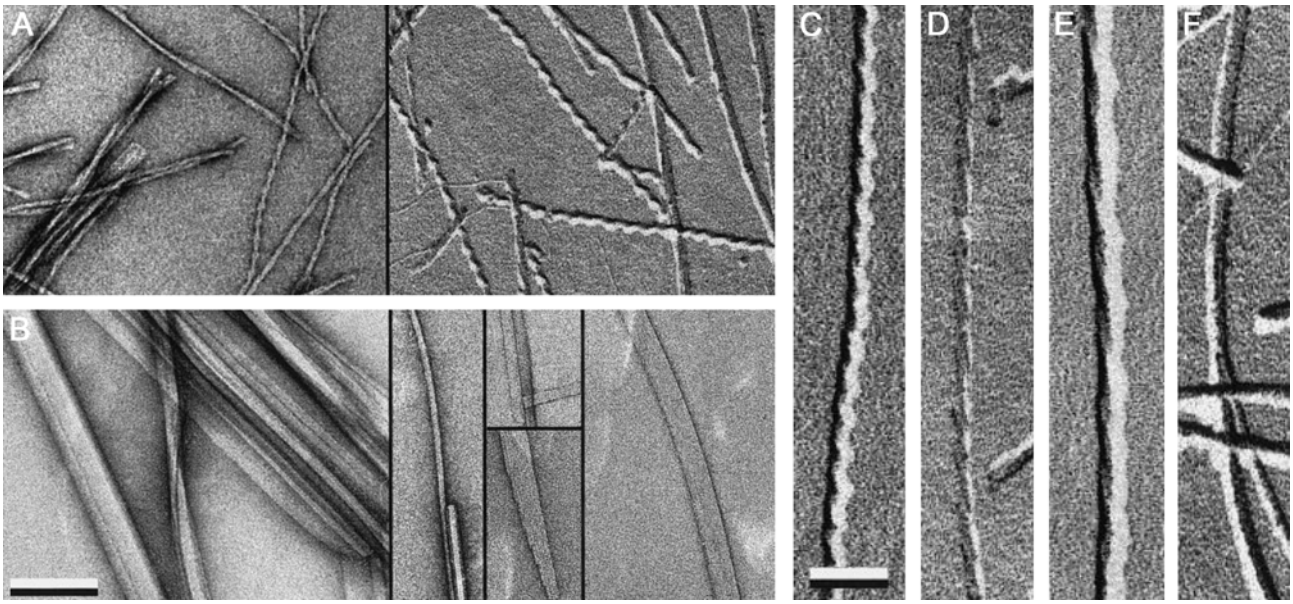

Figure 3. Diversity of fibril morphology (polymorphism) for IAPP (A,C-F) and $IAPP_{20-29}$ (B). Adapted from [68]

not form twisted fibrils but only flat ribbons of 3.6nm-wide filaments (figure 3.B) signifying the influence of the non-core regions in determining fibril morphology. Twisting of protofilaments and fibrils is predominantly left-handed propagating from the tendency towards inter-stand twisting within β-sheets determined by amino acid chirality and steric constraints [50]. Correspondingly, fibrils formed from the *D*-form have right-handed twists [83, 84]. The diverse appearance of IAPP fibrils reflects the frequent observation of a wide range of fibril morphologies [80, 85-88], which include tubular structures with electron-translucent centres and straight or twisted fibres with occasional branching and frayed ends exposing individual protofilaments.

Growth micro- and macro-conditions can have a strong impact on morphology and condition-dependent polymorphism is a frequent observation such as pH and agitation for $A\beta_{1-40}$ and fragments thereof [89, 90] solution polarity for insulin [91] or peptide concentration, fibrillation temperature, ionic strength and presence of ions that may acts as ligands for the pancreatic hormone glucagon [67, 92]. Finally, growth under conditions of high pressure has been shown to lead to formation of highly curved or circular fibrils for insulin [93] underscoring the

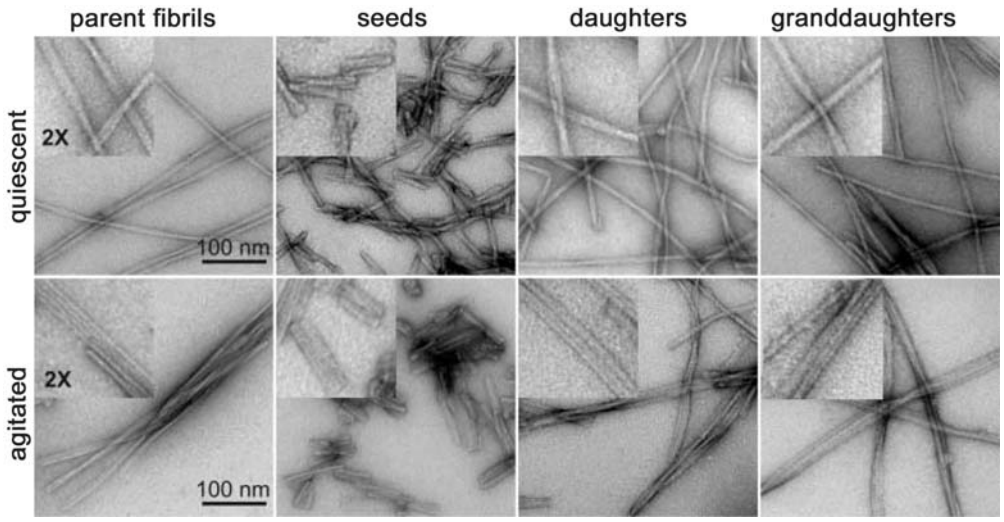

Figure 4. 'Strain' behaviour of Aβ fibrils. The use or absence of agitation during growth give rise to two fibril types. The properties of the seed determines the properties of seeded fibrils [90].

morphological diversity of amyloid-like fibrils. Several of these studies also illustrate the principle of fibril 'strain' (figure 4), which parallels the strain-behaviour of prions. Solutions seeded with fragments of previously formed fibrils showed preservation of morphology in populations of daughter- and granddaughter-fibrils. However, the widespread condition-dependent polymorphism and strain behaviour has raised questions about the generic nature of the fibril structure, which will be discussed further below.

1.2.3 The cross-β fibril structure

The wide range of fibril morphologies raises the question of the basic structure of the protofilament and whether structural polymorphism originate in differences of protofilament packing or illustrates more fundamental differences in structure. Early structural studies of amyloid-like fibrils by X-ray fibre diffraction showed the characteristic diffraction pattern [94, 95] ascribed to the cross-β organisation of the extended pleated sheets first described by Pauling (figure 5.A-B) [96]. The individual β-strands are perpendicular to the fibril axis while the β-sheet is parallel to the fibril direction (figure 5.C) resulting in a diffraction pattern consisting of 4.7-4.8Å meridional and more diffuse 10-11Å equatorial reflections [97]. The former originates from the distance between the extended β-strands within the β-sheet while the latter is attributed to the distance between two or more laminated β-sheet although this distance depends on the type of side chains [98]. X-ray fibre diffraction does not distinguish well between parallel and anti-parallel orientation nor does it provide information about the register of the individual β-strands, the direction of twisting of the β-sheets or about regions of the polypeptide chain outside the regular structure such as loops or turns. However, Blake and Serpell [99, 100] used the observation of a repeating unit of 24 β-strands to construct a basic protofilament structure consisting of four laminated, continuous β-sheets for *ex vivo* fibrils of transthyretin (TTR) variant V30M (figure 6.A). The mature fibril consists of 4 such protofilaments. The full rotation of the laminated β-sheets around a central axis result in an inter-strand twist of 15º similar to the energy-minimising twist observed for β-sheets in globular proteins [102]. An analogous model, constructed from electron-density maps obtained from cryo-electron microscopy of fibrils of the SH3 domain of phosphatidylinositol-3'-kinase [101], shows a double-helix of two pairs of protofilaments, each consisting of two laminated β-sheets. Similarly, an ensemble of polymorph fibrils of insulin

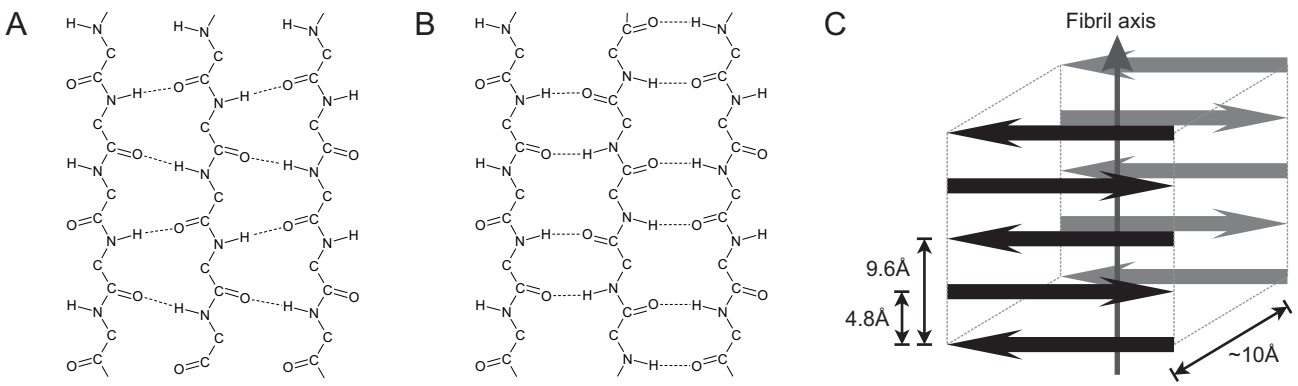

Figure 5. Parallel (A) and anti-parallel (B) pleated sheets [96]. The cross-β structure consist of laminated pleated sheets (shown as anti-parallel) running along the fibril direction with strands oriented perpendicular to the fibril axis. Adapted from [97].

[81] was found to consist of 2, 4, 6 or more protofilaments (figure 6.B-C) that appeared identical under the available resolution.

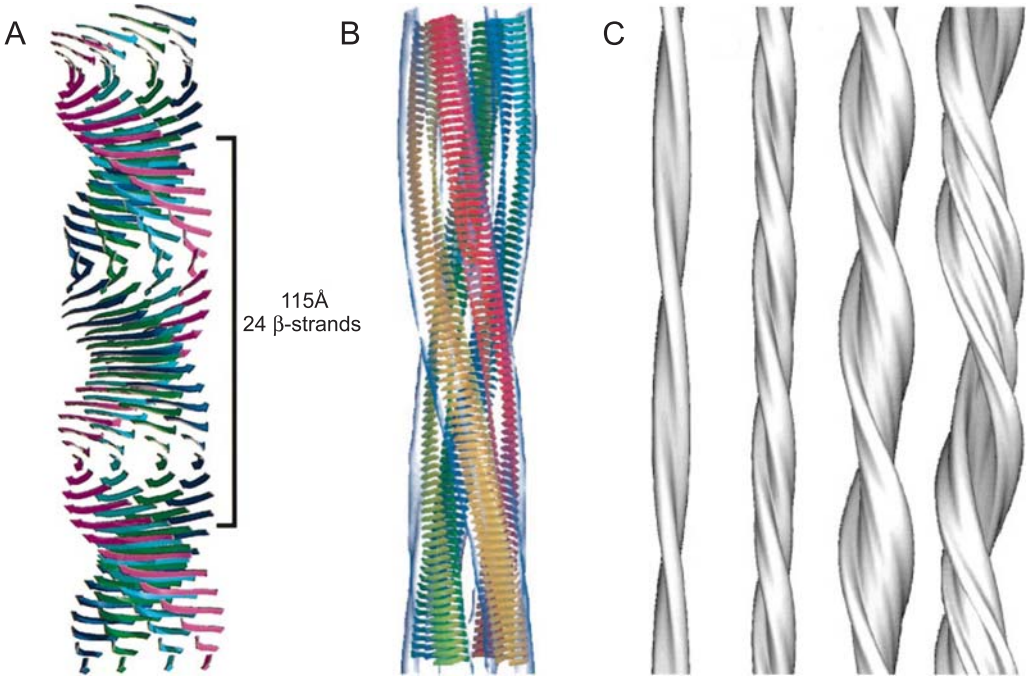

Figure 6. Model of TTR_{V30M} (A) and insulin (B-C) fibril structures. Adapted from [100] and [81], respectively.

1.2.4 Sub-protofilament structure

The advances in high-resolution methods, particularly within the field of nuclear magnetic resonance spectroscopy (NMR), has allowed the collection of more detailed information about the sub-protofilament structure of both short peptides and full-length amyloidogenic polypeptides. Using Aβ as an example, if was found by combination of several methods that the longer peptides $Aβ_{10-35}$, $Aβ_{1-42}$ and $Aβ_{1-42}$ form parallel, in-register β-sheets [103-109] while the shorter $Aβ_{11-25}$ and $Aβ_{16-22}$ form β-sheets in anti-parallel conformation [110, 111]. Interestingly, the latter peptide was found to switch to parallel conformation upon octanoylation of the N-terminus [112]. This can be rationalised in terms of hydrophobic and electrostatic interactions. The longer peptides have asymmetrical hydrophobic segments (residues 17-21 and 29-40) and the parallel, in-register conformation allows for full overlap between these. For the shorter peptides, the segment at residues 17-21 occupies a central, symmetrical position that allows for anti-parallel conformation and interaction between the opposing terminal charges. Octanoylation abolishes the electrostatic interaction and adds an additional hydrophobic region switching $Aβ_{16-22}$ to parallel organisation.

It has been suggested that the structural polymorphism observed for identical peptides at differing growth conditions stems from protofilament surface characteristics [77], e.g. side chains not directly involved in formation of the cross-β core. The parallel-to-anti-parallel conformational switching suggests that polymorphism may correspond to structural difference at the sub-filament level. This is further supported by the observation of significant differences in protofilament-substructure observed by solid state NMR for the previously mentioned polymorphic $Aβ_{1-40}$ fibrils grown with or without agitation [90] (figure 4). Quiescent

Fibril type	Conditions	Characteristics
A	>1g/L glucagon (pH 2.5)	Thin flexible fibrils, sometimes as twisted bundles; high ThT staining.
B	<0.5mg/mL (pH 2.5); agitation	Untwisted parallel bundles of two or more filaments; low ThT staining; CD-spectrum fingerprint at 206nm and characteristic IR peak at ~1635cm^{-1}.
$B_{quiescent}$	<0.5g/L (pH 2.5); no agitation	Twisted thick fibrils; low ThT staining.
C	<0.5g/L (pH 2.5); agitation; elevated temperature (50ºC)	Low ThT staining; large untwisted parallel bundles of several filaments; similar molecular structure as type B.
D	<0.5g/L (pH 2.5); 100-200µM NaCl; agitation	High-pitch twisting; low ThT staining.
S (sulphate type)	~0.5g/L glucagon (pH 2-2.5); 1mM SO_4^{2-}; agitation not required	Regular twisted fibrils; high ThT staining; irregular, α-helix-like CD spectrum.

Table 5. Summary of glucagon fibril types. Adapted from [114].

samples were found to contain two conformations ratio 2:1, and measurements of MPL by STEM further suggested that agitated and quiescent protofilaments contained two and three laminated sheets, respectively. However, monoclonal antibodies specific for fibrils but not precursors or soluble monomers suggest the existence of a common fibril-specific structural epitope [113].

A more extensive description of the dependence of sub-filament structural polymorphism on fibrillation conditions comes from studies of the 29 amino acid glucagon peptide [67, 92, 114]. Numerous fibril 'types' (table 5) have been described exclusively or in mixed populations depending on peptide concentration, agitation, pH, temperature, ionic strength and presence of specific anions during fibrillogenesis. The mature fibril types vary not only in morphology (figure 7.A-D) but also in their stability by thermal or chemical dissociation and their secondary structure. Fourier transform infrared spectroscopy (FTIR) of dried fibril samples show some diversity but all display a major β-sheet component in the 1620-1640cm^{-1} range (figure 7.E). In contrast, circular dichroism (CD) yields very diverse spectra including typical β-structure as well as spectra with α-helical or β-turn characteristics (figure 7.F). Using types B and D as examples, growth in the presence of 250mM NaCl changes the CD spectrum from β-turn-like to a more typical β-sheet-like spectrum without considerably altering the appearance

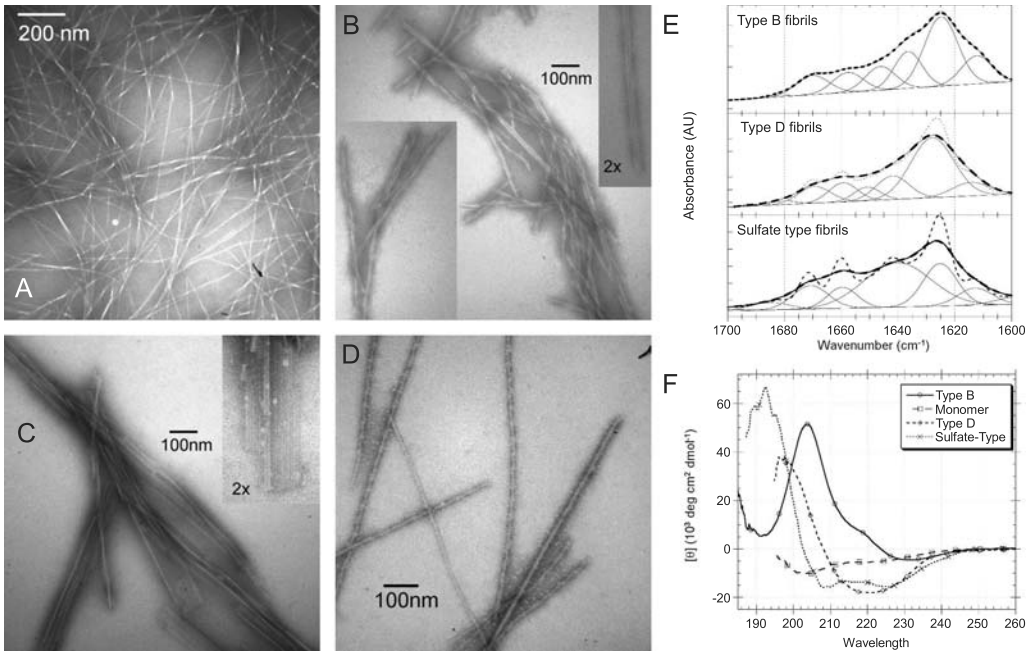

Figure 7. Morphology of glucagon fibril types A-D (A-D) [67]. FTIR (E) and CD (F) spectra of selected types [114].

in FTIR. Similarly, the addition of as little as 1mM sulphate ions favours a fibril type which contains noticeable amounts of α-helical structure (type S), which is also observed for freshly dissolved peptide in the presence of higher concentrations of sulphate ions [92] suggestive of a stabilising role of sulphate towards helical conformation. It thus appears that fibril polymorphism encompasses every level from secondary structure, which must be probed by spectroscopic methods, to quaternary structure, commonly observable as differences in gross morphology. For a given polypeptide, the structural preferences within this polymorphic field of possible conformations are determined by physical (e.g. temperature) and solution (e.g. ionic strength) conditions and these traits are generally conferred to daughter fibrils upon seeding under dissimilar conditions as those used for parent fibrillation. This speaks against a single generic fibril structure representing a global energy minimum and the tendency towards a given fibril type or strain is likely driven by kinetic factors and directed by constraints from solution conditions and imprinting from seed 'templates'.

1.2.5 Models of fibril structure

The extensive work on the structural properties of the Aβ peptides have led to a parallel, in-register structural model of full-length $A\beta_{1\text{-}40}$ [115] (figure 8.A). The two β-strands are folded so the peptide contributes one β-strand to each of the two continuous β-sheets that make up the protofilament. This model is in general agreement with subsequent data obtained from e.g. solution NMR [117], mass spectrometry [118], cryo-EM [119, 120] and mutagenesis studies [121, 122] although a recent structure of $A\beta_{1\text{-}42}$ [116] obtained from solution NMR combined with structural constraints from previous studies suggests a staggered arrangement with the laminated sheet leading to partially unpaired β-strands (figure 8.B).

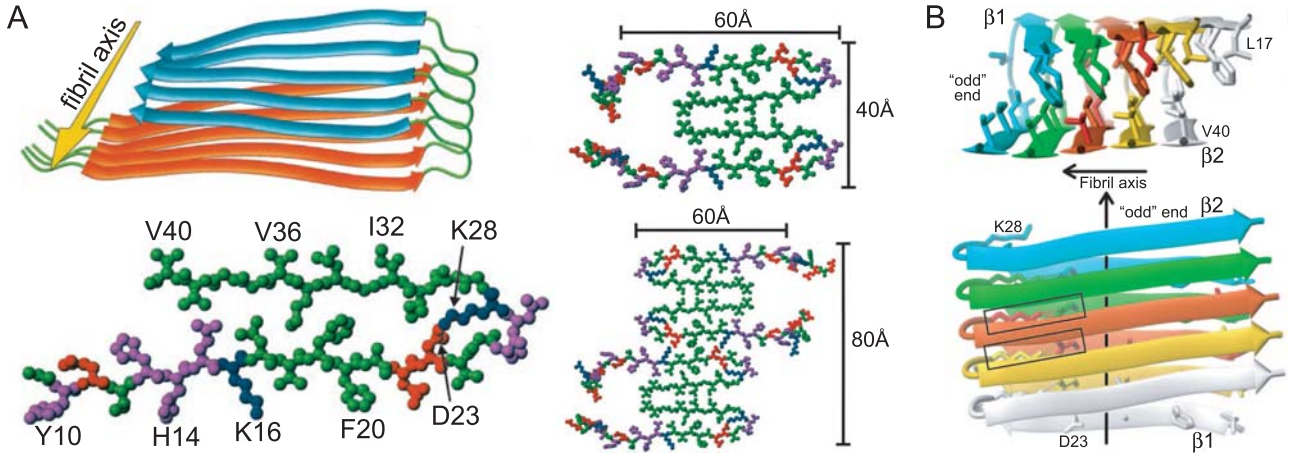

Figure 8. Structural model of $A\beta_{1\text{-}40}$ (A) consisting of two laminated sheets from the same peptide. An alternative model (B) describes a staggered arrangement. Adapted from [115] and [116], respectively.

A similar interpretation of the cross-β organisation comes the ability of certain short, amyloidogenic peptides to form crystalline, fibril-like structures [123, 124]. Two peptides from the N-terminal prion domain of the fungal prion Sup35, GNNQQNY and NNQQNY, were found to form microcrystals that allowed X-ray diffraction to 1.8Å and 1.3Å resolution, respectively, revealing continuous, flat β-sheets with β-strands in parallel, in-register conformation [125]. The inner core of the laminated β-sheets, or 'dry face', is tightly packed with closely nes-

tled, complementary side chains giving the appearance along the protofilament axis of an interlocked 'steric zipper'. The tight packing excludes water from the core, which is compatible with the structural insensitivity of some fibrils towards hydration [126]. The polar Asn and Gln side chains do not form hydrogen bonds between β-sheets but rather 'polar zippers' along the fibril axis [127]. In the absence of hydrogen bond stabilisation, the two β-sheets are held together by van der Waals interactions between the closely packed side chains. Similar structures have been described for a further eight short peptides from amyloidogenic proteins or peptides [128] classified based on β-strand orientation within the β-sheet and with respect to the opposite β-sheet and which β-sheet sides, or faces, are in contact (figure 9). Interestingly, several of the peptides have two conformations suggesting variability in side chain packing and the less specific van der Waals interactions could be a basis for fibril polymorphism.

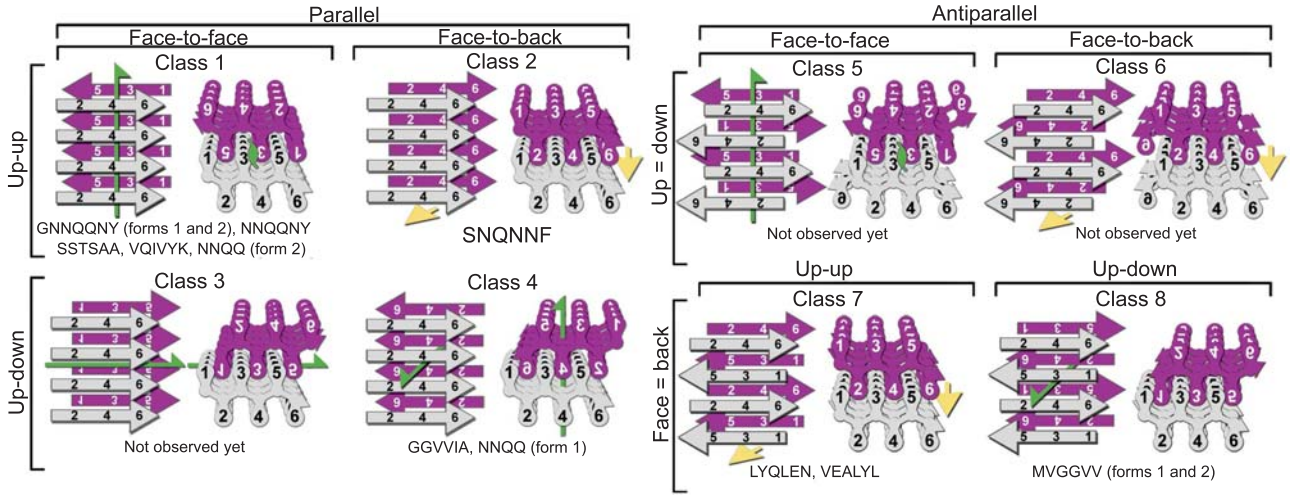

Figure 9. Classes of steric zippers. Adapted from [128].

Several alternative model for fibril structure suggest that cross-β organisation may not be relevant for all fibrils. The late Max Perutz [129] observed that the 10Å equatorial reflection is missing in X-ray fibre diffraction patterns for fibrils of polyglutamine repeats and proposed that amyloid-like fibrils may be water-filled nanotubes composed of ~30nm-wide, cylindrical β-helices with 20 residues per turn. Similar β-helical structures with circular or triangular cross-sections have been suggested for other fibril types [130-134]. A second group of alternative structural models is based on preservation of some native structure [135]: *i*) 'Gain-of-interaction' models in which dislocation of a native β-sheet allows intermolecular contact between edge strands and direct stacking of monomers preserving residual native structure (e.g. TTR) [136-138], *ii*) cross-β spine models in which a central fibril is formed by N- or C-terminal amyloidogenic regions (e.g. yeast prion Ure2p) or by 'gain-of-interaction' association of edge strands conserving extra-fibrillar domains of native structure (e.g. β2m) [139, 140] and *iii*) domain-swapping in which the native structure opens and complementary domains associate across molecules (e.g. cystatin C) [141, 142].

In summary, despite overall similarities amyloid-like fibrils show a striking degree of polymorphism in their gross morphology and in their underlying struc-

ture. The self-assembly *via* hydrogen bonded β-strands into continuous β-sheets or β-helices may the underlying motif of formation of amyloid-like fibrils. This might be a reflection of the inherent ability of the polypeptide backbone to conform to the extended β-strand conformation.

1.3 The mechanism of protein folding and misfolding

1.3.1 The inherent ability of proteins to form fibrils

Many proteins and peptides have been identified in biological amyloid, but two observations paved the way to a more fundamental understanding of fibril assembly: *i*) synthetic disease-related peptides are capable of forming amyloid-like fibrils *in vitro* with comparable tinctorial, morphological and structural properties to their *in vivo* counterparts [143, 144] and *ii*) globular proteins unrelated to disease may by induced to form similar fibrils as in the case of SH3, the ninth type III domain of fibronectin (rm-III9) and acylphosphatase (ACP) [145-147]. The observation of fibrillogenic potential for natively folded proteins led to the proposal that any protein sequence may be capable of forming amyloid-like fibrils under appropriate conditions and that the capacity to conform to the continuous β-sheet structure may be an intrinsic ability of the polypeptide backbone [148]. This is supported by the ever-growing list of proteins and peptides fibrillating *in vitro* or *in vivo*, which includes all-β (SH3, rm-III9, β2m), all-α (apomyoglobin, cytochrome c_{552}), mixed structures (ACP, hen egg white lysozyme, stefin B), fragments of transmembrane helices (Aβ, truncated glycophorin A) and polyamino acids [98, 149-153]. Consequently, the fibril conformation seems to occupy a permanent place in the energy landscape of folding [154]. While the native structure encoded within the protein sequence [155] may represent a local free energy minimum relevant for the isolated polypeptide chain, it has been suggested that the native fold may be considered a metastable state whereas the amyloid-like fold represents the global free energy minimum [156].

Formation of intermolecular contacts opens up the alternative aggregation energy landscape (figure 10) and allows for a range of structures including the

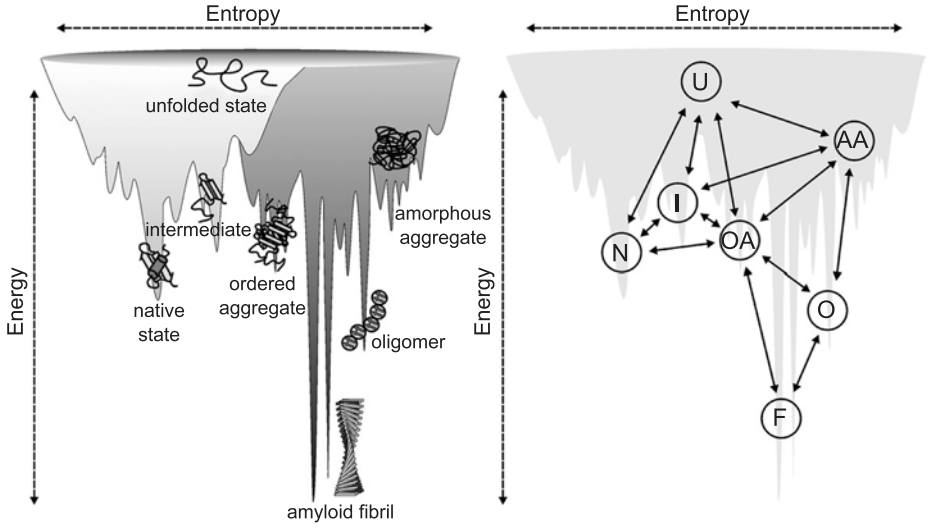

Figure 10. The energy landscape of folding and aggregation. The formation of intermolecular interactions allows access to alternative structures that may be more energitically favourable than the native structure. Adapted from [157].

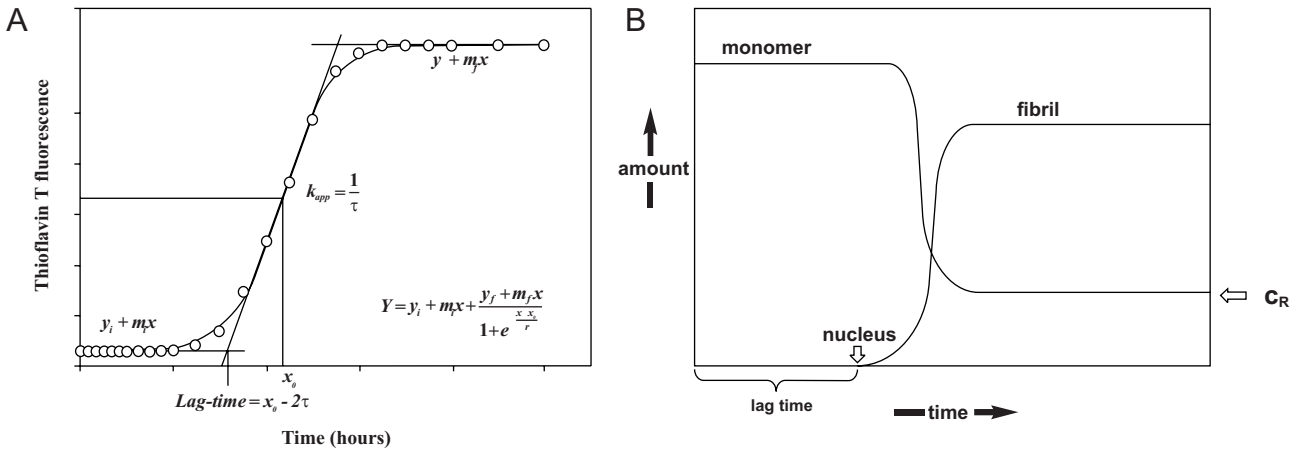

Figure 11. Fibril growth is often characterised by a lag phase followed by rapid growth (A) here shown for ThT-monitored insulin fibrillation [169]. (B) The end of the lag phase is often ascribed to the formation of the critical fibrillation nucleus [162] although this interpretation is inconsistent with the low concentration dependence and rapid onset of elongation observed for several fibril systems.

highly stable amyloid-like fibril [157]. However, a single common and preserved amyloid structural motif can hardly be expected in the light of the absence of evolutionary pressure in the development of fibril structure excluding those few proteins that constitute the functional amyloid group. The evolutionary pressure has rather been on prevention of aggregation-promoting non-native interactions during protein folding, which offers a partial explanation for the relative rarity of *in vivo* amyloidogenesis compared to the readiness with which many otherwise non-pathogenic proteins have been induced to fibrillate *in vitro*. In light of the frequent observation of fibril polymorphism, the nucleation and growth of amyloid-like fibrils appears to be a competitive process involving a collection of highly-ordered structures in a 'survival of the fittest'-like scenario [114]. From a mechanistic strand-point, the fibrillation process begins from the monomeric state, which may belong to an ensemble of unfolded or partially folded conformations [158, 159] or be native-like [135, 160]. The subsequent assembly may involve formation of oligomeric species, ordered or amorphous aggregates, all of which have been implicated on- or off-pathway in the fibrillation process [161].

1.3.2 Models for fibril growth

The classical model of fibrillation is a nucleation-dependent assembly mechanism, which ascribes the frequently observed lag phase before growth of mature fibrils can be detected[2] to a rate-limiting formation of a critical fibrillation nucleus (figure 11), defined as the most unstable and therefore least populate species along the pathway [162, 163]. The assembly proceeds *via* step-wise addition of monomer to the growing fibril [165]. However, the initial equilibria are thermodynamically unfavourable until the critical fibrillation nucleus (n*) is reached:

$$(1) \quad A + A_n \rightleftharpoons A_{n+1} \ldots A_{n^*} + A \rightleftharpoons A_{n^*+1}$$

The end of the observable lag phase corresponds to the end of the initial slow nucleation phase and formation of the rare critical nucleus (figure 12.A). This is followed by thermodynamically favoured end-wise elongation leading to observable fibril growth. The addition of available 'ends' in the form of seeds of preformed fibrils should abolish the lag phase. The nucleation-elongation model also implies a critical concentration (C_R) below which fibril formation does not

2 Detection can be by e.g. ThT or intrinsic fluorescence or time-lapse AFM.

occur and a strong concentration dependence of fibrillation kinetics. The addition of monomers to the growing fibril end may proceed rapidly but can involve a second rate-limiting step as observed for elongation of Sup35 fibrils [166] or separate binding and rearrangement steps as observed for $A\beta_{1\text{-}40}$ [167, 168].

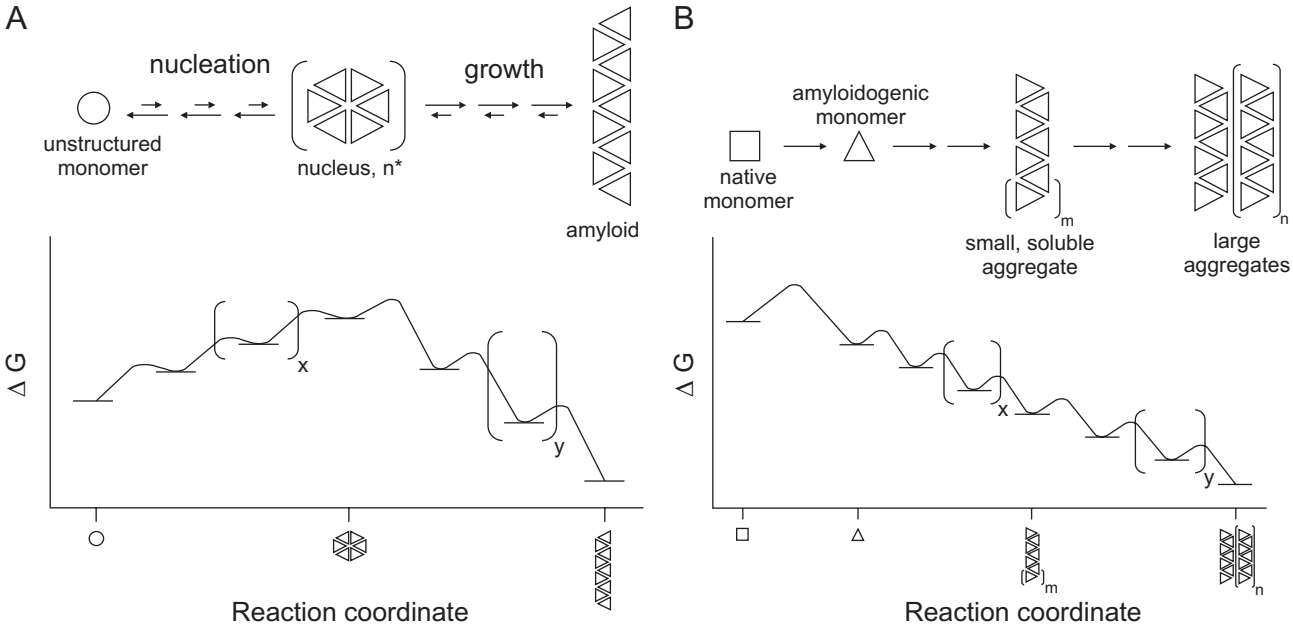

Figure 12. Proposed reaction schemes for the nucleation-dependent fibrillation of Aβ (A) and the downhill polymerisation of TTR (B), which is initiated by conversion of the native monomer to an aggregation-prone conformation. In the former case, the critical nucleus is the highest-energy species. In the latter case, the native monomer occupies this position. Adapted from [164].

Nucleation-dependent models have been used successfully for kinetic interpretation of experimental fibrillation or aggregation data [88, 169-171]. However, the duration of the lag phase can be independent of or only weakly dependent on monomer concentration and the elongation phase may show rapid onset, which is in disagreement with the parabolic early time-course predicted by the nucleation-dependent model [165, 166, 172]. Secondary processes for production of growing ends in the form of branching, nucleus-formation on the fibril surface or fibril fragmentation may result is such abrupt termination of the lag phase [161]. Fragmentation also explains promotion of growth by sonication or agitation [173, 174] and the importance of fibril 'brittleness' for fungal prion phenotypes [175]. Lateral surface recruitment and association of smaller spheroids has been observed for short, rod-like prefibrillar insulin oligomers [176]. The relative independence of concentration has been attributed to formation of off-pathway species lowering the effective monomer concentration [177-179]. Duration of the lag phase can also be affected by stabilisation of on-pathway monomeric or oligomeric species [180-184].

Alternatively, fibrillation may take place without formation of a critical nucleus similar to the process of amorphous aggregation [185]. The aggregation-prone monomer is the highest energy species (figure 12.B) and each essentially irreversible assembly step stabilises the larger species. Consequently, such downhill polymerisation is characterised by first-order dependence on monomer concentration and whereas addition of seeds may affect the distribution of oligomeric species, it has no effect on the time-course of the assembly as observed for TTR under partially denaturing conditions and Aβ covalently modified by aldehyde-

derivatives of cholesterol [164, 186, 187]. Similarly, formation of amorphous but seeding-competent aggregates of a tandem-repeat of SH3 at neutral pH has been shown to follow down-hill polymerisation kinetics [188].

1.3.3 Early oligomeric species, on- or off-pathway intermediates

The initial phases of fibrillation, before the appearance of mature fibrils, are often characterised by nucleation-independent conversion of a portion of the monomer pool into an ensemble of oligomeric species [189-191]. These early intermediates are generally classified based on appearance (EM and AFM) and approximate molecular mass (size-exclusion chromatography [SEC] and gel electrophoresis). A diverse range of structures have been observed including spheroids [69, 192, 193], curvilinear protofibrils [69, 194, 195], 'micelles' produced above a CMC-like threshold monomer concentration [177, 196, 197] and, for Aβ, Aβ-derived diffusible ligands (ADDLs) [198]. Pore-like structures have also been observed with striking similarities to pore-forming bacterial toxins suggesting a role in neurodegeneration [199-203].

The presence of oligomeric species and slow disappearance before mature fibrils can be observed has prompted speculation about their role as potential on-pathway intermediates. Because of their relative abundance they cannot by definition be the critical nucleus, but an on-pathway role is supported by structural studies detecting similar ordered elements for protofibrils as for fibrils [118, 204] and oligomeric intermediate species have been inferred or identified on-pathway in several studies [178, 205-207]. Spheroids have been observed to anneal to form linear or annular structures [200, 203, 208] and participation in fibril elongation by association of oligomers at fibril ends has been proposed for e.g. Sup35 and $A\beta_{1-40}$ [209, 210] although elongation by monomer addition is well-documented in many cases [166, 197]. However, fibrillation can occur under mildly denaturing conditions that prevent formation of oligomers [211] and Goldsbury *et al.* [208] observed that annealed $A\beta_{1-40}$ spheroids separated before disappearing from solution as mature fibrils appeared suggesting an off-pathway role. The latter study also demonstrated protofibrils may originate from spheroids, indicating internal conformational nucleation, and elongate by monomer addition albeit at a slower rate than mature fibril growth suggesting structural differences requiring conformational rearrangement to allow conversion to mature fibrils. The early curliform protofibrils may be on-pathway intermediates that laterally associated to form mature fibrils [212] but protofibrils may coexist with spheroids under conditions that disfavour formation of mature fibrils whereas fibrils are capable of growing under conditions that disfavour the formation of oligomeric species [191]. As such, early oligomeric species may be kinetically trapped on pathways competing with formation of mature fibrils [208, 213, 214] and whereas on-pathway oligomers can be observed for several systems, they are not generally obligate. This is supported by the observation that several small-molecule inhibitors selectively reduces oligomerisation of Aβ without affecting fibrillogenesis indicating that oligomerisation and fibrillation can occur by separate pathways [215].

1.3.4 Formation of aggregation-prone species

Significant work has gone into describing the earliest events in the fibrillation process, i.e. how the relevant polypeptide chain becomes prone to participating in aggregation and which factors influence the process. Fibrillation has been observed to occur for globular proteins, intrinsically unfolded proteins or unfolded proteolytic fragments and the specific formation of the fibrillation-prone monomer depends on the nature of the precursor polypeptide. Fibrillation of globular proteins generally requires conditions under which fibrillation-prone, partially folded conformations are populated [10, 158]. This can happen either *i*) by introduction of mutations that destabilise the native state or stabilise the partially folded conformation [216-218] or *ii*) *via* non-native environmental factors [145, 151, 219, 220] such as low or high pH, high temperature or addition of organic solvents to alter solvent polarity. The unmasking of fibrillation-prone regions allows for interaction with similar regions on other molecules and the formation of higher order species. An example is dislocation within a native β-sheet, through mutation or environment factors, leading to exposure of edge β-strands already in the required extended conformation and available for formation of an intermolecular β-sheet. The importance of such exposed edge β-strands is illustrated in the protective methods used by globular proteins such as strategically placed charges, incorporation of prolines and shortening of edge β-strands to prevent such association [221, 222].

Fibrillation also occurs from intrinsically unfolded conformations include full-length proteins (e.g. α-synuclein), short peptides with low structural propensity (e.g. IAPP and calcitonin) or proteolytic fragments of longer precursor protein (e.g. Aβ and medin [223]). In the latter example, the cleaved peptides will be incapable of folding into a globular shape offering protection of fibrillation-prone regions. However, mutagenesis studies have demonstrated that fibrillation from both unfolded [224] or partially folded [225] states occurs through interactions between a limited number of residues in a manner reminiscent of the native folding nucleus[3] although the residues forming the native and fibrillation nuclei differ. Additionally, intrinsically unfolded proteins or peptides are capable of adopting molten globule-like structures with significant secondary structure and the formation of such transient intermediates, occasionally with significant α-helical elements, have been observed for e.g. IAPP and $A\beta_{1\text{-}40}$ [226-228].

1.3.5 Factors influencing aggregation propensity

There is no single consensus motif for fibrillation but different sequences have markedly different fibrillation propensities and rates. The amyloid stretch theory [229] proposes that the fibril self-assembly occurs through interaction of short segments within the polypeptide chain and that the properties of these aggregation-prone regions or 'hot spots' that can be used for predictive purposes. Several intrinsic physiochemical factors have been described as playing a role in determining aggregation rates [230, 231], e.g. hydrophobicity, β-strand amphiphilicity, charge and β-sheet propensity.

3 Not to be confused with the critical fibrillation nucleus defined for the nucleation-elongation model.

The interaction between unmasked hydrophobic patches is an important driving force in the formation of amyloid-like fibrils as well as amorphous aggregates [232, 233]. However, short peptide fragments consisting of polar amino acids (e.g. GNNQQNY [124]) and long polyglutamine also readily form amyloid-like fibrils *in vitro*, possible stabilised by polar zippers as proposed by Perutz *et al.* [127] and observed for yeast prion Ure2p and several steric zipper structures [125, 128, 234]. Eisenberg and coworkers [235] used threading of sliding window hexapeptides of amyloidogenic proteins through the steric zipper structure obtained from microcystals of the NNQQNY peptide [125] to accurately predict not only potentially amyloidogenic Asn and Gln-rich segments but also known predominantly nonpolar amyloidogenic regions including the final GGVVIA hexapeptide of $A\beta_{1\text{-}42}$ in agreement with the increased fibrillation rate for the longer Aβ variant [39]. Brack and Orgel [236] and later Hecht and coworkers [237] studied the secondary structure preferences of patterns of alternating hydrophilic and hydrophobic residues and found partiality towards β-structure and formation of amyloid-like fibrils. Indeed, such patterns are underrepresented in Nature suggesting an evolutionary disadvantage. However, screening of globular and amyloidogenic proteins did not yield an overrepresentation of alternating patterns [222]. Rather, fibril-forming proteins showed an increased frequency of pure hydrophobic or hydrophilic segments.

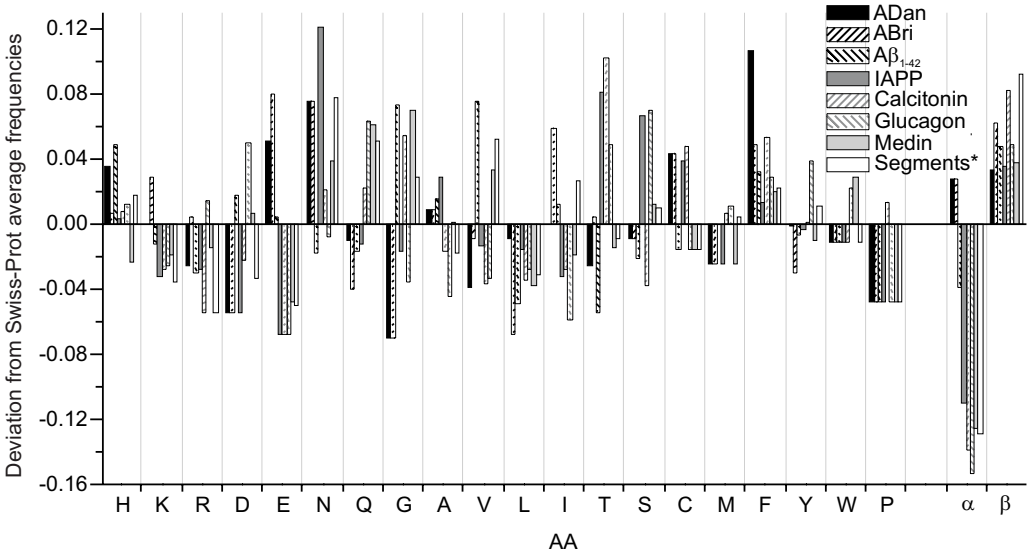

Figure 13. Deviation from the average Swiss-Prot amino acid composition (www.expasy.ch/sprot/relnotes/relstat.html) of small amyloidogenic peptides. *Small peptide segments examined by Eisenberg and co-workers [235].

The β-branched (VIL) and large aromatic (FYW) residues generally favour β-sheet structure [238-240] and these amino acids are overrepresented when examining the deviation of amino acid frequency compared to the average frequencies in the Swiss-Prot database for a selection of short, amyloidogenic peptides associated with disease and with the overall frequencies observed for short fibril-forming segments (figure 13). Similarly, the α-helix promoting amino acids (MALEK) are generally underrepresented. In the case of the α-helix promoting charged amino acids, the low frequencies may arise from the aforementioned net charge effect leading to overrepresentation of low charge among the amyloidogenic peptides. Proline is largely excluded, which is in agreement with its role as secondary structure 'breaker'. Correspondingly, scanning proline mutagenesis has

been used to elucidate the thermodynamic stability and structure of fibrils [131, 241]. The effect of proline in amyloidogenic sequences is illustrated in the lack of amyloid-formation for rat IAPP, which contains a proline-rich segment (NLGPVLPP) in region corresponding to the human amyloidogenic core (NFGAILSS) [242]. Conversely, glycine has diverse effects on fibrillation. Conserved glycine residues have been linked to prevention of ACP-fibrillation by alanine mutagenesis [243] while the G3A substitution in NFGAIL was shown to be without effect [244]. In contrast, the small glycine residue was found to be important in packing of bulky side chains for a fragment of transmembrane, α-helical glycophorin A [150] and glycine has a similar role in the packing of large aromatic side chains and in interstrand interaction for antiparallel β-strands [245, 246].

Aromatic residues appears to play an important role in fibril formation in agreement with the general overrepresentation of particularly phenylalanine in the summarised amyloidogenic sequences (figure 13). Indeed, alanine-substitution of phenylalanine in NFGAIL abolishes fibrillation [244] while tyrosine-substitution significantly inhibits it [247] indicating structure-specificity in the form of π-stacking of aromatic rings [248]. However, Raleigh and coworkers [249] demonstrated that phenylalanine is not required to form fibrils although a large effect upon alanine-substitution and a less dramatic effect of leucine-substitution were observed. The effects ascribed to effects on hydrophobicity and β-structure propensity. Similar observations were made for ACP [250]. However, a microcrystal structure of a designed 12-mer (KFFEAAAKKFFE) showed stabilisation of the packing of parallel β-sheets by means of π-stacking of rows of phenylalanine termed a phenylalanine zipper by the authors [251] and similar packing of aromatic side chains has been described for a pentapeptide of human calcitonin [252].

The role of charge in fibril-formation seemingly involve competition between opposite mechanisms. Chiti and co-workers found that mutations that reduces the net charge promote aggregation of ACP and the N-terminal domain of HypF from *E. coli* (HypF-N) from an ensemble of partially denatured states signifying an inhibitory effect of charge repulsion [232, 253]. Similarly, the tetrapeptide KFFE fibrillates while KFFK and EFFE do not [254] in agreement with the observation that intrinsically unfolded proteins have lower net hydrophobicity and higher net charge than native folded proteins [255]. In contrast, a study of *de novo* designed hexapeptides showed that a charge of +/-1 was essential for fibril-formation to proceed over amorphous aggregation [256] supporting the both importance of charge-interactions in fibril stabilisation and the tendency towards formation of amorphous aggregates at neutral net charge or by charges-screening at high ionic strength [85, 185, 257]. The competition between amorphous β-aggregation and formation of ordered amyloid-like fibrils is reasonable since hydrophobicity and propensity for β-structure are important for both processes [258]. Despite the overlap between β-aggregation and fibrillogenesis, some cautious generalisations can be made about the relationship between the two proc-

esses. Although amorphous, β-rich aggregates do contain significant amounts of ordered structure, their structural flexibility can result in faster kinetics compared to fibrillogenesis [258]. For highly hydrophobic sequences with high β-sheet propensity, the tendency will be towards fast amorphous aggregation while more polar sequences will be more favourable for formation of ordered fibril structure. However, the two processes commonly occur simultaneous and competitively, exemplified by the frequent observation of transient amorphous aggregates during fibrillogenesis.

Table 6. Aggregation propensities of the 20 natural amino acids used for AGGRESCAN (A, [260]) and Zyggregator (B, [261]) methods.

A. Aggregation propensities, de Groot *et al.*		**B. Aggregation propensities, Pawar *et al.***			
Residue		Residue	pH 2	pH 7	pH 13
W	1.037	W	2.92	2.92	2.92
F	1.754	F	2.80	2.80	2.80
C	0.604	C	1.61	1.61	-3.44
Y	1.259	Y	1.03	1.03	1.03
I	1.822	I	0.93	0.93	0.93
V	1.594	V	0.49	0.49	0.49
L	1.380	L	-0.25	-0.25	-0.25
M	0.910	M	-1.06	-1.06	-1.06
T	-0.159	T	-2.12	-2.12	-2.12
A	-0.036	A	-3.31	-3.31	-3.31
G	-0.535	G	-3.96	-3.96	-3.96
H	-1.033	H	-9.36	-4.31	-4.31
S	-0.294	S	-5.08	-5.08	-5.08
Q	-1.231	Q	-6.00	-6.00	-6.00
N	-1.302	N	-6.02	-6.02	-6.02
D	-1.836	D	-4.38	-9.42	-9.42
K	-0.931	K	-9.55	-9.55	-9.47
E	-1.412	E	-6.73	-10.93	-10.93
R	-1.240	R	-11.93	-11.93	-11.85
P	-0.334	P	-11.96	-11.96	-11.96

In recent years, several methods for prediction of aggregation or fibrillation propensity of denatured polypeptides have been developed based on individual amino acids properties within the sequence. Using aggregation propensities obtained from mutagenesis of Aβ [259, 260] (table 6.A) and sliding window analysis, Conchillo-Sole *et al.* [262] developed the AGGRESCAN method for predicition of aggregation 'hot spots' for several amyloidogenic proteins. The Zyggregator algorithm, developed by Vendruscolo and co-workers [261], also uses position-specific aggregational propensities (table 6.B) to calculate aggregation scores, but these are based on α- and β-structure propensities, a score for patterns of alternating polar and nonpolar side chains, hydrophobicity and charge. Aggregation-prone regions are identified by comparison to aggregation scores of a random protein of similar length. The algorithm was recently [263] expanded to allow prediction of aggregation-prone regions in native proteins by incorporation of the CamP method for calculation of flexibility and solvent accessibility [264]. For the TANGO method, Fernandez-Escamilla *et al.* [265] used similar physiochemical factors in combined with the assumption that a given amino acid is fully buried in the fibril fold. The protein is divided into segments and the partitioning within a conformation space including α-helix, β-aggregate and other conformations is calculated to predict aggregation-prone segments. A different approach was chosen by Seno and co-workers [266] for the PASTA method. Se-

quence-specific strand-strand interaction energies were calculated from a library of globular proteins to give parallel and anti-parallel pairing matrices. The prediction algorithm calculates pairing aggregation scores for combinations of potentially interacting regions in parallel and anti-parallel conformations to predict aggregation-prone segments and their orientation as minimal interaction energies. This list of prediction methods is by no means exhaustive but merely represent the methods used in the present work. It is worth mentioning that the close relationship between β-aggregation and fibrillation can limit the predictive power of such methods. A sequence may be predicted as aggregation-prone based on high β-strand propensity, high hydrophobicity and low net charge but this is not in itself indicative of aggregation in the fibrillar form.

1.4 Molecular basis of cellular toxicity

A detailed description of the pathological mechanism of neurodegenerative amyloidoses and diseases with amyloid-like deposits has remained an elusive target. Certainly, the clinical characteristics do not suggest a single, simple underlying mechanism. The diseases have very diverse cardinal symptoms, e.g. bradykinesia, rest tremor, rigidity and postural instability of Parkinson's disease, insomnia and autonomic nervous system dysfunction of Fatal Familial Insomnia (FFI) and uncontrolled body movements, personality changes and dementia of Huntington's disease [267-269]. However, the underlying progressive neuronal dysfunction and apoptosis shows similarities on the cellular level and the diverse symptoms are rather associated with selectivity for specific populations of neurons [270]: Hippocampal and cortical neurons are the primary targets in AD whereas PD is associated with loss of dopaminogenic neurons of the substantia nigra [271, 272]. Likewise, different mutations in the same gene can lead to distinct clinical forms such for mutations in the prion protein gene where Creutzfeldt-Jacob disease is associated with widespread spongiform changes while neuronal loss is limited to the thalamus in FFI [269, 273]. It is likely that numerous of inherited or environmental factors play a role in pathogenesis and that the specific factors and the interplay between may differ for the various neurodegenerative diseases. A number of theses factors will be covered in the following with particular emphasis on the effect of the amyloidogenic protein species and the identification of the primary toxic species among these.

1.4.1 The amyloid and oligomeric hypotheses

The presence of insoluble amyloid co-localised with areas most affected by disease is a general observation of neurodegenerative amyloidoses [274]. This, coupled with the discovery of mutations in the *APP* gene associated with early onset-AD and the inevitable development of AD in individuals with trisomy 21/Down's syndrome who live beyond the age of 40[4] [275], led to the amyloid hypothesis of Alzheimer's disease (figure 14): The accumulation and deposition of amyloid is the primary event of disease leading to a cascade of tau hyperphosphorylation and neuronal death [42, 276]. Additional support for the amyloid hypothesis comes

4 The extra copy of *APP* in trisomy 21 causes life-long overexpression of AβPP and widespread deposition of Aβ [275].

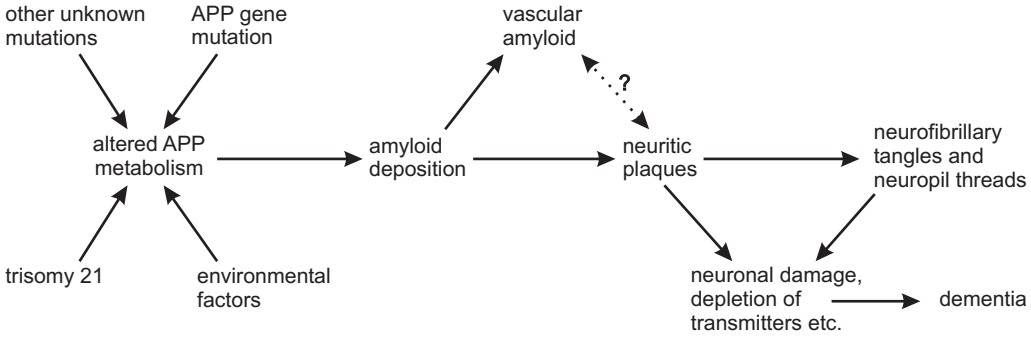

Figure 14. The amyloid hypothesis of Alzheimer's disease. Adapted from [267].

from AD as well as other neurodegenerative amyloidoses in the form of disease-associated phenotypes observed for animal models over-expressing amyloidogenic proteins [277-279], from identification of mutations linked to hereditary disease forms [32, 268] as well as biophysical characterisation of the *in vitro* aggregational tendency of the mutant proteins and peptides [32, 39]. Nevertheless, several factors speak against the validity of the this simple amyloid cascade hypothesis. The correlation between accumulation of amyloid plaques and the severity of AD symptoms is poor [280, 281] whereas the soluble population of Aβ, consisting of monomers and low-molecular mass oligomers, is more predictive for the severity of neurodegeneration [41, 282, 283]. Neurological deposits is a common post-mortem find in the non-demented elderly [284] and symptoms may conversely develop in the absence of extensive deposition such as in the case of juvenile autosomal recessive PD [285, 286]. Correspondingly, symptoms have been shown to precede formation if amyloid plaques in Aβ- or α-synuclein-expressing mouse and *Drosophila* models [287-291]. Disease progression may therefore be independent of formation of mature amyloid plaques and it is plausible that a shared mechanism may exist that unify not only the neurodegenerative amyloidoses but also neurodegenerative disease such as amyotrophic lateral sclerosis (ALS, [292]) that progress in the absence of amyloid plaques but shows formation of similar oligomeric structures.

The presence of non-amyloid aggregates can be demonstrated in the early presymptomatic stage for mouse and *Drosophila* models [293-295] and the emerging view of the relationship between protein structure and progression of disease focuses on the formation of oligomeric species [5, 193, 296], which may be similar to those observed in *in vitro* studies, e.g. spheroid and linear or annular protofibrils. This view is supported by the study of the E693G or 'Arctic' variant of AD for which dementia develops in the absence of compact amyloid plaques. The mutation causes decreased plasma levels of $A\beta_{1-40}$ and the more amyloidogenic $A\beta_{1-42}$ but increases protofibril formation [297]. While the common observation of oligomeric structures *in vitro* may not correspond to biologically relevant species, soluble Aβ oligomers have been isolated from human cerebrospinal fluid (CSF), cultured cells or transgenic mouse models [298-301]. Memory-impairment in the absence of neuronal loss correlated to extra-cellular accumulation of a 56kDa oligomer[5] has been demonstrated in mouse model over-expressing AβPP and comparable reversible memory impairment was observed when the oligomer was injected in rat brain [302]. Similarly, samples from cases of multiple system

5 The 56kDa oligomer theoretically corresponds to a dodecamer of $A\beta_{1-42}$.

atrophy were found to contain annular α-synuclein oligomers [303] with similarities to the annular species observed for recombinant α-synuclein [200].

The detection and characterisation of oligomers in humans is limited but much information has been gleaned from studies on cultured neurons. Mature fibrils can be neurotoxic but commonly at significant higher concentrations than for oligomers, which also speaks against the mature fibril as the primary toxic species *in vivo* [24]. Sub-micromolar concentrations of oligomers are capable of inducing apoptosis with associated calcium homeostasis alterations, unspecific membrane permeabilisation and depolarisation, Golgi and chromatin fragmentation and increased oxidative stress [192, 304-308]. The toxicity of oligomers in cell culture appears to be a general phenomenon [32, 309] and has been reported for proteins or peptides with no association with clinical disease as well as those associated with neurodegenerative and other localised amyloidoses, e.g. Aβ [198, 310], α-synuclein [311, 312], PrP [313], IAPP [314, 315], TTR [316, 317], equine lysozyme [318, 319], SH3 and *E.coli* hydrogenase maturation factor (HypF) [320, 321]. Oligomer-cytotoxicity has also been implicated in the systemic immunoglobulin light chain amyloidosis [31] and may be a contributing factor in other systemic amyloidoses [322].

In recent years, studies have also shed light on the effect of oligomers *in vivo*. Selkoe and coworkers [323-326] have identified $A\beta_{1-42}$ over-expressing cell lines that form intra-cellular and secreted di-, tri- and tetramers, which are potent neurotoxins at picomolar concentration. Direct cerebellar injection in rat caused inhibition of hippocampal long-term potentiation (LTP), cognitive disruption and impairment of complex learned behaviour. Studies of organotypical hippocampal slices *in vivo* also showed inhibition of hippocampal LTP as well as pronounced but reversible effects on dendritic spine density. In all, these results suggest that the mechanism behind the memory and learning deficits of dementia is does not merely involve cell death but also subtle effects on neuron function. Similarly, injection of oligomers of the non-pathogenic HypF into rat brain led to dose-dependent impairment of function although to a lesser degree than in cultured cells suggesting the presence of protective mechanisms [309]. Further support for the role of oligomers in disease process comes from antibody and immunisation studies. Antibodies raised against soluble $A\beta_{1-42}$ oligomers or a molecular mimic of spherical Aβ oligomers have little or no immunoreactivity against low-molecular weight Aβ or fibrils but effectively inhibit the neurotoxicity in cell culture of $A\beta_{1-40}$ and $A\beta_{1-42}$ oligomers [327-329], which is in agreement with the marked improvement in transgenic mice upon immunisation and that neurological improvement can be independent of reduced presence of mature amyloid [330]. However, the oligomer-specific antibodies also inhibit neurotoxicity of oligomers of very diverse sequences including α-synuclein, IAPP, polyglutamine, lysozyme, insulin and $PrP_{106-126}$ [327] suggesting a shared oligomeric structure and common pathological mechanism. The supposed shared structure is interesting in the light of the proposed generic nature of mature fibril structure.

1.4.2 Membrane permeabilisation by amyloidogenic proteins or peptides

The seeming importance of early oligomeric forms of the amyloidogenic proteins combined with the common observations of membrane permeabilisation and depolarisation suggest that the cytotoxic mechanism may include membrane-associated processes [331]. It has been hypothesised that cell death is closely associated with or caused by membrane perturbations through formation of channels by the amyloidogenic protein, changes in membrane fluidity or lipid peroxidation due to increased levels of free radicals or possibly a combination of these factors [332-335]. *In vitro* permeabilisation has been demonstrated for several amyloidogenic system [336-339] using artificial liposomes of neutral and anionic lipids and in- or efflux of Ca^{2+} and various probes. As expected from the available observations of cytotoxicity, the early oligomeric forms have the highest membrane activity, which decreases as mature fibrils are formed [306, 338, 340].

The ability of an amyloidogenic peptide to form transmembrane pores *in vitro* was first demonstrated in 1993 for $A\beta_{1-40}$ [341]. The pores were voltage-independent, moderately cation-selective, Ca^{2+}-permable, of varied conductance in the pS-range and all susceptible to blockage by Al^{3+} (irreversible) and tris (tromethamine, reversible). Further work demonstrated formation of channels with unusually high conductance in the 0.4-4nS range and the authors suggested that the incorporation of such channels in neuronal membranes could alter Ca^{2+} homeostasis and depolarise the membrane within seconds and induce apoptosis [342] leading to the channel hypothesis of Aβ cell toxicity [343]. Indeed, $A\beta_{1-40}$ and $A\beta_{1-42}$ have been shown to kill fibroblasts and to form channels in rat cortical neurons, hNT cells and patches of gonadotropin-releasing neurons [344-347]. Studies have demonstrated formation of several dissimilar and reproducible channel types distinguishable by their conductivity, ion selectivity, voltage activation and kinetic characteristics [341, 342, 348-350], which is consistent with a range of oligomeric assemblies and thereby channels rather than a single well-defined transmembrane structure. The channel hypothesis has since been supported by *in*

Table 7. Examples of channel-formation by amyloidogenic proteins and peptides. Adapted from [335]. [a] C-terminal fragment of APP. [b] Channels open at negative voltages and close at positive voltages. [c] Channels close at positive voltages. N.D. Not determined.

Peptide	Voltage dependence	Single-channel conductance	Ion selectivity	Blockade by zinc	Inhibition by Congo red
$A\beta_{25-35}$	Dependent [b]	10-400pS	Cation	+	+
$A\beta_{1-40}$	Independent	10-2000pS	Cation	+	N.D.
	Independent	50-4000pS	Cation	+	N.D.
$A\beta_{1-42}$	Independent	10-2000pS	Cation	+	+
CT105 [a]	Independent	120pS	Cation	+	+
IAPP	Dependent [c]	7.5pS	Cation	+	+
$PrP_{106-126}$	Independent	10-400pS	Cation	+	+
	Independent	140, 900, 1444pS	Cation	N.D.	N.D.
PrP_{82-146}	Independent		Cation	N.D.	N.D.
SAA	Independent	10-1000pS	Cation	+	+
ANF	Independent	21, 63pS	Cation	+	+
β2m	Independent	0.5-120pS	Non-selective	+	+
Transthyretin	Independent	Variable	Cation (variable)	+	+
Polyglutamine	Independent	19-220pS	Non-selective	-	-
	Independent	17pS	Cation	N.D.	N.D.
α-synuclein$_{65-95}$	Independent	10-300pS		+	+

vitro observation of similar pores for several other amyloidogenic proteins and polypeptides (table 7, figure 15) [199, 202]. Despite very varied conductivities and differences in cation-selectivity, the channels have remarkably similar characteristics including blocking by Zn^{2+} and inhibition of channel formation by CR, which is a known inhibitor of fibrillation [335, 351]. In contrast, conditions that favour oligomerisation generally enhance channel formation, which is also the effect of increasing membrane charge and low concentration of cholesterol [352, 353] illustrating the importance of aggregational state, electrostatic interaction and membrane fluidity on membrane activity.

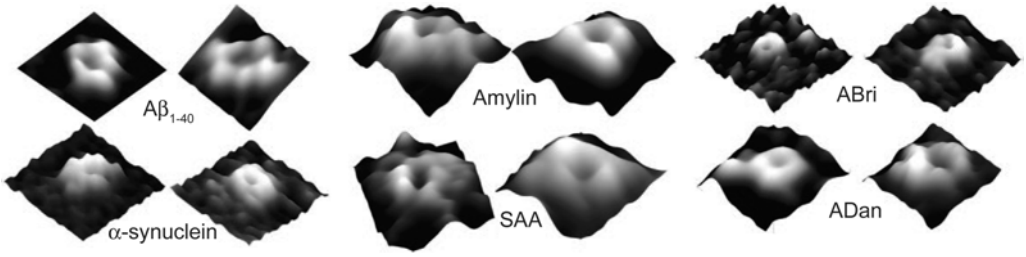

Figure 15.High-resolution AFM images of oligomeric channels. Adapted from [202].

In all, the observations of channel-like permeabilisation suggest the toxicity is linked to the formation of a collection of channels with overall similar structure. However, other mechanisms of membrane permeabilisation have been described. Glabe and co-workers [304] described generalised permeabilisation by oligomers of Aβ, IAPP, polyglutamine and lysozyme while Kayed *et al.* [354] described alterations in membrane conductance by oligomers of $A\beta_{1-40}$, $A\beta_{1-42}$, α-synuclein, polyglutamine, $PrP_{106-126}$ and IAPP that could not be explained by channel formation. IAPP has also been shown to induce non-channel defects in supported lipid bilayers monitored by time-lapse AFM [355] while α-synuclein and the G4R variant of human stefin B cause membrane fragmentation [336, 339]. Interestingly, both the wild type and the more amyloidogenic stB-Y31 isoforms of stefin B permeabilises liposomes by a channel-like mechanism. A different effect has been observed for growing fibrils of e.g. IAPP, endostatin and Aβ *in vitro*, for which alteration of bilayer structure or extraction of lipid into the forming fibril was associated with loss of membrane integrity and increased permeability [356-358]. It is possible that such non-specific alteration of membrane structure could play a direct role in inducing apoptosis *in vivo*.

1.4.3 Membrane modulation of fibril growth

As described previously, the current hypothesis for fibrillogenesis under membrane-free conditions consists of several steps: *i*) Destabilisation and partial unfolding of globular proteins or partial folding/stabilisation of natively unfolded proteins/peptides yielding a fibrillation-prone conformation, *ii*) association of monomers into a critical fibrillation nucleus or seed and *iii*) endwise elongation/addition of monomers to the seed and growing fibril, possibly combined with shearing of fibrils to create additional growing ends. Formation of a variety of morphologically distinct oligomers may or may not be an on-pathway phenomenon and the growing fibril may undergo further maturation. Based on current knowledge, a similar mechanism can be outlined for on-membrane fibrillogenesis

although significant structural differences may exist between solution- and membrane-associated assemblies [359]: *i*) Association of the monomer with the membrane, generally but not solely by electrostatic attraction, *ii*) structural transitioning to a fibrillation-prone conformation, *iii*) oligomerisation of the bound monomers, which for IAPP and α-synuclein appears to proceed in a nucleation-dependent manner and *iv*) fibril growth by monomer addition.

The unique environment afforded by the lipid bilayer may induce and act as a catalyst of fibrillogenesis. Whereas zwitterionic membranes have little or not effect, acceleration of fibrillation by anionic lipids has demonstrated for proteins/peptides associated with disease, e.g. Aβ [360], α-synuclein [361], IAPP [362], lysozyme, transthyretin, as well as proteins without known *in vivo* amyloidogenic activity, e.g. cytochrome c, insulin, myoglobin and endostatin [357, 363]. Effects on oligomerisation of Aβ have also been described for mixed membranes of zwitterionic lipid and gangliosides or cholesterol [364], suggesting that lipids may influence fibrillogenesis by a complex interplay of factors that influence physiochemical characteristics (e.g. charge, interfacial pH and dielectric constant, bilayer thickness and lateral pressure) and that these factors are protein/peptide specific. Destabilisation and partial unfolding at the water-membrane interface has been observed for a variety of globular proteins such as cytochrome c, phospholipase A_2 and acetylcholinesterase [365-367]. Similarly, membrane interaction may stabilise partially folded conformations of natively unfolded proteins or peptides. Aβ is unfolded in solution but recognises and binds to clusters of GM1 gangliosides on the cell membrane, the formation of which is modulated by cholesterol [368]. The unfolded peptide transitions to an α-helical structure at low Aβ:GM1 ratios, whereas higher ratios result in a β-rich conformation, which is hypothesised to facilitate nucleation and fibrillation *in vivo* [369]. Similarly, α-synuclein assumes an α-helical conformation when bound to negatively charged membranes [370].

Preferential membrane binding can increase the local concentration [371] and/or result in regular orientation of the polypeptide chain normal to the membrane plane by e.g. asymmetric charge distribution or partial insertion into the bilayer. An illustrative examples comes from human IAPP. While the peptide binds to zwitterionic liposomes in a β-rich conformation [372], Miranker and co-workers [373] showed that human IAPP partly insert into anionic membranes in an α-helical conformation, which after a lag phase transitions to a β-rich conformation synchronous with fibril formation. The formed α-helix has a highly cationic N-terminus and the authors speculated that the interaction with the anionic lipid headgroups masks the charges allowing the α-helix to form and permits clustering of individual helices in bundles. Random helix-coil sampling then leads to cooperative transition to the β-rich conformation and nucleation of fibril formation (figure 16) yielding fibrils of parallel strand orientation. Such interstrand orientation has been described for IAPP [374] while parallel, in-register alignment appears to be a favoured conformation for fibrils of several Aβ-variants in

solution [375]. Curiously, membrane permeabilisation is observed for the α-helical rather than later states, which offers a possible structural model for non-pore permeabilisation observed for IAPP [304, 354]. The importance of charge in membrane-associated IAPP fibrillogenesis is also illustrated by the observation of an optimal surface charge density of anionic:zwitterionic vesicles for rapid fibril assembly [362].

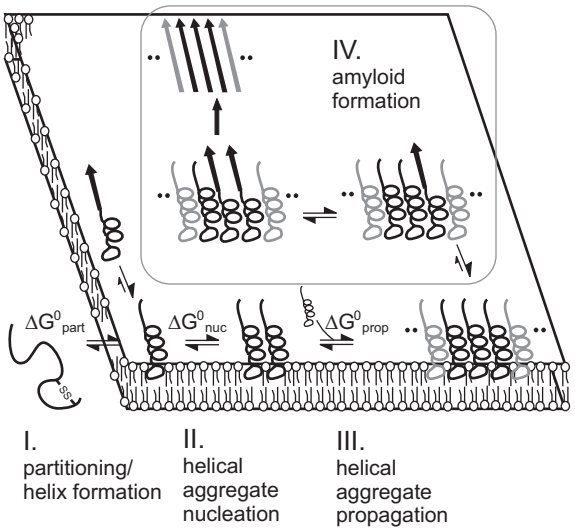

Figure 16. On-membrane fibrillation of IAPP by orientation of the peptide chain *via* α-helical association. Adapted from [373].

The anionic head groups play an important role in preferentially binding the protein or peptide [376] but the properties of the hydrophobic core region of the bilayer have significance for those proteins or peptides that partially inserts into the bilayer and intercalates between the densely packed acyl chains [377-379]. The interaction can inhibit fibrillation but also enhance nucleation and fibril formation. Wild type α-synuclein primarily associate with the polar lipid headgroups where it can act as a heterologous seed for fibrillation in the cytosol whereas the A53T mutant penetrates deeper into the non-polar bilayer core thereby masking the hydrophobic protein regions and inhibiting nucleation [380]. Membrane association and penetration also appears to be of importance for Aβ. The ability of Aβ to insert into mixed zwitterionic lipid/cholesterol monolayers and vesicles increases with increasing cholesterol content [381]. At cholesterol levels the peptide adopts a predominantly α-helical conformation and is effectively protected against fibril formation. Similarly, decreasing cholesterol content of brain lipid liposomes resulted in increased nucleation, surface fibril formation and toxicity for PC-12 and SY5Y cells whereas high cholesterol levels allowed membrane association but not insertion and inhibited fibril formation [382]. The nucleation- and fibrillation-enhancing effect of Aβ associated with anionic membrane surfaces was also demonstrated by Bokvist *et al.* [360] who showed that anionic lipids could stabilise an α-helical, transmembrane conformation of the recently cleaved peptide thereby preventing its release and subsequent fibrillation through surface-associated nucleation. However, an exiting recent study by Rousseau and co-workers [383] revealed a complementary effect of zwitterionic and anionic lipids as well as cholesterol and gangliosides. Vesicles of these lipids converted mature Aβ fibrils into soluble oligomers similar to those formed by 'forward'

oligomerisation. The 'backward' oligomers were cytotoxic in culture and induced cognitive deficits in rats suggesting that a highly dynamic equilibrium exists for lipid-associated oligomers and fibrils and that lipids play an important role in modulation of oligomerisation and thereby toxicity *in vivo*.

1.4.4 Mechanism behind cell death may be complex and involve many factors

There is compelling evidence for oligomers formed during the early steps in fibrillogenesis as the primary toxic species *in vivo*, which allows formulation of a tentative mechanism of cytotoxicity (figure 17.A). In the healthy cell, misfolded proteins should be refolded by chaperone intervention or cleared by the ubiquitin-proteasome system [384]. Similarly, oligomeric assemblies and insoluble aggregates should be degraded *via* the autophagy-lysozyme pathway. However, insufficiency or outright malfunction of these system allows accumulation of misfolded monomers, oligomers and, eventually, mature fibrils. The oligomers most likely have a number of deleterious effects such as membrane destabilisation, mitochondrial dysfunction and alterations in the Ca^{2+} homeostasis [24, 331]. Some or all of these eventually leads to cells dysfunction and death, which present as clinical symptoms although significant cell loss can be required [385].

The focus on oligomers as the neurotoxic agent proposes a useful but somewhat narrow perspective, which may be too simplistic *in vivo*, as demonstrated by the observation of protective mechanisms in rat brain against HypF oligomers. The question also remains what leads to misfolding of proteins and formation of oligomers in tissue in excess of the capacity of cellular clearance pathways. One likely scenario is an interplay of numerous causes (figure 17.B) related to aging, disease or inherited factors including, but not limited to, increased concentration of the amyloidogenic protein or peptide, increased oligomerisation tendency, decreased clearance of misfolded protein or aggregates and increased oxidative stress [5, 311].

The available cellular concentration of the amyloidogenic protein or peptide is determined by synthesis and clearance rates and, in the case of amyloidogenic protein fragments, by alterations of the proteolytic processing of the precursor protein consistent with the correlation between elevated of 'soluble' Aβ, i.e. monomeric and low-molecular mass oligomeric, and disease in AD. Decreasing efficiency and capacity of cellular clearance pathway and increasing oxidative stress are both associated with ageing [384, 386, 387], which offers a possible explanation for why neurodegenerative diseases predominantly are diseases of late life. Oxidative stress arises from the accumulation of reactive oxygen species (ROS) in excess of what the cellular antioxidant systems and has been implicated in pathogenesis of a number of neurodegenerative and other amyloidoses [268, 388], e.g. lipid peroxidation known to induce membrane perturbations and other cellular injuries prompting cell death [389, 390] or accumulation of misfolded proteins [272, 391, 392]. The tendency towards misfolding, oligomerisation and fibrillation can also be driven by pathogenic mutations exemplified by the E693G

A

MISFOLDED PROTEINS OR PEPTIDES DUE TO GENETIC VARIANTS, MUTATIONS AND/OR CHANGES OF THE INTRACELLULAR CONDITIONS (AGEING)

⇓

Exposure of hydrophobic regions and interaction with cell components (membranes)

⇓

Inability of the intracellular mechanisms to chaperone misfolded proteins to their locations

⇓

Triggering of adaptive cellular responses to remove misfolded proteins (UPR, HSR)

⇙	⇓	⇘
Chaperone refolding Enzymatic degradation	Compartmentalization (aggresomes, Lewy or Russel bodies)	Mature fibrils or disordered aggregates

FAILURE OF THESE MECHANISMS, CHAPERONE/PROTEASOME OVERLOAD

⇓

Accumulation of misfolded proteins and their prefibrillar aggregates

⇓

Destabilisations of cell membranes and impairment of the intracellular redox status and ion distribution possibly through formation of aspecific pores

⇓

Vacuolation, loss of electrolyte and redox homeostasis, reduced mitochondrial functionality, apoptosis, necrosis,
cell death

⇓

CLINICAL SYMPTOMS

B

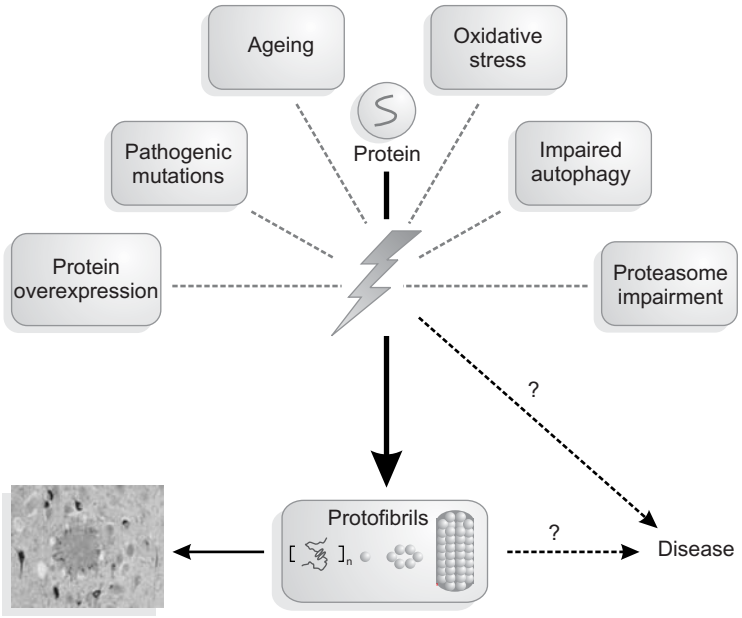

Figure 17. The progression from protein misfolding to clinical symptoms (A [331]) proceeds through several steps. Although the details of the causes of protein misfolding are not known, they likely involve an interplay of numerous factors (B [5]).

Arctic variant of AD described above. Any of these factors could contribute to the accumulation of misfolded protein but amyloidogenic proteins can in turn influence both the oxidative state of the cell and proteasomal efficacy. Binding of metal ions such as Cu^{2+} and Fe^{3+} to Aβ results in production of ROS, peptide oxidation and reduction of the metal ions by reaction with O_2 [393, 394]. Similarly, amyloid plaques are efficient redox catalysts [395] and co-localise with elevated levels of transition metals [396] suggesting that direct production of ROS by Aβ oxidation plays a role in pathogenesis. Interaction with transition metals have also been described as an effective catalyst of oligomerisation [397, 398]. However, Aβ, α-synuclein and polyglutamate have also been implicated directly in mitochondrial dysfunction [399] and enhanced permeability of mitochondrial membranes with channel-like characteristics or through localised oxidative damage to the membrane [400-403]. It is likely that mitochondrial dysfunction will affect the ATP dependent ubiquitin-proteasome system [404] but oligomers of α-synuclein have also been directly linked to proteasome impair-

ment [405, 406]. Consequently, the pathogenesis of neurodegenerative amyloidoses is complex and may be driven by self-propagating factors.

Activation of components of the immune system may play an important role in the clinical progression of neurodegenerative amyloidoses. Activation of microglia and astrocytes leading to overexpression of cytokines is a known cause of neuronal tissue loss and can, in the chronic inflammatory state of AD, act in a self-propagating fashion [407]. Additionally, activation of complement through the classical and alternative pathways occurs early in disease progression. Activation appears to occur at the site of plaques leading to insertion of the membrane-perforating MAC complex in surrounding neurons probably leading to further neuronal death [408]. It remains unknown to what degree immune activation and inflammation actively participates in driving the emergence of clinical symptoms, but they arguable play an important part in the progression of disease [409].

A final potential contributor to neurological abnormalities is cerebral amyloid angiopathy (described in section 1.1.4). The exact role of CAA in the pathology of AD and other neurodegenerative amyloidoses is not known, but CAA has in some cases been linked directly to the development of dementia [410]. CAA-related strokes, micro-haemorrhages and vascular degeneration appears to play a significant role with ischemic lesions as a common post-mortem find in e.g. AD. It is possible that the progressive damage to vasculature arises from direct toxicity of the deposited species [411]. However, the argument can also be made that the pathology of CAA also bears semblance to the systemic amyloidoses in that vascular disruption appears to play an important part in disease development.

1.4.5 Potential therapeutic approaches

Unsurprisingly, much effort has gone into development of therapeutic strategies for intervention in neurodegenerative and other amyloidoses. The current treatment options do not address the underlying cause of disease but are rather focused on alleviating symptoms e.g. by inhibitions of acetylcholinesterase in AD (tacrine, donepezil and rivastigmine approved for treatment) [412, 413] or dopamine-replacement therapy in PD (levodopa, co-careldopa and co-beneldopa) [414]. Disease-modifying treatment requires that the cause of disease be addressed. Considering the case of AD and using the current limited understanding of its pathology, a simplistic sequence of events can be drawn up (figure 18) [5]. Briefly, the full-length AβPP is processed (1) yielding a number of Aβ variants of which $A\beta_{1\text{-}42}$ is the most amyloidogenic. Aβ is in dynamic equilibrium with toxic oligomers, $(A\beta)_n$, (2) and mature fibrils in amyloid plaques (3). The presence of oligomers give rise to disease by a complex mechanism (4). Prevention of clinical symptoms require intervention at any of these steps or by depletion of monomeric Aβ (5, 6). Selected therapeutic approaches are summarised in table 8.

The initial processing of AβPP (1) is a prime candidate for intervention e.g. *via* inhibition or modulation of γ-secretase and shifting of the proteolytic cleavage

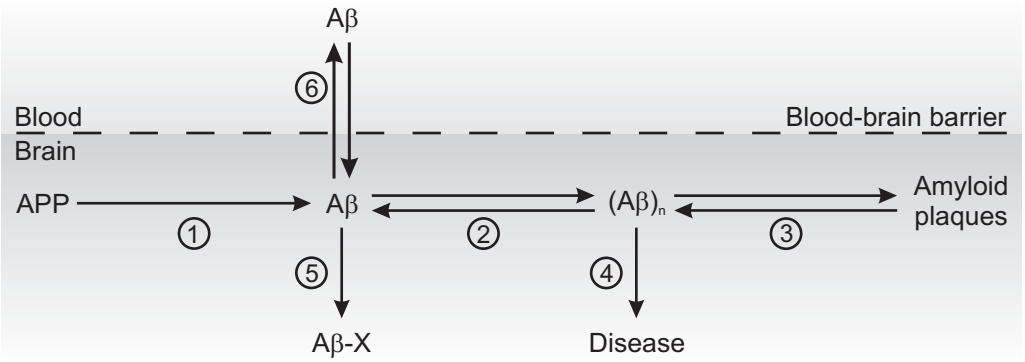

Figure 18. Summary of Aβ processing and fibrillation with possible sites of intervention. Obviously, activity in the CNS requires prospective drugs to be able to cross the blood brain barrier. Adapted from [5].

from $A\beta_{1-42}$ to less amyloidogenic peptide variants. Recent years have seen several potentially effective candidates. The γ-secretase modulator *R*-flurbiprofen (Flurizan) showed promise in animal and phase II trials, but was discarded after lack of effect at phase III [415-417]. Recently, an alternative, LY451039, has entered phase III [418-420].

Assuming that the soluble oligomers that are observed for most amyloidoses indeed are the toxic species, the prevention of this step is essential, either by binding of the monomer thereby preventing self-association (5) or by stabilisation of a non-toxic oligomeric assembly (2). The initial view that the mature fibril is the toxic species led to a focus on the prevention of fibrillation rather than formation of oligomers and diverse small molecule inhibitors were identified *in vitro* including benzoflurans, sulphated or sulphonated compounds, apomorphine, antioxidants, antibiotics, chemotherapeutic agents and natural products such as curcumin from tumeric [421-435]. Several of these compounds also prevent cell death in culture [423, 424, 427, 432, 435]. However, inhibition of oligomerisation or of oligomerisation and fibrillation can only be demonstrated for a subset of the general inhibitors [215]. An example of an oligomerisation inhibitor is tramiprosate (3APS), which is currently in phase III trials. The approach utilises the *in vivo* binding of glycosaminoglycan (GAG) to amyloid. The compound is a sulpho-

Table 8. Examples of compounds being developed for treatment of AD.

Compound name(s)	Clinical trial no.[a]	Phase	Remarks
Inhibition of γ-secretase			
R-flurbiprofen, Flurizan	NCT00105547	III	Lack of effect in phase III, discontinued
LY450139	NCT00244322	II	
	NCT00471211	II	
	NCT00594568	III	
Inhibition/modulation of oligomerisation			
Tramiprosate, 3APS	NCT00314912	III	Sulphonated GAC-mimic
	NCT00088673	III	
	NCT00217763	III	
ELND005, AZD103	NCT00568776	II	*Scyllo* stereoisomer of inositol
Antibody-based approaches			
AN1792	NCT00021723	II	Active immunisation, discontinued after severe adverse effects
Bepaneuzimab, ELN115727	NCT00574132	III	Passive immunisation with monoclonal antibody
	NCT00575055	III	
	NCT00676143	III	
	NCT00667810	III	

[a] http://clinicaltrial.gov

nated GAG mimic, which selectively binds monomeric Aβ (5), maintains it in an α-helical/random coil conformation and thereby prevents formation of toxic oligomers [436-439]. An alternative approach, utilising the *scyllo* stereoisomer of inositol (ELND005, formerly known as AZD-103), targets the equilibrium formation of oligomeric $(A\beta)_n$ (2). The compound stabilises a non-toxic oligomeric Aβ assembly [440-442] and is being investigated in phase II.

Antibody-mediated removal of the amyloidogenic monomer from the brain (6) is a potentially very powerful alternative. Binding of monomeric Aβ and transport across the blood-brain barrier followed by remote degradation would deplete the soluble peptide pool and, *via* the equilibrium, oligomers and higher aggregates. Consistent with this, animal studies have demonstrated that active or passive immunisation against Aβ can result in reduction of amyloid plaques and some reversibility of cognitive deficits [330, 443-447]. A phase II study using pre-aggregated Aβ (AN1792) was prematurely stopped after 6% of participants developed aseptic meningoencephalitis, possibly due to T-cell activation [448, 449] and despite observations of lower levels of aggregated Aβ in test subjects [450], concern remains over the severe adverse effects. An alternative small study using passive immunisation with total human IgG from healthy individuals showed effect in human subjects [451] and several remodelled antigens or monoclonal antibodies are in development [452-455] including the AN1792-derived monoclonal antibody bepaneuzimab [456, 457], which is currently in phase III.

An alternative to inhibition of toxic oligomer formation is intervention at step (4) by e.g. neuroprotective agents such as the antihistamine dimebolin [458, 459], which has been described as an effective blocker of Ca^{2+} channels [460], or metal-protein attenuating compounds such as the quinoline derivative PBT2 [461], which also potentially targets Cu^{2+}-mediated oligomerisation. A consequence of the oligomer toxicity hypothesis is that conversion to mature fibrils could function as a clearing mechanism allowing sequestering of toxic oligomers in relatively benign deposits [462, 463]. Consequently, inhibitors that prevent this step (3) could exacerbate rather than alleviate disease. A compound that catalyses fibril formation could have clinical effect although some studies indicate that mature fibrils may be toxic as well [464, 465]. However, intervention at steps (3) and (4) are associated with progressing build-up of aggregated material, which may lead to tissue damage and disease, particularly considering the pathology of the systemic amyloidoses and CAA.

Chromosome 13 dementias and associated proteins

2

Paper 1 is focused on characterisation of the aggregational behaviour of a modified peptide linked to Familial Danish dementia. This recently described neurodegenerative disease belongs to the chromosome 13 group of rare familial amyloidoses, which also comprises Familial British dementia (FBD). These diseases share a common precursor protein, BriPP, which is located on the long arm of chromosome 13, and constitute an alternative model for neurodegenerative amyloid pathology. Central aspects of these diseases are summarised in the following with emphasis on pathophysiology and the properties of the associated proteins and peptides.

2.1 Aspects of chromosome 13 dementias

2.1.1 Familial British dementia

Familial British dementia was first described by Worster-Drought and collaborators in 1933 as a novel form of familial presenile dementia with spastic paralysis in members of a family residing in South London [466, 467]. The original Worster-Drought pedigree has since been expanded to encompass more than 300 individuals including 36 known cases dating back to the late eighteenth century [468-471]. An additional pedigree containing two cases without clear relation to the main pedigree has been described [472] and could potentially represent an unrelated emergence of the disease-causing mutation although relation to the expanded Worster-Drought pedigree could exist through several members that remain unaccounted for.

FBD is an early-onset autosomal dominant disorder with a median age of onset of 48 years (range 40-60) [469, 473]. Clinically, it initially presents with personality changes and impairment of memory, which progresses to global amnesia. The patients display gradually worsening spastic tetraparesis and cerebellar ataxia. The median length of illness is 9 years with median age of death at 56 years of age (range 48-70). Histopathologic examination of post-mortem samples shows CR and ThS positive parenchymal plaques composed of 10nm-wide fibrils of

varying density and entanglement throughout the central nervous system but particularly affecting the hippocampus and cerebellum with lesser involvement of the amygdala and hypothalamic nuclei [474]. Neurofibrillar tangles are observed with severe pathology in the limbic system associated with plaques in a manner similar to AD. In addition of amyloid plaques, diffuse CR- and ThS-negative non-fibrillar or preamyloid deposits are present in most areas of the CNS. These are composed of amorphous, electron-dense material with sparse fibril presence. CR-negative amorphous material is also found bordering amyloid plaques. Additionally, many amyloid plaques are of the perivascular type and associated with severe CAA throughout the brain and spinal cord affecting white and grey matter. Cerebral haemorrhage is observed rarely in FBD, but stroke-like episode have been described in some cases and ischemic lesions is a common post-mortem find [468]. Overall, the neuropathology of FBD is similar to that observed for AD, but FBD also shows widespread systemic amyloid or non-amyloid, parenchymal and vascular deposits, indistinguishable from those found in the CNS, in organs and skeletal muscle [475, 476]. Systemic, non-amyloid presence of Aβ has been demonstrated for AD [477] while systemic amyloid has been identified for HCHWA-I, for which CNS parenchymal amyloid is absent, but neither shows both neurological and systemic presence of amyloid [478, 479]. The main constituent of FBD amyloid plaques, perivascular plaques, vascular and diffuse deposits has been identified as a ~4kDa peptide, termed ABri, which is a C-terminal proteolytic degradation product of the BriPP protein [480]. The presence of amyloid-associated proteins or other additional components has also been demonstrate including SAP, apolipoproteins E and J, HSPGs [481] and, curiously, C-terminal fragments of α- and β-tubulin [482].

2.1.2 Familial Danish dementia

Familial Danish Dementia was first described in 1970 by Strömgren and collaborators under the name heredopathia ophthalmo-oto-encephalica in a family from Djursland, Denmark [483]. The 48 person pedigree is smaller than that of FBD with 13 identified cases spanning five generations [473, 484]. Like FBD, FDD is an autosomal dominant disease but with earlier age of onset, which can be before the age of 30 and median age of death at 58 years. The first clinical symptom is gradual loss of vision from cataract formation and accumulation of amyloid in the retina and in walls of retinal capillaries leading to loss of glial cells and retinal neovascularisation, vitreous haemorrhage and neovascular glaucoma [485]. Severe or total central hearing loss develops 10-20 years after the initial symptoms followed by gradually worsening cerebellar ataxia [473]. The final decade of life is marked by development of paranoid psychosis and progressive dementia.

One of the major histopathological finds in FDD is severe cerebral amyloid angiopathy throughout the CNS with particularly abundant deposits found in the hippocampus, subiculum and cerebellar cortex where some capillaries appear

completely occluded [484, 486] and with associated volume loss and small areas of infarction. However, unlike FBD and Alzheimer's disease, amyloid plaques rare and principally perivascular with the exception of retinal and subpial paranchymal plaques. Paranchymal deposits are predominantly non-neuritic and observed throughout the CNS with highest concentration in the hypothalamus, midbrain tectum and periaqueductal grey, locus ceruleus, retina, hippocampal formation and other limbic structures. These deposits do not stain with CR or ThS but do bind antibodies to AAPs with particularly high intensity for SAP [481]. The absence of staining with amyloid-specific dyes indicate a lack of fibrillar structure and these possibly preamyloid deposits can be divided into two groups: 1) Compact plaques that appear morphologically similar to cotton-wool plaques observed for spastic paraparesis variants of Alzheimer's disease and 2) ill-defined 'cloudy' deposits that are often peri-neuronal. Neurofibrillar tangles, particularly within the hippocampus, are similar to the neuropathology observed for FBD and AD. The predominance of non-fibrillar deposits highlights the probable importance of oligomeric species in disease progress and suggests that the eventual presence of fibrillar or non-fibrillar, insoluble deposits may be incidental. Similar to other neurodegenerative amyloidoses, immune activation appears to be an important factor in FBD and FDD. Complement activation in FBD and FDD occurs by both the classical and alternative pathways with membrane attack complex activation on level with the activation observed for $A\beta_{1-42}$ [487]. The amyloid, but not the defuse deposits in FBD and FDD, are associated with markers of glial activation and local inflammation [474, 484] and show co-localisation with α-1-antichymotrypsin and cystatin C indicating local inflammation [481].

A novel, 34-amino acid peptide, ADan, has been identified in circulation and in plaques in post-mortem samples [486]. Like ABri, it is a C-terminal proteolytic fragment of BriPP albeit arising from a different mutation. An interesting aspect of FDD is the colocalisation but without complete overlap between deposits of ADan and Aβ by immunostaining [484, 488]. Co-deposition is primarily vascular or within perivascular amyloid plaques and occur predominantly in the hippocampus, limbic structures, neocortex, thalamus and cerebellum while other areas are solely affected by ADan deposition. The most prevalent deposited form is $A\beta_{1-42}$ with N-terminal degradation to position 3-4 [489]. It is possible that Aβ is deposited as an 'innocent bystander' due to interaction with ADan or the precursor protein or that FDD is associated with early-onset Alzheimer's disease through some unknown mechanism. However, the exact mechanism behind such co-localisation remains unknown although overlapping deposition is a well-known phenomenon as exemplified by cystatin C, which co-localises with Aβ in AD brain [490] and with amyloid deposits in FBD and FDD. CST3, encoding cystatin C, has also recently been implicated as a AD susceptibility gene [491] and whereas mutant variants of cystatin C is linked to hereditary amyloidosis and CAA, the wild type has also been shown to inhibit fibrillation *in vitro* [492].

2.2 The precursor proteins

2.2.1 Characteristics of BriPP

The Bri precursor protein (termed BriPP, ABriPP or ADanPP depending on presence of FBD or FDD-related mutation) is a 266AA protein encoded by the *ITM2B* gene on the long arm of chromosome 13 [486]. The gene contains six exons and five introns of which the first is long and possibly contains regulatory elements. The *ITM2* gene family span at least three isoforms (*ITM2A*, *ITM2B* and *ITM2C*) in human and mouse [489], but *ITM2B*, *ITM2C* and *ITM2*-like genes (*ITM2-LGs*) have been identified in a wide range of vertebras and non-vertebras (table 9 and figure 19). The family is highly conserved. Human *ITM2B* shared 41% and 47% similarity with human *ITM2A* and *ITM2C*, respectively, and 60% identity with fruit fly *Q9VPT9*, the most distant identified relative.

Table 9. Examples of ITM2 and ITM2-like genes from vertebras (A) and invertebras (B). [a] Ray-finned fish. [b] Nematodes.

A. Vertebras

Class	Organism	No.	Gene name, SwissProt ID
Actinopterygii [a]	Zebrafish (*Danio rerio*)	1	ITM2B_DANRE, Q803H7
		2	ITM2C_DANRE, Q7SYK5
Amphibia	African clawed frog (*Xenopus laevis*)	3	ITM2B_XENLA, Q8AVF1
	Western clawed frog (*Xenopus tropicalis*)	4	ITM2B_XENTR, Q6P3P6
Aves	Chicken (*Gallus gallus*)	5	ITM2B_CHICK, O42204
Mammalia	Chimpanzee (*Pan troglodytes*)	6	ITM2B_PANTR, A5A6H8
	Cow (*Bos taurus*)	7	ITM2B_BOVIN, Q3T0P7
		8	ITM2C_BOVIN, A2VDN0
	Crab-eating macaque (*Macaca fascicularis*)	9	ITM2B_MACFA, Q60HC1
		10	ITM2C_MACFA, Q4R540
	Human (*Homo sapiens*)	11	ITM2A_HUMAN, O43736
		12	ITM2B_HUMAN, Q9Y287
		13	ITM2C_HUMAN, Q9NQX7
	Mouse (*Mus musculus*)	14	ITM2A_MOUSE, Q61500
		15	ITM2B_MOUSE, O89051
		16	ITM2C_MOUSE, Q91VK4
	Pig (*Sus scrofa*)	17	ITM2B_PIG, Q52N47
		18	ITM2C_PIG, Q06AV4
	Rat (*Rattus norvegicus*)	19	ITM2B_RAT, Q5XIE8
		20	ITM2C_RAT, Q5PQL7
	Sumatran orang-utan (*Pongo abelii*)	21	ITM2B_PONAB, Q5R876
		22	ITM2C_PONAB, Q5NVC3

B. Invertebras

Class	Organism	No.	Abbreviation / SwissProt ID
Insecta	Common fruit fly (*Drosophila melanogaster*)	23	Q9VPT9_DROME,Q9VPT9
Secernentea [b]	*Caenorhabditis briggsae*	24	Q17302_CAEBR, Q17302
	Caenorhabditis elegans	25	Q967F7_CAEEL , Q967F7

The *ITM2* family shows distinct differences in expression profile. Expression or up-regulation of *ITM2A* has been associated with development of bone and cartilage in mouse and with haemopoiesis and T-cell selection with expression restricted to these tissues [493, 494]. *ITM2C* is expressed in brain and other tissues [495, 496], but not with as wide an expression profile as *ITM2B*, which appears ubiquitous [497]. In human and mouse CNS, it is expressed in smooth muscle and endothelial cells of the cerebral vasculature and in microglia, astrocytes and neurons with presence in the neuron body, axons and dendrites [498, 499]. It is

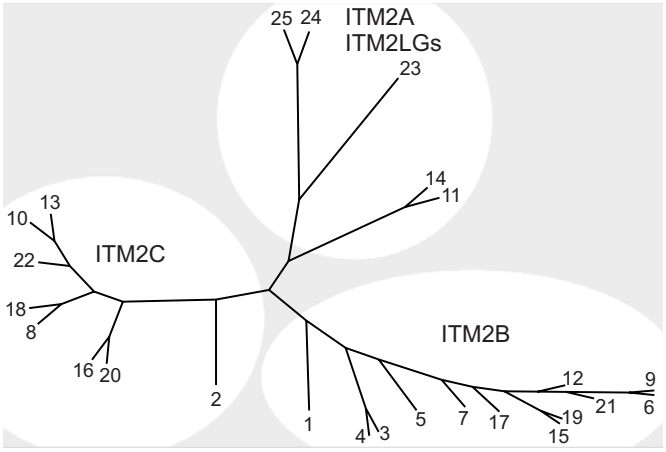

Figure 19. Unrooted phylogenetic tree of selected ITM2 and ITM2-like genes (see table 9 for key). Made using the Phylip server (bioweb2.pasteur.fr/phylogeny/intro-en.html)

present throughout both white and grey matter but is particularly abundant in the hippocampus and cerebellum, which parallels the most intense sites of neuronal loss in FBD and FDD.

Little experimental evidence exists for the domain organisation of the proteins encoded by the *ITM2* genes, but the overall structure appears shared by all members [495, 497, 500]. Using BriPP as a representative example, the *ITM2*-type protein is putative type II transmembrane protein (figure 20.A) with a proteolytically protected region spanning positions 52 to 76 [504]. Transmembrane helix prediction algorithms Phobius [501, 502] and PHDhtm [505] both predict a single transmembrane helix at positions 51-74 and 58-75 (figure 20.B), respectively. This partitions the protein into three domains with the short N-terminal domain located intra-cellularly, a transmembrane region and a larger, possibly globular, extra-cellular C-terminal domain ($BriPP_{EC}$). Using the ScanProsite motif scanning tool [506], a single N-glycosylation site is predicted at position 170. This has been reported previously [497] and is supported by the observation of glycosylation at a similar, conserved site in mouse ITM2A [507]. ScanProsite also predicts a number of potential phosphorylation sites[6] and two N-myristoylation sites at position 48 and 67, which are interesting in light of the predicted membrane localisation.

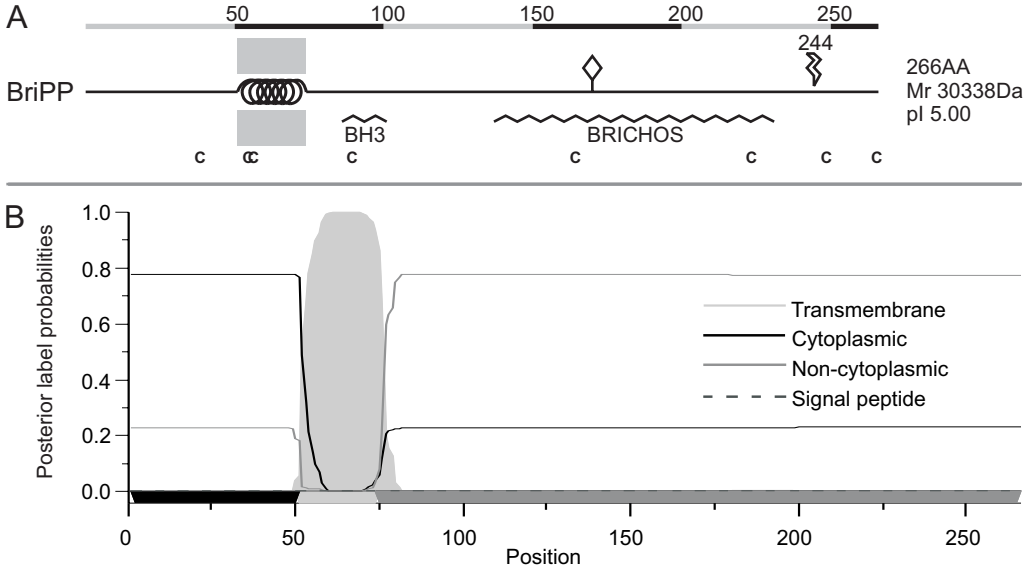

Figure 20. The primary structure of BriPP (A) adapted from [497]. Phobius prediction of a single transmembrane helix (B) [501, 502].

6 Casein kinase II: 22, 114. cAMP- and cGMP-dependent protein kinase: 151, 233. Protein kinase C: 206, 228, 236. Tyrosine kinase: 221.

2.2.2 Proteolytic processing of BriPP

FBD and FDD are associated with mutations that elongate the C-terminal of BriPP creating the two variants ABriPP and ADanPP. In the case of FBD, a T-to-A mutation in the TGA stop codon results in the introduction of an Arg codon and 10 additional amino acids (RTVKKNIIEEN) before the sequence terminates at a pre-existing stop codon [480]. For FDD, a 10bp insertion/deletion (tttaatttgt) in codon 265 results in S266F mutation and an 11 amino acid elongation ((S-to-F)NLFLNSQEKHY) and termination at a previously out-of-frame stop codon [486]. Consequently, both variant proteins contain 277 residues but with drastically different C-terminal elongations.

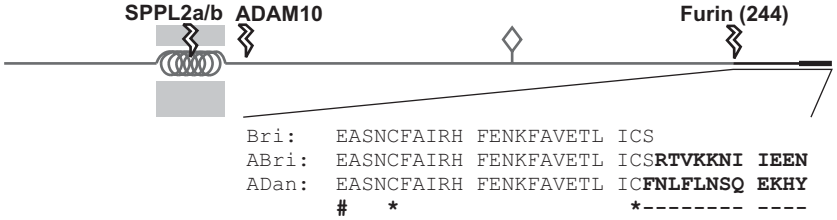

Figure 21. The proteolytic processing of BriPP (C) and the three resulting peptides Bri, ABri and ADan [503, 512].

BriPP, ABriPP and ADanPP are all cleaved before position 244 to release the C-terminal Bri, ABri and ADan peptides, respectively (figure 21). The proprotein convertase furin colocalises with ABri amyloid in FBD [508]. Furin also cleaves BriPP, ABriPP and ADanPP effectively in cell culture of which a fraction occurs intracellulary in the *trans*-Golgi [504, 509, 510]. Other members of the subtilisin/kexin-like proprotein convertase family also cleaves the precursor proteins but with less efficiency [509]. Interestingly, the release of ABri is elevated compare to release of the wild-type Bri peptide. The production of ADan is also increased but this peptide appears to accumulate intra-cellularly. The observation by Kim *et al*. that furin is 'both necessary and sufficient' for processing of the precursor proteins contrasts somewhat with work by Choi and co-workers [511]. This group found that cleavage is not prevented by inhibition of cellular furin or expression in furin-deficient cells and that processing takes place in the *cis*- or *medial*-Golgi indicating that while furin has proteolytic activity, another protease may be responsible for processing *in vivo*. Additionally, they observed a novel proteolytic variant arising from cleavage N-terminally to the N-glycosylation site at position 170. This is in agreement with a recent study by Haass and co-workers [512] that demonstrates proteolytic processing by the ADAM metallopeptidase domain 10 (ADAM10) and release of the C-terminal $BriPP_{EC}$ domain to the extra-cellular space. The cleavage is independent of prior removal of the Bri peptide. The N-terminal domain further undergoes intramembrane proteolysis by signal peptidase-like proteases 2a and 2b (SPPL2a and SPPL2b).

2.2.3 Structure of BriPP, extra-cellular domain

The structure and function of $BriPP_{EC}$ is highly interesting in light of the proteolytic cleavage and the disease-associate peptides that result. The 191AA domain is sufficiently long to allow for folding. The DISPro [513], FoldIndex [514], IUPred [515, 516] and DisEMBL [517] methods all indicated that $BriPP_{EC}$ is folded into a compact globular shape although the DisEMBL method did return several po-

tentially unfolded regions by the loops/coils definition (figure 22.A). However, none of these were sufficiently long to indicate that the domain is intrinsically unfolded. To further elucidate the possible structure of the precursor protein, five neural network-based secondary prediction servers were chosen: HNN [518], SSPro [519, 520], PROF [521], PSIPred [522, 523] and Jpred [524]. The presence of the N-terminal and transmembrane regions did not significantly influence the predictions and these were omitted for clarity. The resulting predictions were not in general agreement (figure 22.B), but a consensus prediction was built by demanding three or more positives per position and three or more consecutive residues. The consensus is robust for several regions of the sequence and $BriPP_{EC}$ appears to be a mixed α/β protein with alternating helices and strands although several regions lacked agreement between the used methods. Overall, the prediction is too poor to allow comprehensive structural analysis, particularly in light of the absence of evolutionary conserved homologues outside the *ITM2* family.

A

```
                 80         90        100        110        120        130        140
      AA:       YKYFA LQPDDVYYCG IKYIKDDVIL NEPSADAPAA LYQTIEENIK IFEEEEVEFI SVPVPEFADS
     SEG:       _____ __________ __________ __________ ____xxxxxx xxxxxxxxxx xxxxxxx___
DisEMBL 1:      xxxxx xxxxxxxxxx xxxxxxxxxx xxxxxxxx__ __________ ____xxxxxx xxxxxxxxxx
DisEMBL 2:      xxxxx xxxxxx____ __________ __________ __________ __________ __________

                150        160        170        180        190        200        210
      AA: DPANIVHDFN KKLTAYLDLN LDKCYVIPLN TSIVMPPRNL LELLINIKAG TYLPQSYLIH EHMVITDRIE
     SEG: __________ __________ __________ __________ __________ __________ __________
DisEMBL 1: xxxxxx____ _________x xxxxxxxxxx xxxxxxx___ _______xxx xxxxxxxxx_ __________
DisEMBL 2: __________ __________ __________ __________ __________ __________ __________

                220        230        240        250        260
      AA: NIDHLGFFIY RLCHDKETYK LQRRETIKGI QKREASNCFA IRHFENKFAV ETLICS
     SEG: __________ __________ __________ __________ __________ ______
DisEMBL 1: __________ __________ __________ __________ __________ ______
DisEMBL 2: __________ __________ __________ __________ __________ ______
```

B

```
                 80         90        100        110        120        130        140
      AA:       YKYFA LQPDDVYYCG IKYIKDDVIL NEPSADAPAA LYQTIEENIK IFEEEEVEFI SVPVPEFADS
     HNN:       -EEEE E-----EHEH HHH----EEE -------HHH HHHHHHHHHH HHHH--EEEE EE--------
   SSPro:       --EEE E----EEEEE EEEE------ ---------- -HHHHHHHEE EEHH---EEE E---------
    PROF:       -eeee .---.eEEEE EEEee..... ----------. ....hhheee ....--eeEE e....-----
  PSIPred:      -..ee .---.EEEEE EEEee..... .---.--... ...eeeeeee e.....EEEE e-----.---
    Jpred:      --... .----eeEEE EEEe...... ...--.---- --..eeeeEe ee---.eeEE e..-------
Consensus:      -      ---- EEEE EEE        ---------               -  EEE   --------

                150        160        170        180        190        200        210
      AA: DPANIVHDFN KKLTAYLDLN LDKCYVIPLN TSIVMPPRNL LELLINIKAG TYLPQSYLIH EHMVITDRIE
     HNN: ----HHHHHH HHHHHHEH-- ---EEEEE-- ---E--HHHH HHHHHHE--- ------EEEE EHHEHH-HHH
   SSPro: -HHHHHHHHH HHHHHHHH-- ---EEEEE-- -EEE--HHHH HHHHHHH--- -----EEEEE EEEEEE--H-
    PROF: -.hhHHHhhh hh.hhhhh.. --.eEEEe.- -.ee.-hhhH HHHHHHhh.- -.--..eeee eeeEee....
  PSIPred: -..eeeee.. --.eEEEE.- --eEEEEe-- -.ee.--.-H HHHHHHh..- ..-..eEEEE EeeEE.-...
    Jpred: --eeeeee.. ...eEEEe.- --.EEEe..- ..e..--..h HHHHhh..-- ...-..eeee ...e......
Consensus: -   HHH          e  - -- EEEE -- -    -   H HHHHHH  -- - --  EEEE E  e

                220        230        240        250        260
      AA: NIDHLGFFIY RLCHDKETYK LQRRETIKGI QKREASNCFA IRHFENKFAV ETLICS
     HNN: HH-H--HHHH EE------HH HHHHHHHH-- -HHHHHHHHH HHHHH---EE EEEEE-
   SSPro: -HHHHHHHHH HH------EH HHHHHHHHHH HHHHHH-HHH HEE----EEE EEEE--
    PROF: .hhhhhHHHH Hh.----eee ee.hhh.... .......... ee...-.eeE EeeE.-
  PSIPred: .hHHhhHHHH HHh----.EE EeehHhh.-. .hhhh..... eee.--.eEE EEEe.-
    Jpred: ....hhHHHH Hh..---eeE EeeeeeeeeE Ee.......e e.----.eeE EEee--
Consensus:    h  HHHH H  ----       h                   -  EE EEEE -
```

Figure 22. Prediction of folding (A) by DisEMBL [506] and prediction of secondary structure (B) [517-523] of the BriPP extra-cellular domain.

2.2.4 Biological function of BriPP

BLAST and FastA homology searches return only identified members of the ITM2 family. However, BriPP does contain a conserved BRICHOS domain (position 137-231) which is also found in such functionally distant proteins as chondromodulin and lung surfactant C [525]. The specific function of the BRICHOS domain remains unknown, but given that the identified BRICHOS

proteins all are type II membrane proteins and all are proteolytically cleaved, it has been speculated that the domain may be involved in secretory targeting or intra-cellular protease processing. BriPP and lung surfactant C are both prone to aggregation and BRICHOS could also have evolved to function as an intramolecular chaperone.

Finally, Fleischer and co-workers [526] identified a preserved BH3 domain in a short form of BriPP beginning at position 57 ($BriPP_S$). The BH3 domain is one among several domains preserved among the *Bcl-2* family of proapoptotic or prosurvival proteins and $BriPP_S$ was found to be capable of caspase-3 and caspase-9 activation and of inducing p53-independent apoptosis in cell culture [527, 528]. The shortening of the protein affects the transmembrane helix and could potentially involve solvent exposure of the highly hydrophobic region. It is interesting to speculate that this property of $BriPP_S$ could be related to the proapoptotic effect observed for Aβ, which is also characterised by an exposed, partial transmembrane helix [411, 529].

Induction of apoptosis is not the only potential function ascribed to BriPP. *ITM2B* is located in the 13q14.3 region of chromosome 13 and loss of heterozygosity in this region has been connected to head and neck squamous cell carcinoma, pituitary tumours and ovarian carcinoma [530-532]. *ITM2B* is one of several genes down-regulated in primary prostate cancer [533] suggesting a role in tumour suppression. Interestingly in the light of the strong link between prostate cancer and testosterone level, ITM2B was found to be strongly regulated by testosterone in rat reproductive tissue [534]. Expression was significantly down-regulated upon castration of mature rats and up-regulate upon testosterone replacement.

The perhaps most interesting putative function of BriPP is in the regulation of AβPP processing. A region of BriPP stretching from V46 to S104 and including the first 24 residues of $BriPP_{EC}$ was found to interact in *cis* with $A\beta PP_{648-719}$ in transfected cells [535, 536]. This region includes the uncleaved Aβ sequence, the transmembrane helix and the cleavage sites for the three secretases. Indeed, BriPP was found to strongly modulate secretase activity and production of Aβ. The activity of β-secretase increased while the α- and γ-secretases were inhibited resulting in decreased release of Aβ. This interaction could explain the observed colocalisation of ADan and Aβ in FDD. The high expression of BriPP in the CNS also suggests a role in neuron function. Immunostaining of healthy brain tissue and tissue from pathological cases reveals that *ITM2B* expression is upregulated near ischemic or hypoxic lesions and in dystrophic neurites in AD [498]. Similar to AβPP [537], BriPP or its proteolytic fragments appear to be transported in axons [511] and expression of the protein was also found to induce neuron outgrowth suggesting a role in plasticity of neuronal processes.

A part of the aim of the present work was biophysical characterisation of BriPP, ABriPP and ADanPP. While the C-terminal globular domain could be effectively

expressed in *E. coli* and purified by a combination of methods, the high number of cysteines made the following refolding difficult. The applied methods and relevant observations are summarised in annex 1.

2.3 Amyloidogenic and aggregation-prone ABri and ADan peptides

2.3.1 Heterogeneity of circulating and deposited forms

The proteolytic cleavage of the pre-proteins releases the amyloidogenic subunits ABri and ADan to circulation where they are found in serum, CNS deposits and, for FBD, systemic deposits [475, 488]. ABri was initially identified in leptomeningeal vascular amyloid extracted by formic acid with Mr 3935.5Da and in a form that prevented N-terminal sequencing [480]. This suggests an intramolecular disulphide bond between cysteines 5 and 22 and N-terminal cyclisation of glutamate to form pyroglutamyl. ABri isolated from systemic and CNS deposits are indistinguishable. The peptide was also identified in serum at an estimated concentration of 20ng/mL (5nM) and with an unmodified N-terminal glutamate [475]. Studies of ADan gave similar findings [486, 488]. The circulating form was not N-terminally modified while deposits of rising complexity contained peptide of increasing diversity (figure 23). Soluble fractions in PBS or 2% sodium dodecylsulphate (SDS) contained monomers and dimers with pyroglytamyl (ADan-pE) and unmodified N-terminals in a ratio of 60:40. The monomeric form dominated PBS and SDS-solubilised vascular samples while the dimer prevailed in parenchymal SDS fractions. However, deposits solubilised in formic acid showed only extensively oligomerised ADan-pE, which was N- and C-terminally truncated at positions 3 and 27, 28, 30 and 33, respectively. $ADan_{1\text{-}33}$-pE, $ADan_{1\text{-}28}$-pE and $ADan_{1\text{-}34}$-pE were more prevalent. Similarly, formic acid-solubilised ABri was highly oligomerised but with less extensive internal cleavage. It is not known whether the pattern of truncation demonstrates peptide variability the time of deposition or the body's attempt at clearing the deposits.

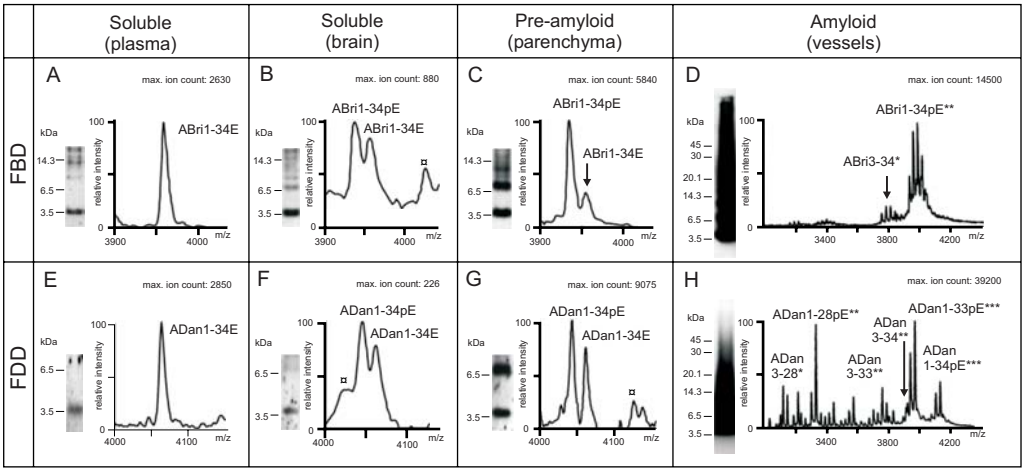

Figure 23. Western blot and mass spectrometry analysis of circulating (plasma) and deposited ABri and ADan. Adapted from [473].

The absence of ABri-pE and ADan-pE in serum and the gradual conversion with increasing deposit complexity could indicate increased aggregation-susceptibility of the pE forms but it is equally likely that circulating peptide does not origi-

nate from cleared deposits and that the cyclisation of glutamate happens *in situ* as deposits age. N-terminal blocking by pyroglutamyl has been described in forms of Aβ truncated at position 4 and for several hormones and neuropeptides [538-542]. For the latter two, the reaction is an enzymatic deamination catalysed by glutaminyl cyclase with glutamine as substrate [543, 544] whereas the substrate is glutamate for ABri, ADan and $A\beta_{4\text{-}x}$. Although cyclisation of Glu has been demonstrate in *Aplysia* neurons [545], the specific pathway has not been identified. Interestingly, the presence of ABri-pE in systemic deposits suggests that the catalysing enzyme or enzymes are not restricted to the CNS in activity.

2.3.2 In vitro aggregation and fibrillation of ABri and ADan

Despite their differences in the C-terminal elongation, ABri and ADan both aggregate readily *in vitro* although important differences can be observed. Early studies on ABri aggregation suggested that the intramolecular disulphide bond was essential for fibrillation [546]. Neither reduced ABri (redABri) nor wild-type Bri peptide oligomerised or displayed appreciable cytotoxicity in human neuroblastoma SHSY-5Y cells [547]. In contrast, the oxidised form (oxABri) formed dimers and an extensive array of SDS-stable, DTT-sensitive higher oligomers (SDS-stable non-fibrillar oligomeric species, SSNFOS) at pH 9.0. The predicted pI is 6.9 and the high pH-value was chosen to avoid this region of low solubility. Upon ageing over a period of three weeks short, curly protofibrils (2.5-8.5nm-wide and 10-60nm-long) and later long, intertwined, CR-birefringent fibrils (5-9nm-wide) were produced. Fresh samples containing SSNFOS showed significantly higher concentration-dependent toxicity than aged samples in SHSY-5Y cells measured by lactate dehydrogenase-release, inhibition of MTT[7] reduction and positive staining with of apoptotic cells with annexin A5. However, the later finding that the intramolecular disulphide bond is labile and prone formation of intermolecular covalent species [548] at pH 9 suggests that the oligomerisation pattern may be an artefact of the experimental procedure. OxABri is does indeed appear aggregation-prone in the absence of reducing agents as shown by circular dichroism of aged samples in the absence or presence of cysteine [549]. Under reducing conditions, the peptide remained in solution in a β-rich conformation but precipitates in the absence of reducing agent.

Zagorski and coworkers [548] used disaggregation with hexafluoropropan-2-ol (HFIP) prior to use to prevent disulphide scrambling for a systematic investigation of the pH and concentration-dependence of oxABri structure. At low pH (3.1) the peptide is predominantly random coil, which converts to a β-rich form as the pH is raised incrementally to pH 8.9. At low peptide concentration significant random coil is retained throughout the interval whereas high concentration (44μM) decreased the tipping point from random coil to β-rich conformation to between pH 4.7 and 5.9. Aging at pH 4.9 for 48 hours leads to formation of spherical aggregates (0.5-1.5nm diameter) and 1.5-2.2nm-wide curved or branched protofilaments (termed protofibrils by the authors) with 20-30nm periodicity (figure 24). The protofibrils may appear as beaded chains, ring-like or pore-like struc-

7 MTT: 3-(4,5-dimethylthiazol-2-yl)-2.5-diphenyltetrazolium bromide.)

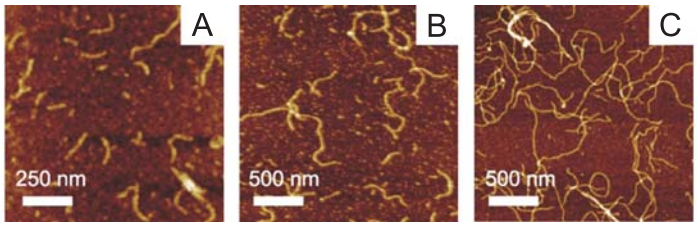

Figure 24. AFM images of ageing samples of 56μM oxABri at pH 4.9 for 48 (A), 144 (B) and 336 (C) hours. Adapted from [547].

tures with symmetry indicative of a tetramer [550] as previously observed by Quist *et al.* [202]. After two weeks, longer 4-6nm-wide fibrils with 37-45nm periodicity emerge [548]. These are composed of several protofilaments, which retain the curving and branching of the thinner filaments. When followed by ThT fluorescence, the emission reaches a plateau after approximately 80 hours suggesting that the protofilaments are structurally similar to mature fibrils. Higher pH- values (pH 7.3-8.4) favours production of amorphous species. Spherical aggregates (2-8nm diameter) form within a day and slowly coalesce into dense, amorphous structures with 100-200nm dimensions. The addition of fibrils formed at pH 4.9 to solutions at higher pH seeds protofilaments but not mature fibrils suggesting that the assembly of mature fibrils from protofilaments may be influences by the charge state of the peptide. These finding are in agreement with the previous studies where spherical aggregates coalescing into denser structures were observed at similar concentrations and basic pH [546, 547].

The pH-sensitivity of ABri fibrillation suggests that the charge state of the peptide plays a significant part in the thermodynamic and kinetic partitioning between solution-stable species, aggregation and fibrillation. The peptide contains multiple glutamate residues (figure 25) and the presence of stable monomeric species at low pH is likely attributable to charge repulsion. Examination of the charge state of the peptide suggests that the narrow pH range for fibrillation is dependent upon the deprotonation of the single histidine residue with nominal pKa at pH 6. Above this value, ABri is neutral and faster β-aggregation is likely favoured. The absence of aggregation for redABri could suggest that gradual deprotonation of the free cysteines play a role. However, a different interpretation of the available data is that the disulphide bond for oxABri restricts the peptide chain and efficiently brings together the misfolding nucleus tipping the balance from a soluble monomer to an aggregation- or fibrillation-prone species.

```
pH 5
      +-       ++ - +   -     +  ++   -- -
ABri:  EASNCFAIRHFENKFAVETLICSRTVKKNIIEEN  +1
ADan:  EASNCFAIRHFENKFAVETLICFNLFLNSQEKHY  +1
      +-       ++ - +   -            -++ -
pH 7
      +-       +  - +   -     +  ++   -- -
ABri:  EASNCFAIRHFENKFAVETLICSRTVKKNIIEEN   0
ADan:  EASNCFAIRHFENKFAVETLICFNLFLNSQEKHY  -1
      +-       +  - +   -            -+  -
```

Figure 25. Charge distribution of ABri and ADan at either side (pH 5 and 7) of the predicted isoelectric points. Red, negative; blue, positive; green, histidine; yellow: cysteine.

ADan has the same net charge as ABri at pH 5.0 despite containing significantly fewer charged residues (figure 25) and fibrillation of oxidised ADan (oxADan) has similar pH preference as oxABri [551]. Fibrillation occurs over a broad concentration range from 18 to 140 μM and comparable timescale. At pH 4.8, freshly

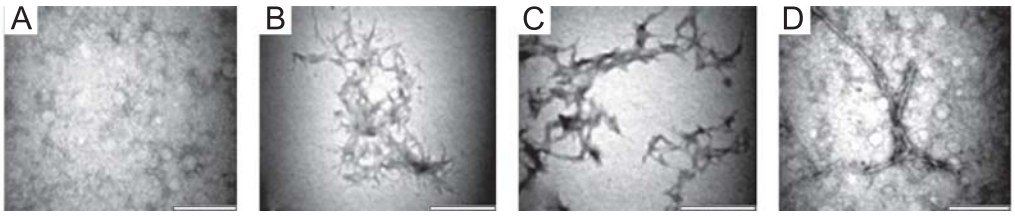

Figure 26. TEM images of ageing oxADan at pH 4.9 for 2 (A), 10 (B, C) and 30 (D) days. Adapted from [550].

prepared oxADan contains a low-molecular weight species, which could be a mono- or dimer, and a ~35kDa oligomer. Protofibrils and then filaments and mature fibrils are formed over 10-15 days as the low-molecular weight species disappears. Unlike oxABri, for which increasing concentration results in faster kinetics [548], ThT-monitored oxADan fibrillation shows increasing lag time with increasing peptide concentration from 22 hours at 35μM to 94 hours at 140μM suggestive of one or more kinetically favoured off-pathway oligomeric species stabilised at higher peptide concentrations. EM and AFM of the mature fibrils reveals slender, straight approximately 4nm-wide fibrils without observable periodicity and composed of thinner, ~2nm-wide protofilaments (figure 26). In addition, the samples occasionally show annular forms with average diameters of 100nm diameter and 8-9nm in height, which is lower than observed for e.g. oxABri and α-synuclein although the morphology do not appear 'beaded' from lateral association of spheroids.

The similar pH-preference for oxidised ABri and ADan is interesting in the light of the distinct C-terminal elongations. ABri is predominantly polar with multiple charged side chains whereas ADan combines a hydrophobic stretch (figure 27) containing several phenylalanines with a charge-rich C-terminus. The shorter Bri peptide does not readily aggregate and is not related to any human disease suggesting that the elongations are solely responsible for the increased aggregation propensity. However, the fact that the two disease-related peptides form amyloid-like fibrils, albeit over a narrow pH range, despite their dissimilar properties implies that the wild type peptide contains latent amyloidogenic potential. This is consistent with the presence of two predicted aggregation-prone regions by the

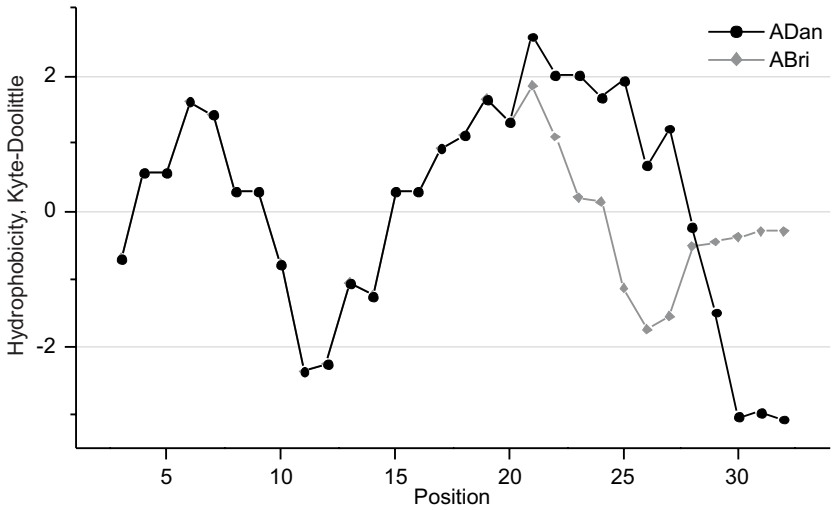

Figure 27. Hydrophobicity of ABri and ADan estimated using the ProtScale tool [551] (www.expasy.org/tools/protscale.html) with the Kyte-Doolittle scale [552] and a sliding window of 7. The Eisenberg scale [553] gives similar results.

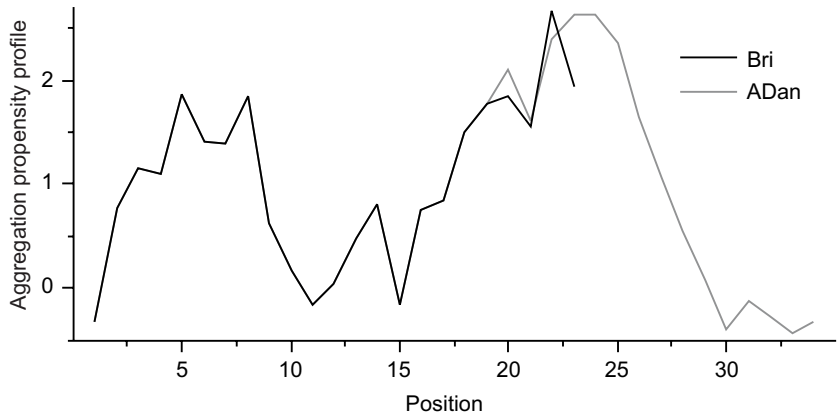

Figure 28. Prediction of β-aggregation-prone regions by the Zyggregator method at pH 7.5 [263, 554, 555].

Zyggregator method [263, 555, 556] (figure 28.A) at positions 3-8 and 18-23 that are shared with the ADan peptide.

Whereas oxADan does form amyloid-like fibrils over a narrow pH-range, reduced ADan (redADan) has not been induced to form fibrils. Freshly prepared samples at pH 4.8 contain a range low-molecular mass oligomers [551]. Ageing results in formation of spherical amorphous aggregates that are 30-40nm in height and lack structural features. Simultaneously, the oligomeric species disappear. However, even fresh samples contain insoluble material. As expected, the formation of amorphous aggregates by redADan occurs significantly faster than ordered fibril formation by oxADan. At higher pH (7.4), a non-covalent dimer and a higher-molecular mass oligomer (Mr ~70kDa) dominate for both oxADan and redADan. Over several weeks, spherical species and later electron-dense larger aggregates are formed in a manner similar to oxABri (figure 29) although aggregated oxADan shows mild birefringence after CR binding [557].

In contrast to the similar aggregational properties of the oxidised forms, reduced ABri and ADan have remarkable differences. redADan readily aggregates at slightly acidic and neutral pH whereas redABri remains in solution [548, 551]. ADan contains fewer charged residues than ABri despite a similar net charge and the presence of two histidine residues likely results in a more abrupt charge transition around pH 6. As a consequence, the aggregation appears to be chiefly driven by the presence of the extended hydrophobic region at positions 17-27 that, com-

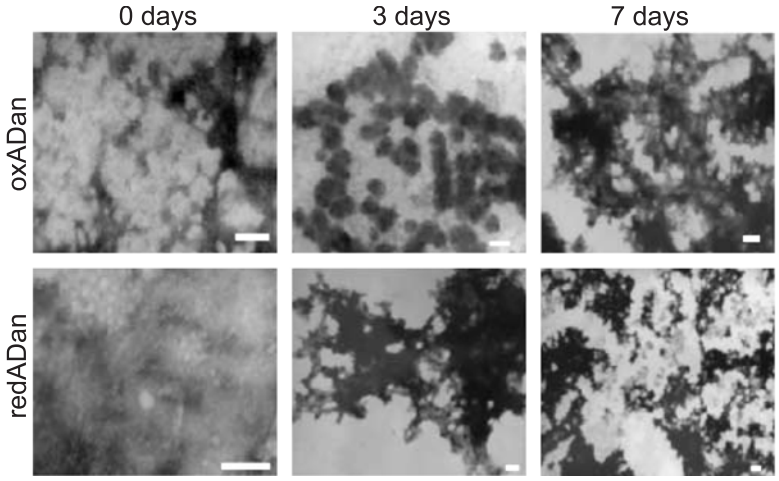

Figure 29. TEM images of ageing oxADan and redADan at pH 7.4. Adapted from [556].

bined with high β-structure propensity, results in either β-aggregation or fibrillation. The presence of the disulphide bond appears to favour fibrillation over segregation in amorphous aggregates in competition with charge effects in a similar manner as for ABri, possibly due to formation of a similar misfolding nucleus.

Perhaps the most striking difference between ADan and ABri is that while redABri is snows minimal toxicity in SHSY-5Y assays, redADan is more toxic than oxADan at low concentration in both SHSY-5Y and neuro2a cell assays and induces marked caspase activation [551, 557]. At higher concentration, the oxidised and reduced form appear equally toxic. Additionally, redADan is also more toxic than oxABri. The low or absent cytotoxicity for non-oligomerising and non-aggregating species, Bri and redABri, and the higher toxicity for fresh samples containing predominantly oligomeric species is in agreement with the oligomer hypothesis of cytotoxicity. The absence of the restricting disulphide bond for redADan allows higher conformational freedom and the high toxic potential of redADan could be ascribed to an alternative, more toxic conformation.

DISCUSSION

Presentation and discussion of Papers 1 and 2

3

3.1 Introduction to Paper 1

Nesgaard, L., Vad, B., Christiansen, G., Otzen, D. Kinetic partitioning between aggregation and vesicle permeabilization by modified ADan. *Biochim Biophys Acta* (2009) 1794 p. 84-93.

The identification of the ABri and ADan peptides in FBD and FDD deposits is a very recent discovery, which may explain why our understanding of their biophysical characteristics is still relatively limited. Certainly, when compared to the volume of work on Aβ and α-synuclein, chromosome 13 dementias appear decidedly underrepresented although it must be admitted that they are not only rare diseases but, in the case of FDD, among the rarest of diseases. Nonetheless, they offer an interesting alternative to Aβ as model systems of aggregational behaviour. Chromosome 13 dementias and AD share many similarities such as parenchymal preamyloid and amyloid deposits, neurofibrillar tangles, cerebral amyloid angiopathy and extensive inflammation. Despite being dissimilar in sequence, ABri/ADan and Aβ can associate to oligomers and fibrils through a comparable series of events and are capable of forming transmembrane channels.

Of the two peptides, ADan is by far the least investigated despite having a number of highly interesting properties. Firstly, despite being the most likely causative agent of a highly aggressive amyloid disease with remarkably early onset, ADan does not fibrillate readily *in vitro*. Secondly, while the *in vivo* redox state of ADan is not known, it has been speculated that it is the reduced form of the peptide (redADan), which circulate in plasma. redADan is also the most toxic to cultured neurons. Conversely, only the oxidised peptide (oxADan) has been induced to form amyloid-like fibrils. Accordingly, the conditions under which ADan can be induced to form fibrils are associated with significantly lower cytotoxicity than conditions that favour production of oligomers and large, presumably amorphous aggregates. This is entirely in keeping with the hypothesis that amyloid toxicity is mediated by toxic oligomers and in line with the observation of transmembrane channels with similar properties as those described for Aβ and other well-known amyloidogenic peptides [5, 558]. The cyclisation of cysteines 5 and 22 effectively constrains the structure while the linear peptide has a wider field of

available conformations. It is likely that the variation in aggregational propensity for oxADan and redADan reflects structural differences at the monomer level. However, the structural properties of redADan along the assembly pathway and of the mature aggregates themselves are largely unknown. A number of questions can be posed as a consequence of these reflections: Is it possible to delineate a mechanism of assembly for the non-amyloid aggregates of the linear ADan peptide? What morphologies can be observed during aggregation and what are their structural properties? What, if any, similarities exist with other know fibrillation or aggregation processes? Finally, in light of the higher cytotoxicity, is redADan able to interact with or permeabilise membranes and in which form of the peptide does such interaction take place? The aim of the present work was to answer these questions in part or in full, but initial observations of the redox behaviour of the redADan peptide in solution led me to alter my approach somewhat.

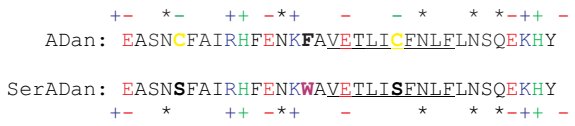

Figure 30. Primary structure of SerADan peptide. Red, negative charge; blue, positive charge; green, neutral or positive in the mid-pH region; yellow, cystein; *, asparagine and glutamine; underlined, hydrophobic region.

3.1.1 SerADan, a linear ADan variant

The experimental protocol called for ageing of samples over a period of days to weeks prompting concern that prolonged ageing and frequent aliquot removal could result in intramolecular oxidation or intermolecular cross-linking. Stock solutions of redADan were prepared in 10M urea or 6M guanidine to limit the presence of aggregate seeds prior to use, but despite the presence of powerful chaotropes, the concentration of redADan steadily dropped as small amounts of insoluble aggregates formed. Their low concentration and the presence of urea or guanidine prevented examination of secondary structure or morphology, but the addition of dithiothreitol (DTT) limited aggregation without abolishing it entirely suggesting that the aggregates were cross-linked *via* intermolecular disulphide bonds. To ensure that the peptide remained in the linear form, thereby preventing artefacts brought on by small amounts of oxidised monomer or cross-linked oligomers, I designed an alternative peptide termed SerADan (figure 30) by replacement of the two cysteines with serine (C5S, C22S), which decisively eliminated the intramolecular disulphide bond. Additionally, phenylalanine 15 (F15W) was substituted with tryptophan. The aim was to obtain a higher intrinsic fluorescence and to incorporate a polarity-sensitive probe in the central region of the peptide where packing into large aggregates could conceivable be monitored. As discussed in section 1.3.5, the importance of phenylalanine in stabilisation of the fibril structure has been observed for fibril of NFGAIL and ACP due to π-stacking or its inherent β-sheet propensity and hydrophobicity. However, the β-sheet propensity is essentially preserved and the previously described redADan aggregates are amorphous so the additional bulkiness of the larger tryptophan side chain could conceivably be accommodated within the structure.

The cysteine-to-serine and phenylalanine-to-tryptophan substitutions are largely conservative under the assumption that cysteine is uncharged, but lead to an overall

Pairing	Energy	Length	Segment 1	Segment 2	Orientation
1	-6.99347	23	6-28	6-28	parallel
2	-6.84909	12	17-28	17-28	parallel
3	-6.84653	22	6-27	6-27	parallel

Table 10. Prediction of aggregation-prone SerADan segments by the PASTA algorithm.

reduction in hydrophobicity and β-sheet propensity, which could alter the aggregation propensity. To estimate the effect of the substitutions, the original and substituted variants were assessed using the four prediction methods Zyggregator [263, 555, 556], TANGO [258, 265, 559], AGGRESCAN [262] and PASTA [266, 560] (figure 31.A, B-C, D and table 10, respectively). The three predictors of aggregation-prone regions give strikingly similar results for ADan, predicting a low-value region at approximately positions 3-8 (SNCFAI) and a region of higher propensity at positions 18-27 (ETLICFNLFL) with the exception of TANGO, which does not predict the former region. As expected, the substitutions lower the predicted aggregation propensity for both regions, although Zyggregator eliminates the first region altogether. The predictions show little variance with pH and similar observations can be made for variations in concentration (10-50μM) and ionic strength (0.05-0.15M) when using the TANGO algorithm for which these values can be specified (not shown).

For SerADan, the predicted aggregation-prone region (ETLISFNLFL) overlaps with the hydrophobic region (VETLISFNLF, see also section 2.3.2), which is asymmetrical and surrounded by charged and polar stretches containing several

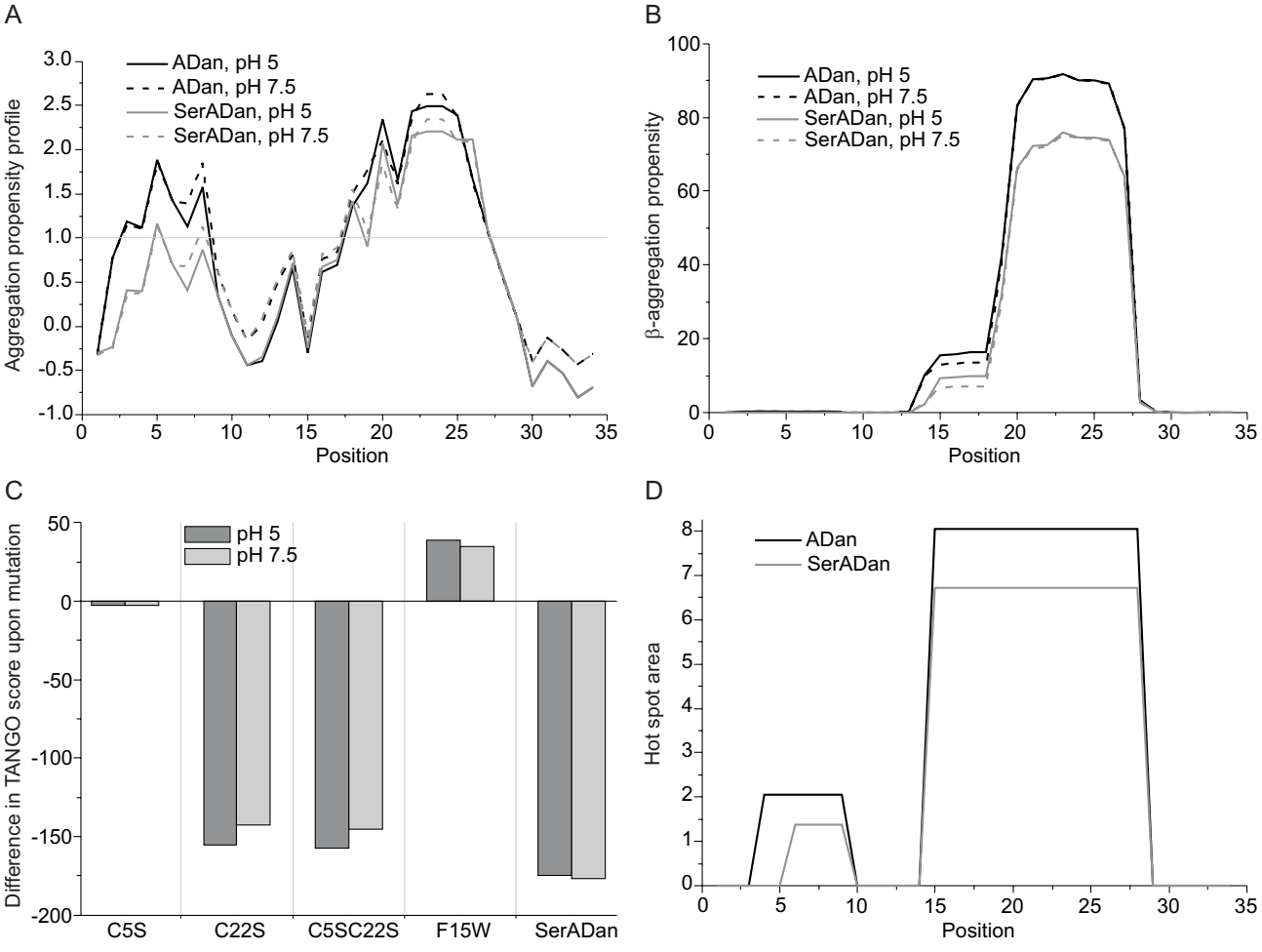

Figure 31. Prediction of aggregation-prone regions in SerADan by various prediction methods: Zyggregator (A), TANGO (B-C), AGGRESCAN (D).

asparagines and a single glutamine residue. These amino acids have been implicated in stabilisation of continuous β-sheets through the 'polar zipper'. By comparison, the PASTA algorithm return parallel orientations of similar energies suggesting a preference for β-sheet self-association in the parallel orientation. Interestingly, the asymmetric position of the non-polar region shows similarities to the properties of longer Aβ peptides, which assemble into fibrils with parallel interstrand orientation. Overall, SerADan appears to retain a strong if somewhat lower propensity for β-aggregation when compared to the linear redADan.

3.1.2 Methods for characterisation of aggregation

Describing the mechanistic and structural characteristics of SerADan aggregation required observation of secondary and tertiary structure by time-resolved and static techniques as well as particle size and overall morphology of the formed species (table 11). The F15W substitution allowed the use of intrinsic peptide fluorescence as a probe of peptide environment and thereby indirectly of tertiary structure in solution [561]. The situation is somewhat more complex in the presence of lipids since spectral changes observed during shielding of the Trp from the aqueous environment may be ascribed to structural changes or burial of the aromatic residue within the membrane. Intrinsic Trp fluorescence was monitored either by recording full emission spectra at a fixed excitation wavelength (290nm) at various time-points during aggregation or as time-resolved measurements in second- or minute increments at fixed excitation and emission (290 and 350nm, respectively). Similarly, information regarding particle size was obtained by dynamic light scattering [562] by measurements in minute intervals although this method is particularly sensitive to particulate matter, e.g. dust, which occasionally led to excessive noise despite careful buffer filtering and centrifugation of peptide stocks.

Secondary structure was monitored by a combination of three techniques. Attenuated total reflection FTIR (ATR-FTIR) is a powerful tools for secondary structure analysis [563, 564], but was used exclusively for end-point measurements of mature aggregates because of its poor suitability for time-resolved studies[8]. CD is useful for time-resolved single-wavelength measurements as well as estimation of secondary structure from spectra [564-566] but ill-suited for large aggregates due to non-uniform concentration throughout solution and light scattering effects. When applied to SerADan aggregates, the method showed significant variability in signal intensity and noise between individual scans for aged samples. In addition, the acquisition of spectral information at high energies is limited by the presence of salts, urea and other contaminants. While some inferences could be made about secondary structure from spectra obtained from the commercially available Jasco J-810 instrument (Jasco, Hachioji, Tokyo, Japan), insufficient spectral data prevented an actual estimate of secondary structure content. The use of synchrotron UV radiation, with its much higher intensity, allows spectral acquisition at higher energies and the results obtained by this method

8 Due to interference from urea and salts, aggregates were washed in milliQ water prior to spectral acquisition. The aggregates were stable in structure and morphology over several days under these conditions.

will be discussed further in section 3.4. The secondary and supramolecular structure of mature fibre-like aggregates were also examined by X-ray fibre diffraction [97], which was kindly performed by Christian Beyschau Andersen at the Protein Structure and Biophysics group, Novo Nordisk A/S. However, the presence of salts and the relatively low signal intensity limited the data quality.

The morphology of amorphous and structured aggregates was observed by EM at several time points during assembly. The extended time (~10 minutes) required for sample preparation at each time point results in poor resolution in time, but the method does nonetheless offer a snapshot of the aggregate population during assembly. AFM was used for corroboration of morphological properties. EM and AFM are both powerful methods, but while the shapes and sizes of aggregates can be observed at good resolution [77, 567], it must be stressed that the images offer little or no information about the exact nature the structures. The methods are therefore susceptible to numerous artefacts from presence of salts, lipids, dust and other contaminants as well as method-specific concerns, e.g. sample deformation and tip broadening effects for AFM. The interpretation of images must be performed with careful consideration of such artefacts.

Table 11. Methods for characterisation of SerADan aggregation and lipid interaction.

Method	What is detected?	Ref.
Intrinsic tryptophan fluorescence	Changes in Trp environment. Reports on tertiary structure.	[561]
Liposome calcein release	Calcein trapped in liposomes at self-quenching concentration. Release into solution by liposome permeabiliation abolishes self-quenching.	[568]
Congo Red absorbance	Amount of CR bound to fibril. Specific for amyloid.	[9]
Thioflavin T fluorescence	Amount of ThT bound to fibril. Specific for amyloid.	[52, 53]
Electron microscopy (EM)	Morphology.	[567]
Atomic force microscopy (AFM)	Morphology. Always run in contact mode on washed and dried samples.	[77]
Dynamic light scattering (DLS)	Particle size. Sensitive to pollutants, e.g. dust particles.	[562]
Fourier transform IR (FTIR)	Secondary structure. Practical for dried, insoluble samples but sensitive to salt and other solutes.	[563-564]
Circular dichroism (CD)	Secondary structure. Sensitive to some solutes. Scattering effects from large particles.	[564-566]
Synchrotron radiation CD (SRCD)	Secondary structure. High-intensity light source yields good signal/noise ratio and spectral acquisition at higher energies.	[607]
X-ray fibre diffraction	Secondary and supramolecular organisation. Sensitive to presence of salts and other solutes.	[97]

The interaction of peptide and lipids was examined using extruded large unilamillar vesicles of the zwitterionic 1,2-dioleoyl-*sn*-glycero-3-phosphocholine (DOPC) and anionic 1,2-dioleoyl-*sn*-glycero-3-[phospho-*rac*-(1-glycerol)] (DOPG) *via* Trp fluorescence, DLS, AFM and calcein release. The latter method utilised the the fluorophore calcein, which is trapped within the liposomes at high, self-quenching concentrations [568]. Permabilisation of the vesicles led to release of the fluorophore into the surrounding solution and increased intensity. For comparison, total release was obtained using the detergent Triton X-100 and the permeabilisation efficiency expressed as the percentage of total calcein release.

Early in the experimental phase it became clear that an efficient protocol was required for disaggregation of the SerADan peptide prior to use. The presence of small pre-formed nuclei capable of effectively seeding fibrillation makes the ag-

gregation process highly stochastic [165, 569]. Indeed, the time-course of aggregation of SerADan freshly dissolved from powder form was observed to vary greatly. The halogenated alcohol 1,1,1,3,3,3-hexafluoropropan-2-ol (HFIP) has been used for disaggregation of the ABri and ADan peptides [548, 551] but proved insufficient for suppression of the stochastic aggregation of SerADan. Instead, disaggregation was accomplished by overnight incubation in 10M urea, which was highly effective. However, urea decomposes in solution to isocyanic acid with resulting carbamylation of arginine, lysine and the polypeptide N-terminus [570, 571]. Consequently, urea was prepared fresh, the peptide stocks fast-frozen in aliquots of appropriate size and only thawed immediately prior to usage.

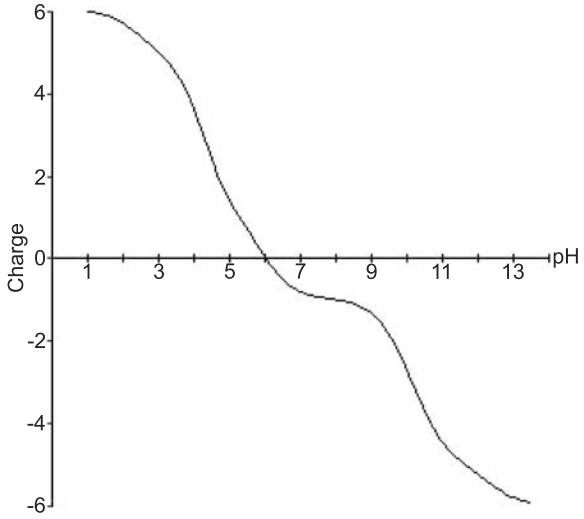

Figure 32. Theoretical titration curve of SerADan (www.iut-arles.up.univ-mrs.fr/w3bb/d_abim/compo-p.html).

Irrespective of the used technique, the aggregation process was in all cases initiated by dilution of the peptide from 10M to 0.2M urea in sodium phosphate or Tris buffer at pH 5.0 and 7.5, respectively. It should be mentioned acceleration of fibrillation by urea has been described [572], but at significantly higher concentrations (5M). The lower pH value was chosen with reference to the pH interval where oxADan has been induced to form fibrils. The predicted charge is +1 at pH 5.0 and the higher pH value was chosen to give an overall peptide charge of -1 after examination of the theoretical titration curve (figure 32).

Biochimica et Biophysica Acta 1794 (2009) 84–93

Contents lists available at ScienceDirect

Biochimica et Biophysica Acta

journal homepage: www.elsevier.com/locate/bbapap

Kinetic partitioning between aggregation and vesicle permeabilization by modified ADan

Lise Nesgaard [a], Brian Vad [a,b], Gunna Christiansen [c], Daniel Otzen [a,b,*]

[a] Department of Life Sciences, Aalborg University, Sohngaardsholmsvej 49, DK-9000 Aalborg, Denmark
[b] Interdisciplinary Nanoscience Centre, Department of Molecular Biology, University of Aarhus, Gustav Wieds Vej 10C, DK-8000 Aarhus C, Denmark
[c] Institute of Medical Microbiology and Immunology, The Bartholin Building, University of Aarhus, DK-8000 Aarhus C, Denmark

ARTICLE INFO

Article history:
Received 18 June 2008
Received in revised form 19 September 2008
Accepted 28 September 2008
Available online 15 October 2008

Keywords:
Familial Danish Dementia
Non-amyloid aggregate
β-sheet structure
Oligomer
Vesicle permeabilization

ABSTRACT

The neurodegenerative illness Familial Danish Dementia (FDD) is linked to formation and aggregation of the 34-residue ADan peptide, whose cytotoxicity may be mediated by membrane interactions. Here we characterize the derived peptide SerADan, in which the two cysteines found in ADan have been changed to serines to emulate the reduced peptide. SerADan aggregates rapidly at pH 5.0 and 7.5 in a series of conformational transitions to form β-sheet rich fibril-like structures, which nevertheless do not bind amyloid-specific dyes, probably due to the absence of organized β-sheet contacts. Aggregation is prevented at neutral/acidic pH and low ionic strength by anionic lipid vesicles. These vesicles are permeabilized by monomeric SerADan assembling on the membrane to form stable β-sheet structures which are different from the solution aggregates. In contrast, solution ageing of SerADan first reduces and then abolishes permeabilization properties. The competition between lipid binding and aggregation may reflect bifurcating pathways for the ADan peptide *in vivo* between accumulation of inert aggregates and formation of cytotoxic permeabilizing species. Our work demonstrates that non-fibrillar aggregates can assemble in a series of steps to form a hierarchy of higher-order assemblies, where rapid formation of stable local β-sheet structure may prevent rearrangement to amyloid proper.

1. Introduction

Familial Danish Dementia, first described in 1970 [1] as *heredopathia ophthalmo-oto-encephalica*, is an example of a degenerating neurofibrillar disease of the same type as the more common and better characterized Alzheimer's disease (AD) [2]. The illness involves progressive dementia and is fatal with death occurring at the age of 50–60. The earliest clinical manifestation is cataract formation before the age of thirty followed by progressive hearing loss and cerebellar ataxia. A 34-amino acid peptide, ADan, has been identified in circulation and in plaques in post-mortem tissue samples [2]. In contrast to the Aβ aggregates formed in AD, these plaques appear to be predominantly pre-amyloid in nature with amorphous morphology containing sparse and disperse fibrils, and are negative for staining with the amyloid-specific dyes Congo red and thioflavin S [3]. The ADan peptide is formed due to a decamer duplication in the 3′-end of the *Bri* gene causing a frameshift and generating a larger-than-normal precursor protein [2]. C-terminal degradation of the precursor by furin yields the 34-amino acid ADan peptide rather than the native 23-amino acid Bri peptide [4] (Fig. 1). Both wild-type Bri and mutant ADan peptide circulate in plasma, but only ADan has been found to accumulate in tissue [5]. The oxidation state of the two cysteines in serum-circulating and plaque-deposited ADan is controversial, with some groups claiming it to be reduced [6] and others oxidized between Cys5 and Cys22 [7]. The deposited form of the peptide is highly heterogeneous [7], with the N-terminal glutamate modified to pyroglutamate in a large percentage of the peptide chains, which are also N- and C-terminally processed at position 3, 28 and 33.

Previous studies of the aggregational tendencies of ADan in both the reduced and oxidized forms [8,9] did not observe classical fibril-formation of the type routinely observed for Aβ and similar fibrillation protein peptides under physiological conditions. Formation of amyloid-like material was only possible for the oxidized form of ADan under mildly acidic conditions (pH 4.8) and after extensive ageing (10–15 days). At other experimental condition, including a wide range of pH values and peptide concentrations, oxidized and reduced ADan were found to readily aggregate into various amorphous structures. However, studies using SH-SY5Y or neuro2a cell lines showed that the reduced form of ADan had higher cytotoxicity than the oxidized form and led to marked caspase activation [8]. The distinct prevalence of pre-amyloid over amyloid deposits makes ADan an interesting case

Abbreviations: AD, Alzheimer's Disease; DLS, Dynamic light scattering; DOPC, 1,2-Dioleoyl-*sn*-glycero-3-phosphocoline; DOPG, 1,2-Dioleoyl-*sn*-glycero-3-[phospho-*rac*-(1-glycerol)]; FDD, Familial Danish Dementia; IAPP, Islet Amyloid Polypeptide

* Corresponding author. Interdisciplinary Nanoscience Centre, Department of Molecular Biology, University of Aarhus, Gustav Wieds Vej 10C, DK-8000 Aarhus C, Denmark. Tel.: +45 89 42 50 46; fax: +45 98 12 31 78.
E-mail address: dao@inano.dk (D. Otzen).

1570-9639/$ – see front matter © 2008 Elsevier B.V. All rights reserved.
doi:10.1016/j.bbapap.2008.09.021

```
wtBri     EASNCFAIRHFENKFAVETLICS
ADan    pEASNCFAIRHFENKFAVETLICFNLFLNSQEKHY
SerADan   EASNSFAIRHFENKWAVETLISFNLFLNSQEKHY
          #    *          ¤       *------------
```

Fig. 1. Primary structure of wildtype Bri (wtBri), ADan and SerADan peptides. #: Location of pyroglutamate found in physiological aggregates of ADan peptide. *: Mutation of cysteine to serine. ¤: Mutation of phenylalanine to tryptophane. -: Elongation found in physiological aggregates of ADan peptide.

study, that may provide further insight into the nature of aggregate cytotoxicity. Here we examine the aggregational properties of a modified ADan-like peptide, termed SerADan, designed to prevent any oxidation by replacing Cys5 and Cys22 with Ser. Besides mimicking the reduced state which has been shown to be more neurotoxic than the oxidized state in cell cultures [8], it also avoids the formation of covalent crosslinks that complicate *in vitro* studies of ADan. Additionally, the phenylalanine in position 14 was replaced with the fluorescent probe tryptophan, which may also be considered a conservative mutation. To address charge effects, the peptide was investigated at both the approximately neutral pH-value 7.5 and the slightly acidic pH 5.0, which is similar to the pH-value at which the oxidized variant form amyloid-like structures. These two pH values are on either side of the estimated isoelectric point of pH 6.05.

In order to elucidate the possible mechanism of cytotoxicity, we investigated the direct interaction of SerADan with lipid membranes. Several fibrillation-prone peptides are known to interact with anionic lipid membranes but with different outcomes. Anionic membranes stimulate fibrillation of Islet Amyloid Polypeptide (IAPP) [10,11], while $A\beta_{40}$ is protected from fibrillation when fully inserted in anionic membranes but experiences accelerated fibrillation when surface bound [12]. Interestingly, zwitterionic lipids may also reverse fibrillation of amyloid and lead to cytotoxic species [13]. The anionic lipid phosphatidylserine has been shown to trigger fibril formation for a number of peptides and proteins including lysozyme, insulin and transthyretin [14]. In contrast, annular structures that exhibit heterogeneous single-channel conductance have been observed for ADan bound to zwitterionic phosphatidylcholine membranes in a manner highly similar to those of other fibrillation-prone peptides *e.g.* α-synuclein and Aβ [15]. We consequently examined peptide-membrane interactions using fluorescence spectroscopy and calcein release assays for vesicles of anionic and zwitterionic phospholipids.

2. Materials and methods

2.1. Materials

SerBri (EASNSFAIRH FENKWAVETL ISS) and SerADan (EASNSFAIRH FENKWAVETL ISFNLFLNSQ EKHY, in which Cys5 and Cys22 found in ADan are replaced by Ser) peptides were obtained >90% pure (EZBiolab Inc., Westfield, IN, USA). 1,2-Dioleoyl-*sn*-glycero-3-phosphocoline (DOPC) and 1,2-Dioleoyl-*sn*-glycero-3-[phospho-*rac*-(1-glycerol)] (DOPG) were from Avanti Polar Lipids (Alabaster, AL). Thioflavin T and other chemicals were from Sigma (Sigma-Aldrich, St. Louis, MO).

2.2. Preparation of SerADan samples

Freeze-dried SerADan peptide was dissolved in 10 M urea and allowed to disaggregate overnight at room temperature to obtain a monodisperse monomeric population in the random coil conformation according to circular dichroism. Concentration was monitored by absorbance at 280 nm (extinction coefficient estimate obtained using the ProtParam tool at http://www.expasy.org) and found to be within 5% of the weighed amount. Stock concentration was adjusted to 2.5 mM. Stock aliquots were flash frozen and stored at −80 °C. They were thawed and centrifuged immediately before use. Samples for aggregation were prepared by freshly thawed peptide stock to the appropriate concentration (10–75 μM) in either 50 mM sodium acetate (pH 5.0) or 50 mM Tris (pH 7.5) with or without 100 mM NaCl.

2.3. Preparation of liposomes and calcein release assay

Vesicles were prepared from stock solutions of lipids dissolved in chloroform and dried overnight in vacuum. Lipids were then resuspended by vortexing in milliQ water to a final concentration of 10 g/L (~14 mM), exposed to at least seven cycles of freezing in liquid nitrogen, followed by thawing in a 50 °C water bath, before extrusion through a 100 nm pore filter 12 times using a 10 mL thermo barrel extruder (Northern Lipids, Vancouver, Canada). Vesicle size was verified by DLS and vesicles were used the same day they were made.

Calcein-containing vesicles, which were made immediately before each experiment, were prepared similarly, except that lipid was dispersed in 1.5 mL calcein-containing buffer (70 mM calcein, 50 mM Tris, pH 7.5) prior to freeze–thawing and extrusion. Vesicles were isolated from the calcein buffer by filtration through a pre-equilibrated Pharmacia PD-10 column and small aliquots of the collected fractions were monitored by fluorescence (excitation 490 nm, emission 500–600 nm) using Triton X-100 to obtain release of calcein and thereby increased fluorescence of vesicle-containing fraction(s). Those with the highest signal-to-background ratio were selected for further use. The fluorescence measurements were conducted on a Cary Eclipse Fluorescence Spectrophotometer (Varian, Palo Alto, CA) using a 10 mm quartz cuvette with magnetic stirring. The vesicles were diluted in 50 mM Tris buffer pH 7.5 to a concentration of ~0.017 mg/mL (21 μM), yielding a maximum signal of around 90 U under these settings. For ageing experiments, SerADan was diluted from a 2.5 mM stock in 10 M urea to 10 μM peptide and 0.04 M urea in 50 mM Tris buffer pH 7.5. At different time points, 10 μL of this solution was diluted 10-fold to 1 μM SerADan in the presence of 21 μM calcein-filled vesicles and calcein release was monitored by measuring fluorescence emission intensity at 515 nm (excitation at 490 nm, 5 nm slits for both monochromators) every 11 s until it reached a plateau. Spectra were normalized with regards to maximum fluorescence, *i.e.* the fluorescence level achieved when 1% of Triton X-100 is added. For permeabilization experiments with different concentrations of SerADan, the peptide was first diluted from 2.5 mM stock in urea to 50 μM peptide and immediately diluted to the appropriate concentration in the presence of 21 μM calcein vesicles.

2.4. Circular dichroism

Circular dichroism (CD) spectra were recorded on a Jasco J-810 spectropolarimeter (Jasco, Hachioji, Tokyo, Japan; 110QS cuvette, Hellma, Müllheim, Germany) using averaging over 10 scans, resolution 0.1 nm and 10–50 μM peptide.

2.5. Fourier transform infrared spectroscopy

Spectra were recorded on a Bruker Tensor 27 infrared spectrometer (Bruker Optik GmbH, Ettlingen, Germany) with a Specac Golden Gate single-reflection ATR unit (Specac Ltd., Orpington, UK). Aged aggregates were washed twice in milliQ water and isolated by centrifugation. Three independent samples were investigated (64 scans, 2 cm^{-1} resolution). The secondary structure was estimated using OPUS 5.5. If needed, the presence of water vapor was corrected for by subtraction of a fresh vapor spectrum or the inbuilt atmospheric compensation function. Peaks were assigned from the 2nd derivative and deconvolution of spectra [16]. The non-deconvoluted spectra were fitted using the Levenberg–Maquardt method, the areas of individual peaks calculated and the secondary structure content estimated.

2.6. Fluorescence spectroscopy

Time-resolved fluorescence spectroscopy was performed on a Cary Eclipse fluorometer (Varian, Palo Alto, CA), excitation at 290 nm and emission measured at 350 nm. Freshly thawed peptide stock was diluted to 10–50 μM in buffer with or without lipid (LP 0.1–10). Aggregation was monitored for 30 min in 10 s increments and for the following 600–1200 min in 1 min increments. Initial reaction rates were calculated by linear regression as the slope of the timecurve over the initial 10 min. Emission spectra were obtained at start and at end points before and after vigorous agitation of the sample to resuspend sediments. Time resolved emission spectra were recorded similarly on a LS55 fluorometer (Perkin-Elmer, Wellesley, MA), excitation at 290 nm, emission 310 nm–390 nm.

2.7. Dynamic light scattering

Time-resolved estimates of the hydrodynamic radius were obtained by dynamic light scattering on a PDDLS/CoolBatch+90T system (Precision Detectors, Bellingham, MA). Buffers were filtrated to remove dust particles. Samples were prepared by dilution of freshly thawed and centrifuged peptide stock into buffer (50 μM peptide, 50 mM Tris, pH 7.5) with or without freshly prepared and centrifuged lipid vesicles (LP 0.1–10). Temperature was held at 22.5 °C and R_{hyd} estimates were obtained every 2–3 min.

2.8. Electron microscopy

Electron microscopy was performed as described [17] by placing 5 μL aliquots on 400-mesh carbon-coated, glow-discharged grids for 30 s followed by washing with distilled water and staining with phosphotungstic acid (pH 6.8). Samples were visualized using a Jeol 1010 transmission electron microscope. For time-based electron microscopy on the hour timescale, aliquots were removed directly from the aging sample. For longer experimental periods, the aliquots were flash-frozen in liquid nitrogen and stored at −80 °C.

3. Results

3.1. SerADan is sparsely soluble and quickly forms β-rich but non-amyloid aggregates

The serine-variant of the short non-toxic wildtype Bri peptide (SerBri) readily dissolves in dilute buffer to adopt a predominantly random coil-like structure when examined with circular dichroism (data not shown). In contrast, the longer SerADan peptide forms large, insoluble aggregates when diluted from 10 M urea to 0.2 M urea at pH 5.0 (Fig. 2) and 7.5 (Fig. 3) as shown by time-resolved electron microscopy. The aggregates can be observed within minutes of dilution (Figs. 2A–B, 3A) and have μm-scale dimensions, consisting of thin filaments that persist over the entire visualized time-span of 5 days (Figs. 2D, 3C, E). At pH 5.0, a more electron-dense and less organized morphology can be observed for samples obtained 19 min after dilution, but not for later time points. Smaller, transient amorphous structures were also present during the first hour of aggregation (Fig. 3B, shown for pH 7.5 only) but slowly disappeared. When studied by attenuated total reflection infrared spectroscopy (ATR-FTIR, Fig. 4A) the secondary structure of aged (12 h) and washed samples, which are structurally stable over a period of several days, appear rich in β-sheet with similar sheet content for pH 5.0 and 7.5 (34–36%). Circular dichroism spectra (Fig. 4B) show that β-structure with a characteristic minimum around 215 nm appears within a few minutes of dilution from the stock solution (within the dead-time of the measurement), suggesting that the peptide rapidly collapses into a β-rich structure in solution. Over time, the spectra diminish in intensity, particularly within the first 100 min of incubation (insert to Fig. 4B), but retain the overall β-sheet appearance. At pH 7.5 there is a lag phase of around 30 min before the ellipticity starts to decline, while the lag phase is absent at pH 5.0.

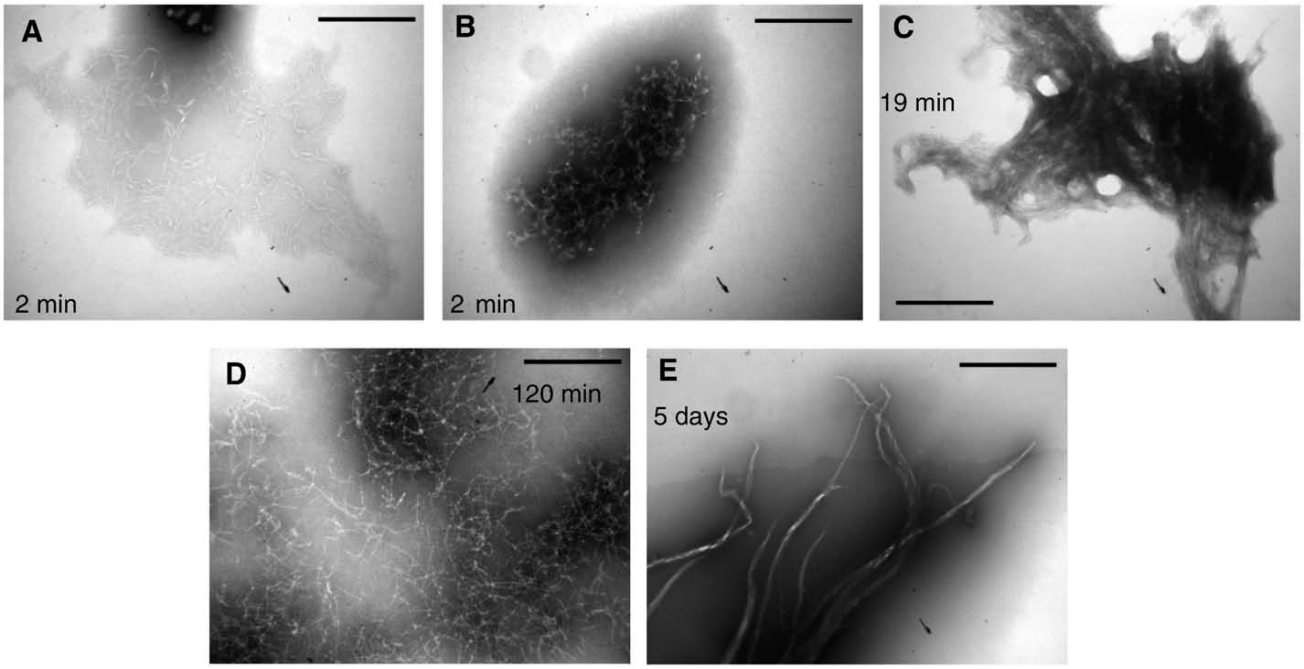

Fig. 2. Time-resolved electron micrographs of 50 μM SerADan at pH 5.0. Black bar corresponds to 400 μm. (A) Thin filaments observed within the method deadtime (2–3 min). (B) Same sample as A. but showing a more electron-dense morphology. (C) Sample obtained after 19 min showing dense, less organized morphology, which coexisted with the type of structures shown in B. (D) Sample obtained after 2 h and frozen for later imaging. Morphology consists of long, thin filaments. (E) Sample obtained and frozen after 5 days aging. The shown morphology coexists with thin filaments.

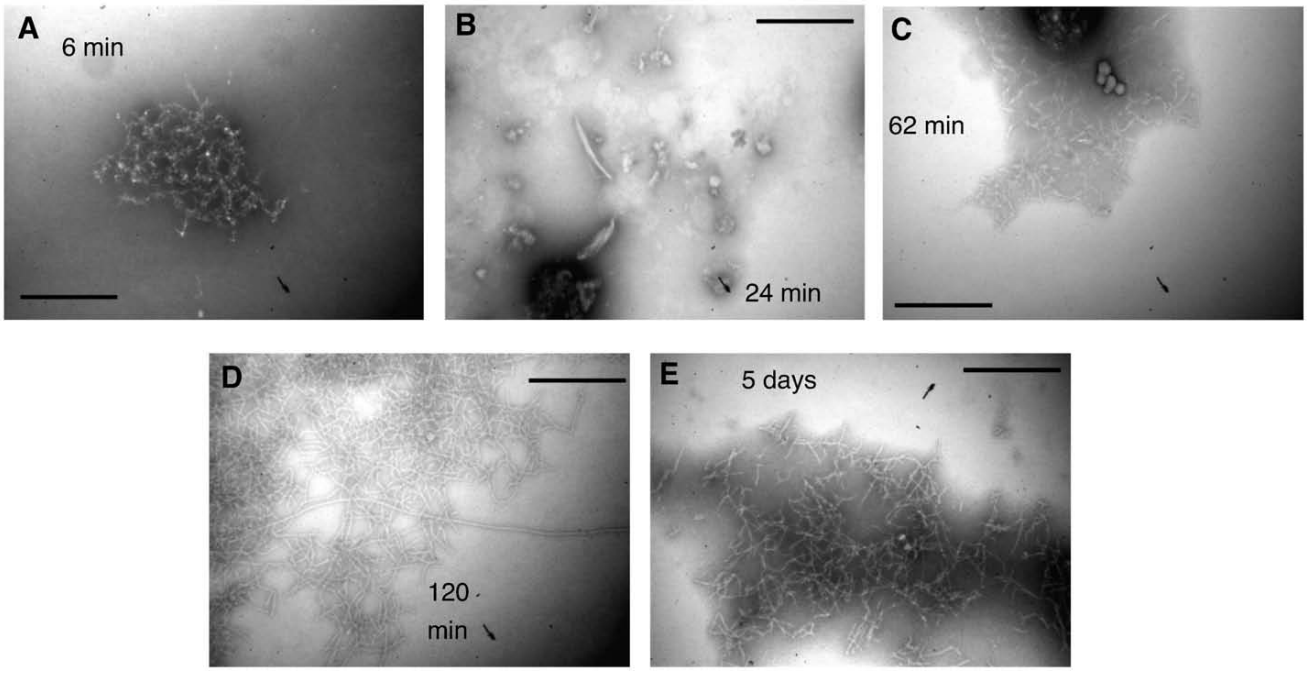

Fig. 3. Time-resolved electron micrographs of 50 μM SerADan at pH 7.5. Black bar corresponds to 400 μm. (A) Morphology after 6 min. (B) Amorphous structures observed after 24 min. Structures coexistent with structure of the type shown in A. (C) Sample obtained after 62 min contains filaments and amorphous elements. (D) Long, thin filaments of clear morphology obtained after 2 h and frozen for later imaging. (E) Sample obtained and frozen after 5 days aging. Thin filaments persist as dominating structure.

The fibril-like structure and β-sheet signature are amyloid hallmarks. However, no binding of Congo Red or Thioflavin T can be observed (data not shown), just as reported for wildtype ADan deposits [2,3]. This indicates a different arrangement of the β-structure within the observed filaments. Our previous X-ray fiber diffraction data show a strong signal at 4.76 Å arising from the distance between adjacent β-strands [18]. However, signals at 10–11 Å (which are strong in regular amyloid fibrils and reflect inter-sheet distances) are essentially absent for pH 7.5 aggregates and very diffuse for the pH 5.0 aggregates [18], indicating a lack of organized higher-order structure.

3.2. Time-resolved fluorescence data shows two distinct phases

The images obtained by EM show that the aggregates form within a very short time span of a few minutes. The Phe11Trp substitution provides a fluorescent probe to follow the time course of the aggregate formation (Fig. 5A).

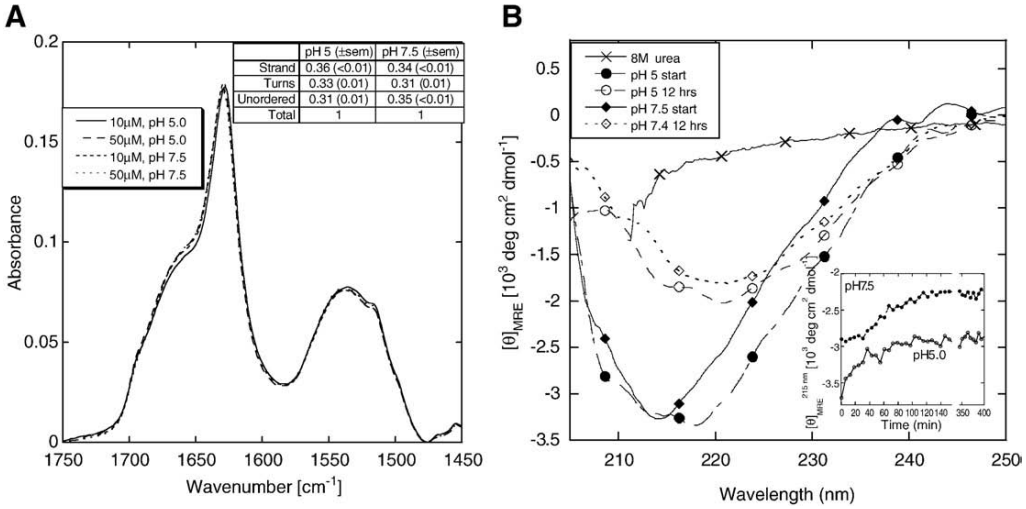

Fig. 4. Secondary structure of aggregated SerADan. (A) Fourier transform infrared spectroscopy of 10 and 50 μM SerADan at pH 5.0 and 7.5, aged for 12 h at 10 and 50 μM peptide. The aggregates were washed in water and found to be stable over several days. The secondary structure appears independent of pH and concentration. Table: Estimate of secondary structure content by curve fitting. (B) CD spectra of 50 μM SerADan in 10 M urea (no buffer) and at pH 5.0 and 7.5 after 50-fold dilution into 0.2 M urea. Immediately after dilution, there is a clear minimum around 215–220 nm, indicative of β-sheet structure. The spectra reduce in intensity over the next 12 h but retain minimum around 215–220 nm. Insert: change in molar ellipticity at 215 nm over time when 50 μM SerADan is diluted into 0.2 M urea from 10 M urea, indicating that most of the ellipticity change occurs over the first 100 min. Ellipticity levels for the two runs have been offset for clarity. Note the lag phase at pH 7.5 which is absent at pH 5.0.

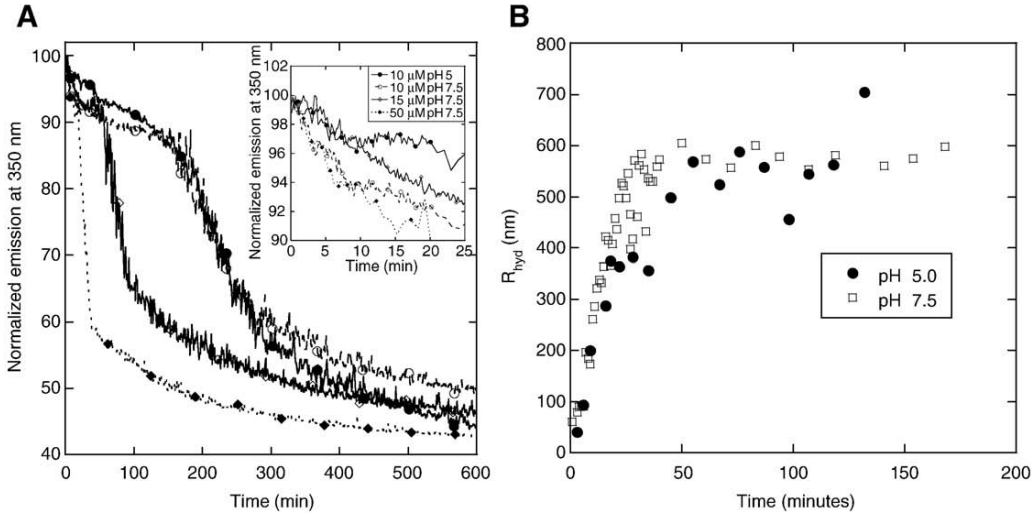

Fig. 5. Aggregation behavior of SerADan at pH 7.5 and 22.5 °C. (A) Time-resolved intrinsic fluorescence (excitation 290 nm, emission 350 nm) at 10 μM, 15 μM and 50 μM, respectively. An exponential decline of ~5–7% is followed by a linear decline of ~5%, a steep drop of ~30% and a slower decline of ~20%. Insert shows a blow-up of the first 25 min of the reaction. (B) Dynamic light scattering data for 50 μM SerADan at pH 5.0 and 7.5 followed over time. Note the immediate increase in particle size in contrast to the lag observed by CD and fluorescence.

When 10–50 μM SerADan is incubated at pH 7.5 and 22.5 °C and the fluorescence emission was monitored over time, we observe a rapid and only slightly concentration-dependent ~5–7% decline in the signal over the first 5–10 min, followed by a ~5% linear decline (~5%). After an additional 10–100 min (depending on concentration), there is a very steep decline over 10–100 min in emission down to ~60% of the initial fluorescence intensity, which slowly declines further by ~20% over the next 6–9 h. Incubation at pH 5.0 also leads to a similar 20% decline in signal although the change is somewhat slower (Fig. 5A, insert). In conjunction with the differences in the time-profile for the CD signal between pH 5.0 and 7.5 (Fig. 4B), this suggests subtle differences in the initial conformational changes at these two pH values. The rapid fluorescence phase completed within 5–10 min at pH 7.5 coincides with the formation of β-sheet structure within the dead-time of the recording of the first CD spectrum (Fig. 4B). The subsequent 5% signal change occurs over the next ~100 min at 10 μM peptide, and the rate of the linear decline (raw fluorescence emission intensity per time unit) scales with protein concentration with a slope of 1 in a log–log plot, indicating that this step does not involve a change in the molecularity of the SerADan aggregate formed at this stage (data not shown). However, the length of this phase (ending at the onset of the steep fluorescence decline) is shortened dramatically at 50 μM to around 15 min, indicating that the next step involves aggregation. In fact we have two observations that indicate that the large decline in emission to around 60% is simply caused by bulk sedimentation of aggregated material. Firstly, there is no decline if the experiment is performed with agitation, which prevents sedimentation (data not shown). Secondly, resuspension of the aggregates returns fluorescence to the plateau value reached after the first 20% decline in signal (data not shown).

Emission spectra recorded at different times at both pH-values reveals that change in fluorescence signal within the initial exponential phase and slow linear decline (prior to the sedimentation step) is due to changes in fluorescence intensity rather than a major shift in maximum emission wavelength, since we only observe a slight blue-shift from ~353 nm to ~350 nm (data not shown).

The rapid fluorescence decline to a 60% level (completed after 20 min at a concentration of 50 μM SerADan) is complemented by DLS data for 50 μM SerADan at both pH 5.0 and 7.5 which show an increase in particle size to a plateau level within 20–30 min (Fig. 5B). During this period there is no change in the CD signal at 50 μm SerADan (Fig. 4B insert). Rather, the slow decline in CD signal seen for 50 μM SerADan (Fig. 4B insert) coincides with the slower decay over several hundreds of seconds from ~60 to ~40% intensity after the rapid fluorescence decline. Thus there appears to be several phases in the sedimentation process, of which only the last one is detected by CD. As a reporter of tertiary and quaternary structure, Trp fluorescence is a more sensitive reporter of protein changes than CD signal and it is therefore not unexpected that more phases are revealed by the former method.

Early onset of formation of large aggregates and thereby sedimentation can also be triggered by addition of seeds of preformed aggregates, which is a well-known characteristic of batch fibrillation *in vitro*. Thus, addition of 1.5% seeds reduces the sedimentation half-time from around 200 to around 120 min, while 15% seeds have little further effect (data not shown).

3.3. SerADan interacts with the anionic lipid DOPG

Wildtype ADan is cytotoxic to the commonly used SH-SY5Y neuronal cell line [8,9] in both oligomeric and more extensively aggregated forms. The known interaction between cytotoxic peptides and cell membranes prompted us to study the membrane interactions of the SerADan peptide. Fibrillation of numerous proteins has previously been shown to be stimulated by the presence of anionic lipids [10–12,14] so we investigated the effect on aggregation by both the zwitterionic DOPC and anionic DOPG. While little interaction was observed with DOPC at both pH values (data not shown), DOPG interacted strongly with freshly diluted peptide. The presence of anionic lipid prevented the sedimentation of large aggregates (Fig. 6A). This effect was pronounced at even 1:10 lipid:protein ratios at pH 7.5 while 10:1 lipid:protein ratios were required at pH 5.0 (data not shown). For pH 7.5, the anti-sedimentation effect was abolished for all but the highest lipid concentration (LP 10) by the presence of 100 mM NaCl, indicating electrostatic forces as an important factor in the interaction. However, the lone tryptophan also appears involved in the interaction as the peptide fluorescence spectrum shows a clear blueshift from ~353 nm to ~340 nm when incubated with lipid (Fig. 6B insert). In contrast, the far-UV CD spectrum has a minimum around 210 nm (Fig. 6B) which is different from and more intense than that in the absence of lipid (Fig. 4B). Furthermore, it does not undergo any significant band shifts or intensity changes over time. Interestingly, the small pre-sedimentation exponential decay in emission (within the first 20 min, Fig. 5A) is not affected by lipids, suggesting

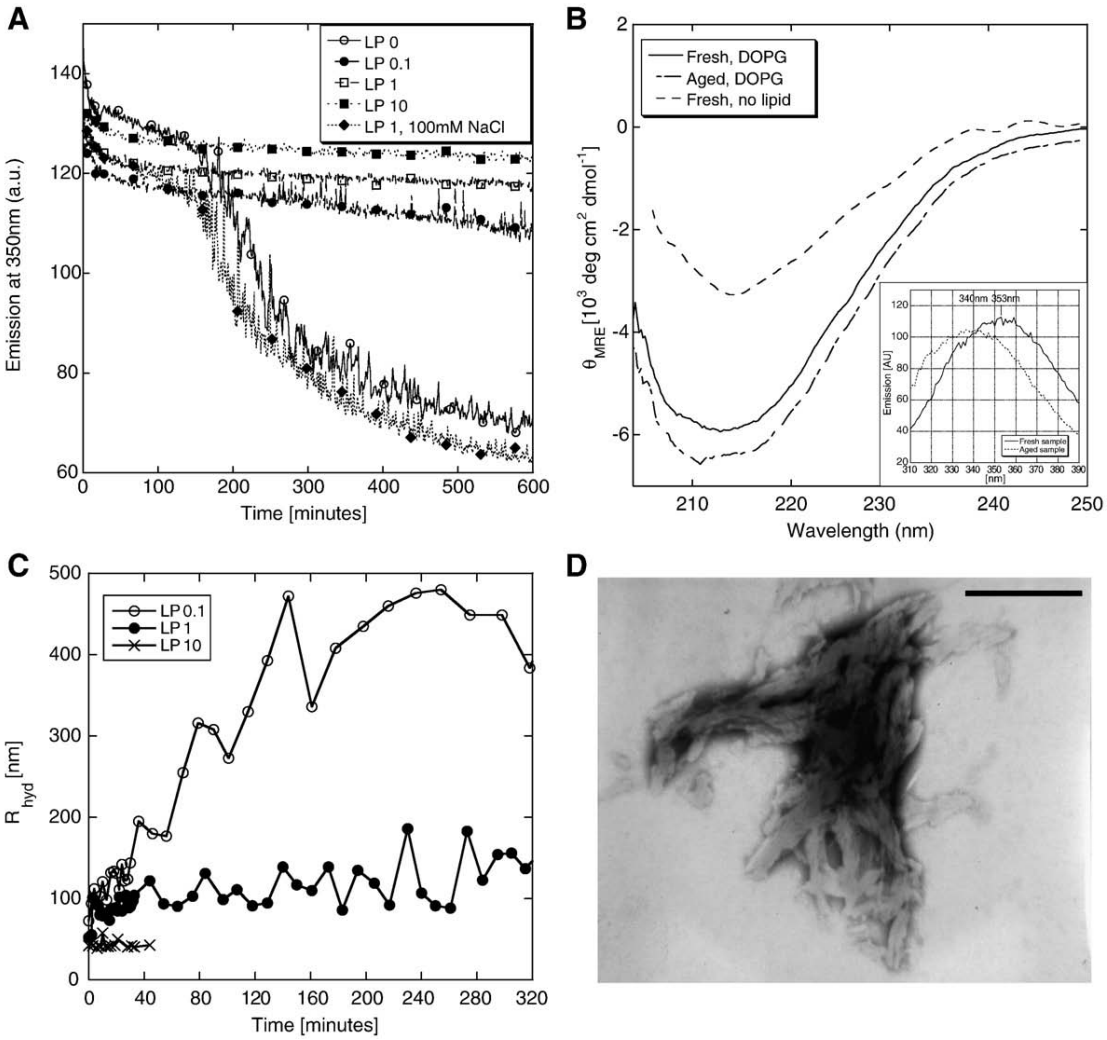

Fig. 6. Spectroscopic and microscopic investigations of SerADan lipid interactions at pH 7.5 and 22.5 °C. (A) The effect of anionic lipid (DOPG) at high and low ionic strength on the change in fluorescence signal (excitation 290 nm, emission 350 nm) of 10 μM SerADan over time. The presence of lipids prevents sedimentation but the effect is abolished by the presence of 100 mM NaCl at lipid-to-protein ratios (LP) of 1 and below. (B) CD spectra for fresh (immediately after dilution from stock in 10 M urea) and aged (12 h after dilution) SerADan (10 μM) in the presence of DOPG, LP 10 at pH 7.5 (no NaCl). Fresh spectrum in absence of DOPG (from Fig. 4B) included for comparison. Insert: Emission spectra showing significant blue-shifting. (C) Time-resolved DLS of 10 μM SerADan showing inhibition of aggregation at LP 1 and 10. (D) Electron micrograph of 50 μM SerADan with DOPG (LP 10) at pH 7.5 after 5 days aging. Black bar corresponds to 400 μm. The previously observed thin filaments are absent in favour of amorphous material.

that this conformational change is a prerequisite for lipid binding or can occur on the lipid surface.

When examined at pH 7.5 by DLS, the formation of large species is highly dependent on the presence of lipids (Fig. 6C). As described previously the formation of large species is fast in the absence of lipids, while the presence of small amounts (LP 0.1) slows the formation of large species considerably. At higher lipid concentrations, the formation of large species is negligible within the observed time window. Electron microscopy of samples aged for 16 h or 6 days did not show straight fibril-like structures but rather small amounts of wool-like morphologies (Fig. 6D), suggesting mixed, amorphous lipid/peptide material. This suggests that the presence of anionic lipid prevents the formation of fibril-like aggregates instead of just preventing their sedimentation.

3.4. SerADan affects release of calcein from vesicles in competition with ageing

To investigate more closely the interactions of SerADan with lipids, we studied the ability of the peptide to release calcein from different vesicles. In this assay, calcein is initially trapped in vesicles at self-quenching concentrations and subsequent release of calcein leads to a large rise in fluorescence which for SerADan follows an approximately exponential time course (Fig. 7A). This permeabilization ability towards DOPG vesicles is maintained at peptide:lipid molar concentrations down to 1:500 (Fig. 7B). SerADan's ability to release calcein is highly dependent on its age. While SerADan freshly diluted from a stock in 10 M urea is able to affect release of almost 60% of all trapped calcein from 21 μM DOPG vesicles, this figure drops precipitously to around 30% within 15 min of ageing (Fig. 7C), and subsequently remains at a plateau until it drops further after around 3 h of ageing (corresponding to the onset of precipitation seen in Fig. 5A). Over the same 15 min ageing time range, the rate constant at which calcein release occurs (approximated by a first order fitting to the release data) drops by around a factor of 10, after which it remains at a very low value. The ability to release calcein is also sensitive to vesicle type. SerADan diluted from a stock in 10 M urea and aged for about 10 min is able to effect only release of around 31% of the trapped calcein from pure DOPG vesicles (Fig. 7A) over a period of about an hour, and the figure

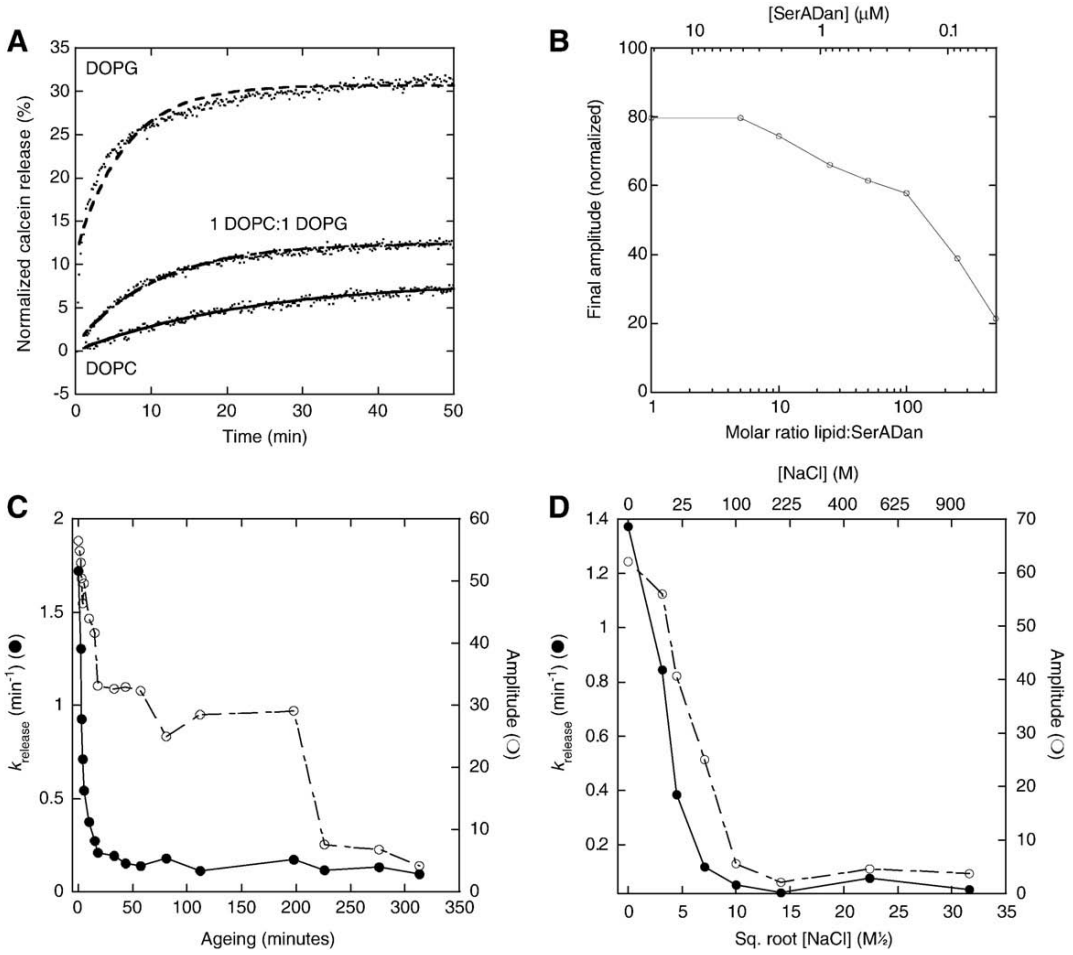

Fig. 7. Ability of SerADan to permeabilize vesicles at pH 7.5 and 22.5 °C. (A) Time profile of the release of calcein from 21 μM of vesicles of different compositions by 1 μM SerADan (50-fold diluted from a 50 μM solution in 0.2 M urea that had been aged for an hour after 50-fold dilution from a 2.5 mM stock in 10 M urea). Lines indicate best fits to single exponential decays. The fit is not particularly good for DOPG, but the associated rate constant and amplitude provide useful (if approximate) measures of the efficacy of permeabilization. (B) Ability of different concentrations of freshly diluted SerADan to permeabilize 21 μM calcein-filled DOPG vesicles. SerADan was first diluted from 2.5 mM peptide in 10 M urea to 50 μM peptide in 0.2 M urea, and then immediately diluted to the indicated concentrations in the presence of vesicles. SerADan permeabilizes a significant proportion of the vesicles at molar protein:lipid ratios down to 1:500. (C) Effect of ageing on ability of SerADan to permeabilize DOPG vesicles, measured in terms of the rate constant and amplitude of calcein release (derived from exponential decays as in panel A). SerADan was aged at a concentration of 10 μM in 0.04 M urea (diluted 250-fold from a 2.5 mM stock in 10 M urea) and subsequently diluted to 1 μM in the presence of 21 μM DOPG. The time profile thus reports on the ageing at 10 μM concentration. (D) Effect of ionic strength on ability of 1.0 μM SerADan to permeabilize 21 μM DOPG vesicles, measured as in panel A.

declines to around 13 and 8% for 1:1 DOPG:DOPC vesicles and pure DOPC vesicles, respectively. Just as high NaCl concentrations abolish the interaction between lipids and SerADan (Fig. 6A), they also prevent SerADan from permeabilizing vesicles (Fig. 7D).

4. Discussion

4.1. The multifaceted nature of SerADan aggregation

SerADan is an interesting model aggregation system for several reasons. Firstly, the close similarity to the original ADan peptide provides a direct link to aggregation processes occurring *in vivo*. Secondly, despite the preponderance of β-sheet structure and the overall amyloid-like appearance of the aggregates at longer time points, it presents no *bona fide* amyloid structure (according to both tinctorial assays and X-ray fiber diffraction studies). Diffraction data [18] indicate that the peptide is able to form organized β-stranded structure at the local level, but cannot assemble the ensuing β-sheets into supramolecular structures that are sufficiently organized to provide binding sites for amyloid-specific dyes such as Thioflavin T and Congo Red. In this sense SerADan occupies an intermediate position between classical amyloid and more diffuse protein aggregates, which may occur naturally as reversible associations in secretory granules [19]. These less well organized structures can be stabilized by local interactions in competition with proper amyloid structures [20] or may be held together by *e.g.* complementary charges mediated by detergent molecules [21].

The conformational and functional transitions identified for SerADan based on the use of 6 different techniques (circular dichroism, FTIR, Trp fluorescence, dynamic light scattering, electron microscopy and the release of calcein entrapped in vesicles) indicate that non-fibrillar aggregates can also assemble in numerous steps. We can thus build up a rather detailed picture of the different steps involved in SerADan aggregation after it has been diluted out from 10 M urea into buffer (summarized in Fig. 8). The following data pertain to behavior at pH 7.5 but are essentially the same at pH 5.0 unless indicated otherwise. SerADan is calculated to have a negative charge of −1 to −2 at pH 7.5 and ~+1 at pH 5, but the minor difference in behavior at these two pH values reveals that the overall charge does not play a significant role.

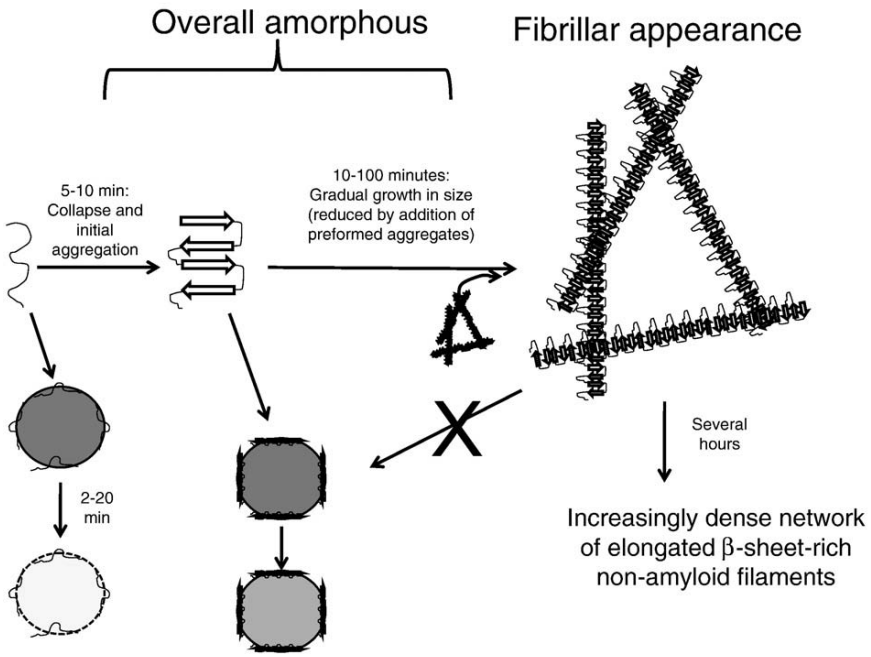

Fig. 8. Model of the different aggregation steps for SerADan and its interaction with lipids. Times indicate the approximate lengths required to complete the step in question (at concentration ranges spanning 10–50 μM SerADan). The first phase (first 10 min) involves formation of β-sheet structure, a ~5% loss in Trp fluorescence, initial aggregation and ~50% loss of permeabilization ability. Over the next 10–100 min aggregation levels increase, leading eventually to a multi-step sedimentation of large aggregates with loss of permeabilization ability, CD and Trp signals. Calcein-containing vesicles are denoted by circles. The different shades of grey indicate different levels of ability of SerADan aggregates to permeabilize the vesicles.

Within the first 5–10 min, there is a small (~15%) concentration-independent decline in Trp fluorescence; concomitantly a large amount of β-sheet structure forms rapidly according to circular dichroism, after which it stabilizes temporarily. In this period, SerADan's ability to permeabilize calcein-loaded membranes declines 50% in terms of the amount of calcein that can be released and around 10-fold in terms of the rate constant of permeabilization. This initial Trp decline is not so evident at pH 5.0, and at this pH the CD signal starts to decline straight away, suggesting that the rearrangement step occurs more rapidly at pH 5.0 or is bypassed to some extent. Over the next 5–100 min (depending on peptide concentration), there is a minor (~5%) linear and concentration-independent decline in fluorescence which may indicate a modest conformational rearrangement, but no change in permeabilization efficiency or CD signal at pH 7.5. Compared to the initial non-aggregated species which can permeabilize up to 60% of the vesicles, the aggregates present at this stage have a two-fold reduced membrane permeabilization activity, perhaps based on a limited ability to dissociate and re-aggregate productively in the membrane environment. Alternatively, these aggregates do not rearrange in the membrane, but simply possess a more modest permeabilization activity than the aggregated species formed by assembly of monomers in the membrane environment; the assembly process in the membrane is likely to be different from that in solution and also leads to β-sheet assemblies with stronger CD signals and more blue-shifted Trp fluorescence than in solution. In this time range, we also observe a marked growth in aggregate size by dynamic light scattering and the transient appearance and disappearance of amorphous aggregates according to electron microscopy. Although we do not include this as a separate step, it is likely that there is a gradual build-up of soluble species of increasing size in this period. From 2 h onwards, fibril-like aggregates (which already appear after a few minutes but not as the major species) dominate the EM images and there is a marked increase in aggregate size (probably due to the formation of intermeshed structures), leading to precipitation from solution and the complete loss of membrane permeabilization activity. This aggregation process is complex and proceeds in several stages; the steep drop in fluorescence to around 60% of the initial value (which is not paralleled by CD changes) is followed by a more measured fluorescence decline towards 40% over the next 2–10 h as well as a decline in CD signal. Although EM provides no categorical distinction between the different levels of aggregation on these time scales, the final decline is nevertheless accompanied by the consolidation of large filament-like structures by EM (Fig. 3). No major rearrangements occur over longer time intervals at the level of secondary structure (FTIR) or ultrastructure (EM). The modest decline in fluorescence prior to precipitation can be viewed as an apparent lag phase, as it represents the time required for accumulation of aggregates of a certain size. Similar to other nucleation-limited process, precipitation can be accelerated by the addition of preformed aggregates around which the smaller aggregates can coalesce as well as by an increase in the protein concentration.

In the presence of sufficient amounts of lipids, and provided there is not significant amount of electrostatic screening, there is only a small decline in Trp fluorescence (*i.e.* no precipitation) but a marked increase in β-sheet structure compared to the absence of lipids. Nevertheless EM does not indicate formation of straight fibril-like structure in lipids but rather wool-like threads. The decline in Trp fluorescence is accompanied by a ~13 nm blueshift, suggesting direct hydrophobic interaction between the aromatic residue and lipid. In contrast, the lipid-free process associated with the 15% Trp fluorescence decline gives rise to a negligible shift. Thus there is a kinetic partitioning between lipid binding and aggregation. In fact the inability of fresh SerADan to permeabilize vesicles 100% could be due to dead-time formation of aggregated species. Aggregation will dominate under physiological conditions (cfr. the screening effect of 100 mM NaCl), but permeabilization is not completely abolished and will be facilitated by higher lipid: peptide ratios, so that its effects may accumulate over longer time spans.

4.2. Similarities between SerADan and ADan

The previous studies of the reduced form of ADan showed no formation of amyloid-like structures but did demonstrate the presence of a dimer in fresh samples, which aggregated over several days [8,9] into an electron-dense matrix. That matrix shares some morphological similarities with the electron micrographs we present here although a stronger similarity can be seen with so-called immature fibers formed by oxidized ADan [9]. However, the kinetics of SerADan aggregation at pH 5.0 and 7.5 alike are an order of magnitude more rapid than those previously measured for the cysteine-containing ADan variants. This acceleration of aggregation is unexpected given the nature of the substitutions (Cys→Ser and Phe→Trp). These do not significantly alter the β-sheet propensity [22,23] or, in the case of F15W, the propensity for β-aggregation [24]. For C5S and C22S, the substitution theoretically lowers the β-aggregation propensity rather than increasing it. However, due to the proximity to the theoretical pKa for cysteine (~8.0), ~17% of the Cys residues in reduced ADan will be charged at pH 7.5. In principle, the elimination of charge by the mutations in SerADan could play a role at pH 7.5, but not at pH 5.0 where only 0.1% of the Cys residues will be charged. However, since the kinetics are rapid at both pH 5.0 and 7.5, we conclude that charge elimination by the Cys-Ser mutations will not contribute significantly. An alternative explanation for the effect of the mutations is that the elimination of cysteine prevents shuffling and formation of intermolecular disulphide bonds that could trap the peptide in 'aggregation-protected' conformations. Thus the mutations in SerADan allow us to filter out the covalent interactions and focus entirely on how non-covalent interactions affect the aggregation process.

4.3. SerADan interacts strongly with anionic phospholipids

SerADan shows the preference for anionic lipids that is seen for most other lipid-interacting aggregating proteins. These interactions are mediated by electrostatics, as they are reduced at medium ionic strength. At pH 7.5, the charge is predicted to be −1 to −2, leading to overall repulsion from anionic lipid membranes. Inspection of the primary structure does not reveal an obvious basic region that could account for the interaction with the negatively charged lipid. However, several authors have attempted molecular modeling of the ADan peptide based on (a) the 101–123 segment of transthyretin [9] or (b) a previous model for the related ABri peptide [8,25]. The former (a) resulted in a double-stranded β-sheet stabilized by disulphide and hydrogen bonding and terminating in a long loop with the C-terminal tyrosine residue hydrogen bonded to the β-sheet. The latter (b) showed a triple β-sheet in which strands one and two are similar to the double-stranded model while the third strand consist of the C-terminal region. Both of these models are interesting in that they largely isolate the charged residues at one or both ends of the β-sheet albeit not in a manner that creates a clear cationic region. In addition, the peptide contains two histidine residues and local environmental effects could very well shift the effective pK_a of this group. The residue corresponding to the single tryptophan in SerADan is also located at one end of both models. Together with the observed strong blueshifting of the emission spectrum in SerADan, it is tempting to speculate that Trp is buried within the core or border region of the membrane while a local basic region of the peptide interacts with the lipid head group; this whole interacting region is located at one end of a double- or triple-stranded β-sheet.

4.4. SerADan share characteristics with antimicrobial peptides

The rapid release of calcein from vesicles demonstrates that SerADan (and by implication ADan) has a potent perturbing effect on lipid membranes at molar peptide:lipid ratios down to 1:500, which is comparable to *bona fide* antimicrobial peptides [26]. Unlike small antimicrobial peptides such as Novispirin [27], lipid-bound SerADan does not contain notable amounts of α-helical structure. However, amphiphilic antimicrobial peptides forming β-hairpins in the active form have been identified such as the cationic β-defensins and bactenecin [28,29], and self-assembling β-sheet peptides are able to form transient pores in membranes [30]. Furthermore, formation of α-helix structure is not a prerequisite for the ability of Novicidin to permeabilize *e.g.* zwitterionic lipids (B.S. Vad and D.E. Otzen, unpublished observations).

SerADan's predilection for β-sheet structure in lipids is in marked contrast to IAPP, which in the presence of anionic lipids is able to form α-helical assemblies that lead to membrane leakage and subsequent fibril assembly through α-to-β conversion within the α-helical assembly [31]. Similarly, the fibrillating polypeptides α-synuclein [32] and Aβ [33] both form α-helical structures in lipid bilayers which may be intermediates in fibril formation [34]. Although programmes such as TANGO [35] predict Aβ to have a significantly higher β-sheet propensity in buffer than SerADan (whose propensity in turn is much higher than that of IAPP), this may be overruled by the pronounced tendency of SerADan to associate rapidly by a more general collapse. SerADan's inability to form highly organized fibrillar structures may thus reflect that it is quickly trapped in locally well-organized aggregates that are unable to reorganize at the molecular level to make regular β-sheet contacts. It is tempting to speculate that the swiftness with which these oligomeric structures are formed in solution and in lipid bilayers is a key factor that will facilitate an aggressive behavior towards cellular membranes at the monomeric and early oligomeric level.

Acknowledgements

L.W.N. and B.S.V. are supported by pre-doctoral grants from Aalborg University, the Danish Research Training Council and the BioNET research network, funded by the Villum Kann Rasmussen Foundation. D.E.O. is supported by the Villum Kann Rasmussen Foundation and the Danish Research Foundation.

References

[1] E. Strömgren, A. Dalby, M.A. Dalby, B. Ranheim, Cataract, deafness, cerebellar ataxia, psychosis and dementia—a new syndrome. Acta Neurol. Scand. 46 (Suppl. 43) (1970) 97–98.
[2] R. Vidal, T. Revesz, A. Rostagno, E. Kim, J.L. Holton, T. Bek, M. Bojsen-Moller, H. Braendgaard, G. Plant, J. Ghiso, B. Frangione, A decamer duplication in the 3′ region of the BRI gene originates an amyloid peptide that is associated with dementia in a Danish kindred, Proc. Natl. Acad. Sci. U. S. A. 97 (2000) 4920–4925.
[3] J.L. Holton, T. Lashley, J. Ghiso, H. Braendgaard, R. Vidal, C.J. Guerin, G. Gibb, D.P. Hanger, A. Rostagno, B.H. Anderton, C. Strand, H. Ayling, G. Plant, B. Frangione, M. Bojsen-Moller, T. Revesz, Familial Danish dementia: a novel form of cerebral amyloidosis associated with deposition of both amyloid-Dan and amyloid-beta, J. Neuropathol. Exp. Neurol. 61 (2002) 254–267.
[4] S.H. Kim, J.W. Creemers, S. Chu, G. Thinakaran, S.S. Sisodia, Proteolytic processing of familial British dementia-associated BRI variants: evidence for enhanced intracellular accumulation of amyloidogenic peptides, J. Biol. Chem. 277 (2002) 1872–1877.
[5] A. Rostagno, Y. Tomidokoro, T. Lashley, D. Ng, G. Plant, J. Holton, B. Frangione, T. Revesz, J. Ghiso, Chromosome 13 dementias, Cell. Mol. Life Sci. 62 (2005) 1814–1825.
[6] B. Austen, O.M.A. El-Agnaf, S. Nagala, B. Patel, N. Gunasekera, M. Lee, V. Lelyveld, Properties of neurotoxic peptides related to the BRI gene, Biochem. Soc. Trans. 30 (2002) 557–559.
[7] Y. Tomidokoro, T. Lashley, A. Rostagno, T.A. Neubert, M. Bojsen-Møller, H. Brændgaard, G. Plant, J.M. Holton, B. Frangione, T. Revesz, J. Ghiso, Familial Danish dementia: co-existence of Danish and Alzheimer amyloid subunits (ADan AND Aβ) in the absence of compact plaques, J. Biol. Chem. 280 (2005) 36883–36894.
[8] G. Gibson, N. Gunasekera, M.T. Lee, V. Lelyveld, O.M.A. El-Agnaf, A. Wright, B. Austen, Oligomerization and neurotoxicity of the amyloid ADan peptide implicated in familial Danish dementia, J. Neurochem. 88 (2004) 281–290.
[9] I. Surolia, G.B. Reddy, S. Sinha, Hierarchy and the mechanism of fibril formation in ADan peptides, J. Neurochem. 99 (2006) 537–548.

[10] J.D. Knight, A.D. Miranker, Phospholipid catalysis of diabetic amyloid assembly, J. Mol. Biol. 341 (2004) 1175–1187.
[11] Y.A. Domanov, P.K. Kinnunen, Islet amyloid polypeptide forms rigid lipid–protein amyloid fibrils on supported phospholipid bilayers, J. Mol. Biol. 376 (2008) 42–54.
[12] M. Bokvist, F. Lindstrom, A. Watts, G. Grobner, Two types of Alzheimer's beta-amyloid (1–40) peptide membrane interactions: aggregation preventing transmembrane anchoring versus accelerated surface fibril formation, J. Mol. Biol. 335 (2004) 1039–1049.
[13] I.C. Martins, I. Kuperstein, H. Wilkinson, E. Maes, M. Vanbrabant, W. Jonckheere, P. Van Gelder, D. Hartmann, R. D'Hooge, B. de Strooper, J. Schymkowitz, F. Rousseau, Lipids revert inert Aβ amyloid fibrils to neurotoxic protofibrils that affect learning in mice, EMBO J. 27 (2008) 224–233.
[14] H. Zhao, E.K. Tuominen, P.K. Kinnunen, Formation of amyloid fibers triggered by phosphatidylserine-containing membranes, Biochemistry 43 (2004) 10302–10307.
[15] A. Quist, I. Doudevski, H. Lin, R. Azimova, D. Ng, B. Frangione, B. Kagan, J. Ghiso, R. Lal, Amyloid ion channels: a common structural link for protein-misfolding disease, Proc. Natl. Acad. Sci. U. S. A. 102 (2005) 10427–10432.
[16] D.M. Byler, H. Susi, Examination of the secondary structure of proteins by deconvolved FTIR spectra, Biopolymers 25 (1986) 469–487.
[17] J.S. Pedersen, G. Christiansen, D.E. Otzen, Modulation of S6 fibrillation by unfolding rates and gatekeeper residues, J. Mol. Biol. 341 (2004) 575–588.
[18] L. Nesgaard, A. Malmendal, S.V. Hoffmann, D.E. Otzen, Characterization of dry globular proteins and proteins fibrils by synchrotron radiation circular dichroism, Biopolymers 89 (2008) 779–795.
[19] C. Keeler, M.E. Hodsdon, P.S. Dannies, Is there structural specificity in the reversible protein aggregates that are stored in secretory granules? J. Mol. Neurosci. 22 (2004) 43–49.
[20] O.P. Bliznyukov, L.D. Kozmin, L.L. VYsotskaya, A.K. Golenkov, V.M. TIshchenko, M.P. Samyolovich, V.B. Klimovich, Human immunoglobulin light chains lambda form amyloid fibrils and granular aggregates in solution, Biochemistry (Mosc.) 70 (2005) 458–466.
[21] D.E. Otzen, L. Nesgaard, K.K. Andersen, J.H. Hansen, G. Christiansen, H. Doe, P. Sehgal, Aggregation of S6 in a quasi-native state by monomeric SDS, Biochim. Biophys. Acta 1784 (2008) 400–414.
[22] P.Y. Chou, G.D. Fasman, Conformational parameters for amino acids in helical, beta-sheet, and random coil regions calculated from proteins, Biochemistry 13 (1974) 211–222.
[23] P. Koehl, M. Levitt, Structure-based conformational preferences of amino acids, Proc. Natl. Acad. Sci. U. S. A. 96 (1999) 12524–12529.
[24] A.P. Pawar, K.F. DuBay, J. Zurdo, F. Chiti, M. Vendruscolo, C.M. Dobson, Prediction of "Aggregation-prone" and "Aggregationsusceptible" regions in proteins associated with neurodegenerative diseases, J. Mol. Biol. 2005 (2005) 379–392.
[25] O.M. El-Agnaf, J.M. Sheridan, C. Sidera, G. Siligardi, R. Hussain, P.I. Haris, B.M. Austen, Effect of the disulfide bridge and the C-terminal extension on the oligomerization of the amyloid peptide ABri implicated in familial British dementia, Biochemistry 40 (2001) 3449–3457.
[26] R.E.W. Hancock, H.G. Sahl, Antimicrobial and host-defense peptides as new anti-infective therapeutic strategies, Nat. Biotechnol. 24 (2006) 1551–1557.
[27] R. Wimmer, K. Andersen, B. Vad, M. Davidsen, S. Mølgaard, L.W. Nesgaard, H.H. Kristensen, D.E. Otzen, Versatile interactions of the antimicrobial peptide Novispirin with detergents and lipids, Biochemistry 45 (2006) 481–497.
[28] M. Pazgier, X. Li, W. Lu, J. Lubkowski, Human defensins: synthesis and structural properties, Curr. Pharm. Des. 13 (2007) 3096–3118.
[29] D. Romeo, B. Skerlavaj, M. Bolognesi, R. Gennaro, Structure and bactericidal activity of an antibiotic dodecapeptide purified from bovine neutrophils, J. Biol. Chem. 263 (1988) 9573–9575.
[30] J.M. Rausch, J.R. Marks, R. Rathinakumar, W.C. Wimley, Beta-sheet pore-forming peptides selected from a rational combinatorial library: mechanism of pore formation in lipid vesicles and activity in biological membranes, Biochemistry 46 (2007) 12124–12139.
[31] J.D. Knight, J.A. Hebda, A.D. Miranker, Conserved and cooperative assembly of membrane-bound alpha-helical states of islet amyloid polypeptide, Biochemistry 45 (2006) 9496–9508.
[32] E. Jo, J. McLaurin, C.M. Yip, P. St. George-Hyslop, P.E. Faser, alpha-Synuclein membrane interactions and lipid specificity, J. Biol. Chem. 275 (2000) 34328–34334.
[33] E. Terzi, G. Holzemann, J. Seelig, Interaction of Alzheimer beta-amyloid peptide (1–40) with lipid membranes, Biochemistry 36 (1997) 14845–14852.
[34] M.D. Kirkitadze, M.M. Condron, D.B. Teplow, Identification and characterization of key kinetic intermediates in amyloid beta-protein fibrillogenesis, J. Mol. Biol. 312 (2001) 1103–1119.
[35] A.M. Fernandez-Escamilla, F. Rousseau, J. Schymkowitz, L. Serrano, Prediction of sequence-dependent and mutational effects on the aggregation of peptides and protein, Nat. Biotechnol. 22 (2004) 1302–1306.

Co-author statement for Paper 1

Nesgaard, L., Vad, B., Christiansen, G. and Otzen, D.: Kinetic partitioning between aggregation and vesicle permeabilization by modified ADan. *Biochim Biophys Acta* (2009) 1794 p. 84-93.

- Lise W. Nesgaard performed all experimental work except electron microscopy and liposome calcein release and wrote the article with Daniel Otzen
- Gunna Christiansen performed all electron microscopy.
- Brian Vad performed all liposome calcein release work.
- Daniel Otzen supervised design and execution of the experiments, contributed extensively to the writing of the article and took care of submission, revision and galley proofs.

Brian Vad		31st March 2009
Gunna Christiansen		30th March 2009
Daniel Otzen		16th March 2009
Lise W. Nesgaard		31st March 2009
	Signature	Date

3.2 Discussion of Paper 1

3.2.1 SerADan aggregates by a step-wise mechanism

The aggregation of SerADan was followed by several methods (table 11), which in collaboration demonstrate an assembly mechanism that falls in several steps. The earliest detectable event in the assembly process, occurring within the first minute, is the collapse from a random coil structure into a β-rich conformation following dilution from 10M to 0.2M urea (paper 1/figure 4). Considering the intrinsic Trp fluorescence, the assembly of SerADan aggregates takes place in three roughly defined phases (figure 33, paper 1/figure 5). During the initial phase, the fluorescence intensity declines by approximately 20% associated with a minimal peak blue-shift (~353nm to ~350nm). For pH 7.5, the reduced intensity can be further divided into two sub-phases as discussed in section 3.2.4. The length of phase I varies with the initial peptide concentration between ~20 and ~160 minutes for 50μM and 10μM peptide, respectively. During this phase, DLS shows a steady increase in particle size starting immediately after dilution and into the second phase observable by Trp-fluoresence (paper 1/figure 5.B). The eventual plateau in particle size, which for a peptide concentration of 50μM is reached after approximately 40 minutes, is rather due to limitations imposed by instrument settings than a genuine arrest of aggregate growth. This is consistent with sedimentation as the cause of the abrupt reduction in Trp fluorescence to ~60% of the initial emission intensity. The role of sedimentation is also supported by the absence of phase II and III in continuously stirred samples (figure 34.A) and the recovery of emission intensity by agitation of quiescent samples (figure 34.B).

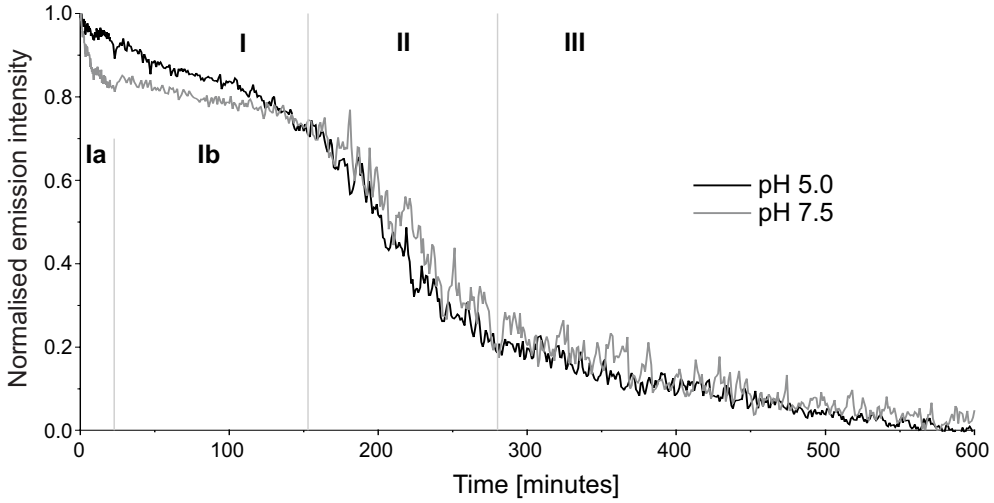

Figure 33. The time-course of SerADan aggregation followed by intrinsic Trp fluorescence falls into three phases. The first phase can be divided further for pH 7.5.

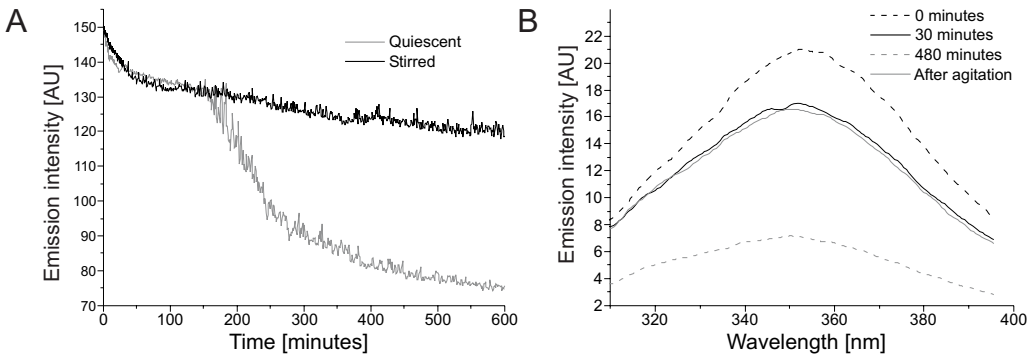

Figure 34. (A) Intrinsic Trp fluorescence time-course for quiescent and stirred aggregation of 10μM SerADan. (B) Time-resolved emission spectra of a similar sample.

In parallel with aggregate growth observed by DLS and indirectly by Trp fluorescence, EM shows the transient appearance of amorphous structures followed by very large particles composed of tightly interwoven linear, fibre-like aggregates (figure 35.A, paper 1/figure 2). Nevertheless, linear filaments are observable in the very earliest EM images albeit as a minor species and with less well-defined and uniform structure, which could suggest that they function as precursors to the mature, linear aggregates. However, the obtained EM images do not allow discrimination between the observed structures with sufficient confidence to make conclusions regarding their relative position on or off the aggregation pathway.

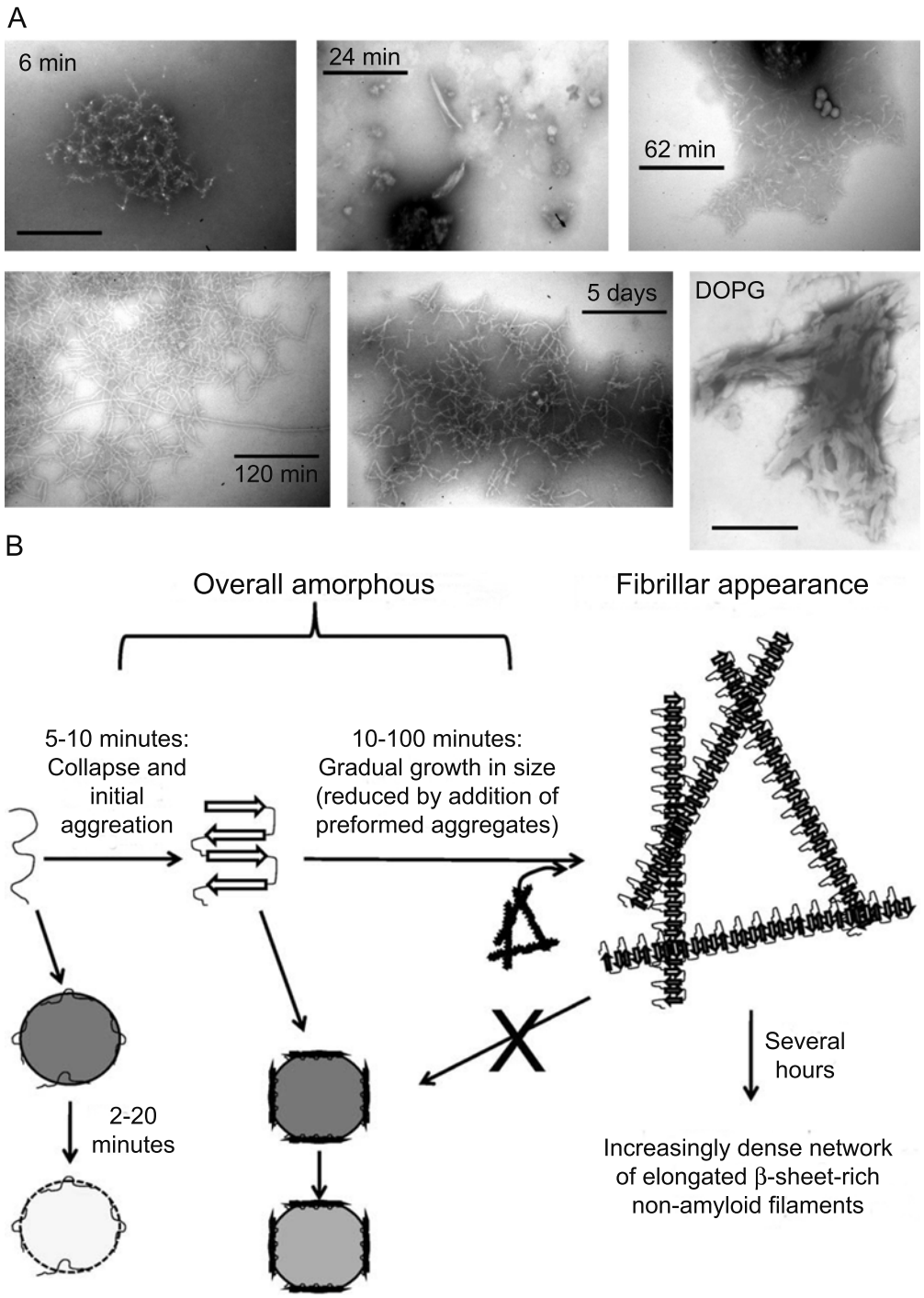

Figure 35. (A) Examples of morphology by EM for aggregation of 50μM SerADan at pH 7.5. Scale bars correspond to 400nm. (B) Putative mechanism of SerADan aggregation and lipid interaction.

Based on these observations, a putative assembly mechanism can be draw up (figure 35.B) consisting of an early collapse of the monomer into a β-rich confor-

mation followed by association of monomers into oligomers and later aggregates of increasing size. The onset of sedimentation appears to correlate with the formation of increasingly large aggregates of closely intertwined fibres with fibril-like appearance. A more detailed description of the steps involved in the assembly process is not possible, but it is likely that the early phase of aggregation involves gradual build-up of soluble and insoluble oligomers in equilibrium with the amorphous structures observed by EM. Aspects of this assembly mechanism, the structure of SerADan aggregates and the circumvention of aggregation by liposome binding are discussed in the following.

3.2.2 SerADan forms linear, β-rich, non-amyloid aggregates

The assembly of SerADan aggregates is rapid with formation of the final mature structures accomplished within a few hours depending on concentration. A minor fibrous species emerges for pH 5.0 within a few days, but overall stable and static mature aggregates are established within the initial few hours whether in secondary structure or in the observable morphology. The final fibre-like, ThT and CR

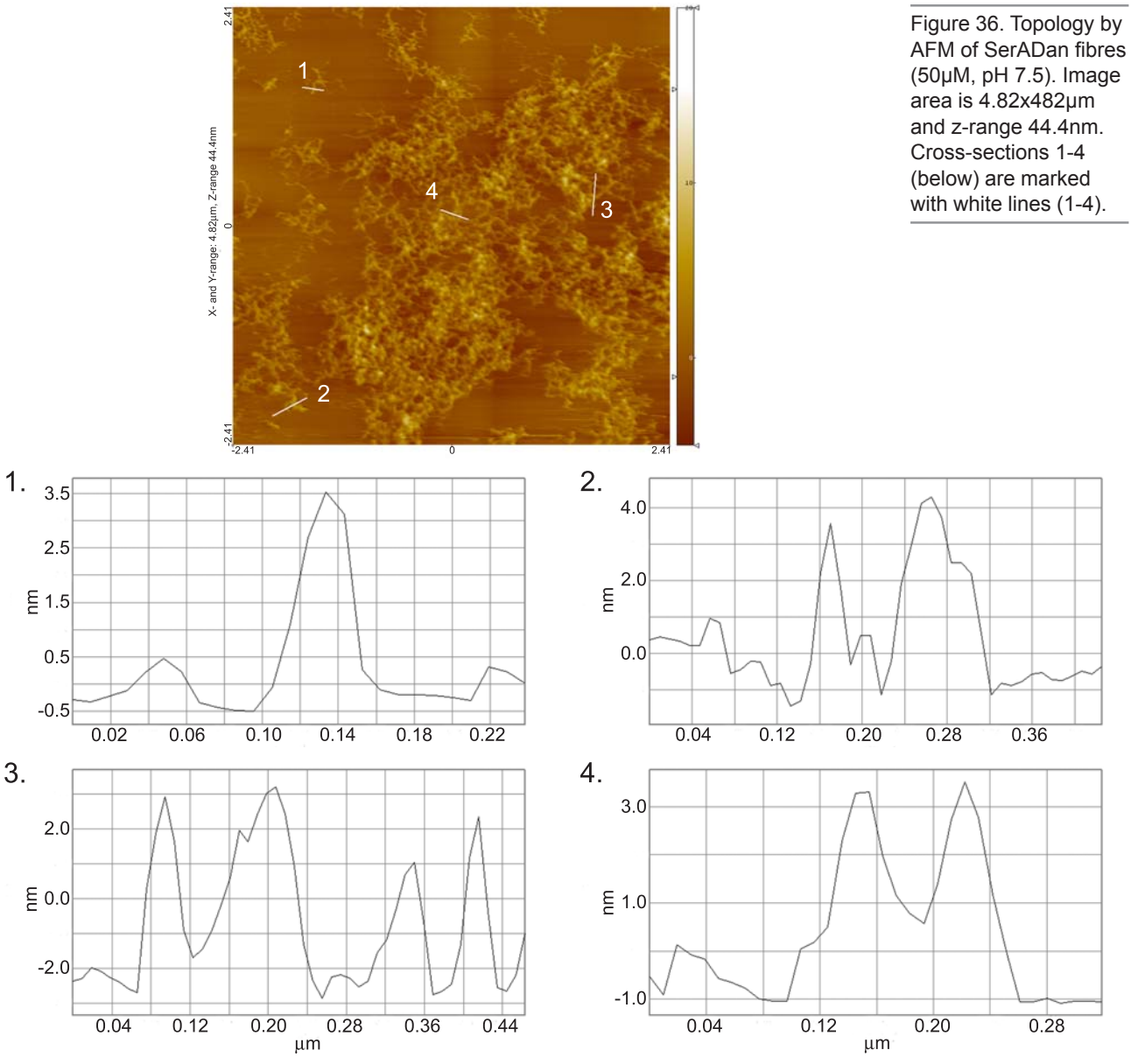

Figure 36. Topology by AFM of SerADan fibres (50µM, pH 7.5). Image area is 4.82x482µm and z-range 44.4nm. Cross-sections 1-4 (below) are marked with white lines (1-4).

negative structures are highly curved and intertwined to the point of preventing imaging of single fibres although sonication prior to imaging for some samples was found to cause shearing of the micron-scale aggregates allowing AFM images to be obtained along their edges. The final fibre-like structures are of variable length but reasonably consistent height in the 3-5nm range (figure 36). The estimated dimensions and the curvilinear appearance are suggestive of the protofibrillar aggregates described as intermediates during the fibrillation of many polypeptides including oxADan [547]. It is worth noticing that protofibrils in general have little or no affinity for CR or ThT, which is consistent with the binding model of CR and ThT that places the dye molecules parallel along the fibril axis and bound in groves between protofilaments. According to this model, binding of the dyes would not expected for fibrous structures without such multifilament substructure. However, a possible structural relationship between SerADan fibres and protofibrils must remain a suggestion in the absence of more detailed structural information.

The fibres are undoubtedly composed of β-sheet organised to form linear aggregates, but the supramolecular arrangement is puzzling. Our initial observations by X-ray fibre diffraction, included in paper 2, did show a reflection at 4.8Å in agreement with the interstrand distance in regular β-sheets but absent or very diffuse reflection as higher distances inconsistent with cross-β structure and strongly suggesting the absence of supersecondary structure (figure 37). It must be noted that the overall signal intensity was very low, possibly due to poor alignment of the fibres.

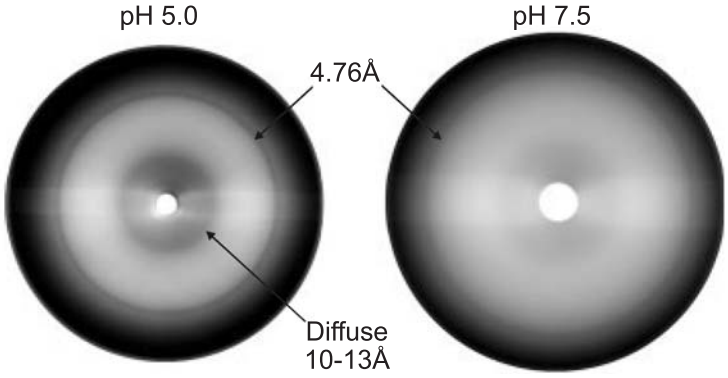

Figure 37. X-ray fibre diffractograms of aligned SerADan fibres formed at pH 5.0 and 7.5. Adapted from paper 2/figure 10,

Martin Jeppesen and Daniel Otzen continued this work by X-ray fiber diffraction on recombinant SerADan, in collaboration with Kim Hein and Poul Nissen, allowing collection of high quality X-ray diffractograms (figure 38.A). The peptide preparation and aggregation conditions were somewhat different [573]. The SerADan peptide was expressed as a SUMO fusion product in *E. coli*, disaggregated in HFIP and could be induced for form ThT-binding aggregates at 25μM peptide and pH 5.5, 37ºC with vigorous shaking[9]. Aggregation at other pH values in the range 4.8-7.5 showed less or no binding of ThT. However, despite the affinity for ThT, the appearance in EM was not one of linear, fibril-like structures but rather short strands intermixed with amorphous material (figure 38.B). The complex diffraction pattern showed several reflections including the charac-

9 Aggregation of synthetic SerADan was independent of temperature between 13ºC and 40ºC.

teristic peak at 4.67Å, but only a single reflection at 11.5Å in the 10-11Å region expected for cross-β organisation. However, the multiple reflections do suggest significant supersecondary structure and illustrates that SerADan has capacity for forming regular structures with a high degree of intermolecular organisation.

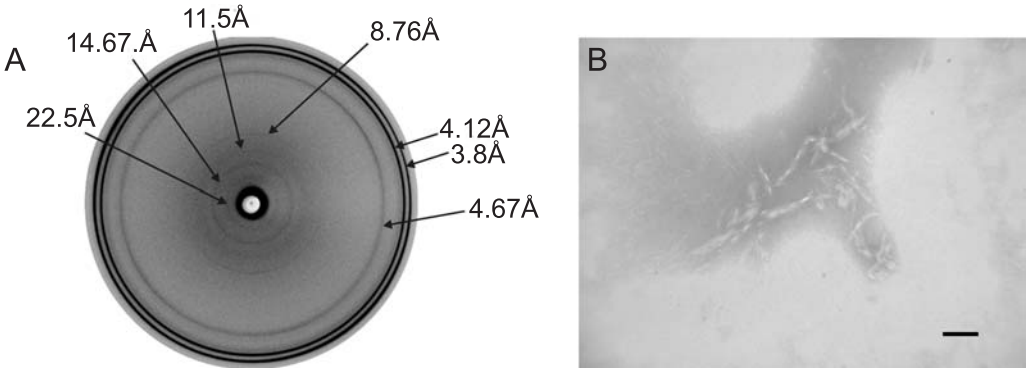

Figure 38. (A) X-ray fibre diffractogram of ThT-positive aggregates of recombinant SerADan, disaggregated in HFIP, incubated at pH 5.5 with shaking. (B) Aggregate morphology by EM. Scale bar corresponds to 90nm. Adapted from [573]

As discussed in section 1.2.5, several structures have been suggested as alternatives to the canonical fibril model, in which the fibril is composed of multiple protofilaments of cross-β structure. A particularly interesting alternative in light of the SerADan X-ray diffraction data is the nanotube model suggested by Max Perutz for polyglutamine fibrils [129]. Rather than a semi-flat continuous β-sheet, the nanotube model describes a continuous β-helix with 20 residues per turn forming a water-filled tube with a mean diameter of 20Å. In this model, the 3.2Å and 3.6Å reflections observed for polyglutamine were interpreted as side-chain repeats along the inner and outer cylindrical phases, respectively.

The observation of β-rich, linear fibres is not limited to structures with the classical amyloid-like characteristics of dye binding, linear morphology and cross-β organisation. Natural fibres such as spider drag line silk are composed of highly organised β-sheets while β-rich fibres without classical cross-β organisation has also been described for e.g. domain-swapped fibres of cystatin C or ribonuclease A [574, 575] as well as edge-associated superoxide dismutase (SOD-1) [576]. These structures contain a large degree of preserved native structure. In all, preservation of native structure appears to be a more common feature for protein aggregation than previously believed. We have in our group demonstrated that ribosomal subunit S6 from *Thermus thermophilus* can be induced to aggregated in a quasi-native state by electrostatic attraction mediated by the anionic detergent SDS [577]. A certain degree of structural specificity has also been observed for secretory granules [578]. An interesting example of the balance between native and β-rich aggregate structure was described by Alakoskela *et al.* [579] who demonstrated heterogeneity along the long axis of fibres formed by cytochrome c in the presence of anionic lipids varying from near-native to classical cross-β amyloid-like organisation. This highlights the possibility of structural polymorphism, not only between fibrils formed of the same polypeptide under differing circumstances but also within the same sample. It also speaks to the plasticity of the polypeptide backbone when moving from globular protein folding, with its dependence upon sequence as described by Anfinsen [155], to the apparently

generic ability of proteins to form aggregates and fibrils [10], which in the absence of evolutionary pressure gives rise to wide-ranging structural polymorphism dependent on external conditions [114].

Based on these reflections, it is possible that the β-rich and linear but non-amyloid fibres observed here for SerADan could represent an intermediary between conventional amyloid structure and one or more alternative linear arrangements of β-sheets. The obtained results suggest that the linear SerADan arrangement is considerably less organised than that of amyloid, and lacks the surface characteristics required for CR and ThT binding. The exact structural properties of such alternative structures is of great interest and could provide a greater understanding of β-sheet interaction in linear aggregates as well as their assembly. Structural studies with the potential to answer these questions are currently underway.

3.2.3 The onset of sedimentation is accelerated by seeding

The rapid decline in intrinsic Trp fluorescence (phase II) can be ascribed to sedimentation of very large aggregates and as a result, the kinetic behaviour of SerADan cannot be followed reliably by Trp fluorescence beyond the early stages of aggregation. Nor is DLS suitable since even low concentrations of large aggregates skewer the results towards high particle size and polydispersity. In the absence of more specific time-resolved methods, inferences must be made based on indirect methods.

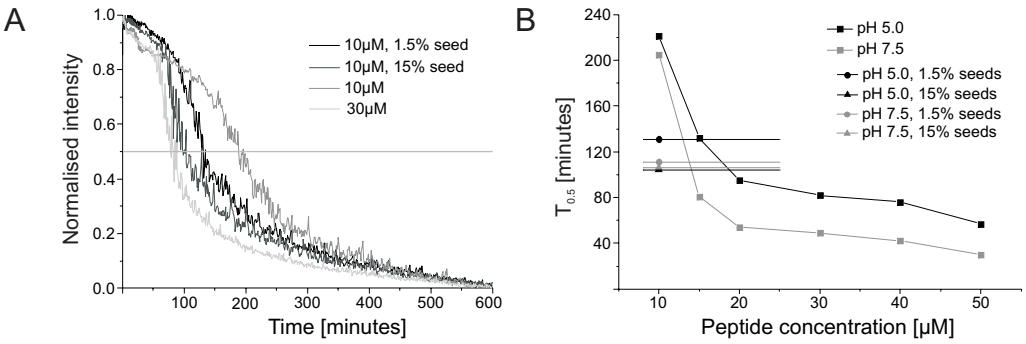

Figure 39. (A) Effect of seeding with 1.5% or 15% preformed aggregates on SerADan aggregation followed by intrinsic Trp fluorescence. (B) Dependence of $T_{0.5}$ (time at normalised intensity=0.5) on peptide concentration without seeds and with 1.5% or 15% seeds (horisontal lines).

The addition of 1.5% sonicated, preformed, mature aggregates to 10µM SerADan approximately halves the apparent lag phase ($T_{0.5}$), here defined as the time-point corresponding to a normalised emission intensity of 0.5 (figure 39.A-B). Further addition to 15% seeds did not considerably shorten the delay before onset of sedimentation. Whereas this could be interpreted as the circumvention of nucleation during growth of the fibres and thereby as an indirect sign of a nucleated growth process, a different interpretation is likely. It must be expected that the period required for formation of sedimentation-prone particles would be shortened by the presence of large particles at the onset of aggregation around which smaller oligomeric species can coalesce. However, process of seeding in formation of ordered aggregates, e.g. during fibrillogenesis, is complex and poorly understood. Dobson and co-workers [188] observed that a tandem repeat of the SH3 domain of the α-subunit of bovine phosphatidyl-3'-kinase forms amorphous oligomers of various sizes at pH 3.6 by a down-hill oligomerisation process and

that oligomers over a certain size efficiently seed amyloid-like fibrils at pH 2.3. The authors attributed this activity to a structural conversion within the amorphous oligomers to form curly fibrils. Similar seeding of ABri fibrils was described when spherical aggregates formed at pH 7.3 was transferred to pH 4.9 [548]. In all, the underlying role of amorphous structures in seeding is unresolved, but seems to involve internal structural conversion, seeding *via* surface structures of amyloid-like conformation or a role as reservoir for aggregation-prone monomers [188, 208, 209, 580]. The mature SerADan aggregates do not appear to have classical amyloid-like structure and the function of preformed aggregates in acceleration of the assembly of sedimentation-prone aggregates could involve a number of such mechanisms.

3.2.4 Charge may play a role in the early aggregation phase

The difference in pH does not result in significant disparities in later phases of aggregation in terms of secondary structure, gross morphology or in the time-profiles obtained by fluorescence and dynamic light scattering. However, clear differences can be observed in intrinsic Trp fluorescence in the initial phases immediately following the collapse into from random coil to β-structure. At pH 7.5, an initial ~15% decline in emission intensity can be observed over 5-10 minutes (phase Ia, figure 33) followed by a less steep, linear reduction of approximately 5% (phase Ib). The normalised data sets, used for easy comparison, do not demonstrate concentration dependence of phase I, but when the non-normalised time-courses are examined, a different picture emerges (figure 40).

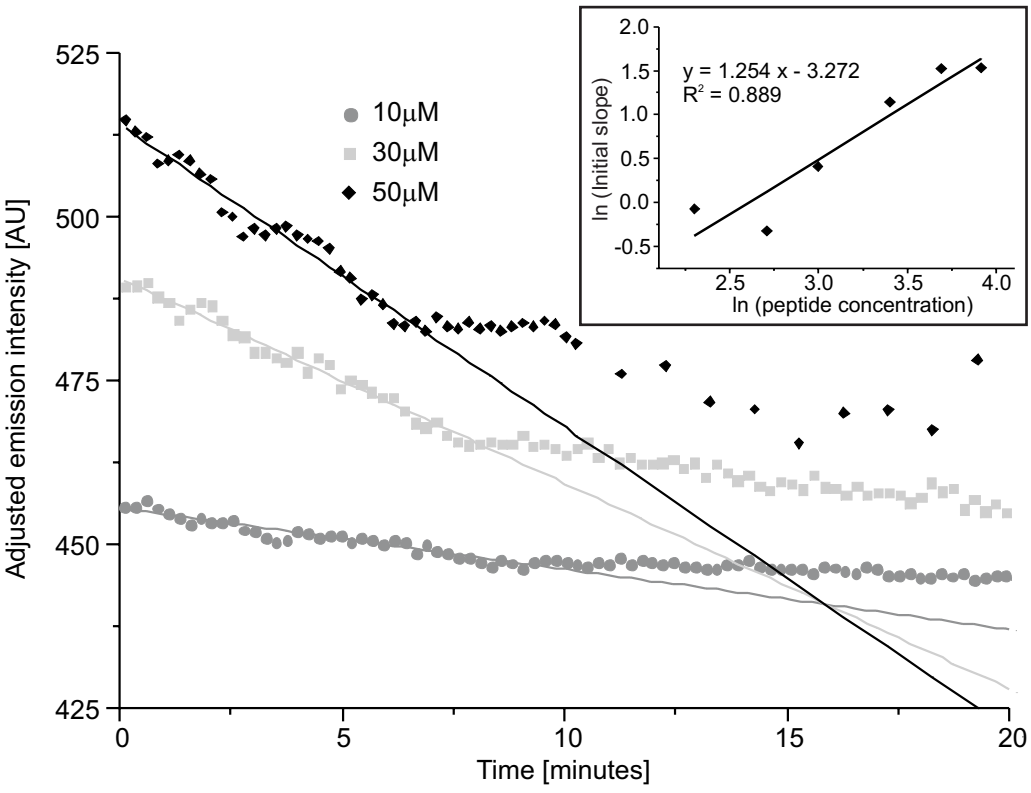

Figure 40. Linear fits to the initial 7 minutes of the raw emission intensities (only adjusted in the y-direction to allow graphical comparison). Insert: Log-log plot of peptide concentration *vs*. initial slope.

At pH 7.5 a log-log plot of the initial reaction rates[10] versus initial monomer concentration yields a reaction order in peptide concentration of ~1.3 (figure 40,

10 Initial reaction rates were obtained as the initial slope by linear regression over the first five minutes of non-normalised emission intensity per time unit.

insert). This value is more consistent with a complex reaction than a simple monomeric collapse or dimerisation. In contrast, this sub-phase division is absent at pH 5.0 for which a single linear reduction to ~80% of the initial intensity can be observed. The first 4-5 minutes at pH 5.0 are marked by significant noise of unknown origin preventing the direct calculation of initial reaction rates. However, under the assumption that the following linear decline is representative, the slopes of the curve versus peptide concentration in a log-log plot yields a reaction order of approximately 1, similarly to phase Ib for pH 7.5, suggesting an unchanged aggregate molecularity. Similarly, time-resolved CD shows distinct differences over a comparable time period. While the decline in intensity of the β-component of the spectrum begins immediately after dilution at pH 5.0, the time profile for pH 7.5 shows a lag phase. In all, these results are suggestive of subtle differences between the aggregate assembly mechanisms with particular emphasis during the initial phase. Given the differing predicted charges at pH 5.0 and 7.5, the pH-dependence of the time profiles points towards an electrostatic cause for the disparity in assembly, e.g. by charge repulsion or alternative electrostatic interaction for the β-rich monomeric conformation or within oligomeric structures. However, this charge dependency also speaks to the possible effects of the C5S and C22S mutations. While cysteine is neutral at pH 5.0, pH 7.5 is sufficiently close to the theoretical pKa for cysteine that a considerable proportion of the residues (~17%) will be negatively charged at pH 7.5. It must be emphasised that this difference between redADan and SerADan may make the kinetic observations of early aggregation irrelevant for the biological peptide.

In addition to the possible charge-related effects on the early events in aggregation of the Cys-to-Ser substitutions, the absence of the intramolecular disulphide must be considered. It is possible that the disulphide maintain the ADan peptide in a aggregation-protected conformation that only slowly converts to a more aggregation-prone conformation. The absence of the disulphide would allow the SerADan peptide to sample possible conformation, including aggregation-prone ones, more rapidly thereby significantly increasing the observable aggregation rate in spite of the lower predicted β-aggregational propensity. In the light of the solution condition-dependent partitioning between fibrillation and amorphous aggregation described for monoclonal human immunoglobulin light chain [581], this line or reasoning also offers a possible rationalisation for the transition from amorphous aggregates observed for ADan to the linear aggregates described here for SerADan. Slow conversion to the aggregation-prone conformation combined with rapid aggregation of the ADan peptide could lead to kinetic trapping of the peptide in β-rich but amorphous aggregates with limited ability to structurally reorganise into ordered, linear aggregates. In contrast, the lowered aggregational propensity predicted for SerADan could permit formation of repeatable intermolecular contacts and thereby linear aggregates without permitting formation of canonical fibrils. It is possible that further mutational studies could tune the intrinsic aggregational propensity of SerADan to allow formation fibrils with classical tinctorial, structural and morphological characteristics.

3.2.5 SerADan interacts with anionic lipids by a combination of factors

The presence of anionic lipids dramatically alters the aggregational properties of SerADan. Whereas the early changes in fluorescence appear conserved, the later sedimentation phase is effectively prevented within the monitored time frame (paper 1/figure 6). Similarly, DLS shows that formation of large aggregates is either prevented (lipid-to-protein, LP, ratios of 1 mole/mole or higher) or significantly delayed (LP 0.1). The fibrous aggregates are also absent in EM and AFM in favour of amorphous, wool-like structures, which show a combination of characteristic lipid and protein bands in the amide-sensitive 1750-1500cm^{-1} region in FTIR (figure 41). The appearance in FTIR is of a β-rich polypeptide similarly to the CD spectra, which suggest that the lipid-bound peptide contains significantly more β-structure than in the absence of lipid. This β-rich conformation is established within the first few minutes and on a similar timescale as the β-structure observed in the absence of lipid. Despite the higher β-content, the elements involved in peptide-peptide interaction (i.e. a form of monomer-level aggregation nucleus similar to the folding nucleus described for folding of globular proteins) may well be similar. The reaction is associated with a strong peak blue-shift (353nm to 340nm) within the dead time of the fluorescence measurement that remains stable throughout the monitored time window. In all, it is likely that the peptide interacts with lipid vesicles in a manner that leads to a highly ordered β-rich structure at the monomer level associated with partial or complete burial of the Trp residue within the membrane. However, the presence of NaCl in the physiological range re-establishs the formation of large aggregates and this combined with the preference for anionic over zwitterionic lipids clearly indicate a strong electrostatic component to the interaction between lipid and peptide. It thus appears that the interaction of SerADan with lipids occurs as a combination of both electrostatic and hydrophobic factors, which is intuitively consistent with a peptide containing both predominantly hydrophobic and highly charged regions.

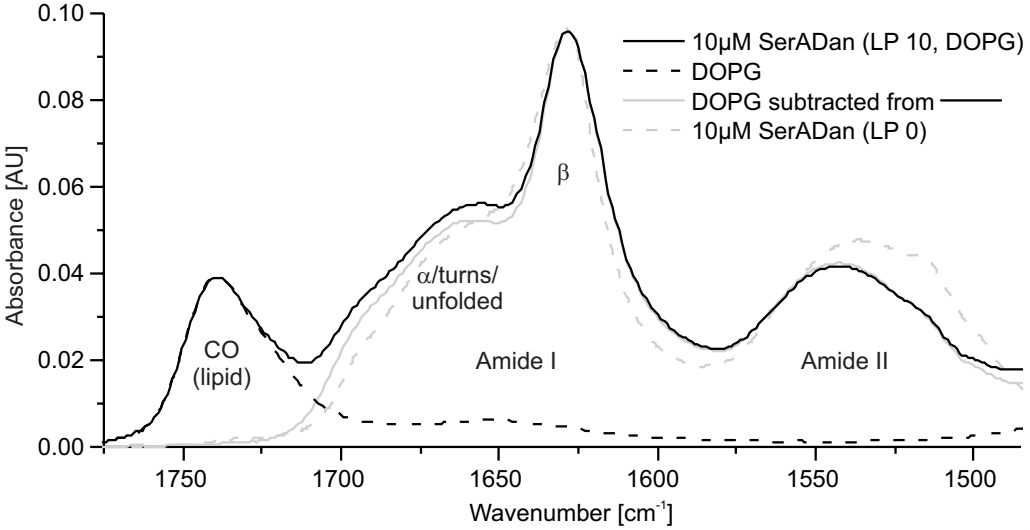

Figure 41. ATR-FTIR of SerADan with/without DOPG at pH 7.5. pH 5.0 gave similar spectra. The samples were aged 12h and dialysed overnight against diluted (10mM) aggregation buffer to remove urea and excess buffer. The spectra were baseline-adjusted and normalised to the same intensity.

3.2.6 Membrane permeabilisation and aggregation are kinetically partitioned

The strong effect of the anionic lipid DOPG, particularly at pH 7.5, led us to further investigate the interaction during early stages of aggregation at this pH

value by calcein release, which shows a strong dependence of sample ageing on the effectiveness of vesicle permeabilisation. Addition of freshly diluted peptide to calcein-containing vesicles allows release of nearly 60% compared to levels obtained by addition of detergent (paper 1/figure 7). The membrane-disturbing effects can be observed down to a lipid-to-peptide ration of 500:1, which makes SerADan a very effective membrane de-stabiliser on par with the efficiency of antimicrobial peptides [582]. However, within the initial 15 minutes, the rate constant of the time course of calcein release[11] decreased rapidly while the obtained final emission level drops to a plateau of ~30% before decreasing to practically nil concurrent with the onset of precipitation[12].

The distinct three-phased dependence upon sample ageing suggests that whereas the peptide becomes effectively sequestered in the mature aggregates of linear fibres, earlier forms of the peptide fall in two classes. The most effective agent or agents of liposome permeabilisation are the earliest and presumable smallest and least structurally complex species. The second class of oligomers may have an observable but lower intrinsic permeabilisation activity. However, an alternative and fascinating interpretation is that peptides aggregating in the absence of liposomes attain a stable, energetically favourable or kinetically trapped structure for which some degree of structural rearrangement is required for permeabilisation to occur. However, despite the dead time peak blue shift, the early fluorescence time course is preserved both in terms of time and emission intensity scales indicating that the freshly dissolved and thereby effectively penetrating peptide does display some degree of oligomerisation with similarities to the process under lipid-free conditions. Alternatively, the conformational transition associated with the decreased emission intensity could be a prerequisite of membrane binding rather than a process occurring both on- and off-membrane. It thus appears that peptide oligomerisation, membrane interaction and permeabilisation is a complex process composed to two competing and partially overlapping but kinetically partitioned pathways in the presence or absence of anionic lipids. Interestingly, the permeabilisation of the calcein-containing vesicles by freshly dissolved peptide is not complete when compared to the effect of detergent and in the kinetic partitioning scenario, this could be due to limited but significant formation of stable lipid-free aggregates. It is possible that addition of pre-incubated peptide/non-calcein vesicle samples to calcein-containing liposomes could illuminate the structural dynamics of the lipid-bound peptide ensemble, e.g. whether the membrane-bound and permeabilisation-competent peptide is effectively immobilised or capable of transfer to the calcein-containing vesicles.

3.2.7 Membrane interaction inhibits aggregation rather than enhancing it

The cessation of large-scale aggregation in the presence of anionic liposomes suggests that the lipid association plays a pivotal role in effectively preventing self-association of the peptide into large aggregates although formation of smaller oligomers appears preserved as judged by the early fluorescence changes. This is in contrast to the majority of observations for the interaction of amyloidogenic

11 The release of calcein fits well with a single exponential decay.
12 The sample was agitated so the decreasing permeabilisation is not due to disappearance of peptide from solution.

polypeptides and anionic lipids for which membrane interaction results in acceleration of fibril formation. However, inhibitory effects of anionic lipids have been demonstrated for Aβ and α-synuclein purportedly due to burial of hydrophobic segments within the membrane protecting these aggregation-promoting regions from protein self-association (see section 1.4.3).

A similar scenario could be relevant for the non-amyloidogenic SerADan given the central hydrophobic region, which could be involved in such interaction [583], and the likely membrane insertion of the Trp residue suggesting that the lipid interaction of SerADan is dependent upon a combination of electrostatic and hydrophobic effects. However, the general lack of effect of zwitterionic lipids demonstrate that the mere availability of a hydrophobic environment is not sufficient for binding to occur whereas the electrostatic interaction appears crucial. A recent study from our group [584] demonstrated the dependence of membrane surface electrostatics. Using a simple but descriptive binding-and-folding model Lars Kjær *et al.* showed that the membrane association and folding of α-synuclein into an α-rich conformation is highly dependent upon lipid gel-to-liquid disordered phase transition but also that the binding and folding was critically dependent upon the presence of anionic lipids of sufficient charge density. The kinetic partitioning between strong membrane interaction and aggregation is also curious in the light of the pH preference for membrane interaction. A significantly stronger anti-aggregational effect of the negatively charged lipids at pH 7.5 (predicted charge -1) compared with pH 5.0 (predicted charge +1). The blue-shift in Trp-emission is indicative of direct membrane contact, but an inspection of the adjacent protein sequence does not suggest an obvious and intuitive way for such charge-dependent interaction to occur. Rather, the peptide consists of the hydrophobic region with high predicted aggregational propensity flanked by two zwitterionic segments predicted to be overall neutral at pH 7.5.

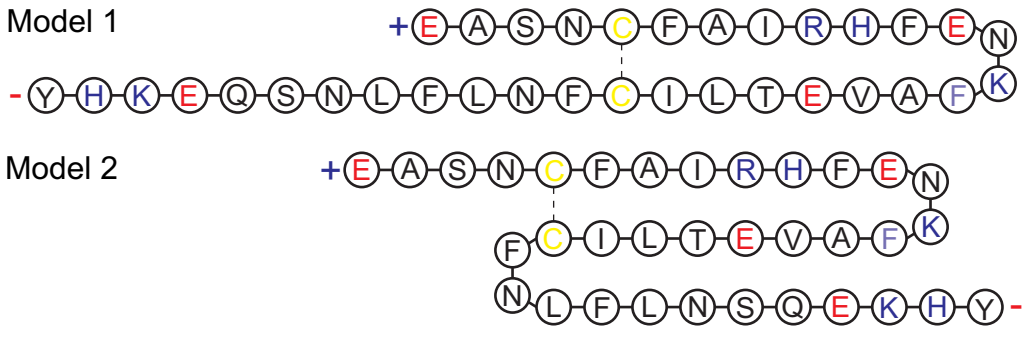

Figure 42. Models of ADan in fibrils, adapted from [557] (model 1) and [551] (model 2). Red, negative charge; blue, positive charge; yellow, cysteine; purple, Phe15 (replaced with Trp in SerADan).

A survey of literature reveals two proposed structural models for the oxADan peptide in the aggregate form (figure 42). Surolia *et al.* [551] modelled a double-stranded β-sheet (model 1) based on the 101-123 segment of transthyretin whereas Austen and co-workers [557] based their triple-stranded β-sheet (model 2) on a previously model of oxABri, which in turn was derived from multiple alignment secondary structure predictions yielding a β-strand-turn-β-strand motif for the N-terminal residues 1-23 [546]. The two models are similar for these initial 23 residues but whereas model 1 suggests a loosely coordinated loop for the 11 C-

terminal residues, model 2 describes a third anti-parallel β-strand stabilised by van den Waals interactions and electrostatic attraction between K14 and the C-terminus. Despite the differences in peptide composition as well as the absence of the intramolecular disulphide, it is interesting to speculate that the membrane-bound peptide exists in such a β-rich conformation, which allows partly or complete burial or W15 as well as interaction with the negatively charged lipid headgroups *via* a localised positively charged patch. Model 2 in particular describes the concentration of several charges at one end of the structure and in vicinity of the F15W mutation, which is interesting in light of the preference of aromatic residues for the membrane interface region [585, 586]. The charge state of histidine is malleable to the surrounding electrostatic environment, e.g. in the dipole charge stabilisation at the C-terminus of α-helices [587], and charge-stabilisation specific to the structure formed at pH 7.5 beyond the nominal pKa could conceivably explain the peculiar preference for neutral over acidic pH. However, in the absence of conclusive experimental information, it must be presumed that the residue has neutral charge at pH 7.5 and under such circumstances neither model adequately explains the preference for anionic lipids. An alternative and attractive possible explanation is that the interaction with anionic lipids is dependent upon a delicate balance between charge and hydrophobicity pushing the peptide towards lipid binding when the hydrophobicity increases as histidine is deprotonated without increasing the hydrophobic effect to the point where interaction with zwitterionic membranes becomes favourable. Studies of oligomer/detergent complexes are ongoing and could potentially shed light on the structural characteristics of these kinetically trapped species.

3.2.8 Mechanisms of increased membrane permeability

A simple structural model of SerADan binding to liposomes could involve binding of monomeric or oligomeric species to the membrane surface. In contrast to the many amyloidogenic polypeptides, which have preference for anionic liposomes, the increased concentration at the membrane surface, neutralisation of repulsive charges, non-random orientation and other surface-specific effects that could be expected from such binding does not lead to acceleration of nucleation or elongation of linear fibres. However, the structure of the membrane-bound monomer or oligomer may very well differ from the aggregation-prone species found in solution and furthermore homogeneous orientation of the peptide by membrane binding cannot be assumed. An alternative mechanism to surface membrane binding is lipid-mediated formation of size-limited β-rich oligomeric structures with burial of the Trp residue within the lipid/peptide structure. These mechanisms are both consistent with the permeabilisation of vesicles observed by calcein-release. In the former case, direct membrane permeabilisation could occur by a pore-like mechanism or by non-specific alteration of membrane permeability, which has been extensively described from amyloidogenic polypeptides. In the latter case, IAPP could serve as an instructive example. It has been proposed that extraction of lipid molecules could directly cause membrane leakage [356], but a recent study of permeability changes associated with on-membrane

fibril growth [588] suggests that it is the growth itself which disturbs the membrane, possible due to bilayer perturbation and distortion associated with peptide structural rearrangement within the membrane leading to increased membrane permeability. On-membrane fibre growth has not been observed for SerADan, but it is possible that structural rearrangement or lipid extraction could play a similar role as for IAPP.

The proposed mechanisms of SerADan-induced membrane instability share many similarities with the antimicrobial peptides (AMPs), a class of small (10-40AA) and amphipathic peptides that often, but not exclusively, are positively charged and preferentially bind to anionic membranes [589, 590]. Unlike SerADan, the majority of AMPs are random coil in solution but form amphipathic α-helices upon membrane binding with concomitant increased membrane permeability. However, there does not seem to be a single unified mechanism behind the action of AMPs. While some AMPs appear to form well-defined transmembrane pores or 'helical bundles' [591, 592], antimicrobial activity has been demonstrated for both natural AMPs and synthetic peptides in parallel orientation to the membrane [593], which is inconsistent with such pore models. For these peptides, the increased membrane permeability has been suggested to arise from transient channel formation *via* a combination of mechanisms, e.g. 'carpet'-like membrane binding and disruption, transient perturbation of lipid packing and membrane stability by diffusing peptides or detergent-like lipid extraction and membrane disintegration [591, 594-597]. Despite the prevalence of α-helical structure, a smaller subset of β-rich AMPs have been identified such as the β-hairpin forming bactenecin or the mammalian defensins (figure 43.A), which bind to membranes as triple-stranded β-sheets stabilised by several disulphide bonds [590, 598].

Figure 43. (A) Tertiary structure of human β-defensins (HBD) 1-3 (left to right). Adapted from [598]. (B) Multiple sequence alignment (www.ebi.ac.uk/Tools/clustalw2/) of SerADan and HBD1-3. * denotes preserved cysteines.

It is possible that the β-rich AMPs have similar mechanisms of action as the α-helical AMPs [598]. Similarly, self-assembled, β-rich channels are well-known for toxins such as α-latrotoxin and α-haemolysin [599-601] while formation of transient transmembrane pores have been demonstrated for β-hairpin forming peptides [602]. In general, the physiochemical properties of the lipid or detergent, e.g. charge, strongly influence the structural preferences for AMPs and the disruptive effect of AMPs hinges on a combination of electrostatic interactions and the hydrophobic effect related to the burial of hydrophobic residues in the membrane proper [589, 603-605]. While SerADan does not share e.g. the canonical multiple-cysteine defensin motif or an overall positive charge (figure 43.B), the peptide does share the strong preference for anionic lipids, the importance of electrostatic attraction in the lipid-peptide interaction, the likely burial of hydrophobic residues and, interestingly, the low concentration threshold for

membrane activity. The pore-forming ability of ABri and ADan have previously been described [202, 550], but such structures could not be identified by EM or AFM in the samples examined here However, it is conceivable that SerADan affects membrane integrity by one or several AMP-like mechanisms such as formation of well-defined channels or by less specific membrane perturbation. As such, SerADan does not only occupy an interesting position between amorphous and fibrillar aggregates but also between aggregating polypeptides and the antimicrobial peptides. Further studies of the mechanisms and effects the analogous serine-mutants of the ABri peptide *in vitro* and *in vivo* are currently in the early stages under the direction of Dr Jorge Ghiso (Departments of Pathology and Psychiatry, New York University, New York, NY, USA) and in collaboration with our group.

3.2.9 The relevance of the SerADan peptide

The balance between self-association in the form of large aggregates or membrane association and permeabilisation appears controlled by solution conditions *via* charge screening at close to physiological ion concentrations. This curious characteristic does suggest that the biological activity of the relevant ADan peptide may be similarly affected in tissue although this does assume that the observations for the SerADan peptide carries physiological relevance. My initial interest in ADan as an aggregation model system was through the combination of predominantly non-amyloid deposits *in vivo* and the aggressive nature of the disease. The design of the SerADan peptide does raise obvious questions about the biological validity of the results, but it does provide a direct link to aggregation processes occurring *in vivo*. Furthermore, the SerADan peptide combines a number of highly interesting properties. It is both capable of forming organised, linear, β-rich but non-amyloid aggregates with a puzzling lack of supersecondary structure based on our results and the ability to effectively and specifically permeabilise anionic liposomes during the very early phases of aggregation. In this light, I would argue that the peptide has proven to be of interest in its own right. The putative mechanism of SerADan aggregation *in vitro* demonstrates that mature aggregates that do not bind ThT and CR, and therefore cannot be classified as amyloid-like, can occur as a step-wise assembly process and have ordered, linear appearance.

3.3 Introduction to Paper 2

Nesgaard, L.W., Hoffmann, S.V., Andersen, C.B., Malmendal, A., Otzen, D.E. Characterization of dry globular proteins and protein fibrils by synchrotron radiation vacuum UV circular dichroism. *Biopolymers* (2008) 89 p. 779-95.

The mature linear aggregates formed by SerADan do not share classical amyloid characteristics, but seem to occupy a intermediate position between β-rich amorphous aggregates and canonical fibril structure. It is likely that more refined structural methods such as solid phase NMR [573] will yield more detailed structural information, but my structural analysis was restricted to gross morphology and secondary structure estimation. For the latter purpose, I used ATR-FTIR, which showed negligible variation among samples, and solution far-UV circular dichroism, which is somewhat unsuitable for insoluble aggregates due to scattering effects as well as the inherent non-uniform concentration throughout solution.

3.3.1 Features of circular dichroism

The circular dichroism signal is measured as the difference, rather than the ratio, between left and right circularly polarised light making the signal particularly sensitive to noise at low light intensities [606]. At wavelengths below ~190nm, the absorbance of the polypeptide, solvent and solutes increases beyond the limited light intensity of commercially available instruments fitted with xenon lamps although the practical cut-off may be well above 200nm in the presence of e.g. chloride ions or, as the case is here, urea. The 250-190nm spectral window provides a great deal of information about secondary structure, and should allow distinction between 4-5 structural elements [607, 608]. A light source with higher intensity is required to permit more detailed structural characterisation by extending the spectral window further into the far-UV range. High-flux synchrotron radiation allows spectral collection down to 160-175nm [609] (figure 44), which allows full recording of the nπ* transition and perpendicular and parallel exciton peaks of the $\pi_{nb}\pi^*$ transition as well as the interamide charge transfer

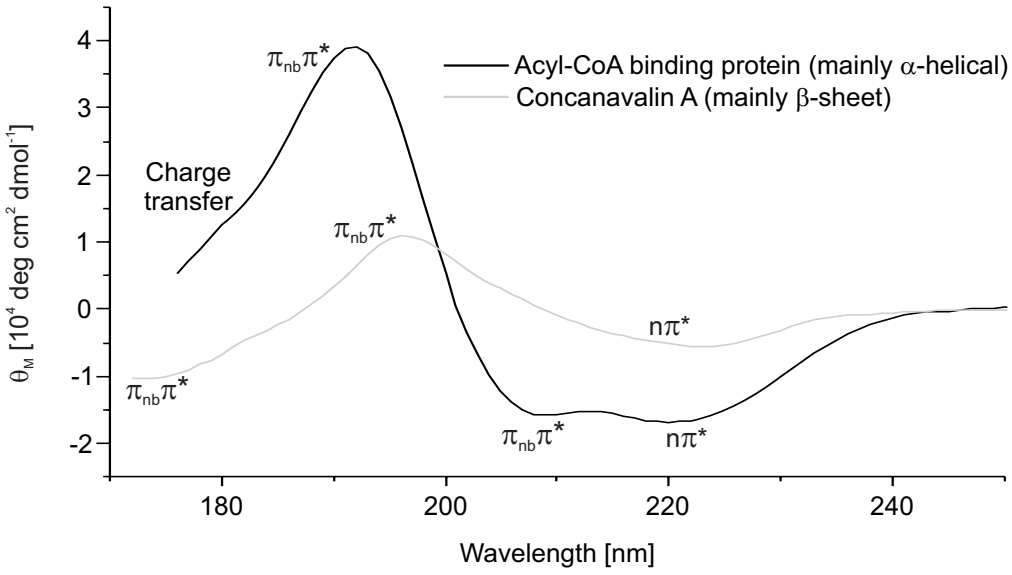

Figure 44. Representative SRCD spectra of all-α and all-β proteins from paper 2 with relevant transitions [610]. Note the difference in relative intensity. nb, non-bonding; *, anti-bonding.

transitions around 180nm. The high light influx and well-defined characteristics makes it well-suited to the purpose, but the production of high-energy synchrotron radiation requires access to expensive and technically complex accelerator equipment. Currently, only a handful of centres are exploiting synchrotron radiation for CD studies world-wide including the ASTRID (Aarhus STorage RIng in Denmark) facility at Aarhus University, Denmark. In cooperation with Dr Søren V. Hoffmann, I was given the opportunity to record synchrotron radiation vacuum UV CD (SRCD) spectra of mature SerADan aggregates. While the more detailed spectra did not lead to new extensive and conclusive structural information about the SerADan aggregates, it was the beginning of an exciting collaboration.

3.3.2 Synchrotron radiation vacuum ultraviolet circular dichroism

The information content of CD spectra dramatically increases as the spectral window is extended further into the far-UV region. Whereas spectra in the 250-190nm range only allow discrimination between four to five structural elements [608, 611], extension to 178nm could increase the information content sufficiently to allow for seven to eight structural classes (e.g. α-helix, 3_{10}-helix, β-sheet, random coil, various turns), which should suffice for meaningful estimates of secondary structure content [607]. This approach assumes highly standardised spectral contributions for each structural element. However, the practical analysis of protein β-sheet content presents a special challenge, which must be considered for β-rich structures such as fibrils or the linear SerADan aggregates. Firstly, proteins with predominant β-sheet structure but differing fold can be highly diverse in their circular dichroism [607]. The splitting of the $\pi_{nb}\pi^*$ band at ~190nm into two apparent components is a known spectral deviation observed to varying degree for e.g. immunoglobulin-like folds [612]. The nature of this variation could be unusual negative spectral contributions from e.g. aromatic residues [613, 614] or attributable to variations in β-sheet twist. The β-sheet geometry has also been implicated in the intensity differences observed for the $n\pi^*$ (~215nm) and $\pi_{nb}\pi^*$ (~198nm) bands [615] with higher relative intensity of the $\pi_{nb}\pi^*$ band for highly twisted β-sheets. Secondly, the β-sheet CD signal has a significantly lower intensity than several of the other common structural elements [607, 610]. This impedes accurate estimation of the spectral β-sheet contribution proteins of e.g. mixed α/β or α+β, but also influences the spectra obtained for proteins otherwise identified as β-rich from their crystal or NMR structures. This is demonstrated by the subdivision of all-β spectra into βI and βII types [616]. While βI-type spectra are similar to those for model β-sheets, βII-type spectra resemble those obtained for unordered polypeptides, which in turn have great similarity with poly(L-proline) II helix-like P_2-type spectra (figure 45). Sreerama and Woody [616] showed that the partitioning between βI- or βII-type spectra depends on the relative content of β-sheet (f_β) and P_2 (f_{P2}) structure, the latter of which can account for a considerable fraction of the secondary structure of globular proteins [617]. At low ratios ($f_{P2}/f_\beta < 0.4$), β-sheet dominates the spectrum but this contribution is counteracted by the higher intensity P_2 contribution at higher ratios. Spectral perturbations can also come from the intrinsic CD of aromatic residues

and disulphide bonds above 225nm [614], which can distort the low-intensity β-type spectra significantly. As a result, the extraction of structural characteristics of β-rich proteins may be poor from spectra with atypical properties despite the otherwise powerful tool provided by e.g. secondary structure estimation using reference data sets. One such example comes from jacalin, which shows a strong negative contribution at ~190nm resulting in particularly inaccurate estimation of the β-sheet content [618]. Extension of the spectral window into the vacuum ultraviolet (VUV) range could provide further structurally sensitive bands for analysis and thereby allow more accurate analysis of rare protein folds as well as potentially offer information on super-secondary and tertiary structure [609, 619, 620]. The prospect of additional spectral information allowing characterisation of subtle alterations in secondary as well as higher levels of structure is of particular interest for fibrils in light of the polymorphism in structure and stability that appears to be a common phenomenon for numerous proteins and peptides.

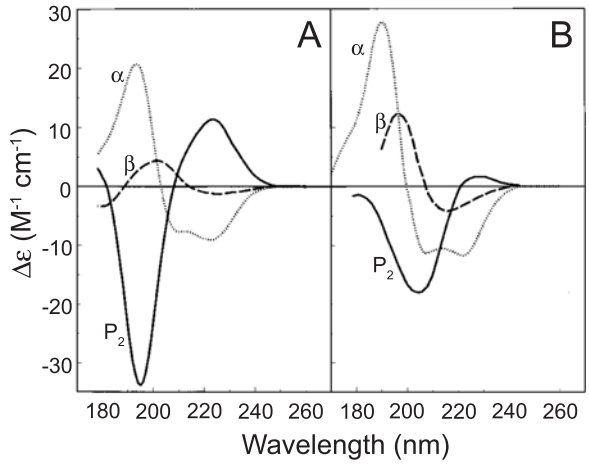

Figure 45. Examples of α-, β- and P_2-type CD spectra deconvoluted from a reference protein set (A) or model polypeptides (B). Adapted from [616].

3.3.3 Experimental approach to synchrotron radiation vacuum UV CD

The absorbance of UV light by water below ~160nm limits solution synchrotron vacuum UV CD to this wavelength and acquisition of CD spectra at higher energies requires either the substitution of water for an alternative non-absorbing solvent or drying of samples. Spectra have been recorded at wavelengths down to ~130nm using fluorinated alcohols, e.g. trifluoroethanol (TFE) and HFIP, as solvents but these alcohols have also been implicated in denaturation of globular and membrane proteins [621, 622] as well as modulation of fibrillation [623] and aggregation, as we have shown for several α-helical and β-barrel membrane proteins [624]. This effect likely arise from the reduction in relative solvent dielectric constant and associated mimicry of membrane-surface conditions [625, 626]. In contrast, amyloid, amyloid-like fibrils and other aggregates types are generally robust and studies by Dobson and co-workers [126] have shown that fibrils tolerate dehydration well without significant structural alteration. We therefore decided to use samples dried on a MgF_2 plate, which only absorb light below 125nm, in a manner similar to that used for FTIR and AFM for which a small volume was air dried or dried under a gentle nitrogen stream. Because of the relatively larger volume, the process was accelerated by placing sample under approximately ~100mbar vacuum during drying.

To allow meaningful interpretation of low wavelength features for fibril spectra if was necessary to obtain spectre for a range of globular proteins of known structure in the dry phase. For this purpose, a selection of 13 globular model proteins was chosen based on relevance, availability and the need for sufficient structural diversity to cover a range of all-α, αβ and all-β proteins. Although the former two groups are included in the selection, special emphasis was placed on β-rich proteins in light of the predominance of β-sheet in fibrils and aggregates and the structural diversity of all-β proteins. The model proteins were dried and otherwise treated similarly to fibril and aggregate samples for the dry phase spectra. Globular proteins are less tolerant towards drying and dehydration than aggregates although the preservation of native-like structure under ambient temperature is a recurrent observation [627-629]. As the primary purpose of the study was to obtain information about structurally sensitive features below ~160nm, elucidation of the overall preservation of spectral features upon drying became a secondary purpose. To this end, spectra for both model proteins and aggregate or fibril samples were obtain for in aqueous solution (or 'wet phase') using quartz cuvettes, which are opaque below 165nm, as well as in the dry phase.

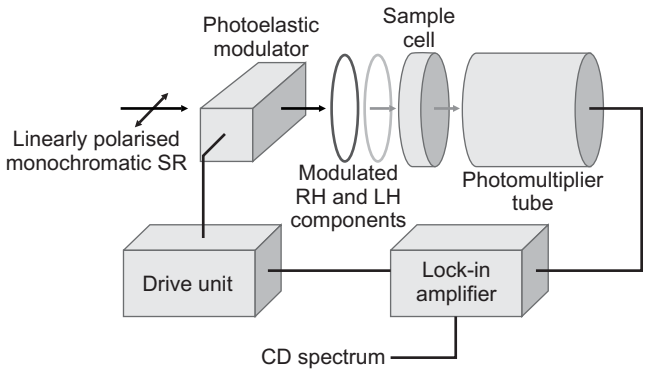

Figure 46. Schematic overview of SRCD instrumentation on the UV1 beamline (www.isa.au.dk/facilities/astrid/beamlines/uv1/)

ASTRID has several beamlines including the custom-built synchrotron vacuum-UV CD (SRCD) facility (figure 46) using the high-flux UV1 beamline [630]. Briefly, the highly linear polarised UV1 beam was converted to circularly polarised light with alternating left- and right-handed orientation at a frequency of 50Hz by a CaF_2 Photo Elastic Modulator (PEM, model I/CF50, Hinds Instruments, Hillsboro, Oregon, USA). The light beam was passed through the sample and sample chamber, which was continuously purged with nitrogen to limit absorbance from atmospheric oxygen, and detected with a UV-sensitive photomultiplier tube (PMT, model 9402B, Electron Tubes, Uxbridge, UK) and lock-in amplifier. The pre-use calibration with camphor sulphonic acid (CSA), baseline and sample spectrum acquisition as well as post-acquisition data treatment was similar for wet and dry phase with exception of a lower wavelength end-point for the dry phase spectra. For comparison between wet and dry phase spectra, the concentration-sensitive detector voltage for the protein-specific peak at 190nm was used for normalisation of the dry phase spectrum to the known concentration for the wet phase spectrum.

Characterization of Dry Globular Proteins and Protein Fibrils by Synchrotron Radiation Vacuum UV Circular Dichroism

Lise W. Nesgaard,[1] Søren V. Hoffmann,[2] Christian Beyschau Andersen,[1,3] Anders Malmendal,[4] Daniel E. Otzen[1,5]

[1] *Department of Life Sciences, Aalborg University, Sohngaardsholmsvej 49, DK-9000 Aalborg, Denmark*

[2] *Institute for Storage Ring Facilities (ISA), Aarhus University, Ny Munkegade, DK-8000 Aarhus C, Denmark*

[3] *Protein Structure and Biophysics, Novo Nordisk A/S, Novo Nordisk Park, DK - 2760 Måløv, Denmark*

[4] *Interdisciplinary Nanoscience Center (iNANO) and Department of Chemistry, Center for Insoluble Protein Structures (inSPIN), Aarhus University, Ny Munkegade, DK-8000 C, Denmark*

[5] *Department of Molecular Biology, Interdisciplinary Nanoscience Centre, Faculty of Natural Sciences, Aarhus University, Gustav Wieds Vej 10C, DK-8000 Aarhus C, Denmark*

Received 26 February 2008; revised 10 April 2008; accepted 11 April 2008
Published online 5 May 2008 in Wiley InterScience (www.interscience.wiley.com). DOI 10.1002/bip.21011

ABSTRACT:

Circular dichroism using synchrotron radiation (SRCD) can extend the spectral range down to ~130 nm for dry proteins, potentially providing new structural information. Using a selection of dried model proteins, including α-helical, β-sheet, and mixed-structure proteins, we observe a low-wavelength band in the range 130–160 nm, whose intensity and peak position is sensitive to the secondary structure of the protein and may also reflect changes in super-secondary structure. This band has previously been observed for peptides but not for globular proteins, and is compatible with previously published theoretical calculations related to π-orbital transitions. We also show that drying does not lead to large changes in the secondary structure and does not induce orientational artifacts. In combination with principal component analysis, our SRCD data allow us to distinguish between two different types of protein fibrils, highlighting that bona fide *fibrils formed by lysozyme are structurally more similar to the nonclassical fibrillar aggregates formed by the SerADan peptide than with the amyloid formed by α-synuclein. Thus, despite the lack of direct structural conclusions, a comprehensive SRCD-based database of dried protein spectra may provide a useful method to differentiate between various types of supersecondary structure and aggregated protein species.* © *2008 Wiley Periodicals, Inc. Biopolymers 89: 779–795, 2008.*

Keywords: structural classes; protein films; band shift; hydration effects; orientational artifacts

This article was originally published online as an accepted preprint. The "Published Online" date corresponds to the preprint version. You can request a copy of the preprint by emailing the Biopolymers editorial office at biopolymers@wiley. com

INTRODUCTION

The deposition of soluble proteins or peptides in the form of insoluble amyloid plaques is associated with many systemic and neurodegenerative diseases such as Alzheimer's disease, Parkinson's disease and Type II diabetes mellitus.[1] Because of their insolubility, amyloid-like fibrils do not lend themselves easily to structural studies, but some insight has been gleaned from e.g. cryo-electron microscopy and X-ray diffraction studies of model fibrils formed in vitro.[2–5] These methods offer detailed

Correspondence to: Daniel Otzen; e-mail: dao@inano.dk
Contract grant sponsors: Aalborg University, Novo Nordisk A/S, the Danish Ministry of Science, Technology and Innovation, Danish Research Foundation

structural information, but are technically demanding and not well suited for high-throughput studies. In contrast, several spectroscopic methods allow fast and reliable estimation of secondary structure. Among the commonly used methods are infrared, Raman, and far-UV circular dichroism spectroscopy (CD).[6] Each method has advantages and drawbacks. Infrared spectroscopy, usually in the form of Fourier-transform infrared spectroscopy (FTIR), is useful for secondary structure characterization, but high confidence estimates require spectra of high quality, whose acquisition is complicated by the presence of strongly absorbing water as solvent and vapor. This demands meticulous sample handling and use of deuterium oxide or dried protein films.[7,8] Circular dichroism offers simpler sample handling and experimental conditions closer to physiological values. The method, when using conventional lamp-based CD instruments, is highly useful for α-rich proteins but has lower accuracy for proteins with a low α-helix content due to a number of factors such as presence of aromatic residues and the relatively lower signal intensity of β-sheet compared to α-helix above 190 nm.[9,10]

Circular dichroism is measured as the difference in absorption of left- and right-handed circularly polarized light ($\Delta A = A_L - A_R$) and commonly expressed as mean residue molar ellipticity. The magnitude of the difference is small for protein samples leading to the need for high light influx. A commercially available instrument equipped with a xenon arc lamp typically gives meaningful information down to ~190 nm although the spectral window can be further limited by the presence of species that absorb strongly in the far-UV range such as chloride ions.[11] This only allows distinction between a handful of structural classes, but extension of the spectral window into the vacuum ultra violet (VUV) range would provide additional information about secondary structure and potentially allow assessment of super-secondary and tertiary structure information.[12–14] Synchrotron radiation is eminently suited for this purpose given its high intensity and well-defined electromagnetic characteristics and has been used successfully to increase the accuracy of secondary structure prediction by allowing spectra to be measured down to 160 nm. The lower limit for synchrotron radiation CD (SRCD[1]) is dictated by the presence of water.[10] This is not a major problem for protein fibrils and aggregates, because sample heterogeneity and insolubility makes it more appropriate to study them in the form of thin protein films.[15–17] By eliminating water, it should be possible to extend the available spectral range down to 130 nm and thereby obtain additional structural information.

Based on these considerations, we here present the use of circularly polarized far-UV synchrotron radiation (SRCD) on dried protein samples.

To elucidate the usefulness of the method, thirteen globular model proteins were selected with varying structural motifs (Table I). The list of potential model proteins was winnowed down based on availability and relevance to include proteins with α-rich, mixed α-β, and β-rich structures. Spectra were obtained for both solubilised proteins and dried proteins films to assess the advantage of extending the spectroscopic window weighed against the risk of structural rearrangement of proteins due to altered hydration. Structural effects of drying have previously been described,[18,19] suggesting that drying at ambient temperatures preserves structure whereas e.g. freeze-drying might lead to conformational changes. In this study our concern is to elucidate whether the drying process perturbs the CD spectra to an extent that prevents a meaningful interpretation of the spectra for dried samples.

We used an over representation of β-rich proteins to allow further examination of various β-sheet configurations, particularly sandwiched sheets. The characterization of β-rich proteins was of special importance because of the wide range of structural motifs observed in β-sheet globular proteins and the prospect that information could be gleaned from spectra features at lower wavelengths, which could assist in differentiating structural motifs. Including a high number of β-rich proteins was also of interest for the characterization of protein fibrils, which are known to have high β-sheet content. Nevertheless, although all fibrils display a characteristic stacking of β-strands, there is an increasing number of reports of fibrillar polymorphisms, which include subtle variations in secondary structure and associated stability.[20–22] This is substantiated by recent X-ray microcrystal structures revealing several different types of β-strand arrangements in fibrils.[23] Our results suggest that SRCD may provide a method for more detailed classification of such polymorphism.

RESULTS

Spectral Features Are Preserved for Dry Phase Spectra

Denaturation caused by disruption of native protein-solvent interactions is a major concern when protein samples are dried to form protein films. It has previously been shown for globular proteins (including serum albumin, ConA, trypsin, and lysozyme) that secondary structure maybe preserved during film-formation and that protein films can be used for structural studies.[17,24] To investigate whether protein films retain the same structure as in solution under the conditions of our experiments, we recorded

Table I Model Proteins and Fibrillar Samples Used for Wet and Dry Phase Synchrotron Circular Dichroism

Protein/Peptide	Class	Architecture	Topology	Remarks	Pdb
Acyl-CoA-binding protein (ACBP, bovine)	Mainly α	Up-down bundle	ACBP		1HB6
α-lactalbumin (bovine milk)	Mainly α	Orthogonal bundle	Lysozyme		1HFX
β-galactosidase (*Escherichia coli*)	α β	Complex		Complex, multidomain protein. Predominantly β	1DP0
Carbonic anhydrase (bovine)	α β	Roll	Carbonic anhydrase II	Single sheet, 10 strands. Predominantly β	1V9E
Concanavalin A (ConA, *Canavalia ensiformis*)	Mainly β	Sandwich	Jelly roll	Sandwich, 12 strands in two sheets, complex topology	1NLS
Jacalin (*Artocarpus integrifolia*)	Mainly β	Aligned prism	Vittelline		1KU8
Porcine serum albumin (PSA)	Mainly α	Orthogonal bundle	Serum albumin		1HK1
S6, ribosomal subunit (*Thermus thermophilus*)	α β	2-layer sandwich	α-β plaits		1RIS
Tenescin, third fibronectin type III repeat (Tnfn3, human)	Mainly β	Sandwich	Immunoglobulin-like (Fibronectinv type III)	7 strands in two sheets	1TEN
Thaumatin (*Thaumatococcus danielli*)	Mainly β	Sandwich	Thaumatin	11 strands in two sheets	1RQW
Titin, Ig repeat 27 (TII27, human)	Mainly β	Sandwich	Immunoglobulin-like (Immunoglobulins)	7 strands in two sheets	1TIT
Transthyretin (human)	Mainly β	Sandwich	Immunoglobulin-like (Transthyretin)	7 strands in two sheets	1F41
Trypsin (bovine pancreatic)	Mainly β	β-barrel	Thrombin	6-stranded barrel	5PTP
Alpha synuclein (human)	N.A.			Fibrils, two forms	N.A.
Lysozyme (hen egg white)	N.A.			Fibril	N.A
SerADan	N.A.			β-rich aggregates with linear structure, two types	N.A.

Model proteins are described using CATH classification. N.A, not applicable.

spectra for both wet samples and dried proteins films. Since the conversion of spectral raw data to mean molar ellipticity is dependent on knowledge of the protein concentration, the dried spectra were normalized by comparison of the protein absorbance at 190 nm.

For α-helical and mixed α-β proteins (see Figure 1), the main spectral difference lies in the relative intensities of the three $n\pi^*$ and $\pi\pi^*$ bands, which lie approximately at the well-known values of 222, 208, and 190 nm. The spectra display a minimum at 160–170 nm and, for ACBP and serum albumin, a weak shoulder at ∼180 nm. Spectral features in this area have previously been ascribed to $n\pi^*$ or $\pi\pi^*$ charge transfer transitions for α-helical and β-sheet geometries, respectively.[25–27] Only limited band shifting can be observed, predominantly for the perpendicular exciton peak (∼190 nm) for which a slight red-shift occurs upon drying. There is no clear tendency in the intensity differences. This suggests that the shift and intensity differences are protein-specific rather than a general effect of the drying process.

The same overall preservation of spectral features can be observed for the β-rich protein concanavalin A (ConA) and thaumatin (see Figure 2). Both represent nonimmunoglobulin-like sandwich architectures. Although drying mainly affects the relative intensities for ConA, thaumatin shows a slightly larger red-shift of the $n\pi^*$ band (∼215 nm) than ConA. As previously described,[28] thaumatin also displays a positive band at ∼230 nm, consistent with the presence of aromatic side-chains and disulfide bonds.[29] The band is preserved upon drying, although an apparent baseline shift can be observed. Spectral artifacts due to unavoidable scattering in the protein film were minimized by a short sample to detector distance of less than 30 mm. Since any possible scattering increases at lower wavelength, the spectra were recorded up to 330 nm, to ensure that any discrepancy between the baseline and the sample

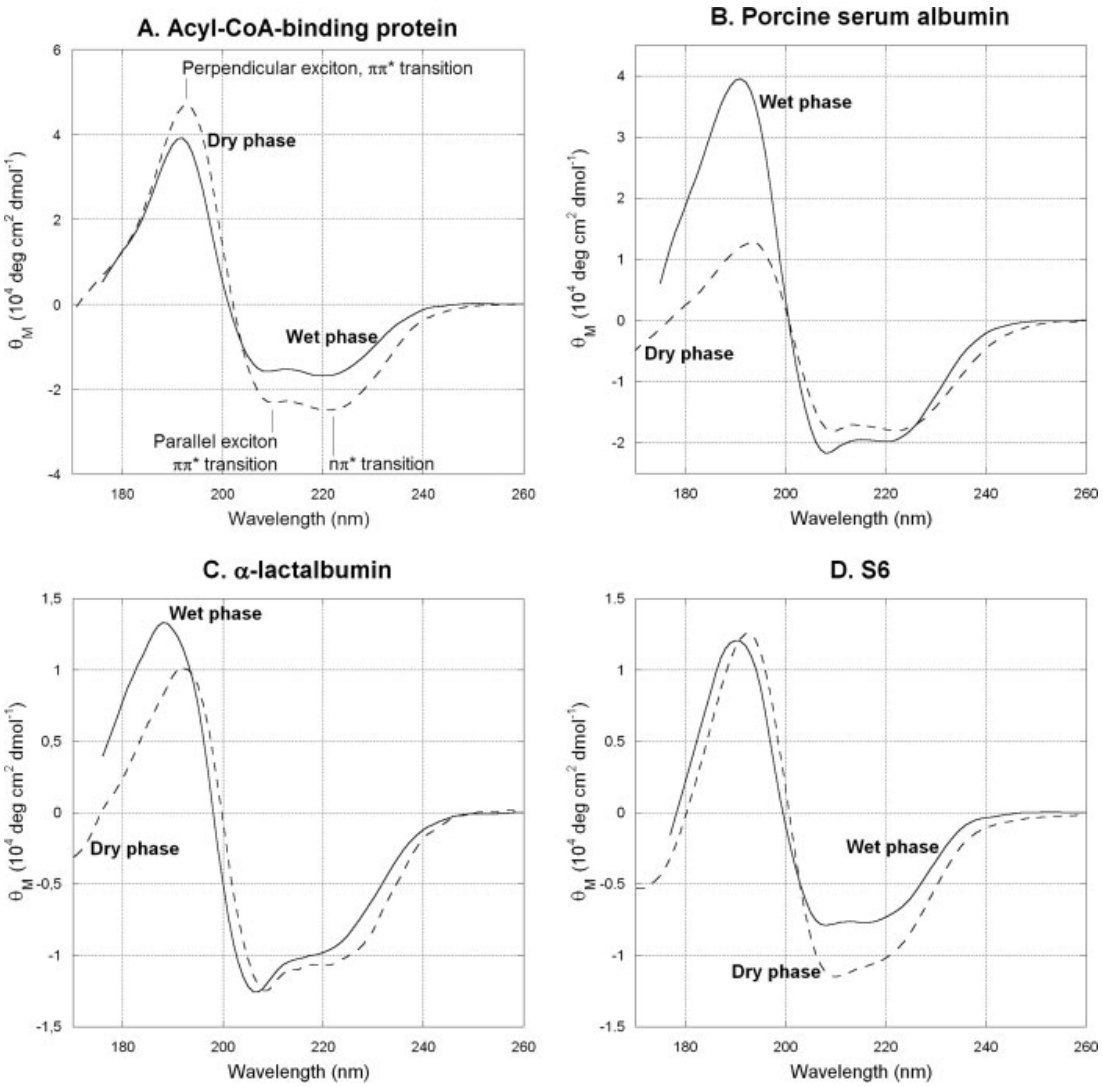

FIGURE 1 Wet and dry phase CD spectra for mainly α-helix and mixed α+β structural classes. A. Acyl-CoA-binding protein (ACBP) with peaks corresponding to nπ* and ππ* electronic transitions marked. B. Porcine serum albumin. C. α-lactalbumin. D. S6.

spectra were due to properties of the protein film, and not an instrumental artifact.

The presence of a similar strong, positive band at higher wavelengths (∼230 nm) combined with a relatively weak nπ* band can be observed for the immunoglobulin-like proteins (see Figure 3). This unusual appearance of the typical β-sheet spectrum is well known for Bence Jones-like structures and likewise attributed to side-chain interference.[30,31] A comparable shift in baseline, which partially obscures the presence of aromatic side-chains, combined with a striking shift in relative peak intensities can also be seen for the immunoglobulin class. In addition there is a significant red-shift of the nπ* band, while the ππ* band remains largely unaffected, in contrast to the band-shifts observed for predominantly α-helical proteins. Splitting of the ππ* band at ∼200 nm (Figures 3A and 3B) has also been observed for some immunoglobulins.[32]

The remaining four globular proteins, carbonic anhydrase, trypsin, jacalin and β-galactosidase, represent β-rich structural classes that differ from the immunoglobulin-like proteins and, in the case of β-galactosidase, is of a highly complex nature including both β-sandwich and other architectures (see Figure 4). For all proteins, the recorded wet phase spectra correspond well to known spectra obtained from literature.[12,14,33,34] While carbonic anhydrase is classified as a mixed α-β-protein, the predominant structure type

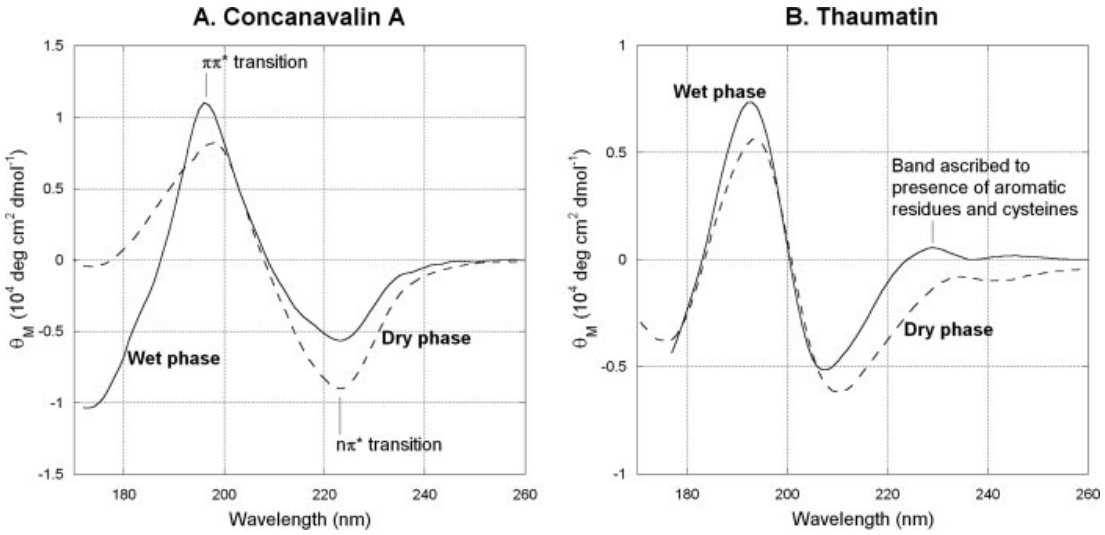

FIGURE 2 Wet and dry phase CD spectra for non-immunoglobulin-like sandwich architectures. A. Concanavalin A (ConA) with peaks corresponding to nπ* and ππ* electronic transitions marked. B. Thaumatin.

is β-sheet and has a spectrum similar to the classical β_I-sheet spectrum.[9,33] Drying causes a similar shift towards negative ellipticity and red-shift of the negative nπ band as observed for sandwich-type folds. A comparable baseline shift is observed for the aligned prism jacalin. This protein is characterized by the atypical negative band at ~190 nm, which has been speculated to be an effect of local environment or β-sheet twisting.[35] A less pronounced but similar splitting is also observed for the two immunoglobulin-like proteins Tnfn3 and TII27.

The only significant red-shifts for jacalin are observed for the bands at ~202 nm and ~182 nm. In contrast, trypsin shows red-shift of both positive and negative peaks, similar to what is observed for the large and complex β-galactosidase, although this protein shows little variance in peak intensities upon drying.

Overall, we observe preservation of spectral features upon drying for all structural classes, which reassures us that the protein films have not undergone significant structural changes compared to the solution state.

Proteins Do Not Significantly Order Within Film

The extent of absorbance for any single chromophore within a protein will depend on the orientation with respect to the direction of polarization of light. For a film with a high degree of cooperative organization between proteins, i.e. organized or maybe even crystalline films, the orientation could have a significant effect on the obtained spectrum with artifacts arising from a potentially very strong linear dichroism signal. To ensure that no in-plane molecular alignment occurred due to the drying process of making the protein film, spectra of dried samples were obtained before and after rotation by 90° of the MgF_2 plate upon which a sample had been dried. No significant difference was observed when the sample plate was rotated (data not shown), indicating that the observed spectrum predominantly demonstrated biologically relevant structural data rather than orientation-related artifacts.

Estimates of Secondary Structure Show Good Correspondence with Known PDB Structures

The general preservation of spectral features prompted us to estimate the secondary structure of the globular model proteins for both the wet and dry phase spectra using the CDSSTR program and reference sets available at DICHROWEB (Table II). CDSSTR is intended for analysis using water as solvent, but the spectral similarities indicated its potential usefulness in analysis of the dried protein films as well. Values for native secondary structure were extracted from crystal structure data using the DSSP algorithm and grouped by simple partitioning into α-helical, β-sheet and other structure as described by Oberg et al.,[36] which has previously been used successfully for comparison of CD and PBD data.[37] We cannot exclude that a different grouping of assignments might lead to differences in the analysis, but that is outside the scope of this article. We are here concerned with overall similarity to crystal structure.

For the majority of spectra, both wet and dry phase yield estimates the approximate values obtained from crystal structures. The main inaccuracy is related to estimates

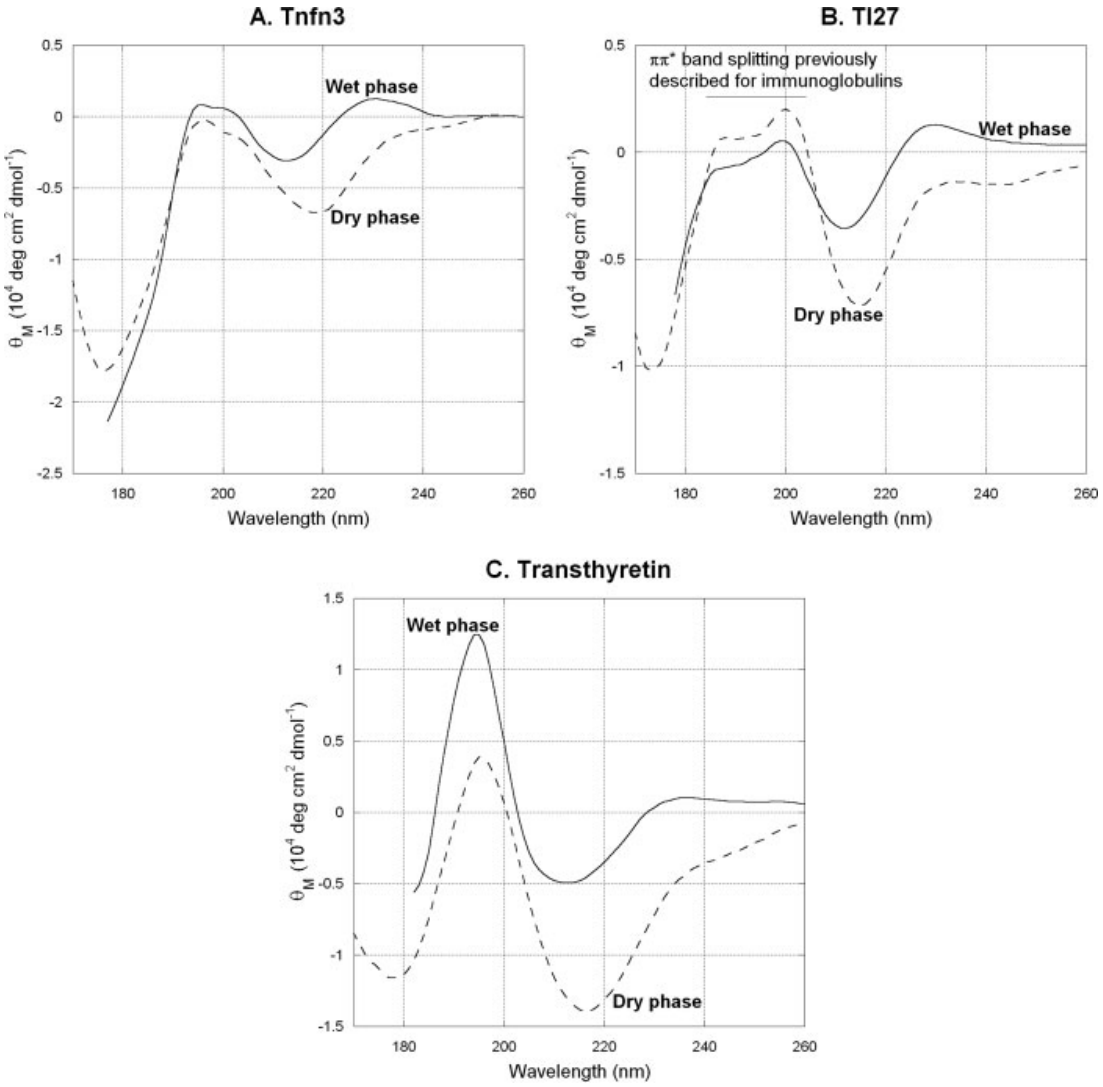

FIGURE 3 Wet and dry phase CD spectra for immunoglobulin-like folds.

predicting a small presence of β-sheet in predominantly α-helical proteins or vice versa. For the immunoglobulin-like proteins, the estimates have a higher deviation from the crystal structure predictions, which is expected, given the side-chain interference superimposed on a low-intensity β-sheet signal. Curiously, transthyretin shows good agreement for the wet phase and PDB data, but with little similarity to the values obtained for the dry phase. The estimates for jacalin are also predictably poor because of the atypical spectra. Overall the correspondence between PBD and CD data is sufficient to determine the structural class for both solubilised protein and protein film with the exception of dry phase transthyretin.

A subset of the model proteins was also investigated in the dried state using ATR-FTIR (see Figure 5) followed by secondary structure estimation (Table III). These were compared to data for the native structures obtained as described above. FTIR and PDB values correspond reasonably well for β-galactosidase, carbonic anhydrase, serum albumin, and thaumatin, but with lower accuracy for α-lactalbumin although the protein is estimated to have mixed α/β-content. In all cases, the content of the predominant structural class was overestimated at the expense of loops and other structural elements.

The various structural elements do not give rise to well-separated structural bands in infrared spectroscopy but rather to a single, relatively featureless overall band, which can only be cautiously analyzed by use of Fourier self-deconvolution. A likely reason for the inconsistency in the data for α-lactalbumin is this overlap between the bands corresponding to

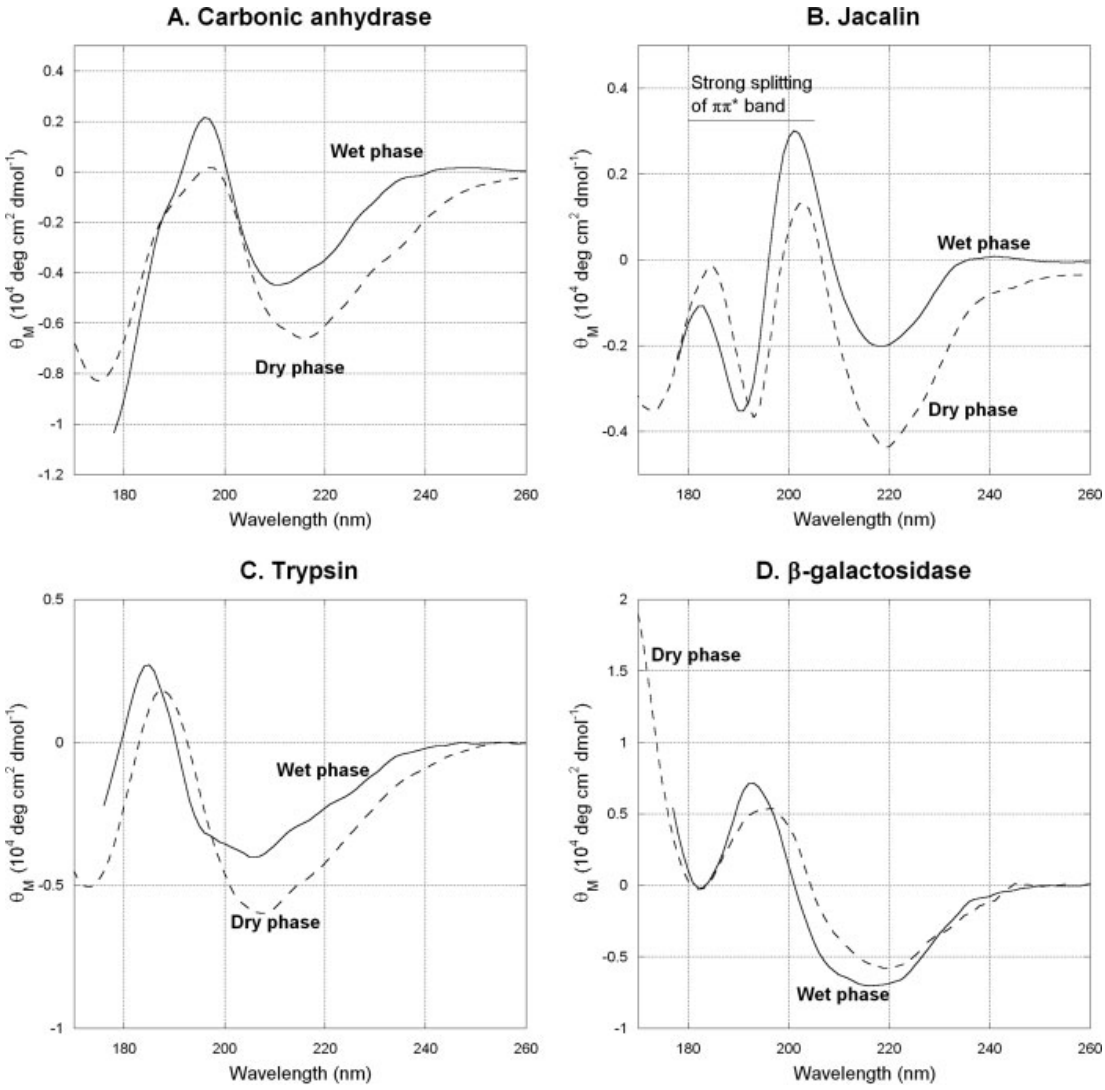

FIGURE 4 Wet and dry phase CD spectra for other mainly β folds and complex structures.

individual structural elements. Overall, the data obtained by FTIR support our previous conclusion from CD spectra that drying does not cause significant loss of structure.

Principal Component Analysis of Wet and Dry Spectra Correspond Well to Estimated Structural Content

To obtain correlations which are not obvious from the general structural analysis, we performed principal component analysis (PCA) for wet and dry spectra. PCA provides a ranked series of components that describe the changes among a collection of spectra. The first principal component accounts for the great majority of the spectral variance, but useful modulations within this variance may be provided by the second component. Spectra were analyzed both as separate data sets and as a combined wet and dry data set. For all data-sets, the first principal component (PC 1) was found to correlate well with estimated helical content (see Figure 6). The correlation was best for the combined wet and dry data set (R^2 0.9499) and weaker for the isolated wet and dry data sets. The β-sheet content of globular proteins correlates with α-helix content because these two constitute the major structural classes so that low β-sheet content corresponds to high α-helix content. PC 1 was therefore found to correlate well also with β-sheet content. The subsequent components did not show correlation with estimated structural content of less abundant structural classes such as turns. This could be due to the low frequency of residues in such conformations, lack of well-defined spectral characteristics for the structural type or the actual PCA method used.

For more in-depth analysis, subsequent PCs were plotted against the primary principal component for the isolated wet

Table II Structure Estimates from Circular Dichroism and Crystal or NMR Structure

Model Protein	α-helix[a]	β-sheet[a]	Other[a]	NMRSD[a]
ACBP	0.56	0.10	0.34	0.022
	0.72	0.01	0.27	0.012
	0.64	0	0.36	
α-lactalbumin	0.31	0.14	0.56	0.012
	0.35	0.13	0.51	0.025
	0.29	0.08	0.63	
β-galactosidase	0.15	0.32	0.53	0.033
	0.08	0.40	0.52	0.053
	0.10	0.38	0.51	
Carbonic anhydrase	0.05	0.37	0.58	0.043
	0.07	0.32	0.61	0.049
	0.08	0.29	0.63	
ConA	0.06	0.44	0.49	0.045
	0.08	0.39	0.53	0.026
	0	0.46	0.54	
Jacalin	0	0.44	0.53	0.190
	0.05	0.40	0.54	0.052
	0	0.62	0.38	
Serum albumin[b]	0.64	0.05	0.29	0.009
	0.59	0.13	0.28	0.007
	0.66	0	0.34	
S6	0.19	0.29	0.51	0.027
	0.28	0.24	0.49	0.017
	0.26	0.28	0.47	
Tnfn3	0.01	0.43	0.55	0.111
	0.07	0.37	0.57	0.022
	0	0.53	0.47	
Thaumatin	0.03	0.42	0.54	0.028
	0.07	0.39	0.53	0.088
	0.11	0.36	0.54	
TII27	0	0.47	0.50	0.098
	0.06	0.35	0.60	0.143
	0	0.33	0.67	
Transthyretin	0.05	0.46	0.48	0.018
	0.34	0.29	0.38	0.009
	0.06	0.48	0.46	
Trypsin	0.03	0.33	0.62	0.043
	0.06	0.34	0.58	0.075
	0.07	0.32	0.61	

[a] 1st row, wet phase CD; 2nd row, dry phase CD; 3rd row, estimate from DSSP.

[b] Both human and porcine types of serum albumin were analyzed and gave similar values.

and dry data sets. If the second principal component (PC2) is plotted against PC1 (Figures 7A and 7B), a clear separation is seen based on structural class. α- and α/β proteins, with the exception of the dry-phase values for the complex β-galactosidase, lie in two groups separate from the larger area containing β proteins. However, there is an interesting variance within the β-protein group. In the wet phase, the three Ig-like folds Tnfn3, TII27, and transthyretin have similar PC1 values but highly different PC2 values. In the dry phase, both PC1 and PC2 differ but in a similar pattern with Tnfn3 lying close to the main β-protein area and transthyretin furthest away. This variance could illustrate a structural difference but could also be due to the positive aromatic and cysteine signal at ∼230 nm, which is strong for these folds. However, it should be mentioned that transthyretin does not have an apparent strong aromatic signal for either wet or dry phase. If the third principal component (PC3) is plotted against PC1 (Figures 7C and 7D), the observed clustering is similar to that observed for PC2 although the Ig-fold variance is not observed. Overall, the PCA yields a meaningful clustering of structural classes for both wet and dry phases, further affirming that drying does not significantly alter structure.

Low Wavelength Features Correlated to Structural Class and Architecture

Drying of samples expanded the spectroscopic window towards 130 nm and revealed new spectral features. For the majority of proteins, the spectrum climbs from the negative band at ∼160–175 nm for α-helical proteins and 170–180 nm for β-sheet proteins to a well-defined positive band centered at 140–160 nm. The positive band has previously been observed for UVCD studies of α-helical oligomers or cyclic amino acid dimers in halogenated alcohols or dried films[38–40] (see DISCUSSION). However, the band has not been correlated with other structural features of either peptide or globular proteins. To elucidate this in more detail, we have therefore recorded spectra down to 130 nm for a number of

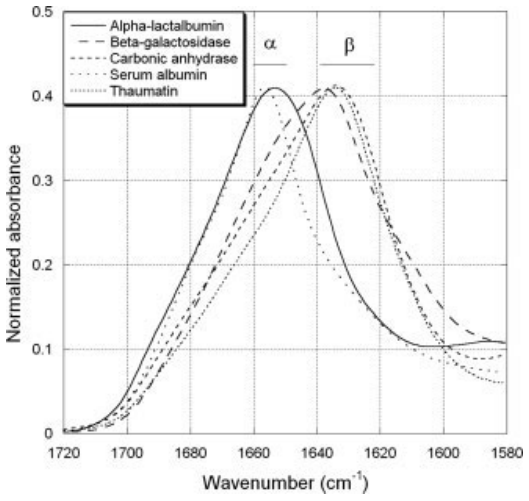

FIGURE 5 Representative ATR-FTIR spectra of model proteins shown for the structurally sensitive amide I area. α-helical signals predominate at ∼1655 cm^{-1} and β-sheet signals between 1622–1638 cm^{-1}.

Table III Structure estimates from AT-FTIR and PDB file

Model Protein	α-helix[a]	β-sheet[a]	Other[a]
α-lactalbumin	0.54 (0.04)	0.06 (0.03)	0.40 (0.02)
	0.29	0.08	0.63
β-galactosidase	0.19 (0.03)	0.37 (0.02)	0.44 (0.03)
	0.10	0.38	0.51
Carbonic anhydrase	0.08 (0.04)	0.29 (0.02)	0.63 (0.03)
	0.08	0.29	0.63
Serum albumin	0.75 (0.04)	0.01 (<0.01)	0.24 (0.03)
	0.66	0	0.34
Thaumatin	0.10 (0.04)	0.54 (0.02)	0.36 (0.03)
	0.11	0.36	0.54

[a] 1st row, FTIR (+/− s.e.m.); 2nd row, estimated from DSSP.

globular proteins covering a wide range of structures. Interestingly, the position of the 140–160 nm band appears to be associated with secondary structure as discussed below (summarized in Table IV). However, there is no clear correlation between the intensity of this band and bands at higher wavelengths, although the bands largely fall within the same intensity range, i.e. α-helical proteins show higher intensity than β-sheet proteins.

Proteins containing significant α-helical structure (i.e. >25%) have a common band position at 140–142 nm (Figure 8A). In the case of S6, which contains similar fractions of α-helix and β-sheet, the spectrum also displays a shoulder at ∼160 nm, which could be attributable to the mixed structure since the β-rich proteins show bands at higher wavelengths. For both immunoglobulin-like and other sandwich architectures, the band is centered at higher wavelengths, such as 149–152 nm for ConA, thaumatin, TII27 and Tnfn3 and 157 nm for transthyretin (Figure 8B). The third group of proteins, mainly β-sheet with more complex architectures, shows a wider variety of spectral features as expected (Figure 8C). Jacalin and trypsin both have well-defined bands located at 147-148 nm. It is possible that a similar band could be observed for carbonic anhydrase, but the considerable increase in background absorbance from 145 nm onwards, possibly because of opacity of the dried film, interferes with the spectrum. As a result, the spectrum for carbonic anhydrase could not be quantified below 147 nm. This is also likely to be the cause of the final shape of the spectrum for TII27. The final example, β-galactosidase, has the highest band position among the model proteins at 166 nm (Figure 8D), which is a sufficiently high wavelength that the tail of the peak is also detectable on the wet phase spectrum. This high position could be caused by a number of factors including the tertiary structure of the 116 kDa protein, which is a combination of several structural motifs including immunoglobulin-like β-sandwich and triosephosphate isomerase α/β-barrel-like folds. Contributions from aromatics and cysteines, which are known to affect the region around 240–220 nm, could also play a part.[29]

Fibril Spectra Show Spectral Features Similar to β-Rich Globular Proteins

Spectra of protein aggregates and fibrils of various types were obtained in wet and dry phase to acquire both far-UV and VUV-range structural information. One of the well-known in vitro models of amyloid is lysozyme fibrillated at low pH, for which there is good correspondence with the typical β_1-sheet spectrum (Figure 9A). The low-wavelength band at 145

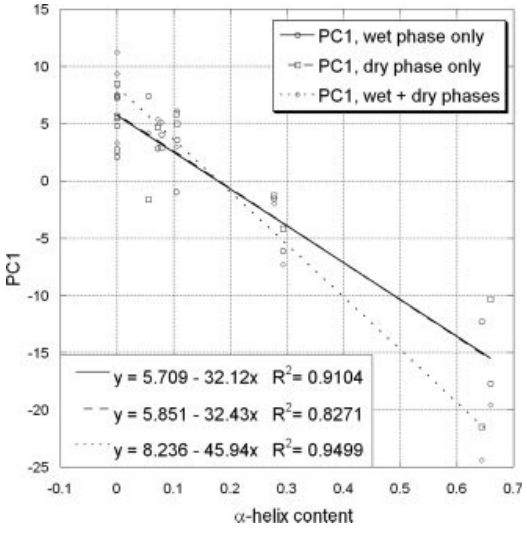

FIGURE 6 Correlation between α-helical content and first principal component for three data sets: Wet phase spectra only, dry phase spectra only and wet and dry phase spectra combined. All three datasets show similar linear correlation between the fraction of α-helical structure and PC1.

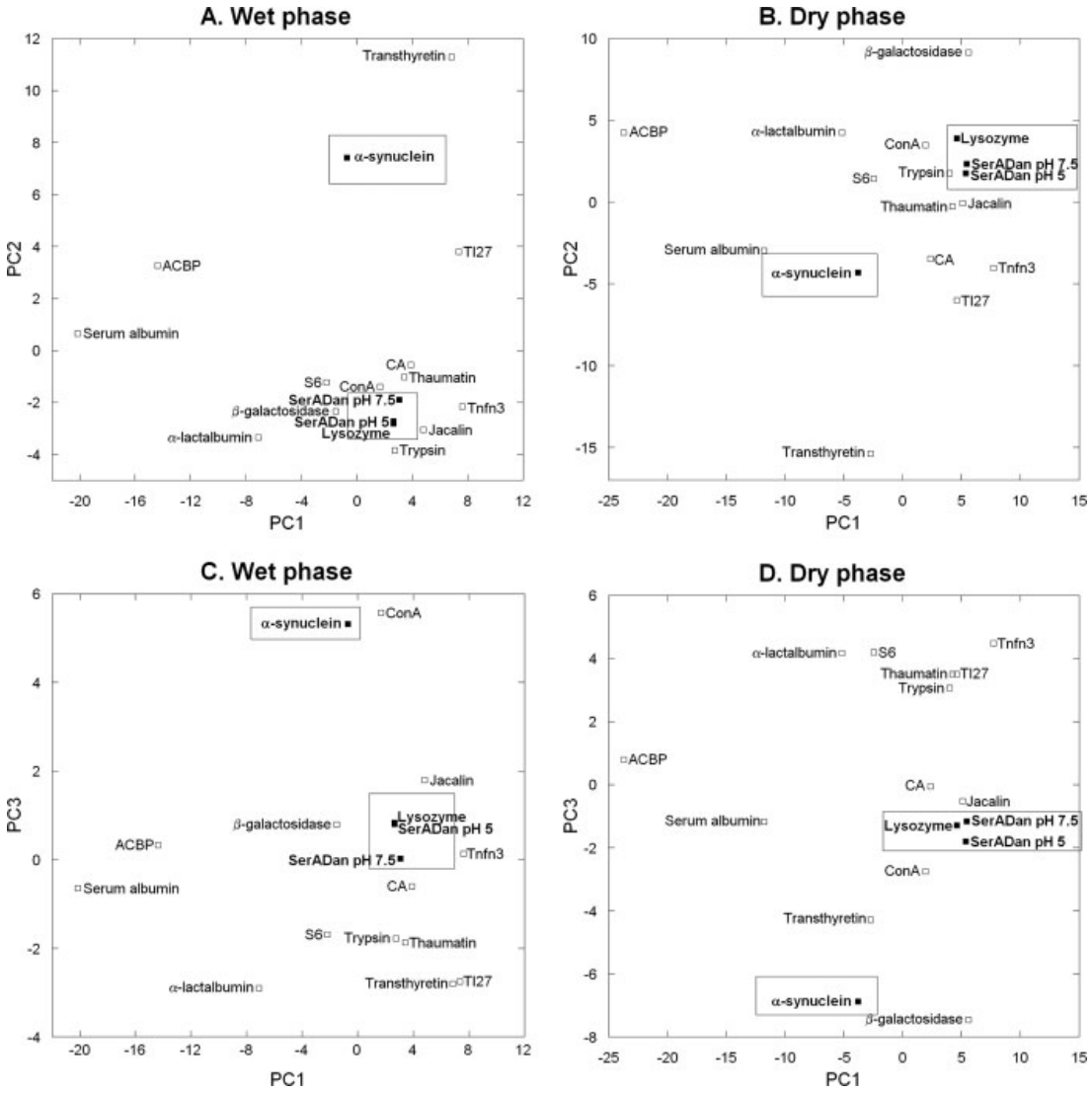

FIGURE 7 Clustering of model proteins into structural classes from primary (PC1) and secondary (PC2) or tertiary (PC3) principal components. Fibril and aggregate samples are circled.

nm is located slightly lower than the 149–152 nm seen for the β-rich model protein spectra described above, although not as low as the α-rich proteins. In contrast, fibrils formed by α-synuclein, which is the predominant protein isolated from the insoluble amyloid found in Parkinson's disease, shows a low-wavelength peak at 151 nm, similar to the β-rich proteins. The fibrils, which are formed in the presence of phosphate and NaCl, show the same features in wet and dry phase (Figure 9B).

The third example of fibril or aggregate structures is for the nonamyloidogenic peptide SerADan (Figure 9C). The peptide is derived from the parent peptide ADan by substituting the two Cys residues (positions 5 and 22) with Ser to prevent covalent crosslinking. This is justified by the observation of ADan aggregates in the reduced state. In addition, Phe11 is replaced by Trp to provide better quantitation and monitoring of its behavior. ADan does not bind the fibril-specific dyes Congo red and Thioflavin T in its reduced form[41] and the same is observed for SerADan (L.W.N. and D.E.O. unpublished observations). However, AFM (Figure 9D) and ATR-FTIR (data not shown) indicates that SerADan forms β-rich, linearly structured aggregates indicative of a fibril-like superstructure. This is further corroborated by a distinctive X-ray fiber diffraction pattern that is characteristic for amyloid-like fibrils in Figure 10. Despite long accumulation times, diffraction patterns were weak, possibly owing to the fact that fibrils were aligned in solution by centrifugation in a capillary tube. Nevertheless, the X-ray fiber diffraction

Table IV Spectral Features and Bands Observed at Low Wavelengths

Model Protein	Structure Class/Architecture	Observed Low-Wavelength Features
ACBP	Mainly α, up-down bundle	Peak at 140 nm
α-lactalbumin	Mainly α, orthogonal bundle	Peak at 141 nm
β-galactosidase	α β, complex	Peak at 166 nm
Carbonic anhydrase	α β, roll, predominantly *β-sheet	Shoulder at 157 nm, increases towards 145 nm without reaching max
ConA	Mainly β, sandwich, jelly roll	Peak at 150 nm
Jacalin	Mainly β, aligned prism	Peak at 148 nm
Serum albumin	Mainly α, orthogonal bundle	Peak at 141 nm
S6	α β, 2-layer sandwich	Peak at 142 nm with shoulder at 150–160 nm
Tnfn3	Mainly β, sandwich, immunoglobulin-like	Peak at 152 nm
Thaumatin	Mainly β, sandwich	Peak at 149 nm
TI27	Mainly β, sandwich, immunoglobulin-like	Peak at ∼152 nm
Transthyretin	Mainly β, sandwich, immunoglobulin-like	Peak at 157 nm
Trypsin	Mainly β, β-barrel	Peak at 147 nm

patterns have sharp diffraction peaks at 4.76 Å (typical of the inter-strand distance in β-sheets). In well-organized fibrils, the inter-sheet distance gives rise to a sharp peak at 10–11 Å, but in the case of SerADan, the diffuse peaks at 10–13 Å suggest only partly aligned fibrils. There were subtle differences between the fibrils formed at the two pH values, as indicated by the shoulder around 5.0–5.5 Å for the pH 7.5 (but not pH 5.0) fibrils, and the greater intensity of the 10–15 Å diffraction peaks for pH 5.0 fibrils compared to the pH 7.5 fibrils. The pseudo-fibril properties of SerADan made it particularly interesting to examine these fibrils by VUV-CD. The aggregates were formed at two pH values and spectra were collected for both wet and dry phase. All peaks corresponded well with β-rich structures. Interestingly, the dry-phase spectra show pH-dependent splitting of the positive band at 190 nm similar to that observed for some immunoglobulin-like folds, corroborating the pH-dependent differences observed in fiber-diffraction data. Furthermore, the low-wavelength band lies in the area populated by β-rich proteins with values of 149 nm for pH 5 and 148 nm for pH 7.5. These peak positions are midway between those of lysozyme and α-synuclein.

We calculated the PC values for the fibril spectra (in Figure 7) based on the PCA analysis of the globular proteins. When the fibril values (represented by circled entries) are included in Figure 7, an interesting pattern emerges. The values for SerADan aggregates and lysozyme fibrils fall at the centre of the main β-protein area for all plots. However, α-synuclein fibrils lie outside the main β-protein area with PC1 values similar to mixed α/β-proteins, possibly indicating a biologically relevant structural difference. This distribution of points is virtually identical to that obtained if the spectra for the fibrils and globular proteins are combined and used in a new PCA analysis (data not shown).

Overall, the fibril and aggregate sample all have the expected β-rich characteristics, but varying intensities of the low-wavelength band compared with the intensity of the positive $\pi\pi^*$ band particularly for α-synuclein fibrils. This is also observed for the globular model proteins.

DISCUSSION

Drying Has Limited Effect on Protein Structure

A key objective of the present study is to examine the VUV spectral region for bands potentially carrying structural information. Our strategy was to use a number of model proteins including both α- and β-rich structural classes as well as mixed α/β species. β-rich proteins are over represented to allow subsequent analysis of β-rich fibrils. Since this region is only accessible by removal of water, it is assumed that gentle drying of proteins into film form does not cause significant loss of secondary structure, which would negate any advantages that removal of water might bring. How well is this assumption borne out? Previous studies have suggested that gentle drying does not lead to major structural changes,[18,19] but we found it necessary to investigate the extent to which the synchrotron radiation spectra were affected to support the validity of our conclusions. Overall, the spectral elements are well preserved when aqueous samples and dried films are compared, although red-shifting and changes in relative intensity of bands were observed for some samples in a manner that could not immediately be correlated to structure class. The normalization procedure used for the dried spectra utilized the protein absorbance at 190 nm for the dry and wet phase spectra and includes the assumption that drying does not affect the absorbance, which could conceivably be inaccurate. This normalization procedure makes it clear that dry-

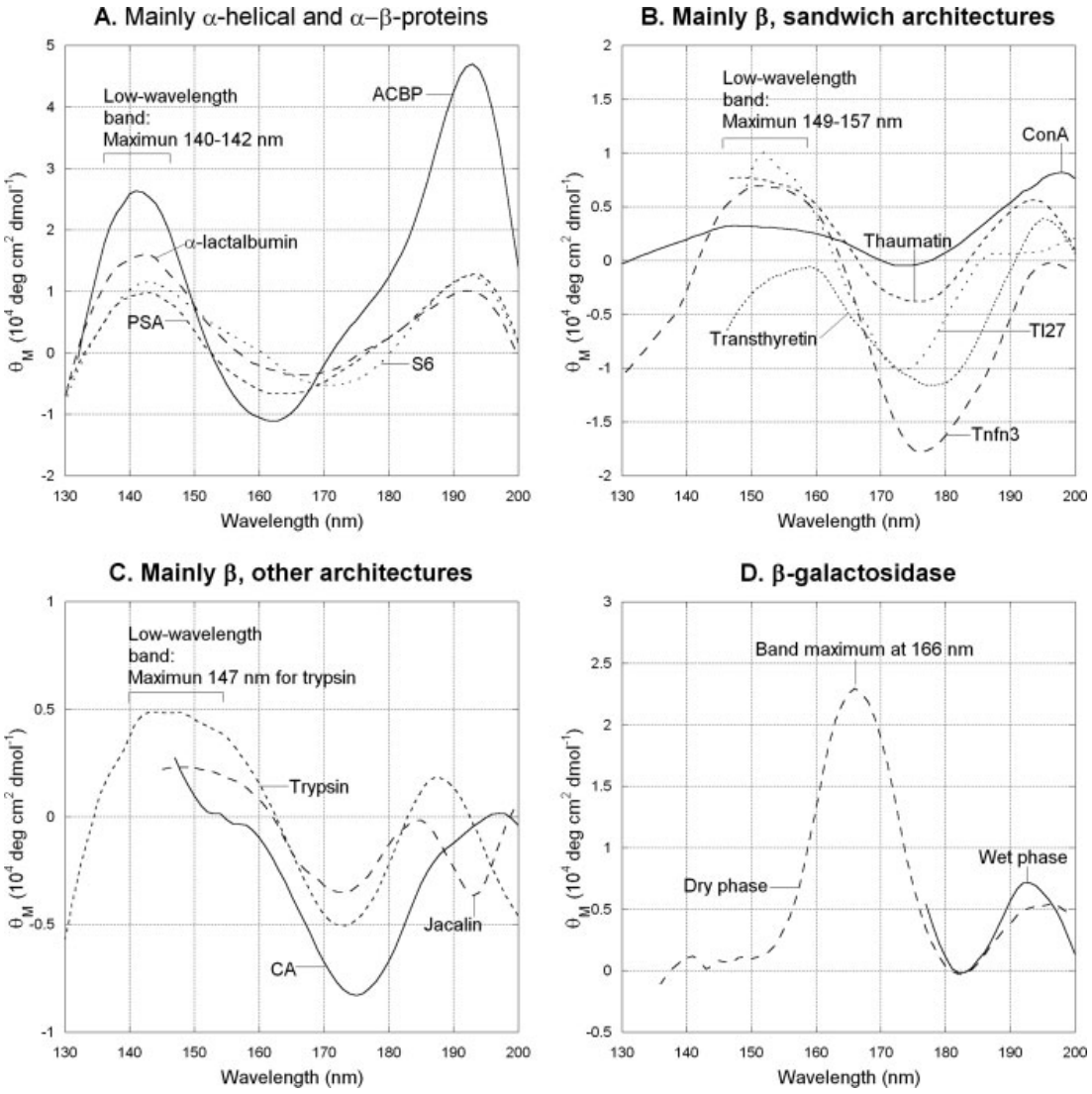

FIGURE 8 Spectral features at low wavelengths correspond to secondary structure. (A) Mainly α-helical and α-*β*-proteins. (B) Sandwich architectures. (C) Mainly *β*-sheet proteins with more complex architectures. Note that while carbonic anhydrase is classed as α-*β*, it is contains mainly *β*-sheet.

ing led to changes in relative peak intensity, as previously reported.[17]

Analysis by conventional secondary structure analysis tools revealed that both wet and dry phase spectra correspond well to the secondary structure obtained from PDB data with the exception of transthyretin in the wet phase and the unusually structured jacalin. It should be mentioned that such tools are designed specifically for use on spectra obtained for aqueous samples of soluble globular proteins. FTIR secondary structure analysis of a subset of proteins likewise showed correspondence between spectral data collected for dried films and native structure with the main structural elements either estimated accurately or overestimated. Similarly, the PCA yielded structurally relevant correlations for both wet and dried samples as well as for fibril samples. Interestingly, the immunoglobulin-like folds appeared particularly sensitive in the analysis with transthyretin as the extreme outlier. This could be due to loss of structure but also underlying structural differences or the effect of the presence of aromatic and cysteine residues. Otherwise, the proteins were found to cluster according to structural class.

Overall, this indicates that drying does not cause widespread protein denaturation and the proteins can be accurately associated with the correct structural class. However, it cannot be ruled out that local denaturation occurs either due to loss of hydration, protein–protein interactions within the

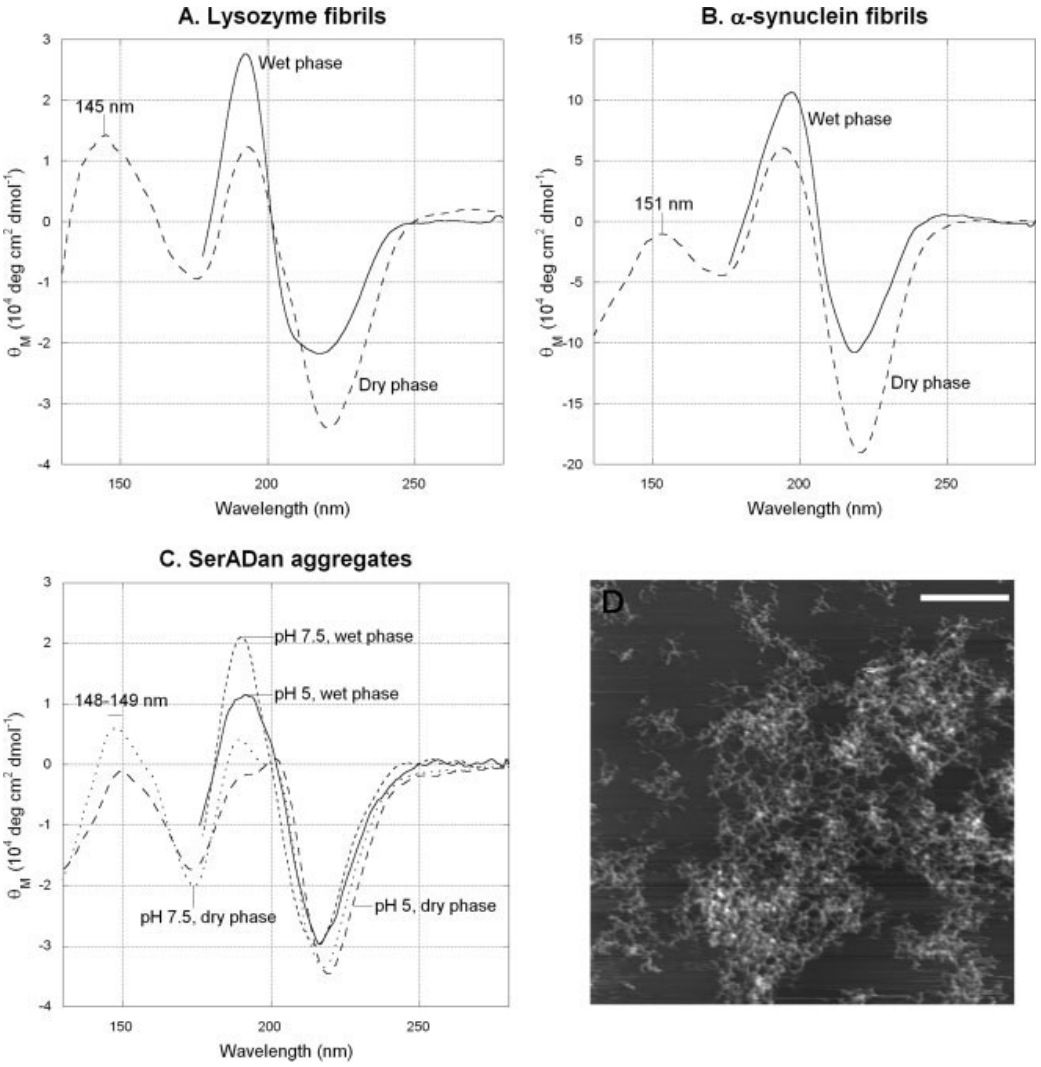

FIGURE 9 A–C. Dry phase CD spectra for fibril and aggregate samples. D. AFM of SerADan aggregates formed at pH 7.5, white bar is 1 mm.

film or interaction with the surface upon which the film is formed although the latter would be limited to the protein interacting with the surface and therefore small compared to the total thickness of the film.

Spectral changes accompanying drying might be caused by local changes in hydration. The films are formed under vacuum but subsequently exposed to moist room air before being placed in the dry N_2 atmosphere of the sample chamber. It is therefore not possible to give a precise description of the hydration level of the protein film. Loss of direct interactions with water could alter the spectral characteristics, but one could speculate that removal of water could conceivably lead to local or global structural changes without significantly disturbing the secondary structure content. Although structure appeared well preserved for our model proteins, studies have demonstrated the risk of structure alterations for e.g. freeze-dried samples,[42,43] which indicates that secondary structure perturbations upon drying cannot generally be discounted. Addition of saccharides to protect native secondary structure could be considered in such situations although the additive must allow the formation of transparent protein films. The challenge of structural preservation upon drying is well known in the field of drug stability and delivery.[44] In contrast, a recent study showed very little effect of drying on structure for fibrillar samples,[45] highlighting the usefulness of the technique for such samples.

Calculations on oligopeptides and proteins have previously suggested a connection between β-sheet twisting and the magnitudes of the ~215 nm $n\pi^*$ and ~198 nm $\pi\pi^*$ bands.[46] Such disturbances of individual secondary structure

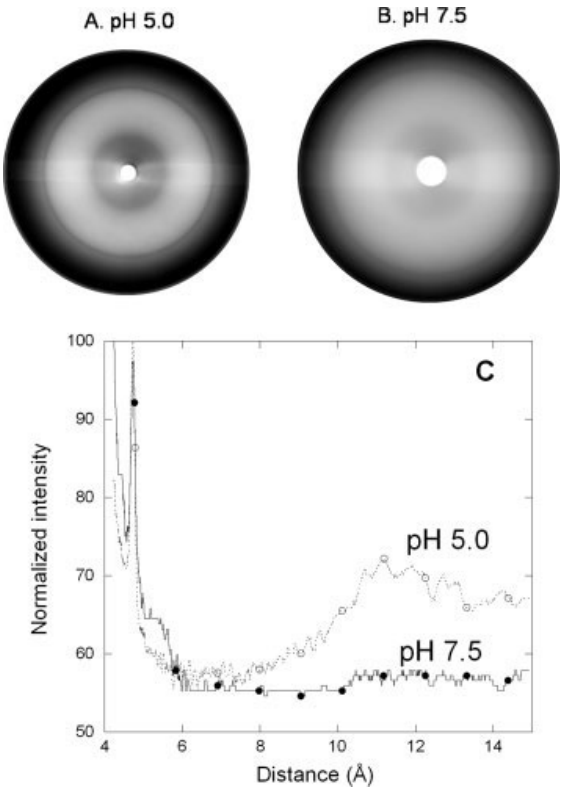

FIGURE 10 X-ray diffractograms of partly aligned SerADan samples formed at (A) pH 5 and (B) 7.5. (C) The diffractograms show a distinct diffraction peak at 4.76 Å and diffuse diffraction peaks at 10–13 Å. The fibrils were aligned in solution in a capillary tube to avoid diffraction from buffer salts, and this accounts for the relatively weak diffraction.

elements could potentially be a cause of spectral distortion for film samples. However, the spectral content obtained for the dry phase does appear to be consistent with known structural data. Consequently, the information obtained from the VUV range is expected to be structurally relevant, although further investigations must be conducted to elucidate the exact nature of the observed structural distortions.

Low-Wavelength Band Is Sensitive to Secondary Structure and May Be Related to a π-Orbital Transition

The second central issue is whether VUV bands confer additional structural information on top of the information provided by the conventional far-UV spectra. The position of the low-wavelength band, observed in the 140–160 nm region, appears sensitive to secondary structure. Both α-rich and mixed α/β proteins showed a low-wavelength band centered at 140–142 nm. However, for β-rich proteins, the band was shifted to higher values, which varied from 147 to 157 nm for different proteins. In addition, the low-wavelength band was either absent from the spectrum for the structurally complex β-galactosidase or positioned very high at 166 nm. Interestingly, the relative intensity of the band was not correlated to the intensity of other bands, suggesting that it may serve as an independent structural indicator, though its direct structural significance remains unclear. Some clues may be obtained from previous studies. In a study on poly-γ-methyl L-glutamate (PMG) in hexafluoro-2-propanol (HFIP) published 35 years ago, Johnson and Tinoco described a spectrum for the α-helical species containing a negative peak at 159 nm and a positive maximum below 140 nm.[38] Similarly, a well-defined positive band centered at 140 nm has been observed for poly(L-alanine) in the form of a dry film produced by evaporation of trifluoroethanol (TFE)[39] although no such band was observed for a poly(L-proline) film formed from water.[47] Instead, the spectrum appeared typical for the polyproline II conformation and showed a negative band was centered at 145 nm and with a positive band below 135 nm. Bowman et al.[40] measured the circular dichroism of cyclic amino acid dimers, which likewise showed a strong, positive band at 140 nm, although cyclic, constrained dimers are geometrically dissimilar to biologically relevant protein structures. One might expect exciton-splitting of the transition between the π-bonding and π-antibonding orbitals ($\pi_b\pi^*$) for α-helical proteins in a manner similar to that observed for the $\pi_{nb}\pi^*$ transition, but the transition is nonetheless energetically relevant. Serrano-Andrés and Fülcher[48] calculated the transition energies for several small amides to lie within 9.6–10.5 eV (118–129 nm). Similarly, calculations on formamide and *N*-methylacetamide (NMA) by Besley et al.[49] showed that the $\pi_b\pi^*$ transition occurs at 9.4–9.6 eV (129–132 nm) for NMA and 10.4eV (119 nm) for formamide in water. These energies are within the same range as the VUV band albeit somewhat higher. The VUV band could arise from the $\pi_b\pi^*$ transition but other contributions such as Rydberg states should be considered although an in-depth analysis falls outside the scope of this work. However, based on the present experimental data, the involved transitions must be sensitive to the secondary structure of the proteins' backbone.

The protein distribution in the PCA plot was broadly retained whether based on wet or dry spectra, but there were clear shifts among different proteins due to the inclusion of the VUV band. The position and intensity of the VUV band also appears useful in differentiating between different types of aggregates. For α-synuclein, the band position was within the range described by the β-rich globular proteins, while that of lysozyme was shifted to a lower wavelength. Both SerADan spectra had band positions that fell in between. Never-

theless, the SerADan fibrils showed relative and absolute peak intensities much closer to those of lysozyme than of α-synuclein, leading to a close clustering of SerADan and lysozyme in the PCA plots in Figure 7.

Protein fibrils and aggregates are well-suited for study in film form and detailed study of these and other aggregate structures might reveal underlying structural differences in otherwise similar fibrillar samples. We are currently investigating a number of different fibrillar states by SRCD in order to elucidate potential changes in super-secondary or tertiary structure and anticipate that the present study will be the start of a comprehensive database for the classification of aggregated protein species.

MATERIALS AND METHODS

Materials

α-lactalbumin, β-galactosidase, carbonic anhydrase, jacalin, hen egg-white lysozyme, porcine serum albumin, thaumatin, transthyretin, trypsin, Thioflavin T and other chemicals were from Sigma (Sigma-Aldrich, St. Louis, MO). Concanavalin A was obtained from CalBioChem (La Jolla, CA). Acyl-CoA-binding protein was purified as described in Ref. 50. S6 was purified as described in Ref. 51. Tnfn3 and TII27 were purified as described in Ref. 52. Expression and purification of wild-type α-synuclein was performed according to Ref. 53. SerADan peptide (EASNSFAIRH FENKWAVETL ISFNLFLNSQ EKHY) was obtained >90% pure from EZBiolab (EZBiolab Inc., Westfield, IN).

Sample Preparation for Wet and Dry Phase

Model proteins were used without further purification. For dried samples, the proteins were weighed and dissolved in water and in 6*M* guanidine followed by spectroscopic concentration measurement at 280 nm using extinction coefficients available in literature or predicted using the ProtParam tool (http://www.expasy.org/tools/protparam.html). The weighed amount was found to be in agreement with the spectroscopically determined concentration for all proteins within a margin of 5%. For proteins supplied in the liquid phase, only spectroscopic concentration measurements were used. Dried proteins were dissolved in either fresh milliQ water or dilute phosphate buffer (20 m*M*, pH 7.5). Proteins supplied as dissolved stocks were dialyzed for >2 h against the dilute phosphate buffer to remove traces of chloride ions and other contaminants.

Instrument Preparation

The spectra were recorded at the SRCD facility at the UV1 beamline[54] on the storage ring ASTRID at Institute for Storage Ring Facilities (ISA), University of Aarhus, Denmark. The light exiting UV1 through a CaF_2 window was passed into the custom built CD instrument, which was constantly purged with nitrogen to avoid absorption from atmospheric oxygen. In the CD instrument the highly linear polarized light from UV1 was converted into alternating left and right handed circularly polarized light with a CaF_2 Photo Elastic Modulator (PEM) [model I/CF50, Hinds Instruments, USA] at a frequency of 50 kHz. The modulated light was passed through the sample and detected with a UV-sensitive photomultiplier tube (PMT) [model 9402B, Electron Tubes, UK]. The 50 kHz CD signal from the PMT was detected using a lock-in amplifier. The instrument was carefully calibrated with respect to CD signal magnitude using camphor sulfonic acid (chemical shift anisotropy [CSA]) after each daily beam fill of the storage ring.

Circular Dichroism for Wet Samples

All wet sample spectra were recorded using a 0.1 mm path length quartz SUPRASIL cell (Hellma GmbH, Germany), over a wavelength range of 260–170 nm in 1 nm steps and a dwell time of 3 s per wavelength point. The sample cell was carefully cleaned with milliQ water or HCl if needed and dried before recording of a baseline spectrum (average of three single spectra) of the relevant solvent. The cell was cleaned again and loaded with 15 μL sample solution and the sample spectrum collected (average of five individual spectra). The protein concentration was adjusted until a detector voltage of 800–900 V was obtained at the 190 nm protein absorption peak, corresponding to a sample absorbance of about 0.8. The cell was cleaned and filled with solvent before a second baseline spectrum was obtained for comparison.

Circular Dichroism for Dry Samples

Quartz cuvettes are opaque below 165 nm, so all measurements with dry samples were performed using MgF_2 plates, which only absorb below 125 nm. For the dry spectra, one MgF_2 plate was fitted to be used at stable orientation to the incident light. The plate was carefully cleaned with milliQ water and dried before a baseline spectrum was collected as above. A 15-μL sample was applied as a droplet of approximately ellipsoid shape. The sample was dried under low vacuum (about 100 mbar) for ∼10 min and visually inspected for particles or opaque areas. The sample was transferred to the CD instrument and a sample spectrum was obtained as described above. After cleaning of the plate, a second baseline spectrum was obtained. For comparison of the wet and dry spectra, the detector voltage for the polypeptide specific peak at 190 nm was used to normalize the dry phase spectrum against the known concentration of the wet phase spectrum. Although the amount of protein transferred to the MgF_2 plate was known, local unavoidable variations in protein film thickness made it necessary to perform this normalization.

Preparation of Aggregated Samples

Purified α-synuclein was dialyzed against milliQ water, lyophilized and stored at −20°C. Protein stock solution was prepared according to Ref. 55. Samples were prepared containing 1 mg/mL of protein (20 m*M* phosphate, pH 7.4, 150 m*M* NaCl) and incubated as 1 mL aliquots at 37°C in a fluorometer (Cary Ellipse, Varian Inc., Palo Alto, CA) with constant stirring. Addition of the fibril-specific flurophore thioflavin T (ThT, 40 μ*M*) allowed in situ monitoring of fibril formation using excitation at 450 nm and emission at 485 nm.

Lysozyme fibrils (10 mg/mL protein) were formed in 500 m*M* NaCl adjusted to pH 2 with HCl. Samples were incubated overnight at 57°C with mechanical agitation. Presence of fibrils was monitored using ThT (emission 490 nm).

Freeze-dried SerADan peptide was dissolved in 10*M* urea and allowed to disaggregate overnight at room temperature. Concentration was monitored by absorbance at 280 nm and found to be within 5% of the weighed amount. Stock concentration was adjusted to 2.5 m*M*. Stock aliquots were fast frozen, stored at −80°C and thawed immediately before use. Aggregates were prepared by dilution of the stock to 50 μM peptide (0.2*M* urea) in 50 m*M* sodium acetate (pH 5) or 50 m*M* Tris (pH 7.5) and incubation overnight at room temperature. Presence of aggregates was verified by atomic force microscopy (AFM) and secondary structure analyzed by ATR-FTIR.

X-Ray Fiber Diffraction

Fibrillated sample solution was pipetted into a thin glass capillary sealed at one end and centrifuged at 4000*g* for several hours until a visible precipitate had formed. Fibrils in the capillary tube are partly aligned due to the centrifugation, and as the fibrils are still in solution, the buffer salts do not give rise to unwanted diffraction. The capillary tube was sealed and mounted on a rotating anode setup with a wavelength of 1.5418 Å and a Mar345 image plate detector (Mar Research). The sample-detector distance was 35 and 40 cm for the SerADan samples formed at pH 5 and 7.5, respectively. "Wet" fibers diffract poorly, and to that end each diffractogram was collected by accumulating data over night. A single data set consisted of 40 or 100 images each accumulated over 10 min and averaged by use of Marcombine (Mar Research). The diffractogram was radially averaged by use of Datasqueeze (Datasqueeze Software).

Circular Dichroism for Fibril Samples

To separate protein fibrils or aggregates from the reaction solution, the samples were centrifuged for 10 min before aspiration of the supernatant. The pellet was washed in milliQ water and centrifuged again before being resuspended in milliQ water. All aggregate and fibrils samples used here were known to be stable over several hours in water. Otherwise, the samples were treated as described for dry phase spectra.

Analysis of Secondary Structure from Circular Dichroism

The CDSSTR program,[56] available at DICHROWEB,[57,58] was used to estimate secondary structure based on wet and dry phase spectra employing the SP175 reference set[35] when possible. The DSSP[59] algorithm was used for assignment of secondary structure from PDB files giving eight output classes, which were grouped in a simple manner to give α-helical (H), β-sheet (E), and "other" as discussed in Ref. 36.

Primary Component Analysis of Wet and Dry Phase Spectra

PCA[60] was conducted on data sets containing wet, dry, or wet and dry spectra of globular proteins and of globular and fibrillating proteins. The data was scaled to obtain unit variance (i.e. the intensities at each frequency were divided by the standard deviation of the intensities of that frequency within the entire data set) and then centered. This scaling reduces the weight of stochastic large amplitude variations and increases the weight of small correlated changes. The resulting scores and loadings were then rescaled to the original intensities. The PCA was performed using Simca-P (Umetrics, Umeå, Sweden).

Fourier Transform Infrared Spectroscopy

Spectra were recorded on a Bruker Tensor 27 infrared spectrometer (Bruker Optik GmbH, Ettlingen, Germany) with a Specac Golden Gate single-reflection ATR unit (Specac Ltd., Orpington, UK). Proteins were dissolved in milliQ water and ∼2 μg protein were dried on the ATR element under a gentle stream of nitrogen. Three independent samples were investigated (64 scans, 2 cm^{-1} resolution). The secondary structure was estimated using OPUS 5.5. If needed, the presence of water vapor was corrected for by subtraction of a fresh vapor spectrum or the built-in atmospheric compensation function. Peaks were assigned from the 2nd derivative and deconvolution of spectra.[61] A fitting scheme composed of nine peaks of mixed Lorentzian and Gaussian shapes was found to fit well for all spectra. Of the eight peaks, six were assigned to amide band I, two to amide band II and one to weak side-chain contributions between the amide bands. The nondeconvoluted spectra were fitted using the Levenberg-Marquardt method, the areas of individual peaks calculated and the secondary structure content estimated.

ACBP was kindly provided by Kell Andersen, TII27 and Tnfn3 by Mette Nielsen and α-synuclein fibrils by Lise Giehm, Aalborg University. We thank Anders Svensson, Mathias Norrman and Gerd Schluckebier at Novo Nordisk A/S for help with the collection of fiber diffraction data.

REFERENCES

1. Stefani, M.; Dobson, C. M. J Mol Med 2003, 81, 678–699.
2. Sunde, M.; Serpell, L. C.; Bartlam, M.; Fraser, P. E.; Pepys, M. B.; Blake, C. C. J Mol Biol 1997, 273, 729–739.
3. Serpell, L. C.; Sunde, M.; Benson, M. D.; Tennent, G. A.; Pepys, M. B.; Fraser, P. E. J Mol Biol 2000, 300, 1033–1039.
4. Sumner Makin, O.; Serpell, L. C. J Mol Biol 2004, 335, 1279–1288.
5. Jimenez, J. L.; Guijarro, J. I.; Orlova, E.; Zurdo, J.; Dobson, C. M.; Sunde, M.; Saibil, H. R. Embo J 1999, 18, 815–821.
6. Pelton, J. T.; McLean, L. R. Anal Biochem 2000, 277, 167–176.
7. Jackson, M.; Mantsch, H. H. Crit Rev Biochem Mol Biol 1995, 30, 95–120.
8. Goormaghtigh, E.; Ruysschaert, J. M.; Raussens, V. Biophys J 2006, 90, 2946–2957.
9. Sreerama, N.; Woody, R. W. Methods Enzymol 2004, 383, 318–351.
10. Wallace, B. A.; Janes, R. W. Curr Opin Chem Biol 2001, 5, 567–571.
11. Miles, A. J.; Wallace, B. A. Chem Soc Rev 2006, 35, 39–51.
12. Wallace, B. A.; Wien, F.; Miles, A. J.; Lees, J. G.; Hoffmann, S. V.; Evans, P.; Wistow, G. J.; Slingsby, C. Faraday Discuss 2004, 126, 237–243; discussion 245–254.
13. Matsuo, K.; Yonehara, R.; Gekko, K. J Biochem (Tokyo) 2005, 138, 79–88.
14. Matsuo, K.; Yonehara, R.; Gekko, K. J Biochem (Tokyo) 2004, 135, 405–411.

15. McPhie, P. Biopolymers 2004, 75, 140–147.
16. Calero, M.; Gasset, M. Methods Mol Biol 2005, 299, 129–151.
17. Safar, J.; Roller, P. P.; Ruben, G. C.; Gajdusek, D. C.; Gibbs, C. J., Jr. Biopolymers 1993, 33, 1461–1476.
18. Hill, J. J.; Shalaev, E. Y.; Zografi, G. J Pharm Sci 2005, 94, 1636–1667.
19. Rupley, J. A.; Careri, G. Adv Protein Chem 1991, 41, 37–172.
20. Pedersen, J. S.; Dikov, D.; Flink, J. L.; Hjuler, H. A.; Christiansen, G.; Otzen, D. E. J Mol Biol 2006, 355, 501–523.
21. Pedersen, J. S.; Dikov, D.; Flink, J. L.; Otzen, D. E. Biophys J 2006, 90, 4181–4194.
22. Petkova, A. T.; Leapman, R. D.; Guo, Z.; Yau, W.-M.; Mattson, M. P.; Tycko, R. Science 2005, 307, 262–265.
23. Sawaya, M. R.; Sambashivan, S.; Nelson, R.; Ivanova, M. I.; Sievers, S. A.; Apostol, M. I.; Thompson, M. J.; Balbirnie, M.; Wiltzius, J. J.; McFarlane, H. T.; Madsen, A. O.; Riekel, C.; Eisenberg, D. Nature 2007, 447, 453–457.
24. Shanmugam, G.; Polavarapu, P. L. J Am Chem Soc 2004, 126, 10292–10295.
25. Serrano-Andres, L.; Fulscher, M. P. J Phys Chem B 2001, 105, 9323–9330.
26. Oakley, M. T.; Hirst, J. D. J Am Chem Soc 2006, 128, 12414–12415.
27. Bulheller, B. M.; Miles, A. J.; Wallace, B. A.; Hirst, J. D. J Phys Chem B 2008, 112, 1866–1874.
28. Kaneko, R.; Kitabatake, N. Chem Senses 2001, 26, 167–177.
29. Woody, R. W.; Dunker, A. K. In Circular Dichroism and the Conformational Analysis of Biomolecules; Fasman, G. D., Ed.; Plenum Press: New York, 1996, pp 109–158.
30. Ross, D. L.; Jirgensons, B. J Biol Chem 1968, 243, 2829–2836.
31. Tetin, S. Y.; Mantulin, W. W.; Denzin, L. K.; Weidner, K. M.; Voss, E. W., Jr. Biochemistry 1992, 31, 12029–12034.
32. Tetin, S. Y.; Prendergast, F. G.; Venyaminov, S. Y. Anal Biochem 2003, 321, 183–187.
33. Freskgard, P. O.; Martensson, L. G.; Jonasson, P.; Jonsson, B. H.; Carlsson, U. Biochemistry 1994, 33, 14281–14288.
34. Mahanta, S. K.; Sastry, M. V.; Surolia, A. Biochem J 1990, 265, 831–840.
35. Lees, J. G.; Miles, A. J.; Wien, F.; Wallace, B. A. Bioinformatics 2006, 22, 1955–1962.
36. Oberg, K. A.; Ruysschaert, J. M.; Goormaghtigh, E. Eur J Biochem 2004, 271, 2937–2948.
37. Lees, J. G.; Miles, A. J.; Janes, R. W.; Wallace, B. A. BMC Bioinformatics 2006, 7, 507.
38. Johnson, W. C., Jr.; Tinoco, I, Jr. J Am Chem Soc 1972, 94, 4389–4392.
39. Young, M. A.; Pysh, E. S. Macromolecules 1973, 6, 790–791.
40. Bowman, R. L.; Kellerman, M.; Johnson, W. C. Biopolymers 1983, 22, 1045–1070.
41. Surolia, I.; Reddy, G. B.; Sinha, S. J Neurochem 2006, 99, 537–548.
42. Schwegman, J. J.; Carpenter, J. F.; Nail, S. L. J Pharm Sci 2007, 96, 179–195.
43. Luthra, S.; Kalonia, D. S.; Pikal, M. J. J Pharm Sci 2007, 96, 2910–2921.
44. Frokjaer, S.; Otzen, D. E. Nat Rev Drug Discov 2005, 4, 298–306.
45. Squires, A. M.; Devlin, G. L.; Gras, S. L.; Tickler, A. K.; MacPhee, C. E.; Dobson, C. M. J Am Chem Soc 2006, 128, 11738–11739.
46. Woody, R. W. In Circular Dichroism and the Conformational Analysis of Biomolecules; Fasman, G. D., Ed.; Plenum Press: New York, 1996, pp 25–67.
47. Young, M. A.; Pysh, E. S. J Am Chem Soc 1975, 97, 5100–5103.
48. Serrano-Andrés, L.; Fülscher, M. P. J Am Chem Soc 1998, 118, 12190–12199.
49. Besley, N. A.; Hirst, J. D. J Phys Chem A 1998, 102, 10791–10797.
50. Kragelund, B. B.; Knudsen, J.; Poulsen, F. M. Biochim Biophys Acta 1999, 1441, 150–161.
51. Otzen, D. E.; Kristensen, O.; Proctor, M.; Oliveberg, M. Biochemistry 1999, 38, 6499–6511.
52. Nielsen, M. M.; Andersen, K. K.; Westh, P.; Otzen, D. E. Biophys J 2007, 92, 3674–3685.
53. Huang, C.; Ren, G.; Zhou, H.; Wang, C. C. Protein Expr Purif 2005, 42, 173–177.
54. Eden, S.; Limão-Vieira, P.; Hoffmann, S. V.; Mason, N. J. Chem Phys 2005, 323, 313–333.
55. Kaylor, J.; Bodner, N.; Edridge, S.; Yamin, G.; Hong, D. P.; Fink, A. L. J Mol Biol 2005, 353, 357–372.
56. Johnson, W. C. Proteins 1999, 35, 307–312.
57. Lobley, A.; Whitmore, L.; Wallace, B. A. Bioinformatics 2002, 18, 211–212.
58. Whitmore, L.; Wallace, B. A. Nucleic Acids Res 2004, 32, W668–W673.
59. Kabsch, W.; Sander, C. Biopolymers 1983, 22, 2577–2637.
60. Spearman, C. Am J Psychol 1904, 15, 201–293.
61. Byler, D. M.; Susi, H. Biopolymers 1986, 25, 469–487.

Reviewing Editor: Laurence Nafie

Co-author statement for Paper 2

Nesgaard, L. W., Hoffmann, S. V., Andersen, C. B., Malmendal, A. and Otzen, D. E.: Characterization of dry globular proteins and protein fibrils by synchrotron radiation vacuum UV circular dichroism. *Biopolymers* (2008) 89 p. 779-95.

- Lise W. Nesgaard performed all experimental work related to synchrotron CD.
- Søren S. Hoffmann supervised the experimental work and performed post-experimental spectral smoothing and baseline-correction.
- Christian B. Andersen performed X-ray fibre diffraction.
- Anders Malmendal performed the principal component analysis.
- Lise W. Nesgaard wrote the article and took care of revisions.
- Daniel E. Otzen supervised the experiments and the writing of the article and took care of submission, revision and galley proofs.

Søren V. Hoffmann	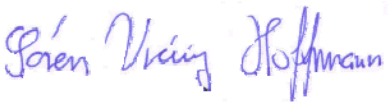	31st March 2009
Christian B. Andersen		31st March 2009
Anders Malmendal		31st March 2009
Daniel E. Otzen		16th March 2009
Lise W. Nesgaard	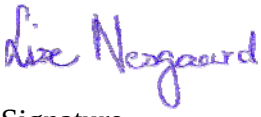	31st March 2009
	Signature	Date

3.4 Discussion of Paper 2

3.4.1 Spectral features are generally preserved after drying

The aim of the present study was to investigate the 130-170nm range for structurally sensitive bands. This required the use of dried samples and the recording of spectra for a number globular model proteins (paper 2/table 1), which may not be tolerant towards dehydration. However, we observed limited effect of dehydration for our model proteins, but there can be little doubt that the general sensitivity of globular proteins towards dehydration limits the applicability of the 130-170nm region that we have explored here. Comparison of wet and dry phase spectra for the model proteins as well as for protein aggregates or fibrils showed that the structurally sensitive bands in the 170-230nm range were generally well-preserved despite some changes in relative intensities and shifting of positions for the $n\pi^*$ and $\pi_{nb}\pi^*$ bands (paper 2/1-4). Fibril samples, which are generally less sensitive to hydration state, displayed similar spectral effects of the drying process. Similarly, principle component analysis (PCA) of wet and dry phase spectra showed correlation between the first principle component (PC1) and the α-helical content for the model proteins as well as structurally meaningful clustering from PC1/PC2 and PC1/PC3 comparisons for both model proteins and aggregate/fibril samples (paper 2/figure 6-7). We therefore believe that information gleaned from the 130-170nm range contains meaningful information.

3.4.2 Drying reveals a novel structure-sensitive, low-wavelength band

The extension of the spectra into the higher-energy area accessible by drying showed known negative bands at 162-171nm for all-α or mixed proteins or ~175nm for β-rich proteins followed by a positive band in the 140-160nm region. The position of this band is sensitive to protein structure (figure 47.A, paper 2/figure 8) and while it is lower in intensity for β-rich proteins, its intensity does not correlate with that of bands at lower energy suggesting a possible role as an independent structural indicator. Whereas the proteins with predominant β-helical structure (ACBP, α-lactalbumin and serum albumin) display a band centred at 141-142nm (figure 47.B no. 1-3), this position was red-shifted by approximately 10nm (mean value 151nm) for β-rich model proteins albeit within a large range consistent with a more structurally diverse structural element. It is noteworthy that the immunoglobulin-like folds (TI27, Tnfn3, transthyretin, no. 9-11) all fall above the mean at 151nm while the lowest values observed for β-structure belong to the closed β-barrel of trypsin (no. 5) and the aligned prism of jacalin (no. 6). It is possible the relative position and intensity of this band could provide information about super-secondary structure, but further studies are needed to elucidate of the relationship with protein architecture/fold. A second interesting observation is that S6, which contains significant β-structure, shows α-helical characteristics at first glance, but the spectrum also contain a shoulder at 150-160nm and a β-sheet-like negative band at ~170nm suggesting that structural distinction of these predominantly a-helical and mixed structures may furthered by information in this wavelength range. Similarly, jacalin contains clearly β-

sheet-like bands below 170nm despite the atypical appearance in the 180-200nm range.

The low-wavelength band has not previously been described for globular proteins or aggregates. However, the study by Young and Pysh published in 1973 [631] of α-helical poly(L-alanine) in a film produced by TFE evaporation details negative and positive bands at ~160nm and ~140nm, respectively. The sign and position of these bands are in agreement with the spectrum of helical poly-c-methyl L-glutamate (PMG) in HFIP by Johnson and Tinoco from 1972 [632], which contains a negative peak centred at 159nm climbing to a maximum below 140nm, and the later study by Bowman *et al.* [633] of cyclic amino acid dimers that showed a strong positive band at ~140nm. Cyclic amino acid dimers are highly geometrically constrained and structurally unrelated to biological polypeptides so the preserved band at 140nm speaks against structural sensitivity. However, the spectrum of a poly-(L-proline) film [634], formed by evaporation of water, shows a P_2-like spectrum in the 160-250nm range, but a negative

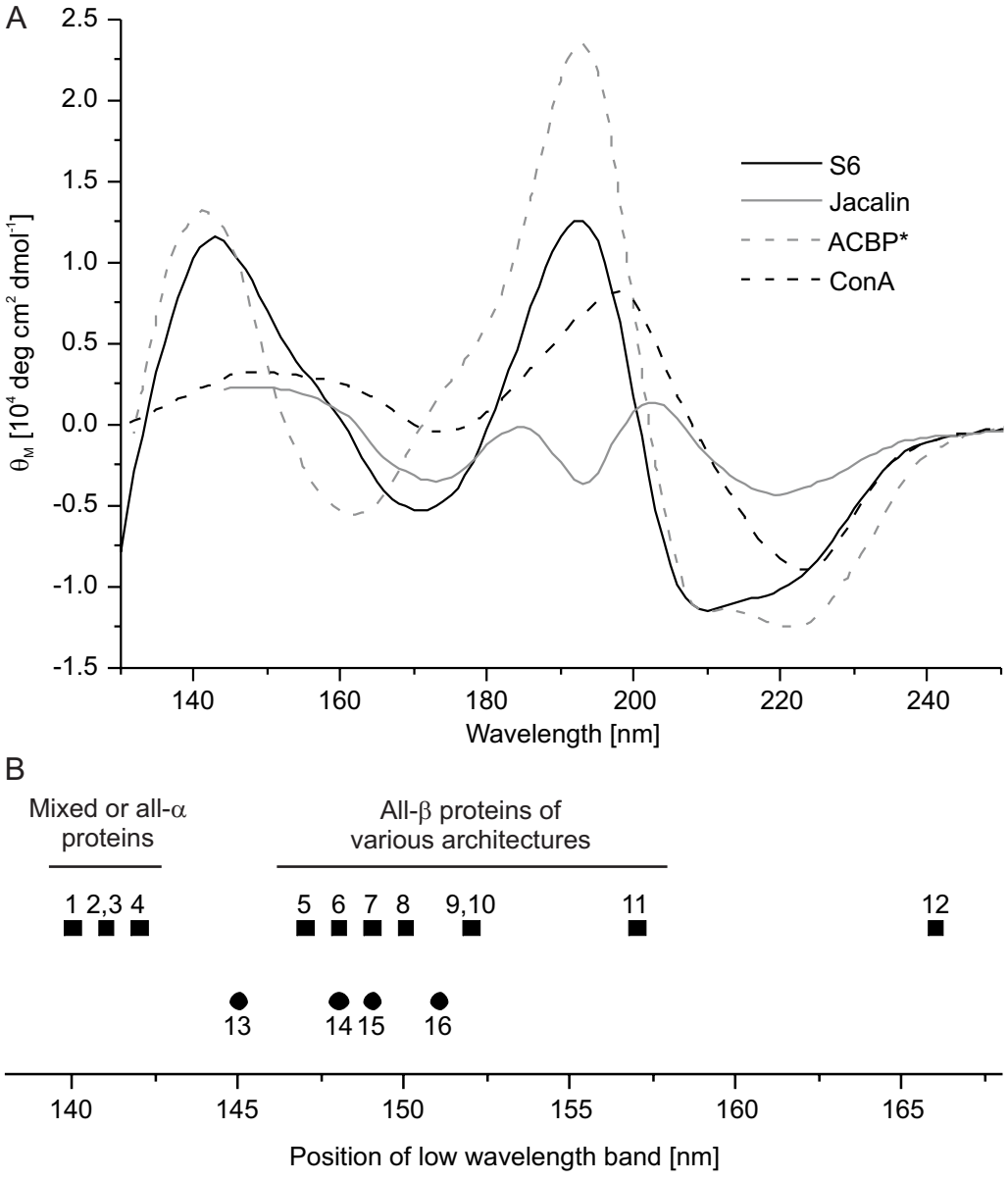

Figure 47. (A) The low-wavelength region for a selection of globular proteins. * ACBP: Acyl-CoA binding protein, ConA: Concanavalin A. (B) Position of peak for low-wavelength band. Proteins: *1* ACBP, *2* α-lactalbumin, *3* serum albumin, *4* S6, *5* trypsin, *6* jacalin, *7* thaumatin, *8* ConA, *9* TI27, *10* Tnfn3, *11* transthyretin, *12* β-galactosidase. Fibrils/aggregates: *13* lysozyme, *14* SerADan, pH 7.5, *15* SerADan, pH 5.0, *16* α-synuclein.

band centred at 145nm with positive bands at ~165nm and below 135nm. The same study by Young and Pysh [634] also shows that the poly-(L-proline) I helix spectrum is essentially featureless below 190nm but that gradual conversion to poly-(L-proline) II conformation is associated with emergence of the 145nm and 165nm bands. Based on these observations and the results from the present work, it is plausible that the 135-160nm VUV region contains structurally sensitive bands and could potentially aid in characterisation of protein structure by CD. The origin of the low-wavelength band remains unknown, but it is worth noting that Besley and Hirst [635] and Serrano-Andrés and Fülscher [636] calculated the π-bonding-to-antibonding orbital transition ($\pi_b\pi^*$) for a number of small amides to fall within the 118-132nm region. It is possible that the low-wavelength band originates from this transition although other contributions cannot be ruled out.

3.4.3 Potential uses of the low-wavelength band in analysis of β-rich spectra

As summarised in section 3.3.2., all-β proteins are highly diverse in their spectral properties. The intensity of the low-wavelength band is significantly lower for β-sheet compared to the α-helical spectra, but it is possible that the separation into distinct α- and β-regions, as the spectrum for S6 demonstrates, could aid in the discrimination and characterisation of these two structural elements. This structural specificity of the 130-160nm region is also interesting in light of the alternative P_2-like βII-type spectra, which were not included among the model proteins. The exact spectral properties for βII-type all-β proteins in this region cannot be predicted, but it would be reasonable to expect a negative band at or near 145nm by comparison to the previous P_2-like film spectrum [634] and it is interesting to speculate that this region could provide an unambiguous marker of β-structure, which in not otherwise clearly visible in the βII-type spectrum.

The availability of an additional structurally sensitive band is also interesting for fibril and aggregate samples, particularly because these typically are more tolerant to dehydration and harsh treatment than globular proteins. One of the central characteristics of amyloid-like fibrils is their high β-sheet content, but widespread heterogeneity has been described for secondary structure and particularly for CD spectral properties. Using the well-characterised glucagon as example, this peptide is capable of forming several types of fibrils with distinct structure and stability depending on conditions during fibrillogenesis [67, 92, 114] (also see section 1.2.4). FTIR appears less sensitive to structural diversity and generally displays spectra consistent with a high β-sheet content, while the corresponding CD spectra show much greater variety including spectra with characteristic for α-helical or β-turn bands as well as typical β-structure. The underlying cause of this diversity it most likely genuine structural variability combined with the low relative intensity of the β-sheet bands. While FTIR provides a straightforward method for estimation of the secondary structure content, it is possible that information contained in the low wavelength band could aid in more sophisticated structural analysis. The examination of fibril and aggregates samples by SRCD

shows that the position and intensity of the low-wavelength band varies significantly in a similar region and over a similar range as the globular model proteins (figure 47.B, paper 2/figure 9). Whereas the position of the low-wavelength band for fibril of lysozyme (no. 13) lies between the β-rich proteins and the α-helical/mixed protein region, the position of the band for fibrils of α-synucleins (no. 16) hints at structural similarities with the sandwich-like architectures, e.g. concanavalin A. This is not inconsistent with the available models of sub-filament structure widely agree on a fibril structure consisting of two or more laminated, regular β-sheets with little or no twist. In contrast, the α-synuclein fibrils fall outside the main β-rich area when examined by PCA suggesting subtle structural variations but highlighting the potential value of the low-wavelength band in analysis of secondary and super-secondary structure. However, as for the globular model proteins, a meaningful interpretation of the structural content of the structural information contained in the low-wavelength band requires further studies and a wider range of model as well as fibril structures.

3.4.4 SRCD reveals subtle pH-dependent differences for SerADan aggregates

The examination of secondary structure of the mature aggregates by FTIR showed no significant variability depending on concentration or pH value indicating that the secondary structure was similar and primarily dependent on peptide properties rather than solution conditions. Whereas the low-quality spectra obtainable on our commercial CD spectrometer also showed minor variability, the high-resolution spectra obtain by SRCD yielded spectra that included splitting of the $\pi_{nb}\pi^*$ band at ~190nm, which has been described for proteins with immunoglobulin-like folds but is also observed for e.g. jacalin, which has an aligned prism architecture. Interestingly, the splitting of this band shows different intensity of the two components depending on pH. The underlying differences that result in observable spectral differences are not clear, but the difference in pH can be assumed to alter the charge state of the peptide and it is likely that the underlying structural cause is connected to differences in charge distribution. Curiously, the low-wavelength bands for the SerADan aggregates fall within the β-rich region and share overall position and shape, but vary in intensity. It is likely that the ongoing effort in structural characterisation by solid state NMR [573] may provide answers to not only the differences observed by CD spectroscopy, but also the overall question of the structure of the mature SerADan aggregates.

APPENDIX

4 Cloning, expression and purification of BriPP and variants

The biophysical and structural properties of BriPP and the two disease-related variants, ABriPP and ADanPP, are of interest because of the possible effect of the C-terminal elongations on stability and aggregational propensity. Consequently, the gene encoding BriPP, *ITM2B*, was isolated from cDNA, the relevant mutations introduced by site-directed mutagenesis and the coding sequences inserted in an appropriate vector system (summary of constructs and vectors in figure 48). Protein expression, in the form of inclusion bodies, was verified and a purification protocol established followed by screening of refolding conditions.

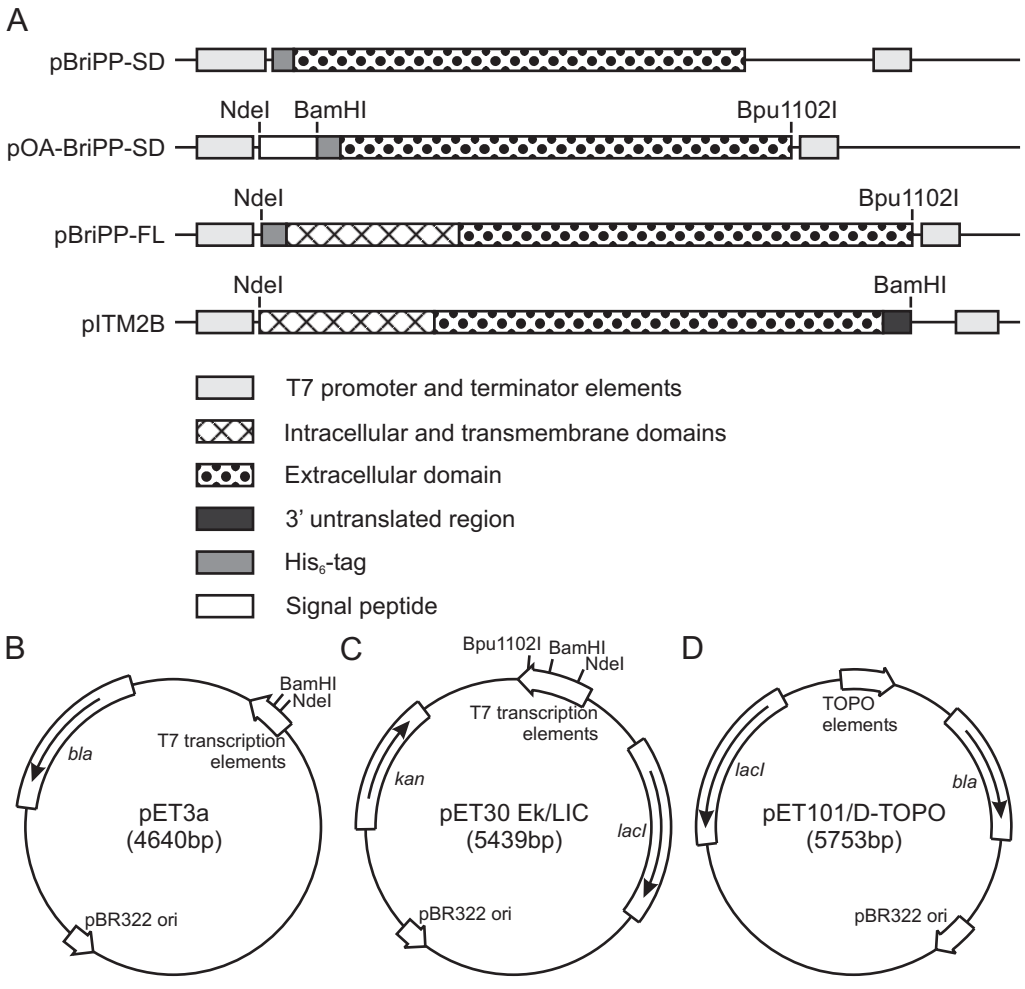

Figure 48. Overview of constructs (A) and empty vector maps of pET3a (B), pET30Ek/LIC (C) and pET101/D-TOPO (D).

4.1 Results and discussion

Isolation of ITM2B coding sequence from cDNA

ITM2B is ubiquitously expressed but has particularly high expression levels in most regions of the CNS including cerebellum. Consequently, a cDNA library obtained from human cerebellum (HL1128b, Clontech, Palo Alto, CA, USA) was chosen for isolation of the *ITM2B* encoding sequence by polymerase chain reaction (PCR). Based on the AY341247 genomic DNA sequence (www.ebi.ac.uk/embl/), the forward and reverse primers (table 12) were designed to introduce NdeI and BamHI restriction sites, respectively, and to allow inclusion of the *ITM2B* 3'-untranslated region, which is activated in the two disease-related mutants.

Despite repeated attempts, *ITM2B* could not be isolated from cerebellar cDNA and the search was widened to include a comparable library from adult lung tissue (Clontech), which yielded a fragment of approximately the expected size

Table 12. Primer and other oligonucleotides. T, target sequence.

Isolation of ITM2B+3'UTR from cDNA and insertion in pET3a		
	Forward	5'-aggccgcgcc atggtgaaggtgacgttcaa-3' **T**
1		5'-ggaattccat atggtgaaggtgacgttcaa-3'
	Reverse	5'-aaacattattgaggaaaattaatat cacagcata-3' **T**
2		3'-tttgtaataactccttttaattata cctaggcgc-5'
Introduction of mutations in pITM2B		
3	ABriPP	5'-ccgtggaaactttaatttgttct **cgc** acagtcaagaaaaacattattgag-3'
		5'-ccgtggaaactttaatttgttct **tga** acagtcaagaaaaacattattgag-3' **T**
4		3'-ggcacctttgaaattaaacaaga **gcg** tgtcagttctttttgtaataactc-5'
5	ADanPP	5'-caaatttgccgtggaaac**tttaatttgt**tttaatttgttcttgaacagtc-3'
		5'-caaatttgccgtggaaac tttaatttgttcttgaacagtc-3' **T**
6		3'-gtttaaacggcacctttg**aaattaaaca**aaattaaacaagaacttgtcag-5'
Construction of OmpA signal sequence		
7		5'-ggaattccatatgaaaaagacagctatcgcgattg**cagtggcactggctgg**-3'
8		3'-**gtcaccgtgaccgacc**aaagcgatggcaccgcgtccggcgacctagggcg-5'
Insertion of ITM2B, full length and soluble domain, in pET30Ek/LIC		
	Forward, full length	5'-taattttgtttaactttaagaaggagatatacatatg gtgaaggtgacgttcaac-3' **T**
9		5'-ggaattccatatgcatcaccatcaccatcacggtgct gtgaaggtgacgttcaac-3'
	Forward, soluble domain	5'-cttgcaggcgttattctaggaggagcatacttg tacaaatattttgcacttcaa-3' **T**
10		5'-cgcggatcccatcaccatcaccatcacggggct tacaaatattttgcacttcaa-3'
	Reverse	5'-cgtggaaactttaatttgttct tgaacagtcaagaaaaacat-3' **T**
11	BriPP	3'-gcacctttgaaattaaacaaga attattcgactcgccttaag -5'
		5'-gaaaaacattattgaggaaaattaa tatggatccggctgcta-3' **T**
12	ABriPP	3'-ctttttgtaataactccttttaatt attcgactcgccttaag-5'
		5'-ttgaacagtcaagaaaaacattat tgaggaaaattaatatggat-3' **T**
13	ADanPP	3'-aacttgtcagttctttttgtaata attattcgactcgccttaag-5'
Insertion of ITM2B, soluble domain, in pTOPO101/D		
	Forward	5'-tgcaggcgttattctaggaggagcatacttg tacaaatattttgcacttcaacc-3' **T**
14		5'-caccatgcatcatcatcatcatcatggtacc tacaaatattttgcacttcaacc-3'
	Reverse	5'-cgtggaaactttaatttgttct tgaaca-3' **T**
15	BriPP	3'-gcacctttgaaattaaacaaga attatt-5'
		5'-gaaaaacattattgaggaaaattaa tat-3' **T**
16	ABriPP	3'-ctttttgtaataactccttttaatt att-5'
		5'-ttgaacagtcaagaaaaacattat tgagga-3' **T**
17	ADanPP	3'-aacttgtcagttctttttgtaata attatt-5'

(856bp, figure 49). The pET3a plasmid (Novagen, Madison, Wisconsin, USA) was chosen as template for vector construction. Rapid ligation at 22ºC was unsuccessful but overnight ligation at 4ºC gave numerous colonies compared to controls (insert or empty vector). Ten colonies were cultured for plasmid purification and sequencing. Mutations were identified in all clones, but one of these (pITM2B) contained only silent mutations (ggc-to-ggt at codon 67, cct-to-ccc at codon 133 and gca-to-gcg at codon 138) and was chosen for further modification.

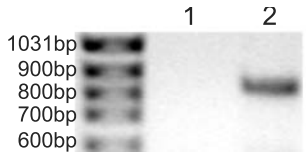

Figure 49. 1% agarose gel of PCR from cDNA of cerebellum (1) and lung tissue (2).

Construction of recombinant expression vectors

The pITM2B plasmid contained not only the *ITM2B* coding sequence but also sufficient 3'-UTR to allow introduction of the two disease related mutations directly on the vector by site-directed mutagenesis (SDM) as opposed to elongation of the 3' sequence by successive rounds of PCR. The forward and reverse primers were designed for the two mutations (table 12). As expected, the method yielded few colonies per mutation (3-5), all of which were picked for plasmid amplification and sequencing using the T7 forward primer combined with a custom primer (table 12) allowing better visualisation of the 3'-region. Despite the low number of colonies, correctly introduced mutations were identified in all but one clone. The purpose of the introduction of the disease-related mutations was to obtain templates for PCR amplification and modification to allow insertion in an appropriate expression vector. To this end, a single clone was picked for each mutation (pITM2B-AB and pITM2B-AD for ABriPP and ADanPP, respectively) containing only the disease-related mutation and the three silent mutations.

BriPP is a predicted type I transmembrane proteins with a short 51AA N-terminal cytoplasmic region, a 25AA transmembrane helix and a 190AA C-terminal extra-cellular domain. To allow characterisation of both the full-length membrane protein (FL form) and the presumably soluble extra-cellular domain (SD form), two sets of expression vectors were designed based on the pET30Ek/LICS plasmid (Novagen). This kanamycin-conferring plasmid was chosen to minimise false-positive clones of pITM2B vectors, which carry ampicillin resistance. The BriPP-FL, ABriPP-FL and ADanPP-FL constructs were designed to yield simple N-terminally His-tagged proteins which would presumably form inclusion bodies. The His-tag was introduced by PCR as an additional overhang and the coding sequence inserted between the plasmid NdeI and BlpI restriction sites. As for pITM2B, rapid ligation yielded only colonies bearing the empty vector and similar results were obtained by cold overnight ligation. However, the addition of a desphosphorylation step for the vector fragment prior to gel purification gave multiple colonies of which 8 were picked for sequencing for each variant and one chosen per construct (pBriPP-FL, pABriPP-FL and pADanPP-FL).

The BriPP-SD and variant constructs were initially designed for transport to the periplasm by introduction of the OmpA signal sequence (OA, table 12) to allow purification of native protein rather than inclusion bodies. The vector was to be assembled in two steps: *i*) Insertion of the OA between plasmid restriction sites NdeI and BamHI (pOA plasmid) and *ii*) insertion of the soluble domain coding sequence including an 5' His-tag sequence between plasmid restriction sites BamHI and BlpI (pOASS-<variant>-SD plasmids). However, while the signal sequence was readily incorporated into the empty vector, the subsequent ligation of the vector and SD domain (produced by PCR) proved difficult. Similar lack of results were observed for ligation of the SD-sequence into an unmodified vector (pET3a and pET30Ek/LICS both). An alternative approach was chosen based on the TOPO 101/D cloning system (Invitrogen, Carlsbad, CA, USA). The method omits the use of restriction sites, restriction enzymes and conventional ligation. The PCR product is cloned into the linear plasmid by the activity of covalently linked topoisomerase I from the *Vaccinia* virus (figure 50).

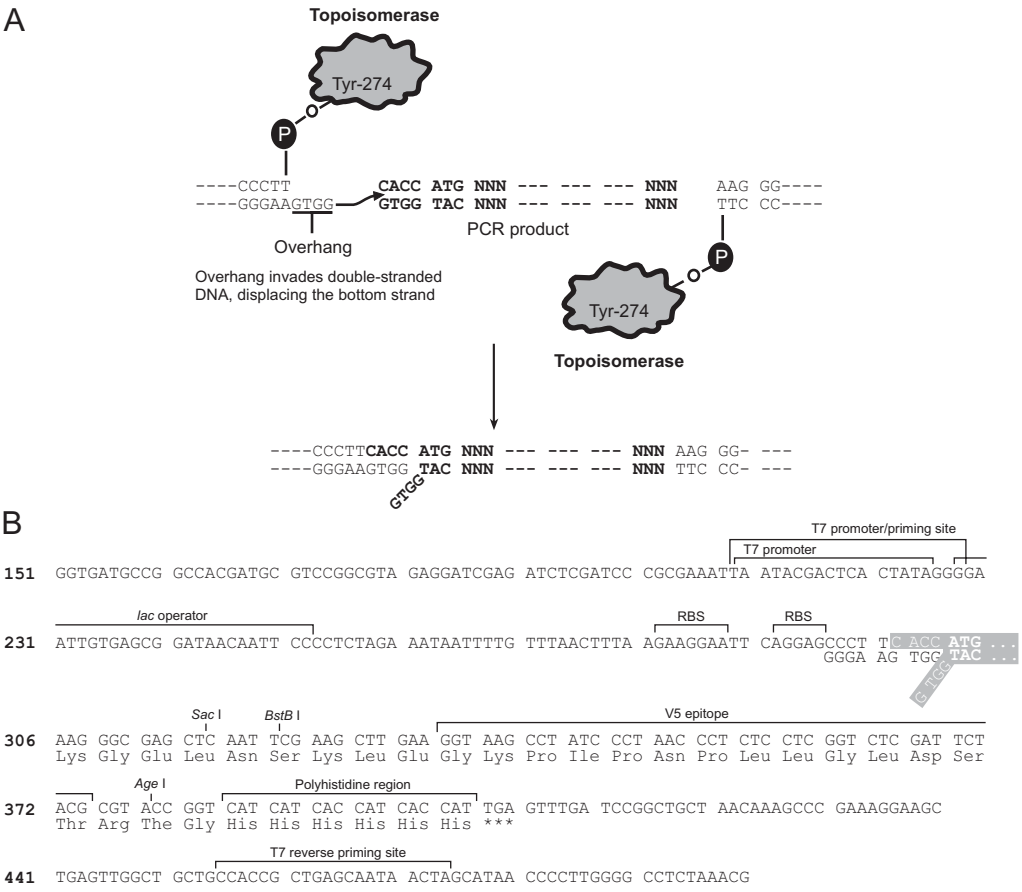

Figure 50. Principle of TOPO cloning (A) and sequence of the cloning region (B) (tools.invitrogen.com/content/sfs/manuals/pettopo_man.pdf).

Directional cloning is made possible by adding a 4bp, 5'-overhang during PCR amplification. An N-terminal His_6-tag introduced by PCR was preferred over the C-terminal His-tags available on the vector due to the C-terminal localisation of the two mutations. Therefore, the TOPO cloning primers included the cacc overhang for directional cloning, an N-terminal MH_6T peptide, and a two C-terminal stop codons (table 12). The colony-yield was low (with no control plate colonies) but subsequent sequencing showed that the correct sequence had been obtained for all three variants (pBriPP-SD, pABriPP-SD and pADanPP-SD).

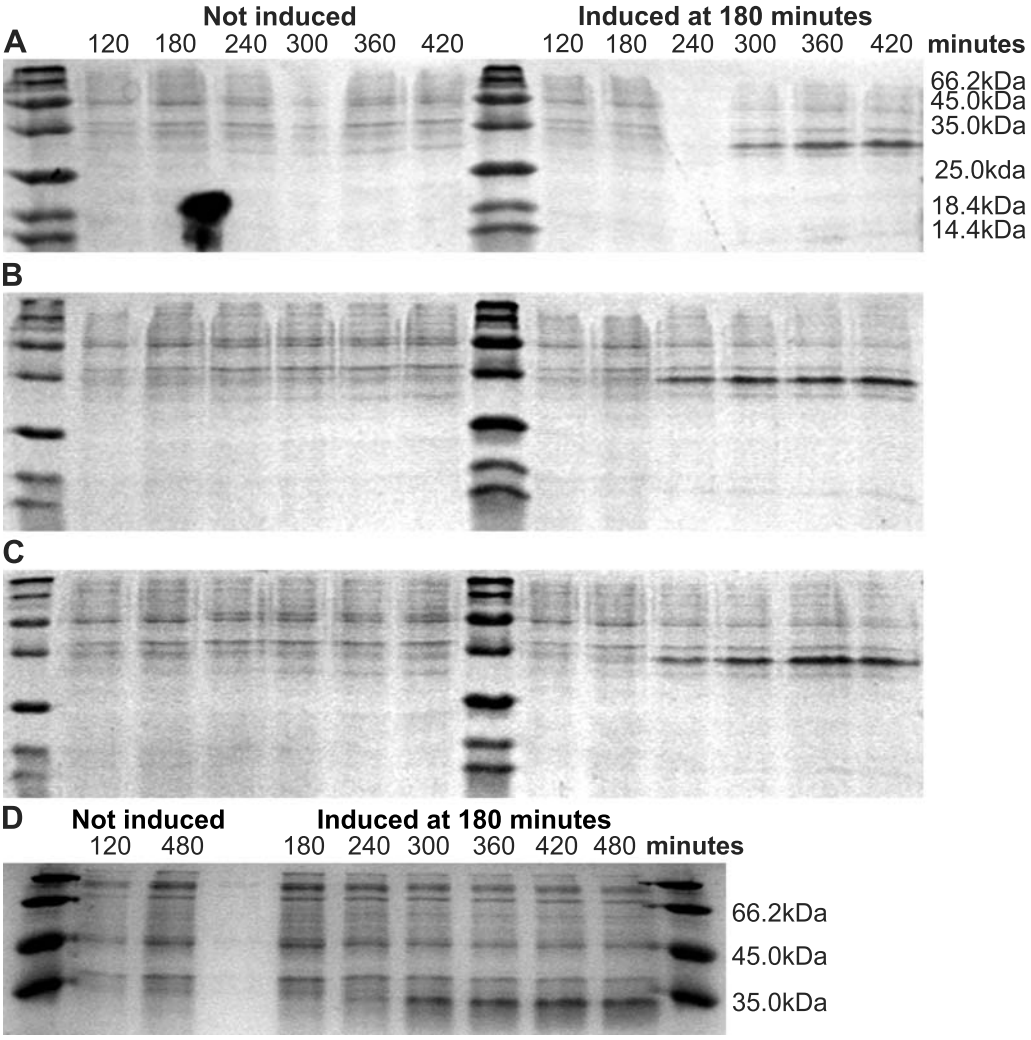

Figure 51. Expression of BriPP (A), ABriPP (B) and ADanPP (C) in LB medium and BriPP in M9 medium (D).

Verification of protein expression in rich and minimal medium

A series of culture experiments was designed to monitor expression of the soluble domain (SD) of BriPP, ABriPP and ADanPP by *E. coli* BL21 (DE3) in rich (LB) and minimal (M9) medium at 37ºC. Briefly, *E.coli* BL21 (DE3) cells transformed with the appropriate plasmids were grown under batch conditions and cell samples were removed at regular intervals for SDS-PAGE analysis (figure 51). Following induction, a band appears at approximately 30kDa with increasing intensity. The apparent value is somewhat higher than the expected molecular weight of the soluble domain (23.4 kDa). This is the case for both rich (figure 51.A) and minimal medium (figure 51.D) and a similar behaviour can be observed for the soluble domain of the mutant ABriPP and ADanPP (figure 51.B-C). Since the protein was expressed to the cytoplasm, and appears to be present in large amounts, it is reasonable to assume that the protein deposits as inclusion bodies rather than as native protein.

To verify the presence of BriPP-SD, cells were harvested and the inclusion bodies isolated and re-dissolved in 8M urea (20mM Tris, 8M urea, pH 7.4). Unsurprisingly, the roughly purified inclusion bodies had a very intense band at ~30kDa (figure 52). The His-tagged protein was further purified by nickel affinity chromatography (NAC). The resulting fractions were analysed on 15% SDS-

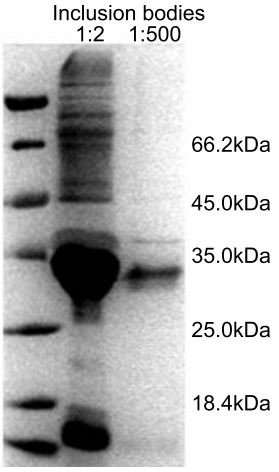

Figure 52. Roughly purified inclusion bodies of BriPP at 1:2 and 1:500 dilutions (15% SDS-PAGE).

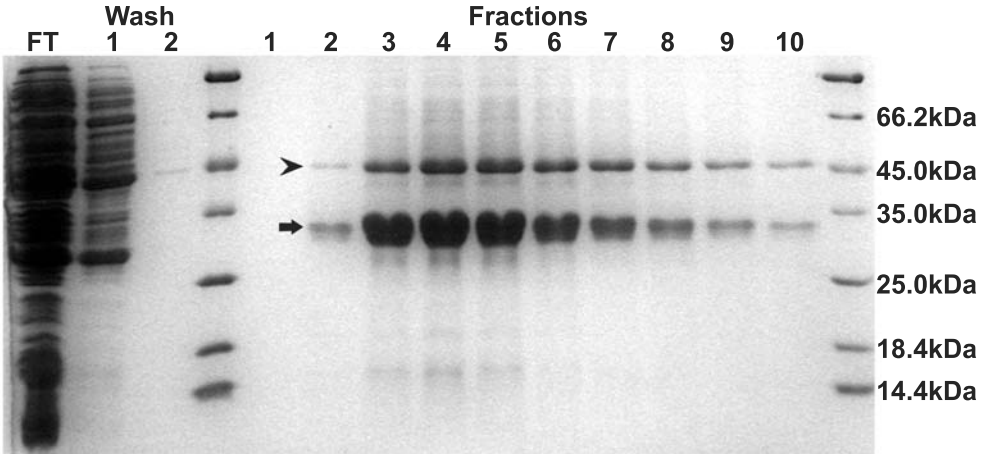

Figure 53. NAC-purified BriPP (15% SDS-PAGE). Arrow, recombinant band; arrowhead, contiminant band.

PAGE (figure 53) and did show overall increased purity of the supposed recombinant band (arrow) but also a marked degree of impurity including a strong band at ~46kDa (arrowhead), which closely follows the supposed recombinant band in intensity. The position corresponds to the expected dimer mass (46.6kDa) although the monomer runs with a higher apparent mass. The two bands were analysed by in-gel tryptic digestion and mass spectroscopy and both were identified as variants of the recombinant protein. The presence of a high-molecular weight band of the recombinant protein suggests formation of a covalent dimer by partially dithiothreitol (DTT)-resistant disulphide formed from any of the 5 cysteines. Indeed, incubation with 40mM DTT decreased the intensity of higher order bands but did not entirely suppress the formation of dimers or higher oligomers (figure 54).

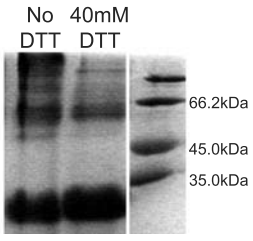

Figure 54. Effect of DTT on oligomerisation of BriPP (15% SDS-PAGE).

Establishment of purification protocol

The initial purification experiment suggested that affinity-chromatography could be an effective method provided that the formation of covalent dimers and higher

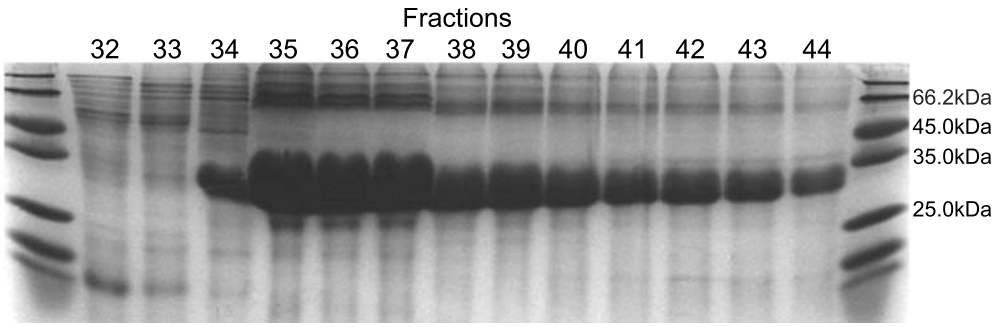

Figure 55. AEC-purified BriPP.

oligomers could be suppressed and that the presence of additional impurities minimised. To this end, an initial anion-exchange chromatography (AEC) step was introduced using a high capacity Source™ 15Q column. The AEC step did improve overall purity but the highest-concentration fractions still required further purification (fractions 35-37, figure 55). BriPP eluted at approximately 200mM NaCl, which allowed binding to the NAC matrix without intervening dialysis. To limit cross-linking without reducing Ni^{2+}, 25mM 2-mercaptoethanol (2me) was added to the equilibration, wash and elution buffers. The resulting fractions appear pure but low in concentration (figure 56). To asses the purity, the highest-concentration fractions (2-3) were pooled and concentrated by ultrafiltration/centrifugation. By comparison to a samples purified only by NAC and in the absence of 2me, the combination of the two methods appears to yield sufficiently pure protein with limited disulphide cross-linking (figure 57).

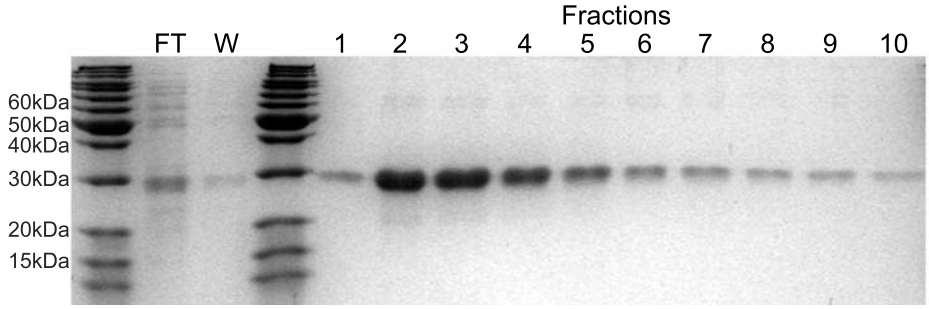

Figure 56. BriPP purified by NAC and AEC in the presence of reducing agents.

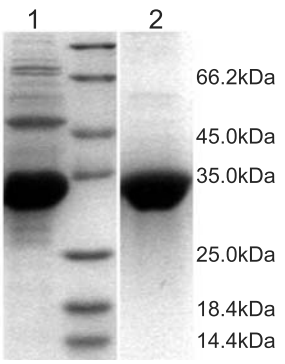

Figure 57. Concentrate of purified BriPP in the presence of 2me (2) compared to the same concentration of protein purified by AEC alone and in the absence of reducing agent.

Screening of refolding conditions

The attained purity cannot be said to be sufficient for advanced characterisation, e.g. crystallisation, but was deemed sufficient for screening conditions under which folding into a stable, supposed native-like conformation could be accomplished. The micro-well plate method was adopted from [637] with special emphasis on the effect of reducing (2me, GSH/GSSG) and stabilising agents (glycerol, glucose, PEG 400 and 4000) as well as the effect of salts (KCl, NaCl). In addition, a

A	1	2	3	4	5	6	7	8	9	10	11	12
	pH 4.0		pH 5.0		pH 6.0		pH 7.0		pH 8.0		pH 9.0	
A	N.a.a.	2me Glycerol	N.a.a.	2me EDTA	N.a.a.	2me 0.1M NaCl	N.a.a.	Cocktail	N.a.a.	2-bme	N.a.a.	----
B	0.1M KCl	2me 0.1M KCl	KCl	2me Glycerol	0.1M KCl	2me 0.2M NaCl Glucose	0.1M NaCl	2me	0.1M NaCl	2me 0.1M NaCl	0.1M NaCl	2me 0.2M NaCl
C	EDTA	2me 0.1M NaCl	0.2M NaCl	2me PEG 4000	EDTA	2me	0.2M NaCl	2me 0.1M NaCl	0.2M NaCl	2me 0.2M NaCl Glucose	0.1M NaCl Glucose	0.1M KCl Glucose
D	Glycerol	2me 0.2M NaCl	0.1M NaCl	2me PEG 400	Glucose	2me Glycerol	0.1M KCl	2me EDTA	Glucose	2me Glucose	0.2M NaCl	PEG 400
E	PEG 400 Glucose	2me Glucose	Cocktail	2me 0.1M NaCl	Glycerol	2me Glucose	EDTA	2me Glycerol	EDTA Glucose	2me Glycerol	Glycerol	2me EDTA
F	PEG 4000 Glucose	Cocktail	EDTA	2me Glucose EDTA	PEG 400	2me PEG 400	Glucose	2me PEG 4000	PEG 400	2me 0.1M KCl	PEG 400	PEG 4000 Glucose
G	2-bme	2me PEG 400 Glucose	2me	Glucose EDTA	PEG 4000	Cocktail	PEG 4000	2me PEG 400 Glucose	PEG 4000	Cocktail	Cocktail	2me 0.1M NaCl Glycerol
H*	5mM GSH	5mM GSSG	10mM GSSG	5mM GSH 5mM GSSG	5mM GSH 2mM GSSG	2mM GSH 5mM GSSG	----	----	----	----	----	----

*50mM Tris, pH 8, 150mM NaCl, 1mM EDTA. N.a.a. No additional additives; ----, used for background; 2me, 2-mercaptoethanol; GSH, glutathione; GSSG, glutathione disulphide. Other concentrations: EDTA, 1mM ; glycerol, 20%(v/w); PEG 400 and PEG 4000, 0.5%(m/m); glucose, 500mM; 2me, 10mM. Cocktail: 50µM each of thiamine(HCl), $CaCl_2$, $CuSO_4$, $ZnSO_4$, $NiCl_2$.

B	1	2	3	4	5	6	7	8	9	10	11	12
	pH 4.0		pH 5.0		pH 6.0		pH 7.0		pH 8.0		pH 9.0	
A	0.115	0.108	0.061	0.071	*0.029*	0.072	**0.001**	**0.010**	**0.001**	**0.001**	**0.001**	----
B	0.122	0.102	0.097	0.047	0.069	0.074	**0.001**	**0.001**	**0.002**	**0.001**	**0.001**	**0.002**
C	0.121	0.104	0.095	0.069	0.033	*0.029*	*0.013*	**0.002**	**0.001**	**0.002**	**0.001**	**0.001**
D	0.103	0.096	0.095	0.060	*0.025*	*0.027*	**0.003**	**0.001**	**0.002**	**0.001**	**0.001**	**0.001**
E	0.106	0.102	0.058	0.088	0.033	*0.029*	**0.001**	**0.002**	**0.001**	**0.001**	**0.001**	**0.001**
F	0.105	0.110	0.057	0.059	0.037	0.031	**0.001**	**0.002**	**0.001**	**0.001**	**0.001**	**0.001**
G	0.105	0.037	0.054	0.030	0.033	0.033	**0.001**	**0.001**	**0.001**	**0.008**	**0.008**	**0.001**
H*	**0.010**	**0.008**	**0.007**	*0.013*	**0.008**	**0.006**	----	----	----	----	----	----

* pH 8.0; ----, Empty

C	1	2	3	4	5	6	7	8	9	10	11	12
	pH 4.0		pH 5.0		pH 6.0		pH 7.0		pH 8.0		pH 9.0	
A	0.117	0.110	0.063	0.073	*0.030*	0.075	**0.001**	**0.007**	**0.001**	**0.001**	**0.001**	----
B	0.121	0.103	0.097	0.049	0.072	0.076	**0.005**	**0.002**	**0.002**	**0.002**	**0.002**	**0.002**
C	0.120	0.112	0.095	0.070	0.034	*0.030*	*0.019*	**0.004**	**0.002**	**0.003**	**0.002**	**0.002**
D	0.107	0.102	0.097	0.063	*0.028*	*0.028*	**0.006**	**0.001**	**0.002**	**0.002**	**0.001**	**0.002**
E	0.111	0.109	0.059	0.092	0.033	*0.030*	**0.002**	**0.002**	**0.001**	**0.001**	**0.001**	*0.013*
F	0.106	0.108	0.059	0.061	0.044	0.032	**0.001**	**0.002**	**0.002**	**0.001**	**0.002**	**0.002**
G	0.105	0.099	0.054	0.054	*0.030*	0.036	**0.001**	**0.001**	**0.001**	**0.005**	**0.003**	**0.001**
H*	*0.015*	**0.007**	**0.010**	*0.013*	**0.010**	**0.007**	----	----	----	----	----	----

* pH 8.0; ----, Empty

cocktail of trace metal ions was screened (table 13.A). The results showed a clear tendency towards aggregation at low pH and high salt concentration (table 13.B-C). The latter could be partially alleviated by the presence of glucose, but not altogether abolished. After two weeks, the protein remained in solution in all samples at pH 8.0 and 9.0 with exception of those containing 0.2M NaCl. No clear effect was observed for other additives or trace metal ions.

Table 13 (opposite). Refolding assay (A) and OD_{340} after 15 min. (B) and overnight storage (C) at 4ºC. Classification: 'Soluble' (bold) <0.01; 'partly soluble' (italics) <0.03.

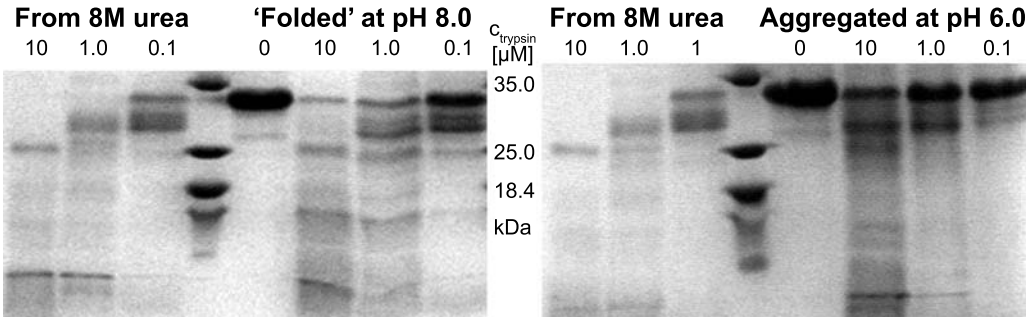

Figure 58. Trypsin digest of urea-denatued, aggregated and 'folded' BriPP.

Following 14 days of storage, the stability of the protein against tryptic digest was estimated for aggregated and soluble samples at pH 6.0 and 8.0, respectively (wells A5 and A9, figure 58), and compared to stability of the protein diluted directly from 8M urea to comparable protein concentration in digestion buffer. Both the soluble and aggregated protein were significantly more resistant to proteolysis than the denatured form. It is expected that protein aggregates are protected from proteolysis. The somewhat lower but nonetheless apparent resistance of the soluble form at pH 8.0 suggests that the protein is folded in what must assumed to be a native-like conformation. Circular dichroism spectra were obtained for protein freshly diluted into folding buffer at pH 8.0 and after overnight folding (figure 59). The initial conformation appear β-like albeit with significant

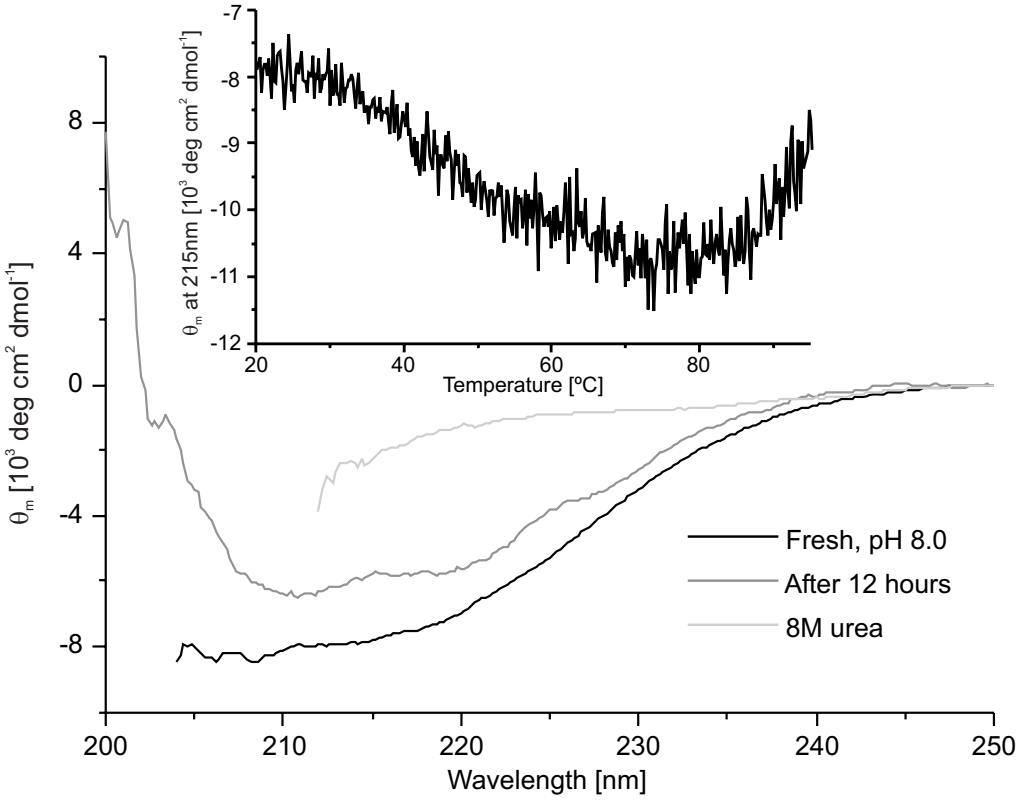

Figure 59. CD spectra of 5µM BriPP (A) in the denatured, freshly dissolved and aged state. Insert: Thermal scan of a similar sample.

noise. Over the longer folding period, the spectrum changes to a more α-like appearance. However, following the CD-signal at 215nm during heating does not reveal corporative loss of secondary structure suggesting a non-native conformation (figure 59, insert).

An important issue raised by the observations summarised above, is the formation of dimers and higher oligomers, presumably by disulphide cross-linking. For long-term storage, including storage at -80ºC, neither DTT nor 2me was found to suppress cross-linking while the addition of 25mM Tris(2-carboxyethyl)phoshine (TCEP) was found to be more effective without suppressing the cross-binding entirely. The role of cysteines is also of concern since the protein largely aggregates in solution at pH-values below 8. The use of refolding under basic conditions also leads to higher lability and shuffling of disulphide bonds [638], which could aid in refolding by allowing a higher degree of conformational freedom. However, considering the tendency towards cross-binding, suppression of intermolecular disulphide formation may well be a requirement for folding to occur and for long term stability of the protein in solution. Conversely, the high number of cysteines suggest a structural role of disulphide formation and the suppression of oxidation could significantly and adversely affect the stabilisation of the protein structure. Similarly, the *in vivo* quartenary structure of BriPP is not at all clear but potential dimerisation or higher oligomerisation must be kept in mind particularly in light of the odd number of cysteines is found in both the full-length protein and extra-cellular domain. A recent study by Tsachaki *et al.* [639] on BriPP expressed in culture demonstrated the presence of BriPP dimers formed by disulphide cross-linking at position 89 in the transmembrane region. It is possible that prevention of intermolecular bonding could prevent the protein from attaining native structure. As such, the highly reducing conditions do not reflect biologically relevant conditions and any structural or functional properties must be viewed with some doubt. One possible approach to elucidating the role of cysteines in BriPP folding and function would be a Cys-to-Ser combinatorial mutational study.

4.2 Materials and methods

Materials

All chemicals were supplied by Sigma (St. Louis, MO, USA) unless otherwise indicated. Medium components (tryptone, yeast extract, bacto-agar) were from International Diagnostics Group (Bury, UK). NaCl was supplied by J.T. Baker (Deventer, Holland). XL1 Blue and BL21 (DE3) cell lines were generic laboratory strains. QuikChange® Site-Directed Mutagenesis kit and Champion™ Directional TOPO® 101/D expression kit including specific supercompetent cells were from Strategene (La Jolla, CA, USA) and Invitrogen (Carlsbad, CA, USA), respectively. pET3a and pET30Ek/LIC vector backbones were from Novagen (Madison, WI). Lung tissue and whole cerebellum 5'-STRETCH cDNA libraries (λgt11) were supplied by ClonTech (). Plasmids were purified using the

GenElute™ Plasmid Miniprep kit (Sigma, St. Louis, MO, USA). The NucleoSpin Extract kit (Macherey-Nagel, Düren, Germany) was used for purification of PCR products and agarose gel extraction of DNA. Primers were supplied by DNA Technology (Aarhus, Denmark). The *Taq* and Herculase polymerases were from New England Biolabs (Beverly, MA, USA) and Stratagene (La Jolla, CA, USA). T4 DNA ligase and restriction enzyme NdeI were from New England Biolabs (Beverly, MA, USA). Restriction enzymes BamHI and BlpI (isoschizomer of Bpu1102I), shrimp alkaline phosphatase (SAP), sequencing reagents, DNA and protein weight standards were supplied by MBI Fermentas (Hanover, MD, USA). Acrylamide:bis-acrylamide (37.5:1, 30% solution) and sodium dodecylsulfate (SDS) were supplied by AppliChem (Darmstadt, Germany). All lipids were from Avanti Polar Lipids (Alabaster, AL, USA).

DNA-based methods

Polymerase chain reaction (PCR) was performed using 16nM of each primer, 0.2mM dNTP, 0.04units/100µL *Taq* or Herculase polymerase and 2µL template (plasmid or λ phase cDNA). Templates, primers, temperatures and cycle lengths are summarised in table 14. All PCR products were visualised on 1% agarose and purified before further use.

The appropriate and purified PCR fragment was sequentially digested according to manufacturer's recommendations followed by a second round of gel purification. Vector DNA was treated similarly but also dephosphorylated (SAP) prior to gel purification. Ligation using T4 ligase was performed either for 1 hour at 22ºC or overnight at 4ºC according to manufacturer's protocol. For each ligation, a maximum of ten colonies were picked for analysis by PCR using insert-specific primers. Positive colonies were further analysed by sequencing. The alternative TOPO method was performed according to the supplied protocol, but otherwise analysed similarly. Site-directed mutagenesis on the pITM2B plasmid was performed using the Quik-Change® method (Stratagene) according to manufacturer's protocol.

Relevant colonies were picked for plasmid purification and used as PCR template with specific sequencing primers followed by treatment with SAP and exonuclease I. Dye terminated fragments were obtained by second PCR using dye-dNTPs. The dye-terminated fragments were separated by capillary chromatography (Megabace, GE Health Care, Little Chalfont, UK)

Growth and expression of BriPP and variants

Chemically competent *E.coli* BL21 (DE3) cells were transformed with the appropriate plasmid and plated on LB-agar under selection pressure (100µg/mL ampicillin). Single colonies were picked for overnight starter cultures (37ºC, LB or M9 medium, table 15). Growth batch cultures were inoculated with 5% starter culture and grown to an optical density at 600nm (OD_{600}) of ~0.2 before induction with 0.5mM IPTG. Cell samples were removed at regular intervals, OD_{600}

measured and aliquots centrifuged and stored at -20ºC for subsequent analysis. All cell samples were re-dissolved in PBS buffer to similar OD and aliquots were mixed with SDS-PAGE sample buffer (0.2M Tris, 2% (w/v) SDS, 20% (v/v) glycerol, 40mM DTT, pH 6.8) and heated (60 seconds, 95ºC). Samples were analysed by Laemmli-type SDS-PAGE [640] (4% stacking, 15% separation gels). Proteins were visualised by Coomassie staining.

Inclusion body purification

Cells were harvested by centrifugation (8000rpm, 10 minutes, Sorvall® RC5C Plus, SLA3000 rotor, Kendro Laboratory Products,Newtown, California, USA). The pelleted cells were re-suspended in 50mL PBS and lysed by repeated sonication (10 x 60 seconds with 30 second intervals) on ice. Inclusion bodies and remaining whole cells were isolated by centrifugation (5800rpm, 2 hours, SS34 rotor, Kendro Laboratory Products). The pellet was resuspended in 20mL TEN-Triton buffer (50mM Tris, 1mM EDTA, 100mM NaCl, 1mM DTT, 2% (w/v) Triton X100, pH 8) and incubated overnight at 37ºC, 150rpm shaking. The sample was centrifuged (5800rpm, 20 minutes, SS34 rotor), the pellet re-suspended in 20mL TEN buffer (without Triton) and centrifuged again under the same conditions. The pellet was re-suspended in 20mL TN buffer (50mM Tris, 100mM NaCl, 1mM DTT, pH 8.8 for AEC and pH 7.4 for NAC) and mixed with 4 volumes TN buffer with 10M urea. The inclusion bodies were allowed to dissolved for 3 hours at 37ºC before removal of remaining whole cells and non-inclusion body cellular debris by centrifugation (19000rpm, 20 minutes, SS34 rotor). The supernatant was decanted, fast-frozen and stored at -80ºC. Samples taken during the purification and the final supernatant were analysed by 15% SDS-PAGE and visualised by Coomassie staining.

Anion-exchange chromatography

Anion-exchange chromatography was performed on an ÄKTAexplorer system (GE Healthcare, Little Chalfont, UK) fitted with a 30mL Source™ 15Q anion exchange column (GE Healthcare). Due to the high back pressure cause by running in 8M urea, flow was restricted to 0.5mL/minute. The column material was equilibrated in buffer AEC A (20mM Tris, 8M urea, 10mM DTT, pH 8.8). Protein (5mL) was loaded on the column and washed with two column volumes of buffer AEC A. Elution was performed as a linear 0-500mM NaCl gradient (0-50% buffer AEC B, 20mM Tris, 1M NaCl, 8M urea, 10mM DTT, pH 8.8) over two column volumes and the eluent collected as 0.5mL fractions. The elution was followed by absorbance at 280nm and selected fractions were analysed by 15% SDS-PAGE.

Nickel affinity chromatography

The HIS-Select™ Nickel Affinity gel (Sigma) was chosen for the NAC step. The tolerance of the binding capacity towards reducing agents was examined prior to use. DTT reduced Ni^{2+}, while 2me could be used up to a concentration of ~30mM.

The Ni^{2+}-charged agarose gel beads were drained and equilibrated (20mM Tris, 6M urea, 20mM 2me, 100mM NaCl, which was omitted when binding AEC samples). The slurry was mixed with four volumes of sample and left overnight at 4ºC with rotational agitation. The material was transferred to a column and washed twice (20mM Tris, 100mM NaCl, 5mM imidazole, 6M urea, 20mM 2me) by gravity draining. Protein was eluted in 10 x 5mL elution buffer (20mM Tris, 100mM NaCl, 250mM imidazole, 6M urea, 20mM 2me), which were analysed by 15% SDS-PAGE. The relevant fractions were pooled and dialysed overnight (20mM Tris, 8M urea, 30mM DTT or TCEB, pH 7.4) at 4ºC. The sample was then concentrated (~10x) in a Centricon® YM10 filter (Millipore, Billerica, MA, USA), aliquoted, fast-frozen and stored at -80ºC.

Refolding assay

Screening of refolding conditions was performed according to Vincentelli *et al.* [637] with some modifications (assay summarised in table 13.A). The buffer concentration was 50mM of sodium acetate (pH 4.0), MES (pH 5.0 and 6.0) or Tris (pH 7.0, 8.0 and 9.0). Buffers were prepared, filtered (0.22µM syringe filter, Millipore) to prevent microbial growth and aliquots of 95µL were transferred to a clear 96 microwell plate (Greiner Bio-One, Frickenhausen, Germany). The concentration of the dialysed protein was estimated from absorbance at 280nm (A_{280}, ε_{280}=18130$M^{-1}cm^{-1}$) and adjusted to a stock concentration of ~5mg/mL of which 5µL were transferred to each well to a concentration of ~0.25mg/mL (11µM). The formation of protein aggregates was measured (U1500, Hitachi, Tokyo, Japan) as optical density at 340nm (OD_{340}) after 15 minutes, overnight and 14 days storage of the closed plate at 4ºC. Samples were classified as 'soluble' for OD_{340} at or below 0.01 and 'partly soluble' for OD_{340} between 0.01 and 0.03.

Trypsin stability assay

For examination of protein stability towards trypsin digest, protein samples were mixed with 1:1 with trypsin digest buffer (50mM sodium phosphate, pH 7.6) containing 0.1, 1 and 10µM freshly prepared and chilled trypsin. Sample were incubated at 37ºC for 15 minutes. Proteolysis was stopped with 1mM phenylmethanesulphonyl fluoride (PMSF) and samples examined by 15% SDS-PAGE. Protein diluted directly from 8M urea into trypsin digest buffer was included as control and otherwise treated similarly.

Circular dichroism

Circular dichroism (CD) spectra were recorded using 5µM protein on a Jasco J-810 spectropolarimeter (Jasco, Hachioji, Tokyo, Japan; 1mm 110-QS cuvette, Hellma, Müllheim, Germany) with averaging over 10 scans, resolution 0.1nm, response time 2s. Thermal scanning was monitored at 215nm for every 0.2ºC with linear ramping from 20 to 95ºC at a speed of 90ºC/hour (resolution 2nm, response time 2s).

References

5

1. Frokjaer, S. and Otzen, D. E.: Protein drug stability: a formulation challenge. *Nat Rev Drug Discov* (2005) 4 p. 298-306.
2. Thomas, P. J., Qu, B. H. and Pedersen, P. L.: Defective protein folding as a basis of human disease. *Trends Biochem Sci* (1995) 20 p. 456-9.
3. Chaudhuri, T. K. and Paul, S.: Protein-misfolding diseases and chaperone-based therapeutic approaches. *Febs J* (2006) 273 p. 1331-49.
4. Westermark, P.: Aspects of human amyloid forms and their fibril polypeptides. *Febs J* (2005) 272 p. 5942-9.
5. Lansbury, P. T., Jr. and Lashuel, H. A.: A century-old debate on protein aggregation and neurodegeneration enters the clinic. *Nature* (2006) 443 p. 774-9.
6. Aterman, K.: A historical note on the iodine-sulphuric acid reaction of amyloid. *Histochemistry* (1976) 49 p. 131-43.
7. Sipe, J. D. and Cohen, A. S.: Review: history of the amyloid fibril. *J Struct Biol* (2000) 130 p. 88-98.
8. Westermark, P., Benson, M. D., Buxbaum, J. N., Cohen, A. S., Frangione, B., Ikeda, S., Masters, C. L., Merlini, G., Saraiva, M. J. and Sipe, J. D.: Amyloid: toward terminology clarification. Report from the Nomenclature Committee of the International Society of Amyloidosis. *Amyloid* (2005) 12 p. 1-4.
9. Westermark, G. T., Johnson, K. H. and Westermark, P.: Staining methods for identification of amyloid in tissue. *Methods Enzymol* (1999) 309 p. 3-25.
10. Chiti, F. and Dobson, C. M.: Protein misfolding, functional amyloid, and human disease. *Annu Rev Biochem* (2006) 75 p. 333-66.
11. Linke, R. P., Joswig, R., Murphy, C. L., Wang, S., Zhou, H., Gross, U., Rocken, C., Westermark, P., Weiss, D. T. and Solomon, A.: Senile seminal vesicle amyloid is derived from semenogelin I. *J Lab Clin Med* (2005) 145 p. 187-93.
12. Dobson, C. M.: Protein folding and misfolding. *Nature* (2003) 426 p. 884-90.
13. Alexandrescu, A. T.: Amyloid accomplices and enforcers. *Protein Sci* (2005) 14 p. 1-12.
14. Lindquist, S.: Mad cows meet psi-chotic yeast: the expansion of the prion hypothesis. *Cell* (1997) 89 p. 495-8.
15. Wickner, R. B., Edskes, H. K., Maddelein, M. L., Taylor, K. L. and Moriyama, H.: Prions of yeast and fungi. Proteins as genetic material. *J Biol Chem* (1999) 274 p. 555-8.
16. Glover, J. R., Kowal, A. S., Schirmer, E. C., Patino, M. M., Liu, J. J. and Lindquist, S.: Self-Seeded Fibers Formed by Sup35, the Protein Determinant of [PSI+], a Heritable Prion-like Factor of S. cerevisiae. *Cell* (1997) 89 p. 811-9.
17. Prusiner, S. B.: Molecular biology of prion diseases. *Science* (1991) 252 p. 1515-22.
18. DePace, A. H. and Weissman, J. S.: Origins and kinetic consequences of diversity in Sup35 yeast prion fibers. *Nat Struct Biol* (2002) 9 p. 389-96.
19. Larsen, P., Nielsen, J. L., Dueholm, M. S., Wetzel, R., Otzen, D. and Nielsen, P. H.: Amyloid adhesins are abundant in natural biofilms. *Environ Microbiol* (2007) 9 p. 3077-90.
20. Larsen, P., Nielsen, J. L., Otzen, D. and Nielsen, P. H.: Amyloid-like adhesins produced by floc-forming and filamentous bacteria in activated sludge. *Appl Environ Microbiol* (2008) 74 p. 1517-26.
21. Fowler, D. M., Koulov, A. V., Alory-Jost, C., Marks, M. S., Balch, W. E. and Kelly, J. W.: Functional Amyloid Formation within Mammalian Tissue. *PLoS Biol* (2005) 4 p. e6.
22. Fowler, D. M., Koulov, A. V., Balch, W. E. and Kelly, J. W.: Functional amyloid - from bacteria to humans. *Trends Biochem Sci* (2007) 32 p. 217-24.
23. Otzen, D. and Nielsen, P. H.: We find them here, we find them there: functional bacterial amyloid. *Cell Mol Life Sci* (2008) 65 p. 910-27.
24. Stefani, M. and Dobson, C. M.: Protein aggregation and aggregate toxicity: new insights into protein folding, misfolding diseases and biological evolution. *J Mol Med* (2003) 81 p. 678-99.
25. Rocchi, A., Pellegrini, S., Siciliano, G. and Murri, L.: Causative and susceptibility genes for Alzheimer's disease: a review. *Brain Res Bull* (2003) 61 p. 1-24.
26. Tan, S. Y. and Pepys, M. B.: Amyloidosis. *Histopathology* (1994) 25 p. 403-14.
27. Pepys, M. B., Hawkins, P. N., Booth, D. R., Vigushin, D. M., Tennent, G. A., Soutar, A. K., Totty, N., Nguyen, O.,

Blake, C. C., Terry, C. J. and et al.: Human lysozyme gene mutations cause hereditary systemic amyloidosis. *Nature* (1993) 362 p. 553-7.
28. Benson, M. D.: Ostertag revisited: the inherited systemic amyloidoses without neuropathy. *Amyloid* (2005) 12 p. 75-87.
29. Soto, C.: Unfolding the role of protein misfolding in neurodegenerative diseases. *Nat Rev Neurosci* (2003) 4 p. 49-60.
30. Cornwell, G. G., 3rd, Johnson, K. H. and Westermark, P.: The age related amyloids: a growing family of unique biochemical substances. *J Clin Pathol* (1995) 48 p. 984-9.
31. Bellotti, V., Mangione, P. and Merlini, G.: Review: immunoglobulin light chain amyloidosis—the archetype of structural and pathogenic variability. *J Struct Biol* (2000) 130 p. 280-9.
32. Hardy, J. and Selkoe, D. J.: The amyloid hypothesis of Alzheimer's disease: progress and problems on the road to therapeutics. *Science* (2002) 297 p. 353-6.
33. Wisniewski, H. M., Bancher, C., Barcikowska, M., Wen, G. Y. and Currie, J.: Spectrum of morphological appearance of amyloid deposits in Alzheimer's disease. *Acta Neuropathol* (1989) 78 p. 337-47.
34. Masters, C. L., Simms, G., Weinman, N. A., Multhaup, G., McDonald, B. L. and Beyreuther, K.: Amyloid plaque core protein in Alzheimer disease and Down syndrome. *Proc Natl Acad Sci U S A* (1985) 82 p. 4245-9.
35. Friedhoff, P., von Bergen, M., Mandelkow, E. M. and Mandelkow, E.: Structure of tau protein and assembly into paired helical filaments. *Biochim Biophys Acta* (2000) 1502 p. 122-32.
36. Gandy, S. and Petanceska, S.: Regulation of Alzheimer [beta]-amyloid precursor trafficking and metabolism. *Biochimica et Biophysica Acta (BBA) - Molecular Basis of Disease* (2000) 1502 p. 44-52.
37. Selkoe, D. J.: Folding proteins in fatal ways. *Nature* (2003) 426 p. 900-4.
38. Vassar, R., Bennett, B. D., Babu-Khan, S., Kahn, S., Mendiaz, E. A., Denis, P., Teplow, D. B., Ross, S., Amarante, P., Loeloff, R., Luo, Y., Fisher, S., Fuller, J., Edenson, S., Lile, J., Jarosinski, M. A., Biere, A. L., Curran, E., Burgess, T., Louis, J.-C., Collins, F., Treanor, J., Rogers, G. and Citron, M.: Beta-secretase cleavage of Alzheimer's amyloid precursor protein by the transmembrane aspartic protease BACE. *Science* (1999) 286 p. 735-41.
39. Jarrett, J. T., Berger, E. P. and Lansbury, P. T., Jr.: The carboxy terminus of the beta amyloid protein is critical for the seeding of amyloid formation: Implications for the pathogenesis of Alzheimer's disease. *Biochemistry* (1993) 32 p. 4693-7.
40. Mayeux, R., Tang, M. X., Jacobs, D. M., Manly, J., Bell, K., Merchant, C., Small, S. A., Stern, Y., Wisniewski, H. M. and Mehta, P. D.: Plasma amyloid beta-peptide 1-42 and incipient Alzheimer's disease. *Ann Neurol* (1999) 46 p. 412-6.
41. Lue, L. F., Kuo, Y. M., Roher, A. E., Brachova, L., Shen, Y., Sue, L., Beach, T., Kurth, J. H., Rydel, R. E. and Rogers, J.: Soluble amyloid beta peptide concentration as a predictor of synaptic change in Alzheimer's disease. *Am J Pathol* (1999) 155 p. 853-62.
42. Selkoe, D. J.: The molecular pathology of Alzheimer's disease. *Neuron* (1991) 6 p. 487-98.
43. Yamaguchi, H., Nakazato, Y., Hirai, S., Shoji, M. and Harigaya, Y.: Electron micrograph of diffuse plaques. Initial stage of senile plaque formation in the Alzheimer brain. *Am J Pathol* (1989) 135 p. 593-7.
44. Joachim, C. L., Morris, J. H. and Selkoe, D. J.: Diffuse senile plaques occur commonly in the cerebellum in Alzheimer's disease. *Am J Pathol* (1989) 135 p. 309-19.
45. Crook, R., Verkkoniemi, A., Perez-Tur, J., Mehta, N., Baker, M., Houlden, H., Farrer, M., Hutton, M., Lincoln, S., Hardy, J., Gwinn, K., Somer, M., Paetau, A., Kalimo, H., Ylikoski, R., Poyhonen, M., Kucera, S. and Haltia, M.: A variant of Alzheimer's disease with spastic paraparesis and unusual plaques due to deletion of exon 9 of presenilin 1. *Nat Med* (1998) 4 p. 452-5.
46. Karlstrom, H., Brooks, W. S., Kwok, J. B., Broe, G. A., Kril, J. J., McCann, H., Halliday, G. M. and Schofield, P. R.: Variable phenotype of Alzheimer's disease with spastic paraparesis. *J Neurochem* (2008) 104 p. 573-83.
47. Yamada, M.: Cerebral amyloid angiopathy: an overview. *Neuropathology* (2000) 20 p. 8-22.
48. Revesz, T., Ghiso, J., Lashley, T., Plant, G., Rostagno, A., Frangione, B. and Holton, J. L.: Cerebral amyloid angiopathies: a pathologic, biochemical, and genetic view. *J Neuropathol Exp Neurol* (2003) 62 p. 885-98.
49. Revesz, T., Holton, J. L., Lashley, T., Plant, G., Rostagno, A., Ghiso, J. and Frangione, B.: Sporadic and familial cerebral amyloid angiopathies. *Brain Pathol* (2002) 12 p. 343-57.
50. Serpell, L. C., Sunde, M. and Blake, C. C.: The molecular basis of amyloidosis. *Cell Mol Life Sci* (1997) 53 p. 871-87.
51. Jarrett, J. T. and Lansbury, P. T., Jr.: Seeding "one-dimensional crystallization" of amyloid: a pathogenic mechanism in Alzheimer's disease and scrapie? *Cell* (1993) 73 p. 1055-8.
52. LeVine, H.: Quantification of beta-sheet amyloid fibril structures with Thioflavin T. *Methods Enzymol* (1999) 309 p. 274-84.
53. Jin, L.-W., Claborn, K. A., Kurimoto, M., Geday, M. A., Maezawa, I., Sohraby, F., Estrada, M., Kaminksy, W. and Kahr, B.: Imaging linear birefringence and dichroism in cerebral amyloid pathologies. *Proc Natl Acad Sci U S A* (2003) 100 p. 15294-8.
54. Inouye, H., Nguyen, J. T., Fraser, P. E., Shinchuk, L. M., Packard, A. B. and Kirschner, D. A.: Histidine residues underlie Congo red binding to A beta analogs. *Amyloid* (2000) 7 p. 179-88.
55. Carter, D. B. and Chou, K. C.: A model for structure-dependent binding of Congo red to Alzheimer beta-amyloid

fibrils. *Neurobiol Aging* (1998) 19 p. 37-40.
56. Turnell, W. G. and Finch, J. T.: Binding of the dye congo red to the amyloid protein pig insulin reveals a novel homology amongst amyloid-forming peptide sequences. *J Mol Biol* (1992) 227 p. 1205-23.
57. Klunk, W. E., Jacob, R. F. and Mason, R. P.: Quantifying amyloid by Congo red spectral shift analysis. *Methods Enzymol* (1999) 309 p. 285-305.
58. Stopa, B., Piekarska, B., Konieczny, L., Rybarska, J., Spolnik, P., Zemanek, G., Roterman, I. and Krol, M.: The structure and protein binding of amyloid-specific dye reagents. *Acta Biochim Pol* (2003) 50 p. 1213-27.
59. Khurana, R., Uversky, V. N., Nielsen, L. and Fink, A. L.: Is Congo red an amyloid-specific dye? *J Biol Chem* (2001) 276 p. 22715-21.
60. Klunk, W. E., Pettegrew, J. W. and Abraham, D. J.: Quantitative evaluation of congo red binding to amyloid-like proteins with a beta-pleated sheet conformation. *J Histochem Cytochem* (1989) 37 p. 1273-81.
61. LeVine, H.: Thioflavine T interaction with amyloid beta-sheet structures. *Amyloid* (1995) 2 p. 1-6.
62. Groenning, M., Olsen, L., van de Weert, M., Flink, J. M., Frokjaer, S. and Jorgensen, F. S.: Study on the binding of Thioflavin T to beta-sheet-rich and non-beta-sheet cavities. *J Struct Biol* (2007) 158 p. 358-69.
63. De Ferrari, G. V., Mallender, W. D., Inestrosa, N. C. and Rosenberry, T. L.: Thioflavin T is a fluorescent probe of the acetylcholinesterase peripheral site that reveals conformational interactions between the peripheral and acylation sites. *J Biol Chem* (2001) 276 p. 23282-7.
64. Naiki, H., Higuchi, K., Hosokawa, M. and Takeda, T.: Fluorometric determination of amyloid fibrils in vitro using the fluorescent dye, thioflavin T1. *Anal Biochem* (1989) 177 p. 244-9.
65. Voropai, E. S., Samtsov, M. P., Kaplevskii, K. N., Maskevich, A. A., Stepuro, V. I., Povarova, O. I., Kuznetsova, I. M., Turoverov, K. K., Fink, A. L. and Uversky, V. N.: Spectral properties of Thioflavin T and its complexes with amyloid fibrils. *J App Spectroscopy* (2003) 70 p. 868-74.
66. LeVine, H., 3rd: Stopped-flow kinetics reveal multiple phases of thioflavin T binding to Alzheimer beta (1-40) amyloid fibrils. *Arch Biochem Biophys* (1997) 342 p. 306-16.
67. Pedersen, J. S., Dikov, D., Flink, J. L., Hjuler, H. A., Christiansen, G. and Otzen, D. E.: The changing face of glucagon fibrillation: Structural polymorphism and conformational imprinting. *J Mol Biol* (2006) 355 p. 501-23.
68. Goldsbury, C., Goldie, K., Pellaud, J., Seelig, J., Frey, P., Muller, S. A., Kistler, J., Cooper, G. J. S. and Aebi, U.: Amyloid fibril formation from full-length and fragments of amylin. *J Struct Biol* (2000) 130 p. 352-62.
69. Goldsbury, C., Wirtz, S., Muller, S. A., Sunderji, S., Wicki, P., Aebi, U. and Frey, P.: Studies on the in Vitro Assembly of Abeta 1-40: Implications for the Search for Abeta Fibril Formation Inhibitors. *J Struct Biol* (2000) 130 p. 217-31.
70. Khurana, R., Coleman, C., Ionescu-Zanetti, C., Carter, S. A., Krishna, V., Grover, R. K., Roy, R. and Singh, S.: Mechanism of thioflavin T binding to amyloid fibrils. *J Struct Biol* (2005) 151 p. 229-38.
71. Krebs, M. R., Bromley, E. H. C. and Donald, A. M.: The binding of thioflavin-T to amyloid fibrils: localisation and implications. *J Struct Biol* (2005) 149 p. 30-7.
72. Groenning, M., Norrman, M., Flink, J. M., van de Weert, M., Bukrinsky, J. T., Schluckebier, G. and Frokjaer, S.: Binding mode of Thioflavin T in insulin amyloid fibrils. *J Struct Biol* (2007) 159 p. 483-97.
73. Ye, L., Morgenstern, J. L., Gee, A. D., Hong, G., Brown, J. and Lockhart, A.: Delineation of positron emission tomography imaging agent binding sites on beta-amyloid peptide fibrils. *J Biol Chem* (2005) 280 p. 23599-604.
74. Lockhart, A., Ye, L., Judd, D. B., Merritt, A. T., Lowe, P. N., Morgenstern, J. L., Hong, G., Gee, A. D. and Brown, J.: Evidence for the presence of three distinct binding sites for the thioflavin T class of Alzheimer's disease PET imaging agents on beta-amyloid peptide fibrils. *J Biol Chem* (2005) 280 p. 7677-84.
75. Müller, S. A., Goldie, K. N., Bürki, R., Häring, R. and Engel, A.: Factors influencing the precision of quantitative scanning transmission electron microscopy. *Ultramicroscopy* (1992) 46 p. 317-34.
76. Shirahama, T. and Cohen, A. S.: High-resolution electron microscopic analysis of the amyloid fibril. *J Cell Biol* (1967) 33 p. 679-708.
77. Chamberlain, A. K., MacPhee, C. E., Zurdo, J., Morozova-Roche, L. A., Hill, H. A., Dobson, C. M. and Davis, J. J.: Ultrastructural organization of amyloid fibrils by atomic force microscopy. *Biophys J* (2000) 79 p. 3282-93.
78. Bauer, H. H., Aebi, U., Haner, M., Hermann, R., Muller, M., Arvinte, T. and Merkle, H. P.: Architecture and polymorphism of fibrillar supramolecular assemblies produced by in vitro aggregation of human calcitonin. *J Struct Biol* (1995) 115 p. 1-15.
79. Makin, O. S. and Serpell, L. C.: Structures for amyloid fibrils. *Febs J* (2005) 272 p. 5950-61.
80. Serpell, L. C., Sunde, M., Benson, M. D., Tennent, G. A., Pepys, M. B. and Fraser, P. E.: The protofilament substructure of amyloid fibrils. *J Mol Biol* (2000) 300 p. 1033-9.
81. Jimenez, J. L., Nettleton, E. J., Bouchard, M., Robinson, C. V., Dobson, C. M. and Saibil, H. R.: The protofilament structure of insulin amyloid fibrils. *Proc Natl Acad Sci U S A* (2002) 99 p. 9196-201.
82. Goldsbury, C., Cooper, G. S., Goldie, K. N., Muller, S. A., Saafi, E. L., Gruijters, W. T. M., Misur, M. P., Engel, A., Aebi, U. and Kistler, J.: Polymorphic fibrillar assembly of human amylin. *J Struct Biol* (1997) 119 p. 17-27.
83. Harper, J. D., Lieber, C. M. and Lansbury, P. T., Jr.: Atomic force microscopic imaging of seeded fibril formation and fibril branching by the Alzheimer's disease amyloid-beta protein. *Chem Biol* (1997) 4 p. 951-9.
84. Wadai, H., Yamaguchi, K., Takahashi, S., Kanno, T., Kawai, T., Naiki, H. and Goto, Y.: Stereospecific amyloid-like fibril formation by a peptide fragment of beta2-microglobulin. *Biochemistry* (2005) 44 p. 157-64.
85. Hoyer, W., Antony, T., Cherny, D., Heim, G., Jovin, T. M. and Subramaniam, V.: Dependence of alpha-synuclein

aggregate morphology on solution conditions. *J Mol Biol* (2002) 322 p. 383-93.
86. Khurana, R., Ionescu-Zanetti, C., Pope, M., Li, J., Nielson, L., Ramirez-Alvarado, M., Regan, L., Fink, A. L. and Carter, S. A.: A general model for amyloid fibril assembly based on morphological studies using atomic force microscopy. *Biophys J* (2003) 85 p. 1135-44.
87. Malinchik, S. B., Inouye, H., Szumowski, K. E. and Kirschner, D. A.: Structural Analysis of Alzheimer's beta(1-40) Amyloid: Protofilament Assembly of Tubular Fibrils. *Biophys J* (1998) 74 p. 537-45.
88. Chen, S., Berthelier, V., Hamilton, J. B., O'Nuallain, B. and Wetzel, R.: Amyloid-like Features of Polyglutamic Aggregates and Their Assembly Kinetics. *Biochemistry* (2002) 41 p. 7391-9.
89. Fraser, P. E., Nguyen, J. T., Surewicz, W. K. and Kirschner, D. A.: pH-dependent structural transitions of Alzheimer amyloid peptides. *Biophys J* (1991) 60 p. 1190-201.
90. Petkova, A. T., Leapman, R. D., Guo, Z., Yau, W.-M., Mattson, M. P. and Tycko, R.: Self-propagating, molecular-level polymorphism in Alzheimer's beta-amyloid fibrils. *Science* (2005) 307 p. 262-5.
91. Dzwolak, W., Smirnovas, V., Jansen, R. and Winter, R.: Insulin forms amyloid in a strain-dependent manner: an FT-IR spectroscopic study. *Protein Sci* (2004) 13 p. 1927-32.
92. Pedersen, J. S., Dikov, D., Flink, J. L. and Otzen, D. E.: Sulfates dramatically stabilize a salt dependent type of glucagon fibrils. *Biophys J* (2006) 90 p. 4181-94.
93. Jansen, R., Grudzielanek, S., Dzwolak, W. and Winter, R.: High pressure promotes circularly shaped insulin amyloid. *J Mol Biol* (2004) 338 p. 203-6.
94. Glenner, G. G., Eanes, E. D. and Page, D. L.: The relation of the properties of Congo red-stained amyloid fibrils to the beta-conformation. *J Histochem Cytochem* (1972) 20 p. 821-6.
95. Eanes, E. D. and Glenner, G. G.: X-ray diffraction studies on amyloid filaments. *J Histochem Cytochem* (1968) 16 p. 673-7.
96. Pauling, L. and Corey, R. B.: Configurations of Polypeptide Chains With Favored Orientations Around Single Bonds: Two New Pleated Sheets. *Proc Natl Acad Sci U S A* (1951) 37 p. 729-40.
97. Serpell, L. C., Fraser, P. E. and Sunde, M.: X-ray fiber diffraction of amyloid fibrils. *Methods Enzymol* (1999) 309 p. 526-36.
98. Fandrich, M. and Dobson, C. M.: The behaviour of polyamino acids reveals an inverse side chain effect in amyloid structure formation. *Embo J* (2002) 21 p. 5682-90.
99. Blake, C. and Serpell, L.: Synchrotron X-ray studies suggest that the core of the transthyretin amyloid fibril is a continuous beta-sheet helix. *Structure* (1996) 4 p. 989-98.
100. Sunde, M., Serpell, L. C., Bartlam, M., Fraser, P. E., Pepys, M. B. and Blake, C. C.: Common core structure of amyloid fibrils by synchrotron X-ray diffraction. *J Mol Biol* (1997) 273 p. 729-39.
101. Jimenez, J. L., Guijarro, J. I., Orlova, E., Zurdo, J., Dobson, C. M., Sunde, M. and Saibil, H. R.: Cryo-electron microscopy structure of an SH3 amyloid fibril and model of the molecular packing. *Embo J* (1999) 18 p. 815-21.
102. Chothia, C.: Conformations of twisted beta-sheets in proteins. *J Mol Biol* (1973) 75 p. 295-302.
103. Benzinger, T. L. S., Gregory, D. M., Burkoth, T. S., Miller-Auer, H., Lynn, D. G., Botto, R. E. and Meredith, S. C.: Propagating structure of Alzheimer's beta-amyloid (10-35) is parallel beta-sheet with residue in exact register. *Proc Natl Acad Sci U S A* (1998) 95 p. 13407-12.
104. Antzutkin, O. N., Balbach, J. J. and Tycko, R.: Site-specific identification of non-beta-strand conformations in Alzheimer's beta-amyloid fibrils by solid-state NMR. *Biophys J* (2003) 84 p. 3326-35.
105. Antzutkin, O. N., Balbach, J. J., Leapman, R. D., Rizzo, N. W., Reed, J. and Tycko, R.: Multiple quantum solid-state NMR indicates a parallel, not antiparallel, organization of beta-sheets in Alzheimer's beta-amyloid fibrils. *Proc Natl Acad Sci U S A* (2000) 97 p. 13045-50.
106. Benzinger, T. L. S., Gregory, D. M., Burkoth, T. S., Miller-Auer, H., Lynn, D. G., Botto, R. E. and Meredith, S. C.: Two-dimensional structure of beta-amyloid(10-35) fibrils. *Biochemistry* (2000) 39 p. 3491-9.
107. Torok, M., Milton, S., Kayed, R., Wu, P., McIntire, T., Glabe, C. G. and Langen, R.: Structural and dynamic features of Alzheimer's Abeta peptide in amyloid fibrils studied by site-directed spin labeling. *J Biol Chem* (2002) 277 p. 40810-5.
108. Balbach, J. J., Petkova, A. T., Oyler, N. A., Antzutkin, O. N., Gordon, D. J., Meredith, S. C. and Tycko, R.: Supramolecular structure in full-length Alzheimer's beta-amyloid fibrils: evidence for a parallel beta-sheet organization from solid-state nuclear magnetic resonance. *Biophys J* (2002) 83 p. 1205-16.
109. Antzutkin, O. N., Leapman, R. D., Balbach, J. J. and Tycko, R.: Supramolecular structural constraints on Alzheimer's beta-amyloid fibrils from electron microscopy and solid-state nuclear magnetic resonance. *Biochemistry* (2002) 41 p. 15436-50.
110. Petkova, A. T., Buntkowsky, G., Dyda, F., Leapman, R. D., Yau, W.-M. and Tycko, R.: Solid State NMR Reveals a pH-dependent Antiparallel beta-Sheet Registry in Fibrils Formed by a beta-Amyloid Peptide. *J Mol Biol* (2004) 335 p. 247-60.
111. Balbach, J. J., Ishii, Y., Antzutkin, O. N., Leapman, R. D., Rizzo, N. W., Dyda, F., Reed, J. and Tycko, R.: Amyloid fibril formation by A beta 16-22, a seven-residue fragment of the Alzheimer's beta-amyloid peptide, and structural characterization by solid state NMR. *Biochemistry* (2000) 39 p. 13748-59.
112. Gordon, D. J., Balbach, J. J., Tycko, R. and Meredith, S. C.: Increasing the Amphiphilicity of an Amyloidogenic Peptide Changes the beta-Sheet Structure in the Fibrils from Antiparallel to Parallel. *Biophys J* (2004) 86 p. 428-34.

113. O'Nuallain, B. and Wetzel, R.: Conformational Abs recognizing a generic amyloid fibril epitope. *Proc Natl Acad Sci U S A* (2002) 99 p. 1485-90.
114. Pedersen, J. S. and Otzen, D. E.: Amyloid-a state in many guises: survival of the fittest fibril fold. *Protein Sci* (2008) 17 p. 2-10.
115. Petkova, A. T., Ishii, Y., Balbach, J. J., Antzutkin, O. N., Leapman, R. D., Delaglio, F. and Tycko, R.: A structural model for Alzheimer's beta-amyloid fibrils based on experimental constraints from solid state NMR. *Proc Natl Acad Sci U S A* (2002) 99 p. 16742-7.
116. Luhrs, T., Ritter, C., Adrian, M., Riek-Loher, D., Bohrmann, B., Dobeli, H., Schubert, D. and Riek, R.: 3D structure of Alzheimer's amyloid-beta(1-42) fibrils. *Proc Natl Acad Sci U S A* (2005) 102 p. 17342-7.
117. Whittemore, N. A., Mishra, R., Kheterpal, I., Williams, A. D., Wetzel, R. and Serpersu, E. H.: Hydrogen-deuterium (H/D) exchange mapping of Abeta 1-40 amyloid fibril secondary structure using nuclear magnetic resonance spectroscopy. *Biochemistry* (2005) 44 p. 4434-41.
118. Kheterpal, I., Chen, M., Cook, K. D. and Wetzel, R.: Structural Differences in Abeta Amyloid Protofibrils and Fibrils Mapped by Hydrogen Exchange - Mass Spectrometry with On-line Proteolytic Fragmentation. *J Mol Biol* (2006) 361 p. 785-95.
119. Sachse, C., Xu, C., Wieligmann, K., Diekmann, S., Grigorieff, N. and Fandrich, M.: Quaternary Structure of a Mature Amyloid Fibril from Alzheimer's Abeta(1-40) Peptide. *J Mol Biol* (2006) 362 p. 347-54.
120. Sachse, C., Fandrich, M. and Grigorieff, N.: Paired beta-sheet structure of an Abeta(1-40) amyloid fibril revealed by electron microscopy. *Proc Natl Acad Sci U S A* (2008) 105 p. 7462-6.
121. Shivaprasad, S. and Wetzel, R.: An intersheet packing interaction in A beta fibrils mapped by disulfide cross-linking. *Biochemistry* (2004) 43 p. 15310-7.
122. Shivaprasad, S. and Wetzel, R.: Scanning cysteine mutagenesis analysis of Abeta-(1-40) amyloid fibrils. *J Biol Chem* (2006) 281 p. 993-1000.
123. Diaz-Avalos, R., Long, C., Fontano, E., Balbirnie, M., Grothe, R., Eisenberg, D. and Caspar, D. L. D.: Cross-beta Order and Diversity in Nanocrystals of an Amyloid-forming Peptide. *J Mol Biol* (2003) 330 p. 1165-75.
124. Balbirnie, M., Grothe, R. and Eisenberg, D. S.: An amyloid-forming peptide from the yeast prion Sup35 reveals a dehydrated beta-sheet structure for amyloid. *Proc Natl Acad Sci U S A* (2001) 98 p. 2375-80.
125. Nelson, R., Sawaya, M. R., Balbirnie, M., Madsen, A. Ø., Riekel, C., Grothe, R. and Eisenberg, D.: Structure of the cross-beta spine of amyloid-like fibrils. *Nature* (2005) 435 p. 773-8.
126. Squires, A. M., Devlin, G. L., Gras, S. L., Tickler, A. K., MacPhee, C. E. and Dobson, C. M.: X-ray scattering study of the effect of hydration on the cross-beta structure of amyloid fibrils. *J Am Chem Soc* (2006) 128 p. 11738-9.
127. Perutz, M. F., Johnson, T., Suzuki, M. and Finch, J. T.: Glutamine repeats as polar zippers: their possible role in inherited neurodegenerative diseases. *Proc Natl Acad Sci U S A* (1994) 91 p. 5355-8.
128. Sawaya, M. R., Sambashivan, S., Nelson, R., Ivanova, M. I., Sievers, S. A., Apostol, M. I., Thompson, M. J., Balbirnie, M., Wiltzius, J. J., McFarlane, H. T., Madsen, A. O., Riekel, C. and Eisenberg, D.: Atomic structures of amyloid cross-beta spines reveal varied steric zippers. *Nature* (2007) 447 p. 453-7.
129. Perutz, M. F., Finch, J. T., Berriman, J. and Lesk, A.: Amyloid fibers are water-filled nanotubes. *Proc Natl Acad Sci U S A* (2002) 99 p. 5591-5.
130. Govaerts, C., Wille, H., Prusiner, S. B. and Cohen, F. E.: Evidence for assembly of prions with left-handed beta-helices into trimers. *Proc Natl Acad Sci U S A* (2004) 101 p. 8342-7.
131. Williams, A. D., Portelius, E., Kheterpal, I., Guo, J.-T., Cook, K. D., Xu, Y. and Wetzel, R.: Mapping abeta amyloid fibril secondary structure using scanning proline mutagenesis. *J Mol Biol* (2004) 335 p. 833-42.
132. Wetzel, R.: Ideas of order for amyloid fibril structure. *Structure* (2002) 10 p. 1031-6.
133. Lazo, N. D. and Downing, D. T.: Amyloid fibrils may be assembled from beta-helical protofibrils. *Biochemistry* (1998) 37 p. 1731-5.
134. Kheterpal, I., Lashuel, H. A., Hartley, D. M., Walz, T., Lansbury, P. T., Jr. and Wetzel, R.: Abeta protofibrils possess a stable core structure resistant to hydrogen exchange. *Biochemistry* (2003) 42 p. 14092-8.
135. Nelson, R. and Eisenberg, D.: Recent atomic models of amyloid fibril structure. *Curr Opin Struct Biol* (2006) 16 p. 260-5.
136. Laidman, J., Forse, G. J. and Yeates, T. O.: Conformational change and assembly through edge beta strands in transthyretin and other amyloid proteins. *Acc Chem Res* (2006) 39 p. 576-83.
137. Olofsson, A., Ippel, J. H., Wijmenga, S. S., Lundgren, E. and Ohman, A.: Probing solvent accessibility of transthyretin amyloid by solution NMR spectroscopy. *J Biol Chem* (2004) 279 p. 5699-707.
138. Serag, A. A., Altenbach, C., Gingery, M., Hubbell, W. L. and Yeates, T. O.: Arrangement of subunits and ordering of beta-strands in an amyloid sheet. *Nat Struct Biol* (2002) 9 p. 734-9.
139. Ivanova, M. I., Sawaya, M. R., Gingery, M., Attinger, A. and Eisenberg, D.: An amyloid-forming segment of beta2-microglobulin suggests a molecular model for the fibril. *Proc Natl Acad Sci U S A* (2004) 101 p. 10584-9.
140. Baxa, U., Taylor, K. L., Wall, J. S., Simon, M. N., Cheng, N., Wickner, R. B. and Steven, A. C.: Architecture of Ure2p Prion Filaments. *J Biol Chem* (2003) 278 p. 43717-27.
141. Staniforth, R. A., Giannini, S., Higgins, L. D., Conroy, M. J., Hounslow, A. M., Jerala, R., Craven, C. J. and Waltho, J. P.: Three-dimensional domain swapping in the folded and molten-globule states of cystatins, an amyloid-forming structural superfamily. *Embo J* (2001) 20 p. 4774-81.

142. Janowski, R., Kozak, M., Jankowska, E., Grzonka, Z., Grubb, A., Abrahamson, M. and Jaskolski, M.: Human cystatin C, an amyloidogenic protein, dimerizes through three-dimensional domain swapping. *Nat Struct Biol* (2001) 8 p. 316-20.
143. Castano, E. M., Ghiso, J., Prelli, F., Gorevic, P. D., Migheli, A. and Frangione, B.: In vitro formation of amyloid fibrils from two synthetic peptides of different lengths homologous to Alzheimer's disease beta-protein. *Biochem Biophys Res Commun* (1986) 141 p. 782-9.
144. Kirschner, D. A., Inouye, H., Duffy, L. K., Sinclair, A., Lind, M. and Selkoe, D. J.: Synthetic peptide homologous to beta protein from Alzheimer disease forms amyloid-like fibrils in vitro. *Proc Natl Acad Sci U S A* (1987) 84 p. 6953-7.
145. Chiti, F., Webster, P., Taddei, N., Clark, A., Stefani, M., Ramponi, G. and Dobson, C. M.: Designing conditions for in vitro formation of amyloid protofilaments and fibrils. *Proc Natl Acad Sci U S A* (1999) 96 p. 3590-4.
146. Guijarro, J. I., Sunde, M., Jones, J. A., Campbell, I. D. and Dobson, C. M.: Amyloid fibril formation by an SH3 domain. *Proc Natl Acad Sci U S A* (1998) 95 p. 4224-8.
147. Litvinovich, S. V., Brew, S. A., Aota, S., Akiyama, S. K., Haudenschild, C. and Ingham, K. C.: Formation of amyloid-like fibrils by self-association of a partially unfolded fibronectin type III module. *J Mol Biol* (1998) 280 p. 245-58.
148. Dobson, C. M.: Protein misfolding, evolution and disease. *Trends Biochem Sci* (1999) 24 p. 329-32.
149. Zerovnik, E., Turk, V. and Waltho, J. P.: Amyloid fibril formation by human stefin B: influence of the initial pH-induced intermediate state. *Biochem Soc Trans* (2002) 30 p. 543-7.
150. Liu, W., Crocker, E., Zhang, W., Elliott, J. I., Luy, B., Li, H., Aimoto, S. and Smith, S. O.: Structural Role of Glycine in Amyloid Fibrils Formed from Transmembrane Alpha-Helices. *Biochemistry* (2005) 44 p. 3591-7.
151. Krebs, R. H., Wilkins, D. K., Chung, E. W., Pitkeathly, M. C., Chamberlain, A. K., Zurdo, J., Robinson, C. V. and Dobson, C. M.: Formation and seeding of amyloid fibrils from wild-type hen lysozme and a peptide fragment from the beta-domain. *J Mol Biol* (2000) 300 p. 541-9.
152. Fandrich, M., Fletcher, M. A. and Dobson, C. M.: Amyloid fibrils from muscle myoglobin. *Nature* (2001) 410 p. 165-6.
153. Pertinhez, T. A., Bouchard, M., Tomlinson, E. J., Wain, R., Ferguson, S. J., Dobson, C. M. and Smith, L. J.: Amyloid fibril formation by a helical cytochrome. *FEBS Lett* (2001) 495 p. 184-6.
154. Wolynes, P. G.: Energy landscapes and solved protein-folding problems. *Philosophical Transactions of the Royal Society A* (2005) 363 p. 453-67.
155. Anfinsen, C. B.: Principles that govern the folding of protein chains. *Science* (1973) 181 p. 223-30.
156. Gazit, E.: The "Correctly Folded" state of proteins: is it a metastable state? *Agnew Chem Int Ed* (2002) 41 p. 257-9.
157. Jahn, T. R. and Radford, S. E.: Folding versus aggregation: polypeptide conformations on competing pathways. *Arch Biochem Biophys* (2008) 469 p. 100-17.
158. Uversky, V. N. and Fink, A. L.: Conformational constraints for amyloid fibrillation: the importance of being unfolded. *Biochim Biophys Acta* (2004) 1698 p. 131-53.
159. Chiti, F., Taddei, N., Bucciantini, M., White, P., Ramponi, G. and Dobson, C. M.: Mutational analysis of the propensity for amyloid formation by a globular protein. *Embo J* (2000) 19 p. 1441-9.
160. Eakin, C. M., Attenello, F. J., Morgan, C. J. and Miranker, A. D.: Oligomeric assembly of native-like precursors precedes amyloid formation by beta-2 microglobulin. *Biochemistry* (2004) 43 p. 7808-15.
161. Kodali, R. and Wetzel, R.: Polymorphism in the intermediates and products of amyloid assembly. *Curr Opin Struct Biol* (2007) 17 p. 48-57.
162. Harper, J. D. and Lansbury, P. T., Jr.: Models of amyloid seeding in Alzheimer's disease and scrapie: mechanistic truths and physiological consequences of the time-dependent solubility of amyloid proteins. *Annu Rev Biochem* (1997) 66 p. 385-407.
163. Jarrett, J. T. and Lansbury, P. T., Jr.: Amyloid fibril formation requires a chemically discriminating nucleation event: Studies of an amyloidogenic sequence from the bacterial protein OsmB. *Biochemistry* (1992) 31 p. 12345-52.
164. Hurshman, A. R., White, J. T., Powers, E. T. and Kelly, J. W.: Transthyretin aggregation under partially denaturing conditions is a downhill polymerization. *Biochemistry* (2004) 43 p. 7365-81.
165. Ferrone, F.: Analysis of protein aggregation kinetics. *Methods Enzymol* (1999) 309 p. 256-74.
166. Collins, S. R., Douglass, A., Vale, R. D. and Weissman, J. S.: Mechanism of prion propagation: Amyloid growth occurs by monomer addition. *PLoS Biol* (2004) 2 p. e321.
167. Cannon, M. J., Williams, A. D., Wetzel, R. and Myszka, D. G.: Kinetic analysis of beta-amyloid fibril elongation. *Anal Biochem* (2004) 328 p. 67-75.
168. Petty, S. A. and Decatur, S. M.: Experimental Evidence for the Reorganization of beta-Strands within Aggregates of the Abeta(16-22) Peptide. *J Am Chem Soc* (2005) 127 p. 13488-9.
169. Nielsen, L., Khurana, R., Coats, A., Frokjaer, S., Brange, J., Vyas, S., Uversky, V. N. and Fink, A. L.: Effect of environmental factors on the kinetics of insulin fibril formation: elucidation of the molecular mechanism. *Biochemistry* (2001) 40 p. 6036-46.
170. Chen, S., Ferrone, F. A. and Wetzel, R.: Huntington's disease age-of-onset linked to polyglutamine aggregation nucleation. *Proc Natl Acad Sci U S A* (2002) 99 p. 11884-9.
171. Fink, A. L.: The aggregation and fibrillation of alpha-synuclein. *Acc Chem Res* (2006) 39 p. 628-34.

172. Librizzi, F. and Rischel, C.: The kinetic behavior of insulin fibrillation is determined by heterogeneous nucleation pathways. *Protein Sci* (2005) 14 p. 3129-34.
173. Stathopulos, P. B., Scholz, G. A., Hwang, Y.-M., Rumfeldt, J. A. O., Lepock, J. R. and Meiering, E. M.: Sonication of proteins causes formation of aggregates that resemble amyloid. *Protein Sci* (2004) 13 p. 3017-27.
174. Sasahara, K., Yagi, H., Sakai, M., Naiki, H. and Goto, Y.: Amyloid nucleation triggered by agitation of beta2-microglobulin under acidic and neutral pH conditions. *Biochemistry* (2008) 47 p. 2650-60.
175. Tanaka, M., Collins, S. R., Toyama, B. H. and Weissman, J. S.: The physical basis of how prion conformations determine strain phenotypes. *Nature* (2006) 442 p. 585-9.
176. Jansen, R., Dzwolak, W. and Winter, R.: Amyloidogenic self-assembly of insulin aggregates probed by high resolution atomic force microscopy. *Biophys J* (2005) 88 p. 1344-53.
177. Rhoades, E. and Gafni, A.: Micelle formation by a fragment of human islet amyloid polypeptide. *Biophys J* (2003) 84 p. 3480-7.
178. Serio, T. R., Cashikar, A. G., Kowal, A. S., Sawicki, G. J., Moslehi, J. J., Serpell, L. C., Arnsdorf, M. F. and Lindquist, S. L.: Nucleated conformational conversion and the replication of conformational information by a prion determinant. *Science* (2000) 289 p. 1317-21.
179. Padrick, S. B. and Miranker, A. D.: Islet amyloid: Phase partitioning and secondary nucleation are central to the mechanism of fibrillogenesis. *Biochemistry* (2002) 41 p. 4694-703.
180. Souillac, P. O., Uversky, V. N., Millett, I. S., Khurana, R., Doniach, S. and Fink, A. L.: Elucidation of the molecular mechanism during the early events in immunoglobulin light chain amyloid fibrillation. Evidence for an off-pathway oligomer at acidic pH. *J Biol Chem* (2002) 277 p. 12666-79.
181. Hokenson, M. J., Uversky, V. N., Goers, J., Yamin, G., Munishkina, L. A. and Fink, A. L.: Role of individual methionines in the fibrillation of methionine-oxidized alpha-synuclein. *Biochemistry* (2004) 43 p. 4621-33.
182. Uversky, V. N., Yamin, G., Souillac, P. O., Goers, J., Glaser, C. B. and Fink, A. L.: Methionine oxidation inhibits fibrillation of human alpha-synuclein in vitro. *FEBS Lett* (2002) 517 p. 239-44.
183. Glaser, C. B., Yamin, G., Uversky, V. N. and Fink, A. L.: Methionine oxidation, alpha-synuclein and Parkinson's disease. *Biochim Biophys Acta* (2005) 1703 p. 157-69.
184. Souillac, P. O., Uversky, V. N., Millett, I. S., Khurana, R., Doniach, S. and Fink, A. L.: Effect of association state and conformational stability on the kinetics of immunoglobulin light chain amyloid fibril formation at physiological pH. *J Biol Chem* (2002) 277 p. 12657-65.
185. Chi, E. Y., Krishnan, S., Randolph, T. W. and Carpenter, J. F.: Physical stability of proteins in aqueous solution: mechanism and driving forces in nonnative protein aggregation. *Pharm Res* (2003) 20 p. 1325-36.
186. Bieschke, J., Zhang, Q., Bosco, D. A., Lerner, R. A., Powers, E. T., Wentworth, P. and Kelly, J. W.: Small molecule oxidation products trigger disease - associated protein misfolding. *Acc Chem Res* (2006) 39 p. 611-9.
187. Bieschke, J., Zhang, Q., Powers, E. T., Lerner, R. A. and Kelly, J. W.: Oxidative metabolites accelerate Alzheimer's amyloidogenesis by a two-step mechanism, eliminating the requirement for nucleation. *Biochemistry* (2005) 44 p. 4977-83.
188. Bader, R., Bamford, R., Zurdo, J., Luisi, B. and Dobson, C. M.: Probing the Mechanism of Amyloidogenesis through a Tandom Repeat of the PI3-SH3 Domain Suggests a Generic Model for Protein Aggregation and Fibril Formation. *J Mol Biol* (2006) 356 p. 189-208.
189. Modler, A. J., Gast, K., Lutsch, G. and Damaschun, G.: Assembly of amyloid protofibrils via critical oligomers—a novel pathway of amyloid formation. *J Mol Biol* (2003) 325 p. 135-48.
190. Gosal, W. S., Morten, I. J., Hewitt, E. W., Smith, D. A., Thompson, N. H. and Radford, S. E.: Competing Pathways Determine Fibril Morphology in the Self-assembly of beta2-Microglobulin into Amyloid. *J Mol Biol* (2005) 351 p. 850-64.
191. Smith, A. M., Jahn, T. R., Ashcroft, A. E. and Radford, S. E.: Direct Observation of Oligomeric Species formed in the Early Stages of Amyloid Fibril Formation using Electrospray Ionisation Mass Spectrometry. *J Mol Biol* (2006) 364 p. 9-19.
192. Hoshi, M., Sato, M., Matsumoto, S., Noguchi, A., Yasutake, K., Yoshida, N. and Sato, K.: Spherical aggregates of beta-amyloid (amylospheroid) show high neurotoxicity and activate tau protein kinase I/glycogen synthase kinase-3beta. *Proc Natl Acad Sci U S A* (2003) 100 p. 6370-5.
193. Conway, K. A., Lee, S. J., Rochet, J. C., Ding, T. T., Williamson, R. E. and Lansbury, P. T., Jr.: Acceleration of oligomerization, not fibrillization, is a shared property of both alpha-synuclein mutations linked to early-onset Parkinson's disease: implications for pathogenesis and therapy. *Proc Natl Acad Sci U S A* (2000) 97 p. 571-6.
194. Walsh, D. M., Lomakin, A., Benedek, G. B., Condron, M. M. and Teplow, D. B.: Amyloid beta-protein fibrillogenesis. Detection of a protofibrillar intermediate. *J Biol Chem* (1997) 272 p. 22364-72.
195. Harper, J. D., Wong, S. S., Lieber, C. M. and Lansbury, P. T.: Observation of metastable Abeta amyloid protofibrils by atomic force microscopy. *Chem Biol* (1997) 4 p. 119-25.
196. Yong, W., Lomakin, A., Kirkitadze, M. D., Teplow, D. B., Chen, S. H. and Benedek, G. B.: Structure determination of micelle-like intermediates in amyloid beta -protein fibril assembly by using small angle neutron scattering. *Proc Natl Acad Sci U S A* (2002) 99 p. 150-4.
197. Lomakin, A., Teplow, D. B., Kirschner, D. A. and Benedek, G. B.: Kinetic theory of fibrillogenesis of amyloid beta-protein. *Proc Natl Acad Sci U S A* (1997) 94 p. 7942-7.

198. Lambert, M. P., Barlow, A. K., Chromy, B. A., Edwards, C., Freed, R., Liosatos, M., Morgan, T. E., Rozovsky, I., Trommer, B., Viola, K. L., Wals, P., Zhang, C., Finch, C. E., Krafft, G. A. and Klein, W. L.: Diffusible, nonfibrillar ligands derived from Abeta1-42 are potent central nervous system neurotoxins. *Proc Natl Acad Sci U S A* (1998) 95 p. 6448-53.
199. Lashuel, H. A., Hartley, D., Petre, B. M., Walz, T. and Lansbury, P. T., Jr.: Neurodegenerative disease: amyloid pores from pathogenic mutations. *Nature* (2002) 418 p. 291.
200. Ding, T. T., Lee, S. J., Rochet, J. C. and Lansbury, P. T., Jr.: Annular alpha-synuclein protofibrils are produced when spherical protofibrils are incubated in solution or bound to brain-derived membranes. *Biochemistry* (2002) 41 p. 10209-17.
201. Lashuel, H. A., Hartley, D. M., Petre, B. M., Wall, J. S., Simon, M. N., Walz, T. and Lansbury, P. T., Jr.: Mixtures of wild-type and a pathogenic (E22G) form of Abeta40 in vitro accumulate protofibrils, including amyloid pores. *J Mol Biol* (2003) 332 p. 795-808.
202. Quist, A., Doudevski, I., Lin, H., Azimova, R., Ng, D., Frangione, B., Kagan, B., Ghiso, J. and Lal, R.: Amyloid ion channels: a common structural link for protein-misfolding disease. *Proc Natl Acad Sci U S A* (2005) 102 p. 10427-32.
203. Lashuel, H. A., Petre, B. M., Wall, J., Simon, M., Nowak, R. J., Walz, T. and Lansbury, P. T., Jr.: Alpha-synuclein, especially the Parkinson's disease-associated mutants, forms pore-like annular and tubular protofibrils. *J Mol Biol* (2002) 322 p. 1089-102.
204. Mukhopadhyay, S., Nayak, P. K., Udgaonkar, J. B. and Krishnamoorthy, G.: Characterization of the formation of amyloid protofibrils from barstar by mapping residue-specific fluorescence dynamics. *J Mol Biol* (2006) 358 p. 935-42.
205. Plakoutsi, G., Bemporad, F., Calamai, M., Taddei, N., Dobson, C. M. and Chiti, F.: Evidence for a Mechanism of Amyloid Formation Involving Molecular Reorganisation within Native-like Precursor Aggregates. *J Mol Biol* (2005) 351 p. 910-22.
206. Krishnan, R. and Lindquist, S. L.: Structural insights into a yeast prion illuminate nucleation and strain diversity. *Nature* (2005) 435 p. 765-72.
207. Christensen, P. A., Pedersen, J. S., Christiansen, G. and Otzen, D. E.: Spectroscopic evidence for the existence of an obligate pre-fibrillar oligomer during glucagon fibrillation. *FEBS Lett* (2008) 582 p. 1341-5.
208. Goldsbury, C., Frey, P., Olivieri, V., Aebi, U. and Muller, S. A.: Multiple assembly pathways underlie amyloid-beta fibril polymorphisms. *J Mol Biol* (2005) 352 p. 282-98.
209. Blackley, H. K., Sanders, G. H., Davies, M. C., Roberts, C. J., Tendler, S. J. and Wilkinson, M. J.: In-situ atomic force microscopy study of beta-amyloid fibrillization. *J Mol Biol* (2000) 298 p. 833-40.
210. Scheibel, T., Bloom, J. and Lindquist, S. L.: The elongation of yeast prion fibers involves separable steps of association and conversion. *Proc Natl Acad Sci U S A* (2004) 101 p. 2287-92.
211. Hong, D. P., Ahmad, A. and Fink, A. L.: Fibrillation of Human Insulin A and B Chains. *Biochemistry* (2006) 45 p.
212. Bitan, G., Kirkitadze, M. D., Lomakin, A., Vollers, S. S., Benedek, G. B. and Teplow, D. B.: Amyloid beta -protein (Abeta) assembly: Abeta 40 and Abeta 42 oligomerize through distinct pathways. *Proc Natl Acad Sci U S A* (2003) 100 p. 330-5.
213. Nichols, M. R., Moss, M. A., Reed, D. K., Lin, W.-L., Mukhopadhyay, R., Hoh, J. H. and Rosenberry, T. L.: Growth of beta-amyloid(1-40) protofibrils by monomer elongation and lateral association. Characterization of distinct products by light scattering and atomic force microscopy. *Biochemistry* (2002) 41 p. 6115-27.
214. Pellarin, R., Guarnera, E. and Caflisch, A.: Pathways and intermediates of amyloid fibril formation. *J Mol Biol* (2007) 374 p. 917-24.
215. Necula, M., Kayed, R., Milton, S. and Glabe, C. G.: Small molecule inhibitors of aggregation indicate that amyloid beta oligomerization and fibrillization pathways are independent and distinct. *J Biol Chem* (2007) 282 p. 10311-24.
216. Booth, D. R., Sunde, M., Bellotti, V., Robinson, C. V., Hutchinson, W. L., Fraser, P. E., Hawkins, P. N., Dobson, C. M., Radford, S. E., Blake, C. C. and Pepys, M. B.: Instability, unfolding and aggregation of human lysozyme variants underlying amyloid fibrillogenesis. *Nature* (1997) 385 p. 787-93.
217. Funahashi, J., Takano, K., Ogasahara, K., Yamagata, Y. and Yutani, K.: The structure, stability, and folding process of amyloidogenic mutant human lysozyme. *J Biochem (Tokyo)* (1996) 120 p. 1216-23.
218. Smith, A. M., Jones, S., Serpell, L. C., Sunde, M. and Radford, S. E.: A Systematic Investigation into the Effect of Protein Destabilisation on Beta 2-Microglobulin Amyloid Formation. *J Mol Biol* (2003) 330 p. 943-54.
219. Morozova-Roche, L. A., Zurdo, J., Spencer, A., Noppe, W., Receveur, V., Archer, D. B., Joniau, M. and Dobson, C. M.: Amyloid fibril formation and seeding by wild-type human lysozyme and its disease-related mutational variants. *J Struct Biol* (2000) 130 p. 339-51.
220. Khurana, R., Gillespie, J. R., Talapatra, A., Minert, L. J., Ionescu-Zanetti, C., Millett, I. and Fink, A. L.: Partially folded intermediates as critical precursors of light chain amyloid fibrils and amorphous aggregates. *Biochemistry* (2001) 40 p. 3525-35.
221. Richardson, J. S. and Richardson, D. C.: Natural beta-sheet proteins use negative design to avoid edge-to-edge aggregation. *Proc Natl Acad Sci U S A* (2002) 99 p. 2754-9.
222. Mandel-Gutfreund, Y. and Gregoret, L.: On the significance of alternating patterns of polar and non-polar residues in beta-strands. *J Mol Biol* (2002) 323 p. 453-61.

223. Haggqvist, B., Naslund, J., Sletten, K., Westermark, G. T., Mucchiano, G., Tjernberg, L. O., Nordstedt, C., Engstrom, U. and Westermark, P.: Medin: An intergral fragment of aortic smooth muscle cell-produced lactadherin forms the most common human amyloid. *Proc Natl Acad Sci U S A* (1999) 96 p. 8669-74.
224. Chiti, F., Taddei, N., Baroni, F., Capanni, C., Stefani, M., Ramponi, G. and Dobson, C. M.: Kinetic partitioning of protein folding and aggregation. *Nat Struct Biol* (2002) 9 p. 137-43.
225. Pedersen, J. S., Christensen, G. and Otzen, D. E.: Modulation of S6 fibrillation by unfolding rates and gatekeeper residues. *J Mol Biol* (2004) 341 p. 575-88.
226. Kirkitadze, M. D., Condron, M. M. and Teplow, D. B.: Identification and characterization of key kinetic intermediates in amyloid beta-protein fibrillogenesis. *J Mol Biol* (2001) 312 p. 1103-19.
227. Walsh, D. M., Hartley, D. M., Kusumoto, Y., Fezoui, Y., Condron, M. M., Lomakin, A., Benedek, G. B., Selkoe, D. J. and Teplow, D. B.: Amyloid beta-protein fibrillogenesis. Structure and biological activity of protofibrillar intermediates. *J Biol Chem* (1999) 274 p. 25945-52.
228. Kayed, R., Bernhagen, J., Greenfield, N., Sweimeh, K., Brunner, H., Voelter, W. and Kapurniotu, A.: Conformational transitions of islet amyloid polypeptide (IAPP) in amyloid formation in vitro. *J Mol Biol* (1999) 287 p. 781-96.
229. Esteras-Chopo, A., Serrano, L. and Lopez de la Paz, M.: The amyloid stretch hypothesis: recruiting proteins toward the dark side. *Proc Natl Acad Sci U S A* (2005) 102 p. 16672-7.
230. Chiti, F., Stefani, M., Taddei, N., Ramponi, G. and Dobson, C. M.: Rationalization of the effects of mutations on peptide and protein aggregation rates. *Nature* (2003) 424 p. 805-8.
231. DuBay, K. F., Pawar, A. P., Chiti, F., Zurdo, J., Dobson, C. M. and Vendruscolo, M.: Prediction of the absolute aggregation rates of amyloidogenic polypeptide chains. *J Mol Biol* (2004) 341 p. 1317-26.
232. Calamai, M., Taddei, N., Stefani, M., Ramponi, G. and Chiti, F.: Relative influence of hydrophobicity and net charge in the aggregation of two homologous proteins. *Biochemistry* (2003) 42 p. 15078-83.
233. Fink, A. L.: Protein aggregation: folding aggregates, inclusion bodies and amyloid. *Fold Des* (1998) 3 p. R9-23.
234. Chan, J. C., Oyler, N. A., Yau, W. M. and Tycko, R.: Parallel beta-sheets and polar zippers in amyloid fibrils formed by residues 10-39 of the yeast prion protein Ure2p. *Biochemistry* (2005) 44 p. 10669-80.
235. Thompson, M. J., Sievers, S. A., Karanicolas, J., Ivanova, M. I., Baker, D. and Eisenberg, D.: The 3D profile method for identifying fibril-forming segments of proteins. *Proc Natl Acad Sci U S A* (2006) 103 p. 4074-8.
236. Brack, A. and Orgel, L. E.: Beta structures of alternating polypeptides and their possible prebiotic significance. *Nature* (1975) 256 p. 383-7.
237. West, M. W., Wang, W., Patterson, J., Mancias, J. D., Beasley, J. R. and Hecht, M. H.: De novo amyloid proteins from designed combinatorial libraries. *Proc Natl Acad Sci U S A* (1999) 96 p. 11211-16.
238. Chou, P. Y. and Fasman, G. D.: Conformational parameters for amino acids in helical, beta-sheet, and random coil regions calculated from proteins. *Biochemistry* (1974) 13 p. 211-22.
239. Street, A. G. and Mayo, S. L.: Intrinsic beta-sheet propensities result from van der Waals interactions between side chains and the local backbone. *Proc Natl Acad Sci U S A* (1999) 96 p. 9074-6.
240. Smidt, C. K., Withka, J. M. and Regan, L.: A thermodynamic scale for the beta-sheet forming tendencies of the amino acids. *Biochemistry* (1994) 33 p. 5510-7.
241. Chiba, T., Hagihara, Y., Higurashi, T., Hasegawa, K., Naiki, H. and Goto, Y.: Amyloid fibril formation in the context of full-length protein: Effects of proline mutations on the amyloid fibril formation of beta2-microglobulin. *J Biol Chem* (2003) 278 p. 47016-24.
242. Westermark, P., Engstrom, U., Johnson, K. H., Westermark, G. T. and Betsholtz, C.: Islet amyloid polypeptide: Pinpointing amino acid residues linked to amyloid fibril formation. *Proc Natl Acad Sci U S A* (1990) 87 p. 5036-40.
243. Parrini, C., Taddei, N., Ramazzotti, M., Degl'Innocenti, D., Ramponi, G., Dobson, C. M. and Chiti, F.: Glycine residues appear to be evolutionarily conserved for their ability to inhibit aggregation. *Structure* (2005) 13 p. 1143-51.
244. Azriel, R. and Gazit, E.: Analysis of the minimal amyloid-forming fragment of the islet amyloid polypeptide. An experimental support for the key role of the phenylalanine residue in amyloid formation. *J Biol Chem* (2001) 276 p. 34156-61.
245. Merkel, J. S. and Regan, L.: Aromatic rescue of glycine in beta sheets. *Fold Des* (1998) 3 p. 449-55.
246. Gazit, E.: Global analysis of tandem aromatic octapeptide repeats: the significant of the aromatic glycine motif. *Bioinformatics* (2002) 18 p. 880-3.
247. Porat, Y., Mazor, Y., Efrat, S. and Gazit, E.: Inhibition of islet amyloid polypeptide fibril formation: a potential role for heteroaromatic interactions. *Biochemistry* (2004) 43 p. 14454-62.
248. Gazit, E.: A possible role for pi-stacking in the self-assembly of amyloid fibrils. *Faseb J* (2002) 16 p. 77-83.
249. Tracz, S. M., Abedini, A., Driscoll, M. and Raleigh, D. P.: Role of aromatic interactions in amyloid formation by peptides derived from human Amylin. *Biochemistry* (2004) 43 p. 15901-8.
250. Bemporad, F., Taddei, N., Stefani, M. and Chiti, F.: Assessing the role of aromatic residues in the amyloid aggregation of human muscle acylphosphatase. *Protein Sci* (2006) 15 p. 862-70.
251. Makin, O. S., Atkins, E., Sikorski, P., Johansson, J. and Serpell, L. C.: Molecular basis for amyloid fibril formation and stability. *Proc Natl Acad Sci U S A* (2005) 102 p. 315-20.
252. Naito, A., Kamihira, M., Inoue, R. and Saito, H.: Structural diversity of amyloid fibril formed in human calcitonin as revealed by site-directed 13C solid-state NMR spectroscopy. *Magn Reson Chem* (2004) 42 p. 247-57.

253. Chiti, F., Calamai, M., Taddei, N., Stefani, M., Ramponi, G. and Dobson, C. M.: Studies of the aggregation of mutant proteins in vitro provide insights into the genetics of amyloid diseases. *Proc Natl Acad Sci U S A* (2002) 99 Suppl 4 p. 16419-26.
254. Tjernberg, L., Hosia, W., Bark, N., Thyberg, J. and Johansson, J.: Charge attraction and beta propensity are necessary for amyloid fibril formation from tetrapeptides. *J Biol Chem* (2002) 277 p. 43243-6.
255. Uversky, V. N., Gillespie, J. R. and Fink, A. L.: Why are "natively unfolded" proteins unstructured under physiologic conditions? *Proteins* (2000) 41 p. 415-27.
256. Lopez De La Paz, M., Goldie, K., Zurdo, J., Lacroix, E., Dobson, C. M., Hoenger, A. and Serrano, L.: De novo designed peptide-based amyloid fibrils. *Proc Natl Acad Sci U S A* (2002) 99 p. 16052-7.
257. Zurdo, J., Guijarro, J. I., Jimenez, J. L., Saibil, H. R. and Dobson, C. M.: Dependence on solution conditions of aggregation and amyloid formation by an SH3 domain. *J Mol Biol* (2001) 311 p. 325-40.
258. Rousseau, F., Schymkowitz, J. and Serrano, L.: Protein aggregation and amyloidosis: confusion of the kinds? *Curr Opin Struct Biol* (2006) 16 p. 118-26.
259. de Groot, N. S., Aviles, F. X., Vendrell, J. and Ventura, S.: Mutagenesis of the central hydrophobic cluster in Abeta42 Alzheimer's peptide. Side-chain properties correlate with aggregation propensities. *Febs J* (2006) 273 p. 658-68.
260. de Groot, N. S., Pallares, I., Aviles, F. X., Vendrell, J. and Ventura, S.: Prediction of "hot spots" of aggregation in disease-linked polypeptides. *BMC Struct Biol* (2005) 5 p. 18.
261. Pawar, A. P., DuBay, K. F., Zurdo, J., Chiti, F., Vendruscolo, M. and Dobson, C. M.: Prediction of "Aggregation-prone" and "Aggregationsusceptible" Regions in Proteins Associated with Neurodegenerative Diseases. *J Mol Biol* (2005) 2005 p. 379-92.
262. Conchillo-Sole, O., de Groot, N. S., Aviles, F. X., Vendrell, J., Daura, X. and Ventura, S.: AGGRESCAN: a server for the prediction and evaluation of "hot spots" of aggregation in polypeptides. *BMC Bioinformatics* (2007) 8 p. 65.
263. Tartaglia, G. G., Pawar, A. P., Campioni, S., Dobson, C. M., Chiti, F. and Vendruscolo, M.: Prediction of Aggregation-Prone Regions in Structured Proteins. *J Mol Biol* (2008) x p. x.
264. Tartaglia, G. G., Cavalli, A. and Vendruscolo, M.: Prediction of local structural stabilities of proteins from their amino acid sequences. *Structure* (2007) 15 p. 139-43.
265. Fernandez-Escamilla, A. M., Rousseau, F., Schymkowitz, J. and Serrano, L.: Prediction of sequence-dependent and mutational effects on the aggregation of peptides and proteins. *Nat Biotechnol* (2004) 22 p. 1302-6.
266. Trovato, A., Chiti, F., Maritan, A. and Seno, F.: Insight into the structure of amyloid fibrils from the analysis of globular proteins. *PLoS Comput Biol* (2006) 2 p. e170.
267. Gutekunst, C. A., Li, S. H., Yi, H., Mulroy, J. S., Kuemmerle, S., Jones, R., Rye, D., Ferrante, R. J., Hersch, S. M. and Li, X. J.: Nuclear and neuropil aggregates in Huntington's disease: relationship to neuropathology. *J Neurosci* (1999) 19 p. 2522-34.
268. Mizuno, Y., Hattori, N., Kubo, S., Sato, S., Nishioka, K., Hatano, T., Tomiyama, H., Funayama, M., Machida, Y. and Mochizuki, H.: Progress in the pathogenesis and genetics of Parkinson's disease. *Philos Trans R Soc Lond B Biol Sci* (2008) 363 p. 2215-27.
269. Lugaresi, E., Medori, R., Montagna, P., Baruzzi, A., Cortelli, P., Lugaresi, A., Tinuper, P., Zucconi, M. and Gambetti, P.: Fatal familial insomnia and dysautonomia with selective degeneration of thalamic nuclei. *N Engl J Med* (1986) 315 p. 997-1003.
270. Mattson, M. P.: Apoptosis in neurodegenerative disorders. *Nat Rev Mol Cell Biol* (2000) 1 p. 120-9.
271. Selkoe, D. J.: Alzheimer disease: mechanistic understanding predicts novel therapies. *Ann Intern Med* (2004) 140 p. 627-38.
272. Dauer, W. and Przedborski, S.: Parkinson's disease: mechanisms and models. *Neuron* (2003) 39 p. 889-909.
273. Johnson, R. T. and Gibbs, C. J., Jr.: Creutzfeldt-Jakob disease and related transmissible spongiform encephalopathies. *N Engl J Med* (1998) 339 p. 1994-2004.
274. Caughey, B. and Lansbury, P. T., Jr.: Protofibrils, Pores, Fibrils, and Neuredegeneration: Separating the Responsible Protein Aggregates from The Innocent Bystanders. *Annu Rev Neurosci* (2003) 26 p. 267-98.
275. Lott, I. T. and Head, E.: Alzheimer disease and Down syndrome: factors in pathogenesis. *Neurobiol Aging* (2005) 26 p. 383-9.
276. Hardy, J. and Allsop, D.: Amyloid deposition as the central event in the aetiology of Alzheimer's disease. *Trends Pharmacol Sci* (1991) 12 p. 383-8.
277. Wong, P. C., Cai, H., Borchelt, D. R. and Price, D. L.: Genetically engineered mouse models of neurodegenerative diseases. *Nat Neurosci* (2002) 5 p. 633-9.
278. Urbanc, B., Cruz, L., Le, R., Sanders, J., Ashe, K. H., Duff, K., Stanley, H. E., Irizarry, M. C. and Hyman, B. T.: Neurotoxic effects of thioflavin S-positive amyloid deposits in transgenic mice and Alzheimer's disease. *Proc Natl Acad Sci U S A* (2002) 99 p. 13990-5.
279. Masliah, E., Rockenstein, E., Veinbergs, I., Mallory, M., Hashimoto, M., Takeda, A., Sagara, Y., Sisk, A. and Mucke, L.: Dopaminergic loss and inclusion body formation in alpha-synuclein mice: implications for neurodegenerative disorders. *Science* (2000) 287 p. 1265-9.
280. Terry, R. D., Masliah, E., Salmon, D. P., Butters, N., DeTeresa, R., Hill, R., Hansen, L. A. and Katzman, R.: Physical basis of cognitive alterations in Alzheimer's disease: synapse loss is the major correlate of cognitive impairment. *Ann Neurol* (1991) 30 p. 572-80.

281. Lemere, C. A., Blusztajn, J. K., Yamaguchi, H., Wisniewski, T., Saido, T. C. and Selkoe, D. J.: Sequence of deposition of heterogeneous amyloid beta-peptides and APO E in Down syndrome: implications for initial events in amyloid plaque formation. *Neurobiol Dis* (1996) 3 p. 16-32.
282. Kuo, Y. M., Emmerling, M. R., Vigo-Pelfrey, C., Kasunic, T. C., Kirkpatrick, J. B., Murdoch, G. H., Ball, M. J. and Roher, A. E.: Water-soluble Abeta (N-40, N-42) oligomers in normal and Alzheimer disease brains. *J Biol Chem* (1996) 271 p. 4077-81.
283. McLean, C. A., Cherny, R. A., Fraser, F. W., Fuller, S. J., Smith, M. J., Beyreuther, K., Bush, A. I. and Masters, C. L.: Soluble pool of Abeta amyloid as a determinant of severity of neurodegeneration in Alzheimer's disease. *Ann Neurol* (1999) 46 p. 860-6.
284. Dickson, D. W., Crystal, H. A., Mattiace, L. A., Masur, D. M., Blau, A. D., Davies, P., Yen, S. H. and Aronson, M. K.: Identification of normal and pathological aging in prospectively studied nondemented elderly humans. *Neurobiol Aging* (1992) 13 p. 179-89.
285. Mori, H., Kondo, T., Yokochi, M., Matsumine, H., Nakagawa-Hattori, Y., Miyake, T., Suda, K. and Mizuno, Y.: Pathologic and biochemical studies of juvenile parkinsonism linked to chromosome 6q. *Neurology* (1998) 51 p. 890-2.
286. Takahashi, H., Ohama, E., Suzuki, S., Horikawa, Y., Ishikawa, A., Morita, T., Tsuji, S. and Ikuta, F.: Familial juvenile parkinsonism: clinical and pathologic study in a family. *Neurology* (1994) 44 p. 437-41.
287. Iijima, K., Liu, H. P., Chiang, A. S., Hearn, S. A., Konsolaki, M. and Zhong, Y.: Dissecting the pathological effects of human Abeta40 and Abeta42 in Drosophila: a potential model for Alzheimer's disease. *Proc Natl Acad Sci U S A* (2004) 101 p. 6623-8.
288. Crowther, D. C., Kinghorn, K. J., Miranda, E., Page, R., Curry, J. A., Duthie, F. A., Gubb, D. C. and Lomas, D. A.: Intraneuronal Abeta, non-amyloid aggregates and neurodegeneration in a Drosophila model of Alzheimer's disease. *Neuroscience* (2005) 132 p. 123-35.
289. Moechars, D., Dewachter, I., Lorent, K., Reverse, D., Baekelandt, V., Naidu, A., Tesseur, I., Spittaels, K., Haute, C. V., Checler, F., Godaux, E., Cordell, B. and Van Leuven, F.: Early phenotypic changes in transgenic mice that overexpress different mutants of amyloid precursor protein in brain. *J Biol Chem* (1999) 274 p. 6483-92.
290. Hsia, A. Y., Masliah, E., McConlogue, L., Yu, G. Q., Tatsuno, G., Hu, K., Kholodenko, D., Malenka, R. C., Nicoll, R. A. and Mucke, L.: Plaque-independent disruption of neural circuits in Alzheimer's disease mouse models. *Proc Natl Acad Sci U S A* (1999) 96 p. 3228-33.
291. Mucke, L., Masliah, E., Yu, G. Q., Mallory, M., Rockenstein, E. M., Tatsuno, G., Hu, K., Kholodenko, D., Johnson-Wood, K. and McConlogue, L.: High-level neuronal expression of abeta 1-42 in wild-type human amyloid protein precursor transgenic mice: synaptotoxicity without plaque formation. *J Neurosci* (2000) 20 p. 4050-8.
292. Pasinelli, P. and Brown, R. H.: Molecular biology of amyotrophic lateral sclerosis: insights from genetics. *Nat Rev Neurosci* (2006) 7 p. 710-23.
293. Goldberg, M. S. and Lansbury, P. T., Jr.: Is there a cause-and-effect relationship between alpha-synuclein fibrillization and Parkinson's disease? *Nat Cell Biol* (2000) 2 p. E115-9.
294. Koistinaho, M., Ort, M., Cimadevilla, J. M., Vondrous, R., Cordell, B., Koistinaho, J., Bures, J. and Higgins, L. S.: Specific spatial learning deficits become severe with age in beta -amyloid precursor protein transgenic mice that harbor diffuse beta -amyloid deposits but do not form plaques. *Proc Natl Acad Sci U S A* (2001) 98 p. 14675-80.
295. Westerman, M. A., Cooper-Blacketer, D., Mariash, A., Kotilinek, L., Kawarabayashi, T., Younkin, L. H., Carlson, G. A., Younkin, S. G. and Ashe, K. H.: The relationship between Abeta and memory in the Tg2576 mouse model of Alzheimer's disease. *J Neurosci* (2002) 22 p. 1858-67.
296. Lansbury, P. T., Jr.: Evolution of amyloid: what normal protein folding may tell us about fibrillogenesis and disease. *Proc Natl Acad Sci U S A* (1999) 96 p. 3342-4.
297. Nilsberth, C., Westlind-Danielsson, A., Eckman, C. B., Condron, M. M., Axelman, K., Forsell, C., Stenh, C., Luthman, J., Teplow, D. B., Younkin, S. G., Naslund, J. and Lannfelt, L.: The 'Arctic' APP mutation (E693G) causes Alzheimer's disease by enhanced Abeta protofibril formation. *Nat Neurosci* (2001) 4 p. 887-93.
298. Roher, A. E., Chaney, M. O., Kuo, Y. M., Webster, S. D., Stine, W. B., Haverkamp, L. J., Woods, A. S., Cotter, R. J., Tuohy, J. M., Krafft, G. A., Bonnell, B. S. and Emmerling, M. R.: Morphology and toxicity of Abeta-(1-42) dimer derived from neuritic and vascular amyloid deposits of Alzheimer's disease. *J Biol Chem* (1996) 271 p. 20631-5.
299. Pitschke, M., Prior, R., Haupt, M. and Riesner, D.: Detection of single amyloid beta-protein aggregates in the cerebrospinal fluid of Alzheimer's patients by fluorescence correlation spectroscopy. *Nat Med* (1998) 4 p. 832-4.
300. Gong, Y., Chang, L., Viola, K. L., Lacor, P. N., Lambert, M. P., Finch, C. E., Krafft, G. A. and Klein, W. L.: Alzheimer's disease-affected brain: presence of oligomeric A beta ligands (ADDLs) suggests a molecular basis for reversible memory loss. *Proc Natl Acad Sci U S A* (2003) 100 p. 10417-22.
301. Mukai, H., Isagawa, T., Goyama, E., Tanaka, S., Bence, N. F., Tamura, A., Ono, Y. and Kopito, R. R.: Formation of morphologically similar globular aggregates from diverse aggregation-prone proteins in mammalian cells. *Proc Natl Acad Sci U S A* (2005) 102 p. 10887-92.
302. Lesne, S., Koh, M. T., Kotilinek, L., Kayed, R., Glabe, C. G., Yang, A., Gallagher, M. and Ashe, K. H.: A specific amyloid-beta protein assembly in the brain impairs memory. *Nature* (2006) 440 p. 352-7.
303. Pountney, D. L., Lowe, R., Quilty, M., Vickers, J. C., Voelcker, N. H. and Gai, W. P.: Annular alpha-synuclein species from purified multiple system atrophy inclusions. *J Neurochem* (2004) 90 p. 502-12.

304. Demuro, A., Mina, E., Kayed, R., Milton, S. C., Parker, I. and Glabe, C. G.: Calcium dysregulation and membrane disruption as a ubiquitous neurotoxic mechanism of soluble amyloid oligomers. *J Biol Chem* (2005) 280 p. 17294-300.
305. Simoneau, S., Rezaei, H., Sales, N., Kaiser-Schulz, G., Lefebvre-Roque, M., Vidal, C., Fournier, J. G., Comte, J., Wopfner, F., Grosclaude, J., Schatzl, H. and Lasmezas, C. I.: In vitro and in vivo neurotoxicity of prion protein oligomers. *PLoS Pathog* (2007) 3 p. e125.
306. Volles, M. J. and Lansbury, P. T., Jr.: Zeroing in on the pathogenic form of alpha-synuclein and its mechanism of neurotoxicity in Parkinson's disease. *Biochemistry* (2003) 42 p. 7871-8.
307. Janson, J., Ashley, R. H., Harrison, D., McIntyre, S. and Butler, P. C.: The mechanism of islet amyloid polypeptide toxicity is membrane disruption by intermediate-sized toxic amyloid particles. *Diabetes* (1999) 48 p. 491-8.
308. Gosavi, N., Lee, H. J., Lee, J. S., Patel, S. and Lee, S. J.: Golgi fragmentation occurs in the cells with prefibrillar alpha-synuclein aggregates and precedes the formation of fibrillar inclusion. *J Biol Chem* (2002) 277 p. 48984-92.
309. Baglioni, S., Casamenti, F., Bucciantini, M., Luheshi, L. M., Taddei, N., Chiti, F., Dobson, C. M. and Stefani, M.: Prefibrillar amyloid aggregates could be generic toxins in higher organisms. *J Neurosci* (2006) 26 p. 8160-7.
310. Hartley, D. M., Walsh, D. M., Ye, C. P., Diehl, T., Vasquez, S., Vassilev, P. M., Teplow, D. B. and Selkoe, D. J.: Protofibrillar intermediates of amyloid beta-protein induce acute electrophysiological changes and progressive neurotoxicity in cortical neurons. *J Neurosci* (1999) 19 p. 8876-84.
311. Zhou, W., Hurlbert, M. S., Schaack, J., Prasad, K. N. and Freed, C. R.: Overexpression of human alpha-synuclein causes dopamine neuron death in rat primary culture and immortalized mesencephalon-derived cells. *Brain Res* (2000) 866 p. 33-43.
312. Xu, J., Kao, S. Y., Lee, F. J., Song, W., Jin, L. W. and Yankner, B. A.: Dopamine-dependent neurotoxicity of alpha-synuclein: a mechanism for selective neurodegeneration in Parkinson disease. *Nat Med* (2002) 8 p. 600-6.
313. Kazlauskaite, J., Young, A., Gardner, C. E., Macpherson, J. V., Venien-Bryan, C. and Pinheiro, T. J.: An unusual soluble beta-turn-rich conformation of prion is involved in fibril formation and toxic to neuronal cells. *Biochem Biophys Res Commun* (2005) 328 p. 292-305.
314. Lorenzo, A., Razzaboni, B., Weir, G. C. and Yankner, B. A.: Pancreatic islet cell toxicity of amylin associated with type-2 diabetes mellitus. *Nature* (1994) 368 p. 756-60.
315. Ritzel, R. A., Meier, J. J., Lin, C. Y., Veldhuis, J. D. and Butler, P. C.: Human islet amyloid polypeptide oligomers disrupt cell coupling, induce apoptosis, and impair insulin secretion in isolated human islets. *Diabetes* (2007) 56 p. 65-71.
316. Reixach, N., Deechongkit, S., Jiang, X., Kelly, J. W. and Buxbaum, J. N.: Tissue damage in the amyloidoses: Transthyretin monomers and nonnative oligomers are the major cytotoxic species in tissue culture. *Proc Natl Acad Sci U S A* (2004) 101 p. 2817-22.
317. Sousa, M. M., Cardoso, I., Fernandes, R., Guimaraes, A. and Saraiva, M. J.: Deposition of transthyretin in early stages of familial amyloidotic polyneuropathy: evidence for toxicity of nonfibrillar aggregates. *Am J Pathol* (2001) 159 p. 1993-2000.
318. Malisauskas, M., Ostman, J., Darinskas, A., Zamotin, V., Liutkevicius, E., Lundgren, E. and Morozova-Roche, L. A.: Does the Cytotoxic Effect of Transient Amyloid Oligomers from Common Equine Lysozyme in Vitro Imply Innate Amyloid Toxicity? *J Biol Chem* (2005) 280 p. 6269-75.
319. Malisauskas, M., Darinskas, A., Zamotin, V. V., Gharibyan, A., Kostanyan, I. A. and Morozova-Roche, L. A.: Intermediate amyloid oligomers of lysozyme: Is their cytotoxicity a particular case or general rule for amyloid? *Biochemistry (Mosc)* (2006) 71 p. 505-12.
320. Bucciantini, M., Giannoni, E., Chiti, F., Baroni, F., Formigli, L., Zurdo, J., Taddei, N., Ramponi, G., Dobson, C. M. and Stefani, M.: Inherent toxicity of aggregates implies a common mechanism for protein misfolding diseases. *Nature* (2002) 416 p. 507-11.
321. Bucciantini, M., Calloni, G., Chiti, F., Formigli, L., Nosi, D., Dobson, C. M. and Stefani, M.: Prefibrillar amyloid protein aggregates share common features of cytotoxicity. *J Biol Chem* (2004) 279 p. 31374-82.
322. Merlini, G. and Westermark, P.: The systemic amyloidoses: clearer understanding of the molecular mechanisms offers hope for more effective therapies. *J Intern Med* (2004) 255 p. 159-78.
323. Walsh, D. M., Klyubin, I., Fadeeva, J. V., Cullen, W. K., Anwyl, R., Wolfe, M. S., Rowan, M. J. and Selkoe, D. J.: Naturally secreted oligomers of amyloid beta protein potently inhibit hippocampal long-term potentiation in vivo. *Nature* (2002) 416 p. 535-9.
324. Selkoe, D. J.: Soluble oligomers of the amyloid beta-protein impair synaptic plasticity and behavior. *Behav Brain Res* (2008) 192 p. 106-13.
325. Cleary, J. P., Walsh, D. M., Hofmeister, J. J., Shankar, G. M., Kuskowski, M. A., Selkoe, D. J. and Ashe, K. H.: Natural oligomers of the amyloid-beta protein specifically disrupt cognitive function. *Nat Neurosci* (2005) 8 p. 79-84.
326. Podlisny, M. B., Ostaszewski, B. L., Squazzo, S. L., Koo, E. H., Rydell, R. E., Teplow, D. B. and Selkoe, D. J.: Aggregation of secreted amyloid beta-protein into sodium dodecyl sulfate-stable oligomers in cell culture. *J Biol Chem* (1995) 270 p. 9564-70.
327. Kayed, R., Head, E., Thompson, J. L., McIntire, T. M., Milton, S. C., Cotman, C. W. and Glabe, C. G.: Common structure of soluble amyloid oligomers implies common mechanism of pathogenesis. *Science* (2003) 300 p. 486-9.

328. Lambert, M. P., Viola, K. L., Chromy, B. A., Chang, L., Morgan, T. E., Yu, J., Venton, D. L., Krafft, G. A., Finch, C. E. and Klein, W. L.: Vaccination with soluble Abeta oligomers generates toxicity-neutralizing antibodies. *J Neurochem* (2001) 79 p. 595-605.
329. Klyubin, I., Walsh, D. M., Lemere, C. A., Cullen, W. K., Shankar, G. M., Betts, V., Spooner, E. T., Jiang, L., Anwyl, R., Selkoe, D. J. and Rowan, M. J.: Amyloid beta protein immunotherapy neutralizes Abeta oligomers that disrupt synaptic plasticity in vivo. *Nat Med* (2005) 11 p. 556-61.
330. Morgan, D., Diamond, D. M., Gottschall, P. E., Ugen, K. E., Dickey, C., Hardy, J., Duff, K., Jantzen, P., DiCarlo, G., Wilcock, D., Connor, K., Hatcher, J., Hope, C., Gordon, M. and Arendash, G. W.: A beta peptide vaccination prevents memory loss in an animal model of Alzheimer's disease. *Nature* (2000) 408 p. 982-5.
331. Stefani, M.: Protein misfolding and aggregation: new examples in medicine and biology of the dark side of the protein world. *Biochim Biophys Acta* (2004) 1739 p. 5-25.
332. Kremer, J. J., Pallitto, M. M., Sklansky, D. J. and Murphy, R. M.: Correlation of beta-amyloid aggregate size and hydrophobicity with decreased bilayer fluidity of model membranes. *Biochemistry* (2000) 39 p. 10309-18.
333. Butterfield, D. A., Castegna, A., Lauderback, C. M. and Drake, J.: Evidence that amyloid beta-peptide-induced lipid peroxidation and its sequelae in Alzheimer's disease brain contribute to neuronal death. *Neurobiol Aging* (2002) 23 p. 655-64.
334. Kagan, B. L., Hirakura, Y., Azimov, R., Azimova, R. and Lin, M. C.: The channel hypothesis of Alzheimer's disease: current status. *Peptides* (2002) 23 p. 1311-5.
335. Kagan, B. L., Azimov, R. and Azimova, R.: Amyloid peptide channels. *J Membr Biol* (2004) 202 p. 1-10.
336. Volles, M. J., Lee, S. J., Rochet, J. C., Shtilerman, M. D., Ding, T. T., Kessler, J. C. and Lansbury, P. T., Jr.: Vesicle permeabilization by protofibrillar alpha-synuclein: implications for the pathogenesis and treatment of Parkinson's disease. *Biochemistry* (2001) 40 p. 7812-9.
337. Relini, A., Torrassa, S., Rolandi, R., Gliozzi, A., Rosano, C., Canale, C., Bolognesi, M., Plakoutsi, G., Bucciantini, M., Chiti, F. and Stefani, M.: Monitoring the process of HypF fibrillization and liposome permeabilization by protofibrils. *J Mol Biol* (2004) 338 p. 943-57.
338. Anguiano, M., Nowak, R. J. and Lansbury, P. T., Jr.: Protofibrillar islet amyloid polypeptide permeabilizes synthetic vesicles by a pore-like mechanism that may be relevant to type II diabetes. *Biochemistry* (2002) 41 p. 11338-43.
339. Rabzelj, S., Viero, G., Gutierrez-Aguirre, I., Turk, V., Dalla Serra, M., Anderluh, G. and Zerovnik, E.: Interaction with model membranes and pore formation by human stefin B: studying the native and prefibrillar states. *Febs J* (2008) 275 p. 2455-66.
340. Volles, M. J. and Lansbury, P. T., Jr.: Vesicle permeabilization by protofibrillar alpha-synuclein is sensitive to Parkinson's disease-linked mutations and occurs by a pore-like mechanism. *Biochemistry* (2002) 41 p. 4595-602.
341. Arispe, N., Rojas, E. and Pollard, H. B.: Alzheimer disease amyloid beta protein forms calcium channels in bilayer membranes: blockade by tromethamine and aluminum. *Proc Natl Acad Sci U S A* (1993) 90 p. 567-71.
342. Arispe, N., Pollard, H. B. and Rojas, E.: Giant multilevel cation channels formed by Alzheimer disease amyloid beta-protein [A beta P-(1-40)] in bilayer membranes. *Proc Natl Acad Sci U S A* (1993) 90 p. 10573-7.
343. Arispe, N., Pollard, H. B. and Rojas, E.: beta-Amyloid Ca(2+)-channel hypothesis for neuronal death in Alzheimer disease. *Mol Cell Biochem* (1994) 140 p. 119-25.
344. Furukawa, K., Abe, Y. and Akaike, N.: Amyloid beta protein-induced irreversible current in rat cortical neurones. *Neuroreport* (1994) 5 p. 2016-8.
345. Sanderson, K. L., Butler, L. and Ingram, V. M.: Aggregates of a beta-amyloid peptide are required to induce calcium currents in neuron-like human teratocarcinoma cells: relation to Alzheimer's disease. *Brain Res* (1997) 744 p. 7-14.
346. Kawahara, M., Arispe, N., Kuroda, Y. and Rojas, E.: Alzheimer's disease amyloid beta-protein forms Zn(2+)-sensitive, cation-selective channels across excised membrane patches from hypothalamic neurons. *Biophys J* (1997) 73 p. 67-75.
347. Zhu, Y. J., Lin, H. and Lal, R.: Fresh and nonfibrillar amyloid beta protein(1-40) induces rapid cellular degeneration in aged human fibroblasts: evidence for AbetaP-channel-mediated cellular toxicity. *Faseb J* (2000) 14 p. 1244-54.
348. Hirakura, Y., Lin, M. C. and Kagan, B. L.: Alzheimer amyloid abeta1-42 channels: effects of solvent, pH, and Congo Red. *J Neurosci Res* (1999) 57 p. 458-66.
349. Kourie, J. I., Henry, C. L. and Farrelly, P.: Diversity of amyloid beta protein fragment [1-40]-formed channels. *Cell Mol Neurobiol* (2001) 21 p. 255-84.
350. Arispe, N., Pollard, H. B. and Rojas, E.: Zn2+ interaction with Alzheimer amyloid beta protein calcium channels. *Proc Natl Acad Sci U S A* (1996) 93 p. 1710-5.
351. Arispe, N., Diaz, J. C. and Simakova, O.: Abeta ion channels. Prospects for treating Alzheimer's disease with Abeta channel blockers. *Biochim Biophys Acta* (2007) 1768 p. 1952-65.
352. Mirzabekov, T. A., Lin, M. C. and Kagan, B. L.: Pore formation by the cytotoxic islet amyloid peptide amylin. *J Biol Chem* (1996) 271 p. 1988-92.
353. Lin, M. C. and Kagan, B. L.: Electrophysiologic properties of channels induced by Abeta25-35 in planar lipid bilayers. *Peptides* (2002) 23 p. 1215-28.
354. Kayed, R., Sokolov, Y., Edmonds, B., McIntire, T. M., Milton, S. C., Hall, J. E. and Glabe, C. G.: Permeabilization of lipid bilayers is a common conformation-dependent activity of soluble amyloid oligomers in protein misfolding diseases. *J Biol Chem* (2004) 279 p. 46363-6.

355. Green, J. D., Kreplak, L., Goldsbury, C., Li Blatter, X., Stolz, M., Cooper, G. S., Seelig, A., Kistler, J. and Aebi, U.: Atomic force microscopy reveals defects within mica supported lipid bilayers induced by the amyloidogenic human amylin peptide. *J Mol Biol* (2004) 342 p. 877-87.
356. Sparr, E., Engel, M. F., Sakharov, D. V., Sprong, M., Jacobs, J., de Kruijff, B., Hoppener, J. W. and Antoinette Killian, J.: Islet amyloid polypeptide-induced membrane leakage involves uptake of lipids by forming amyloid fibers. *FEBS Lett* (2004) 577 p. 117-20.
357. Zhao, H., Jutila, A., Nurminen, T., Wickstrom, S. A., Keski-Oja, J. and Kinnunen, P. K.: Binding of endostatin to phosphatidylserine-containing membranes and formation of amyloid-like fibers. *Biochemistry* (2005) 44 p. 2857-63.
358. Michikawa, M., Gong, J. S., Fan, Q. W., Sawamura, N. and Yanagisawa, K.: A novel action of alzheimer's amyloid beta-protein (Abeta): oligomeric Abeta promotes lipid release. *J Neurosci* (2001) 21 p. 7226-35.
359. Gorbenko, G. P. and Kinnunen, P. K.: The role of lipid-protein interactions in amyloid-type protein fibril formation. *Chem Phys Lipids* (2006) 141 p. 72-82.
360. Bokvist, M., Lindstrom, F., Watts, A. and Grobner, G.: Two types of Alzheimer's beta-amyloid (1-40) peptide membrane interactions: aggregation preventing transmembrane anchoring versus accelerated surface fibril formation. *J Mol Biol* (2004) 335 p. 1039-49.
361. Zhu, M., Li, J. and Fink, A. L.: The association of alpha-synuclein with membranes affects bilayer structure, stability, and fibril formation. *J Biol Chem* (2003) 278 p. 40186-97.
362. Knight, J. D. and Miranker, A. D.: Phospholipid catalysis of diabetic amyloid assembly. *J Mol Biol* (2004) 341 p. 1175-87.
363. Zhao, H., Tuominen, E. K. and Kinnunen, P. K.: Formation of amyloid fibers triggered by phosphatidylserine-containing membranes. *Biochemistry* (2004) 43 p. 10302-7.
364. Vestergaard, M., Hamada, T. and Takagi, M.: Using model membranes for the study of amyloid beta:lipid interactions and neurotoxicity. *Biotechnol Bioeng* (2008) 99 p. 753-63.
365. Shin, I., Kreimer, D., Silman, I. and Weiner, L.: Membrane-promoted unfolding of acetylcholinesterase: a possible mechanism for insertion into the lipid bilayer. *Proc Natl Acad Sci U S A* (1997) 94 p. 2848-52.
366. Tatulian, S. A., Biltonen, R. L. and Tamm, L. K.: Structural changes in a secretory phospholipase A2 induced by membrane binding: a clue to interfacial activation? *J Mol Biol* (1997) 268 p. 809-15.
367. Muga, A., Mantsch, H. H. and Surewicz, W. K.: Membrane binding induces destabilization of cytochrome c structure. *Biochemistry* (1991) 30 p. 7219-24.
368. Kakio, A., Nishimoto, S. I., Yanagisawa, K., Kozutsumi, Y. and Matsuzaki, K.: Cholesterol-dependent formation of GM1 ganglioside-bound amyloid beta-protein, an endogenous seed for Alzheimer amyloid. *J Biol Chem* (2001) 276 p. 24985-90.
369. Matsuzaki, K.: Physicochemical interactions of amyloid beta-peptide with lipid bilayers. *Biochim Biophys Acta* (2007) 1768 p. 1935-42.
370. Davidson, W. S., Jonas, A., Clayton, D. F. and George, J. M.: Stabilization of alpha-synuclein secondary structure upon binding to synthetic membranes. *J Biol Chem* (1998) 273 p. 9443-9.
371. Zhu, M., Souillac, P. O., Ionescu-Zanetti, C., Carter, S. A. and Fink, A. L.: Surface-catalyzed amyloid fibril formation. *J Biol Chem* (2002) 277 p. 50914-22.
372. McLean, L. R. and Balasubramaniam, A.: Promotion of beta-structure by interaction of diabetes associated polypeptide (amylin) with phosphatidylcholine. *Biochim Biophys Acta* (1992) 1122 p. 317-20.
373. Knight, J. D., Hebda, J. A. and Miranker, A. D.: Conserved and Cooperative Assembly of Membrane-Bound alpha-Helical States of Islet Amyloid Polypeptide. *Biochemistry* (2006) 45 p. 9496-508.
374. Jayasinghe, S. A. and Langen, R.: Identifying structural features of fibrillar islet amyloid polypeptide using site-directed spin labeling. *J Biol Chem* (2004) 279 p. 48420-5.
375. Antzutkin, O. N.: Amyloidosis of Alzheimer's Abeta peptides: solid-state nuclear magnetic resonance, electron paramagnetic resonance, transmission electron microscopy, scanning transmission electron microscopy and atomic force microscopy studies. *Magn Reson Chem* (2004) 42 p. 231-46.
376. Hertel, C., Terzi, E., Hauser, N., Jakob-Rotne, R., Seelig, J. and Kemp, J. A.: Inhibition of the electrostatic interaction between beta-amyloid peptide and membranes prevents beta-amyloid-induced toxicity. *Proc Natl Acad Sci U S A* (1997) 94 p. 9412-6.
377. Gorbenko, G. P., Ioffe, V. M. and Kinnunen, P. K.: Binding of lysozyme to phospholipid bilayers: evidence for protein aggregation upon membrane association. *Biophys J* (2007) 93 p. 140-53.
378. Necula, M., Chirita, C. N. and Kuret, J.: Rapid anionic micelle-mediated alpha-synuclein fibrillization in vitro. *J Biol Chem* (2003) 278 p. 46674-80.
379. Chirita, C. N., Necula, M. and Kuret, J.: Anionic micelles and vesicles induce tau fibrillization in vitro. *J Biol Chem* (2003) 278 p. 25644-50.
380. Lee, H. J., Choi, C. and Lee, S. J.: Membrane-bound alpha-synuclein has a high aggregation propensity and the ability to seed the aggregation of the cytosolic form. *J Biol Chem* (2002) 277 p. 671-8.
381. Ji, S. R., Wu, Y. and Sui, S. F.: Cholesterol is an important factor affecting the membrane insertion of beta-amyloid peptide (A beta 1-40), which may potentially inhibit the fibril formation. *J Biol Chem* (2002) 277 p. 6273-9.
382. Yip, C. M., Elton, E. A., Darabie, A. A., Morrison, M. R. and McLaurin, J.: Cholesterol, a modulator of membrane-

associated Abeta-fibrillogenesis and neurotoxicity. *J Mol Biol* (2001) 311 p. 723-34.
383. Martins, I. C., Kuperstein, I., Wilkinson, H., Maes, E., Vanbrabant, M., Jonckheere, W., Van Gelder, P., Hartmann, D., D'Hooge, R., De Strooper, B., Schymkowitz, J. and Rousseau, F.: Lipids revert inert Abeta amyloid fibrils to neurotoxic protofibrils that affect learning in mice. *Embo J* (2008) 27 p. 224-33.
384. Rubinsztein, D. C.: The roles of intracellular protein-degradation pathways in neurodegeneration. *Nature* (2006) 443 p. 780-6.
385. Kruger, R., Kuhn, W., Leenders, K. L., Sprengelmeyer, R., Muller, T., Woitalla, D., Portman, A. T., Maguire, R. P., Veenma, L., Schroder, U., Schols, L., Epplen, J. T., Riess, O. and Przuntek, H.: Familial parkinsonism with synuclein pathology: clinical and PET studies of A30P mutation carriers. *Neurology* (2001) 56 p. 1355-62.
386. Checler, F., Alves da Costa, C., Ancolio, K., Chevallier, N., Lopez-Perez, E. and Marambaud, P.: Role of the proteasome in Alzheimer's disease. *Biochimica et Biophysica Acta (BBA) - Molecular Basis of Disease* (2000) 1502 p. 133-8.
387. Finkel, T. and Holbrook, N. J.: Oxidants, oxidative stress and the biology of ageing. *Nature* (2000) 408 p. 239-47.
388. Smith, M. A., Rottkamp, C. A., Nunomura, A., Raina, A. K. and Perry, G.: Oxidative stress in Alzheimer's disease. *Biochimica et Biophysica Acta (BBA) - Molecular Basis of Disease* (2000) 1502 p. 139-44.
389. Mattson, M. P.: Modification of ion homeostasis by lipid peroxidation: roles in neuronal degeneration and adaptive plasticity. *Trends Neurosci* (1998) 21 p. 53-7.
390. Farooqui, A. A. and Horrocks, L. A.: Lipid peroxides in the free radical pathophysiology of brain diseases. *Cell Mol Neurobiol* (1998) 18 p. 599-608.
391. Rakhit, R., Cunningham, P., Furtos-Matei, A., Dahan, S., Qi, X. F., Crow, J. P., Cashman, N. R., Kondejewski, L. H. and Chakrabartty, A.: Oxidation-induced misfolding and aggregation of superoxide dismutase and its implications for amyotrophic lateral sclerosis. *J Biol Chem* (2002) 277 p. 47551-6.
392. Smith, W. W., Margolis, R. L., Li, X., Troncoso, J. C., Lee, M. K., Dawson, V. L., Dawson, T. M., Iwatsubo, T. and Ross, C. A.: Alpha-synuclein phosphorylation enhances eosinophilic cytoplasmic inclusion formation in SH-SY5Y cells. *J Neurosci* (2005) 25 p. 5544-52.
393. Huang, X., Atwood, C. S., Hartshorn, M. A., Multhaup, G., Goldstein, L. E., Scarpa, R. C., Cuajungco, M. P., Gray, D. N., Lim, J., Moir, R. D., Tanzi, R. E. and Bush, A. I.: The A beta peptide of Alzheimer's disease directly produces hydrogen peroxide through metal ion reduction. *Biochemistry* (1999) 38 p. 7609-16.
394. Huang, X., Cuajungco, M. P., Atwood, C. S., Hartshorn, M. A., Tyndall, J. D., Hanson, G. R., Stokes, K. C., Leopold, M., Multhaup, G., Goldstein, L. E., Scarpa, R. C., Saunders, A. J., Lim, J., Moir, R. D., Glabe, C., Bowden, E. F., Masters, C. L., Fairlie, D. P., Tanzi, R. E. and Bush, A. I.: Cu(II) potentiation of alzheimer abeta neurotoxicity. Correlation with cell-free hydrogen peroxide production and metal reduction. *J Biol Chem* (1999) 274 p. 37111-6.
395. Sayre, L. M., Perry, G., Harris, P. L., Liu, Y., Schubert, K. A. and Smith, M. A.: In situ oxidative catalysis by neurofibrillary tangles and senile plaques in Alzheimer's disease: a central role for bound transition metals. *J Neurochem* (2000) 74 p. 270-9.
396. Lovell, M. A., Robertson, J. D., Teesdale, W. J., Campbell, J. L. and Markesbery, W. R.: Copper, iron and zinc in Alzheimer's disease senile plaques. *J Neurol Sci* (1998) 158 p. 47-52.
397. Bush, A. I., Pettingell, W. H., Multhaup, G., d Paradis, M., Vonsattel, J. P., Gusella, J. F., Beyreuther, K., Masters, C. L. and Tanzi, R. E.: Rapid induction of Alzheimer A beta amyloid formation by zinc. *Science* (1994) 265 p. 1464-7.
398. Atwood, C. S., Moir, R. D., Huang, X., Scarpa, R. C., Bacarra, N. M., Romano, D. M., Hartshorn, M. A., Tanzi, R. E. and Bush, A. I.: Dramatic aggregation of Alzheimer abeta by Cu(II) is induced by conditions representing physiological acidosis. *J Biol Chem* (1998) 273 p. 12817-26.
399. Hsu, L. J., Sagara, Y., Arroyo, A., Rockenstein, E., Sisk, A., Mallory, M., Wong, J., Takenouchi, T., Hashimoto, M. and Masliah, E.: alpha-synuclein promotes mitochondrial deficit and oxidative stress. *Am J Pathol* (2000) 157 p. 401-10.
400. Rodrigues, C. M., Sola, S., Silva, R. and Brites, D.: Bilirubin and amyloid-beta peptide induce cytochrome c release through mitochondrial membrane permeabilization. *Mol Med* (2000) 6 p. 936-46.
401. Kim, H. S., Lee, J. H., Lee, J. P., Kim, E. M., Chang, K. A., Park, C. H., Jeong, S. J., Wittendorp, M. C., Seo, J. H., Choi, S. H. and Suh, Y. H.: Amyloid beta peptide induces cytochrome C release from isolated mitochondria. *Neuroreport* (2002) 13 p. 1989-93.
402. Rodrigues, C. M., Sola, S., Brito, M. A., Brondino, C. D., Brites, D. and Moura, J. J.: Amyloid beta-peptide disrupts mitochondrial membrane lipid and protein structure: protective role of tauroursodeoxycholate. *Biochem Biophys Res Commun* (2001) 281 p. 468-74.
403. Panov, A. V., Gutekunst, C. A., Leavitt, B. R., Hayden, M. R., Burke, J. R., Strittmatter, W. J. and Greenamyre, J. T.: Early mitochondrial calcium defects in Huntington's disease are a direct effect of polyglutamines. *Nat Neurosci* (2002) 5 p. 731-6.
404. Tanaka, K., Waxman, L. and Goldberg, A. L.: ATP serves two distinct roles in protein degradation in reticulocytes, one requiring and one independent of ubiquitin. *J Cell Biol* (1983) 96 p. 1580-5.
405. Lindersson, E., Beedholm, R., Hojrup, P., Moos, T., Gai, W., Hendil, K. B. and Jensen, P. H.: Proteasomal inhibition by alpha-synuclein filaments and oligomers. *J Biol Chem* (2004) 279 p. 12924-34.
406. McNaught, K. S., Belizaire, R., Isacson, O., Jenner, P. and Olanow, C. W.: Altered proteasomal function in sporadic Parkinson's disease. *Exp Neurol* (2003) 179 p. 38-46.
407. Griffin, W. S., Sheng, J. G., Royston, M. C., Gentleman, S. M., McKenzie, J. E., Graham, D. I., Roberts, G. W. and

Mrak, R. E.: Glial-neuronal interactions in Alzheimer's disease: the potential role of a 'cytokine cycle' in disease progression. *Brain Pathol* (1998) 8 p. 65-72.
408. Emmerling, M. R., Watson, M. D., Raby, C. A. and Spiegel, K.: The role of complement in Alzheimer's disease pathology. *Biochim Biophys Acta* (2000) 1502 p. 158-71.
409. Wyss-Coray, T.: Inflammation in Alzheimer disease: driving force, bystander or beneficial response? *Nature Medicine* (2006) 12 p. 1005-15.
410. Kalaria, R. N.: The role of cerebral ischemia in Alzheimer's disease. *Neurobiol Aging* (2000) 21 p. 321-30.
411. Miravalle, L., Tokuda, T., Chiarle, R., Giaccone, G., Bugiani, O., Tagliavini, F., Frangione, B. and Ghiso, J.: Substitutions at codon 22 of Alzheimer's abeta peptide induce diverse conformational changes and apoptotic effects in human cerebral endothelial cells. *J Biol Chem* (2000) 275 p. 27110-6.
412. Kaduszkiewicz, H., Zimmermann, T., Beck-Bornholdt, H. P. and van den Bussche, H.: Cholinesterase inhibitors for patients with Alzheimer's disease: systematic review of randomised clinical trials. *Bmj* (2005) 331 p. 321-7.
413. Mayeux, R. and Sano, M.: Treatment of Alzheimer's disease. *N Engl J Med* (1999) 341 p. 1670-9.
414. Rao, S. S., Hofmann, L. A. and Shakil, A.: Parkinson's disease: diagnosis and treatment. *Am Fam Physician* (2006) 74 p. 2046-54.
415. Weggen, S., Eriksen, J. L., Das, P., Sagi, S. A., Wang, R., Pietrzik, C. U., Findlay, K. A., Smith, T. E., Murphy, M. P., Bulter, T., Kang, D. E., Marquez-Sterling, N., Golde, T. E. and Koo, E. H.: A subset of NSAIDs lower amyloidogenic Abeta42 independently of cyclooxygenase activity. *Nature* (2001) 414 p. 212-6.
416. Morihara, T., Chu, T., Ubeda, O., Beech, W. and Cole, G. M.: Selective inhibition of Abeta42 production by NSAID R-enantiomers. *J Neurochem* (2002) 83 p. 1009-12.
417. Eriksen, J. L., Sagi, S. A., Smith, T. E., Weggen, S., Das, P., McLendon, D. C., Ozols, V. V., Jessing, K. W., Zavitz, K. H., Koo, E. H. and Golde, T. E.: NSAIDs and enantiomers of flurbiprofen target gamma-secretase and lower Abeta 42 in vivo. *J Clin Invest* (2003) 112 p. 440-9.
418. Fleisher, A. S., Raman, R., Siemers, E. R., Becerra, L., Clark, C. M., Dean, R. A., Farlow, M. R., Galvin, J. E., Peskind, E. R., Quinn, J. F., Sherzai, A., Sowell, B. B., Aisen, P. S. and Thal, L. J.: Phase 2 safety trial targeting amyloid beta production with a gamma-secretase inhibitor in Alzheimer disease. *Arch Neurol* (2008) 65 p. 1031-8.
419. Abramowski, D., Wiederhold, K. H., Furrer, U., Jaton, A. L., Neuenschwander, A., Runser, M. J., Danner, S., Reichwald, J., Ammaturo, D., Staab, D., Stoeckli, M., Rueeger, H., Neumann, U. and Staufenbiel, M.: Dynamics of Abeta turnover and deposition in different beta-amyloid precursor protein transgenic mouse models following gamma-secretase inhibition. *J Pharmacol Exp Ther* (2008) 327 p. 411-24.
420. Spilman, P., Lessard, P., Sattavat, M., Bush, C., Tousseyn, T., Huang, E. J., Giles, K., Golde, T., Das, P., Fauq, A., Prusiner, S. B. and Dearmond, S. J.: A gamma-secretase inhibitor and quinacrine reduce prions and prevent dendritic degeneration in murine brains. *Proc Natl Acad Sci U S A* (2008) 105 p. 10595-600.
421. Yang, F., Lim, G. P., Begum, A. N., Ubeda, O. J., Simmons, M. R., Ambegaokar, S. S., Chen, P. P., Kayed, R., Glabe, C. G., Frautschy, S. A. and Cole, G. M.: Curcumin inhibits formation of amyloid beta oligomers and fibrils, binds plaques, and reduces amyloid in vivo. *J Biol Chem* (2005) 280 p. 5892-901.
422. Cheng, X. and van Breemen, R. B.: Mass spectrometry-based screening for inhibitors of beta-amyloid protein aggregation. *Anal Chem* (2005) 77 p. 7012-5.
423. De Felice, F. G., Houzel, J. C., Garcia-Abreu, J., Louzada, P. R., Jr., Afonso, R. C., Meirelles, M. N., Lent, R., Neto, V. M. and Ferreira, S. T.: Inhibition of Alzheimer's disease beta-amyloid aggregation, neurotoxicity, and in vivo deposition by nitrophenols: implications for Alzheimer's therapy. *Faseb J* (2001) 15 p. 1297-9.
424. Howlett, D. R., George, A. R., Owen, D. E., Ward, R. V. and Markwell, R. E.: Common structural features determine the effectiveness of carvedilol, daunomycin and rolitetracycline as inhibitors of Alzheimer beta-amyloid fibril formation. *Biochem J* (1999) 343 Pt 2 p. 419-23.
425. Howlett, D. R., Perry, A. E., Godfrey, F., Swatton, J. E., Jennings, K. H., Spitzfaden, C., Wadsworth, H., Wood, S. J. and Markwell, R. E.: Inhibition of fibril formation in beta-amyloid peptide by a novel series of benzofurans. *Biochem J* (1999) 340 (Pt 1) p. 283-9.
426. Lashuel, H. A., Hartley, D. M., Balakhaneh, D., Aggarwal, A., Teichberg, S. and Callaway, D. J.: New class of inhibitors of amyloid-beta fibril formation. Implications for the mechanism of pathogenesis in Alzheimer's disease. *J Biol Chem* (2002) 277 p. 42881-90.
427. Lorenzo, A. and Yankner, B. A.: Beta-amyloid neurotoxicity requires fibril formation and is inhibited by congo red. *Proc Natl Acad Sci U S A* (1994) 91 p. 12243-7.
428. Ono, K., Hasegawa, K., Naiki, H. and Yamada, M.: Anti-amyloidogenic activity of tannic acid and its activity to destabilize Alzheimer's beta-amyloid fibrils in vitro. *Biochim Biophys Acta* (2004) 1690 p. 193-202.
429. Ono, K., Hasegawa, K., Naiki, H. and Yamada, M.: Curcumin has potent anti-amyloidogenic effects for Alzheimer's beta-amyloid fibrils in vitro. *J Neurosci Res* (2004) 75 p. 742-50.
430. Ono, K., Yoshiike, Y., Takashima, A., Hasegawa, K., Naiki, H. and Yamada, M.: Vitamin A exhibits potent antiamyloidogenic and fibril-destabilizing effects in vitro. *Exp Neurol* (2004) 189 p. 380-92.
431. Pappolla, M., Bozner, P., Soto, C., Shao, H., Robakis, N. K., Zagorski, M., Frangione, B. and Ghiso, J.: Inhibition of Alzheimer beta-fibrillogenesis by melatonin. *J Biol Chem* (1998) 273 p. 7185-8.
432. Pollack, S. J., Sadler, II, Hawtin, S. R., Tailor, V. J. and Shearman, M. S.: Sulfonated dyes attenuate the toxic effects of beta-amyloid in a structure-specific fashion. *Neurosci Lett* (1995) 197 p. 211-4.

433. Sadler, II, Hawtin, S. R., Tailor, V., Shearman, M. S. and Pollack, S. J.: Glycosaminoglycans and sulphated polyanions attenuate the neurotoxic effects of beta-amyloid. *Biochem Soc Trans* (1995) 23 p. 106S.
434. Sadler, II, Smith, D. W., Shearman, M. S., Ragan, C. I., Tailor, V. J. and Pollack, S. J.: Sulphated compounds attenuate beta-amyloid toxicity by inhibiting its association with cells. *Neuroreport* (1995) 7 p. 49-53.
435. Tomiyama, T., Asano, S., Suwa, Y., Morita, T., Kataoka, K., Mori, H. and Endo, N.: Rifampicin prevents the aggregation and neurotoxicity of amyloid beta protein in vitro. *Biochem Biophys Res Commun* (1994) 204 p. 76-83.
436. Aisen, P. S., Saumier, D., Briand, R., Laurin, J., Gervais, F., Tremblay, P. and Garceau, D.: A Phase II study targeting amyloid-beta with 3APS in mild-to-moderate Alzheimer disease. *Neurology* (2006) 67 p. 1757-63.
437. Gervais, F., Paquette, J., Morissette, C., Krzywkowski, P., Yu, M., Azzi, M., Lacombe, D., Kong, X., Aman, A., Laurin, J., Szarek, W. A. and Tremblay, P.: Targeting soluble Abeta peptide with Tramiprosate for the treatment of brain amyloidosis. *Neurobiol Aging* (2007) 28 p. 537-47.
438. Aisen, P. S., Gauthier, S., Vellas, B., Briand, R., Saumier, D., Laurin, J. and Garceau, D.: Alzhemed: a potential treatment for Alzheimer's disease. *Curr Alzheimer Res* (2007) 4 p. 473-8.
439. Gervais, F., Chalifour, R., Garceau, D., Kong, X., Laurin, J., McLaughlin, R., Morissette, C. and Paquette, J.: Glycosaminoglycan mimetics: a therapeutic approach to cerebral amyloid angiopathy. *Amyloid* (2001) 8 Suppl 1 p. 28-35.
440. Sun, Y., Zhang, G., Hawkes, C. A., Shaw, J. E., McLaurin, J. and Nitz, M.: Synthesis of scyllo-inositol derivatives and their effects on amyloid beta peptide aggregation. *Bioorg Med Chem* (2008) 16 p. 7177-84.
441. Fenili, D., Brown, M., Rappaport, R. and McLaurin, J.: Properties of scyllo-inositol as a therapeutic treatment of AD-like pathology. *J Mol Med* (2007) 85 p. 603-11.
442. McLaurin, J., Golomb, R., Jurewicz, A., Antel, J. P. and Fraser, P. E.: Inositol stereoisomers stabilize an oligomeric aggregate of Alzheimer amyloid beta peptide and inhibit abeta -induced toxicity. *J Biol Chem* (2000) 275 p. 18495-502.
443. Frenkel, D., Dewachter, I., Van Leuven, F. and Solomon, B.: Reduction of beta-amyloid plaques in brain of transgenic mouse model of Alzheimer's disease by EFRH-phage immunization. *Vaccine* (2003) 21 p. 1060-5.
444. Schenk, D., Barbour, R., Dunn, W., Gordon, G., Grajeda, H., Guido, T., Hu, K., Huang, J., Johnson-Wood, K., Khan, K., Kholodenko, D., Lee, M., Liao, Z., Lieberburg, I., Motter, R., Mutter, L., Soriano, F., Shopp, G., Vasquez, N., Vandevert, C., Walker, S., Wogulis, M., Yednock, T., Games, D. and Seubert, P.: Immunization with amyloid-beta attenuates Alzheimer-disease-like pathology in the PDAPP mouse. *Nature* (1999) 400 p. 173-7.
445. Janus, C., Pearson, J., McLaurin, J., Mathews, P. M., Jiang, Y., Schmidt, S. D., Chishti, M. A., Horne, P., Heslin, D., French, J., Mount, H. T., Nixon, R. A., Mercken, M., Bergeron, C., Fraser, P. E., St George-Hyslop, P. and Westaway, D.: A beta peptide immunization reduces behavioural impairment and plaques in a model of Alzheimer's disease. *Nature* (2000) 408 p. 979-82.
446. Bard, F., Cannon, C., Barbour, R., Burke, R. L., Games, D., Grajeda, H., Guido, T., Hu, K., Huang, J., Johnson-Wood, K., Khan, K., Kholodenko, D., Lee, M., Lieberburg, I., Motter, R., Nguyen, M., Soriano, F., Vasquez, N., Weiss, K., Welch, B., Seubert, P., Schenk, D. and Yednock, T.: Peripherally administered antibodies against amyloid beta-peptide enter the central nervous system and reduce pathology in a mouse model of Alzheimer disease. *Nat Med* (2000) 6 p. 916-9.
447. DeMattos, R. B., Bales, K. R., Cummins, D. J., Dodart, J. C., Paul, S. M. and Holtzman, D. M.: Peripheral anti-A beta antibody alters CNS and plasma A beta clearance and decreases brain A beta burden in a mouse model of Alzheimer's disease. *Proc Natl Acad Sci U S A* (2001) 98 p. 8850-5.
448. Nicoll, J. A., Wilkinson, D., Holmes, C., Steart, P., Markham, H. and Weller, R. O.: Neuropathology of human Alzheimer disease after immunization with amyloid-beta peptide: a case report. *Nat Med* (2003) 9 p. 448-52.
449. Ferrer, I., Boada Rovira, M., Sanchez Guerra, M. L., Rey, M. J. and Costa-Jussa, F.: Neuropathology and pathogenesis of encephalitis following amyloid-beta immunization in Alzheimer's disease. *Brain Pathol* (2004) 14 p. 11-20.
450. Bombois, S., Maurage, C. A., Gompel, M., Deramecourt, V., Mackowiak-Cordoliani, M. A., Black, R. S., Lavielle, R., Delacourte, A. and Pasquier, F.: Absence of beta-amyloid deposits after immunization in Alzheimer disease with Lewy body dementia. *Arch Neurol* (2007) 64 p. 583-7.
451. Dodel, R. C., Du, Y., Depboylu, C., Hampel, H., Frolich, L., Haag, A., Hemmeter, U., Paulsen, S., Teipel, S. J., Brettschneider, S., Spottke, A., Nolker, C., Moller, H. J., Wei, X., Farlow, M., Sommer, N. and Oertel, W. H.: Intravenous immunoglobulins containing antibodies against beta-amyloid for the treatment of Alzheimer's disease. *J Neurol Neurosurg Psychiatry* (2004) 75 p. 1472-4.
452. Moretto, N., Bolchi, A., Rivetti, C., Imbimbo, B. P., Villetti, G., Pietrini, V., Polonelli, L., Del Signore, S., Smith, K. M., Ferrante, R. J. and Ottonello, S.: Conformation-sensitive antibodies against alzheimer amyloid-beta by immunization with a thioredoxin-constrained B-cell epitope peptide. *J Biol Chem* (2007) 282 p. 11436-45.
453. Geylis, V. and Steinitz, M.: Immunotherapy of Alzheimer's disease (AD): from murine models to anti-amyloid beta (Abeta) human monoclonal antibodies. *Autoimmun Rev* (2006) 5 p. 33-9.
454. Geylis, V., Kourilov, V., Meiner, Z., Nennesmo, I., Bogdanovic, N. and Steinitz, M.: Human monoclonal antibodies against amyloid-beta from healthy adults. *Neurobiol Aging* (2005) 26 p. 597-606.
455. Lee, E. B., Leng, L. Z., Zhang, B., Kwong, L., Trojanowski, J. Q., Abel, T. and Lee, V. M.: Targeting amyloid-beta peptide (Abeta) oligomers by passive immunization with a conformation-selective monoclonal antibody improves learning and memory in Abeta precursor protein (APP) transgenic mice. *J Biol Chem* (2006) 281 p. 4292-9.

456. Melnikova, I.: Therapies for Alzheimer's disease. *Nat Rev Drug Discov* (2007) 6 p. 341-2.
457. Lemere, C. A., Maier, M., Jiang, L., Peng, Y. and Seabrook, T. J.: Amyloid-beta immunotherapy for the prevention and treatment of Alzheimer disease: lessons from mice, monkeys, and humans. *Rejuvenation Res* (2006) 9 p. 77-84.
458. Bachurin, S., Bukatina, E., Lermontova, N., Tkachenko, S., Afanasiev, A., Grigoriev, V., Grigorieva, I., Ivanov, Y., Sablin, S. and Zefirov, N.: Antihistamine agent Dimebon as a novel neuroprotector and a cognition enhancer. *Ann N Y Acad Sci* (2001) 939 p. 425-35.
459. Doody, R. S., Gavrilova, S. I., Sano, M., Thomas, R. G., Aisen, P. S., Bachurin, S. O., Seely, L. and Hung, D.: Effect of dimebon on cognition, activities of daily living, behaviour, and global function in patients with mild-to-moderate Alzheimer's disease: a randomised, double-blind, placebo-controlled study. *Lancet* (2008) 372 p. 207-15.
460. Lermontova, N. N., Redkozubov, A. E., Shevtsova, E. F., Serkova, T. P., Kireeva, E. G. and Bachurin, S. O.: Dimebon and tacrine inhibit neurotoxic action of beta-amyloid in culture and block L-type Ca(2+) channels. *Bull Exp Biol Med* (2001) 132 p. 1079-83.
461. Lannfelt, L., Blennow, K., Zetterberg, H., Batsman, S., Ames, D., Harrison, J., Masters, C. L., Targum, S., Bush, A. I., Murdoch, R., Wilson, J. and Ritchie, C. W.: Safety, efficacy, and biomarker findings of PBT2 in targeting Abeta as a modifying therapy for Alzheimer's disease: a phase IIa, double-blind, randomised, placebo-controlled trial. *Lancet Neurol* (2008) 7 p. 779-86.
462. Kopito, R. R.: Aggresomes, inclusion bodies and protein aggregation. *Trends Cell Biol* (2000) 10 p. 524-30.
463. Chen, L. and Feany, M. B.: Alpha-synuclein phosphorylation controls neurotoxicity and inclusion formation in a Drosophila model of Parkinson disease. *Nat Neurosci* (2005) 8 p. 657-63.
464. Pieri, L., Bucciantini, M., Nosi, D., Formigli, L., Savistchenko, J., Melki, R. and Stefani, M.: The yeast prion Ure2p native-like assemblies are toxic to mammalian cells regardless of their aggregation state. *J Biol Chem* (2006) 281 p. 15337-44.
465. Isaacs, A. M., Senn, D. B., Yuan, M., Shine, J. P. and Yankner, B. A.: Acceleration of amyloid beta-peptide aggregation by physiological concentrations of calcium. *J Biol Chem* (2006) 281 p. 27916-23.
466. Worster-Drought, C., Hill, T. and McMenemey, W.: Familial Presenile Dementia with Spastic Paralysis. *J Neurol Psychopathol* (1933) 14 p. 27-34.
467. Worster-Drought, C., Greenfield, J. and McMenemey, W.: A form of familial presenile dementia with spastic paralysis (including the pathological examination of a case). *Brain* (1940) 63 p. 237-54.
468. Mead, S., James-Galton, M., Revesz, T., Doshi, R. B., Harwood, G., Pan, E. L., Ghiso, J., Frangione, B. and Plant, G.: Familial British dementia with amyloid angiopathy: early clinical, neuropsychological and imaging findings. *Brain* (2000) 123 (Pt 5) p. 975-91.
469. Plant, G. T., Revesz, T., Barnard, R. O., Harding, A. E. and Gautier-Smith, P. C.: Familial cerebral amyloid angiopathy with nonneuritic amyloid plaque formation. *Brain* (1990) 113 (Pt 3) p. 721-47.
470. Love, S. and Duchen, L. W.: Familial cerebellar ataxia with cerebrovascular amyloid. *J Neurol Neurosurg Psychiatry* (1982) 45 p. 271-3.
471. Griffiths, R. A., Mortimer, T. F., Oppenheimer, D. R. and Spalding, J. M.: Congophilic angiopathy of the brain: a clinical and pathological report on two siblings. *J Neurol Neurosurg Psychiatry* (1982) 45 p. 396-408.
472. Doshi, R. B., Revesz, T., Harwood, G. and Plant, G.: Familial cerebral amyloid angiopathy (British type) with nonneuritic plaque formation is not restricted to a single family. *Neuropathol Appl Neurobiol* (1996) 22 p. 2.
473. Ghiso, J., Rostagno, A., Tomidokoro, Y., Lashley, T., Bojsen-Moller, M., Braendgaard, H., Plant, G., Holton, J., Lal, R., Revesz, T. and Frangione, B.: Genetic alterations of the BRI2 gene: familial British and Danish dementias. *Brain Pathol* (2006) 16 p. 71-9.
474. Holton, J. L., Ghiso, J., Lashley, T., Rostagno, A., Guerin, C. J., Gibb, G., Houlden, H., Ayling, H., Martinian, L., Anderton, B. H., Wood, N. W., Vidal, R., Plant, G., Frangione, B. and Revesz, T.: Regional distribution of amyloid-Bri deposition and its association with neurofibrillary degeneration in familial British dementia. *Am J Pathol* (2001) 158 p. 515-26.
475. Ghiso, J. A., Holton, J., Miravalle, L., Calero, M., Lashley, T., Vidal, R., Houlden, H., Wood, N., Neubert, T. A., Rostagno, A., Plant, G., Revesz, T. and Frangione, B.: Systemic amyloid deposits in familial British dementia. *J Biol Chem* (2001) 276 p. 43909-14.
476. Holton, J. L., Ghiso, J., Lashley, T., Ganguly, M., Strand, K., Rostagno, A., Plant, G., Frangione, B. and Revesz, T.: Familial British dementia (FBD): a cerebral amyloidosis with systemic amyloid deposition. *Neuropathol Appl Neurobiol* (2002) 28 p. 148-.
477. Joachim, C. L., Mori, H. and Selkoe, D. J.: Amyloid beta-protein deposition in tissues other than brain in Alzheimer's disease. *Nature* (1989) 341 p. 226-30.
478. Gudmundsson, G., Hallgrimsson, J., Jonasson, T. A. and Bjarnason, O.: Hereditary cerebral haemorrhage with amyloidosis. *Brain* (1972) 95 p. 387-404.
479. Benedikz, E., Blondal, H. and Gudmundsson, G.: Skin deposits in hereditary cystatin C amyloidosis. *Virchows Arch A Pathol Anat Histopathol* (1990) 417 p. 325-31.
480. Vidal, R., Frangione, B., Rostagno, A., Mead, S., Revesz, T., Plant, G. and Ghiso, J.: A stop-codon mutation in the BRI gene associated with familial British dementia. *Nature* (1999) 399 p. 776-81.
481. Lashley, T., Holton, J. L., Verbeek, M. M., Rostagno, A., Bojsen-Moller, M., David, G., van Horssen, J., Braendgaard, H., Plant, G., Frangione, B., Ghiso, J. and Revesz, T.: Molecular chaperons, amyloid and preamyloid lesions in the

BRI2 gene-related dementias: a morphological study. *Neuropathol Appl Neurobiol* (2006) 32 p. 492-504.
482. Baumann, M. H., Wisniewski, T., Levy, E., Plant, G. T. and Ghiso, J.: C-terminal fragments of alpha- and beta-tubulin form amyloid fibrils in vitro and associate with amyloid deposits of familial cerebral amyloid angiopathy, British type. *Biochem Biophys Res Commun* (1996) 219 p. 238-42.
483. Stromgren, E., Dalby, A., Dalby, M. A. and Ranheim, B.: Cataract, deafness, cerebellar ataxia, psychosis and dementia—a new syndrome. *Acta Neurol Scand* (1970) 46 p. Suppl 43:261+.
484. Holton, J. L., Lashley, T., Ghiso, J., Braendgaard, H., Vidal, R., Guerin, C. J., Gibb, G., Hanger, D. P., Rostagno, A., Anderton, B. H., Strand, C., Ayling, H., Plant, G., Frangione, B., Bojsen-Moller, M. and Revesz, T.: Familial Danish dementia: a novel form of cerebral amyloidosis associated with deposition of both amyloid-Dan and amyloid-beta. *J Neuropathol Exp Neurol* (2002) 61 p. 254-67.
485. Bek, T.: Ocular changes in heredo-oto-ophthalmo-encephalopathy. *Br J Ophthalmol* (2000) 84 p. 1298-302.
486. Vidal, R., Revesz, T., Rostagno, A., Kim, E., Holton, J. L., Bek, T., Bojsen-Moller, M., Braendgaard, H., Plant, G., Ghiso, J. and Frangione, B.: A decamer duplication in the 3' region of the BRI gene originates an amyloid peptide that is associated with dementia in a Danish kindred. *Proc Natl Acad Sci U S A* (2000) 97 p. 4920-5.
487. Rostagno, A., Revesz, T., Lashley, T., Tomidokoro, Y., Magnotti, L., Braendgaard, H., Plant, G., Bojsen-Moller, M., Holton, J., Frangione, B. and Ghiso, J.: Complement activation in chromosome 13 dementias. Similarities with Alzheimer's disease. *J Biol Chem* (2002) 277 p. 49782-90.
488. Tomidokoro, Y., Lashley, T., Rostagno, A., Neubert, T. A., Bojsen-Moller, M., Braendgaard, H., Plant, G., Holton, J., Frangione, B., Revesz, T. and Ghiso, J.: Familial Danish dementia: co-existence of Danish and Alzheimer amyloid subunits (ADan AND Abeta) in the absence of compact plaques. *J Biol Chem* (2005) 280 p. 36883-94.
489. Rostagno, A., Tomidokoro, Y., Lashley, T., Ng, D., Plant, G., Holton, J., Frangione, B., Revesz, T. and Ghiso, J.: Chromosome 13 dementias. *Cell Mol Life Sci* (2005) 62 p. 1814-25.
490. Levy, E., Sastre, M., Kumar, A., Gallo, G., Piccardo, P., Ghetti, B. and Tagliavini, F.: Codeposition of cystatin C with amyloid-beta protein in the brain of Alzheimer disease patients. *J Neuropathol Exp Neurol* (2001) 60 p. 94-104.
491. Bertram, L., McQueen, M. B., Mullin, K., Blacker, D. and Tanzi, R. E.: Systematic meta-analyses of Alzheimer disease genetic association studies: the AlzGene database. *Nat Genet* (2007) 39 p. 17-23.
492. Sastre, M., Calero, M., Pawlik, M., Mathews, P. M., Kumar, A., Danilov, V., Schmidt, S. D., Nixon, R. A., Frangione, B. and Levy, E.: Binding of cystatin C to Alzheimer's amyloid beta inhibits in vitro amyloid fibril formation. *Neurobiol Aging* (2004) 25 p. 1033-43.
493. Deleersnijder, W., Hong, G., Cortvrindt, R., Poirier, C., Tylzanowski, P., Pittois, K., Van Marck, E. and Merregaert, J.: Isolation of markers for chondro-osteogenic differentiation using cDNA library subtraction. Molecular cloning and characterization of a gene belonging to a novel multigene family of integral membrane proteins. *J Biol Chem* (1996) 271 p. 19475-82.
494. Mao, M., Fu, G., Wu, J. S., Zhang, Q. H., Zhou, J., Kan, L. X., Huang, Q. H., He, K. L., Gu, B. W., Han, Z. G., Shen, Y., Gu, J., Yu, Y. P., Xu, S. H., Wang, Y. X., Chen, S. J. and Chen, Z.: Identification of genes expressed in human CD34(+) hematopoietic stem/progenitor cells by expressed sequence tags and efficient full-length cDNA cloning. *Proc Natl Acad Sci U S A* (1998) 95 p. 8175-80.
495. Vidal, R., Calero, M., Revesz, T., Plant, G., Ghiso, J. and Frangione, B.: Sequence, genomic structure and tissue expression of Human BRI3, a member of the BRI gene family. *Gene* (2001) 266 p. 95-102.
496. Choi, S. C., Kim, J., Kim, T. H., Cho, S. Y., Park, S. S., Kim, K. D. and Lee, S. H.: Cloning and characterization of a type II integral transmembrane protein gene, Itm2c, that is highly expressed in the mouse brain. *Mol Cells* (2001) 12 p. 391-7.
497. Pittois, K., Deleersnijder, W. and Merregaert, J.: cDNA sequence analysis, chromosomal assignment and expression pattern of the gene coding for integral membrane protein 2B. *Gene* (1998) 217 p. 141-9.
498. Akiyama, H., Kondo, H., Arai, T., Ikeda, K., Kato, M., Iseki, E., Schwab, C. and McGeer, P. L.: Expression of BRI, the normal precursor of the amyloid protein of familial British dementia, in human brain. *Acta Neuropathol (Berl)* (2004) 107 p. 53-8.
499. Pickford, F., Onstead, L., Camacho-Prihar, C., Hardy, J. and McGowan, E.: Expression of mBRI2 in mice. *Neurosci Lett* (2003) 338 p. 95-8.
500. Pittois, K., Wauters, J., Bossuyt, P., Deleersnijder, W. and Merregaert, J.: Genomic organization and chromosomal localization of the Itm2a gene. *Mamm Genome* (1999) 10 p. 54-6.
501. Kall, L., Krogh, A. and Sonnhammer, E. L.: A combined transmembrane topology and signal peptide prediction method. *J Mol Biol* (2004) 338 p. 1027-36.
502. Kall, L., Krogh, A. and Sonnhammer, E. L.: Advantages of combined transmembrane topology and signal peptide prediction—the Phobius web server. *Nucleic Acids Res* (2007) 35 p. W429-32.
503. Ghiso, J., Revesz, T., Holton, J., Rostagno, A., Lashley, T., Houlden, H., Gibb, G., Anderton, B., Bek, T., Bojsen-Moller, M., Wood, N., Vidal, R., Braendgaard, H., Plant, G. and Frangione, B.: Chromosome 13 dementia syndromes as models of neurodegeneration. *Amyloid* (2001) 8 p. 277-84.
504. Kim, S. H., Wang, R., Gordon, D. J., Bass, J., Steiner, D. F., Lynn, D. G., Thinakaran, G., Meredith, S. C. and Sisodia, S. S.: Furin mediates enhanced production of fibrillogenic ABri peptides in familial British dementia. *Nat Neurosci* (1999) 2 p. 984-8.
505. Rost, B., Fariselli, P. and Casadio, R.: Topology prediction for helical transmembrane proteins at 86% accuracy.

Protein Sci (1996) 5 p. 1704-18.
506. de Castro, E., Sigrist, C. J., Gattiker, A., Bulliard, V., Langendijk-Genevaux, P. S., Gasteiger, E., Bairoch, A. and Hulo, N.: ScanProsite: detection of PROSITE signature matches and ProRule-associated functional and structural residues in proteins. *Nucleic Acids Res* (2006) 34 p. W362-5.
507. Kirchner, J. and Bevan, M. J.: ITM2A is induced during thymocyte selection and T cell activation and causes downregulation of CD8 when overexpressed in CD4(+)CD8(+) double positive thymocytes. *J Exp Med* (1999) 190 p. 217-28.
508. Schwab, C., Hosokawa, M., Akiyama, H. and McGeer, P. L.: Familial British dementia: colocalization of furin and ABri amyloid. *Acta Neuropathol (Berl)* (2003) 106 p. 278-84.
509. Kim, S. H., Creemers, J. W., Chu, S., Thinakaran, G. and Sisodia, S. S.: Proteolytic processing of familial British dementia-associated BRI variants: evidence for enhanced intracellular accumulation of amyloidogenic peptides. *J Biol Chem* (2002) 277 p. 1872-7.
510. Kim, S. H., Wang, R., Gordon, D. J., Bass, J., Steiner, D. F., Thinakaran, G., Lynn, D. G., Meredith, S. C. and Sisodia, S. S.: Familial British dementia: expression and metabolism of BRI. *Ann N Y Acad Sci* (2000) 920 p. 93-9.
511. Choi, S. I., Vidal, R., Frangione, B. and Levy, E.: Axonal transport of British and Danish amyloid peptides via secretory vesicles. *Faseb J* (2004) 18 p. 373-5.
512. Martin, L., Fluhrer, R., Reiss, K., Kremmer, E., Saftig, P. and Haass, C.: Regulated intramembrane proteolysis of Bri2 (Itm2b) by ADAM10 and SPPL2a/SPPL2b. *J Biol Chem* (2008) 283 p. 1644-52.
513. Cheng, J., Sweredoski, M. and Baldi, P.: Accurate Prediction of Protein Disordered Regions by Mining Protein Structure Data. *Data Mining and Knowledge Discovery* (2005) 11 p. 213-22.
514. Prilusky, J., Felder, C. E., Zeev-Ben-Mordehai, T., Rydberg, E. H., Man, O., Beckmann, J. S., Silman, I. and Sussman, J. L.: FoldIndex: a simple tool to predict whether a given protein sequence is intrinsically unfolded. *Bioinformatics* (2005) 21 p. 3435-8.
515. Dosztanyi, Z., Csizmok, V., Tompa, P. and Simon, I.: The pairwise energy content estimated from amino acid composition discriminates between folded and intrinsically unstructured proteins. *J Mol Biol* (2005) 347 p. 827-39.
516. Dosztanyi, Z., Csizmok, V., Tompa, P. and Simon, I.: IUPred: web server for the prediction of intrinsically unstructured regions of proteins based on estimated energy content. *Bioinformatics* (2005) 21 p. 3433-4.
517. Linding, R., Jensen, L. J., Diella, F., Bork, P., Gibson, T. J. and Russell, R. B.: Protein disorder prediction: implications for structural proteomics. *Structure* (2003) 11 p. 1453-9.
518. Guermeur, Y.: Combinaison de classifieurs statistiques, Application a la prediction de structure secondaire des proteines. p.
519. Baldi, P., Brunak, S., Frasconi, P., Soda, G. and Pollastri, G.: Exploiting the past and the future in protein secondary structure prediction. *Bioinformatics* (1999) 15 p. 937-46.
520. Pollastri, G., Przybylski, D., Rost, B. and Baldi, P.: Improving the prediction of protein secondary structure in three and eight classes using recurrent neural networks and profiles. *Proteins* (2002) 47 p. 228-35.
521. Ouali, M. and King, R. D.: Cascaded multiple classifiers for secondary structure prediction. *Protein Sci* (2000) 9 p. 1162-76.
522. Bryson, K., McGuffin, L. J., Marsden, R. L., Ward, J. J., Sodhi, J. S. and Jones, D. T.: Protein structure prediction servers at University College London. *Nucleic Acids Res* (2005) 33 p. W36-8.
523. Jones, D. T.: Protein secondary structure prediction based on position-specific scoring matrices. *J Mol Biol* (1999) 292 p. 195-202.
524. Cuff, J. A., Clamp, M. E., Siddiqui, A. S., Finlay, M. and Barton, G. J.: JPred: A consensus secondary structure prediction server. *Bioinformatics* (1998) 14 p. 892-3.
525. Sanchez-Pulido, L., Devos, D. and Valencia, A.: BRICHOS: a conserved domain in proteins associated with dementia, respiratory distress and cancer. *Trends Biochem Sci* (2002) 27 p. 329-32.
526. Fleischer, A., Ayllon, V., Dumoutier, L., Renauld, J. C. and Rebollo, A.: Proapoptotic activity of ITM2B(s), a BH3-only protein induced upon IL-2-deprivation which interacts with Bcl-2. *Oncogene* (2002) 21 p. 3181-9.
527. Fleischer, A., Ayllon, V. and Rebollo, A.: ITM2BS regulates apoptosis by inducing loss of mitochondrial membrane potential. *Eur J Immunol* (2002) 32 p. 3498-505.
528. Fleischer, A. and Rebollo, A.: Induction of p53-independent apoptosis by the BH3-only protein ITM2Bs. *FEBS Lett* (2004) 557 p. 283-7.
529. Davis, J., Cribbs, D. H., Cotman, C. W. and Van Nostrand, W. E.: Pathogenic amyloid beta-protein induces apoptosis in cultured human cerebrovascular smooth muscle cells. *Amyloid* (1999) 6 p. 157-64.
530. Dodson, M. K., Cliby, W. A., Xu, H. J., DeLacey, K. A., Hu, S. X., Keeney, G. L., Li, J., Podratz, K. C., Jenkins, R. B. and Benedict, W. F.: Evidence of functional RB protein in epithelial ovarian carcinomas despite loss of heterozygosity at the RB locus. *Cancer Res* (1994) 54 p. 610-3.
531. Pei, L., Melmed, S., Scheithauer, B., Kovacs, K., Benedict, W. F. and Prager, D.: Frequent loss of heterozygosity at the retinoblastoma susceptibility gene (RB) locus in aggressive pituitary tumors: evidence for a chromosome 13 tumor suppressor gene other than RB. *Cancer Res* (1995) 55 p. 1613-6.
532. Yoo, G. H., Xu, H. J., Brennan, J. A., Westra, W., Hruban, R. H., Koch, W., Benedict, W. F. and Sidransky, D.: Infrequent inactivation of the retinoblastoma gene despite frequent loss of chromosome 13q in head and neck squamous cell carcinoma. *Cancer Res* (1994) 54 p. 4603-6.

533. Latil, A., Chene, L., Mangin, P., Fournier, G., Berthon, P. and Cussenot, O.: Extensive analysis of the 13q14 region in human prostate tumors: DNA analysis and quantitative expression of genes lying in the interval of deletion. *Prostate* (2003) 57 p. 39-50.
534. Rengaraj, D., Liang, X. H., Gao, F., Deng, W. B., Mills, N. and Yang, Z. M.: Differential expression and regulation of integral membrane protein 2b in rat male reproductive tissues. *Asian J Androl* (2008) 10 p. 503-11.
535. Matsuda, S., Giliberto, L., Matsuda, Y., Davies, P., McGowan, E., Pickford, F., Ghiso, J., Frangione, B. and D'Adamio, L.: The familial dementia BRI2 gene binds the Alzheimer gene amyloid-beta precursor protein and inhibits amyloid-beta production. *J Biol Chem* (2005) 280 p. 28912-6.
536. Fotinopoulou, A., Tsachaki, M., Vlavaki, M., Poulopoulos, A., Rostagno, A., Frangione, B., Ghiso, J. and Efthimiopoulos, S.: BRI2 interacts with amyloid precursor protein (APP) and regulates amyloid beta (Abeta) production. *J Biol Chem* (2005) 280 p. 30768-72.
537. Koo, E. H., Sisodia, S. S., Archer, D. R., Martin, L. J., Weidemann, A., Beyreuther, K., Fischer, P., Masters, C. L. and Price, D. L.: Precursor of amyloid protein in Alzheimer disease undergoes fast anterograde axonal transport. *Proc Natl Acad Sci U S A* (1990) 87 p. 1561-5.
538. Mori, H., Takio, K., Ogawara, M. and Selkoe, D. J.: Mass spectrometry of purified amyloid beta protein in Alzheimer's disease. *J Biol Chem* (1992) 267 p. 17082-6.
539. Saido, T. C., Iwatsubo, T., Mann, D. M., Shimada, H., Ihara, Y. and Kawashima, S.: Dominant and differential deposition of distinct beta-amyloid peptide species, A beta N3(pE), in senile plaques. *Neuron* (1995) 14 p. 457-66.
540. Saido, T. C., Yamao-Harigaya, W., Iwatsubo, T. and Kawashima, S.: Amino- and carboxyl-terminal heterogeneity of beta-amyloid peptides deposited in human brain. *Neurosci Lett* (1996) 215 p. 173-6.
541. Sykes, P. A., Watson, S. J., Temple, J. S. and Bateman, R. C., Jr.: Evidence for tissue-specific forms of glutaminyl cyclase. *FEBS Lett* (1999) 455 p. 159-61.
542. Tekirian, T. L., Saido, T. C., Markesbery, W. R., Russell, M. J., Wekstein, D. R., Patel, E. and Geddes, J. W.: N-terminal heterogeneity of parenchymal and cerebrovascular Abeta deposits. *J Neuropathol Exp Neurol* (1998) 57 p. 76-94.
543. Busby, W. H., Jr., Quackenbush, G. E., Humm, J., Youngblood, W. W. and Kizer, J. S.: An enzyme(s) that converts glutaminyl-peptides into pyroglutamyl-peptides. Presence in pituitary, brain, adrenal medulla, and lymphocytes. *J Biol Chem* (1987) 262 p. 8532-6.
544. Fischer, W. H. and Spiess, J.: Identification of a mammalian glutaminyl cyclase converting glutaminyl into pyroglutamyl peptides. *Proc Natl Acad Sci U S A* (1987) 84 p. 3628-32.
545. Garden, R. W., Moroz, T. P., Gleeson, J. M., Floyd, P. D., Li, L., Rubakhin, S. S. and Sweedler, J. V.: Formation of N-pyroglutamyl peptides from N-Glu and N-Gln precursors in Aplysia neurons. *J Neurochem* (1999) 72 p. 676-81.
546. El-Agnaf, O. M., Sheridan, J. M., Sidera, C., Siligardi, G., Hussain, R., Haris, P. I. and Austen, B. M.: Effect of the disulfide bridge and the C-terminal extension on the oligomerization of the amyloid peptide ABri implicated in familial British dementia. *Biochemistry* (2001) 40 p. 3449-57.
547. El-Agnaf, O. M., Nagala, S., Patel, B. P. and Austen, B. M.: Non-fibrillar oligomeric species of the amyloid ABri peptide, implicated in familial British dementia, are more potent at inducing apoptotic cell death than protofibrils or mature fibrils. *J Mol Biol* (2001) 310 p. 157-68.
548. Srinivasan, R., Jones, E. M., Liu, K., Ghiso, J., Marchant, R. E. and Zagorski, M. G.: pH-Dependent Amyloid and Protofibril Formation by the ABri Peptide of Familial British Dementia. *J Mol Biol* (2003) 333 p. 1003-23.
549. Mahadevan, D., Chattopadhyay, T. and Palmer, R. A.: Predicted fold for the ABri Amyloid Subunit: A Model for Amyloidogenesis in Familial British Dementia. *Prot Pep Let* (2001) 8 p. 171-8.
550. Srinivasan, R., Marchant, R. E. and Zagorski, M. G.: ABri peptide associated with familial British dementia forms annular and ring-like protofibrillar structures. *Amyloid* (2004) 11 p. 10-3.
551. Surolia, I., Reddy, G. B. and Sinha, S.: Hierarchy and the mechanism of fibril formation in ADan peptides. *J Neurochem* (2006) 99 p. 537-48.
552. Gasteiger, E., Hoogland, C., Gattiker, A., Duvaud, S., Wilkins, M. R., Appel, R. D. and Bairoch, A.: Protein identification and analysis tools on the ExPASy server. *The Proteomics Protocols Handbook* (2005) p. 571-607.
553. Kyte, J. and Doolittle, R. F.: A simple method for displaying the hydropathic character of a protein. *J Mol Biol* (1982) 157 p. 105-32.
554. Eisenberg, D., Schwarz, E., Komaromy, M. and Wall, R.: Analysis of membrane and surface protein sequences with the hydrophobic moment plot. *J Mol Biol* (1984) 179 p. 125-42.
555. Luheshi, L. M., Tartaglia, G. G., Brorsson, A. C., Pawar, A. P., Watson, I. E., Chiti, F., Vendruscolo, M., Lomas, D. A., Dobson, C. M. and Crowther, D. C.: Systematic in vivo analysis of the intrinsic determinants of amyloid Beta pathogenicity. *PLoS Biol* (2007) 5 p. e290.
556. Tartaglia, G. G. and Vendruscolo, M.: The Zyggregator method for predicting protein aggregation propensities. *Chem Soc Rev* (2008) 37 p. 1395-401.
557. Gibson, G., Gunasekera, N., Lee, M., Lelyveld, V., El-Agnaf, O. M., Wright, A. and Austen, B.: Oligomerization and neurotoxicity of the amyloid ADan peptide implicated in familial Danish dementia. *J Neurochem* (2004) 88 p. 281-90.
558. Lashuel, H. A. and Lansbury, P. T., Jr.: Are amyloid diseases caused by protein aggregates that mimic bacterial pore-forming toxins? *Q Rev Biophys* (2006) 39 p. 167-201.

559. Linding, R., Schymkowitz, J., Rousseau, F., Diella, F. and Serrano, L.: A comparative study of the relationship between protein structure and beta-aggregation in globular and intrinsically disordered proteins. *J Mol Biol* (2004) 342 p. 345-53.
560. Trovato, A., Seno, F. and Tosatto, S. C.: The PASTA server for protein aggregation prediction. *Protein Eng Des Sel* (2007) 20 p. 521-3.
561. Lakowicz, J. R.: Principles of Fluorescence Spectroscopy. (2006) p. 954.
562. Shen, C. L., Scott, G. L., Merchant, F. and Murphy, R. M.: Light scattering analysis of fibril growth from the amino-terminal fragment beta(1-28) of beta-amyloid peptide. *Biophys J* (1993) 65 p. 2383-95.
563. Goormaghtigh, E., Ruysschaert, J. M. and Raussens, V.: Evaluation of the information content in infrared spectra for protein secondary structure determination. *Biophys J* (2006) 90 p. 2946-57.
564. Calero, M. and Gasset, M.: Fourier transform infrared and circular dichroism spectroscopies for amyloid studies. *Methods Mol Biol* (2005) 299 p. 129-51.
565. Bouchard, M., Zurdo, J., Nettleton, E. J., Dobson, C. M. and Robinson, C. V.: Formation of insulin amyloid fibrils followed by FTIR simultaneously with CD and electron microscopy. *Protein Sci* (2000) 9 p. 1960-7.
566. Kelly, S. M., Jess, T. J. and Price, N. C.: How to study proteins by circular dichroism. *Biochim Biophys Acta* (2005) 1751 p. 119-39.
567. Nielsen, E. H., Nybo, M. and Svehag, S.-E.: Electron microscopy of prefibrillar structures and amyloid fibrils. *Methods Enzymol* (1999) 309 p. 491-5.
568. Mogensen, J. E., Ferreras, M., Wimmer, R., Petersen, S. V., Enghild, J. J. and Otzen, D. E.: The major allergen from birch tree pollen, Bet v 1, binds and permeabilizes membranes. *Biochemistry* (2007) 46 p. 3356-65.
569. Hortschansky, P., Schroeckh, V., Christopeit, T., Zandomeneghi, G. and Fandrich, M.: The aggregation kinetics of Alzheimer's beta-amyloid peptide is controlled by stochastic nucleation. *Protein Sci* (2005) 14 p. 1753-9.
570. Stark, G. R.: Reactions of cyanate with functional groups of proteins. 3. Reactions with amino and carboxyl groups. *Biochemistry* (1965) 4 p. 1030-6.
571. Stark, G. R.: Reactions of cyanate with functional groups of proteins. IV. Inertness of aliphatic hydroxyl groups. Formation of carbamyl- and acylhydantoins. *Biochemistry* (1965) 4 p. 2363-7.
572. Hamada, D. and Dobson, C. M.: A kinetic study of beta-lactoglobulin amyloid fibril formation promoted by urea. *Protein Sci* (2002) 11 p. 2417-26.
573. Petersen, S. V., Jeppesen, M. D., Bjerring, M., Hein, K. L., Christiansen, G., Enghild, J. J., Otzen, D. E., Kristensen, T. and Nielsen, N. C.: Preparation of SerADan fibrils for solid-state NMR structural analysis: Expression, purification, and fibril formation. Submitted (2009).
574. Sambashivan, S., Liu, Y., Sawaya, M. R., Gingery, M. and Eisenberg, D.: Amyloid-like fibrils of ribonuclease A with three-dimensional domain-swapped and native-like structure. *Nature* (2005) 437 p. 266-9.
575. Sanders, A., Jeremy Craven, C., Higgins, L. D., Giannini, S., Conroy, M. J., Hounslow, A. M., Waltho, J. P. and Staniforth, R. A.: Cystatin forms a tetramer through structural rearrangement of domain-swapped dimers prior to amyloidogenesis. *J Mol Biol* (2004) 336 p. 165-78.
576. Elam, J. S., Taylor, A. B., Strange, R., Antonyuk, S., Doucette, P. A., Rodriguez, J. A., Hasnain, S. S., Hayward, L. J., Valentine, J. S., Yeates, T. O. and Hart, P. J.: Amyloid-like filaments and water-filled nanotubes formed by SOD1 mutant proteins linked to familial ALS. *Nat Struct Biol* (2003) 10 p. 461-7.
577. Otzen, D. E., Nesgaard, L. W., Andersen, K. K., Hansen, J. H., Christiansen, G., Doe, H. and Sehgal, P.: Aggregation of S6 in a quasi-native state by sub-micellar SDS. *Biochim Biophys Acta* (2008) 1784 p. 400-14.
578. Keeler, C., Hodsdon, M. E. and Dannies, P. S.: Is there structural specificity in the reversible protein aggregates that are stored in secretory granules? *J Mol Neurosci* (2004) 22 p. 43-9.
579. Alakoskela, J. M., Jutila, A., Simonsen, A. C., Pirneskoski, J., Pyhajoki, S., Turunen, R., Marttila, S., Mouritsen, O. G., Goormaghtigh, E. and Kinnunen, P. K.: Characteristics of fibers formed by cytochrome c and induced by anionic phospholipids. *Biochemistry* (2006) 45 p. 13447-53.
580. Lundberg, K. M., Stenland, C. J., Cohen, F. E., Prusiner, S. B. and Millhauser, G. L.: Kinetics and mechanism of amyloid formation by the prion protein H1 peptide as determined by time-dependent ESR. *Chem Biol* (1997) 4 p. 345-55.
581. Bliznyukov, O. P., Kozmin, L. D., Vysotskaya, L. L., Golenkov, A. K., Tishchenko, V. M., Samoylovich, M. P. and Klimovich, V. B.: Human immunoglobulin light chains lambda form amyloid fibrils and granular aggregates in solution. *Biochemistry (Mosc)* (2005) 70 p. 458-66.
582. Hancock, R. E. and Sahl, H. G.: Antimicrobial and host-defense peptides as new anti-infective therapeutic strategies. *Nat Biotechnol* (2006) 24 p. 1551-7.
583. White, S. H. and Wimley, W. C.: Hydrophobic interactions of peptides with membrane interfaces. *Biochim Biophys Acta* (1998) 1376 p. 339-52.
584. Kjaer, L., Giehm, L., Heimburg, T. and Otzen, D.: The influence of vesicle size and composition on alpha-synuclein structure and stability. Accepted *Biophys J* (2009) p.
585. Wallace, B. A. and Janes, R. W.: Tryptophans in membrane proteins. X-ray crystallographic analyses. *Adv Exp Med Biol* (1999) 467 p. 789-99.
586. Yau, W. M., Wimley, W. C., Gawrisch, K. and White, S. H.: The preference of tryptophan for membrane interfaces. *Biochemistry* (1998) 37 p. 14713-8.

587. Aqvist, J., Luecke, H., Quiocho, F. A. and Warshel, A.: Dipoles localized at helix termini of proteins stabilize charges. *Proc Natl Acad Sci U S A* (1991) 88 p. 2026-30.
588. Engel, M. F., Khemtemourian, L., Kleijer, C. C., Meeldijk, H. J., Jacobs, J., Verkleij, A. J., de Kruijff, B., Killian, J. A. and Hoppener, J. W.: Membrane damage by human islet amyloid polypeptide through fibril growth at the membrane. *Proc Natl Acad Sci U S A* (2008) 105 p. 6033-8.
589. Khandelia, H., Ipsen, J. H. and Mouritsen, O. G.: The impact of peptides on lipid membranes. *Biochim Biophys Acta* (2008) 1778 p. 1528-36.
590. Kourie, J. I. and Shorthouse, A. A.: Properties of cytotoxic peptide-formed ion channels. *Am J Physiol Cell Physiol* (2000) 278 p. C1063-87.
591. Bechinger, B.: Structure and functions of channel-forming peptides: magainins, cecropins, melittin and alamethicin. *J Membr Biol* (1997) 156 p. 197-211.
592. Kelkar, D. A. and Chattopadhyay, A.: The gramicidin ion channel: a model membrane protein. *Biochim Biophys Acta* (2007) 1768 p. 2011-25.
593. Bechinger, B., Kinder, R., Helmle, M., Vogt, T. C., Harzer, U. and Schinzel, S.: Peptide structural analysis by solid-state NMR spectroscopy. *Biopolymers* (1999) 51 p. 174-90.
594. Oren, Z. and Shai, Y.: Mode of action of linear amphipathic alpha-helical antimicrobial peptides. *Biopolymers* (1998) 47 p. 451-63.
595. Bechinger, B.: The structure, dynamics and orientation of antimicrobial peptides in membranes by multidimensional solid-state NMR spectroscopy. *Biochim Biophys Acta* (1999) 1462 p. 157-83.
596. Bechinger, B.: Detergent-like properties of magainin antibiotic peptides: a 31P solid-state NMR spectroscopy study. *Biochim Biophys Acta* (2005) 1712 p. 101-8.
597. Shai, Y.: Mechanism of the binding, insertion and destabilization of phospholipid bilayer membranes by alpha-helical antimicrobial and cell non-selective membrane-lytic peptides. *Biochim Biophys Acta* (1999) 1462 p. 55-70.
598. Taylor, K., Barran, P. E. and Dorin, J. R.: Structure-activity relationships in beta-defensin peptides. *Biopolymers* (2008) 90 p. 1-7.
599. Song, L., Hobaugh, M. R., Shustak, C., Cheley, S., Bayley, H. and Gouaux, J. E.: Structure of staphylococcal alpha-hemolysin, a heptameric transmembrane pore. *Science* (1996) 274 p. 1859-66.
600. Orlova, E. V., Rahman, M. A., Gowen, B., Volynski, K. E., Ashton, A. C., Manser, C., van Heel, M. and Ushkaryov, Y. A.: Structure of alpha-latrotoxin oligomers reveals that divalent cation-dependent tetramers form membrane pores. *Nat Struct Biol* (2000) 7 p. 48-53.
601. Gouaux, E.: Channel-forming toxins: tales of transformation. *Curr Opin Struct Biol* (1997) 7 p. 566-73.
602. Rausch, J. M., Marks, J. R., Rathinakumar, R. and Wimley, W. C.: Beta-sheet pore-forming peptides selected from a rational combinatorial library: mechanism of pore formation in lipid vesicles and activity in biological membranes. *Biochemistry* (2007) 46 p. 12124-39.
603. Wimmer, R., Andersen, K. K., Vad, B., Davidsen, M., Molgaard, S., Nesgaard, L. W., Kristensen, H. H. and Otzen, D. E.: Versatile interactions of the antimicrobial peptide novispirin with detergents and lipids. *Biochemistry* (2006) 45 p. 481-97.
604. Dathe, M., Nikolenko, H., Meyer, J., Beyermann, M. and Bienert, M.: Optimization of the antimicrobial activity of magainin peptides by modification of charge. *FEBS Lett* (2001) 501 p. 146-50.
605. Wieprecht, T., Dathe, M., Schumann, M., Krause, E., Beyermann, M. and Bienert, M.: Conformational and functional study of magainin 2 in model membrane environments using the new approach of systematic double-D-amino acid replacement. *Biochemistry* (1996) 35 p. 10844-53.
606. Miles, A. J. and Wallace, B. A.: Synchrotron radiation circular dichroism spectroscopy of proteins and applications in structural and functional genomics. *Chem Soc Rev* (2006) 35 p. 39-51.
607. Wallace, B. A. and Janes, R. W.: Synchrotron radiation circular dichroism spectroscopy of proteins: secondary structure, fold recognition and structural genomics. *Curr Opin Chem Biol* (2001) 5 p. 567-71.
608. Manavalan, P. and Johnson, W. C.: Protein secondary structure from circular dichroism spectra. *J Biosci (suppl)* (1985) 8 p. 141-9.
609. Wallace, B. A., Wien, F., Miles, A. J., Lees, J. G., Hoffmann, S. V., Evans, P., Wistow, G. J. and Slingsby, C.: Biomedical applications of synchrotron radiation circular dichroism spectroscopy: identification of mutant proteins associated with disease and development of a reference database for fold motifs. *Faraday Discuss* (2004) 126 p. 237-43; discussion 45-54.
610. Sreerama, N. and Woody, R. W.: Computation and analysis of protein circular dichroism spectra. *Methods Enzymol* (2004) 383 p. 318-51.
611. Toumadje, A., Alcorn, S. W. and Johnson, W. C., Jr.: Extending CD spectra of proteins to 168 nm improves the analysis for secondary structures. *Anal Biochem* (1992) 200 p. 321-31.
612. Tetin, S. Y., Prendergast, F. G. and Venyaminov, S. Y.: Accuracy of protein secondary structure determination from circular dichroism spectra based on immunoglobulin examples. *Anal Biochem* (2003) 321 p. 183-7.
613. Woody, R. W.: Contributions of tryptophan side chains to the far-ultraviolet circular dichroism of proteins. *Eur Biophys J* (1994) 23 p. 253-62.
614. Woody, R. W. and Dunker, A. K.: Aromatic and Cysteine Side-Chain Circular Dichroism in Proteins. *Circular Dichroism and the Conformational Analysis of Biomolecules* (1996) p. 109-58.

615. Manning, M. C., Illangasekare, M. and Woody, R. W.: Circular dichroism studies of distorted alpha-helices, twisted beta-sheets, and beta turns. *Biophys Chem* (1988) 31 p. 77-86.
616. Sreerama, N. and Woody, R. W.: Structural composition of betaI- and betaII-proteins. *Protein Sci* (2003) 12 p. 384-8.
617. Sreerama, N. and Woody, R. W.: Poly(pro)II helices in globular proteins: identification and circular dichroic analysis. *Biochemistry* (1994) 33 p. 10022-5.
618. Lees, J. G., Miles, A. J., Wien, F. and Wallace, B. A.: A reference database for circular dichroism spectroscopy covering fold and secondary structure space. *Bioinformatics* (2006) 22 p. 1955-62.
619. Matsuo, K., Yonehara, R. and Gekko, K.: Secondary-structure analysis of proteins by vacuum-ultraviolet circular dichroism spectroscopy. *J Biochem (Tokyo)* (2004) 135 p. 405-11.
620. Matsuo, K., Yonehara, R. and Gekko, K.: Improved estimation of the secondary structures of proteins by vacuum-ultraviolet circular dichroism spectroscopy. *J Biochem (Tokyo)* (2005) 138 p. 79-88.
621. Wilkinson, K. D. and Mayer, A. N.: Alcohol-induced conformational changes of ubiquitin. *Arch Biochem Biophys* (1986) 250 p. 390-9.
622. Dufour, E., Bertrand-Harb, C. and Haertle, T.: Reversible effects of medium dielectric constant on structural transformation of beta-lactoglobulin and its retinol binding. *Biopolymers* (1993) 33 p. 589-98.
623. Munishkina, L. A., Phelan, C., Uversky, V. N. and Fink, A. L.: Conformational behavior and aggregation of alpha-synuclein in organic solvents: modeling the effects of membranes. *Biochemistry* (2003) 42 p. 2720-30.
624. Otzen, D. E., Sehgal, P. and Nesgaard, L. W.: Alternative membrane protein conformations in alcohols. *Biochemistry* (2007) 46 p. 4348-59.
625. Buck, M.: Trifluoroethanol and colleagues: cosolvents come of age. Recent studies with peptides and proteins. *Q Rev Biophys* (1998) 31 p. 297-355.
626. Bychkova, V. E., Dujsekina, A. E., Klenin, S. I., Tiktopulo, E. I., Uversky, V. N. and Ptitsyn, O. B.: Molten globule-like state of cytochrome c under conditions simulating those near the membrane surface. *Biochemistry* (1996) 35 p. 6058-63.
627. Safar, J., Roller, P. P., Ruben, G. C., Gajdusek, D. C. and Gibbs, C. J., Jr.: Secondary structure of proteins associated in thin films. *Biopolymers* (1993) 33 p. 1461-76.
628. Hill, J. J., Shalaev, E. Y. and Zografi, G.: Thermodynamic and dynamic factors involved in the stability of native protein structure in amorphous solids in relation to levels of hydration. *J Pharm Sci* (2005) 94 p. 1636-67.
629. Rupley, J. A. and Careri, G.: Protein hydration and function. *Adv Protein Chem* (1991) 41 p. 37-172.
630. Eden, S., Limão-Vieira, P., Hoffmann, S. V. and Mason, N. J.: VUV photoabsorption in CF3X (X = Cl, Br, I) fluoroalkanes. *Chem Phys* (2005) 323 p. 313-33.
631. Young, M. A. and Pysh, E. S.: Vacuum Ultraviolet Circular Dichroism of Poly(L-alanine) Films. *Macromolecules* (1973) 6 p. 790-1.
632. Johnson, W. C., Jr. and Tinoco, I., Jr.: Circular dichroism of polypeptide solutions in the vacuum ultraviolet. *J Am Chem Soc* (1972) 94 p. 4389-92.
633. Bowman, R. L., Kellerman, M. and Johnson, W. C.: Optical properties of cyclic dimers of amino acids: An experimental and theoretical study. *Biopolymers* (1983) 22 p. 1045-70.
634. Young, M. A. and Pysh, E. S.: Vacuum ultraviolet circular dichroism of poly(L-proline) I and II. *J Am Chem Soc* (1975) 97 p. 5100-3.
635. Besley, N. A. and Hirst, J. D.: Ab Initio Study of the Effect of Solvation on the Electronic Spectra of Formamide and N-Methylacetamide. *J Phys Chem A* (1998) 102 p. 10791-7.
636. Serrano-Andres, L. and Fulscher, M. P.: Theoretical Study of the Electronic Spectroscopy of Peptides. I. The Peptidic Bond: Primary, Secondary, and Tertiary Amides. *J Am Chem Soc* (1998) 118 p. 12190-9.
637. Vincentelli, R., Canaan, S., Campanacci, V., Valencia, C., Maurin, D., Frassinetti, F., Scappucini-Calvo, L., Bourne, Y., Cambillau, C. and Bignon, C.: High-throughput automated refolding screening of inclusion bodies. *Protein Sci* (2004) 13 p. 2782-92.
638. Creighton, T. E.: Proteins: structures and molecular properties. (1993). ISBN 0-7167-7030-X.
639. Tsachaki, M., Ghiso, J., Rostagno, A. and Efthimiopoulos, S.: BRI2 homodimerizes with the involvement of intermolecular disulfide bonds. *Neurobiol Aging* (2008). *In press*.
640. Laemmli, U. K.: Cleavage of structural proteins during the assembly of the head of bacteriophage T4. *Nature* (1970) 227 p. 680-5.

PAPERS 3-6

Available online at www.sciencedirect.com
ScienceDirect
Biochimica et Biophysica Acta 1784 (2008) 400–414
Biochimica et Biophysica Acta BBA
www.elsevier.com/locate/bbapap

Aggregation of S6 in a quasi-native state by sub-micellar SDS

Daniel E. Otzen [a,b,*], Lise W. Nesgaard [b], Kell K. Andersen [a,b], Jonas Høeg Hansen [b], Gunna Christiansen [c], Hidekazu Doe [d], Pankaj Sehgal [b,1]

[a] *Centre for Insoluble Protein Studies (inSPIN), Interdisciplinary Nanoscience Center (iNANO), University of Aarhus, DK-8000 Aarhus C, Denmark*
[b] *Department of Life Sciences, Aalborg University, Sohngaardsholmsvej 49, DK-9000 Aalborg, Denmark*
[c] *Department of Medical Immunology, Aarhus University, DK-8000 Aarhus C, Denmark*
[d] *Department of Chemistry, Graduate School of Science, Osaka City University, Osaka, Japan*

Received 12 September 2007; received in revised form 9 November 2007; accepted 13 November 2007
Available online 18 December 2007

Abstract

Anionic surfaces promote protein fibrillation *in vitro* and *in vivo*. Monomeric SDS has also been shown to stimulate this process. We describe the dynamics of conformational changes and aggregative properties of the model protein S6 at sub-micellar SDS concentrations. S6 exhibits a rich and pH-sensitive diversity in conformational changes around 0.2–2 mM SDS, in which several transitions occur over time scales spanning milliseconds to hours. Monomeric SDS readily precipitates S6 within minutes at pH-values of 5 and below to form states able to bind the fibril-specific dye thioflavin T. At pH 5.5, the process is much slower and shows a mutagenesis-sensitive lag, leading to different forms of organized but not classically fibrillar aggregates with native-like levels of secondary structure, although the tertiary structure is significantly rearranged. The slow aggregation process may be linked to conformational changes that occur at the second-time scale in the same SDS concentration range, leading to an altered structure, possibly with unfolding around the C-terminal helix. The S6 aggregates may be differently trapped states, equivalent to pre-fibrillar structures seen at early stages in the fibrillation process for other proteins. The low quantities of anionic species required suggest that the aggregates may have parallels *in vivo*.

Keywords: Aggregation; Kinetics; SDS; Anionic surface; Unfolding

1. Introduction

Protein aggregation is a ubiquitous problem with deleterious consequences from both a medical [1] and industrial [2] perspective. In particular, an increasing number of both neurodegenerative and systemic diseases are known to be associated with the formation of ordered needle-like aggregates known as amyloid fibrils. It has been proposed that the ability to aggregate to well-ordered structures is a generic property of proteins [3]. However, amyloid formation is specific (*i.e.* unrelated proteins do not cross-seed each other's fibrillation) and sequence-dependent [4], and there are numerous examples of deposition diseases caused by single amino acid substitutions which have a dramatic effect on aggregation. Recent studies suggest that this intrinsic aggregation propensity can be rationalized on simple physical–chemical properties, making it possible to predict the fibrillogenic effect of different mutations [5–7]. In addition to intrinsic changes in the protein sequence, external factors can contribute. A protein can be induced to aggregate and fibrillate if it is cleaved proteolytically into smaller unstable fragments. This occurs for *e.g.* the Aβ peptide involved in Alzheimer's disease [8], gelsolin [9,10] and ABri/ADan [11]. Aggregation can also be encouraged if the protein concentration increases, as seen for secondary amyloidoses, where chronic inflammation can increase serum concentrations of SAA (serum amyloid A) by a factor of 1000, facilitating amyloid formation [12]. Changes in the environment can also play an important role. *In vitro* fibrillation is often favoured by conditions which stabilize

* Corresponding author. Centre for Insoluble Protein Studies (inSPIN), Interdisciplinary Nanoscience Center (iNANO), University of Aarhus, DK-8000 Aarhus C, Denmark. Tel.: +45 89 42 50 46; fax: + 45 86 12 31 78.
E-mail address: dao@inano.dk (D.E. Otzen).
[1] Present address: Department of Chemistry, Graduate School of Science, Osaka City University, Osaka, Japan.

1570-9639/$ - see front matter © 2007 Elsevier B.V. All rights reserved.
doi:10.1016/j.bbapap.2007.11.010

a flexible yet partially folded state, typically favoured by low pH (S6, [13]), structure-inducing solvents such as trifluoroethanol and hexafluoroisopropanol (β_2-microglobulin, [14]) or negatively charged surfaces (α-synuclein, [15]). Living organisms harbour many fibrillogenic anionic molecules. For example, many proteins including tau fibrillate preferentially in the presence of the anionic proteoglycan heparin [16], while negatively charged lipid vesicles stimulate fibrillation of islet amyloid polypeptide (IAPP) [17,18], whose aggregation is central to non-insulin dependent diabetes mellitus (NIDDM). Similar effects by anionic lipids have been seen for common proteins not associated with disease [19]. Exposure of anionic lipids may in fact be associated with cell dysfunction and thus stimulate binding and aggregation of proteins. For example, during apoptosis, the anionic phosphatidylserine lipids, which normally reside in the inner leaflet, become accessible at the cell surface [20], while anionic lipids accumulate during NIDDM and upon glucose stimulation [21,22]. Polyanion-binding proteins may even constitute a functional network of interactions [23].

The anionic surfactant sodium dodecyl sulphate (SDS), although not found *in vivo*, is a widely used mimetic of anionic lipids. Above its critical micelle concentration (cmc), which is around 1 mM under physiological conditions, it mainly exists as micelles. SDS micelles have excellent solubilizing properties due to the electrostatic inter-micellar repulsion, which counteracts their ability to stimulate aggregation. Nevertheless, just around the cmc, SDS micelles stimulate formation of amyloid-like fibers of Aβ which form after passing through a stage of initial amorphous aggregates [24]. However the resulting fibrils were not able to seed subsequent fibrillation of Aβ monomers, and did not form at higher micelle concentrations. Sub-micellar SDS is also known to stimulate aggregation, for example when mixed with cationic peptides such as Novispirin [25]. Goto *et al.* showed that SDS' ability to stimulate elongation of β_2-microglobulin fibrils [26] and induce fibrillation of a β_2-microglobulin fragment [14] peaked just below the cmc, and similar observations have been made for collagen [27] and a peptide from human complement receptor 1 [28], while fibrillation of lysozyme is stimulated by sub-mM (and thus monomeric) SDS concentrations [29]. Nanomolar concentrations of SDS may also affect calcitonin's ability to interact with lipid membranes [30]. In addition, the temperature at which *Fusarium solani pisi* cutinase aggregates decreases from 70 to 60 °C between 0 and 0.5 mM SDS at pH 7 [31].

It has been suggested that anionic surfaces may stimulate protein aggregation simply by concentrating proteins within a small area [17,24], rather than by altering the proteins' conformational properties. This may be true for inherently flexible peptides such as Aβ and IAPP, but larger proteins are likely to undergo coordinated conformational changes which can have profound bearings on their aggregation. To attempt to shed more light on this, we report a study on the structural basis for sub-micellar SDS' general ability to stimulate protein aggregation. As model protein we use the ribosomal protein S6 from *Thermus thermophilus*, which has been shown to fibrillate upon prolonged incubation at low pH and high salt concentrations [13]. Under these conditions, S6 remains overall native-like but a part of the protein becomes more flexible, and this may be the basis for the subsequent fibrillation. S6 unfolds rapidly in micellar SDS in a manner which is sensitive to mutagenesis [32,33], but its conformational and aggregative behaviour in monomeric SDS has not been investigated in detail. We find that S6 aggregates in a narrow SDS concentration interval, leading to seeding-competent aggregates in a sigmoidal time-profile that is responsive to mutagenesis. However, these aggregates are not classical fibrillar and may represent trapped states that are equivalent to early stages in the fibrillation process.

2. Materials and methods

Sodium dodecyl sulfate (SDS), 8-anilino-1-naphthalenesulfonic acid (ANS), Thioflavin T (ThT) and *N*-phenyl-1-naphthylamine (NPN) were from Sigma-Aldrich (St. Louis, MO). S6 wildtype and mutants were prepared and purified as described [34,35].

2.1. Fluorescence-based equilibrium titration of S6

Buffers used were as follows: 20 mM Tris (pH 8) and 20 mM sodium acetate (pH 5.5 or 4.0). All experiments were done at 25±1 °C. 2 μM S6 was incubated with different concentrations of SDS for at least 1 h before measuring fluorescence on an LS-55 Luminescence spectrometer (Perkin-Elmer Instruments, Welleslay, MA), using an excitation wavelength of 295 nm and measuring the emission between 315 and 375 nm. Measurements were obtained using a 10 mm quartz cuvette (Hellma, Müllheim, Germany) from an average of three scans with a slit width of 8 nm and a scanning speed of 300 nm/min. For solubility studies, 20 μM S6 (or other proteins examined) was incubated with different SDS concentrations for at least an hour. Fluorescence intensities of the supernatant were recorded before and after spinning down 15 min at 14,000 rpm, and the ratio of the two measurements used as a measure of solubility.

2.2. Circular dichroism

Far-UV CD spectra were recorded in a 1 mm quartz cuvette on a J-810 spectropolarimeter (Jasco Spectroscopic Co. Ltd., Hachioji City, Japan) equipped with a PTC-423S temperature control unit. Wavelength scans were recorded from 250 to 195 nm using 25 μM S6 in 20 mM Tris pH 8.0 (preincubated for an hour before measurement) with a band width of 2 nm and a scanning speed of 50 nm/min. Five accumulations were averaged to yield the final spectrum. Near-UV CD spectra were recorded from 320 to 260 nm using 60 μM S6 in a 10 mm quartz cuvette with the same settings as for far-UV CD. Due to the high amount of protein required and limited availability, this was performed as a titration experiment with a single S6 solution. After each SDS aliquot, the sample was equilibrated for 10 min before spectra were recorded. In both cases, background contributions from the buffer were subtracted.

2.3. Determination of cmc

This was done in three different ways, namely using NPN fluorescence, interfacial tensiometry and pyrene fluorescence.

2.4. NPN fluorescence

5 μM NPN was incubated with different concentrations of SDS and the fluorescence (excitation 350 nm, emission 430 nm, slits 10 nm) recorded. Inclusion of NPN into the micelles results in an increase in the fluorescence intensity of NPN. Fluorescence intensity was plotted against surfactant concentrations, and the cmc was estimated from the break-point of the curve.

2.5. Tensiometry

Interfacial tension was measured with an EZ-PI interfacial tensiometer (Kibron Inc., Finland). A known volume of sample was introduced in the cuvette

and placed onto the cuvette holder. Before starting measurements, the instrument was calibrated with Milli-Q water.

2.6. Pyrene fluorescence

In the presence of bulk micelles or hemi-micellar aggregates on *e.g.* protein surfaces, pyrene undergoes a shift in the emission intensity at 383.5 nm (I_3) and 372.5 nm (I_1), allowing us to use the I_3/I_1 ratio to measure the cmc value [36] and the formation of surfactant aggregates on surfaces. Pyrene was added to a final concentration of 0.2 μM (from a 20 μM stock solution in ethanol) to a solution containing 0–12 mM SDS and 0 or 2 μM S6. The solution was excited at 335 nm and the emission between 350 and 440 was monitored. Each measurement was recorded as an average of three emission scans in a 10 mm quartz cuvette. Subsequently the I_3/I_1 ratio was plotted versus SDS concentration. The cmc in the absence of S6 could be estimated by the break-point as for NPN.

2.7. Plate-reader assays

These were recorded on a SpectraMax Gemini XS (Molecular Devices, Sunnyvale CA) fluorescence plate reader at 42 °C using 100 μM S6. Samples were incubated in triplicate in 96 well black polystyrene microtiter plates (Greiner Bio-one, Frickenhausen, Germany). Tryptophan emission intensities at 330 nm and 355 nm (both with excitation at 295 nm) were read every 15 min. Each reading was preceded by 150 s of automixing. To prevent evaporation during long incubations, the microtiter plates were covered with Crystal Clear Sealing Tape (Hampton Research, Aliso Viejo, CA), which absorbs only a small fraction of UV light. For time profiles showing lag phases, the lag time was estimated as the interpolated time point for the intersection of the pre-aggregation baseline and the tangent to the elongation or ramp phase.

2.8. ANS and ThT fluorescence

S6 was incubated with 40 μM ANS or 40 μM ThT (in both cases prepared from 100 mM stock solutions in ethanol). ANS was excited at 375 nm and emission recorded at 470 nm. ThT was excited at 450 nm and emission recorded at 485 nm.

2.9. Solubility studies

20 μM S6 or hen egg white lysozyme (Sigma-Aldrich) was incubated in 20 mM buffer with different concentrations of SDS at 25 °C for 1 h. Samples were spun down for 15 min at 14,000 rpm. The fluorescence of the supernatant was measured as described above using excitation at 280 nm and emission at 350 nm.

2.10. Stopped flow kinetics

Unfolding kinetics were monitored on an SX18MV stopped-flow micro-analyzer (Applied Photophysics, Leatherhead, UK) in a thermostatically controlled sample-handling unit. S6 and surfactant were mixed 1:10 to a final protein concentration of 2 μM, samples were excited at 280 nm and the emission above 320 nm was monitored using a cut-off filter.

2.11. Isothermal titration calorimetry

The calorimetric measurements were conducted on a VP-ITC (MicroCal Inc., Northampton, MA). The reference cell was filled with water and in a typical experiment, the sample cell was loaded with a solution of 0.1–0.4 mg/ml S6. The cell solution was titrated with aliquots of 2.5–4 μl of 99 mM SDS in 10 mM Tris, pH 8. All experiments were done at 22 °C, where SDS demicellization gives a minimal thermal signal [37]. Therefore the enthalpic contribution from demicellization of SDS upon injection can be neglected in data analysis. The obtained heat signals from the ITC were integrated using the Origin software supplied by MicroCal Inc.

2.12. Electron microscopy

Electron microscopy was carried out as described [38]. Briefly, a 5 μl aliquot of BSA was placed on a 400-mesh, carbon-coated, glow-discharged grid for 30 s. Grids were washed in two drops of double-distilled water and stained with 1% (w/v) phosphotungstic acid (pH 6.8) and blotted dry on filter paper. Samples were viewed with a Jeol 1010 transmission electron microscope (JEOL, Japan).

2.13. FTIR spectroscopy

Spectra were recorded on a Bruker Tensor 27 infrared spectrometer (Bruker Optik GmbH, Ettlingen, Germany) with a Specac Golden Gate single-reflection ATR unit (Specac Ltd., Orpington, UK). Aggregates were allowed to sediment in the eppendorf tube and samples for FTIR were removed from the bottom of the tube. Approximately 1–3 μg protein was dried under a gentle stream of nitrogen. Three independent samples were investigated (64 scans at 2 cm^{-1} resolution). If needed, the presence of water vapour was corrected for by subtraction of a fresh vapour spectrum. Peaks were assigned from the 2nd derivative and deconvolution of spectra. Amide bands I and II of the non-deconvoluted spectra were fitted using the Levenberg–Marquardt method to 7 Lorentzian peaks of which 4 were assigned to secondary structure elements and 3 to modes in amide band II.

2.14. Atomic Force Microscopy

The solution was centrifuged at 14,000 rpm for 10 min. The supernatant was removed by aspiration and the pellet washed in water. 100 μL of 0.5 μM protein was applied to freshly cleaved mica and dried at 80 °C. Samples were imaged in contact mode on a PicoSPMI (Molecular Imaging, Tempe, Arizona) using silicon nitride cantilevers (BudgetSensors, Sofia, Bulgaria) with force constant 0.27 N/m.

2.15. Limited proteolysis and N-terminal sequencing

10 μM S6 was incubated with 10 nM alcalase (kindly provided by Ture Damhus, Novozymes A/S) in 20 mM NaOAc pH 5.5 or 20 mM Tris–Cl pH 8.0 in 1.5 mM SDS for 30 min at 25 °C. The stacking gel was allowed to polymerize one day prior to electrophoresis and samples were heated in SDS-PAGE loading buffer for 3 min at 80 °C only before loading on the gel. After electrophoresis, selected S6 bands were transferred to a polyvinylidene diflouride membrane (Immobilon-P, Millipore, Bedford, MA) in 10 mM CAPS, 10% (v/v) methanol, pH 11 as described [39]. Samples were analyzed by automated Edman degradation using a Procise amino acid sequencer (Applied Biosystems, Foster City, CA) with on-line phenylthiohydantoin analysis by HPLC.

3. Results

3.1. S6 undergoes significant multi-step conformational changes at sub-micellar concentrations

The purpose of this study was to investigate the conformational changes of relevance for aggregation processes that sub-micellar SDS concentrations can induce in a model protein. We start by titrating in SDS at low concentrations, monitoring the process through S6′ single Trp residue (Trp 62). Under our buffer conditions (20 mM Tris pH 8), the cmc of SDS is around 2.5–3.3 mM (Fig. 1A and 4A) according to three different assessment methods (see legend to figure).The tryptophan signal undergoes several changes below 6 mM SDS, leading to a general decline in intensity and a slight blue-shift in the peak position (Fig. 1B insert). Monitoring the emission intensity at the emission peak around 350 nm (typical of exposed Trp residues), there is a lag region between 0 and 0.25 mM SDS

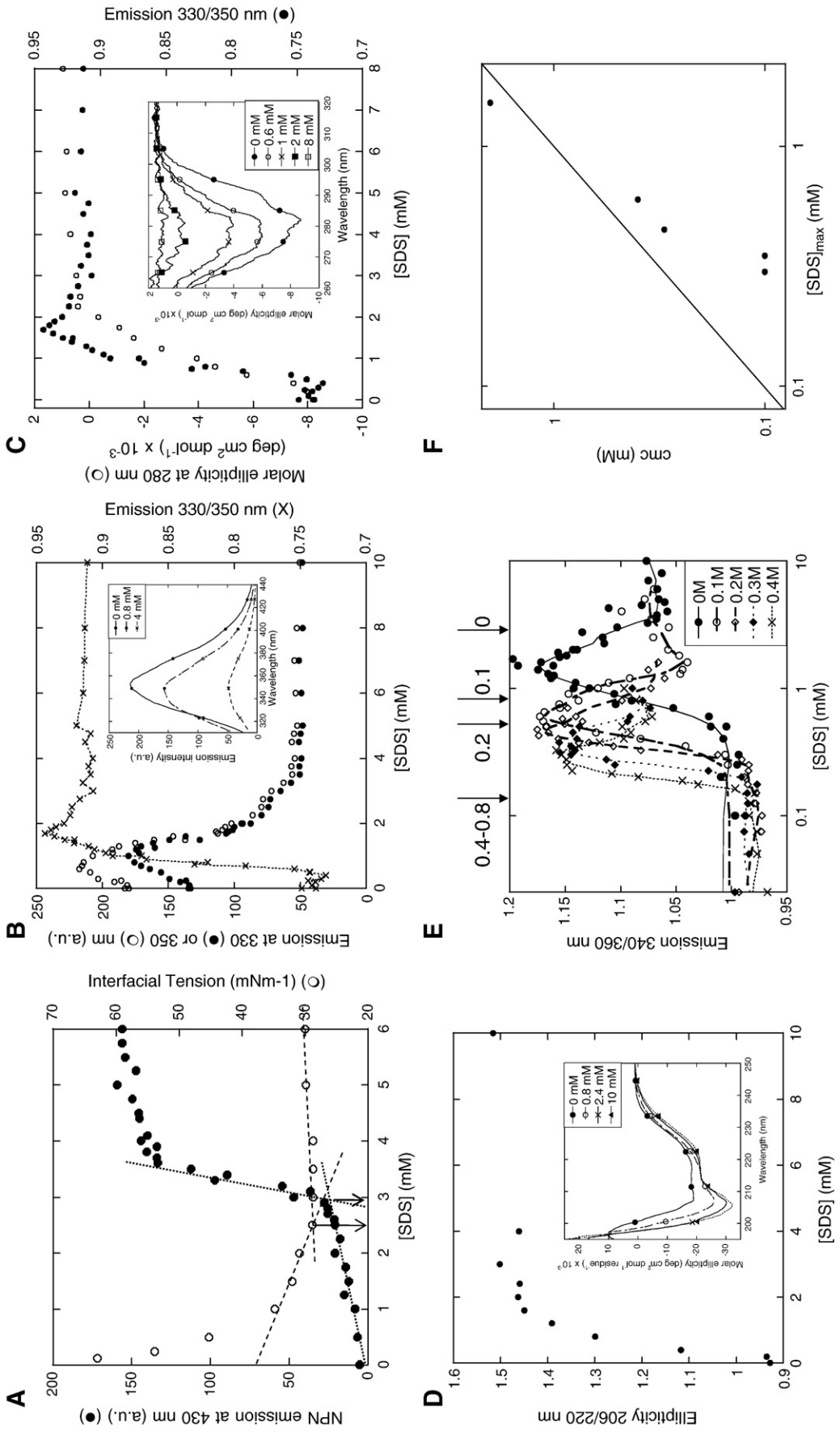

Fig. 1. (A) Determination of cmc of SDS in 20 mM Tris pH 7 according to NPN fluorescence (the emission at 430 nm upon excitation at 350 nm) and interfacial tensiometry. In both cases, the cmc can be estimated from the intersection of the two linear regions on either side of the break-point. The arrows indicate the cmc values obtained by tensiometry (2.5 mM) and NPN measurements (2.9 mM). (B) Change in S6′ Trp fluorescence emission intensity at 330 and 350 nm and the ratio of 330 and 360 nm emission (in 20 mM Tris pH 8.0 at 25 °C), as a function of SDS concentration. *Insert*: Fluorescence spectra of 2 μM S6 in 0–4 mM SDS. (C) Change in near-UV ellipticity at 280 nm for S6 as a function of SDS concentration in 20 mM Tris pH 8.0 at 25 °C. *Insert*: Near-UV CD spectra of 60 μM S6 in 0–8 mM SDS. (D) Ratio of ellipticity for S6 at 206 and 220 nm as a function of SDS concentration in 20 mM Tris pH 8.0 at 25 °C. *Insert*: Far-UV CD spectra of 25 μM S6 in in 0–10 mM SDS. (E) Ratio of emission at 340 and 360 nm for 2 μM S6 as a function of SDS concentration in 0–0.8 M NaCl and 20 mM Tris pH 8.0 at 25 °C. Arrows indicate cmc values at different NaCl concentrations. (F) Position of maximum intensity of fluorescence at different NaCl concentrations (from panel C) versus cmc values at the corresponding NaCl concentration. The straight line is the identity function.

before the signal rises to a maximum around 1.5 mM SDS and then declines to a plateau level around 4 mM SDS, where it remains up to 10 mM SDS (Fig. 1B). The same behaviour is seen using emission at 330 nm (typical of buried Trp residues). The ratio between these two intensities also shows the same type of behaviour, although the maximum signal is reached around 1.9 mM SDS (rather than 1.5 mM SDS) and the signal change is greatest for the first phase (0.3–1.9 mM) rather than the second (1.9–6 mM). Although the ratio between two wavelengths may not always be as quantitative a measure of conformational changes as the actual intensities, it provides a useful trend for the changes that occur.

Although Trp fluorescence is generally a highly sensitive probe of conformational changes, it will also be influenced by changes in the polarity of the medium due to binding of surfactant molecules. Near-UV CD spectroscopy, although requiring ~1000-fold more sample, only reflects changes in the conformational freedom of the aromatic side chains and was used to investigate whether both transitions seen in Fig. 1B are associated with changes in the mobility of the aromatic side chains (due to conformational changes) rather than just surfactant binding. Addition of SDS effectively abolishes the near-UV spectral features (Fig. 1C insert), and the concentration dependence nicely correlates with Trp fluorescence (Fig. 1C): there is a steep rise up to ca. 1.6 mM, commensurate with the first Trp transition, and a less steep rise up to around 2–3 mM, corresponding to the second Trp transition. Thus both transitions reflect conformational changes.

When we monitor changes in secondary structure using far-UV circular dichroism, we see changes in the relative intensities of the two minima around 220 and 206–209 nm (Fig. 1D insert). At increasing SDS concentrations, the second minimum blue-shifts from 209 to 206 nm and the ratio of the intensities at 206 and 220 nm rises steeply to a plateau around 1.6 mM SDS, after which no further changes occur (Fig. 1D). This suggests that the changes in secondary structure only occur in one transition from around 0.2 to 1.6 mM SDS. Although the spectra retain their overall α-helical appearance, the change in intensity ratios suggests that the helices dissociate from each other to form more isolated entities (cfr. [40–42], which is entirely consistent with the loss of tertiary structure seen in this transition according to Trp fluorescence and near-UV CD.

Thus interaction of S6 with low concentrations of SDS at pH 8 appears to involve at least two conformational transitions below cmc. The first change (up to around 1.5–2 mM SDS) involves changes in both secondary and tertiary structure, while the second change primarily involves changes in tertiary structure. The second change is completed just before the formation of micellar structures around 3 mM.

To probe whether the second change is connected with micelle formation, we titrated S6 fluorescence in the presence of 0.1–0.8 M NaCl, which leads to a strong reduction in cmc. At all concentrations, we see the same general trend, namely a short lag phase before a rise in intensity followed by a steep decline (Fig. 1E). The position of the signal maximum always occurs at slightly higher concentrations when measured by emission ratios rather than actual emission values (data not shown). Importantly,

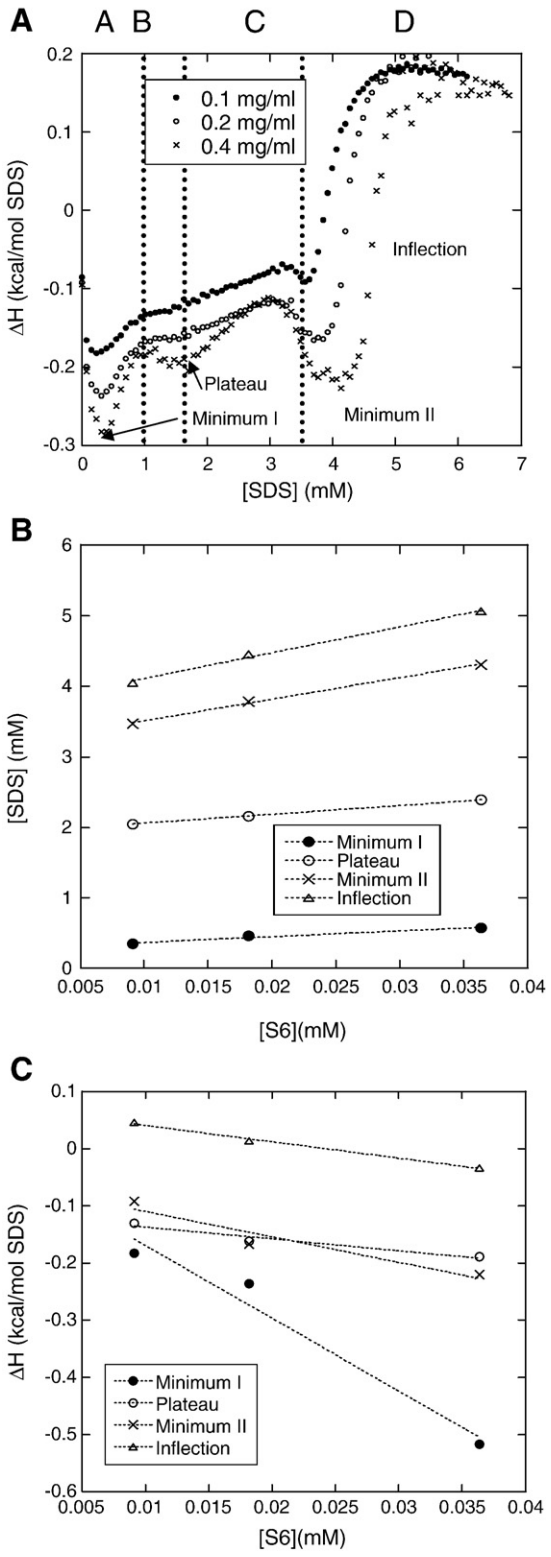

Fig. 2. (A) ITC enthalpograms of the interaction of SDS with different concentrations of S6 in 20 mM Tris pH 8.0 at 22 °C. The sections A–D denote regions with different types of interactions between SDS and S6. (B) SDS concentrations and (C) enthalpy values at which the four characteristic transitions in Fig. 2A occur, plotted versus S6 concentration. Data are summarized in Table 1.

although the position of the SDS maximum does shift to lower values with increasing [NaCl], the maximum does not decrease as strongly as the cmc value (Fig. 1F). This suggests that the second step reflects an independent conformational change rather than a trivial fluorescence change caused by the binding of micelles to S6.

3.2. Isothermal titration calorimetry experiments reveal several binding regions

To complement our spectroscopic studies on the binding of SDS to S6, we turned to ITC, which is a sensitive method that may monitor and quantitate spectroscopically invisible binding of SDS to proteins. When we titrate different concentrations of S6 with SDS, we obtain enthalpograms which change in a characteristic fashion (Fig. 2A). These enthalpograms may be divided into four sections (A–D). Section A shows a significant exothermic (negative) heat flow, which peaks at low concentrations (0.3–0.5 mM SDS. referred to as minimum I). This is followed by a plateau up to around 2 mM SDS (section B), after which there is a steady linear decrease in the signal until it forms a small but distinct peak (section C). This peak has been seen for a number of other protein–SDS systems, and has been assigned to the (endothermic) enthalpy change of protein denaturation [43–45]. Subsequently, the system undergoes a marked exothermic effect in section D, reaching a minimum around 3–4 mM SDS (minimum II). This is also a general observation in ITC studies on protein–SDS interactions, and it most likely reflects the association of SDS and denatured protein [43]. The saturation of this binding occurs around the inflection point (around 3.5–4.5 mM SDS). This also corresponds to the apparent critical micelle concentration (cmc_{app}) in the presence of protein [37]. SDS injected beyond this point mainly remains in micellar form and has far fewer protein molecules to interact with [43,46]. Finally, at high SDS concentrations, the heat flow levels out, indicating that the injected SDS remains in a micellar form and interacts only weakly with the existing protein–SDS complex.

To estimate the number of surfactant molecules bound to S6 at various stages in this process, we can plot the total SDS concentrations ($[SDS]_{tot}$) at these stages against the corresponding protein concentration. Provided that the SDS concentration is low enough to neglect SDS in bulk micellar form (a safe assumption when working below 4–5 mM SDS and at protein concentrations sufficient to bind a substantial amount of SDS),

Table 1
Interactions between S6 and SDS in 20 mM Tris pH 8.0 at 22 °C as determined by isothermal titration calorimetry

Position	Slope (SDS molecules bound per S6)	$[SDS]_o$ (mM)	Slope (cal/mol/mM S6)	ΔH_o (cal/mol SDS)
Minimum I	8.1±1.6	0.29±0.04	−12.7±2.4	−43±57
Plateau	12.4±0.1	1.94±0.01	−2.1±0.5	−117±12
Minimum II	30.56±1.22	3.21±0.03	−4.4±1.3	−66±31
Inflection	36.5±2.6	3.75±0.06	−2.85±0.23	69±6

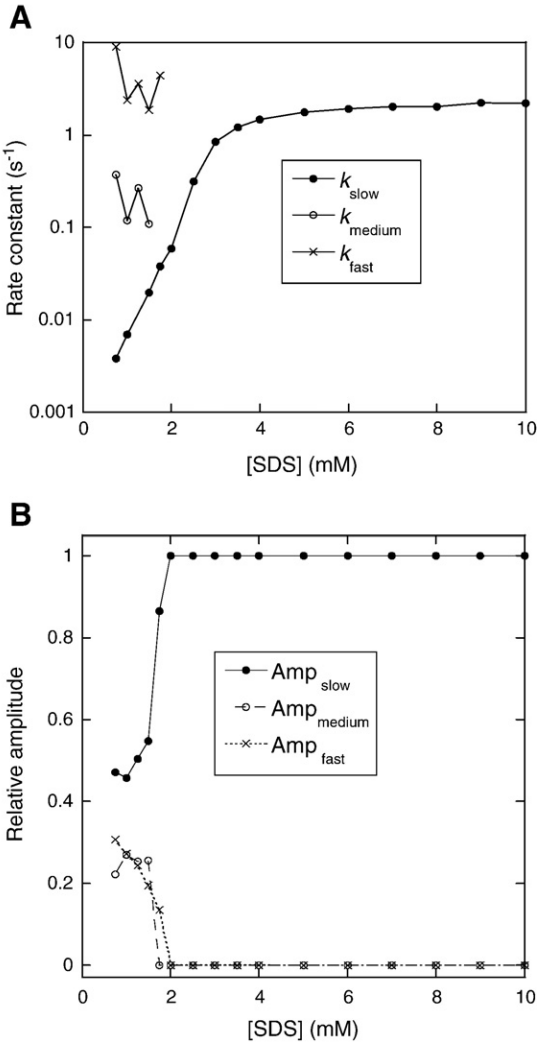

Fig. 3. Kinetics of unfolding of 2 μM S6 in SDS in 20 mM Tris pH 8 at 25 °C. Parameters are obtained by fitting the data to the appropriate number of exponential decays. (A) Rate constants. (B) Relative amplitudes.

SDS binding at each peak can be expressed by the mass balance equation [31]:

$$[SDS]_{tot} = [SDS]_{aq} + [protein]^{*}N \quad (1)$$

where $[SDS]_{aq}$ denotes aqueous (non-bound) SDS and N is the average number of bound SDS per protein molecule [37]. The plots for the transition points illustrated in Fig. 2A give satisfactory linear relationships (Fig. 2B) and the parameters are summarized in Table 1. At minimum I (interpreted as the binding of non-denaturing SDS), 8.1±1.6 molecules of SDS bind S6 in the presence of 0.29±0.04 mM free SDS. This corresponds nicely to the lag region seem from fluorescence titration, suggesting that the SDS molecules bind at different places on S6 without any significant conformational changes. At the end of the plateau region, an additional 4 molecules have bound, leading to 0.32 g SDS/g protein which is comparable to the 0.4 g SDS/g protein reported by Reynolds and Tanford for a number of proteins just below the cmc [47]. However, at this stage in our

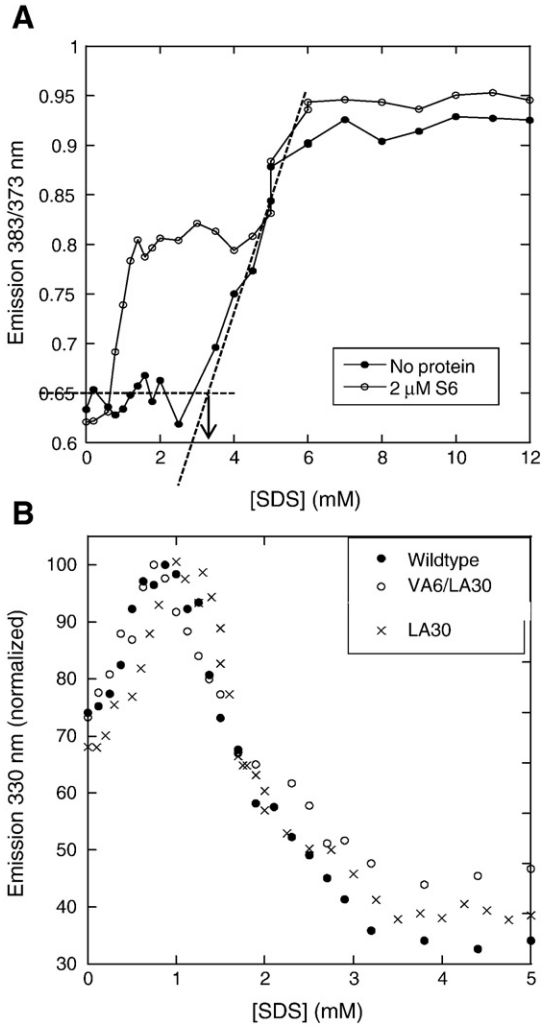

Fig. 4. (A) Pyrene fluorescence (ratio of intensities at 373 and 383 nm) as a function of SDS concentration in the absence and presence of 2 μM S6 in 20 mM Tris pH 8.0 at 25 °C. Based on the break-point in the curve in the absence of S6, we estimate the cmc to be around 3.3 mM SDS. (B) Equilibrium denaturation of 2 μM S6 wildtype (●), LA30 (○) and VA6/LA30 (×) as a function of SDS monitored using emission at 330 nm in 20 mM Tris pH 8.0 at 25 °C.

experiments, the free SDS concentration has risen to 1.94 mM which is still well below cmc. The small increase in the amount of bound SDS over a fairly wide SDS concentration range may explain the lack of a discernible signal in this plateau region, alternatively the SDS molecules bind in a way that does not elicit a strong enthalpic signal.

31 molecules SDS bind at minimum II, leading to a free SDS concentration of 3.21 mM SDS. Finally, at binding saturation (inflection point), 37 molecules of SDS have bound and the free SDS concentration (cmc) is 3.75 mM. This binding corresponds to 1.05±0.07 g SDS per gram protein, only slightly lower than the 1.17 g SDS per gram protein seen for many other proteins [47]. The binding data are summarized in Table 1.

The enthalpy associated with the four different points also scales linearly with protein concentration, although data are slightly more scattered (Fig. 2C and Table 1).

3.3. Multiphasic relaxation phases coincide with hemi-micelle formation on S6

We can analyse this phenomenon in more detail by following the kinetics of these conformational changes. Changes in fluorescence caused by simple binding of SDS micelles, and concomitant change in the polarity of the Trp environment, should be virtually instantaneous, while conformational rearrangements tend to occur on a slower time-scale. Interestingly, at SDS concentrations between 0.75 and 1.75 mM, corresponding to the first conformational change seen in equilibrium titrations, we observe three conformational changes (Fig. 3A). Of these, the fast phase with rate constants around 2–8 s^{-1} and the intermediate phase with rate constants 0.1–0.4 s^{-1} disappear around 1.75 mM SDS, slightly below the onset of micelle formation. The slow phase dominates in terms of amplitude (Fig. 3B), and the log of the slow rate constant increases linearly with increasing [SDS] until it reaches a plateau around 4 mM SDS,

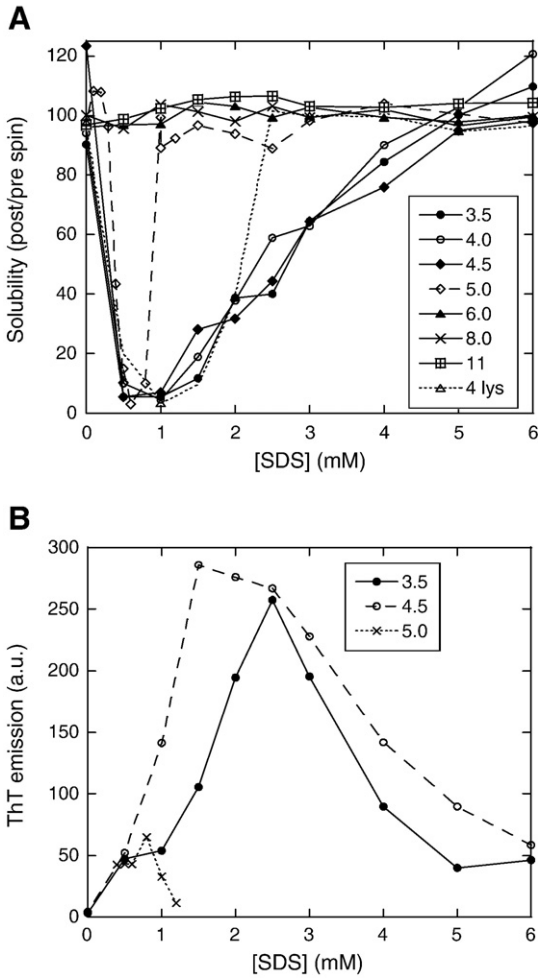

Fig. 5. (A) Solubility of 20 μM S6 as a function of SDS at pH 3–11. Solubility measured as the ratio of the Trp emission intensity of the supernatant (excitation 280 nm, emission 350 nm) before and after centrifugation. Solubility of lysozyme (lys) at pH 4 also shown. (B) ThT fluorescence of pellets obtained from panel A (excitation 350 nm, emission 485 nm) by centrifugation and resuspension in the same volume and same buffer as in (A) but without SDS.

coinciding with the plateau in equilibrium fluorescence. We have described its subsequent dependence on SDS concentration in detail elsewhere [32,33]. Thus kinetics also illuminate a fundamental distinction in the behaviour of S6, namely a multiphasic change below cmc versus single-step unfolding above the cmc.

Next we wanted to probe whether SDS remains monomeric when interacting with S6 below the cmc. It is possible for SDS to form aggregates termed hemi-micelles on protein surfaces which provide binding sites for multiple SDS molecules. This can be investigated using the probe pyrene whose fluorescence (quantified as the ratio of the two emission bands at 383 and 373 nm) changes in a micellar – as well as a hemi-micellar – environment [36], making it a useful tool to determine cmc values. In the absence of protein, pyrene shows a rise in the I_3/I_1 ratio from ca. 2 mM SDS onwards. However, in the presence of S6, there is an intermediate rise in the I_3/I_1 ratio already around 0.6 mM SDS, which only converges with the protein-free pyrene data around 4 mM SDS (Fig. 4A). This is evidence that SDS forms organized structures on the S6 surface in the concentration range 0.5–2 mM SDS, and the formation of these organized structures leads to multiphasic conformational changes. Note that since these hemi-micelles only form on the surface of the protein (they are not observed in the absence of S6 in Fig. 4A), they do not exist as bulk species but form part of the mass balance described in Eq. (3), and therefore do not violate the underlying assumption of this equation.

Note that pyrene does not appear to bind to native S6, since S6 does not lead to any change in the I_3/I_1 ratio at 0 mM SDS. It cannot be excluded that pyrene can bind to S6 once it has undergone conformational changes in the presence of SDS (giving rise to the increase in the I_3/I_1 ratio around 0.6 mM SDS), but we consider this somewhat less likely for several reasons: First of all, there are already 8–12 SDS molecules bound at this stage according to ITC, which provide ready binding sites for pyrene. Secondly, there are no additional changes in the I_3/I_1 ratio in the region around 1–4 mM SDS, where up to 18 additional SDS molecules bind, potentially providing new binding sites for pyrene if it was previously bound to S6.

We then sought to elucidate whether the early stages in the SDS-S6 interactions were sensitive to protein global stability. We compared the SDS-titration of S6 wildtype with two destabilized S6 mutants, namely LA30 (the change in free energy of unfolding compared to wildtype $\Delta\Delta G_{D-N}$=2.6 kcal/mol [35]) and the double mutant VA6/LA30 ($\Delta\Delta G_{D-N}$=5.9 kcal/mol [48]). All three variants showed very similar titration curves (Fig. 4B), with even a hint that the first conformational transition of LA30 occurs at slightly higher SDS concentrations than that

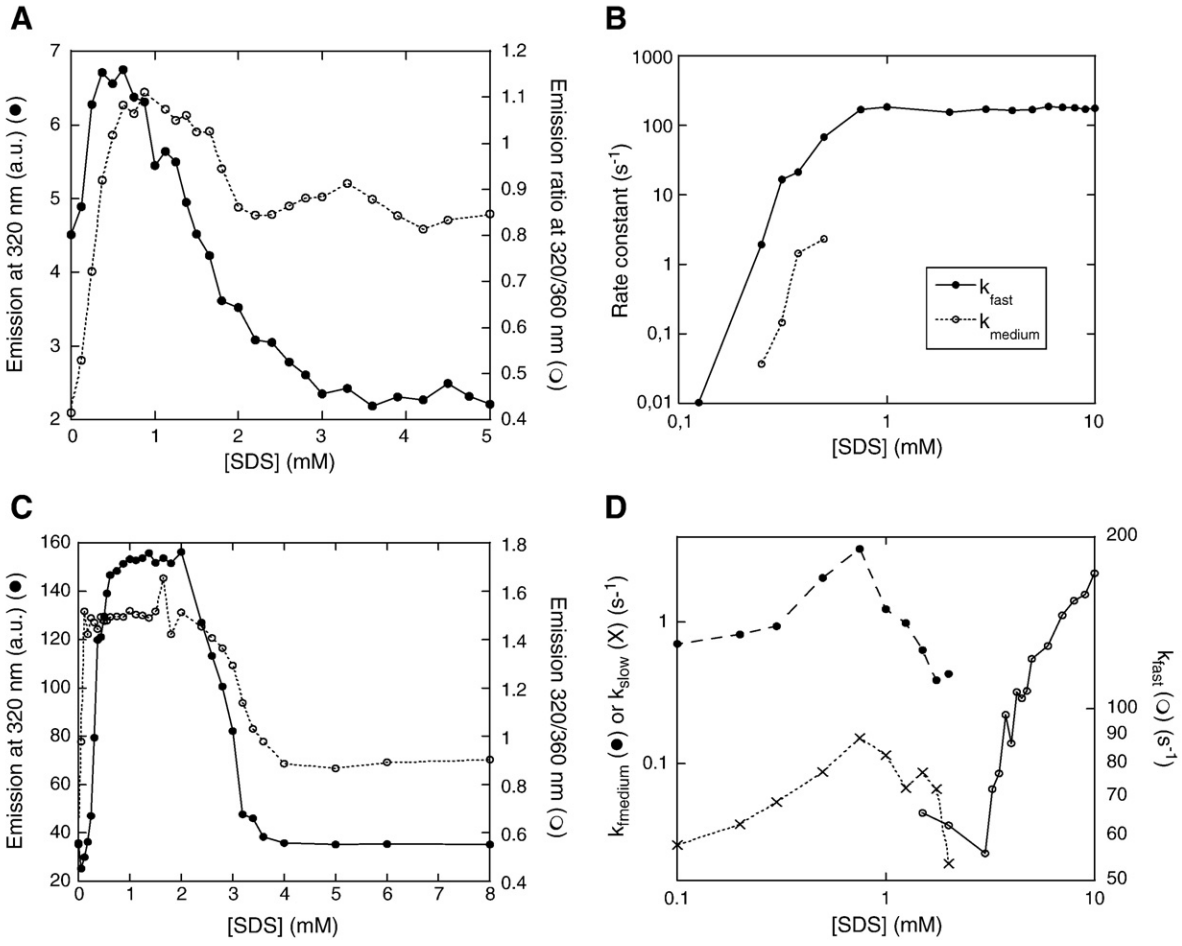

Fig. 6. Equilibrium titration of 2 μM S6 with SDS in 20 mM sodium acetate at (A) pH 5.5 and (C) pH 4. Kinetics of unfolding as a function of SDS concentration in 20 mM sodium acetate at (B) pH 5.5 and (D) pH 4.

of S6 wildtype. This indicates that the equilibrium binding of monomeric SDS to S6 is not coupled to global stability.

3.4. Precipitation of S6 by SDS under acidic conditions

SDS–protein interactions are likely to be mediated to a significant extent by electrostatic interactions which will be altered by changes in pH. Upon incubation of S6 with sub-micellar [SDS] at pH-values below 5, we noticed that the solution became turbid at some concentrations. We systematically analyzed this by incubating 20 μM S6 with 0–6 mM SDS in the pH range 3.5–11 for an hour. Trp fluorescence was then measured before and after spinning down insoluble material, leading to solubility curves (Fig. 5A). These indicated that whereas S6 remains soluble at all SDS concentrations at pH 6 and above, solubility decreases to almost 0% at pH 5 between 0.4 and 0.8 mM SDS; at pH 4.5 and below, solubility is very low between 0.5 and 1 mM SDS, and only recovers to 100% from 5 mM SDS onwards. Interestingly, the spun-down pellet gave rise to a significant rise in the fluorescence of the fibril-sensitive dye Thioflavin T (Fig. 5B). This suggested that SDS might be able to precipitate S6 to orderly aggregates at low pH. The ability of SDS to precipitate proteins appears to be a general feature, as we also observe precipitation of all other proteins we have tested at sub-micellar SDS concentrations at pH 4, including hemoglobin, hen egg white lysozyme, Acyl Co-A binding protein and the all-β sheet protein TNfn3 (data not shown).

To investigate the changes at low pH more systematically, we first carried out equilibrium titrations of S6 at pH 4 and pH 5.5 at a protein concentration where no measurable precipitation occurs at pH 4 (2 μM). At pH 5.5, we see the same increase in intensity followed by a decrease as at pH 8; however, the lag region before the initial rise has essentially disappeared for both absolute intensity values as well as ratios between 320 and 360 nm (Fig. 6A). Similar behaviour is seen at pH 4 (Fig. 6C), although the peak region has broadened to span 0.6–2 mM SDS. In addition, the intensity at pH 4 increases around 8-fold upon addition of SDS. This reflects the fact that Trp fluorescence is severely quenched in the native state below pH 5 (data not shown). In terms of kinetics, the main change is that the dominant phase which persists at higher concentrations remains the fastest phase throughout. At pH 5.5, there is one dominant relaxation phase which increases linearly with [SDS] in a log–log plot and then reaches a plateau, while a minor and slower phase is only observed around 0.25–0.5 mM SDS (Fig. 6B). This latter phase corresponds to the peak region in the equilibrium titration, just as at pH 8. At pH 4, two slow phases are observed only at concentrations up to the end of the peak (2 mM), above which a very fast phase takes over (Fig. 6D).

3.5. Slow precipitation processes with lag phases at pH 5.5

Thus at low pH we still observe the same general conformational changes on the second-to-minute time-scale as at neutral pH, although there are variations in the nature and number of phases. To investigate possible slower processes, we monitored the process in a plate reader where samples were incubated with shaking at 42 °C over a period of several days. At pH 4 and 8, we observe up to 50% increase in Trp fluorescence over a time scale of around 10 h (Fig. 7A). These signal changes

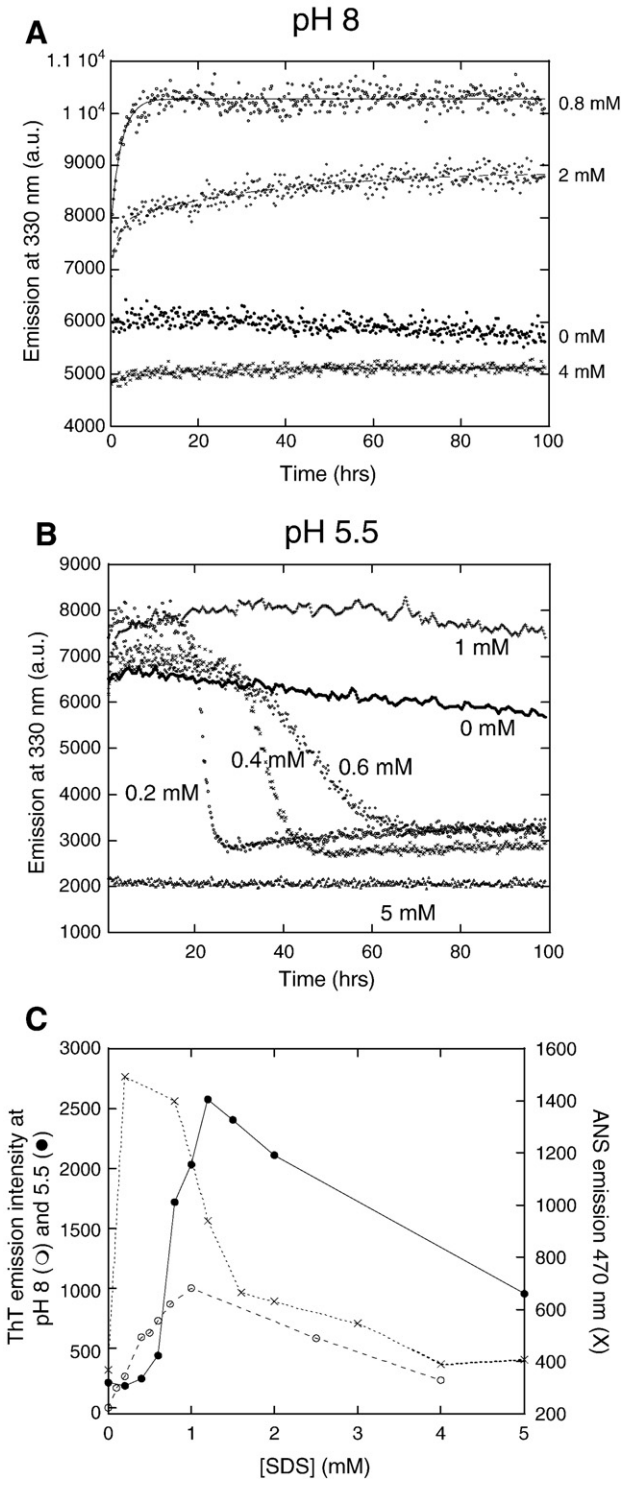

Fig. 7. Plate-reader measurements of S6 emission intensity at 330 nm in (A) 20 mM Tris pH 8 and (B) 20 mM sodium acetate pH 5.5 at the indicated SDS concentrations using 100 μM S6 at 42 °C. (C) ThT fluorescence of samples from the termination of the plate reader assays in (A) and (B). ANS fluorescence of freshly prepared S6 in 20 mM Tris pH 8 in different concentrations of SDS at 25 °C are also shown.

only occur within a narrow range of SDS concentrations, corresponding to the concentration range where a large signal change is seen under equilibrium titrations; at lower and higher SDS concentrations, there is no development. The data fit well to single or double exponential functions. Thus the signal changes monitored by fast reaction kinetics are only the first in a series of

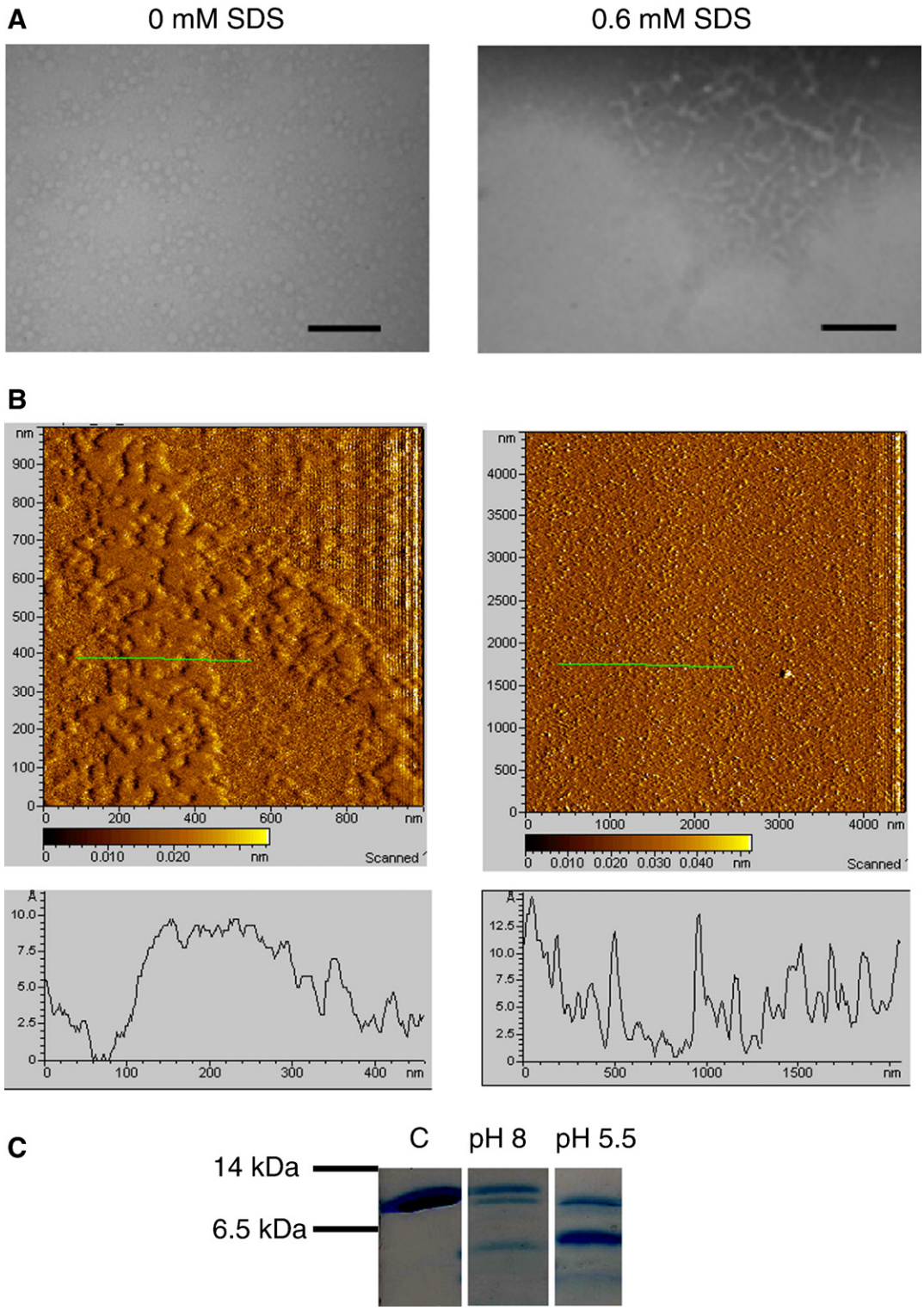

Fig. 8. (A) Electron microscopy images of S6 samples from plate reader in Fig. 6B (20 mM sodium acetate pH 5.5) at (left) 0 and (right) 0.6 mM SDS. No aggregates were seen at 5 mM SDS. The scale bar represents 100 nm. (B) AFM images of S6 after 7 day s of incubation at 42 °C at (left) 0.4 and (right) 1.5 mM SDS in 20 mM sodium acetate pH 5.5. The bottom panel shows the height sampled by the green line. (C) SDS-PAGE analysis of proteolytic degradation of 10 μM S6 in 20 mM Tris pH 8 and 20 mM sodium acetate 5.5 in 1.5 mM SDS (30 min at 25 °C), using the protease Alcalase (10 nM). "C" is undegraded S6.

Table 2
SDS concentrations at pH 5.5 at which lag phase aggregation is observed for different S6 mutants and their associated lag times (in minutes) [a, b]

[SDS]→	0.2 mM	0.4 mM	0.6 mM	0.8 mM	1 mM	1.5 mM	2 mM
Mutant↓							
IA8	–	550	2800	ND	3300	3950	4000
FA60	350	1560	3700	–	–	–	–
Wildtype	1275	2030	ND	2600	–	–	–
LA19	–	–	–	–	–	2150	–
LA52	750	–	–	–	–	–	–
VA9	150	–	–	–	–	–	–
VA90	–	–	–	2150	–	–	–
IA26	125	–	–	–	–	–	–

–: no lag phase observed; ND: not determined.
[a] All experiments in 20 mM NaOAc pH 5.5 and 42 °C using 100 μM protein. Lag times (in minutes) determined as described in Materials and Methods. Standard deviations (from duplicates) 20–30%.
[b] No lag times observed at any SDS concentration for the mutants LA21, VA65,VA37 and IA25.

rearrangements at low concentrations. However, at pH 5.5, a more unusual development is observed between 0.2 and 0.6 mM SDS, in which there is a lag phase of 20–40 h before the signal decreases to a plateau level of around 40% of the original value (Fig. 7B). This time course is similar to that observed for many proteins undergoing fibrillation and has also been observed for S6 fibrillating at pH 2 [13]. However, there are some differences compared to the conventional fibrillation time profiles. Firstly, when Thioflavin T was added at the end of the reaction, the ThT fluorescence peaked around 1 mM SDS and was quite low at the SDS concentrations where the lag phase was observed (Fig. 7C). Furthermore, when the fibril-specific dye Congo Red was added at the end of the reaction, it failed to undergo the spectral band-shift characteristic of the fibril-bound state. In contrast, the hydrophobic probe ANS binds with particular affinity to S6 between 0.2 and 0.8 mM SDS even without prior long-term incubation of S6 with SDS (Fig. 7C).

We next sought to analyze the structure of the aggregates formed in this way. At pH 5.5, electron microscopy pictures reveal no persistent aggregate structure at 0 and 5 mM SDS but at 0.6 mM SDS we observe a few cases of ordered structures similar to fibrils (Fig. 8A), although we did not find many examples and the putative fibrils were difficult to visualize clearly. Atomic force microscopy reveals a compact but non-fibrillar state at 0.4 mM SDS and only scattered aggregates at 1.5 mM (Fig. 8B) (these states were observed consistently and were not observed in the absence of SDS). At both pH 4 and 5.5, Fourier transform infrared spectroscopy of the pelleted aggregates formed at different time points revealed only minor changes in overall secondary structure at different SDS concentrations and as a function of time compared to the native state (data not shown). Thus the aggregates formed by low concentrations of SDS do not appear to contain elevated amounts of β-sheet structure compared to the SDS-free samples. In addition, under all long-time runs, the ratio between emission at 330 and 355 nm remains constant, unlike the case for S6 fibrillation at pH 2, where the ratio increases from 1 to around 1.6 [13].

To compare the flexibility of the structures of S6 at pH 5.5 and 8.0, populated at the onset of the reaction prior to aggregation, we subjected S6 to limited proteolysis at both pH-values in 1.5 mM SDS using the SDS-robust protease Alcalase which is able to cleave after essentially all amino acids, although it shows a preference for hydrophobic amino acids. SDS-PAGE revealed in both cases the formation of a band migrating just below the intact protein (Fig. 8C), which N-terminal sequencing revealed to consist of the sequence 8/9–101 (middle of the first β-strand). The complementary peptide (1–7/8) was too small to be detected on the gel. At pH 8, an additional band, corresponding to a molecular weight around 6 kDa on the SDS gel, was observed with an N-terminus at position 38 and 39 in β-strand 2, (the complementary sequence 1–38/39 was not observed as it was presumably rapidly degraded). At pH 5.5, a major band around 6 kDa and a very faint band around 3 kDa were observed, with N-termini at residue 43 (β-strand 2) and 76 (middle of α-helix 2). This suggests that low concentrations of SDS at both pH-values renders regions of β-sheet 1 and 2 more flexible; at pH 5.5, the region around α-helix 2 also becomes more flexible.

It thus appears that S6 assumes a partially folded state at very low SDS concentrations, which makes it particularly prone to subsequent aggregation, but no significant structural changes occur at the monomer level during the aggregation process.

3.6. Side-chain sensitivity and seeding ability of S6 aggregates

The lack of evidence for well-defined fibrillar structures might be taken to indicate that the aggregates formed at intermediate SDS concentrations lacked specific interactions between proteins. To investigate this further, we monitored the aggregation kinetics of 11 different S6 mutants over longer time scales using a plate reader. Of these, 7 show the characteristic lag phase-decrease in fluorescence; all do so only at pH 5.5 (not at pH 5 and to a much less pronounced extent at pH 6) and in a relatively narrow SDS interval. However, the range of the SDS interval varies quite considerably among the mutants (Table 2), spanning the whole range of 0.4–2 mM for the mutant IA8 and only occurring at a

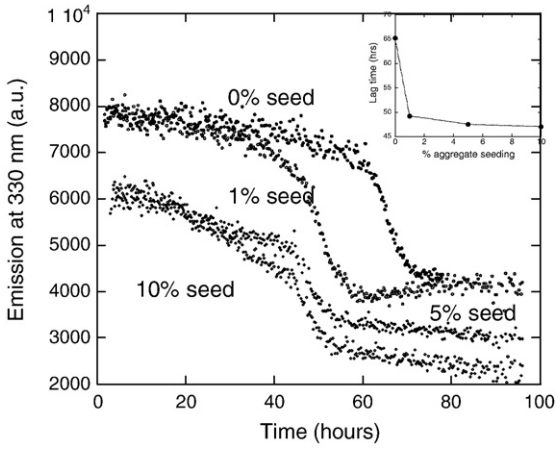

Fig. 9. Plate-reader assay of the seeding of IA8 S6 in 1.5 mM SDS using 1–10% IA8 aggregate from a previous aggregation reaction in 20 mM sodium acetate pH 5.5 at 42 °C. *Insert:* Lag time of fibrillation as a function of aggregate concentration.

single measured concentration for several other mutants. The breadth of the SDS interval does not correlate with the lag time, however, suggesting that aggregation versatility and rapidity of aggregation are different phenomena.

A classical test of the specificity of an aggregation reaction is the ability to seed the reaction by the addition of small amounts of pre-formed aggregates. We see a reduction in aggregation lag time by around 25% when as little as 1% aggregate is added (Fig. 9), although no further effect is observed at higher concentrations (Fig. 9 insert).

4. Discussion

4.1. Three different sub-micellar concentration regimes with different modes of protein–SDS interactions

The purpose of this study was to obtain a better understanding of the ability of sub-micellar SDS to stimulate protein aggregation, previously reported for only a small number of proteins. At the very onset, it is obvious from our data that there is a rich complexity of interactions between S6 and SDS at sub-micellar concentrations. Over time scales spanning seconds to hours, we observe a number of transitions involving changes in conformation and levels of association. These interactions vary significantly as a function of SDS concentration. We can divide the observations into at least 3 concentration regimes:

4.2. Regime 1: Below 0.2 mM SDS

In this range, we observe no binding or conformational changes according to either fluorescence or CD. ITC data indicate that 8 molecules of SDS bind in this concentration region, but clearly this is not sufficient to cause detectable conformational changes. This suggests that the monomers bind separately and loosely on the S6 surface.

4.3. Regime 2: 0.2–2 mM

This region, which is still below the cmc, is the richest in terms of conformational changes. Although the total number of bound SDS molecules only rises to 12 (ITC data, Table 1), our pyrene experiments (Fig. 4A) suggest that they undergo a significant rearrangement to form hemi-micellar aggregates on the protein surface. The total number of aggregated molecules of SDS on BSA increases from 29 to 82 between 17 and 105 mM [49], and in view of of the 6-fold larger size of BSA compared to S6, it would seem quite plausible to have 12 molecules of SDS aggregated on S6. Binding of this number of SDS molecules is sufficient to cause significant changes in both secondary (CD) and tertiary (fluorescence) structure (Fig. 1). As shown in Fig. 7C, the ensuing state is sufficiently flexible over a wide pH-range to bind the probe ANS (or to allow ANS to insert into the hemi-micellar aggregate). The population is probably quite heterogeneous and fluctuating, since absolute fluorescence intensities do not coincide exactly with fluorescence intensity ratios (Fig. 1A). Several mechanistic steps are involved in this change. On the second scale, 2–3 phases are observed (Fig. 3), while even slower phases can be seen over several hours (Fig. 7A). For these very slow phases, there is no change in the ratio of the emission intensities at 330 and 350 nm, suggesting that only subtle changes in conformation or association occur. The main changes are related to protein solubility. Above pH 5.5, these slow phases do not lead to visible aggregation and are characterized by a (relatively small) increase in fluorescence (Fig. 5A). Only a small amount of aggregate is formed, leading to a slight increase in thioflavin T fluorescence. In contrast, at pH 5.0–5.5 over a narrow concentration range (0.2–0.6 mM SDS), a time profile with a characteristic lag phase is observed (Fig. 7B), leading to states which can be spun down and lead to a significant increase in thioflavin T fluorescence (Fig. 7C). The single slow second-scale phase observed around pH 5.5 by stopped-flow kinetics (Fig. 6A) would appear to be a prerequisite for this aggregation, since both phases are only seen over a narrow concentration range. Interestingly, at pH 8.0, two slow second-scale phases are observed by stopped-flow kinetics in the very same concentration range (0.8–2 mM SDS) where the hour-scale increase in fluorescence occurs. This suggests these two pairs of phases are also linked mechanistically, although they must differ qualitatively from the reactions at pH 5.5 where there is a decrease in fluorescence in the same time-scale phase. Below pH 5.0, precipitation happens much faster and is only observed on the hour-scale at SDS concentrations that are either low or close to the cmc. Thus SDS can propel S6 in a number of different conformational directions, depending on pH and concentration. Limited proteolysis data suggest that S6 partially unfolds in the β-sheet region around strands 1 and 2 at both pH-values (Fig. 8C); in addition, the region around the C-terminal helix is rendered more flexible at pH 5.5. The added unfolding in this region may be the basis for the increased aggregation propensity. We have in a previous study identified regions of S6 which appear to be the first sites of unfolding in the presence of low (mode 1) and high (mode 2) concentrations of SDS micelles at pH 8.0 [33]. Interestingly, the region around strand 1 is targeted by SDS in both modes while the C-terminal helix only becomes exposed to SDS in mode 2, leading to rapid unfolding [33]. This suggests that the C-terminal helix is an important determinant of structural integrity in an amphiphilic environment.

4.4. Regime 3: Ca. 2–5 mM

This is a straight-forward transition to the micelle-unfolded state, accompanied by the binding of a large number of SDS molecules, leading eventually to 36 SDS molecules per S6 molecule. We observe an overall decrease in equilibrium fluorescence which stabilizes at plateau level before the cmc is reached (Fig. 1A). The kinetics are simple, since only a single fast relaxation phase is seen, without any further changes over longer time scales and no aggregation occurring (Fig. 3A).

In all cases, these transitions are uncoupled from the conformational stability of S6 measured in the absence of SDS (Fig. 3B). Thus the SDS-induced conformational changes are not coupled to the intrinsic stability of the protein but involve specific ligand-type interactions.

4.5. Ability to precipitate protein requires titration of acidic residues

SDS is known to precipitate proteins under certain conditions, although the basis for this has not been discussed in detail. At pH 3.3 and 90 μM protein, completely soluble SDS-lysozyme complexes are only formed above 5 mM SDS, *i.e.* an SDS:protein molar ratio of 60 [50,51]. This corresponds to an SDS concentration of ca. 1.2 mM in the presence of 20 μM protein (the protein concentration used in our studies). At 20 μM protein and pH 4.0, we see full resolubilization of lysozyme at 2.5 mM SDS (Fig. 5A), in good agreement with this report. Under the same conditions, complete solubilization of S6 is achieved at a slightly higher concentration (5 mM SDS). At pH 4.5 and below, precipitation happens over a relatively broad range (0.5–5 mM SDS), while it is not detectable at pH 6 and above. The pH region 5–6 thus forms a transition region. What is the basis for this precipitation? S6 has an experimentally determined isoelectric point around 6.5 [32], but other proteins with much higher p*I* values (*e.g.* lysozyme, p*I* 10.8) also precipitate below pH 5, excluding a simple isoelectric effect. We have previously reported that the kinetics of unfolding of S6 titrates strongly with pH, increasing 100-fold as we decrease pH from 8 to 5 with an apparent pK_a of around 5.5 [32]. We attributed this effect to the titration of the acidic residues Asp and Glu, whose pK_a values will be increased in the apolar environment provided by the SDS alkyl side chains. In the absence of acidic side chains, this pH-dependence disappears; for example, the anti-microbial peptide Novispirin which only has a C-terminal carboxyl group to offset 4 Lys and 3 Arg, is precipitated by SDS at neutral pH [25]. Although our solubility experiments on S6 were conducted below cmc and thus at most in the presence of hemi-micelles rather than micelles proper, the effect on the pK_a of Asp and Glu are most likely similar. We therefore consider it likely that the electrostatic repulsion of SDS by deprotonated side chains limits the ability of SDS to bind to the protein. Once this can be overcome at sufficiently low pH-values, SDS can bind to the cationic regions and presumably act as a charge neutralizer that allows protein monomers to attach to each other.

4.6. Submicellar SDS induces aggregates but not fibrils in S6

The question now is what kind of aggregates is formed. They possess some of the characteristics of fibrils, increasing the fluorescence of Thioflavin T and forming with a characteristic lag phase. Furthermore, pre-formed aggregates can to some extent accelerate the process for a new batch when added as seeds. The aggregates probably possess some degree of side-chain specificity, since different S6 mutants show considerable differences in their lag phase behaviour. Side-chain sensitivity is even more marked for *bona fide* fibrils of S6 formed at low pH, and mark out a contiguous region which we have suggested to be a flexible domain that is central to the fibrillation process [13]. However, for SDS-induced aggregation, mutant data are somewhat more scattered and do not identify a specific region in the protein. In fact the SDS-induced aggregate is unlikely to be a proper fibril for a number of reasons. Firstly, the increase in Thioflavin T fluorescence is fairly low (Fig. 5B), contrasting with the many orders of magnitude increase that *e.g.* glucagons fibrils can elicit [52]. Secondly, there is no shift in the Congo Red shift. Thirdly, EM and AFM data do not reveal needle-shaped fibril structures (Fig. 8), although the aggregates have a certain degree of regular order. Finally, the FTIR data do not indicate any overall change in secondary structure in the presence of SDS, with little increase in β-sheet signal. So what kind of aggregates has been formed? S6 already possesses extensive β-sheet structure (4 β-sheets as well as 2 α-helices) which could presumably engage in intermolecular contacts. We have persuaded S6 to form tetramers which interface via appropriate mutations in the outward β-strand [53], and it is possible that this can also be exploited by SDS. It is tempting to speculate that such contacts could be further consolidated by hemi-aggregates on different S6 molecules linking up to form micellar structures with alkyl chains facing away from the S6 surface and bridging S6 molecules.

Just as the engineered tetramer represented an association that was trapped at an early stage, it could be imagined that the aggregates represent structures that are trapped at intermediate concentrations *en route* to the actual fibril, because they lack sufficient conformational flexibility to undergo the major structural changes needed to fibrillate. Trapping could occur at several levels. Thus the precipitates at pH 5.5 that lead to the highest ThT signal (around 1.5 mM SDS, which we term Agg2) show less organized structure than those formed around 0.4–0.6 mM SDS (and which have a lag phase, termed Agg1). It is possible that Agg1 represents a more structured aggregate than Agg2 which is nevertheless trapped in a pre-fibrillar structure or which will rearrange to fibrils over longer time scales than tested in the present study. There is precedence for such semi-trapped states: Aβ makes a transition from quasi-amorphous to fibrillar structure over 4 days in the presence of 2 mM SDS. For β_2-microglobulin, agitation-induced amorphous aggregates are an important early step in the aggregation process [54–56]. Incomplete conversion to β-sheet conversion has also been reported for the synthetic insulin variant miniproinsulin [57] which aggregates to non-fibrillar structures, but also shows seeding ability. Unlike human insulin fibrils, MPI shows less than 2-fold increase in ThT fluorescence and also very low ANS binding. Thus it has certain elements in common with SDS-aggregated S6.

In summary, it is notable that we observe a significant change in the properties of the states formed at the very low SDS versus cmc-level concentrations. It is possible that the state formed at very low concentrations is sufficiently "poised" towards flexibility, yet not blocked too much by bound SDS, to allow it to aggregate through slow conformational changes. Despite the unphysiological nature of SDS, the richness of the conformational changes induced in S6 by this molecule over a narrow range of concentration and pH suggests that its cellular equivalents such as free fatty acids may exert considerably influence on protein aggregation behaviour. In this sense, the SDS-bound state could be a model for other slowly aggregating protein species in the cellular cytosol.

Acknowledgements

D.E.O. is supported by the Danish Research Foundation (CureND) and the Villum Kann Rasmussen Foundation (BioNET). Part of this work was funded by a Visiting Scientist grant to D.E.O. from Osaka City University. P.S. and K.K.A. are supported by the Innovation Consortium BIOPRO through a grant from the Danish Ministry of Science, Technology and Innovation. We are very grateful to Professor Peter Westh (Roskilde University) for providing access to the Isothermal Titration Calorimetry apparatus, Ture Damhus (Novozymes A/S) for providing alcalase, and to Professor Jan J. Enghild, Dr. Steen Vang Petersen and Ida Thøgersen for helping with N-terminal sequencing.

References

[1] D.J. Selkoe, Folding proteins in fatal ways, Nature 426 (2003) 900–904.
[2] S. Frokjaer, D.E. Otzen, Protein drug stability — a formulation challenge, Nat. Rev. Drug. Delivery 4 (2005) 298–306.
[3] F. Chiti, P. Webster, N. Taddei, A. Clark, M. Stefani, G. Ramponi, C.M. Dobson, Designing conditions for in vitro formation of amyloid protofilaments and fibrils, Proc. Natl. Acad. Sci. U. S. A. 96 (1999) 3590–3594.
[4] B. O'Nuallain, A.D. Williams, P. Westermark, R. Wetzel, Seeding specificity in amyloid growth induced by heterologous fibrils, J. Biol. Chem. 279 (2004) 17490–17499.
[5] F. Chiti, M. Stefani, N. Taddei, G. Ramponi, C.M. Dobson, Rationalization of the effects of mutations on peptide and protein aggregation rates, Nature 424 (2003) 805–808.
[6] K.F. DuBay, A.P. Pawar, F. Chiti, J. Zurdo, C.M. Dobson, M. Vendruscolo, Predicting absolute aggregation rates of amyloidogenic polypeptide chains, J. Mol. Biol. 341 (2004) 1317–1326.
[7] A.M. Fernandez-Escamilla, F. Rousseau, J. Schymkowitz, L. Serrano, Prediction of sequence-dependent and mutational effects on the aggregation of peptides and protein, Nat. Biotechnol. 22 (2004) 1302–1306.
[8] M.S. Wolfe, The gamma-secretase complex: membrane-embedded proteolytic ensemble, Biochemistry 45 (2006) 7931–7939.
[9] C.-D. Chen, M.E. Huff, J. Matteson, L. Page, R. Phillips, J.W. Kelly, W.E. Balch, Furin initiates gelsolin familial amyloidosis in the Golgi through a defect in Ca2+ stabilization, EMBO J. 20 (2001) 6277–6287.
[10] R.L. Isaacson, A.G. Weeds, A.R. Fersht, Equilibria and kinetics of folding of gelsolin domain 2 and mutants involved in familial amyloidosis-Finnish type, Proc. Natl. Acad. Sci. U. S. A. 96 (1999) 11247–11252.
[11] J.L. Holton, T. Lashley, J. Ghiso, H. Braendgaard, R. Vidal, C.J. Guerin, G. Gibb, D.P. Hanger, A. Rostagno, B.H. Anderton, C. Strand, H. Ayling, G. Plant, B. Frangione, M. Bojsen-Møller, T. Revesz, Familial Danish Dementia: A novel form of cerebral amyloidosis associated with deposition of both amyloid-Dan and amyloid-Beta, J. Neuropath. Exp. Neurol. 61 (2002) 254–267.
[12] J.J. Liepnieks, B. Kluve-Beckerman, M.D. Benson, Characterization of amyloid A protein in human secondary amyloidosis: the predominant deposition of serum amyloid A1, Biochim. Biophys. Acta 1270 (1995) 81–86.
[13] J.S. Pedersen, G. Christiansen, D.E. Otzen, Modulation of S6 fibrillation by unfolding rates and gatekeeper residues, J. Mol. Biol. 341 (2004) 575–588.
[14] K.-I. Yamaguchi, H. Naiki, Y. Goto, Mechanism by which the amyloid-like fibrils of a beta2-microglobulin fragment are induced by fluorine-substituted alcohols, J. Mol. Biol. 363 (2006) 279–288.
[15] M. Necula, C.N. Chirita, J. Kuret, Rapid anionic micelle-mediated alpha-synuclein fibrillization in vitro, J. Biol. Chem. 278 (2003) 46674–46680.
[16] M.D. Murkasch, J. Biernat, M. von Bergen, C. Griesinger, E. Mandelkow, M. Zweckstetter, Sites of tau important for aggregation populate beta-structure and bind to microtubules and polyanions, J. Biol. Chem. 280 (2005) 24978–24986.
[17] J.D. Knight, A.D. Miranker, Phospholipid catalysis of diabetic amyloid assembly, J. Mol. Biol. 341 (2004) 1175–1187.
[18] E. Sparr, M.F.M. Engel, D.V. Sakharov, M. Sprong, J. Jacobs, B. de Kruijff, J.W.M. Höppner, J.A. Killian, Islet amyloid polypeptide-induced membrane leakage involves uptake of lipids by forming amyloid fibers, FEBS Lett. 577 (2004) 117–120.
[19] H. Zhao, E.K.J. Tuominen, P.K.J. Kinnunen, Formation of amyloid fibers triggered by phosphatidylserine-containing membranes, Biochemistry 43 (2004) 10302–10307.
[20] V.A. Fadok, D.R. Voelker, P.A. Campbell, J.J. Cohen, D.L. Bratton, P.M. Henson, Exposure of phosphatidylserine on the surface of apoptotic lymphocytes triggers specific recognition and removal by macrophages, J. Immunol. 148 (1992) 2207–2216.
[21] I. Rustenbeck, A. Matthies, S. Lenzen, Lipid composition of glucose-stimulated pancreatic islets and insulin secreting tumor cells, Lipids 29 (1994) 685–692.
[22] R.V. Farese, P.E. DiMarco, D.E. Barnes, M.A. Sabir, R.E. Larson, J.S. Davis, A.D. Morrison, Rapid glucose-dependent increases in phosphatidic acid and phosphoinositides in rat pancreatic islets, Endocrinology 118 (1986) 1498–1503.
[23] N. Salamat-Miller, J. Fang, C.W. Seidel, Y. Assenov, M. Albrecht, C.R. Middaugh, A network-based analysis of polyanion-binding proteins utilizing human protein arrays, J. Biol. Chem. 282 (2007) 10153–10163.
[24] V. Rangachari, D.K. Reed, B.D. Moore, T.L. Rosenberry, Secondary structure and interfacial aggregation of Amyloid-b(1–40) on sodium dodecyl sulfate micelles, Biochemistry 45 (2006) 8639–8648.
[25] R. Wimmer, K. Andersen, M. Davidsen, S. Mølgaard, B. Vad, D.E. Otzen, Versatile interactions of the antimicrobial peptide Novispirin with detergents and lipids, Biochemistry 45 (2006) 481–497.
[26] S. Yamamoto, K. Kasegawa, I. Yamaguchi, S. Tsutsumi, J. Kardos, Y. Goto, F. Gejyo, H. Naiki, Low concentrations of sodium dodecyl sulfate induces the extension of beta-2-microglobulin-related amyloid fibrils at neutral pH, Biochemistry 43 (2004) 11075–11082.
[27] G.W. Dombi, H.B. Halsall, Collagen fibril formation in the presence of sodium dodecyl sulphate, Biochem. J. 228 (1985) 551–556.
[28] T.A. Pertinhez, M. Bouchard, R.A.G. Smith, C.M. Dobson, L.J. Smith, Stimulation and inhibition of fibril formation by a peptide in the presence of different concentrations of SDS, FEBS Lett. 529 (2002) 193–197.
[29] A.A. Moosavi-Movahedi, P. Pirzadeh, S. Hashemnia, S. Ahmadian, B. Hemmateenejad, M. Amani, A.A. Saboury, F. Ahmad, M. Shamsipur, G.H. Hakimelahi, F.Y. Tsai, H.H. Alijanvand, R. Yousefi, Fibril formation of lysozyme upon interaction with sodium dodecyl sulfate at pH 9.2, Colloids Surf., B Biointerfaces 60 (2007) 55–61.
[30] S. Micelli, D. Meleleo, V. Picciarelli, M.G. Stoico, E. Gallucci, Effect of nanomolar concentrations of sodium dodecyl sulfate, a catalytic inductor of α-helices, on human calcitonin incorporation and channel formation in planar lipid membranes, Biophys. J. 87 (2004) 1065–1075.
[31] A.D. Nielsen, K. Borch, P. Westh, Thermal Stability of *Humicola insolens* cutinase in aqueous SDS, J. Phys. Chem., B 111 (2007) 2941–2947.
[32] D.E. Otzen, Protein unfolding in detergents: effect of micelle structure, ionic strength, pH, and temperature, Biophys. J. 83 (2002) 2219–2230.
[33] D.E. Otzen, M. Oliveberg, Burst-phase expansion of native protein prior to global unfolding in SDS, J. Mol. Biol. 315 (2002) 1231–1240.
[34] D.E. Otzen, M. Oliveberg, Conformational plasticity in folding of the split β-α-β protein S6: evidence for burst-phase disruption of the native state, J. Mol. Biol. 317 (2002) 613–627.
[35] D.E. Otzen, O. Kristensen, M. Proctor, O. Oliveberg, Structural changes in the transition state of protein folding: an alternative interpretation of curved chevron plots, Biochemistry 38 (1999) 6499–6511.
[36] K. Kalyanasundaram, J.K. Thomas, Environmental effects on vibronic band intensities in pyrene monomer fluorescence and their application in studies of micellar systems, J. Am. Chem. Soc. 99 (1977) 2039–2044.
[37] A.D. Nielsen, L. Arleth, P. Westh, Analysis of protein–surfactant interactions — a titration calorimetric and fluorescenc spectroscopic investigation of interactions between *Humicola insolens* cutinase and an anionic surfactant, Biochim. Biophys. Acta 1752 (2005) 124–132.
[38] P. Klemm, G. Christiansen, Three fim genes required for the regulation of length and mediation of adhesion of *Escherichia coli* type 1 fimbriae, Mol. Gen. Genet. 208 (1987) 439–445.

[39] P. Matsudaira, Sequence from picomole quantities of proteins electroblotted onto polyvinylidene difluoride membranes, J. Biol. Chem. 262 (1987) 10035–10038.
[40] N.E. Zhou, C.M. Kay, R.S. Hodges, Synthetic model proteins. Positional effects of interchain hydrophobic interactions on stability of two-stranded a-helical coiled-coils, J. Biol. Chem. 267 (1992) 2664–2670.
[41] S.Y. Lau, A.K. Taneja, R.S. Hodges, Synthesis of a model protein of defined secondary and quaternary structure. Effect of chain length on the stabilization and formation of two-stranded α-helical coiled-coils, J. Biol. Chem. 259 (1984) 13253–13261.
[42] T. Lazarova, K.A. Brewin, K. Stoeber, C.R. Robinson, Characterization of peptides corresponding to the seven transmembrane domains of human adenosine A2a receptor, Biochemistry 43 (2004) 12945–12954.
[43] A.D. Nielsen, L. Arleth, P. Westh, Interactions of *Humicola insolens* cutinase with an anionic surfactant studied by small-angle neutron scattering and isothermal titration calorimetry, Langmuir 21 (2005) 4299–4307.
[44] M.D. Lad, V.M. Ledger, B. Briggs, R.J. Green, R.A. Frazier, Analysis of the SDS-lysozyme binding isotherm, Langmuir 19 (2003) 5098–5103.
[45] D. Kelley, D.J. McClements, Interactions of bovine serum albumin with ionic surfactants in aqueous solutions, Food Hydrocoll. 17 (2003) 73–85.
[46] S. Paula, W. Sus, J. Tuchtenhagen, A. Blume, Thermodynamics of micelle formation as a function of temperature — a high-sensitivity titration calorimetry study, J. Phys. Chem. 99 (1995) 11742–11751.
[47] J.A. Reynolds, C. Tanford, The gross conformation of protein–sodium dodecyl sulfate complexes, J. Biol. Chem. 245 (1970) 5161–5165.
[48] D.E. Otzen, Antagonism, non-native interactions and non-two-state folding in S6 revealed by double-mutant cycle analysis, Prot. Eng. Design Select. 18 (2005) 547–557.
[49] N.J. Turro, X.-G. Lei, K.P. Ananthapadmanabhan, M. Aronson, Spectroscopic probe analysis of protein–surfactant interactions: the BSA/SDS system, Langmuir 11 (1995) 2525–2533.
[50] A. Valstar, W. Brown, M. Almgren, The lysozyme–sodium dodecyl sulfate system studied by dynamic and static light scattering, Langmuir 15 (1999) 2366–2374.
[51] M.N. Jones, P. Manley, in: K.L. Mittal, B. Lindman (Eds.), Surfactants in solution, vol. 2, Plenum Press, London, 1984, p. 1403.
[52] J.S. Pedersen, D. Dikov, J.L. Flink, H.A. Hjuler, G. Christiansen, D.E. Otzen, The changing face of glucagon fibrillation: structural polymorphism and conformational imprinting, J. Mol. Biol. 355 (2006) 501–523.
[53] D.E. Otzen, P. Kristensen, M. Oliveberg, Designed protein tetramer zipped together with an Alzheimer sequence: a structural clue to amyloid assembly, Proc. Natl. Acad. Sci. U. S. A. 97 (2000) 9907–9912.
[54] N.M. Kad, S.L. Myers, D.P. Smith, D.A. Smith, S.E. Radford, E.M. Thomson, Hierarchical assembly of beta2-microglobulin amyloid in vitro revealed by atomic force microscopy, J. Mol. Biol. 330 (2003) 785–797.
[55] P.B. Stathopulos, G.A. Scholtz, Y.M. Hwang, J.A. Rumfeldt, J.R. Lepock, E.M. Meiering, Sonication of proteins causes formation of aggregates that resemble amyloid"", Prot. Sci. 13 (2004) 3017–3027.
[56] Y. Ohhashi, M. Kihara, H. Naiki, Y. Goto, Ultrasonication-induced amyloid fibril formation of beta2-microglobulin, J. Biol. Chem. 280 (2005) 32843–32848.
[57] K. Huang, N.C. Maiti, N.B. Phillips, P.R. Carey, M.A. Weiss, Structure-specific effects of protein topology on cross-beta assembly: studies of insulin fibrillation, Biochemistry 45 (2006) 10278–10293.

4348 *Biochemistry* **2007,** *46,* 4348−4359

Alternative Membrane Protein Conformations in Alcohols†

D. E. Otzen,* P. Sehgal, and L. W. Nesgaard

Department of Life Sciences, Aalborg University, Sohngaardsholmsvej 49, DK-9000 Aalborg, Denmark

Received January 16, 2007; Revised Manuscript Received February 19, 2007

ABSTRACT: Alcohols modulate the oligomerization of membrane proteins in lipid bilayers. This can occur indirectly by redistributing lateral membrane pressure in a manner which correlates with alcohol hydrophobicity. Here we investigate the direct impact of different alcohol−water mixtures on membrane protein stability and solubility, using the two detergent-solubilized α-helical membrane proteins DsbB and NhaA. Both proteins precipitate extensively at intermediate concentrations of alcohols, forming states with extensive (40−60%) *β*-sheet structure and affinity for the fibril-specific dye thioflavin T, although atomic force microscopy images reveal layer-like and spherical deposits, possibly early stages in a fibrillation process trapped by strong hydrophobic contacts. At higher alcohol concentrations, both DsbB and NhaA are resolubilized and form non-native structures with increased (DsbB) or decreased (NhaA) helicity compared to the native state. The alternative conformational states cannot be returned to the functional native state upon dilution of alcohol. The efficiency of precipitation and the degree to which DsbB is destabilized at low alcohol concentrations show the same correlation with alcohol hydrophobicity. Thus, in addition to their effect on the membrane, alcohols perturb membrane proteins directly by solvating the hydrophobic regions of the protein. At intermediate concentrations, this perturbation exposes hydrophobic segments but does not provide sufficient solvation to avoid intermolecular association. Resolubilization requires a reduction in the relative dielectric constant below 65 in conjunction with specific properties of the individual alcohols. We conclude that alcohols provide access to a diversity of conformations for membrane proteins but are not a priori suitable for solution studies requiring reversible denaturation of monomeric proteins.

To remain soluble in the native state, membrane proteins (MPs)[1] need an amphiphilic environment, which can be provided by detergents or lipids. α-Helical MPs typically contain long consecutive sequences of hydrophobic amino acids in the transmembrane segments that allow the helices to dock against each other, stabilized through van der Waals interactions (*1*−*3*). *β*-Barrel MPs are made up of alternating hydrophilic−hydrophobic sequences that alternatively point into the protein interior and out toward the hydrophobic environment (*4*). As a consequence, it is actually possible to solubilize *β*-barrel membrane proteins in high concentrations of chemical denaturants such as guanidinium chloride and urea (*5*−*7*), where they remain in an extensively unfolded state. In contrast, α-helical MPs generally resist this treatment and are most commonly denatured in SDS (*8*−*11*), in which they retain significant amounts of residual helical structure. Thus refolding of *β*-barrel MPs can be followed by diluting the protein from high concentrations of denaturant into lipids or detergents (*6*), whereas α-helical MPs are typically refolded from SDS. The SDS-denatured state of many water-soluble proteins has been the subject of numerous structural studies (*12*−*15*) and appears to consist of isolated detergent-decorated helices joined by more flexible regions. A quantitative way to reversibly denature membrane proteins is to add increasing amounts of SDS in the presence of a constant concentration of a nonionic detergent such as dodecyl maltoside (DM) (*9*, *10*). There appears to be an empirical linear relationship between the SDS mole fraction and the log of the refolding and unfolding rates (*11*, *16*). This relationship also extends to thermal stability, provided account is taken of the micellar rather than bulk composition of detergent (*17*).

The SDS-denatured state retains significant residual structure (*11*, *18*). This may be analogous to the structure of nascent membrane proteins prior to lipid insertion (*19*). Nevertheless, recent reports indicating that this state may have native-like compaction (*20*) have led to the suggestion that the action of SDS may just as well be modeled by simple ligand binding rather than unfolding (*21*). This makes it relevant to look for alternative means of denaturation of membrane proteins.

One possibility is provided by alcohols, which are amphiphilic and contain a hydrophilic headgroup as well as a hydrophobic segment of varying lengths. Alcohols' denaturing action toward soluble proteins (*22*, *23*) is related to their reduction of the relative solvent dielectric constant ϵ_r, which

† D.E.O. is supported by the Danish Research Foundation (CureND) and the Villum Kann Rasmussen Foundation (BioNET). Part of this work was funded by a Visiting Scientist grant to D.E.O. from Osaka City University. P.S. was supported by the Innovation Consortium BIOPRO through a grant from the Danish Ministry of Science, Technology, and Innovation.

* To whom correspondence should be addressed. E-mail: dao@bio.aau.dk.

[1] Abbreviations: DM, dodecyl maltoside; DsbB, disulfide bond forming protein B; HFIP, hexafluoroisopropyl alcohol; iPrOH, 2-propanol; MPs, membrane proteins; NhaA, sodium hydrogen antiporter A; PrOH, *n*-propyl alcohol; TFE, trifluoroethanol.

10.1021/bi700091r CCC: $37.00
Published on Web 03/20/2007

may mimic conditions near the membrane surface (*24*−*26*). Increasing the alcohol concentration generally leads to a uniform increase in α-helicity (*24*, *27*−*30*). The reason for this is not entirely clear (*31*), although the lowered ϵ_r could conceivably strengthen internal hydrogen bonds which can be formed by isolated sequences in the α-helical conformation. However, trifluoroethanol can also induce the accumulation of *β*-sheet-rich aggregation-prone structures at intermediate (20−40%) concentrations and only induce α-helix structures at higher concentrations (*32*). As a further testimony to the versatility of alcoholic conformational switches, methanol but not longer chain alcohols has very recently been reported to induce *β*-sheet structure in an all-α-helix protein (*33*).

This then leads to the interesting question of whether alcohols can be used to reversibly denature membrane proteins for subsequent folding studies. The environment of the membrane protein stabilizing the native state can play a role in the protein's response to alcohols. Previous studies on the *Streptomyces lividans* potassium channel KcsA have shown that the stability of the tetramer in lipids is reduced by molar concentrations of alcohols in an indirect manner which can be related to their ability to alter the lateral membrane pressure and permeabilize the membrane (*34*, *35*). When KcsA is dissolved in detergents and TFE subsequently added, a partially and reversibly unfolded monomeric state is formed at intermediate TFE concentrations, but at higher TFE concentrations this state converts into an irreversibly denatured form (*36*). KcsA is an unusually stable α-helical MP which resists denaturation in SDS, making it possible to monitor its state of oligomerization on SDS−PAGE. Extrapolating on this, a recent study combines 2D gel electrophoresis with exposure to TFE or HFIP (hexafluoroisopropyl alcohol) to identify stable oligomeric membrane protein complexes, based on the criterion that they withstand exposure to SDS and only dissociate in alcohols (*37*). The quoted studies have focused on oligomeric proteins, and while many membrane proteins are found integrated into complexes, a significant number are monomeric. We would like to address the question how monomeric membrane proteins respond to alcohols, more specifically whether they can be unfolded to the same or greater extent by alcohols such as TFE and how reversible this behavior is.

Here we study the response of two α-helical membrane proteins to alcohols, namely, the four-transmembrane helix 176-residue disulfide-exchanging protein DsbB and the 388-residue sodium−hydrogen antiporter NhaA (*38*), both from the inner membrane of *Escherichia coli*. Both proteins can be unfolded in SDS (*39*), and in the case of DsbB, the protein can be reversibly folded into DM micelles as monitored by stopped-flow kinetics (*11*, *16*). We report that incubation with alcohols generally leads to precipitation at intermediate concentrations and the formation of a *β*-rich structure, which at higher concentrations is replaced by a soluble state with altered secondary structure. Both processes are irreversible, precluding the use of this approach for renaturation studies. The alcohols' ability to precipitate proteins, as well as their destabilizing properties at very low concentrations, is directly related to their hydrophobicity. We conclude that alcohols affect intrinsic membrane protein properties as well as exerting an effect via the membrane.

MATERIALS AND METHODS

DsbB (*11*), DsbA (*40*), NhaA (*39*), and AIDA (*41*) were purified as described. The buffer used in all experiments was 25 mM Tris, pH 8, and 0.1 M NaCl. This buffer, including different concentrations of detergent, was completely miscible with all of the alcohols analyzed in this study within the concentration range probed; turbidity was only observed above 40% (v/v) HFIP, 55% TFE, or 75% isopropyl alcohol. Note that the alcohols are expected to alter the pK_a of Tris by little more than 0.1 pH unit (cf. ref *42*). Given that DsbB retains full solubility in detergent over the pH range 3−10 and has unaltered stability over the pH range 8.5−6.5 (data not shown), these small changes in pK_a will not affect solubility or stability by themselves.

Equilibrium Denaturation Experiments. DsbB or NhaA (1.8 *μ*M) was incubated in buffer with 5 mM DM (unless otherwise indicated) and varying concentrations of alcohol in a total volume of 150 *μ*L. Following at least 30 min incubation at room temperature, the solution was centrifuged for 10 min at 14000 rpm and the fluorescence of the supernatant measured by excitation at 295 nm and emission between 310 and 400 nm with slit widths of 8 nm for both excitation and emission, using a LS55 fluorometer (Perkin-Elmer, Wellesley, MA). By using Trp fluorescence for these measurements, we were able to monitor conformational changes in addition to changes in solubility, as well as taking advantage of the superior sensitivity of fluorescence compared to absorbance.

Circular Dichroism. Typically 5 *μ*M protein was incubated in buffer with 5 mM DM and different concentrations of TFE. Circular dichroism spectra were recorded between 195 and 250 nm on a J-810 spectrometer (Jasco Spectroscopic Co. Ltd., Hachioji City, Japan) after at least 30 min of incubation using 1 mm cuvettes and an accumulation of three scans recorded at 20 nm/min with 1 nm bandwidth.

Thermal Scans by CD. These were performed with 5−10 *μ*M protein as described (*16*), following the change at ellipticity at 220 nm as a function of temperature in the presence of different concentrations of alcohols at a concentration range where precipitation did not occur to a significant extent.

Stopped-Flow Kinetics. DsbB in 5 mM DM and buffer was mixed 1:10 with TFE to a final concentration of 2.1 *μ*M DsbB, 5 mM DM, and 20% TFE on an SX18MV stopped-flow microanalyzer (Applied Photophysics, Surrey, Leatherhead, U.K.) at 25 °C. The reaction was followed by exciting at 280 nm and measuring emission above 320 nm using a glass cutoff filter.

DsbB Activity Assays. These were performed essentially as described (*40*, *43*). Typically, 1 *μ*M DsbB was mixed with 10 *μ*M reduced DsbA (from a 167 *μ*M stock where the Cys49−Cys52 bond was reduced in the presence of 10 mM DTT, desalted to remove excess DTT, and stored at −80 °C in 1 mM EDTA to avoid reoxidation) and 30 *μ*M decylubiquinone (from a 0.1 M stock in DMSO) in 300 mM NaCl and 50 mM sodium phosphate, pH 6. Emission was followed at 360 nm with excitation at 295 nm over 1 min. The linear decline in emission, caused by the formation of the Cys49−Cys52 disulfide bond in DsbA by the disulfide bonds in DsbB (*40*), was used as a quantitative measure of DsbB activity.

Thioflavin T Fluorescence. Following incubation with alcohols as described above, the solution was centrifuged for 10 min at 14000 rpm, the supernatant was removed by aspiration, and the pellet was resuspended in 120 μL of buffer containing 40 μM thioflavin T. Fluorescence was measured by excitation at 440 nm and emission at 385 nm using slits of 8 nm.

FTIR Data Acquisition. Spectra were recorded on a Bruker Tensor 27 infrared spectrometer (Bruker Optik GmbH, Ettlingen, Germany) with a Specac Golden Gate single-reflection ATR unit (Specac Ltd., Orpington, U.K.). Following incubation with alcohols as described above (40% for MeOH and EtOH, 30% for iPrOH, and 20% for TFE and PrOH), the solution was centrifuged for 10 min at 14000 rpm, the supernatant was removed by aspiration, and the pellet was resuspended in MilliQ water. Protein (2 μg) was dried under a gentle stream of nitrogen. Three independent samples were investigated (64 scans at 2 cm^{-1} resolution). One spectrum was collected for TFE. When necessary, we corrected for the presence of water vapor by subtracting a fresh water vapor spectrum. Peaks were assigned from the second derivative and deconvolution of spectra. The non-deconvoluted spectra were fitted using the Levenberg−Maquardt method to seven Lorentzian peaks, of which six were assigned to secondary structure elements and one low-intensity peak was assigned to contributions from side chains.

Atomic Force Microscopy. NhaA (5.4 μM) was incubated for 30 min in buffer with 2.8M TFE before centrifugation. The supernatant was removed by aspiration and the pellet washed twice in water. Protein (100 μL of 0.5 μM) was applied to freshly cleaved mica in a sample chamber, dried in an oven at 80 °C (typically 2−3 min), and removed from the oven as soon as the sample had dried. The elevated temperature was required to enable rapid drying and avoid leakage from the sample chamber. This handling does not appear to destroy, e.g., protein fibrils since it allows us to image fibrils of α-synuclein (data not shown). Samples were imaged in contact mode on a PicoSPMI apparatus (Molecular Imaging, Tempe, AZ) using silicon nitride cantilevers (BudgetSensors, Sofia, Bulgaria) with a force constant of 0.27 N/m.

RESULTS

Our initial interest was to analyze whether it was possible to reversibly and cooperatively denature DsbB in the fluorinated alcohol TFE to provide an alternative denaturation method. This would facilitate refolding experiments to compare with refolding from the SDS-denatured state, which is highly structured and contains approximately the same level of α-helicity as the state in DM (*11*).

DsbB Undergoes a Two-Step Irreversible Spectroscopic Change in the Presence of Increasing Concentrations of TFE, Involving Precipitation Followed by Resolubilization. A useful signature for cooperativity is a sigmoidal unfolding curve over a relatively narrow denaturant concentration interval [although sigmoidal unfolding curves can also be obtained from cooperatively and strongly binding ligands (*21*)]. We had failed to observe such cooperative unfolding of DsbB and NhaA when exposed to chemical denaturants in the presence of 5 mM DM. A linear decrease in the ratio of the Trp fluorescence emission at 335 and 350 nm was observed in response to increasing concentrations of guanidinium chloride (0−7 M) and urea (0−9 M) (data not shown). The ratio between these two wavelengths is often taken as a measure of the unfolding of a protein, since unfolding usually leads to a red shift of the emission spectrum (*44*).

We therefore turned to alcohols for denaturation. However, when DsbB was incubated with 0−55% TFE, we saw visible cloudiness over a relatively broad concentration interval. Upon centrifugation, sedimented pellets were observed predominantly around 10−35% TFE. The fluorescence of the supernatants showed a characteristic pattern: the intensity level remained unchanged up to 3% TFE, after which it plunged to around 25% of the original level as the TFE concentration was increased to 12%. The fluorescence remained at a low level up to around 30% TFE and then slowly increased to a level close to two-thirds of the original (Figure 1A). In parallel with this, the 335/350 nm emission ratio remained relatively constant around 1.1 to around 20% TFE, after which it fell to a new level around 0.95 where it remained as the TFE concentration increased to 50%.

The low concentration of DsbB made it unfeasible to use absorption at 280 nm as a measure of solubility. In order to obtain a more direct measure of the solubility of DsbB, we instead measured the ratio of the fluorescence of each sample before and after centrifugation and obtained a profile which was very similar to that of the absolute fluorescence spectrum, except that some lack of solubility was already observed at low concentrations of alcohol and the solubility at high alcohol concentrations reached close to 100% (Figure 1B). For the subsequent analysis, we will use the unprocessed fluorescence emission values for the supernatant rather than the ratio between the solution emission before and after centrifugation, due to problems with light scattering in the presence of suspended precipitates.

As might be expected, the presence of detergents has a significant impact on the ability of TFE to precipitate the protein. If the concentration of DM is decreased from 5 to 1 mM, the midpoint of precipitation is lowered by a factor of at least 2, while replacing DM with SDS increases the midpoint around 3-fold (data not shown). Nevertheless, the same profile involving precipitation and resolubilization was observed under all circumstances. In the following experiments, we kept the DM concentration constant at 5 mM to allow comparison between different alcohols.

CD spectra showed the expected typical α-helical structure in the absence of TFE, but at 20% TFE this is replaced by an essentially featureless spectrum due to extensive precipitation, while the spectrum in 50% TFE (where the solution is visibly clear and precipitation is insignificant; cf. Figure 1B) reveals a state with even higher α-helicity than the native state (insert to Figure 1A). Analysis of the CD spectra by the k2d algorithm (*45*) predicts an α-helix content of 59% (ca. 104 residues) in 0% TFE and 85% (ca. 150 residues) in the presence of 50% TFE, corresponding to an increase in helicity encompassing 46 residues. The transmembrane helices are modeled to consist of ca. 80 residues (*46*), accounting for the majority of the native state helicity. As the two cytoplasmic termini account for only around 25 residues, the increased helicity is most likely to reflect an increase in helicity in the two periplasmic loops as the protein goes from 0 to 50% TFE. We have in a recent thermody-

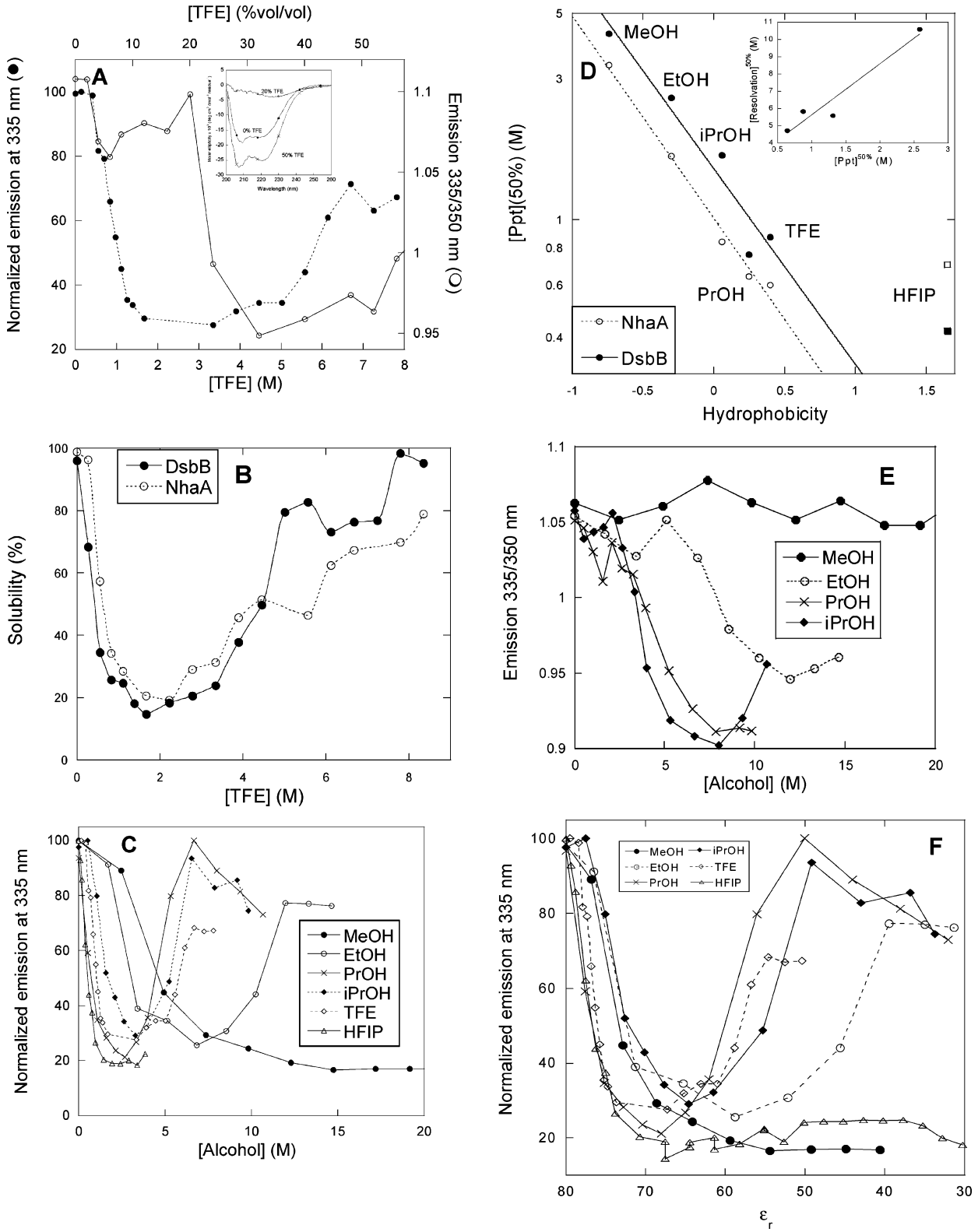

FIGURE 1: (A) Emission at 335 nm and the ratio of emission at 335 and 350 nm for DsbB incubated in different concentrations of TFE. After incubation in TFE for 30 min, the protein solution was spun down and the emission of the supernatant measured. Insert: Far-UV CD spectra of DsbB in the presence of 0−50% TFE. (B) Solubility of DsbB and NhaA at different TFE concentrations. The apparent fluorescence emission at 335 nm of the solution was measured before and after centrifugation. Light scattering due to aggregates contributes to emission before but not after centrifugation. (C) Emission of DsbB at 335 nm as a function of different alcohol concentrations. (D) Midpoint of precipitation $[Ppt]^{50\%}$ for DsbB and NhaA versus alcohol hydrophobicity plotted on a semilogarithmic scale (data for HFIP excluded from the fit). The slopes of the fitted straight lines are -1.53 ± 0.15 (DsbB) and -1.58 ± 0.05 (NhaA). Insert: $[Ppt]^{50\%}$ versus midpoint of resolubilization for DsbB. (E) Ratio of emission at 335 and 350 nm for DsbB incubated at different concentrations of alcohols. (F) Data in (C) plotted versus relative dielectric constant ϵ_r rather than alcohol concentration. Concentrations were converted to ϵ_r values based on data in ref *48*.

namic study concluded by indirect means that residues in the periplasmic loop in the native state are essentially unstructured (*16*), which ties in well with these observations.

The helically enriched species observed in 50% TFE represents a trapped state. If DsbB is transferred from 0 to 4.5% TFE, the protein retains around 80% of its biological activity, i.e., its ability to oxidize the periplasmic chaperone DsbA (see Materials and Methods). This agrees well with its solubility level in 4.5% TFE (Figure 1B). However, transfer from 50% to 4.5% TFE does not restore activity or the original low-TFE CD spectrum with reduced α-helix signals. As expected from the extensive precipitation, no activity was observed in 20% TFE.

On the basis of these observations, it appears that DsbB is not structurally perturbed by TFE until around 3% TFE, after which it starts to precipitate significantly. The soluble state present to a decreasing extent between 3% and 20% TFE appears to be native-like judged by the rather crude measure of the 335/350 nm ratio, but at higher TFE concentrations this is replaced by a state which according to both CD and 335/350 nm is soluble but irreversibly denatured to a non-native state, similar to the membrane protein KcsA (*36*).

Correlation between Hydrophobicity and Precipitation. The precipitation at intermediate TFE concentrations had not been observed for KcsA. We therefore decided to characterize the precipitation behavior in more detail, focusing on (a) the role of general hydrophobicity in precipitating DsbB, (b) the nature of the precipitated state, (c) the mechanism of precipitation, and (d) the generality of this behavior.

We repeated the titration of DsbB using the alcohols methanol (MeOH), ethanol (EtOH), *n*-propyl alcohol (PrOH), isopropyl alcohol (iPrOH), and hexafluoroisopropyl alcohol (HFIP) (listed according to increasing hydrophobicity). In all cases, we saw a characteristic decrease in supernatant fluorescence at relatively low alcohol concentrations. Except for MeOH, which is the least hydrophobic of all the solvents tested, this was always followed by a rise in fluorescence to levels approaching (or in PrOH's case exceeding) that of the native state (Figure 1C). Let us define $[Ppt]^{50\%}$ as the alcohol concentration at which the protein is halfway to the minimal fluorescence level starting from the alcohol-free level; this value can be obtained for each alcohol by simple interpolation. Provided we exclude data for HFIP, Figure 1D shows a clear linear relationship between log $[Ppt]^{50\%}$ and alcohol hydrophobicity [defined by their partitioning between water and octanol (*47*)]. This is similar to the observations made for membrane-embedded KcsA (*34*). However, the slope of the plot for DsbB (-1.53 ± 0.15) is significantly higher than that seen for KcsA using the same hydrophobicity values (slope estimated by us to be around -0.67) (*34*).

Let us similarly define $[resolubilization]^{50\%}$ as the alcohol concentration where the protein is halfway to the highest fluorescence level attained at high alcohol concentration. If the interactions responsible for precipitation and resolubilization are similar in nature, we would expect this parameter to correlate with $[Ppt]^{50\%}$. There is a reasonable linear relationship between the two 50% values (Figure 1D insert), although this may not be significant as the points cluster in one group with a single outlier. The variation in the 335/350 nm ratio with alcohol concentration (Figure 1E) shows a strong correlation with the fluorescence emission intensities: the ratio stays constant until the protein starts to resolubilize, reinforcing the conclusion made from the TFE and activity data that the soluble fraction of the protein remains native-like until it enters the resolubilization range.

As an alternative to alcohol hydrophobicity, we replotted the data in Figure 1C versus the relative dielectric constant ϵ_r of the alcohol−water mixtures, using data from ref *48* to convert concentration to ϵ_r. We see a convergence but not complete coalescence for data between the different alcohols (Figure 1F), suggesting that simple reduction in solvent polarity cannot explain our observations entirely. In particular, it is clear that the resolubilization step differs greatly among alcohols under conditions of comparable polarity.

Aggregation Is Initiated by a Dimerization Reaction. We noted that the final appearance of the titration profile of DsbB in TFE was attained very quickly; overnight incubation did not alter the fluorescence emission levels in the supernatant (data not shown). This indicated that the aggregative processes happened very quickly. We therefore performed stopped-flow experiments to follow the process in more detail, using apparent Trp fluorescence as a sensitive measure of aggregation (similar effects were seen by absorbance changes at 400 nm, but the signal-to-noise ratio was lower). When DsbB is transferred into TFE, there is a lag phase of a few seconds before the (apparent) fluorescence levels rise to a plateau level (Figure 2A). The length of the lag phase is inversely correlated to protein concentration (Figure 2B). In a log−log plot, there is a good linear relationship with a slope of -1.01 ± 0.09. If aggregation is assumed to involve a preequilibrium corresponding to the formation of an oligomeric nucleus, followed by irreversible polymerization, then the first derivative in this log−log plot equals $-n^*/2$, where n^* is the nucleus size (*49*). Our data thus suggest that dimerization is the first step in the aggregation process.

Intermediate Alcohol Concentrations Reduce Membrane Protein Stability. It was of interest to analyze the stability of DsbB at low alcohol concentrations, where a significant fraction of the protein remains soluble and native-like, to see how stability may be coupled to the precipitation process. Thermal stability of DsbB may be monitored via the change in ellipticity at 220 nm (*16*), which provides the midpoint temperature of denaturation t_m. Although DsbB starts to precipitate at the higher end of the alcohol concentration range in these scans, the soluble fraction of DsbB whose stability could be measured by CD-based thermal scanning retained a native far-UV CD spectrum (data not shown). This correlates well with the observation that the 335/350 nm fluorescence emission ratio of the soluble fraction remains roughly constant up to 20% TFE (Figure 1A). Scans at increasing concentrations of different alcohols reveal a linear decline in t_m with alcohol concentration over a restricted concentration range (Figure 3A) (we were unable to obtain satisfactory thermal scans in HFIP). Using the slope of this decline as a measure of the destabilizing influence of the alcohol, we obtain a monotonic and slightly curved relationship with hydrophobicity, which illustrates the clear correlation between increased hydrophobicity and increased destabilizing propensities (Figure 3B). Alternatively, we can estimate the alcohol concentration required to decrease the melting temperature by 10 °C and plot this concentration versus hydrophobicity (Figure 3B). Remarkably, this gives

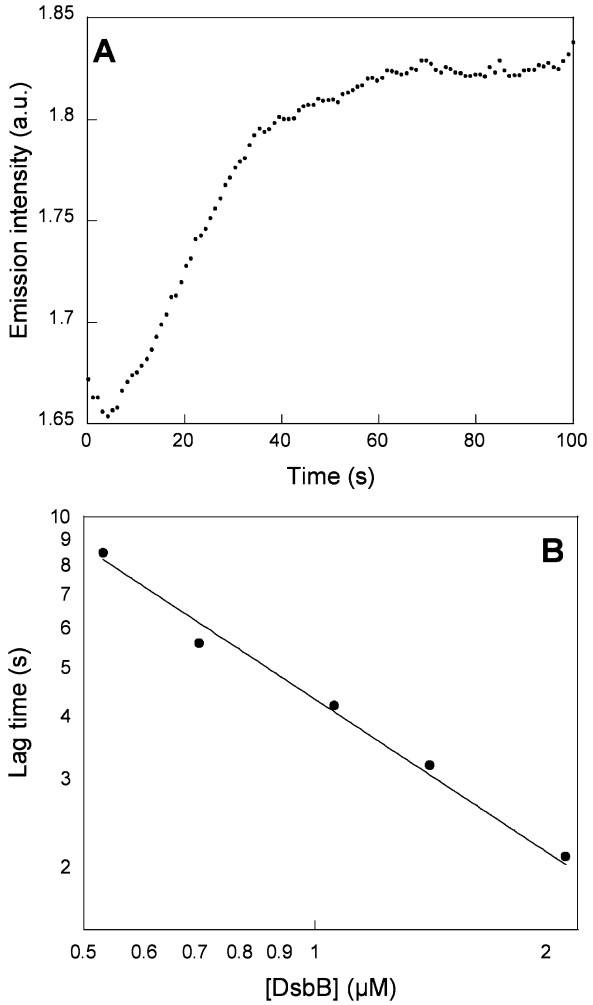

FIGURE 2: (A) Time profile of aggregation of DsbB upon transfer from 0 to 20% TFE. The process was followed by the apparent change in fluorescence, but the magnitude of the signal indicates that significant light scattering is occurring. The lag time t_{lag} is estimated by the intersection of the lag region and the growth region as indicated. (B) Lag time of aggregation as a function of DsbB concentration. The slope of the fitted straight line in the log−log plot is -1.01 ± 0.09.

a linear correlation in a log−log plot with a slope of -1.49 ± 0.17, identical within error to the slope for the precipitation concentrations (Figure 1D). In both cases the slopes show a correlation with hydrophobicity which is significant at the 99% level. This indicates that stability and precipitation are very closely related.

The same relationship between t_m and alcohol concentration was seen when the detergent DM was replaced with octaethylene glycol mono-*n*-dodecyl ether, illustrating that the nature of the detergent is not central in the effect of the alcohol on protein stability (Figure 3C).

The α-Helical Membrane Protein NhaA, but Not the β-Barrel Membrane Protein AIDA, Follows the Same Two-Step Change in Alcohols. To test the generality of alcohols' ability to induce this characteristic sequence of precipitation in membrane proteins, we also tested the behavior of the 388-residue sodium−hydrogen antiporter NhaA, a 12-transmembrane α-helix protein (*38*) which is considerably larger than DsbB. The same general behavior is seen, in which fluorescence decreased sharply at relatively low alcohol

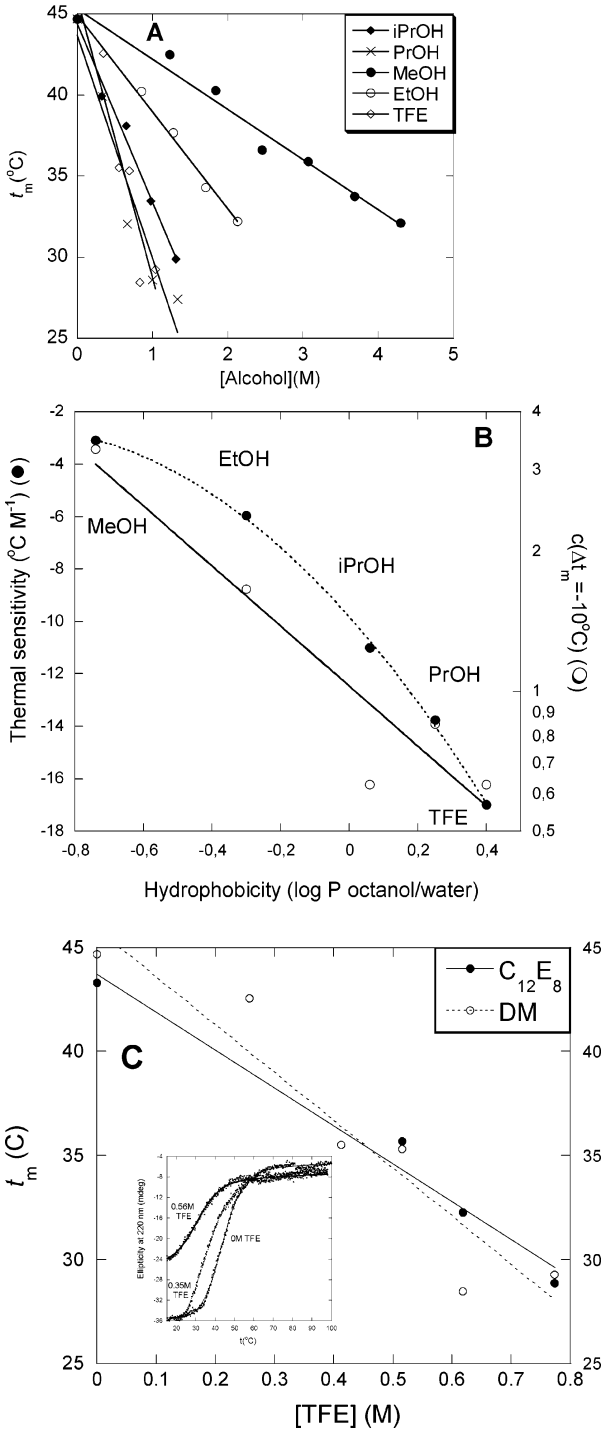

FIGURE 3: (A) Melting temperature t_m of DsbB as a function of different alcohol concentrations. The straight lines represent the best linear fits to the data. (B) The slopes of the fits in (A), and the alcohol concentration required for a 10 °C drop in thermal stability, plotted versus alcohol hydrophobicity. The stippled line is a polynomium intended to guide the eye through the plot of the slope−hydrophobicity data, while the line is the best linear fit of the 10 °C hydrophobicity data. The line has a slope of -1.49 ± 0.17, identical within error to the linear plots in Figure 1D. (C) Change in t_m of DsbB as a function of TFE in two different detergents, namely, DM and $C_{12}E_8$. Insert: Thermal scans for DsbB in 0−0.56 M TFE in the presence of $C_{12}E_8$.

concentrations, followed by a recovery (in the case of PrOH, iPrOH, EtOH, and to some extent TFE) at higher alcohol concentrations (Figure 4A). NhaA solubility increases in

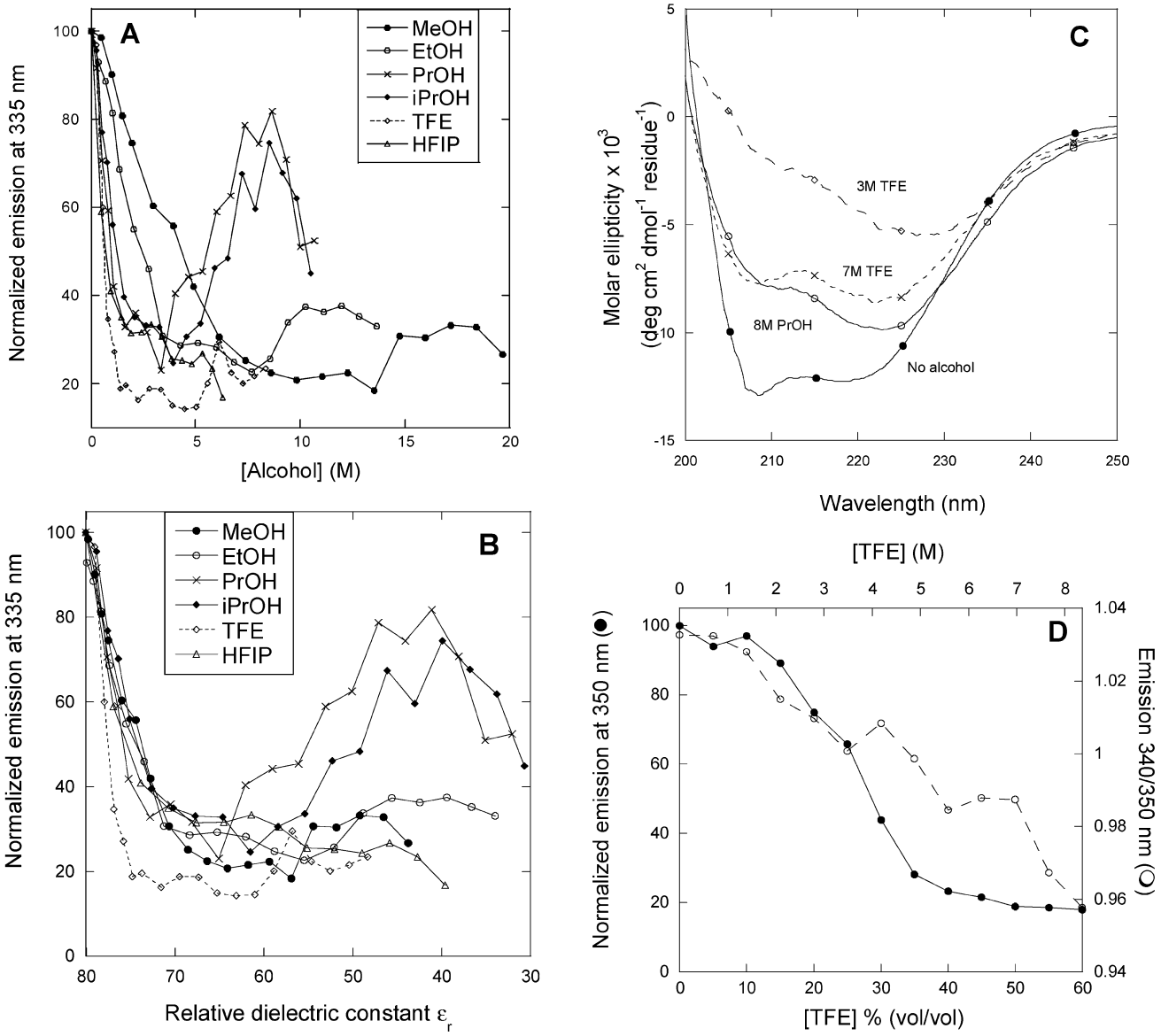

FIGURE 4: (A) Fluorescence emission intensity of NhaA in different alcohols. Emission corresponds closely to solubility (cf. data for TFE in Figure 1B). (B) Data in (A) plotted versus relative dielectric constant ϵ_r rather than alcohol concentration. Concentrations were converted to ϵ_r values based on data in ref *48*. (C) Far-UV CD spectra of NhaA in the native state (no alcohol), the precipitated state (2.8 M TFE), and the resolubilized state (7 M TFE or 8 M PrOH). (D) Emission intensity and emission ratio for the outer membrane β-barrel protein AIDA as a function of TFE concentration.

parallel (Figure 1B). Again, we observe a linear relationship between $[Ppt]^{50\%}$ and alcohol hydrophobicity in a log−log plot when HFIP is excluded, and the slope (-1.58 ± 0.05) is identical within error to that of DsbB (Figure 1D). In the case of NhaA, there is a very marked coalescence of data from different alcohols in the precipitation region when fluorescence data were plotted versus ϵ_r (Figure 4B). There is more divergence in the resolubilization region. Unlike DsbB, NhaA does not show an increase in α-helicity at higher TFE concentrations; according to CD, the α-helical content actually decreases from 41% in 0 M alcohol to 31% in 7 M TFE (Figure 4C). This could partially be due to small light scattering artifacts, since the solution showed a slight opacity in 7 M TFE (data not shown). However, the spectrum in 8 M PrOH (where no opacity is observed) is similar to that in 7 M TFE, although it was not possible to deconvolute it (Figure 4C). Although NhaA only has a slightly higher proportion of transmembrane residues than DsbB [255 residues, corresponding to 66% (*38*)], the residues exposed to the extramembraneous environment are predominantly restricted to form turns between helices and so are presumably less amenable to change to α-helical structures in TFE.

In contrast to the two α-helix membrane proteins DsbB and NhaA, the β-barrel outer membrane protein AIDA (*17*) failed to show any visible precipitation at any TFE concentration with essentially identical fluorescence intensities before and after centrifugation (Figure 4D). Although there was a clear decrease in fluorescence, the linear decline in the 340/350 nm ratio suggested a noncooperative structural transition (Figure 4D).

The Structure of the Precipitated State. It was not feasible to obtain reliable structural information on the aggregates from CD spectra due to excessive light scattering artifacts. However, FTIR is insensitive to the physical state of the

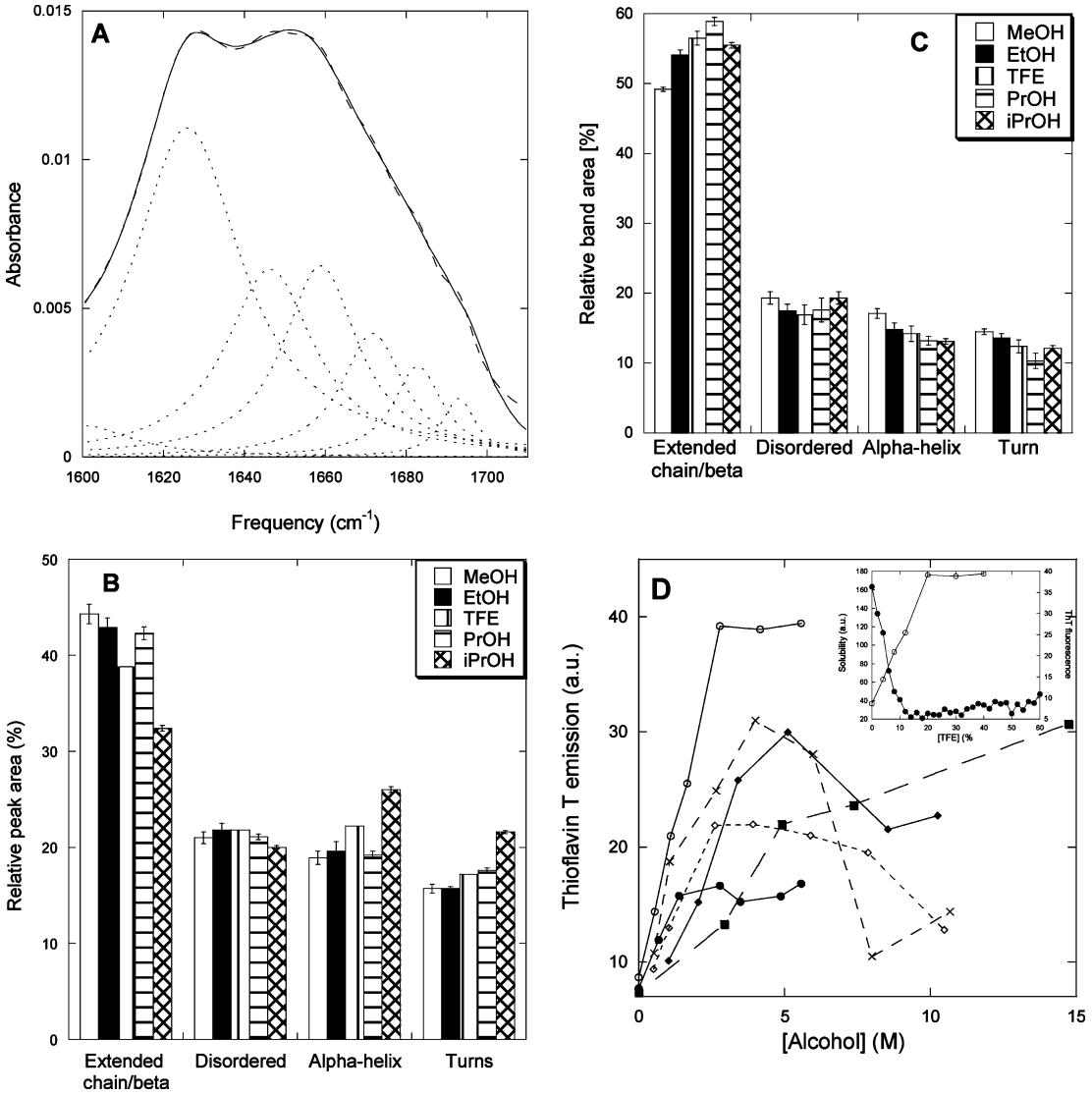

FIGURE 5: (A) FTIR spectrum of DsbB precipitated in 20% (2.8 M) TFE. The stippled lines indicate the deconvoluted peaks assigned to secondary structure elements. (B) Distribution of different secondary structural elements in precipitates of DsbB formed in alcohol concentrations corresponding to lowest solubility (Figure 1A), namely, 2.8 M TFE, 2 M PrOH, 2 M iPrOH, 6 M EtOH, or 15 M MeOH. (C) As in (B) for NhaA in 2.8 M TFE, 15 M MeOH, 6.8 M EtOH, 4.4 M PrOH, or 4 M iPrOH. (D) Thioflavin T fluorescence in the presence of precipitates formed upon incubation of DsbB in (●) TFE and NhaA in (○) TFE, (×) PrOH, (◇) iPrOH, (◆) EtOH, and (■) MeOH at different concentrations. Insert: Correlation between NhaA solubility (●) and ThT fluorescence (○) as a function of TFE concentration.

sample and provides a useful method to characterize these aggregates. Spectra of the DsbB precipitates were recorded at alcohol concentrations where precipitation was maximal. For all alcohols, a clear contribution is observed in the lower β region of the amide I band (Figure 5A). The deconvoluted spectra and the second derivatives showed six contributions for the secondary structure at similar frequencies. A seventh low-intensity Lorentzian peak was added to the fit to account for the contribution of side chains in the lower range of the band. The fitted peaks were centered at 1627 ± 0.2 cm^{-1} (extended chain/β-sheet), 1646 ± 1.0 cm^{-1} (disordered structure), 1659 ± 0.9 cm^{-1} (α-helix), 1672 ± 1.2 and 1684 ± 1.1 cm^{-1} (β turns), and 1694 ± 1.0 cm^{-1} (β-sheet). In all alcohols, the β-sheet structure clearly dominated at the expense of α-helicity. iPrOH showed slightly less β-sheet structure than the other alcohols, with a corresponding increase in the α-helix content as well as β-turns (Figure 5B).

Similar experiments performed for NhaA showed the β-sheet structure to assume an even more dominating role (Figure 5C), with up to 60% β-sheet as opposed to only 40−45% for DsbB.

The increase in β-sheet structure upon incubation at intermediate TFE concentrations raised the question whether the aggregates contained an organized fibrillar structure as seen for water-soluble proteins such as acylphosphatase incubated at 20−30% (2.8−3.8 M) TFE (*32*) and the K3 peptide at 20% TFE (*50*). We therefore incubated samples of DsbB and NhaA at 0.04 mg/mL (i.e., 1.9 μM DsbB or 1 μM NhaA) with TFE for several days, spun down the pellet, and resuspended it in buffer containing the dye thioflavin T (ThT). This dye is known to bind amyloid structures with reasonable specificity (*51*). For both proteins, a significant rise in the ThT signal was observed in the concentration range where DsbB and NhaA precipitate (Figure 5C and insert), although the increase was higher for NhaA. A similar

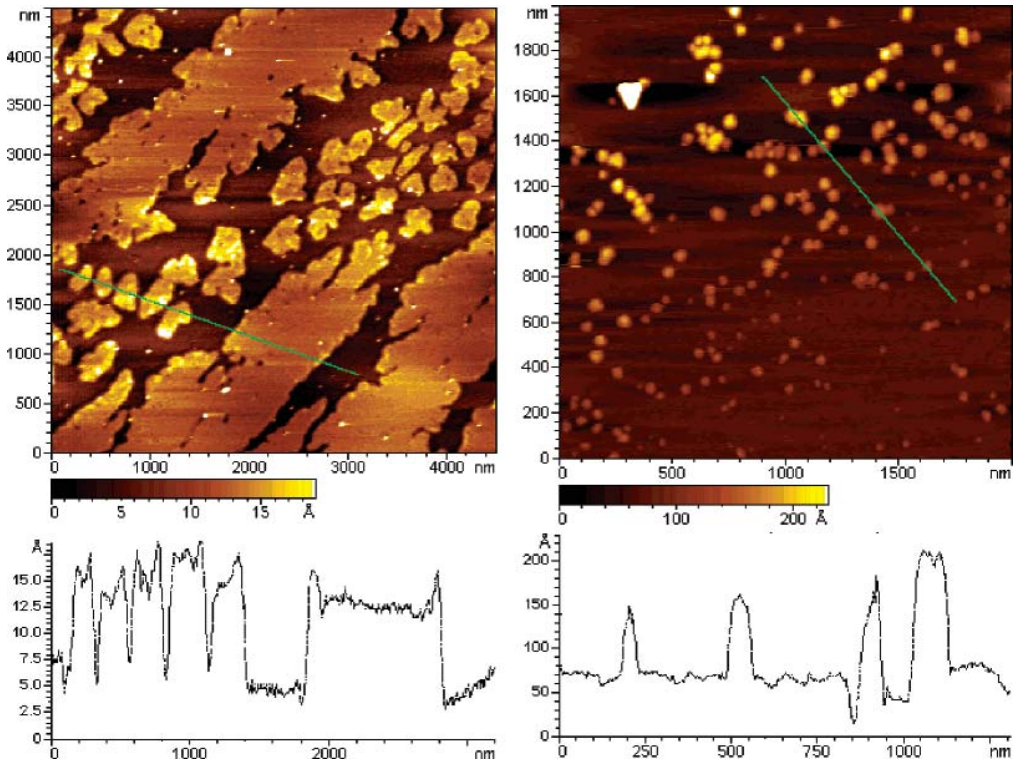

FIGURE 6: Atomic force microscopy images of NhaA precipitates formed in the presence of 2.8 M TFE. The bottom panels display the height profile of the green lines in the AFM images.

analysis of NhaA's structure in other alcohols revealed the same general behavior, in which the ThT signal increases in parallel with the amount of precipitated protein and then declines at high concentrations where the protein becomes resolubilized (Figure 5D).

Nevertheless, the increase in ThT signal is not unequivocal evidence for fibril formation. ThT is also able to bind to nonfibrillar structures, ranging from the acetylcholinerase receptor (*52*) to amorphous aggregates (D. E. Otzen, unpublished observations). Most fibrillation reactions proceed over hours to days and are preceded by a lag time during which nuclei can form (*53*). However, the kinetics of formation of these ThT-positive structures is rapid and the ThT fluorescence level stabilizes within at most 30 min; no further change is seen upon incubation for several days (data not shown). Stronger evidence for the lack of fibrillated aggregates was provided by the amyloid-specific chromophore Congo Red, which did not undergo any spectral change in the presence of these aggregates (data not shown). We used atomic force microscopy to visualize the aggregates of NhaA formed in 2.8M TFE. Much of the mica surface was covered by a layer of a uniform depth of approximately 10 Å (Figure 6A) which coexisted with circular aggregates of varying sizes that were up to 100 Å tall (Figure 6B), indicating a variety of different aggregate structures. However, no bona fide fibrils were observed.

DISCUSSION

We initially hoped to find means of reversibly denaturing monomeric MPs in alcohols as an alternative to detergent solubilization. While alcohols are very useful for reversible dissociation of oligomeric complexes (*36*), it has not been investigated in detail how they affect monomeric membrane proteins. The aim was to be able to obtain reliable estimates of membrane protein stability under conditions where the denatured state is truly denatured and not just a slightly expanded version of the native state, as has been suggested to be the case for the SDS-denatured state (*20*). For the two α-helical MPs tested here, we find no cooperative unfolding in traditional chemical denaturants. In view of recent reports on the ability of the fluorinated alcohol TFE to reversibly denature the membrane protein KcsA at intermediate concentrations (*36*), we therefore decided to systematically test several fluorinated and nonfluorinated alcohols for their ability to induce reversible conformational changes. We find that both proteins irreversibly precipitate at intermediate concentrations of alcohol, and although they are solubilized at higher concentrations of alcohol, dilution does not restore activity. Resolubilization only occurs because the protein is forced into a non-native state which can be more effectively solubilized. These experiments all had to be done in the presence of detergents, since their absence would only make precipitation more pronounced. Thus, increasing detergent concentration simply postponed precipitation to higher alcohol concentrations. We therefore conclude that alcohols, fluorinated or not, do not provide a useful general means of inducing reversible unfolding of membrane proteins in solution. Nevertheless, the conformational changes induced by these alcohols are worthy of further comments.

Precipitation through Destabilization and Structural Frustration. Let us start by focusing on the precipitation occurring at low to medium alcohol concentrations. Cosmotropic salts, such as sodium sulfate, precipitate proteins by hyperstabilizing them; they are preferentially excluded from the protein surface (*54*) and thus favor compact conformations with minimized exclusion zones. At lower salt concentrations, this

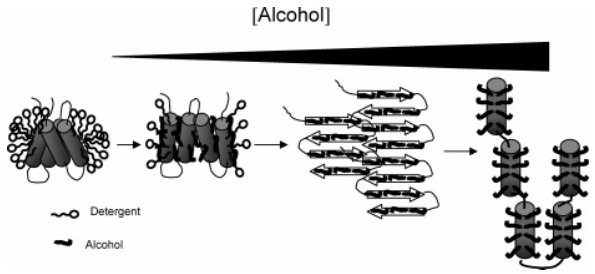

FIGURE 7: Proposed model for alcohol-induced destabilization, precipitation, and resolubilization of membrane proteins. Alcohol molecules may disrupt helix−helix contacts and displace detergent molecules, leading eventually to destabilization and precipitation to β-rich structures, until sufficiently high alcohol concentrations disrupt the β-sheet structure and lead to non-native predominantly α-helical (DsbB) or other non-native (NhaA) states.

will lead to a significant stabilization of the native state relative to the denatured state (*55*), whereas higher salt concentrations eventually induce precipitation of the native state so as to minimize contact with solvent. The alcohols precipitate membrane proteins by a mechanism which is fundamentally different from this. Thermal scans with DsbB indicate that destabilization of the native state of the protein is a prelude to precipitation.

On the basis of this, we speculate that the alcohols are able to bind to hydrophobic parts of the membrane protein via their aliphatic groups, both on the surface-exposed parts of the protein, which are normally sequestered by detergents, and internally in the protein, disrupting tertiary helix−helix contacts which are important stabilizing elements. This will lead to structural frustration, since the alcohol disturbs the normal protein−protein and protein−detergent contacts which maintain the protein in a solubilized native state, while being unable to provide a sufficiently effective solvent to keep the protein in solution (Figure 7). This is corroborated by several observations: First, the good correlation between $[Ppt]^{50\%}$ and hydrophobicity (Figure 1F) is evidence that the more hydrophobic the alcohol, the higher affinity it has for the hydrophobic patches on the protein. In addition, alcohol hydrophobicity is linked to precipitation and destabilization parameters by exactly the same slope (Figures 1D and 3A). Second, the precipitation data for different alcohols converge when plotted versus dielectric constant rather than molar concentration, indicating that exposure of otherwise sequestered parts of membrane proteins to solvents with high polarity will of necessity lead to precipitation. The convergence is particularly clear for NhaA, which has a larger proportion of transmembrane residues than DsbB and is therefore a "cleaner" membrane protein. For water-soluble proteins, where solubility is not such a sensitive issue, the protein will typically respond to changes in ϵ_r by undergoing conformational transitions at the monomeric level (*48*, *56*). Third, the low fraction of the protein population that remains in solution at intermediate alcohol concentrations has native-like fluorescence emission ratios (Figure 1), suggesting that adoption of the non-native conformation induced by alcohols is not compatible with staying in solution. Fourth, the β-barrel membrane protein AIDA remains solubilized throughout the same alcohol concentration range that leads to massive precipitation of DsbB and NhaA, supporting the fact that the tertiary structure of helical membrane proteins is predominantly stabilized by strongly hydrophobic contacts between transmembrane helices that can be disrupted by the alcohols (*2*, *3*). β-Barrel membrane proteins consist of amphiphilic sequences which do not provide such suitable binding sites. In addition to direct alcohol−protein interactions, it could also be expected that the more hydrophobic alcohols more strongly partition into the protein−detergent complex. This could conceivably lead to early disruption of micelles and subsequent precipitation. However, the fact that AIDA, which also requires micellar detergent to stay in solution (*41*), remains solubilized throughout the titration argues that there is little actual stripping of detergents off the membrane protein surface.

Rapid Formation of Stable but Nonfibrillar Precipitates Driven by Hydrophobic Effects. The structural frustration induced by the alcohols leads to very rapid (second-scale) precipitation, driven by the hydrophobic effect. It is a well-defined process with a discernible lag phase where the rate-limiting step is the formation of dimers. This leads to the formation of thioflavin T-positive β-rich precipitates with organized but nonfibrillar structure that also shows great variations in height, indicating a heterogeneous population of aggregates (Figure 6). Thus, under these conditions, formation of intermolecular β-sheet structures is the most effective way of satisfying hydrogen-bonding requirements. Aggregation at intermediate TFE concentrations (peaking at 25%) is also seen for water-soluble proteins such as acylphosphatase (*32*) and the K3 peptide from β_2-microglobulin (*50*). For AcP, aggregation initially leads to the formation of relatively amorphous aggregates which only form ordered structures over a time scale of many days (*57*). No such transitions were observed upon longer term exposure of DsbB and NhaA. Presumably, the strong hydrophobic interactions between the membrane protein molecules effectively trap the precipitated state in a stable conformation which cannot rearrange to other structures. This contrasts with strongly fibrillating peptides such as the 42-residue Alzheimer Aβ peptide, whose C-terminal domain is a fragment of a membrane-spanning helix while the N-terminus is hydrophilic. Similarly, truncation of the transmembrane-spanning part of glycophorin, making it unable to span the membrane bilayer, induces fibrillation within a few days (*58*). The key to their fibrillation propensity, in contrast to full-length membrane proteins, probably lies in (a) their relatively small size, making conformational changes more accessible, and (b) a disruption (truncation) of the normal hydrophobic interactions at a very fundamental level.

Resolubilization Follows Alcohol-Specific Patterns. As we increase the alcohol concentration, it becomes possible to resolubilize the β-rich precipitates to structures rich in α-helicity but with altered tertiary structure, as witnessed by the change in the 335/350 nm emission (Figure 1). In contrast to the alcohols' general ability to precipitate DsbB and NhaA at low concentrations, resolubilization does not follow a simple pattern. To some extent, resolubilization depends on hydrophobicity: the weakly hydrophobic alcohol MeOH cannot resolubilize the precipitates, unlike EtOH, PrOH, iPrOH, and TFE. MeOH, as opposed to other alcohols, has also been shown to induce β-rich structures in the all-helical protein VlsE (*33*) and the α/β protein ervatamin (*59*). However, plotting precipitation data versus ϵ_r (Figure 1D) clearly reveals that changes in ϵ_r cannot explain the resolubilization. In the same ϵ_r range where PrOH, iPrOH, TFE,

and EtOH achieve high solubilization (but starting at different values of ϵ_r), neither MeOH nor HFIP shows any effect. The fluorinated alcohol TFE does not distinguish itself from the nonfluorinated alcohols in precipitation and resolubilization, suggesting that the fluorinated groups do not play any specific role in these phenomena. However, the "hyperfluorinated" alcohol HFIP is not as potent a denaturant as would be predicted from its hydrophobicity. For example, it does not decrease $[Ppt]^{50\%}$ for DsbB and NhaA as much as expected and does not show strong resolubilization properties. The basis for this decreased potency could be related to the inability of fluorine groups in hemifluorinated surfactants to mix with lipids (*60*). On the other hand, HFIP conforms to the general hydrophobicity-driven ability of alcohols to dissociate KcsA tetramers in lipid membranes (*34*). Thus resolubilization appears to be more sensitive to the nature of the alcohol than precipitation, possibly because the alcohol molecules have to bind well to the hydrophobic surfaces to shield the protein against aggregation.

A thought-provoking study on the effect of alcohols on the conformational transitions of the aggregation-prone protein α-synuclein revealed that nonfluorinated alcohols led to β-rich oligomer formation, while HFIP and TFE led to α-rich monomers (*26*). The authors suggested that MeOH and EtOH mimic the environment near the membrane, and TFE and HFIP mimic the environment *in* the membrane, simply because TFE and HFIP are more hydrophobic. These considerations are likely to apply for water-soluble proteins. However, for membrane proteins, which are unequivocally dependent on a membrane-like environment, TFE and HFIP are clearly not sufficiently membrane-like to keep the membrane protein in solution.

TFE and HFIP have also been shown to form higher order clusters at concentrations around 15−65% (v/v) (*48*). However, these clusters cannot be instrumental in resolubilization. TFE only solubilizes DsbB from around 35% onward, whereas HFIP, which has a much greater propensity to form these clusters, does not resolubilize to any significant extent, and the nonclustering alcohol EtOH solubilizes just as efficiently as TFE.

In conclusion, we have shown that alcohols can induce numerous conformational changes in membrane proteins, leading to destabilization, precipitation, and resolubilization. Destabilization and precipitation correlate well with hydrophobicity, whereas resolubilization also involves effects specific for each alcohol. These phenomena highlight the fact that alcohols can exert an effect on membrane proteins, not just by modulating the actual lipid environment (*34*) but also by directly affecting the intrinsic stability of the membrane protein. The effect on membrane protein stability is comparable to the effect on lateral pressure, since the change in the midpoint of precipitation of NhaA and DsbB is more than twice as sensitive to alcohol hydrophobicity as the dissociation midpoints for the KcsA tetramer.

REFERENCES

1. Popot, J.-L., and Engelman, D. M. (1990) Membrane protein folding and oligomerization: the two-stage model, *Biochemistry 29*, 4031−4037.
2. Popot, J. L., and Engelman, D. M. (2000) Helical membrane protein folding, stability, and evolution, *Annu. Rev. Biochem. 69*, 881−922.
3. Stowell, M. H. B., and Rees, D. C. (1995) Structure and stability of membrane proteins, *Adv. Protein Chem. 46*, 279−311.
4. Wimley, W. C. (2002) Toward genomic identification of beta-barrel membrane proteins: composition and architecture of known structures, *Protein Sci. 11*, 301−312.
5. Jähnig, F., and Surrey, T. (1997) Folding and insertion of proteins into membranes in vitro, in *Membrane Protein Assembly* (Von Heijne, G., Ed.) pp 83−98, R. G. Landes Co., Heidelberg, Germany.
6. Kleinschmidt, J. H., and Tamm, L. K. (1996) Folding intermediates of a beta-barrel membrane protein. Kinetic evidence for a multi-step membrane insertion mechanism, *Biochemistry 35*, 12993−13000.
7. Hong, H., and Tamm, L. K. (2004) Elastic coupling of integral membrane protein stability to lipid bilayer forces, *Proc. Natl. Acad. Sci. U.S.A. 101*, 4065−4070.
8. Booth, P. J., Flitsch, S. L., Stern, L. J., Greenhalgh, D. A., Kim, P. S., and Khorana, H. G. (1995) Intermediates in the folding of the membrane protein bacteriorhodopsin, *Nat. Struct. Biol. 2*, 139−143.
9. Faham, S., Yang, D., Bare, E., Yohannan, S., Whitelegge, J. P., and Bowie, J. U. (2004) Side-chain contributions to membrane protein structure and stability, *J. Mol. Biol. 335*, 297−305.
10. Lau, F. W., and Bowie, J. U. (1997) A method for assessing the stability of a membrane protein, *Biochemistry 36*, 5884−5892.
11. Otzen, D. E. (2003) Folding of DsbB in mixed micelles: A kinetic analysis of the stability of a bacterial membrane protein, *J. Mol. Biol. 330*, 641−649.
12. Reynolds, J. A., and Tanford, C. (1970) The gross conformation of protein-sodium dodecyl sulfate complexes, *J. Biol. Chem. 245*, 5161−5165.
13. Tanford, C. (1980) *The Hydrophobic Effect. Formation of Micelles and Biological Membranes*, 2nd ed., Wiley & Sons, New York.
14. Turro, N. J., Lei, X.-G., Ananthapadmanabhan, K. P., and Aronson, M. (1995) Spectroscopic probe analysis of protein-surfactant interactions: the BSA/SDS system, *Langmuir 11*, 2525−2533.
15. Ibel, K., May, R. P., Kirschner, K., Szadkowski, H., Mascher, E., and Lundahl, P. (1990) Protein-decorated micelle structure of sodium-dodecyl-sulfate-protein complexes as determined by neutron scattering, *Eur. J. Biochem. 190*, 311−318.
16. Sehgal, P., and Otzen, D. E. (2006) Thermodynamics of unfolding of an integral membrane protein in mixed micelles, *Protein Sci. 15*, 890−899.
17. Sehgal, P., Mogensen, J. E., and Otzen, D. E. (2005) Using micellar mole fractions to assess membrane protein stability in mixed micelles, *Biochim. Biophys. Acta 1716*, 59−68.
18. Riley, M. L., Wallance, B. A., Flitsch, S. L., and Booth, P. J. (1997) Slow alpha helix formation during folding of a membrane protein, *Biochemistry 36*, 192−196.
19. Woolhead, C. A., McCormick, P. J., and Johnson, A. E. (2004) Nascent membrane and secretory proteins differ in FRET-detected folding far inside the ribosome and in their exposure to ribosomal proteins, *Cell 116*, 725−736.
20. Renthal, R., and Alloor, S. R. (2006) Partially unfolded membrane protein has a compact conformation, *FASEB J. 20* (in press).
21. Renthal, R. (2006) An unfolding story of helical transmembrane proteins, *Biochemistry 45*, 14559−14566.
22. Wilkinson, K. D., and Mayer, A. N. (1986) Alcohol-induced conformational changes of ubiquitin, *Arch. Biochem. Biophys. 250*, 390−399.
23. Dufour, E., Bertrand-Harb, C., and Haertlé, T. (1993) Reversible effects of medium dielectric constant on structural transformation of beta-lactoglobulin and its retinol binding, *Biopolymers 33*, 589−598.
24. Bychkova, V. E., Dujsekina, A. E., Klenin, S. I., Tiktopulo, E. I., Uversky, V. N., and Ptitsyn, O. B. (1996) Molten globule-like state of cytochrome *c* under conditions simulating those near the membrane surface, *Biochemistry 35*, 6058−6063.
25. Buck, M. (1998) Trifluoroethanol and colleagues: cosolvents come of age. Recent studies with peptides and proteins, *Q. Rev. Biophys. 31*, 297−355.
26. Munishkina, L. A., Phelan, C., Uversky, V. N., and Fink, A. L. (2003) Conformational behaviour and aggregation of alpha-synuclein in organic solvents: modeling the effects of membranes, *Biochemistry 42*, 2720−2730.

27. Dzwolak, W., Grudzielanek, S., Smirnovas, V., Ravindra, R., Nocilini, C., Jansen, R., Loksztejn, A., Porowski, S., and Winter, R. (2005) Ethanol-perturbed amyloidogenic self-assembly of insulin: Looking for origins of amyloid strains, *Biochemistry 44*, 8948−8958.
28. Kamatari, Y. O., Konno, T., Kataoka, M., and Akasaka, K. (1998) The methanol-induced transition and the expanded helical conformation in hen lysozyme, *Protein Sci. 8*, 873−882.
29. Shiraki, K., Nishikawa, K., and Goto, Y. (1995) Trifluoroethanol-induced stabilisation of the alfa-helical structure of β-lactoglobulin: Implication for non-hirarchial protein folding, *J. Mol. Biol. 245*, 180−194.
30. Hirota, N., Mizuno, K., and Goto, Y. (1998) Group additive contributions to the alcohol-induced alpha-helix formation of melittin: Implication for the mechanism of the alcohol effects on proteins, *J. Mol. Biol. 275*, 365−378.
31. Jasanoff, A., and Fersht, A. R. (1994) Quantitative determination of helical propensities from trifluoroethanol titration curves, *Biochemistry 33*, 2129−2135.
32. Chiti, F., Taddei, N., Bucciantini, M., White, P., Ramponi, G., and Dobson, C. M. (2000) Mutational analysis of the propensity for amyloid formation by a globular protein, *EMBO J. 19*, 1441−1449.
33. Perham, M., Liao, J., and Wittung-Stafshede, P. (2006) Differential effects of alcohols on conformational switchovers in alpha-helical and beta-sheet protein models, *Biochemistry 45*, 7740−7749.
34. van den Brink-van der Laan, E., Chupin, V., Killian, J. A., and de Kruijff, B. (2004) Small alcohols destabilize the KcsA tetramer via their effect on the membrane lateral pressure, *Biochemistry 43*, 5937−5942.
35. van den Brink-van der Laan, E., Chupin, V., Killian, J. A., and de Kruijff, B. (2004) Stability of KcsA tetramer depends on membrane lateral pressure, *Biochemistry 43*, 4240−4250.
36. Barrera, F. N., Renart, M. L., Molina, M. L., Poveda, J. A., Encinar, J. A., Fernández, A. M., Neira, J. L., and González-Ros, J. M. (2005) Unfolding and refolding in vitro of a tetrameric, alpha-helical membrane protein: The prokaryotic potassium channel KcsA, *Biochemistry 44*, 14344−14352.
37. Spelbrink, R. E. J., Kolkman, Slijper, M., Killian, J. A., and De Kruijff, B. (2005) Detection and identification of stable oligomeric protein complexes in *Escherichia coli* inner membranes: A proteomics approach, *J. Biol. Chem. 280*, 28742−28748.
38. Hunte, C., Screpanti, E., Venturi, M., Rimon, A., Padan, E., and Michel, H. (2005) Structure of a Na^+/H^+ antiporter and insights into mechanism of action and regulation by pH, *Nature 435*, 1197−1202.
39. Otzen, D. E. (2002) Folding of the α-helical membrane proteins DsbB and NhaA, in *Biophysical Chemistry: Membranes and Proteins* (Seddon, J., Ed.) pp 208−214, Royal Society of Chemistry, London.
40. Wunderlich, M., and Glockshuber, R. (1993) Redox properties of protein disulfide isomerase (DsbA) from *Escherichia coli*, *Protein Sci. 2*, 717−726.
41. Mogensen, J. E., Tapadar, D., Schmidt, M. A., and Otzen, D. E. (2005) Barriers to folding of the transmembrane domain of the *Escherichia coli* autotransporter adhesin involved in diffuse adherence, *Biochemistry 44*, 4533−4545.
42. Azab, H. A., El-Nady, A. M., and Saleh, M. S. (1994) Potentiometric determination of the second stage dissociation constant of N-[tris-(hydroxymethyl)-methyl]-2-aminoethane-sulphonic acid (TES) in different solvent mixtures, *Monatsh. Chem. 125*, 233−240.
43. Bader, M., Muse, W., Ballou, D. P., Gassner, C., and Bardwell, J. C. A. (1999) Oxidative protein folding is driven by the electron transport system, *Cell 98*, 217−227.
44. Otzen, D. E., Lundvig, D., Wimmer, R., Hatting, L., Pedersen, J. R., and Jensen, P. H. (2005) p25alpha is flexible but natively folded and binds tubulin in an oligomeric complex, *Protein Sci. 14*, 1396−1409.
45. Andrade, M. A., Chacón, P., Merelo, J. J., and Morán, F. (1993) Evaluation of secondary structure of proteins from UV circular dichroism using an unsupervised learning neural network, *Protein Eng. 6*, 383−390.
46. Jander, G., Martin, N. L., and Beckwith, J. (1994) Two cysteines in each periplasmic domain of the membrane protein DsbB are required for its function in protein disulfide bond formation, *EMBO J. 13*, 5121−5127.
47. Abraham, M. H., Chadha, H. S., Whiting, G. S., and Mitchell, R. C. (1994) Hydrogen bonding. 32. An analysis of water-octanol and water-alkane partitioning and the delta-log P parameter of Seiler, *J. Pharm. Sci. 83*, 1085−1100.
48. Hong, D.-P., Hoshino, M., Kuboi, R., and Goto, Y. (1999) Clustering of fluorine-substituted alcohols as a factor responsible for their marked effects on proteins and peptides, *J. Am. Chem. Soc. 121*, 8427−8433.
49. Goldstein, R. F., and Stryer, L. (1986) Cooperative polymerization reactions. Analytical approximations, numerical examples, and experimental strategy, *Biophys. J. 50*, 583−599.
50. Yamaguchi, K.-I., Naiki, H., and Goto, Y. (2006) Mechanism by which the amyloid-like fibrils of a beta2-microglobulin fragment are induced by fluorine-substituted alcohols, *J. Mol. Biol. 363*, 279−288.
51. Levine, H. I. (1999) Quantification of β-sheet amyloid fibril structures with thioflavin T, *Methods Enzymol. 309*, 274−284.
52. Ferrari, G. V. d., Mallender, W. D., Inestrosa, N. C., and Rosenberry, T. L. (2001) Thioflavin T is a fluorescent probe of the acetylcholinesterase peripheral site that reveals conformational interactions between the peripheral and acylation sites, *J. Biol. Chem. 276*, 23282−23287.
53. Harper, J. D., and Lansbury, P. T. J. (1997) Models of amyloid seeding in Alzheimer's disease and scrapie: mechanistic truths and physiological consequences of the time-dependent solubility of amyloid proteins, *Annu. Rev. Biochem. 66*, 385−407.
54. Timasheff, S. (2002) Protein hydration, thermodynamic binding, and preferential hydration, *Biochemistry 41*, 13473−13482.
55. Parker, M. J., Dempsey, C. E., Lorch, M., and Clarke, A. R. (1997) Acquisition of native beta-strand topology during the rapid collapse phase of protein folding, *Biochemistry 36*, 13396−13405.
56. Uversky, V. N., Narizhneva, N. V., Kirschstein, S. O., Winter, S., and Löber, G. (1997) Conformational transitions provoked by organic solvents in β-lactoglobulin: can a molten globule like intermediate be induced by the decrease in dielectric constant?, *Folding Des. 2*, 163−172.
57. Chiti, F., Webster, P., Taddei, N., Clark, A., Stefani, M., Ramponi, G., and Dobson, C. M. (1999) Designing conditions for *in vitro* formation of amyloid protofilaments and fibrils, *Proc. Natl. Acad. Sci. U.S.A. 96*, 3590−3594.
58. Liu, W., Crocker, E., Zhang, W., Elliott, J. I., Luy, B., Li, H., and Smith, S. O. (2005) Structural role of glycine in amyloid fibrils formed from transmembrane alpha-helices, *Biochemistry 44*, 3591−3597.
59. Sundd, M., Kundu, S., and Jagannadham, M. V. (2000) Alcohol-induced conformational transitions in ervatamin C. An alpha-helix to beta-sheet switchover, *J. Protein Chem. 19*, 169−176.
60. Palchevskyy, S. S., Posokhov, Y. O., Olivier, B., Popot, J. L., Pucci, B., and Ladokhin, A. S. (2006) Chaperoning of insertion of membrane proteins into lipid bilayers by hemifluorinated surfactants: Application to diphtheria toxin, *Biochemistry 45*, 2629−2635.

BI700091R

pH-Dependent Aggregation of Cutinase Is Efficiently Suppressed by 1,8-ANS

Shona Pedersen[1,2]
Lise Nesgaard[1]
Ricardo P. Baptista[3]
Eduardo P. Melo[3,4]
Søren R. Kristensen[2]
Daniel E. Otzen[1]

[1]*Department of Life Sciences, Aalborg University, DK-9000 Aalborg, Denmark*

[2]*Department of Clinical Biochemistry, Aalborg University Hospital, DK-9100 Aalborg, Denmark*

[3]*Centro de Engenharia Biológica e Química, Instituto Superior Técnico, Av. Rovisco Pais, 1049-001 Lisboa, Portugal*

[4]*Centro de Biomedicina Molecular e Estrutural, Universidade do Algarve, Campus de Gambelas, 8005-139 Faro, Portugal*

Received 26 July 2006; revised 14 August 2006; accepted 31 August 2006
Published online 8 September 2006 in Wiley InterScience (www.interscience.wiley.com). DOI 10.1002/bip.20598

Abstract: *We have studied the thermal stability of the triglyceride-hydrolyzing enzyme cutinase from* F. solani pisi *at pH values straddling the pI (pH 8.0). At the pI, increasing the protein concentration from 5 to 80* μM *decreases the apparent melting temperature by 19°C. This effect vanishes at pH values more than one unit away from pI. In contrast to additives such as detergents and osmolytes, the hydrophobic fluorophore 1,8-ANS completely and saturably suppresses this effect, restoring 70% of enzymatic activity upon cooling. ANS binds strongly to native cutinase as a noncompetitive inhibitor with up to 5 ANS per cutinase molecule. Only the first ANS molecule stabilizes cutinase; however, the last 4 ANS molecules decrease* T_m *by up to 7°C. Similar pI-dependent aggregation and suppression by ANS is observed for* T. lanuginosus *lipase, but not for lysozyme or porcine* α*-amylase, suggesting that this behavior is most prevalent for proteins with affinity for hydrophobic substrates and consequent exposure of hydrophobic patches. Aggregation may be promoted by a fluctuating ensemble of native-like states associating via intermolecular* β*-sheet rich structures unless blocked by ANS. Our data highlight the chaperone activity of small molecules with*

Correspondence to: Daniel E. Otzen; e-mail: dao@bio.aau.dk
Contract grant sponsors: Danish Research Foundation and Villum Kann Rasmussen Foundation.
Biopolymers, Vol. 83, 619–629 (2006)

affinity for hydrophobic surfaces and their potential application as stabilizers at appropriate stoichiometries. Biopolymers 83: 619–629, 2006

This article was originally published online as an accepted preprint. The "Published Online" date corresponds to the preprint version. You can request a copy of the preprint by emailing the Biopolymers editorial office at biopolymers@wiley.com

Keywords: *protein aggregation; anionic detergents; urea; ANS binding; thermal stability; enzyme activity*

INTRODUCTION

Temperature-induced protein aggregation has been known for many years.[1,2] The thermally denatured state tends to contain significant amounts of residual structure including contiguous hydrophobic patches that provide contact points between the individual protein molecules and subsequent aggregation. Consequently, aggregation generally occurs above the thermal denaturation temperature T_m. While it is rare for the aggregation process to lower T_m, some proteins aggregate well below T_m.[3] In some cases this can be explained by the formation of partially folded states.[4,5] These states are much more susceptible to aggregation than the native or completely unfolded state, because of the exposure of contiguous hydrophobic regions that are buried in the native state or absent in the denatured state. However, even at temperatures where the protein retains its native structure with intact tertiary interactions, aggregation can occur because of fluctuations in the native state ensemble via transiently expanded conformational subspecies[6] that may require as little as 15% of the surface area expansion required for unfolding.

Higher protein concentration will typically increase aggregation due to simple mass action effects.[7] Efforts to reduce aggregation include the addition of polyols, sugars, polymers, amino acids, detergents, and denaturants, which either stabilize the native state or shield the denatured state against intermolecular contacts.[8–13] In general, these stabilizers work through weak and nonspecific preferential exclusion, although detergents may work by more specific shielding of hydrophobic patches.[14] Salts are less often used, since the effect of ionic strength is very protein dependent.[15] The salt type can also make a significant difference in protein aggregation.[16]

An alternative strategy is to target hydrophobic patches on the protein surface with small water-soluble molecules. For example, the fluorescent dye 1,8-ANS has been shown to suppress thermal aggregation of carbonic anhydrase when present in 150-fold molar excess.[17,18] ANS is traditionally used to detect molten globules, i.e. partly folded proteins that accumulate under mildly denaturing conditions. Binding is believed to occur via solvent-exposed hydrophobic patches, which are a particular characteristic of this protein state.[19] Certain proteins also bind ANS in the native state, however, provided this conformation displays exposed hydrophobic sites,[20–23] as shown initially by Weber in his classic study of ANS binding to BSA.[24] Binding of ANS may in some cases lead to structural changes in the protein, rather than acting as a simple lock-and-key mechanism.[25] This property is shown to even higher extent for the covalent ANS-dimer bis-ANS[20,26] (M.E. Reinau and D.E.O., unpublished observations), although bis-ANS has also been shown to suppress thermal aggregation[27] as well as aggregation of proteins and peptides involved in dementia diseases.[28,29]

Proteins are generally most susceptible to thermal aggregation around their pI, because of the lack of overall electrostatic repulsion. In addition, anisotropic charge distribution at the pI can give rise to dipoles, encouraging intermolecular contacts and aggregation.[30] Therefore, inhibition of aggregation is most efficiently tested around the pI. Here, we report on the observation and inhibition of pronounced pI-dependent aggregation properties of a cutinase from *Fusarium solani pisi*. Cutinase is a compact one-domain 214-residue globular enzyme able to hydrolyze both soluble esters and water-insoluble lipids such as triglycerides. Cutinase has two disulfide bonds and 47 titratable residues, leading to an isoelectric point between 7.8 and 8.0. We show that the thermal stability of cutinase is very sensitive to protein concentration around the pI. Furthermore, we find ANS to be the most efficient inhibitor of this aggregative destabilization at stoichiometric concentrations, with a per mole effect far exceeding that of more conventional formulation agents such as amino acids or detergents. We make similar observations for the lipase from *T. lanuginosus*, another enzyme with hydrophobic substrates. In contrast, lysozyme and porcine α-amylase, whose substrates are much more polar, are not nearly as susceptible to aggregative destabilization.

This highlights the potential of small molecules as efficient chaperones for proteins with "sticky" surface patches.

MATERIALS AND METHODS

Materials

n-Octyl-β-D-maltoside was from Anatrace (Maumee, OH) and *n*-dodecyl-β-D-maltoside was from Calbiochem (La Jolla, CA). All other chemicals were from Sigma (St. Louis, MO). All chemicals were of analytical or biological grade. The following buffers were used, all at 50 m*M*: acetate (pH 4.0 and 5.0), citrate (pH 6.0), Tris-Cl (pH 7.0, 7.5, 8.0, and 8.5), and glycine (pH 9, 10, and 11).

Cutinase Expression and Purification

Cutinase from *Fusarium solani pisi* (SwissProt entry P00590) was cloned and expressed in *Escherichia coli* WK-6 strain, a kind gift from Corvas International N.V. (Gent, Belgium). The recombinant enzyme was produced and purified to >95% purity as described,[41] subsequently dialyzed extensively against water, and lyophilized. Hen egg-white lysozyme (EC 3.2.1.17) and α-amylase (EC 3.2.1.1) were purchased from Sigma and used without further purification. *T. lanuginosus* lipase was a kind gift from Kim Borch, Novozymes A/S.

Protein concentrations were determined spectrophotometrically using molar extinction coefficients of 10,853.5, 37,275, and 37,800M^{-1} cm^{-1} at 280 nm for cutinase, lipase and lysozyme respectively. A stock solution of 0.2 m*M* α-amylase was prepared by weighing out the lyophilized powder (EC 3.2.1.1) (MW = 55,376 g mol^{-1}).

Fluorescence Spectroscopy

Thermal scans were performed on an RTC 2000 spectrometer from Photon Technology International (Lawrenceville, NJ) equipped with a 75-W xenon arc lamp. The wavelength for tryptophan excitation and emission was set to 298 and 350 nm, respectively, in order to avoid contributions from tyrosine fluorescence. The tryptophan fluorescence spectrum of cutinase is unusual in that the fluorescence increases markedly upon unfolding, and this effect will be obscured to some extent if the tyrosine fluorescence contribution is included. The cuvette was thermostated with a Peltier element and the temperature of the solution was followed with a PT100-element submerged into the solution at a scan-rate of 90°C h^{-1}. Because of the highly sloping baseline of the denatured state at high protein concentrations, we found it most reliable to determine T_m as the position of the peak of the first derivative curve. The same instrument was used to measure SLS between 25 and 75°C using excitation and emission wavelengths of 500 nm and sample volumes of 100 μl.

Dye–Cutinase Interaction

A stock solution of ca. 100 m*M* 1,8-ANS in DMSO was prepared and diluted into water. The concentration was determined using the $\varepsilon_{350}^{water}$ of 4990M^{-1} cm^{-1}.[42] ANS fluorescence measurements were carried out on an LS-55 Spectrofluorometer (Perkin-Elmer, Wellesley, MA) using an excitation wavelength of 350 nm and emission at the maximum of fluorescence intensity in the range of 420–550 nm with slit size of 10 nm. For thioflavin T measurements, cutinase was incubated with 40 μM thioflavin T, based on a 100 m*M* stock solution of thioflavin T in ethanol. Excitation was at 450 nm and emission at 485 nm. For Congo red measurements, cutinase was incubated with 20 μM Congo red in buffer and the absorption between 400 and 600 nm recorded.

Far UV CD Spectroscopy

Far UV CD spectra of thermal scans of cutinase in 50 m*M* Tris at pH 8 were performed on a JASCO J-810 spectropolarimeter with a JASCO PTC-348WI temperature control unit and Neslab RTE-111 water bath. For the far UV and near UV CD, ellipticity was measured in the wavelength range of 200–250 nm with the following settings: resolution: 0.1 nm; bandwidth: 1.0 nm; sensitivity: 50 mdeg; response: 2.0 s; speed: 50 nm min^{-1}. Six accumulations were averaged to yield the final spectra. Cuvettes of 1 mm path-length were used.

Thermal scans were performed with a scan rate of 90°C h^{-1} at 223 nm. Raw CD data were fitted in KaleidaGraph (Synergy Software, Reading, PA) to the following equation:[43]

$$\theta = \frac{\alpha_N + \beta_N T + (\alpha_D + \beta_D T) * e^{-(\Delta H_{T_m}(1-\frac{T}{T_m}))/RT}}{1 + e^{-(\Delta H_{T_m}(1-\frac{T}{T_m}))/RT}} \quad (1)$$

where θ is the raw CD signal, α_N and α_D are the θ-values for the folded and denatured states, respectively, at 298 K, β_N and β_D are the slopes of the baselines of the native and denatured states, respectively, and H_{T_m} is the enthalpy of unfolding at the midpoint of denaturation, T_m. Note that this equation is formally only applicable to a reversible two-state unfolding process and not to an irreversible process. However, in practice, the unfolding scans fit very satisfactorily to Eq. (1). In any case, the T_m-values are strictly used for comparative purposes.

$$R_H = \frac{k_b T}{6\pi\eta D_r} \quad (2)$$

where k_b is the Boltzmann constant, T is the temperature in Kelvin and η is the viscosity.

Dynamic Light Scattering

DLS experiments were carried out in triplicate between 25 and 75°C using a Dyna Pro MSTC Dynamic Light Scattering Instrument (Protein Solutions, Charlottesville, VA).

The samples were in-line filtered through a 0.02 μm filter to remove any dust particles and injected into a 50 μl quartz cuvette. Temperature was maintained with an accuracy of better than 1°C by the Peltier cell. The sample was equilibrated for at least 5 min at each temperature before measurement.

Fourier Transform Infrared Spectroscopy

FTIR was carried out on a Bruker Tensor 27 infrared spectrometer (Bruker Optik GmbH, Ettlingen, Germany) with a Specac Golden Gate single-reflection ATR unit (Specac, Orpington, UK). Aggregates were isolated by centrifugation and resuspended in milliQ water. Samples were prepared by drying on the ATR surface under a gentle stream of nitrogen. Spectra were recorded with 128 accumulations and analyzed for secondary structure content of the amide I band using OPUS 5.5 software (Bruker Optik GmbH, Ettlingen, Germany). Estimates of secondary structure were obtained by fitting of Gaussian or Lorentzian curves. Briefly, the number and positions of peaks were determined from the second derivative spectrum and by Fourier self-deconvolution.[44] Peaks fitting was carried out using the Levenberg Maquardt method. Peaks were assigned to secondary structure elements and the relative peak area percentages were calculated. The assignments were: extended chain/β-sheet (1625 $\pm$ 0.2 and 1693 $\pm$ 0.6 cm^{-1}), α-helix (1657 $\pm$ 0.2 cm^{-1}), turns (1670 $\pm$ 0.2 and 1681 $\pm$ 0.2 cm^{-1}), and disordered structure (1643 $\pm$ 0.2 cm^{-1}).

Enzymatic Activity Measurements

The enzymatic activity of cutinase was measured on a UVIKON 943 A (Bio-Tek Kontron Instruments, Milano, Italy) spectrophotometer at 20°C using *p*-NPB as substrate. Hydrolysis of *p*-NPB was monitored as the change in absorbance at 400 nm corresponding to the absorption maximum of the *p*-nitrophenolate anion. *p*-NPB was dissolved in pure acetonitrile to a concentration of 80 m*M* and used at a final concentration of up to 0.8 m*M*. The final enzyme concentration was 3 n*M*. All measurements were performed in 20 m*M* Tris-Cl pH 8 in a volume of 1500 μl. As soon as the enzyme had been added, the cuvette was capped with parafilm, the contents were mixed by gentle inversion, and linear 1 min time profiles were recorded. Time profiles of samples containing different *p*-NPB concentration (0.1–0.8 m*M*) and buffer without enzyme were subtracted as blanks for all spectra to take into account *p*-NPB's autohydrolysis in water. Absorption changes were converted to concentration changes using $e_{400} = 16.000 M^{-1}\ cm^{-1}$. Data both in the absence and presence of ANS were analyzed in a double-reciprocal Lineweaver-Burk plot where the *x*-axis intercept was $-1/K_M$ and the *y*-axis intercept $1/v_{max}$. As seen in Figure 3B, ANS affects the slope but not the *x*-axis intercept, which is an indication of noncompetitive inhibition. In this case, v_{max} is lowered by a factor $(1 + [ANS]/K_I)$, where K_I is the apparent inhibition constant.

RESULTS

Cutinase's Thermal Stability Decreases Strongly with Increasing Protein Concentration Close to Its pI, and Is Related to Aggregation

To elucidate the effect of protein concentration on thermal stability of cutinase close to pI, a concentration-dependent thermal unfolding of 5–80 μM cutinase was monitored by fluorescence spectroscopy, circular dichroism (CD), and light scattering. The native state fluorescence baseline is essentially flat (Figure 1A), in contrast to many other proteins where a strong decrease in fluorescence with temperature is observed because of dynamic solvent quenching. This correlates with the fact that cutinase's single Trp residue is almost totally buried and excluded from solvent contacts in the native state. With increasing protein concentration, the fluorescence unfolding curves change from a typical sigmoidal shape curve to a Gaussian-type curve (Figure 1A). This is suggestive of aggregation and subsequent decline in fluorescence after denaturation (cf. similar data in Ref. 31). It is clear that the T_m decreases with increasing protein concentration (Table I). CD thermal scans (Figure 1B) gave T_m values identical to those obtained by fluorescence (Table I). Far UV CD spectra reveal a significant loss of secondary structural elements upon heating from 25 to 70°C (insert to Figure 1B), although the protein clearly retains a very significant amount of structure.

We used fluorimeter-based static light scattering (SLS) to monitor aggregation associated with thermal denaturation. A concentration-dependent increase in the intensity of scattered light at 500 nm upon thermal unfolding is observed (Figure 1C). At 5 μM cutinase, we only see a 7.4% increase in the intensity of scattered light after protein unfolding, but this increases to more than 100% at 20–60 μM. At 20 and 40 μM, the abrupt increase in intensity occurs above 50°C, while at 60 μM it already starts above 45°C. Thus, thermal denaturation, as monitored by CD and fluorescence, is accompanied by aggregation.

Aggregation Is Suppressed at Low pH and by a Mutation Altering the pI

Comparison of the T_m of cutinase at 5 and 80 μM between pH 4 and 11 reveals that concentration-dependent lowering of the T_m only occurs in a narrow pH range around the pI (Figure 1D). Outside this range, the solutions remain clear upon heating, indicating no macroscopic aggregation. This is confirmed by dynamic light scattering (DLS), which reveals that outside the pI,

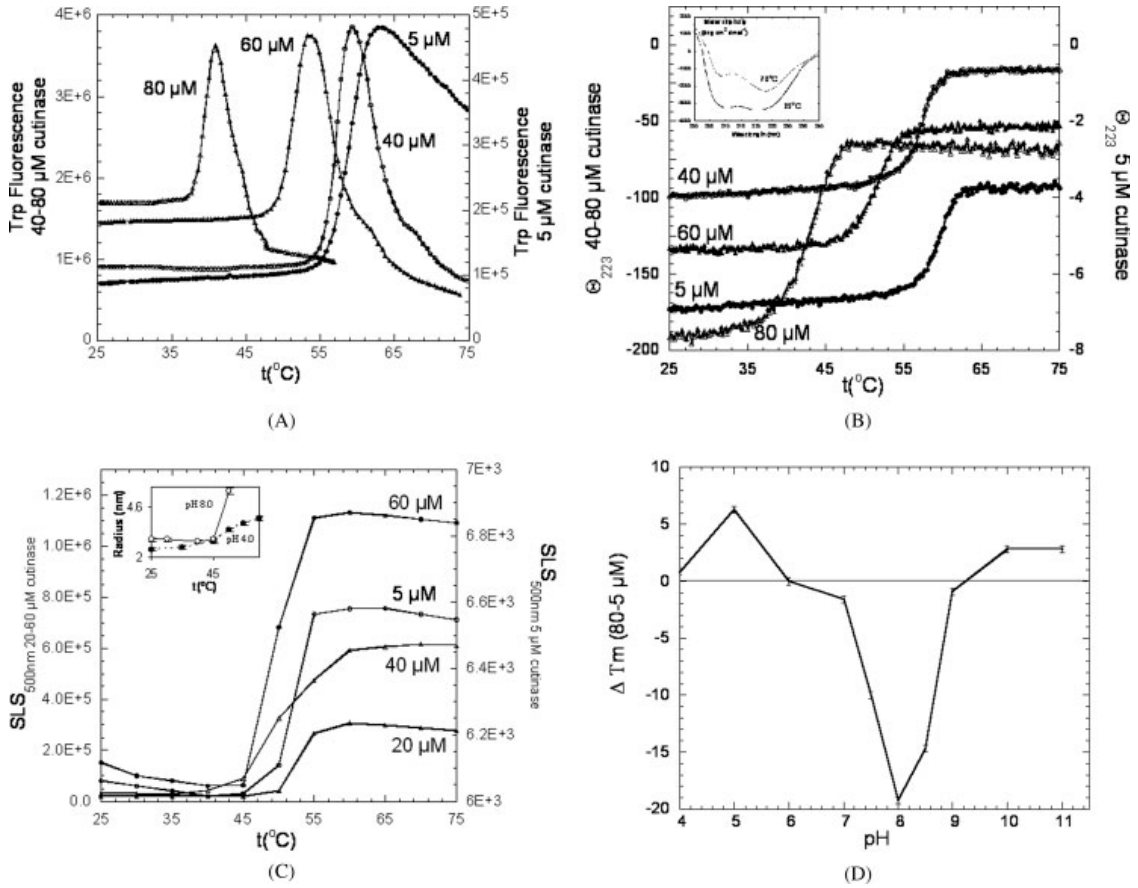

FIGURE 1 A: Thermal stability of 5–80 μM cutinase as monitored by fluorescence spectroscopy at pH 8.0. B: Thermal stability of 5–80 μM cutinase as monitored by CD at 223 nm at pH 8.0. Inset: far-UV CD spectra of 5 μM cutinase at pH 8.0 and 25°C (solid lines) versus 70°C (broken lines). C: SLS of 5–60 μM cutinase at pH 8.0 as a function of temperature. Inset: plot of R_H versus temperature of 60 μM cutinase at pH 4.0 and 8.0. The error bars denote the standard deviation determined for three experiments. R_H is calculated using Eq. (2). D: pH profile of cutinase as a function of ΔT_m (80−5 μM) as monitored by CD at 223 nm. The solid lines are drawn to guide the eye. Error bars are obtained from the fit.

R_H only increases from 2.4 to 2.8 nm upon thermal denaturation (insert to Figure 1C), consistent with a single conformational change from native to unfolded. Furthermore, the mutant E44A, whose pI is shifted upward to 9.5, does not show any aggregation behavior at pH 8.0 between 5 and 80 μM protein, where the T_m-values are 47.3 and 48.0°C, respectively (data not shown).

Fourier Transform Infrared Spectroscopy and Dye-Binding Data Suggest that the Aggregated State Is Rich in β-Content

Thermal aggregation of cutinase leads to temperature-dependent differences in secondary structure according to Fourier transform infrared spectroscopy (FTIR; Figure 2A). As the aggregation temperature increases, a significant increase in the area of the low β-sheet peak at 1625 cm^{-1} is observed (total amount of β-sheet structure at 80°C: 55%), both compared to the lowest aggregation temperature (48% β-sheet structure) and to the native structure (data not shown). The native state shows predominantly α-helical structure, consistent with 41% α-helix, 17% β-strand, 16% β-turns, and 27% disordered in the crystal structure (e.g. PDB file 1CEX). The high extended chain peak (1692 cm^{-1}) does not seem to be influenced by the change in temperature, possibly due to the low intensity. This is also the case for the peak corresponding to disordered structure (1643 cm^{-1}). Overall, the β-sheet content of the aggregated form is far higher than the content for the native protein. In par-

Table I Melting Temperatures T_m of Cutinase, Lysozyme, and α-Amylase at Their Respective pI-Values Followed by Fluorescence (FS) and CD

	Cutinase (T_m (°C); pI = 8.0)		Lipase (T_m (°C); pI = 8.0)	Lysozyme (T_m (°C); pI = 10.5)	Amylase (T_m (°C); pI = 6.0)
[Cutinase] (μM)	FS[a]	CD[b]	FS[a]	CD[b]	FS[a]
0.1	59.3				
5	59.3	59.5	74.4	71.9	58.2
40	57.3	57.2			
60	52.0	51.4			
80	40.3	40.3	68.9	75.7	61.5
ΔT_m (80–5 μM)	−19.0	−19.2	−5.5	+3.8	+3.3

[a] Determined by fluorescence spectroscopy at a scan rate of 90°C/h. Excitation for the fluorescence experiments was set at 295 nm and emission at 350 nm. T_m is calculated as the position of the maximum of the first derivative curve for the thermal unfolding scans. Errors typically 0.1°C.

[b] T_m derived from Eq. (1). CD was monitored at 223 nm. Errors typically 0.1–0.2°C.

allel to the increase in β-content with increasing aggregation temperature, the remaining peaks decrease in intensity although this change is most pronounced for the α-helix peak (1657 cm^{-1}). It is possible that the increase in β-structure is due to exposure of the core β-sheet during thermal unfolding followed by cross β-sheet aggregation and recruitment of neighboring residues into the β-sheet.

The small molecule dyes thioflavin T and Congo red are known to bind to proteins in the misfolded β-sheet rich fibrillated state.[32,33] Incubation with the heat-aggregated state of cutinase (formed by incubation of 80 μM at pH 8.0 at 50–70°C) leads to a distinct red-shift in the Congo red absorption spectrum and a marked increase in thioflavin T fluorescence (Figure 2B), consistent with a high β-sheet content of the aggregates.

Suppression of Cutinase Aggregation by Additives such as Urea, Detergents, and L-Arginine Is Coupled to Destabilization and Irreversible Denaturation

We next investigated the extent to which various additives could reduce the protein's aggregation-induced destabilization. Nonionic detergents, the stabilizing amino acid arginine, and the denaturant urea largely suppressed concentration-dependent destabilization, but all these reagents lowered the thermal stability of cutinase significantly (Table II). Cutinase is known to be destabilized by anionic detergents,[10,34] but nonionic detergents also appear somewhat surprisingly to play a similar role (P. Sehgal and D.O., unpublished observations). In addition, unfolding was far from reversible under these conditions: precipitation above the T_m was observed for detergents, while in urea, the native-level ellipticity was only partially regained upon cooling (data not shown). Thus, detergents could only suppress the aggregation events prior to denaturation but could not keep it in a state able to refold.

Micromolar Concentrations of ANS Efficiently Suppress Aggregation

We reasoned that a probe binding to and shielding exposed hydrophobic regions might suppress the thermal aggregation of cutinase. An obvious candidate is the fluorescent probe 1,8-ANS. We measured the T_m of 80 μM cutinase as a function of ANS concentration, and found that ANS increases the T_m in a hyperbolic fashion, which empirically fits to a simple binding curve. The fit predicts that the T_m-values approach a final value of (63.5 ± 1.0)°C with an apparent dissociation constant K_M of 8.6 ± 1.1 μM (Figure 3A). Importantly, cutinase heated in the presence of ANS retains around 70% of its activity upon cooling, in contrast to cutinase heated in its absence (5% of residual activity), as shown in the insert to Figure 3A. Concentrations up to 80 μM of thioflavin T and Congo red have no effect on the aggregation of 80 μM cutinase (data not shown).

Given that cutinase has a hydrophobic binding patch with an affinity for alkyl chains,[35] it might be expected that ANS could bind to the active site. However, enzymatic activity assays reveal that ANS in fact acts as a noncompetitive inhibitor (i.e. binding outside the active site) (Figure 3B) with unchanged K_D but reduced V_{max} (Table III). The apparent K_I is 62.5 ± 12.5 μM but this need not be identical to the apparent K_D of 8.6 μM identified from thermal scans

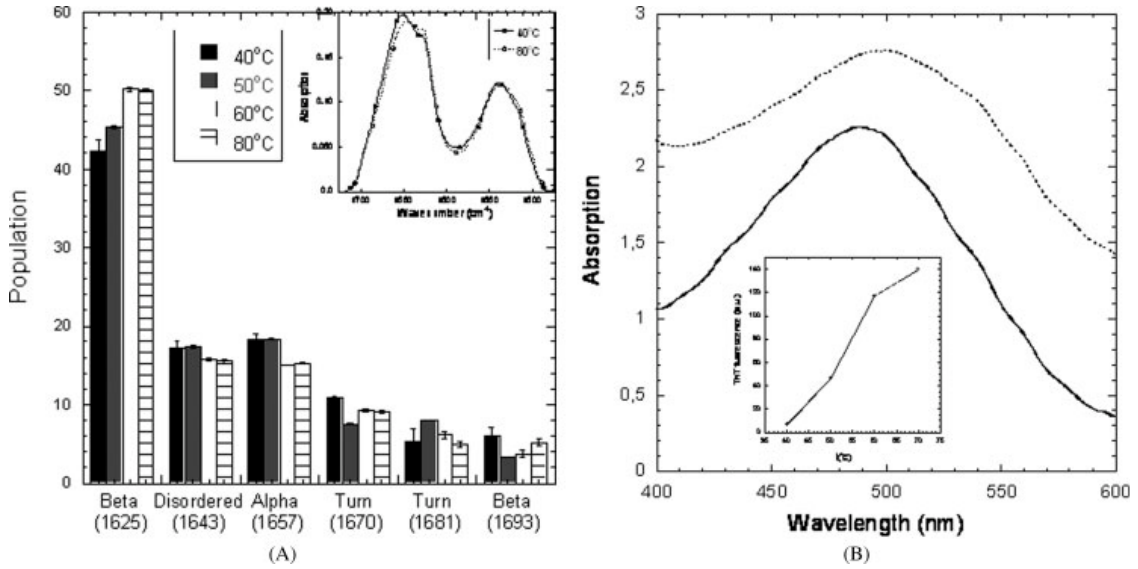

FIGURE 2 A: Secondary structure content of aggregated cutinase at pH 8.0 based on FTIR spectra. Cutinase (80 μM) was incubated at 40–80°C for 15 min. Insert: FTIR spectra of samples incubated at 40 and 80°C. B: Absorption spectra of Congo red alone (joined line) and in the presence of 80 μM cutinase aggregated by exposure to 50°C at pH 8.0 for 15 min (dashed line). Insert: emission intensity of thioflavin T at 485 nm (excitation 450 nm) in the presence of 80 μM cutinase incubated at different temperatures for 15 min at pH 8.0.

(Figure 3A), since the K_I only reports on the binding to sites which directly affect enzymatic activity.

Direct addition of ANS to the native cutinase reveals that ANS binds so tightly to cutinase that a titration plot (with a break-point at saturation) rather that a hyperbolic binding curve is obtained. Data obtained at different cutinase concentrations suggest a 5 ANS:1 cutinase stoichiometry (Figure 3C). Interestingly, when cutinase is present at 4-fold higher concentration than ANS, the protein is either stabilized (pH 7.5–8.5) or not affected (outside pH 7.5–8.5) (Figure 3D). However, when ANS is present in 4-fold excess, the T_m decreases at all pH values (Figure 3D). This suggests that the first binding site for ANS is stabilizing, whereas the occupation of subsequent binding sites leads to destabilization of the protein. This observation is vindicated by Figure 3E, which shows how the T_m of cutinase at 5 μM protein actually increases in the presence of 5 μM ANS but subsequently declines.

Thermal Stability of Lipase, but not Lysozyme and α-Amylase, Is Sensitive to Protein Concentration at the pI

To test the generality of pI-enhanced thermal aggregation and destabilization, we investigated the thermal unfolding of *T. lanuginosus* lipase, lysozyme, and α-amylase at pH-values corresponding to their respective pI-values (Table I). The T_m of lipase decreased by 5.5°C between 5 and 80 μM. This reduction in T_m was completely removed by ANS, which in fact leads to a T_m of 75.8°C at 80 μM lipase, which is 1.4°C higher than the T_m at 5 μM lipase in the absence of ANS. However, for both lysozyme and α-amylase, increasing the protein concentration from 5 to 80 μM resulted in a global thermal stabilization of 3.8 and 3.3°C, respectively, comparable to the stabilization of cutinase by high protein concentrations outside pH 7–9 (Figure 1D). Thus, the concentration-

Table II Effect of Additives on the T_m of 80 μM Cutinase at pH 8.0

Additive	Concentration	T_m (°C)[a] 80 μM	T_m (°C)[a] 5 μM	ΔT_m (°C) 80–5 μM
None	–	40.3	59.3	−19
Urea	2 M	47.5	47.5	0
DM	20 mM	53.8	54.9	−1.1
OG	10 mM	52.1	53.1	–
OM	10 mM	52.5	54.65	–
L-Arg	0.5 M	55.2	56.4	−1.2

[a] Unfolding followed by CD. T_m was obtained by fitting the data to Eq. (1). Errors 0.1–0.2°C.

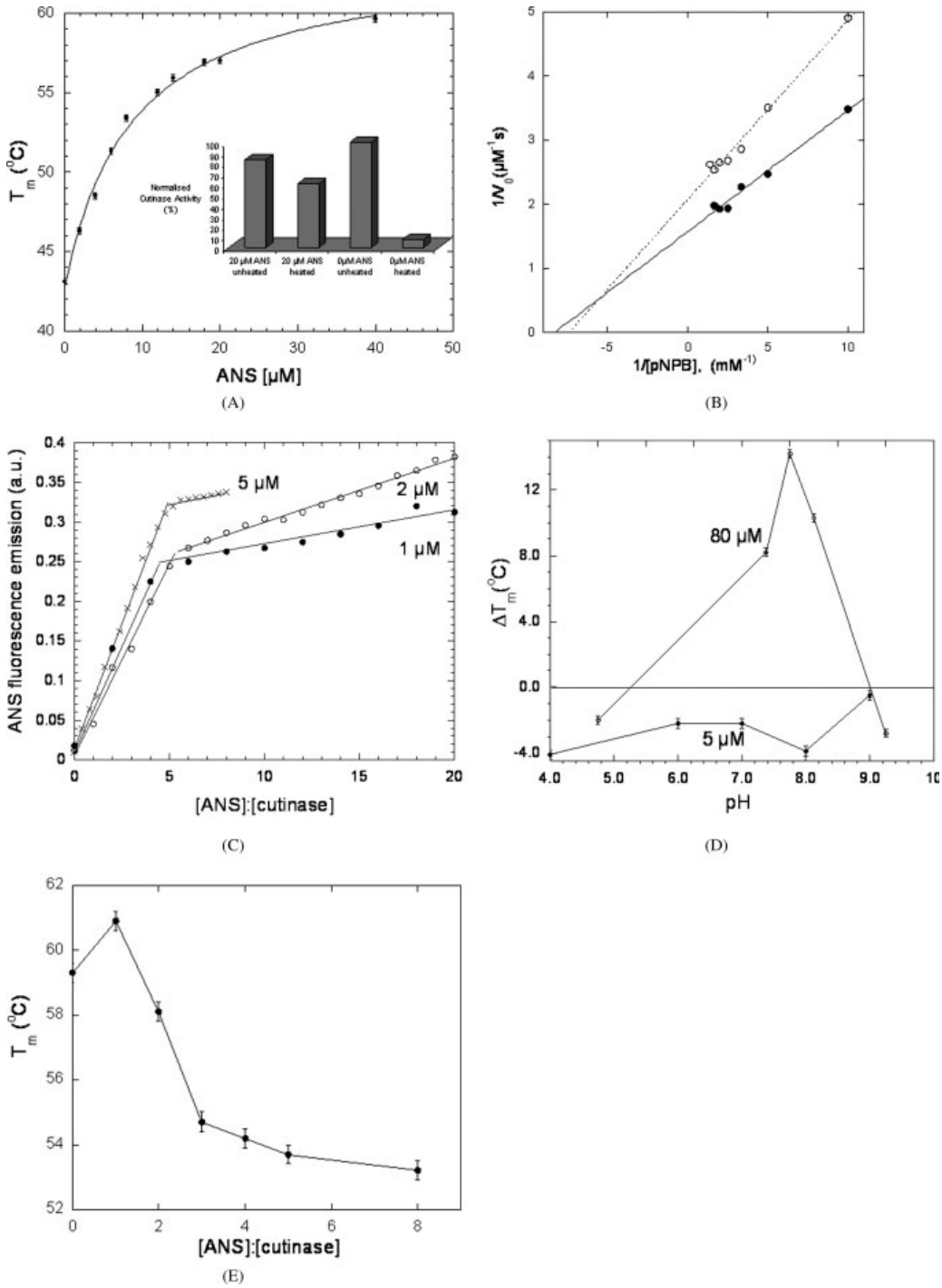

FIGURE 3 A: T_m of 80 μM cutinase at pH 8.0 as a function of ANS concentrations. The solid line is the result of the best fit to a simple binding equation. Inset shows the recovery of enzyme activity after heating of 80 μM cutinase at pH 8.0 in the presence and absence of 20 μM ANS. Errors ca. 5%. B: Double reciprocal plots of cutinase's hydrolytic activity towards *p*-NPB at pH 8.0 in the absence of ANS (filled circles) and in the presence of 20 μM ANS (empty circles). C: Fluorescence profile of cutinase titrated with ANS at pH 8.0 in 1–5 μM cutinase. D: Effects of 20 μM ANS on the T_m of 80 and 5 μM cutinase at different pH values. The solid lines are drawn to guide the eye. E: T_m of 5 μM cutinase at pH 8.0 at different [cutinase]:[ANS] values.

Table III Effect of ANS on Cutinase Activity Towards *p*-NPB

[ANS] (μM)	v_{max} (ΔOD_{410} min^{-1} μM^{-1})$^{-1a,b}$	K_M (μM)^{a,b}
0	0.638 ± 0.024	0.121 ± 0.009
20	0.483 ± 0.015	0.135 ± 0.008

[a] Experiments carried out at pH 8.0 and 20°C using 3 n*M* cutinase.
[b] Values obtained as described in Materials and Methods.

destabilization effect, and its ability to be rescued by ANS, appears specific for enzymes with hydrophobic substrates, i.e. cutinase and lipase.

DISCUSSION

This work shows that the thermal denaturation of the triglyceride-hydrolyzing enzyme cutinase from *F. solani pisi* is particularly sensitive to aggregation around the pI of the protein, where there is minimal electrostatic repulsion. While it is not surprising that protein unfolding around pI should lead to aggregation after thermal denaturation, it seems less obvious why increasing the protein concentration from 5 to 80 μM should decrease the melting temperature from 59.5 to 40.3°C, since the protein is overwhelmingly in the native state at 40°C at low protein concentrations. A simple explanation for such behavior could be that a partially folded intermediate accumulates around 40°C. Intermediates tend to expose hydrophobic patches, which provide contact points to other partially folded molecules, encouraging aggregation.[4] Such an intermediate may accumulate for cutinase under certain conditions. At pH 4.5, cutinase unfolds via a transient unfolding intermediate in guanidinium hydrochloride at 25°C according to stopped-flow experiments.[36] In addition, there was a slight (ca. 0.1*M*) discrepancy between the changes in ANS and Trp fluorescence upon equilibrium unfolding in GdmCl, which is consistent with at least some degree of formation of a partially unfolded state induced by chemical denaturants.[37] Nevertheless, the same study concluded that thermal unfolding proceeded according to a simple two-state model.[37] A careful DSC study on the unfolding of cutinase (conducted at pH 9 and at around 40 μM cutinase, i.e. outside the region of maximal aggregation) also concluded that cutinase unfolding was more complex than a simple Lumry-Eyring model for irreversible unfolding and the authors invoked a thermal unfolding intermediate to explain the discrepancy.[10] However, they acknowledged that there was no direct evidence for an intermediate in the thermogram.

In our study, the perfect correspondence between CD and fluorescence-based data for unfolding of cutinase, the lack of an increase in the fluorescence of ANS (which, in addition to its affinity for sticky patches on native surfaces, should be expected to have particular affinity for partially denatured states) during the thermal scan, as well as the ability to fit the data to a simple two-state unfolding model indicate that a spectroscopically distinct intermediate does not accumulate to any significant effect. On the basis of the fact that the thermal aggregates are rich in β-sheet structure, we propose that aggregation occurs because of fluctuations in the native state ensemble, leading to transient interactions via exposed β-sheets that at high protein concentrations lead to the formation of massive aggregates. This is similar to a model proposed for interferon-γ.[6] What is the nature of these β-sheet interactions? On the one hand, the end-state of the aggregation process binds to the (relatively) fibril-specific dyes thioflavin T and Congo red, indicating the existence of relatively ordered β-sheet structures. On the other hand, these putative β-sheet contacts are unlikely to be as regular as seen for the amyloid state, given that the dyes do not have any effect on the aggregation process. One might otherwise have expected that these dyes could disfavor aggregation in view of their ability to inhibit fibrillation of e.g. the Aβ peptide and huntingtin.[38] It is possible that the well-organized β-sheet structures form at a later stage and the early and rate-limiting formation of intermolecular contacts is driven by more unspecific hydrophobic contacts, such as surface patches found in the native state. These patches are likely to be covered by ANS, reducing the prevalence of intermolecular contacts. Such patches are also found in lipase because of its hydrophobic binding site for substrates but are lacking in lysozyme and α-amylase, thus explaining the different behaviors of these proteins close to their pI.

Aggregation occurs rather abruptly according to SLS data, suggesting that the process may depend on the formation of small nuclei whose formation then lead to an onrush of aggregation. This is compatible with the remarkable efficacy with which ANS suppresses aggregation of cutinase at molar ratios of less than 1 ANS per cutinase molecule. Formation of a propagation-competent aggregation nucleus will be very sensitive to the presence of even small amounts of ANS, which can interfere with the intermolecular contacts, e.g. by binding in the interface between different cutinase molecules. It is also possible that

binding of ANS (at least at low ANS:protein ratios, see later) leads to an overall tightening of cutinase structure, as seen for bovine serum albumin,[25] and suppressing the structural fluctuations that may encourage intermolecular contacts.

Kinetic studies on the aggregation of cutinase during refolding from the chemically denatured state suggest that the rate-limiting step is the formation of dimers (R.B. and D.E.O., unpublished data). In contrast, a previous study on carbonic anhydrase only saw an aggregation-suppressing effect at 150-fold molar excess of ANS, and only a miniscule fraction of activity was retained upon cooling.[17] The key to this difference may be that carbonic anhydrase does not have any obvious binding sites on the surface, since its substrate (hydrated carbon dioxide) is not a large hydrophobic molecule. In contrast, ANS binds so strongly to cutinase that we observe a titration rather than a binding isotherm. The hydrophobicity is so pronounced that several molecules of ANS are able to bind, and this eventually destabilizes the protein when ANS is present in excess, possibly because binding occurs in a cooperative fashion, leading to the partial exposure of otherwise buried parts of the protein and thus an interference with otherwise stabilizing side-chain contacts. Similarly, the dye bis-ANS, consisting of two fused ANS molecules, is able to induce conformational changes and destabilization upon binding.[20] Thus, ANS is not a universal panacea against aggregation of proteins, but appears to be most appropriate when the protein is able to bind the dye in the native state. At the more general level, 1,8-ANS may prove to be a useful aggregation-suppressor for the large number of proteins, which bind hydrophobic or amphiphilic substrates, including both lipolytic enzymes and lipid-transporter molecules. In the case of cutinase, ANS should only be used at equimolar concentrations to avoid destabilization of the protein, but the optimal stoichiometric ratio must be obtained empirically from protein to protein. At low and high pH where aggregation of cutinase does not occur, osmolytes such as trehalose can be used as stabilizers. At these pH values, cutinase stability increases steadily with increasing trehalose concentrations and this effect has been assigned to a shift in the equilibrium towards the native state.[39,40]

REFERENCES

1. Wang, W. Int J Pharm 2005, 289, 1–30.
2. Frokjaer, S.; Otzen, D. E. Nat Rev Drug Delivery 2005, 4, 298–306.
3. Dong, A. C.; Prestrelski, S. J.; Allison, S. D.; Carpenter, J. F. J Pharm Sci 1995, 84, 415–424.
4. Fink, A. L. Fold Des 1998, 3, R9–R29.
5. Carrotta, R.; Bauer, R.; Waninge, R.; Rischel, C. Protein Sci 2001, 10, 1312–1318.
6. Kendrick, B. S.; Carpenter, J. F.; Cleland, J. L.; Randolph, T. W. Proc Natl Acad Sci USA 1998, 95, 14142–14146.
7. Narhi, L. O.; Philo, J. S.; Sun, B.; Chang, B. S.; Arakawa, T. Pharm Res 1999, 16, 799–807.
8. Szenczi, A.; Kardos, J.; Medgyesi, G. A.; Zavodszky, P. Biologicals 2006, 34, 5–14.
9. Shiraki, K.; Kudou, M.; Fujiwara, S.; Imanaka, T.; Takagi, M. J Biochem (Tokyo) 2002, 132, 591–595.
10. Creveld, L. D.; Meijberg, W.; Berendsen, H. J.; Pepermans, H. A.; Philo, J. S. Biophys Chem 2001, 92, 65–75.
11. Tsumoto, K.; Umetsu, M.; Kumagai, I.; Ejima, D.; Philo, J. S.; Arakawa, T. Biotechnol Prog 2004, 20, 1301–1308.
12. Murature, D. A.; Fidelio, G. D. Vox Sang 1995, 68, 1–4.
13. Zhang, J.; Peng, X.; Jonas, A.; Jonas, J. Biochemistry 1995, 34, 8631–8641.
14. Arakawa, T.; Kita, Y. J Pharm Sci 2000, 89, 646–651.
15. Wang, W. Int J Pharm 1999, 185, 129–188.
16. Kita, Y.; Arakawa, T. Biosci Biotechnol Biochem 2002, 66, 880–882.
17. Kundu, B.; Guptasarma, P. Proteins 1999, 37, 321–324.
18. Kundu, B.; Guptasarma, P. Biochem Biophys Res Commun 2002, 293, 572–577.
19. Semisotnov, G. V.; Rodinova, N. A.; Razgulyaev, O. I.; Uversky, V. N.; Gripas, A. F.; Gilmanshin, R. I. Biopolymers 1991, 31, 119–128.
20. Mogensen, J. E.; Wimmer, R.; Larsen, J. N.; Spangfort, M. D.; Otzen, D. E. J Biol Chem 2002, 277, 23684–23692.
21. Schönbrunn, E.; Eschenburg, S.; Luger, K.; Kabsch, W.; Amrhein, N. Proc Natl Acad Sci USA 2000, 97, 6345–6349.
22. Ory, J. J.; Banaszak, L. J. Biophys J 1999, 77, 1107–1116.
23. Slavik, J. Biochim Biophys Acta 1982, 694, 1–25.
24. Daniel, E.; Weber, G. Biochemistry 1966, 5, 1893–1907.
25. Matulis, D.; Baumann, C. G.; Bloomfield, V. A.; Lovrien, R. E. Biopolymers 1999, 49, 451–458.
26. Teschke, C. M.; King, J.; Prevelige, P. E. Biochemistry 1993, 32, 10658–10665.
27. Fu, X.; Zhang, X.; Chang, Z. Biochem Biophys Res Commun 2005, 329, 1098–1093.
28. Cordeiro, Y.; Lima, L. M. T. R.; Gomes, M. P. B.; Foguel, D.; Silva, J. L. J Biol Chem 2004, 279, 5346–5352.
29. Ferrão-Gonzales; Robbs, B. K.; Moreau, V. H.; Ferreira, A.; Juliano, L.; Valente, A. P.; Almeida, F. C. L.; Silva, J. L.; Foguel, D. J Biol Chem 2005, 280, 34747–34754.
30. Chi, E. Y.; Krishnan, R.; Kendrick, B. S.; Chang, B. S.; Carpenter, J. F.; Randolph, T. W. Protein Sci 2003, 12, 903–913.

31. Lo, M.-C.; Aulabaugh, A.; Jin, G.; Cowling, R.; Bard, J.; Malamas, M.; Ellestad, G. Anal Biochem 2004, 332, 153–159.
32. Levine, H. I. Protein Sci 1993, 2, 404–410.
33. Klunk, W. E.; Jacob, R. F.; Mason, R. P. Methods Enzymol 1999, 309, 285–305.
34. Ternström, T.; Svendsen, A.; Akke, M.; Adlercreutz, P. Biochim Biophys Acta 2005, 1748, 74–83.
35. Melo, E. P.; Aires-Barros, M. R.; Cabral, J. M. Appl Biochem Biotechnol 1995, 50, 45–56.
36. Melo, E. P.; Chen, L.; Cabral, J. M.; Fojan, P.; Petersen, S. B.; Otzen, D. E. Biochemistry 2003, 42, 7611–7617.
37. Melo, E. P.; Faria, T. Q.; Martins, L. O.; Goncalves, A. M.; Cabral, J. M. Proteins: Struct Funct Genet 2001, 42, 542–552.
38. Murphy, C. M. Annu Rev Biomed Eng 2002, 4, 155–174.
39. Baptista, R. P.; Chen, L. Y.; Paixao, A.; Cabral, J. M. S.; Melo, E. P. Biotechnol Bioeng 2003, 82, 851–857.
40. Baptista, R. P.; Cabral, J. M.; Melo, E. P. Biotechnol Bioeng 2000, 70, 699–703.
41. Sebastião, M. J.; Joaquim, M. S. C.; Aires-Barros, M. R. Enzyme Microb Technol 1996, 18, 251–260.
42. Kirk, W. R.; Kurian, E.; Prendergast, F. G. Biophys J 1996, 70, 69–83.
43. Yadav, S.; Ahmad, F. Anal Biochem 2000, 283, 207–213.
44. Byler, D. M.; Sussi, H. Biopolymers 1986, 25, 469–487.

Reviewing Editor: Eric J. Toone

Biochemistry **2006,** *45,* 481−497

Versatile Interactions of the Antimicrobial Peptide Novispirin with Detergents and Lipids†

Reinhard Wimmer,‡ Kell K. Andersen,‡ Brian Vad,‡ Mads Davidsen,‡ Søren Mølgaard,‡ Lise W. Nesgaard,‡ Hans H. Kristensen,§ and Daniel E. Otzen*,‡

Department of Life Sciences, Aalborg University, Sohngaardsholmsvej 49, DK-9000 Aalborg, Denmark, and Novozymes A/S, DK-2880 Bagsvaerd, Denmark

Received September 15, 2005; Revised Manuscript Received November 11, 2005

ABSTRACT: Novispirin G-10 is an 18-residue designed cationic peptide derived from the N-terminal part of an antimicrobial peptide from sheep. This derivative is more specific for bacteria than the parent peptide. We have analyzed Novispirin's interactions with various amphipathic molecules and find that a remarkably wide variety of conditions induce α-helical structure. Optimal structure induction by lipids occurs when the vesicles contain 40−80% anionic lipid, while pure anionic lipid vesicles induce aggregation. SDS also forms aggregates with Novispirin at submicellar concentrations but induces α-helical structures above the cmc. Both types of aggregates contain significant amounts of *β*-sheet structure, highlighting the peptide's structural versatility. The cationic detergent LTAC has a relatively strong affinity for the cationic peptide despite the peptide's net positive charge of +7 at physiological pH and total lack of negatively charged side chains. Zwitterionic and nonionic detergents induce α-helical structures at several hundred millimolar detergent. We have solved the peptide structure in SDS and LTAB by NMR and find subtle differences compared to the structure in TFE, which we ascribe to the interaction with an amphiphilic environment. Novispirin is largely buried in the SDS−micelle, whereas it does not enter the LTAC−micelle but merely forms a dynamic equilibrium between surface-bound and nonbound Novispirin. Thus, electrostatic repulsion can be overruled by relatively high-detergent concentrations or by deprotonating a single critical side chain, despite the fact that Novispirin's ability to bind to amphiphiles and form α-helical structure is sensitive to the electrostatics of the amphiphilic environment. This emphasizes the versatility of cationic antimicrobial peptides' interactions with amphiphiles.

Widespread use of conventional antibiotics has resulted in an increasing number of multiresistant microorganisms that pose a problem when dealing with infections and sepsis. In the search for alternatives to traditional antibiotics, antimicrobial peptides (AMPs)[1] have emerged as a possible solution (*1*). These peptides are a part of the innate immune system of almost all kingdoms, ranging from bacteria to animals, indicating that AMPs are an important part of evolution (*2*). The AMPs offer a quick immune response to a broad range of microbes. This is important because the activation of the pathogenic immune response is slow compared to microbial proliferation (*3*). AMPs show enormous sequence diversity but have been classified into four groups. These include linear peptides with or without a hydrophobic C-terminus which form α-helices upon binding to membranes, peptides containing a rigid antiparallel *β*-sheet held together by disulfide bonds, and linear peptides rich in one or two amino acids such as Trp, Pro, or Arg (*2*).

Whatever their structure, AMPs tend to be both amphipathic and cationic. Amphipathicity increases their affinity for biological membranes, while the positive charge increases their specificity toward negatively charged bacterial membranes, instead of the more neutral membrane surrounding eukaryotic cells. Interestingly, this preference for negatively charged membranes is also seen for aggregating proteins such as α-synuclein (*4*), and the ability of such proteins to bind and permeabilize membranes has been suggested to be a central phenomenon in the development of Parkinson's Disease and other dementias (*5*). Unfortunately, several AMPs have shown cytotoxic and hemolytic effect. Current models of AMP action suggest that the peptides bind and disrupt the cell membrane, either by forming holes through

† Daniel E. Otzen is supported by the Villum Kann Rasmussen Foundation and the Danish Research Foundation. Financial support from the Obel Foundation to both R.W. and D.E.O. is gratefully acknowledged.

* To whom correspondence should be addressed. E-mail: dao@bio.aau.dk. Tel: + 45 96 35 85 25. Fax: + 45 98 14 18 08.

‡ Aalborg University.

§ Novozymes A/S.

[1] Abbrevations: 2QF-COSY, double quantum filtered correlation spectroscopy; AMP, antimicrobial peptide; ATR, attenuated total reflection; CD, circular dichroism; CMC, critical micelle concentration; DM, dodecyl maltoside; DOPC, 1,2-dioleoyl-*sn*-glycero-3-phosphocholine; DOPE, 1,2-dioleoyl-*sn*-glycero-3-phosphoethanolamine; DOPG, 1,2-dioleoyl-*sn*-glycero-3-[phosphor-rac-(1-glycerol)]; DPS, 3-(dodecyldimethylammonio)propanesulfonate; EDTA, ethylenediamine tetraacetate; HPLC, high-performance liquid chromatography; IPTG, isopropyl-*β*-D-thiogalactopyranoside; KSI, kesteroid isomerase; LTAB, lauryl-trimethylammonium bromide; LTAC, lauryl-trimethylammonium chloride; MALDI-TOF, matrix-assisted laser desorption ionisation-time-of-flight; NOESY, nuclear Overhauser effect spectroscopy; NPN, 1-*N*-phenylnaphthylamine; PAGE, polyacryl gel electrophoresis; PBS, phosphate buffer saline; PFG, pulsed field gradient; SDS, sodium dodecyl sulfate; TFA, trifluoro acetic acid; TFE, 2,2,2-triflour ethanol; TOCSY, total correlation spectroscopy.

10.1021/bi051876r CCC: $33.50
Published on Web 12/15/2005

the membrane (the barrel-stave model) or by disturbing the lipid arrangement in the outer leaflet (the carpet model), leading to growth inhibition or lysis (*6*−*8*). Until now, only very little resistance has been observed against AMPs (*9*), and the few reported cases involve a reduction in the amount of acidic lipids or the production of specific digestive proteases (*2*).

Besides their direct antimicrobial effect, the AMPs have also proven to have other important roles such as stimulation of adaptive immunity by recruiting memory T-cells and immature dendrite cells (*10*), binding to and inactivating toxic bacterial lipopolysaccharides (*11*), and binding to cellular receptors and activating signaling pathways (*12*).

A number of biophysical features have emerged that influence the interaction between AMPs and membranes. First, electrostatic attraction is very important for initial binding to the membrane surface. Work with synthetic liposomes suggest that negative lipids must be included to achieve high affinity, while screening charge by the presence of salt can reduce or destroy AMP antimicrobial activity (*13*−*15*). Second, interactions with the hydrophobic parts of the membrane are important for the energetics of pore formation. The specific composition of the membrane can be expected to affect the energetics of pore formation through parameters such as bilayer thickness and degree of order, curvature strain, and adsorption energy (*8*, *16*, *17*). Thus, incorporation of PE lipids, which leads to reduced strain in the surface-bound peptide−lipid complex, increases the [peptide]/[lipid] ratio needed for pore formation (*18*), while DOPC encourages membrane insertion to a larger extent than the thinner DLPC (*19*). In addition, physiological features such as membrane proteins, periplasmic components, membrane potential and pH gradients, efflux pumps, and so forth (*20*) can also influence the process of membrane insertion.

Detergents mimic the amphiphilic nature of lipids, but do not provide the bilayer environment needed for pore formation by AMPs. Thus, the interaction between detergents and α-helical AMPs allows us to focus on the first stage of the pore-forming process, namely, binding and formation of α-helical structure. Because of the cationic nature of the AMPs, the anionic detergent SDS is the most popular detergent for such studies (*21*), although a zwitterionic detergent like dodecylphosphocholine can also induce α-helical structure at similar detergent concentrations (*22*). In contrast, nonionic detergents are generally not so effective at inducing structure (*23*), and cationic detergents have, to our knowledge, not been reported to interact significantly with cationic microbial peptides (*24*).

Micellar SDS has, for a long time, been known to stabilize α-helical conformations, even in peptides derived from *β*-sheet structures (*25*). For cationic sequences, this has been shown to be mediated by stable salt bridges between positively charged amino acids and the sulfate group of SDS (*26*), while more hydrophobic sequences probably penetrate into the hydrophobic micellar core (*27*). Because of the specific interactions involved, detergent chain length and headgroup structure can influence the degree of α-helicity of the bound peptide. For example, the helical part of a 15-residue membrane targeting peptide was one residue shorter in sodium nonanesulfonate and 3 residues shorter in sodium hexanesulfonate than in SDS (*28*); SDS was also shown to lead to a structure closest to that observed in the presence of the short chain lipid didecanoyl phosphocholine. The small size of the peptide relative to the detergent means that the micelle size is hardly influenced by the peptide (*28*).

Novispirin is a synthetic peptide (sequence KNLRR IIRKI IHIIK KYG), developed in several steps from the N-terminal part of the 29 residue α-helical AMP SMAP-29 found in sheep. SMAP has shown unusually potent antimicrobial activity (*29*), but its haemolytic and cytotoxic properties have excluded use in humans. Therefore, residues have been introduced which enhance helix stability and create a more pronounced gradient of hydrophobicity along the backbone. This resulted in enhanced bacterial activity and salt tolerance, and the additional Ile → Gly mutation in position 10 decreased haemolytic activity sufficiently to make it a suitable candidate for human use (*30*). The structure of Novispirin in 40% TFE reveals an α-helix from residue 3 to 11, a hinge formed by His12 and Ile 13, and a 3_{10} helix from residue 14 to 16 (*30*). Alcohols such as TFE are known to stimulate α-helix formation (*31*, *32*), probably due to the decrease in solvent polarity which strengthens hydrogen bonding, as well as direct binding to the peptide or protein.

Here, we describe structural studies on the AMP Novispirin G-10 in the presence of different lipids and detergents. The objective was to obtain a better understanding of the relative contributions of electrostatic and hydrophobic effects when Novispirin folds in an amphiphilic environment. Not surprisingly, zwitterionic lipids alone are not able to induce an α-helical structure in Novispirin at experimentally accessible concentrations, unless at least 20% anionic lipid is included. Zwitterionic and nonionic detergents induce an α-helical structure, albeit several orders of magnitude more weakly than SDS. Interestingly, the cationic detergent LTAC is able to induce α-helical structure in Novispirin at detergent concentrations comparable to SDS, although there were subtle changes in the far-UV CD spectrum. We therefore carried out a comparative analysis of the structure and micelle interactions of Novispirin in SDS and LTAB by NMR spectroscopy. To our knowledge, this is the first atomic-level study to address interactions between cationic detergents and antimicrobial peptides.

The peptide formed a helical secondary structure in both SDS and LTAB, although the [detergent]/[peptide] ratio needed to induce secondary structure formation was much higher in LTAB than in SDS. Several NMR techniques were applied to gather information about the relative positioning of the peptide within/on the detergent micelle: H^N-exchange, NOE cross-peaks between the peptide and the lipid, and the addition of paramagnetic ions. These techniques revealed that Novispirin is, to a good part, buried in the SDS−micelle, whereas it does not enter the LTAB−micelle but forms a dynamic equilibrium between surface-bound and nonbound Novispirin. Such a dynamic equilibrium can explain how detergents can override electrostatic repulsion at sufficiently high-detergent concentrations.

MATERIALS AND METHODS

Materials. All lipids, namely, DOPC, DOPE, and DOPG, were from Avanti Polar Lipids (Alabaster, AL). Sodium-dodecyl-d_{25}-sulfate, LTAC, DPS, NPN, and Lipopolysaccharide EH100 from *Escherichia coli* were from Sigma. DM was from Calbiochem and TFE from Aldrich. All chemicals

were of the highest grade available. LTAB-d_{25} (deuterated only on the dodecyl chain but not on the methyl groups) was obtained from QMX Laboratories (U.K.). Note that LTAB-d_{25} was only used for NMR experiments, where deuterated detergent was necessary due to the availability of the deuterated form; for other experiments, LTAC was used due to its lower absorption in the far-UV area.

Cloning, Expression, and Purification of Novispirin G-10. For economy of scale, Novispirin G-10 (KNLRRIIRKGIHIIKKYG) was produced recombinantly in *E. coli* as inclusion bodies. This was achieved through gene-fusion with a fragment of KSI using the commercially available plasmid pET31b+ (www.novagen.com). To facilitate downstream processing and recovery of Novispirin G-10, the Novispirin G-10 gene was preceded by an aspartate−proline (DP) dipeptide, followed by an aspartate−glutamate dipeptide (DE). Thus, the gene-fusion construct encodes the following: KSI−D−P−D−E−NovispirinG-10. The DP dipeptide is prone to mild acid hydrolysis at elevated temperatures (*33*, *34*), and the glutamic acid residue located immediately upstream of the Novispirin G-10 is substrate of a glutamyl endopeptidase I.

The expression plasmid was constructed using the following oligonucleotides encoding Novispirin G-10: (5′-ATT ATT CAG ATG CTG GAT CCG GAC GAA AAA AAC CTG CGT CGC ATT ATC CGC AAA GGC ATC CAT ATC ATT AAA AAA TAT GGC TAA TAA CTC GAG ATT ATT-3′ and 5′-AAT AAT CTC GAG TTA TTA GCC ATA TTT TTT AAT GAT ATG GAT GCC TTT GCG GAT AAT GCG ACG CAG GTT TTT TTC GTC CGG ATC CAG CAT CTG AAT AAT-3′). Enzymatic digestion of introduced flanking restriction endonuclease sites (AlwNI/AvaI) enabled the cloning of the synthetic gene as a fusion construct in pET31b+ (standard procedures as described by the manufacturer (New England Biolabs, Inc., MA)). All standard protocols have been described elsewhere (*35*).

Recombinant pET31b+ was transformed into *E. coli* Novablue as described by the manufacturer (Novagen). Plasmids were recovered by QIAprep Mini Columns (QIAGEN, Inc., CA) and sequenced by automated sequencing using plasmid-specific primers (5′-TGC TAG TTA TTG CTC AGC GG-3′ and 5′-ACC GTA GTT GCG CCC ATC G-3′). Recombinant plasmid was transformed in *E. coli* BLR-DE3 according to the manufacturer (Novagen). Bacteria were cultivated in LB media to $OD_{600} \sim 0.8$, and recombinant protein synthesis was initiated by 1 mM IPTG. Three hours after induction, bacteria were harvested, resuspended in $^1/_{10}$ volume buffer A (50 mM Tris-HCl, 1 mM EDTA, and 100 mM NaCl, pH 8), and lysed by pressure disruption (1500 mbar). The DPDE−Novispirin G-10 is located in inclusion bodies, which were isolated by centrifugation at 24 000*g* for 2 h. The resulting inclusion body pellet was washed twice in buffer B (50 mM Tris-HCl, 10 mM EDTA, 0.5% Triton X-100, and 100 mM NaCl, pH 8). All standard protocols have been described elsewhere (*35*).

The PDE−Novispirin G-10 was liberated from the inclusion bodies by hot acid hydrolysis, which cleaves specifically between Asp−Pro. This sequence was introduced between the KSI (ketosteroid isomerase) fusion partner and N-terminally to the synthetic gene encoding Novispirin G-10. For hot acid hydrolysis, inclusion bodies were resuspended in 100 mM sodium phosphate (pH 2.3) and incubated overnight at 85 °C. Resulting supernatant contained PDE−Novispirin G-10. The sample was neutralized by adding 100 mM sodium phosphate (pH 12.3). The peptide was matured with a glutamyl endopeptidase I from *Bacillus licheniformis* (*36*) produced by Novozymes A/S.

The matured octadecapeptide was purified by cation-exchange chromatography, as follows. The Novispirin G-10 and glutamyl endopeptidase mixture was adjusted to pH 6 and 7 mS/cm prior to application to a CM−sephadex column (Amersham Biosciences). Novispirin G-10 was eluted with a 0−1 M NaCl gradient in 50 mM malonic acid, pH 6, over 10 CV. The fractions were analyzed by MALDI-TOF mass spectrometric analysis (for Novispirin identification) and SDS−PAGE (for high MW impurity detection). The selected fractions were pooled and desalted on Sephadex-G10 column (Amersham Biosciences) equilibrated with PBS, pH 7.4 (50 mM phosphate buffer and 150 mM NaCl). Again the fractions were analyzed by MALDI-TOF mass spectrometric analysis and pooled. The Novispirin G-10 pool was analyzed for purity by SDS−PAGE and RP-HPLC (Jupiter, 5 μm, C18 300 Å, 150 mm × 2 mm, 50 min gradient from 8 to 80% acetonitrile in 0.1% triflouric acid, flow of 0.15 mL/min, $\lambda = 214$ nm). The identity of the peptide was determined by automated N-terminal sequencing using a Procise automatic sequencer (Applied Biosystems Division, Perkin-Elmer), and the concentration was determined by amino acid analysis performed on a Biochrom 20 Plus (Biochrom, Ltd.).

MALDI-TOF Mass Spectrometric Analysis. A 0.5 mL sample was spotted onto a stainless steel target plate. A volume of 0.5 μL of 10 mg/mL 4-hydroxy-α-cyano-cinnapinic acid (HCCA) in 50% acetonitrile and 0.1% TFA was subsequently mixed with the sample on the target plate. The sample spots were allowed to dry at room temperature before analysis (dried droplet method). MALDI analyses were performed on a Voyager DE Pro mass spectrometer with delayed extraction technology and a 337 nm N_2 laser producing 3 ns pulses with a repetition rate of 20 Hz (Applied Biosystems). The instrument was run in reflective mode with positive ionization. External calibration was applied using CalMix2 (Applied Biosystems).

Preparation of Vesicles. Synthetic lipid samples were mixed from stock solutions of lipids dissolved in methanol and dried overnight in a Heto VR-1 centrifuge vacuum drier. Lipids were then resuspended by vortexing in 20 mM sodium phosphate, pH 7.5, to a final concentration of 5 g/L (∼7 mM), exposed to at least seven cycles of freezing in liquid nitrogen, followed by thawing in a 55 °C water bath, before extrusion through a 100 nm pore filter (Nucleopore track etch membrane (Whatman)) 12 times using a 10 mL thermobarrel extruder (Northern Lipids, Vancouver, Canada). Vesicle sizes were confirmed by dynamic light scattering (DynaPro 99, ProteinSolutions). All extruded vesicles were used within 2 days of production. *E. coli* total lipid extract was not extruded due to its high content of phosphoethanolamine lipids but was subjected to 60 min of sonication in a sonication bath after the freeze−thaw step. This yielded a clear solution of vesicles with a hydrodynamic radius of around 75 nm as measured by dynamic light scattering.

CD Spectroscopy. All experiments were carried out in 20 mM sodium phosphate, pH 7.5, at 25 °C unless otherwise stated. Experiments at pH 11 were carried out using 20 mM

Gly as buffer. Equilibrium circular dichroism studies were performed on a Jasco J-810 spectropolarimeter (Jasco Spectroscopic Co., Hachioji City, Japan) with a Jasco PTC-348W1 temperature control unit. At least four scans were averaged to yield the final spectrum. Unless otherwise stated, the peptide concentration was 40 μM, and a 1 mm quartz cuvette was used.

FTIR Spectroscopy. All experiments were carried out in 20 mM Tris, pH 7.5, at 25 °C and at a peptide concentration of 40 μM. Fourier transform infrared spectroscopy was carried out on a Bruker Tensor 27 infrared spectrometer (Bruker Optik GmbH, Ettlingen, Germany) with a Specac Golden Gate single-reflection ATR unit (Specac, Ltd., Orpington, U.K.). The peptide was precipitated in 0.75 mM SDS or 1 mM DOPG. Aggregates were isolated by centrifugation and resuspended in 0.75 mM SDS or 0.2 mM DOPG. Samples were prepared by drying on the ATR surface under a gentle stream of nitrogen. Spectra were recorded with 128 accumulations and analyzed using OPUS 5.5 software (Bruker Optik GmbH, Ettlingen, Germany). For the DOPG samples, a DOPG spectrum was collected and subtracted from the sample spectra to remove the C═O peak at 1740 cm^{-1}. Estimates of secondary structure were obtained by fitting of Gaussian curves by the Levenberg Maquardt method. The number of bands and the positions were determined from the second derivative spectrum and by Fourier self-deconvolution as described (*37*). Bands were grouped by secondary structure type, and the relative band area percentages were calculated.

For comparison with results from CD spectroscopy, transmission spectra were recorded in D_2O using 2 mg/mL Novospirin in 85 mM SDS and 20 mM Tris, pH 7.5.

Determination of Critical Micelle Concentration (Cmc). Cmc was determined by monitoring the conductivity as a function of detergent concentration in the appropriate buffers using a CDM210 conductivity meter (Radiometer, Denmark). The cmc was defined as the detergent concentration where the increase in conductivity with detergent concentration kinks to a lower slope.

Data Analysis. To obtain a quantitative measure of the affinity of Novispirin for different lipids and detergents, titration data (CD signals versus detergent or lipid concentration) were fitted to the following equations.

(1) Hyperbolic binding (only for LPS, DM, DPS, and LTAC):

$$S = S_{\text{start}} + \Delta S \frac{[\text{det}]}{[\text{det}] + K_{\text{d}}} \quad (1)$$

where ΔS is the signal change between the free and bound Novispirin and K_d is an apparent binding constant.

(2) Cooperative binding (sigmoid curve):

$$S = \frac{S_{\text{end}} + S_{\text{start}} 10^{-c(L-L_{50\%})}}{1 + 10^{-c(L-L_{50\%})}} \quad (2)$$

where S_{start} and S_{end} are the CD values at low- and high-lipid concentrations, respectively, concentration L, $L_{50\%}$ is the concentration at which the transition is halfway to completion, and c is the cooperativity constant. The lower c is, the more gradual the transition.

NMR Recording. All NMR spectra were recorded on a BRUKER DRX600 spectrometer operating at a field strength of 14.1 T, equipped with a TXI(H/C/N) probe with triple-axis gradients. Spectra were processed using XWinNMR 2.6 and 3.6.

Titration of Novispirin in LTAC. 1. Constant pH. A sample of novispirin was dissolved in 550 μL of a solution containing 80 mM NaCl, 3 mM NaN_3, 20 mM phosphate buffer, and 5% D_2O. The peptide concentration was 2.5 mM. The pH was adjusted to 5.7 by addition of 1 M H_3PO_4. Solid LTAC was added in small amounts directly into the NMR sample tube. The volume increase (20% at 1 M LTAC) was estimated by help of a graduated sample tube; LTAC concentrations were corrected for the increase in volume. No measures were taken to keep the peptide or salt concentrations unchanged. For each concentration of LTAC, a 1D NMR spectrum and a diffusion spectrum were measured. The 1D NMR spectrum was measured using excitation-sculpting water suppression (*38*) and selective excitation of the region from 6 to 9 ppm by an off-resonance Q5 pulse (*39*) of 3.14 ms duration. This ensured maximum sensitivity on the peptide H^N/aromatic signals by leaving detergent magnetization in the longitudinal state. Experimental details of the diffusion measurements are described below.

2. Constant [LTAC]. A sample of novispirin was dissolved in 550 μL of a solution containing 270 mM LTAC, 80 mM NaCl, 3 mM NaN_3, 20 mM phosphate buffer, and 5% D_2O. The peptide concentration was 2.5 mM. The pH was brought to 9 by addition of 1 M NaOH; thereafter, pH was brought to 4.6 in steps of approximately 0.5 pH units by addition of 1 M H_3PO_4. A 1D NMR spectrum was measured using excitation-sculpting water suppression (*38*) and selective excitation of the region from 6 to 9 ppm by an off-resonance Q5 pulse (*39*) of 3.14 ms duration at each pH value. The solution was diluted by approximately 7% in the course of the titration; no action was taken to compensate for this.

Structure Determination. 1. SDS. The NMR sample was prepared by dissolving novispirin in 350 μL of a 300 mM SDS-d_{25} (Sigma-Aldrich), 300 mM NaCl, 3 mM NaN_3, and 20 mM phosphate buffer solution containing 5% D_2O. The pH of the solution was brought to 4.6 by addition of 1 M H_3PO_4. A 2D NOESY spectrum with 70 ms mixing time was recorded with a WATERGATE water suppression (*40*). [^{1}H,^{1}H]-TOCSY spectra with 40 and 80 ms mixing time, respectively, were recorded using the clean-TOCSY sequence (*41*) with a 15 kHz spin-lock and a WATERGATE water suppression. In addition, a 2QF-COSY experiment was recorded. The assignment was obtained by following the sequential assignment procedure outlined in ref *42*. Spectral analysis was performed with XEASY (*43*) and its PC version NEASY. The temperature for the experiments with SDS was chosen to be 50 °C, since signal intensities at lower temperatures were dissatisfactory, probably due to fast transverse relaxation brought about by high correlation times of the large micellar particles.

2. LTAB. The NMR sample with LTAB was prepared by adding LTAB-d_{25} to a final concentration of 1 M to a solution of 3.1 mM Novispirin in 20 mM phosphate buffer containing 80 mM NaCl and 3 mM NaN_3. The pH was brought to 5.7 by addition of 1 M H_3PO_4. The necessary concentration of LTAB had been determined by titrating a Novispirin sample

with LTAC until the amide protons of Novispirin showed a satisfactory chemical shift dispersion (see Results). A 2D NOESY spectrum with 70 ms mixing time was recorded with a WATERGATE water suppression (*40*). [^{1}H,^{1}H]-TOCSY spectra with 40 and 80 ms mixing time, respectively, were recorded using the clean-TOCSY sequence (*41*) with a 15 kHz spin-lock and a WATERGATE water suppression. In addition, a 2QF-COSY experiment was recorded.

NMR experiments with LTAB were conducted at 25 °C, since higher temperatures led to a loss of amide proton signals, presumably due to fast chemical exchange with the solvent.

Detergent−Peptide Interactions. To investigate interactions between detergent and peptide, 2D NOESY spectra were recorded on samples with nondeuterated SDS and LTAC, but otherwise identical conditions as for the structure determination. In these spectra, the third (and last) 90° pulse was replaced by an off-resonance Q5 pulse (*39*) of 3.14 ms duration selectively exciting a region from 6 to 9 ppm. This leaves the magnetization of water and detergent nuclei in a longitudinal state thus minimizing the signal obtained from them. The remaining water signal was further suppressed by a WATERGATE element.

H^N Exchange. For the experiments determining the H^N exchange, the pH of the sample in SDS-d_{25} used for the structure determination was brought up to pH 5.7, which did not cause large changes in chemical shift. The sample of Novispirin in LTAB-d_{25} was used as for the structure determination. [^{1}H,^{1}H]-TOCSY spectra with 75 ms mixing time were recorded using the clean-TOCSY sequence (*41*) with a 15 kHz spin-lock and a WATERGATE water suppression. The sample of Novispirin in SDS-d_{25} was measured at 50 °C, the sample of Novispirin in LTAB-d_{25} at 25 °C. As a control, an identical TOCSY spectrum was recorded on a sample of 2.5 mM Novispirin at pH 5.7 containing 80 mM NaCl and 3 mM NaN_3 but no detergent. The control spectrum was recorded at 50 °C.

Diffusion Measurements. All diffusion measurements were performed at 17 °C to minimize convection in the sample tube.

1. SDS. The diffusion constant of Novispirin in SDS was measured by the convection-compensated, double-stimulated echo sequence (*44*). A diffusion delay of 100 ms was employed. Sine-shaped gradient pulses of 10 ms duration and 16 different, linearly spaced, strengths ranging from 2.4 to 48 Gcm^{-1} were used. Unlike the case of LTAB-d_{25}, there is no strong protonated signal available from SDS-d_{25}. Therefore, a sample of Novispirin in 284 mM SDS-d_{25} and 16 mM SDS was prepared for these measurements. The regions from 3 to 3.2 ppm (Novispirin arginine $H^{\delta 2,3}$) and 1.0−1.4 ppm (SDS 3-11-CH_2 with a minor contribution of Novispirin isoleucine $H^{\gamma 12}$) were integrated at each gradient strength. The latter signal contains contributions from both SDS and Novispirin ($H^{\gamma 12}$ of Ile side chains). Under these conditions (284 mM SDS-d_{25} with a degree of deuteration of 98%, 16 mM SDS, and 2.5 mM Novispirin), assuming 18 SDS H-atoms (3-11-CH_2) and 5 novispirin atoms ($H^{\gamma 12}$ of Ile side chains) to have their resonance in this area, the total contribution of the ^{1}H on SDS to this signal is 97%, while the Novispirin signals only contribute with 3%.

2. LTAC. Diffusion constants of Novispirin in solutions with increasing amounts of LTAC were measured by the convection-compensated, double-stimulated echo sequence (*44*).

A diffusion delay of 200 ms was employed. Sine-shaped gradient pulses of 4 ms duration and 16 different, linearly spaced, strengths ranging from 2.4 to 48 Gcm^{-1} were used. The signals at 6.76 ppm (Novispirin Y17 $H^{\epsilon 1,2}$) and 3.05 ppm (LTAC N−$(CH_3)_3$) were integrated at each gradient strength. Diffusion constants were obtained from the fitting routine in XWinNMR2.6 and 3.6.

Probing Micelle Penetration with Paramagnetic Reagents. For the experiments with the paramagnetic reagents a [^{1}H,^{1}H]-TOCSY spectrum with 20 ms mixing time was recorded using the clean-TOCSY sequence (*41*) with a 15 kHz spin-lock immediately before the addition of $MnCl_2$ (to a concentration of 0.5 mM for the sample with SDS and 4 mM for the sample with LTAB) and subsequent recording of an identical [^{1}H,^{1}H]-TOCSY spectrum. The mixing time was chosen in order to maximize the intensity of the H^N/H^α cross-peaks. The sample of Novispirin in SDS-d_{25} was measured at 50 °C, the sample of Novispirin in LTAB-d_{25} at 25 °C. Identical rectangular regions were integrated in both spectra, and the integral ratios were determined. Thirty rectangular regions in empty parts of the spectra were integrated, and a standard deviation of the integrals was determined. This was assumed to be the error of the integration. The error of the ratio was determined from the errors of the single values as outlined in ref *45*.

1. Structure Calculation. NOE cross-peaks were identified, integrated, and assigned in the aforementioned NOESY spectra using the program XEASY (*43*) and the NEASY subroutine of CARA (*46*). Backbone torsion angle restraints were obtained from secondary chemical shifts using the program TALOS (*47*). TALOS-derived angle constraints were only accepted for residues, where all the 10 best database hits were situated within the same region of the Ramachandran plot. A deviation from the TALOS-derived value of ±30° was allowed. The CALIBA (*48*) subroutine in CYANA was used to convert cross-peak intensities from NOESY spectra into distance constraints. The CYANA subroutine FOUND (*49*) was used to add angle restraints. On the basis of this input, the structure was calculated using the torsion angle dynamics program CYANA (*50*). Structure calculations were started from 100 conformers with random torsion angle values. The 20 conformers with the lowest final CYANA target function values were embedded in a water shell of 8 Å thickness and energy-minimized against the AMBER force field (*51*) with the program OPALp (*52*).

No further refinement was performed. The structures were checked by PROCHECK_NMR (*53*).

Viscosity Measurements. LTAC micellar diffusion constants were calculated according to the following equation:

$$D_{\mathrm{mic}} = \frac{D_{\mathrm{observed}} - \frac{\mathrm{cmc}}{c} D_{\mathrm{monomer}}}{1 - \frac{\mathrm{cmc}}{c}} \qquad (3)$$

where D_{observed} is the measured diffusion constant of LTAC, D_{monomer} is the diffusion constant for monomeric LTAC, c is the concentration of LTAC, and cmc is the critical micelle concentration (13 mM). Diffusion constants are converted to hydrodynamic radii by help of the Stokes−Einstein

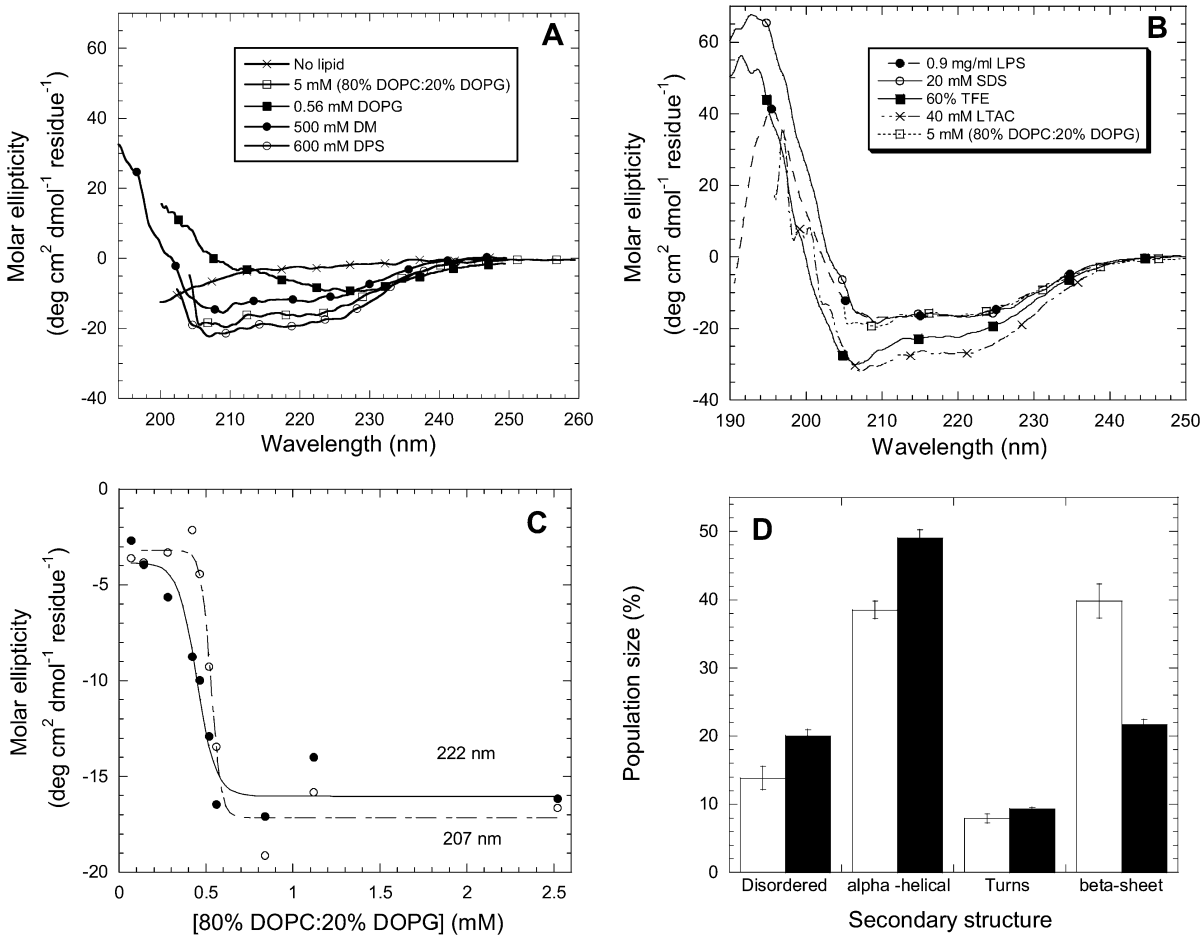

FIGURE 1: (A and B) Representative far-UV CD spectra of Novispirin in different amphiphilic environments. The spectrum in 80% DOPC/20% DOPG is shown in both spectra for ease of comparison. (C) Molar ellipticities of Novispirin at 222 and 207 nm as a function of the concentration of the lipid mixture 80% DOPC/20% DOPG. Data fitted to eq 1 (as shown in Table 2). (D) Secondary structure of the Novispirin aggregates formed in 1 mM DOPG (white columns) or 0.75 mM SDS (black column).

equation to account for changes in sample viscosity at different detergent concentrations:

$$R_h = \frac{kT}{6\pi\eta D} \quad (4)$$

where R_h is the hydrodynamic radius, k is the Boltzmann constant, T is the absolute temperature, η is the kinematic viscosity of the solution, and D is the diffusion constant.

The kinematic viscosity of aqueous solutions of LTAC (0 M ≤ [LTAC] ≤ 1 M) was determined by a Brookfield Digital Viscosimeter DV-II with a UL adapter. Over the interval 0−1 M, the viscosity of LTAC solutions could be fitted to a quadratic curve (data not shown):

$$\eta(c_{LTAC}) = 1.13 + 1.23c_{LTAC} + 1.04c_{LTAC}^2 \quad (5)$$

RESULTS

Importance of Electrostatic Interactions in Novispirin−Lipid Interactions. The first objective of this study was to compare the ability of lipids and detergents to induce the α-helical structure observed for Novispirin in TFE (*30*). This process is followed by far-UV CD spectroscopy. A representative overview of far-UV CD spectra of Novispirin in different amphiphiles and TFE is shown in Figure 1A,B. We start by determining optimal conditions for lipid interactions. In buffer alone, Novispirin only has a weak signal in the far-UV CD spectrum (Figure 1A), indicative of a very low degree of organized structure. Pure zwitterionic DOPC lipid vesicles do not lead to an appreciable increase in Novispirin structure. This is not surprising, as Novispirin has a net charge of +7 at pH 7.5 and would be expected to require negatively charged lipids to bind to vesicles. Nevertheless, vesicles with 10% DOPG do not alter the Novispirin structure compared to DOPC alone. However, this changes as we increase the fraction of anionic lipid. Vesicles containing 20−80% DOPG all show similar spectra with minima at 222 and 209 nm, which are typical of α-helical structure (cf. spectra shown in Figure 1A). There is a cooperative increase in CD signal between 0.5 and 1 mM lipid, after which it reaches a plateau level (shown in Figure 1C for the lipid mixture containing 80% DOPC and 20% DOPG and summarized in Table 1), corresponding to essentially 100% α-helix, according to the deconvolution program Continell (*54*). There is no isodichroic point (data not shown), suggesting that the transition involves more than two states. Thus, the signal changes at the two minima, 207 and 222 nm, though similar, do not coincide completely when plotted versus lipid concentration (Figure 1C). Note the cooperative nature of the transition.

In 100% DOPG, Novispirin forms visible aggregates and the corresponding CD spectrum is significantly altered

Table 1: Cooperative Unfolding Parameters for Novispirin in Different Environments

amphiphile	concentration units	wavelength (nm)	c^a	$L_{50\%}{}^b$
20% DOPC, 80% DOPG	mM	207	15.5 ± 4.9	0.53 ± 0.01
20% DOPC, 80% DOPG	mM	222	8.0 ± 3.2	0.45 ± 0.02
TFE	% (v/v)	222	0.12 ± 0.04	16.6 ± 1.5
TFE	% (v/v)	207	0.13 ± 0.06	17.7 ± 0.4
TFE	% (v/v)	190	0.11 ± 0.04	18.0 ± 060
SDS	mM	222	1.33 ± 0.36	0.98 ± 0.09
SDS	mM	207	4.8 ± 4.3	1.94 ± 0.09
SDS	mM	190	0.68 ± 0.25	1.31 ± 0.17

[a] The cooperativity constant (eq 2). The lower *c* is, the more gradual the transition. [b] The concentration at which the binding transition is halfway to completion (eq 2).

(Figure 1A). This structural change already occurs at low DOPG concentrations, after which no further change is seen (data not shown). Due to light-scattering artifacts, CD is not appropriate to analyze protein aggregates. However, an analysis of the aggregated state by FTIR shows that the α-helix content is reduced to around 50% with a compensating rise in *β*-sheet and turns (Figure 1D). FTIR analysis of Novispirin in solution with SDS shows very little or no *β*-structure (data not shown). Interestingly, the CD spectrum in DOPG is very similar to that of Novispirin in *E. coli* total lipid extract, which contains around 60% PE lipids and 18% PG lipids (data not shown). PE lipids do not appear to play a large role in this structure-induction, since synthetic DOPC lipids containing 10−20% DOPE showed no increase in Novispirin structure compared to pure DOPC (data not shown).

The strong effect of including DOPG clearly indicates electrostatic interactions between Novispirin and lipids. This is confirmed by the screening effect of high ionic strength. In 200 mM NaCl, lipids containing 20% DOPG are unable to induce α-helical structure in Novispirin, whose far-UV CD spectrum under these conditions is identical to that in buffer (data not shown).

Different Modes of Binding of Novispirin to LPS and TFE. Previously, it has been shown that components of the cell wall of Gram-negative and Gram-positive bacteria, namely, lipopolysaccharides from *Pseudomonas aeruginosa* and lipoteichoic acid from *Staphylococcus aureus*, respectively, are able to induce α-helical structure in Novispirin at 1 mg/mL (*30*). However, it is not clear whether this concentration is sufficient to saturate the level of helicity. A more quantitative analysis of the interaction using 0−0.9 mg/mL LPS from *E. coli* EH100 (spectrum shown in Figure 1B) leads to an isodichroic point around 203 nm, suggesting a simple two-state binding-and-folding model (data not shown). Fitting the data to this model using three different wavelengths (eq 1 and Figure 2A) leads to an apparent K_d of 0.7−1.1 mg/mL, indicating that the structural transition is around 60% complete at 1 mg/mL (Table 2). The cmc of LPS is in the low *μ*g/mL range (*55*), indicating that the interactions with Novispirin only involve LPS micelles. It is noteworthy that the affinity of LPS for Novispirin is comparable to that of DOPC/DOPG vesicles; in both cases, the transition nears completion around 1 mg/mL LPS or lipid.

For similar quantitative reasons, we titrated Novispirin with TFE. TFE (33−40%) has been shown to be sufficient to lead to α-helix formation in Novispirin (*30*). The spectra between 0 and 60% TFE reveal a very clear isodichroic point around 202 nm (data not shown; spectrum in 60% TFE shown in Figure 1B) with a cooperative change in the CD signal at different wavelengths (Figure 2B). A plateau is reached around 30% TFE with a midpoint around 16−18% (Table 1), indicating that 33−40% TFE is an appropriate condition for analyzing the NMR structure of Novispirin.

Effect of SDS on Novispirin. The interaction of Novispirin with detergents is interesting, since these substances are lipid-mimetic but more amenable to studies by NMR. Of these, SDS is particularly appropriate due to its well-documented ability to induce α-helical structure. SDS also induces clear α-helical structure in Novispirin in the low millimolar range (Figure 1B). While the 190 and 222 nm data reveal a cooperative transition which can be fitted to eq 2, the data at 207 nm can be divided into three regions, namely, a plateau around 0−0.5 mM, followed by a rather abrupt jump to another plateau between 0.5 and 1.4 mM SDS, leading via a broader transition to a plateau above ca. 2.4 mM (Figure 2C). The midpoint of around 1 mM is only about twice as high as for the vesicles with the highest affinity for Novispirin, namely, 20% DOPC and 80% DOPG (Table 1). Since the cmc of SDS is 2.4 mM under our buffer conditions (20 mM NaP, pH 7.5), SDS is predominantly monomeric in all these regions. There is visible precipitation in the plateau region between 0.5 and 1.4 mM SDS (where the [SDS]/[Novispirin] goes from 12 to 35), confirmed in Figure 2D where it was possible to spin down most of the protein in this detergent range. An FTIR analysis revealed that the α-helix content had decreased to around 40% together with a similar amount of *β*-sheet as well as some turns and disordered structure (Figure 1D). This contrasts with an α-helical content close to 100% at higher SDS concentrations where Novispirin is soluble.

Unlike the case for lipids, the interaction between Novispirin and SDS must involve hydrophobic as well as electrostatic interactions, since addition of up to 500 mM NaCl had no significant effect (data not shown).

Neutral and Zwitterionic Detergents Induce Structure at Higher Concentrations. Interestingly, the neutral detergent dodecyl maltoside as well as the zwitterionic detergent DPS (3-(dodecyldimethylammonio)propane sulfonate) induce α-helical structure, although this requires much higher detergent concentrations than SDS. Both detergents show dichroic points around 204 nm (data not shown; representative spectra shown in Figure 1A), and the solutions show no visible precipitation. Data follow a hyperbolic binding curve with a midpoint around 140−210 nm (DM, Figure 3A) or 82−120 mM (DPS, Figure 3B), which is around 100−200 times as high as for SDS, as well as being high above the cmc of these detergents (0.17 and 4 mM for DM and DPS, respectively).

Ability of LTAC To Induce Structure in Novispirin and Role of Electrostatics. Remarkably, the cationic detergent LTAC clearly induces α-helical structure in Novispirin (Figure 1B), even under conditions where there is a high positive charge on the peptide. At pH 7.5 (overall charge: ca. +7), salt reduces the binding and α-helical folding of Novispirin, but at pH 11 (overall charge ca. +2), salt does not have any significant effect. Helix formation occurs earlier in the presence of salt at pH 11, but this partly reflects NaCl's

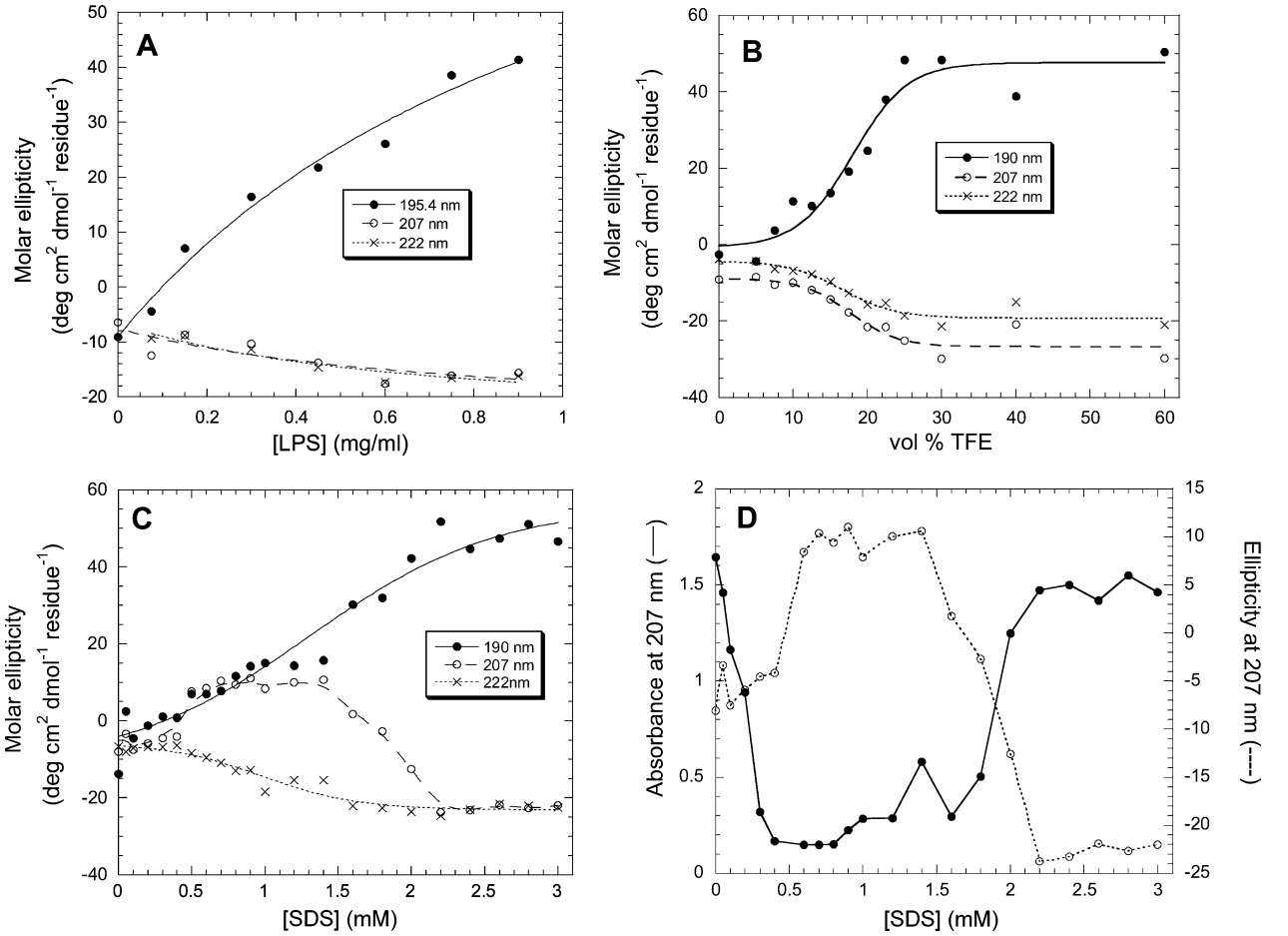

FIGURE 2: (A) Molar ellipticity of 40 μM Novispirin as a function of lipopolysaccharide from *E. coli*. Data fitted to eq 1 (results in Table 3). (B) Molar ellipticity of 40 μM Novispirin as a function of TFE. Data fitted to eq 2. (C) Molar ellipticity of 40 μM Novispirin as a function of SDS. Data for 190 and 222 nm are fitted to eq 2, while data at 207 nm are joined up for clarity. Data are restricted to 0−3 mM for clarity; there are no further transitions beyond 3 mM SDS. Increasing the Novispirin concentration to 400 and 1140 μM leads qualitatively to the same transitions, although the spectral changes occur later at higher SDS concentrations. (D) Solubility of 40 μM Novispirin as a function of SDS concentration. Novispirin was incubated at different SDS concentrations and centrifuged, and the absorbance (joined lines) and ellipticity at 207 nm (stippled lines) of the supernatant were measured.

Table 2: K_d Values for Binding of Novispirin to Detergents Showing Hyperbolic Unfolding Curves[a]

wavelength	LPS (mg/mL)	DM (mM)	DPS (mM)
222	0.67 ± 0.94	190 ± 50	120 ± 20
207	0.80 ± 0.90	210 ± 160	110 ± 25
190 (195.4)	1.15 ± 0.60	140 ± 30	82 ± 22

[a] K_d is defined in eq 1.

reduction of LTAC's cmc due to its ability to reduce electrostatic repulsion between headgroups (Figure 3C, Table 3). As seen for the zwitterionic and nonionic detergents, there is a dichroic point and no precipitation (data not shown).

NMR Assignment and Structure Calculation. A comparison of the far-UV CD spectra of Novispirin in different detergents and solvents reveals that, although the same overall helical structure is observed, there are subtle changes in the distribution of minima (Figure 1B). The spectra in SDS, LPS, and lipid fall in one class, whereas those in LTAC and TFE fall into their own separate classes. Since only the structure of Novispirin in TFE is known in any detail, we have determined the structure of Novispirin in deuterated SDS and LTAB to analyze the effect of detergents on Novispirin structure in more detail. Note that LTAB was only used for NMR experiments that require deuterated detergents, due to the availability of the deuterated form; for all other experiments, LTAC was used because of the prohibitively high absorption of LTAB in the far-UV area.

The concentration of LTAC necessary for helix formation strongly depends on the pH. The presence or absence of secondary structure can be assessed from the H^N region of a ^{1}H NMR spectrum. A high dispersion of chemical shifts as found in the spectrum of Novispirin in 1030 mM LTAC at pH 5.7 (Figure 4) is indicative of the presence of secondary structure, while a low dispersion of chemical shifts as found in the spectrum of Novispirin at pH 5.7 in the absence of LTAC (Figure 4) points at a random-coil structure. The NMR spectrum of Novispirin in 270 mM LTAC at pH 7.5 clearly indicates the presence of secondary structure. This structure is lost upon titration toward the acidic range (Figure 4 and CD, data not shown). This loss of secondary structure can, however, be reversed by adding larger quantities of LTAC (Figure 3C and Figure 4). We therefore chose pH 5.7 and 1030 mM LTAB-d_{25} as suitable conditions for determining Novispirin's structure by NMR.

In SDS, Novispirin retains the same helix-rich CD signal down to pH 3 unaltered (data not shown). NMR analysis

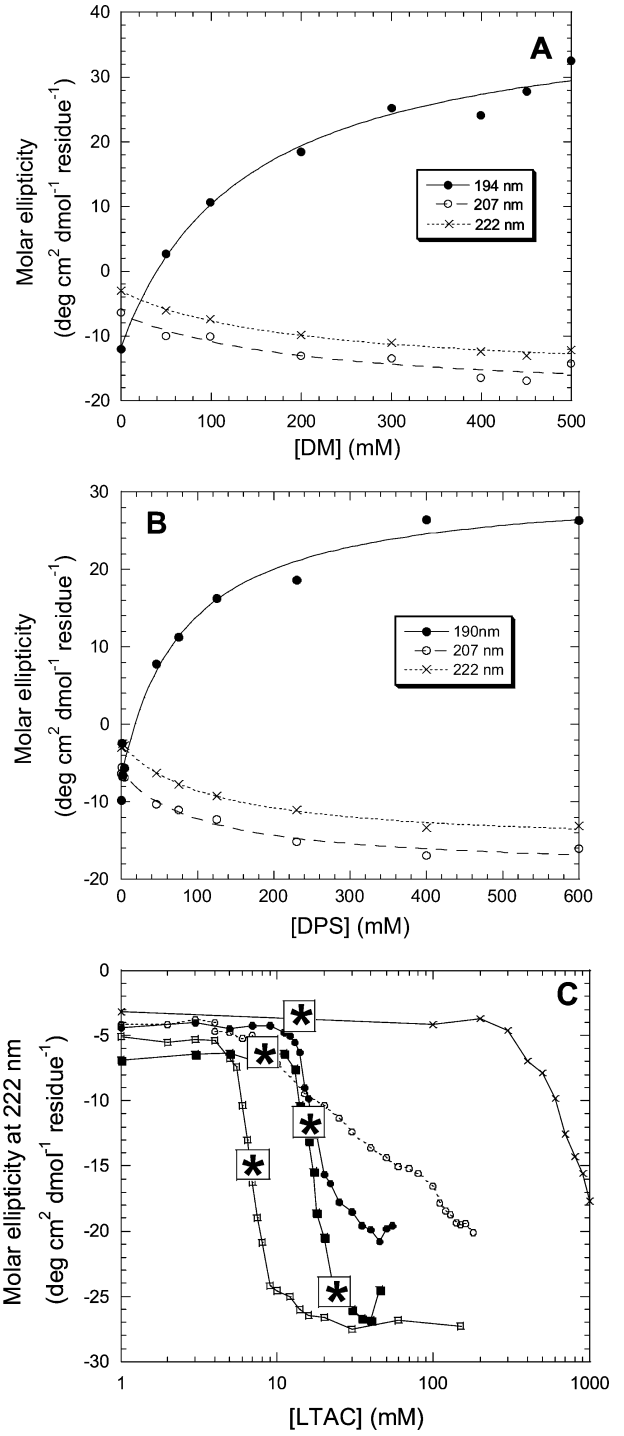

FIGURE 3: (A) Molar ellipticity of Novispirin as a function of DM. Data fitted to eq 1. (B) Molar ellipticity of Novispirin as a function of DPS. Data fitted to eq 1. (C) Titration of Novispirin with LTAC under different conditions: pH 5.7, 0 mM NaCl (×); pH 7.5, 0 mM NaCl (●); pH 7.5, 200 mM NaCl (○); pH 11, 0 mM NaCl (■); pH 11, 200 mM NaCl (□). Asterisks indicate cmc of LTAC under the various experimental conditions. Note the logarithmic scale.

was carried out at pH 4.7. The ^{1}H atoms of Novispirin in SDS could be assigned with the following exceptions: K1 (all protons), N2 H^N, K9, K15, and K16 side-chain atoms (H^β,H^γ,H^δ,H^ϵ,H^ζ). All lysine signals were extremely weak; some lysine side-chain signals could be found but not unambiguously assigned. A set of 20 structures was calculated. Table 4 lists some quality criteria for the structure. The structure shows two well-defined helical regions, whose orientation toward each other was not defined (see Figure 5A). The first helix stretches approximately from residue 2 to 9, the second helix from residue 12 to 17. Residues 10 and 11 form a hinge. From the sequence plot (Figure 6A), it can be seen that helix 1 is well-defined with many $d_{\alpha N(i,i+3)}$

Table 3: Interactions between Novispirin and LTAC at Different pH Values and Ionic Strengths

pH	[NaCl] (mM)	CMC [mM]	C^a	$L_{50\%}{}^a$ (mM)	$[\theta]_{end}$ (deg cm^2 dmol^{-1} residue^{-1})
5.7	0	14.3	—[b]	—[b]	—[b]
7.5	0	16.8	0.17 ± 0.02	17.3 ± 0.3	−19.5 ± 0.3
7.5	200	8.4	(low)	40.5 ± 4	−23.5 ± 0.5
11	0	23	0.20 ± 0.02	17.3 ± 0.2	−25.8 ± 0.3
11	200	7	0.49 ± 0.03	7.0 ± 0.07	−26.4 ± 0.2

[a] Defined in legend to Table 1 and eq 2. [b] Transition not complete.

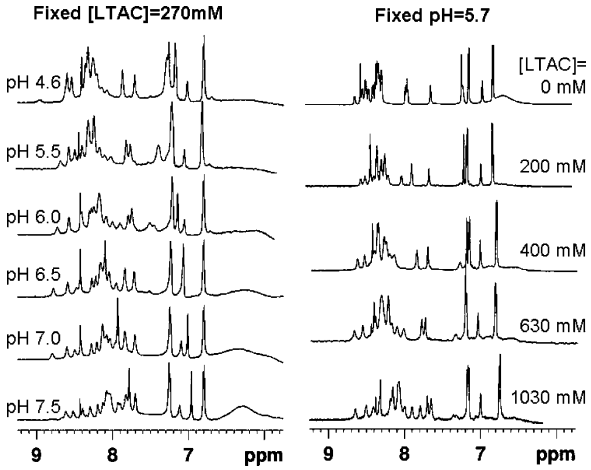

FIGURE 4: H^N/aromatic region of the ^{1}H NMR spectrum of Novispirin. Left panel: constant 270 mM of LTAC, decreasing pH. Right panel: constant pH 5.7, increasing concentrations of LTAC. The spectra were obtained using excitation-sculpting water suppression (*38*) and a selective Q5 pulse of 3.14 ms duration exciting only the region from 6 to 9 ppm.

Table 4: Quality Criteria for the Calculated Novispirin Structures

detergent	SDS	LTAB
number of distance constraints	168	131
- of which intraresidual	96	77
- of which sequential	37	35
- of which medium-range ($2 \le \Delta_{res} \le 4$)	35	19
number of angle constraints[a]	20	18
- of which ϕ	10	9
ψ	10	9
CYANA residual target function	1.0 ± 0.05 Å^2	0.11 ± 0.02 Å^2
distance restraints violated by more than 0.2 Å[b]	0	0
angle restraints violated by more than 5°[b]	0	0
backbone rmsd values residues 2−9[c]	0.66 ± 0.25	0.30 ± 0.09
backbone rmsd values residues 12−17[c]	0.37 ± 0.12	0.23 ± 0.14
Ramachandran plot[d]		
% of residues in most favored regions	78.3%	76%
% of residues in less favored regions	20.3%	22.5%
% of residues in generously allowed regions	1.4%	—
% of residues in disallowed regions	—	1.5%

[a] Only those derived by TALOS (*47*). [b] Per molecule. [c] As calculated by MOLMOL (*64*) from the pairwise rmsd values of each of the 20 structures against a mean structure. [d] As calculated by PROCHECK_NMR (*53*) excluding Gly residues.

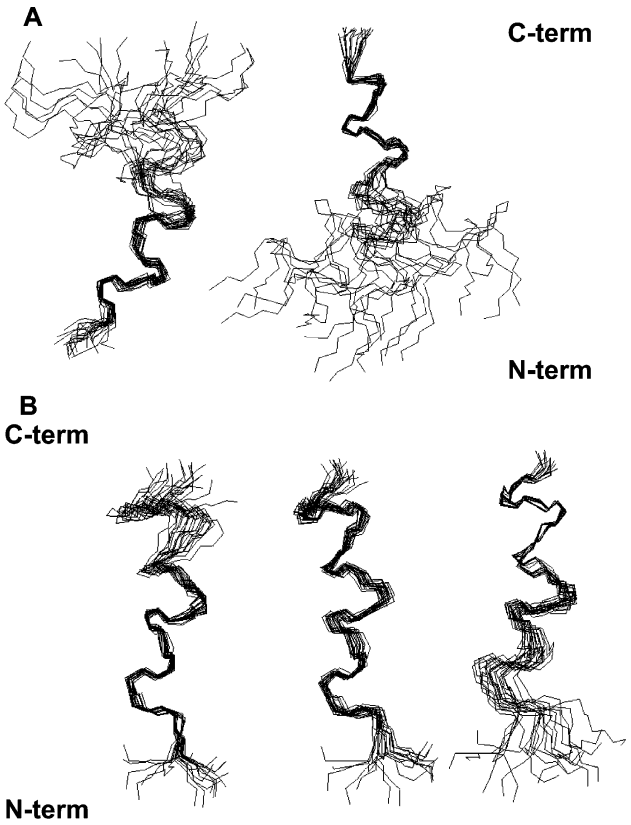

FIGURE 5: Structure of Novispirin in the presence of (A) SDS and (B) LTAB. The aligned bundle of the 20 structures with the lowest residual target function is shown. In the left panel, N, C, and C^{α} atoms of residues 2−9 are aligned; in the right panel, N, C, and C^{α} atoms of residues 12−17 are aligned. In the case of LTAB, a central panel with an alignment of N, C, and C^{α} atoms of residues 2−17 (i.e., the combination of the helical two regions) is also included.

FIGURE 6: Sequence plot of Novispirin NMR data (A) for Novispirin in SDS at 50 °C and (B) for Novispirin in LTAB at 25 °C. The sequential NOE connectivities $d_{\alpha N}$, d_{NN}, and $d_{\beta N}$ are indicated with black bars of a thickness that corresponds to the strength of the NOEs. The medium range connectivities $d_{\alpha N}(i,i+3)$ and $d_{\alpha\beta}(i,i+3)$ are shown by lines starting and ending at the positions of the residues related by the NOE. Residues whose ϕ and ψ angles were constrained based on output from TALOS are underlined. The line CSI gives the chemical shift index. A "+" indicates that the chemical shift of the H^{α} is larger than the random-coil chemical shift +0.1 ppm; a "-" indicates a H^{α} chemical shift lower than the random-coil chemical shift −0.1 ppm. A "0" indicates a shift that is within 0.1 ppm from the random-coil value. Random-coil values were taken from ref *40*.

cross-peaks, whereas helix 2 is only defined by relatively few cross-peaks. However, in addition to those shown in the sequence plot, there are interactions between the aromatic ring protons of Tyr 17 and the side chain of Ile 14. This is also reflected in atypical chemical shifts of the side-chain protons of Ile 14. The helicity of these regions is also corroborated by strong sequential H^N-H^N NOEs. At present, we are unable to decide whether the lack of structural information around residue 12 actually reflects mobility or is caused by an artifact (e.g., lack of NMR signals in this region).

In LTAB, the ^{1}H atoms of Novispirin could be assigned with the following exceptions: K1 (all protons) and N2 H^N. Quality criteria are listed in Table 4. As in SDS micelles, the structure shows 2 helical stretches, but in contrast to the structure in SDS, the kink between the two helices is well-defined and the whole structure (Figure 5B) can be aligned simultaneously. The sequence plot (Figure 6B) clearly shows the presence of two helical stretches.

Micelle Penetration Investigated by Paramagnetic Reagents. In addition to obtaining the structure of Novispirin, it is of interest to investigate to which extent the peptide is buried in the micellar environment or exposed to the surroundings. We have used four complementary techniques to obtain more information on this, namely, quenching of signals by paramagnetic reagents, NOEs between peptide and detergent, PFG-diffusion measurements, and finally H^N exchange.

Table 5: NOESY Cross-Peaks Found between SDS and Novispirin[a]

	SDS-atom				
Novispirin	1-CH_2	2-CH_2	3-CH_2	4−11-CH_2	12-CH_3
R4/R5[b] H^{ϵ}		?		x	
R8 H^{ϵ}		?	x	x	
H12 $H^{\delta 2}$		?	x	x	
H12 $H^{\epsilon 1}$		?		x	
Y17 $H^{\delta 1,2}$			x	x	
Y17 $H^{\epsilon 1,2}$		x	?	x	

[a] Peaks are denoted with an "x". A "?" denotes cases where neither the absence nor the presence of the peak can be proven unambiguously because of spectral overlap with other cross-peaks. [b] The H^{ϵ} of R4 and R5 have the same chemical shift; the cross-peak can, therefore, not be assigned to only one of the two atoms.

Paramagnetic reagents such as Mn^{2+} are useful probes of the solvent-accessibility of different parts of a protein or peptide (*56*). When Mn^{2+} ions come into close proximity with protons, their nuclear magnetic relaxation will be enhanced, leading to signal broadening.

1. SDS. Upon addition of 500 μM $MnCl_2$, several signals of Novispirin were weakened or vanished altogether, whereas others were affected much less. Table 5 and Figure 7 show the results of these experiments. Because of electrostatic interactions, it is assumed that most of the Mn^{2+} is localized on the negatively charged surface of the SDS micelles. The presence of Mn^{2+} ions has only little effect on resonances

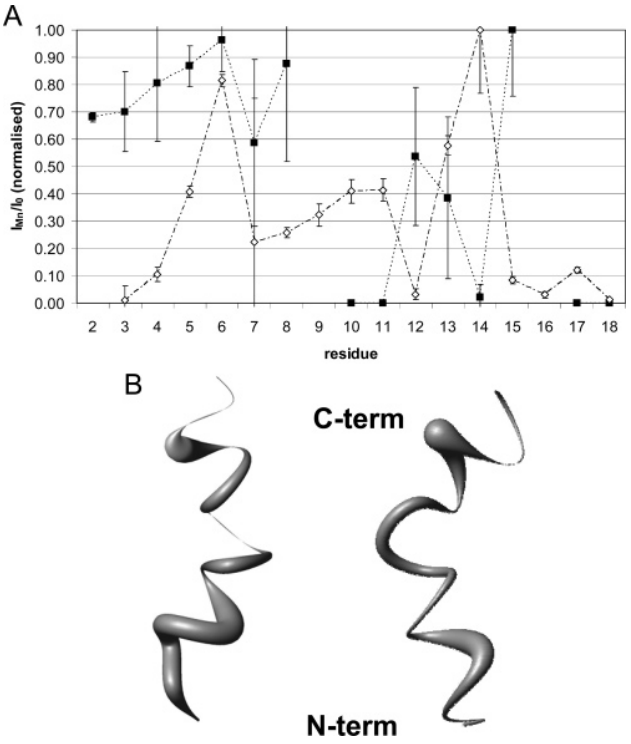

FIGURE 7: (A) Influence of paramagnetic Mn^{2+} ions on relative signal intensity of Novispirin in SDS at 50 °C (closed squares) and LTAB at 25 °C (open diamonds). The top graph shows I_{Mn}/I_0 plotted vs the peptide sequence, where I_{Mn} is the signal intensity in a clean-TOCSY spectrum (*41*) of 20 ms mixing time with a 15 kHz spin-lock and a WATERGATE water suppression (*40*) after addition of 0.5 mM Mn^{2+}, and I_0 is the signal intensity before addition of Mn^{2+}. The highest ratio occurring in each of the samples was normalized to 1, since no comparisons of absolute signal intensity between two different samples could be made. In general, signal intensity ratios are far weaker for LTAB than for SDS. (B) Visualization of the data using the structures for Novispirin in SDS (left) and LTAC (right). The backbone is represented by a spline function, whose radius is proportional to the I_{Mn}/I_0 value plotted in the top graph. The thinner the curve, the more this individual residue is influenced by Mn^{2+} ions.

of residues 2−6 and 8 forming the first helix. A medium effect on residue 7 could be observed. Data on residue 9 have been omitted due to a standard error of more than 100%. Resonances from residues 10 and 11 have disappeared completely, and a moderate effect of the Mn^{2+} ions on residues 12 and 13 can be observed. The resonance of residue 14 has vanished, while that of residue 15 is not affected at all. No data can be obtained on residue 16, and the resonances of the last two residues, 17 and 18, vanish upon addition of Mn^{2+}.

2. LTAB. Upon addition of 4 mM $MnCl_2$, most Novispirin signals diminished or vanished altogether. The fact that a much larger Mn^{2+} concentration was needed to observe an effect compared to SDS micelles is ascribed to the charge of the micellar surface that attracts Mn^{2+} ions in the case of SDS but repels them in the case of LTAB. The data are presented in Table 5 and Figure 7. The only H^N/H^α signals remaining are those of the hydrophobic residues Ile 6, Ile 13, and Ile 14. The signals of the aromatic protons of Tyr 17 remain visible, although its H^N/H^α cross-peak does not.

NOEs between Detergent and Novispirin Molecules. 1. SDS. The 2D-selective NOESY spectrum revealed several cross-peaks from Novispirin side-chain atoms to SDS atoms. The found cross-peaks are summarized in Table 5. No cross-peaks were found from backbone H^N atoms of Novispirin to SDS atoms. Because of severe spectral overlap, only side-chain atoms with a chemical shift >5.5 ppm could be investigated. Neither the presence nor the absence of NOEs between other side-chain atoms, notably Ile and Leu methyl groups, and SDS can be proven. In addition to the cross-peaks given in Table 5, a number of cross-peaks were found that could not be assigned to any peptide atom. They could possibly belong to Lys H^ζ atoms, but as none of them are assigned, this cannot be confirmed.

2. LTAC. No NOEs between any Novispirin atom with a chemical shift >5.5 ppm and LTAC atoms could be detected. NOEs between other Novispirin side-chain atoms and LTAC cannot be ruled out, but they cannot be observed due to spectral overlap.

H^N Exchange in SDS and LTAB. Figure 8 shows the H^N/H^α regions of TOCSY spectra with 75 ms mixing time obtained from Novispirin in SDS, in LTAB, and in the absence of detergents, all at pH 5.7. Although Novispirin in SDS was measured at 50 °C while Novispirin in LTAB was measured at 25 °C, there are numerous H^N/H_2O exchange peaks in the LTAB solution and only a few in the SDS solution. The latter can be attributed to exchangeable arginine side-chain atoms, while not a single H^N exhibits exchange. In LTAB, there is more exchange—only Ile 6, Ile 13, Ile 14, Lys 16, Tyr 17, and Gly 18 H^N definitely do not yield an exchange peak. A control experiment with Novispirin at pH 5.7 and 50 °C in the absence of detergent showed strong backbone H^N exchange. The F2-rows of the TOCSY spectra are shown along with the 1D NMR spectra to demonstrate that the cross-peaks originate from chemical exchange and not from a combination of F1-ridges and insufficient water suppression. Weak examples for the latter can be seen but are having opposite sign to the "true" exchange peaks in the spectra of Novispirin in both detergents.

Novispirin−Micelle Association Probed by PFG Diffusion Experiments. The results of the previous three techniques make it reasonable to infer that Novispirin, at least in part, is buried in the SDS micelle, whereas it is questionable whether Novispirin is at all associated with LTAC micelles (see Discussion). Measurement of the diffusion constant for Novispirin could provide more insight. In the case of SDS, diffusion constants obtained from Novispirin and SDS are equal within the accuracy of the measurement. Under the conditions mentioned above, the diffusion constant for both Novispirin and SDS is 0.11×10^{-10} m^2 s^{-1}, where free Novispirin in water diffuses with 1.75×10^{-10} m^2 s^{-1}. The contribution of monomeric SDS to the measured diffusion constants is negligible at the high salt concentrations used. The diffusion constants obtained from Novispirin and LTAC with increasing amounts of LTAC present are given in Table 6. They show that the diffusion constant of Novispirin drops with increasing LTAC concentration. This is converted to hydrodynamic radius using the Stokes−Einstein equation (eq 4), which also takes into account changes in the viscosity of the solution with increasing LTAC concentration (see Materials and Methods). Diffusion constants of LTAC micelles are higher than those of SDS micelles, which is in agreement with the fact that SDS micelles are larger than LTAC micelles (*57*).

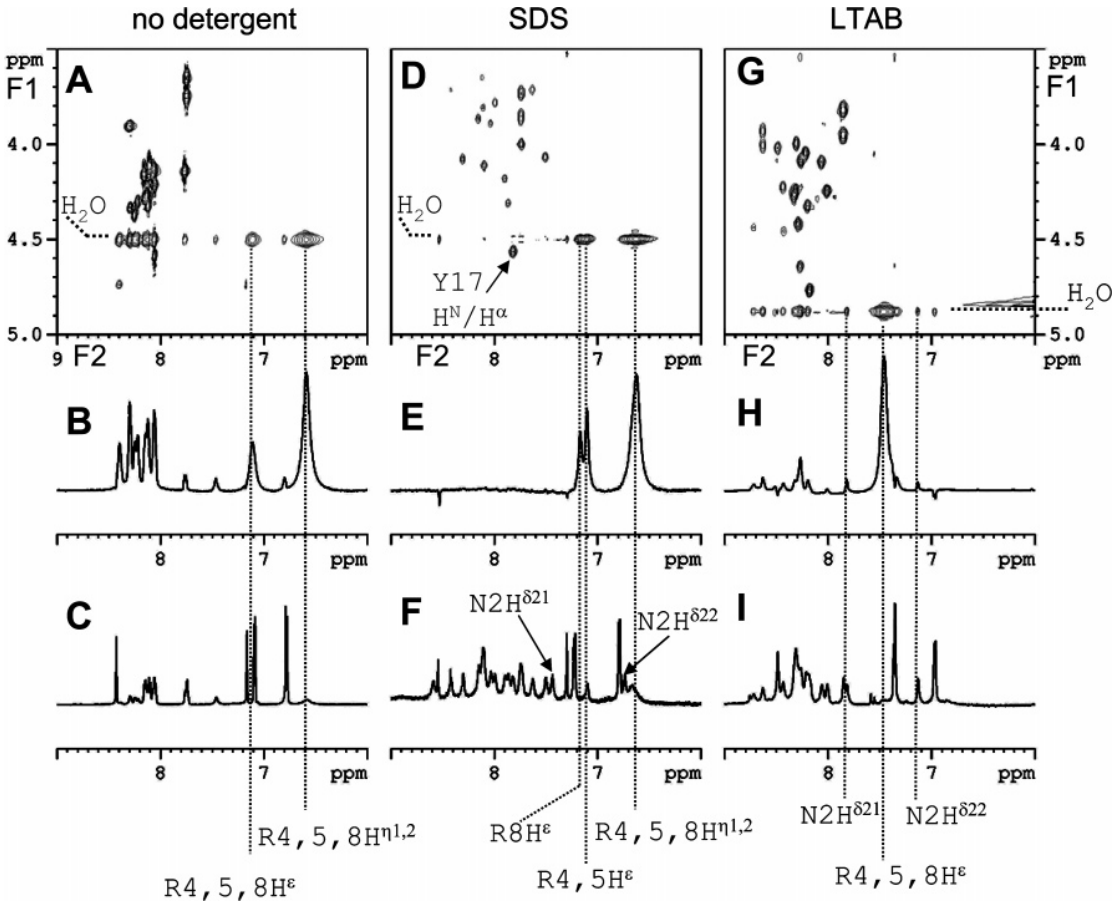

FIGURE 8: H^N/H^α regions of TOCSY spectra with 75 ms mixing time of Novispirin in (A) the absence of detergent, (D) SDS, and (G) LTAB micelles. The spectra were recorded using the clean-TOCSY sequence (*41*) with a 15 kHz spin-lock and a WATERGATE water suppression (*40*) with selective pulses. The chemical shift of water is 4.76 ppm in the spectrum of Novispirin in LTAB (recorded at 25 °C) and 4.50 ppm in the spectra recorded in the presence of SDS and in the absence of detergents (recorded at 50 °C), respectively. The F2-rows of the TOCSY spectrum at the chemical shift of water are presented (B) in the absence of detergent, (E) in SDS micelles, and (H) in LTAB micelles. The bottom line shows 1D NMR spectra recorded using excitation-sculpting water suppression (*38*) and selective excitation of the region from 6 to 9 ppm by an off-resonance Q5 pulse (*39*) of 3.14 ms duration. Spectrum C is from Novispirin in the absence of detergents, spectrum F from Novispirin in SDS, and spectrum I from Novispirin in LTAB.

The hydrodynamic radii of LTAC and Novispirin versus LTAC concentration are plotted in Figure 9. The data show that the apparent hydrodynamic radius of Novispirin remains essentially unchanged up to approximately 630 mM, after which it begins to increase. This is in contrast to the NMR spectra measured at different concentrations of LTAC (Figure 4) which already show signs of chemical shift dispersion of H^N atoms, pointing at the formation of stable secondary structure elements at LTAC concentrations as low as 200 mM. We interpret the data as a sign of beginning secondary structure formation, as detergent concentrations increase, maybe aided by transient interactions with the LTAC micelles. However, the association/dissociation equilibrium at low LTAC concentrations is still shifted toward the free form of Novispirin.

DISCUSSION

In the present work, we have investigated the influence of different detergents and lipids as well as TFE on the secondary structure of Novispirin G-10. For two detergents, SDS and LTAB, we have determined the structures of the peptide by solution-state NMR and obtained information on how the peptide is oriented relative to the detergent micelle.

Different Binding Modes of Novispirin. The titration of Novispirin with different additives clearly follows different binding modes. For lipids, TFE, SDS, and LTAC, there is a cooperative transition, while LPS and the detergents DM and DPS elicit a hyperbolic binding curve. Hyperbolic binding occurs well above the cmc of the detergents in all three cases, suggesting a simple equilibrium between free and micelle-bound peptide. TFE's cooperative transition is a simple consequence of a linear relationship between the free energy of folding and TFE concentration (*31*), similar to that seen for denaturants (*58*). In the case of SDS, the cooperative binding is completed below bulk cmc, and this indicates that SDS monomers must cluster at the Novispirin surface. When a cluster of sufficient density has formed, it presumably generates enough anionic surface area to contact other Novispirin molecules (see below). For LTAC, the cooperative transition overlaps with the cmc under all conditions tested, suggesting that monomers may cluster to a small extent on Novispirin but are superseded by micelles above the cmc. This confirms that a supramolecular structure is required to overcome the electrostatic repulsions between positive side chains and the cationic headgroup of LTAC. The cooperative nature of Novispirin structure formation as a function of lipid

Table 6: Diffusion of Novispirin (c = 2.5 mM) in LTAC, pH 5.7

c_{LTAC}[a] (mM)	η[b] (mPa s)	$D_{obs,novi}$[c] (10^{-10} m^2 s^{-1})	$D_{obs,LTAC}$[d] (10^{-10} m^2 s^{-1})	R_h[e] Novispirin (nm)	R_h LTAC[f] micelles (nm)
0	1.13	1.75		1.10	
18	1.15	1.84	3.20	1.03	
97	1.26	1.65	1.39	1.05	1.46
174	1.37	1.47	1.13	1.08	1.54
247	1.50	1.32	0.99	1.10	1.56
322	1.63	1.33	0.89	1.00	1.57
395	1.78	1.19	0.80	1.04	1.57
478	1.96	1.09	0.74	1.03	1.53
575	2.18	0.94	0.66	1.07	1.53
639	2.34	0.87	0.60	1.07	1.56
711	2.53	0.71	0.55	1.22	1.59
798	2.78	0.60	0.44	1.31	1.80
880	3.02	0.55	0.41	1.31	1.75
1000	3.40	0.46	0.37	1.40	1.74

[a] Concentration of LTAC in millimoles per liter. [b] Viscosity of LTAC solution as calculated from eq 3. [c] Observed Novispirin diffusion constant. [d] Observed LTAC diffusion constant. [e] Hydrodynamic radius of Novispirin calculated from the Stokes−Einstein equation. [f] Hydrodynamic radius of LTAC micelles calculated from the Stokes−Einstein equation separating the contribution of the monomeric LTAC and the micellar LTAC by eq 4.

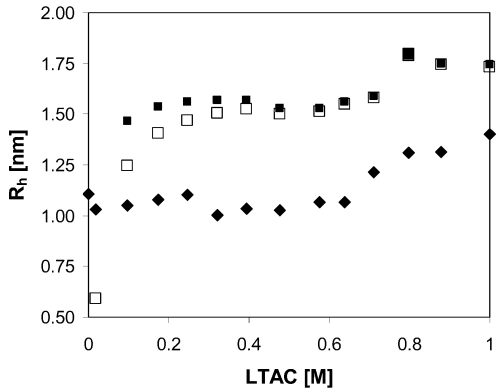

FIGURE 9: Hydrodynamic radii of Novispirin (filled diamonds) and LTAC micelles (filled squares) calculated from the diffusion constants by applying the Stokes−Einstein equation versus the concentration of LTAC. Open squares indicate the apparent hydrodynamic radius for LTAC, which is a population-weighted average of monomeric and micellar form.

concentration is less straightforward to explain, since the amount of peptide is not limiting for Novispirin oligomer formation at the vesicle surface at low-lipid concentrations. We can only speculate that extensive coating of the vesicle surface with Novispirin at very low-lipid concentrations can actually block structural transitions for steric reasons.

The Aggregated State: An Alternative to the Random-Coil and α-Helix. Pure DOPG leads to the formation of water-insoluble, β-sheet-rich aggregates with Novispirin. The same happens with SDS at certain protein/detergent ratios, although the Novispirin−SDS precipitate can be redissolved by adding more detergent. Variations in the amount of secondary structure in DOPG and SDS can be ascribed to differences in the concentrations of detergent versus lipid. LPS, however, which contains a small number of negative charges distributed in a matrix of neutral saccharides, is able to induce structure in its pure form at very low concentrations without forming precipitates to the same extent (although there may be a small amount of aggregation around 0.075 mM LPS, as the CD spectrum at this concentration does not cross the isodichroic point, unlike all other LPS concentrations). Thus, the ability to form aggregates is most likely promoted by electrostatically complementary "sandwich" structures between positively charged Novispirin and negatively charged lipids/detergents. For SDS, this is only possible at relatively low concentrations; at higher SDS concentrations, Novispirin becomes diluted out by SDS molecules, and SDS micelles form, which by themselves are solubilizing due to their high concentration of negative charge. Because of the high degree of light-scattering of DOPG vesicles, we were unable to determine whether higher concentrations of DOPG likewise lead to Novispirin solubilization and α-helix formation.

The aggregation phenomenon is unlikely to have biological significance, since uniformly anionic vesicles do not occur in nature. Nevertheless, it demonstrates that amphiphilic molecules not only necessarily just induce α-helical structure when bound to proteins but also allow them to access other conformational states, depending on the ratio between protein/peptide and amphiphile. SDS at submicellar concentrations has been shown to stimulate fibrillation of proteins (*59*, *60*), and anionic lipid vesicles stimulate the fibrillation of globular proteins and peptides, which at sufficiently high concentrations can even take up and incorporate the lipid in the fibril structures (*61*, *62*).

Novispirin Shows a Versatile Ability To Form Helical Structure in Detergents. Novispirin is able to form regular secondary structures in both anionic, zwitterionic, nonionic, and cationic detergents and phospholipids. The formation of secondary structure proceeds readily if the amphiphilic compounds are negatively charged. Both anionic detergents as SDS and anionic lipids as DOPG can induce secondary structure formation at relatively low concentrations; the latter however only if "diluted" by the zwitterionic DOPC.

The affinity of Novispirin toward negatively charged surfaces is not surprising, since Novispirin at pH 7.5 carries eight positive charges opposed by only one negative charge. Interestingly, Novispirin needs at least 20−40% anionic lipids to form secondary structure, which covers the fraction (around 25%) of anionic lipids present in *E. coli* inner membranes. Our lipid compositions deviate from bacterial membranes in that we used phosphatidylcholine rather than phosphatidylethanolamine due to phosphatidylcholine's superior bilayer-forming properties and the inability to extrude vesicles with high fractions of phosphatidylethanolamine. However, 10−20% of the latter lipid does not affect Novispirin structure.

The pure zwitterionic lipid (DOPC) is not able to induce structure in Novispirin. Uncharged (DM) and zwitterionic (DPS) detergents, however, do induce secondary structure in Novispirin. More counterintuitively, the cationic detergents LTAC and LTAB can likewise induce the formation of secondary structure. The LTAC/LTAB concentration needed to induce structure is strongly pH-dependent. At pH 7.5, a far lower amount of detergent is sufficient than at pH 5.7 (Figure 4). This indicates that the histidine side chain plays an important role in this interaction, since it is the only group titrating in this pH area. In 270 mM LTAC, the chemical shift of the two imidazole protons ($H^{\delta 2}$ and $H^{\epsilon 1}$) titrate with pH to give an apparent pK_a of 6.37 (data not shown). The chemical shift changes are likely to arise from a combination of protonation−deprotonation, association−dissociation, and

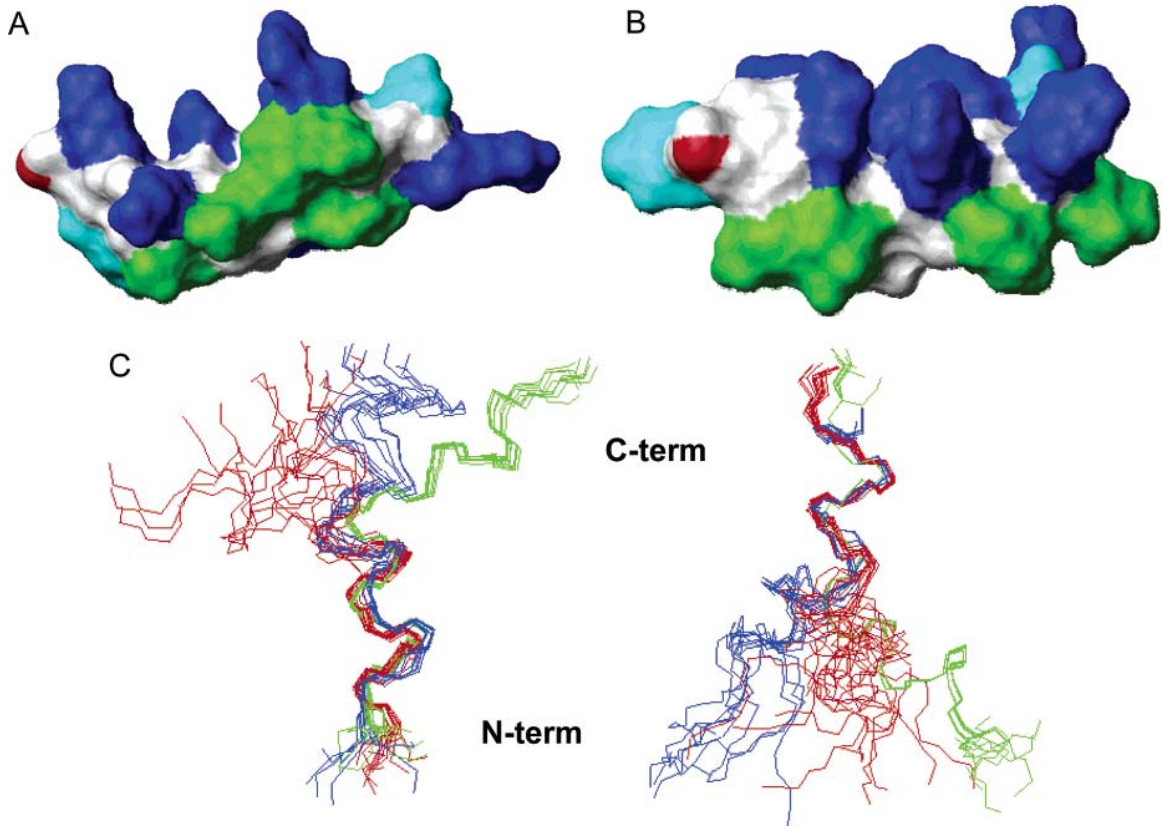

FIGURE 10: Novispirin in SDS (A) and LTAB (B). Contact surface. Green surface regions correspond to Ile and Leu residues, cyan corresponds to Asn and Tyr, red denotes the negatively charged C-terminus, and blue denotes positively charged side chains. The amphipatic nature of the Novispirin helix is evident. The spatial distribution of the positively charged side chains is much narrower in LTAB than in SDS. (C) A superposition of Novispirin in SDS (red), LTAB (blue), and TFE (green). For each structure, a bundle of the 10 best structures is shown. In the left panel, the N-terminal residues are superimposed; in the right panel, the C-terminal residues are superimposed.

folding−unfolding equilibria. However, the protonation−deprotonation generally give rise to the largest shift changes, making the value of 6.37 a reasonable estimate of the imidazole ring's pK_a. Since no positively charged biological membranes are known, the biological significance of this behavior is unknown. However, the observations reveal a surprisingly broad susceptibility of small peptides to form helical structures in micellar environments.

Structure Comparison. CD spectra of Novispirin in SDS, LTAC, and TFE revealed subtle differences. Access to atomic-level structures could elucidate the basis for these differences. Since only the structure in TFE is available (*30*), we have determined the high-resolution NMR structures of Novispirin in two different micellar solutions: SDS and LTAB. In both cases, there are well-defined helical regions interrupted by a less well-defined region around residues 10−12, in agreement with the TFE structure. While the kink in the helix is very well-defined for Novispirin in TFE, it is less so in SDS. This might reflect actual mobility, since the spectra were recorded at 50 °C. Also, recently published molecular dynamics simulations (*63*) point at a higher flexibility of Novispirin G-10 in SDS micelles. It has been pointed out that in the structure of Novispirin in TFE, I13 fills a void in the hydrophobic face of the molecule caused by the I10G mutation (*30*). Such an interaction might be the reason for the observed rigidity of the Novispirin structure. In micellar environments, however, the hydrophobic chains of the detergent molecules can take over this role, thus allowing a more flexible structure of the peptide itself. The structure in LTAB is better-defined. A reason for this might be that only certain orientations of the peptide backbone allow sufficient separation of the positive charges on the peptide from each other and from the positively charged micellar surface; thus, conformational freedom is severely restricted. As noted above, the introduction of an additional positive charge in the middle of the sequence by protonating H12 (at lower pH) greatly reduces the formation of structure at a given LTAC concentration. Figure 10A,B shows the structures of Novispirin in SDS and LTAB. Besides illustrating the amphipathic nature of the helix, it also shows a much narrower spatial distribution of the positively charged side chains when in contact with LTAB.

Figure 10C shows an overlay of the structures of Novispirin in SDS, LTAB, and TFE. It is evident that the structure is better-defined in TFE than in LTAB and SDS. The sequence plots (Figure 6 in this paper and Figure 2B in ref *30*) suggest that Novispirin in LTAB consists of two distinct helical regions of approximately the same number of amino acids, whereas Novispirin in both SDS and TFE consists of a well-defined N-terminal helix and a much less well-defined and smaller (in terms of its number of amino acids) C-terminal helix. The angle between the two helical fragments is different in all three cases, which might be a consequence of the special role of I13 (see above). Thus, although the general structure of the peptide is very similar under all three conditions, there are changes from one structure to another, which reflect the subtle changes observed in the far-UV CD spectra.

Novispirin Is Embedded in the SDS Micelle. It becomes clear that the key to understanding Novispirin's behavior lies in its interaction with the detergent micelles. Three types of experiments were performed to learn more about the relative orientation of Novispirin and the micelle: the backbone H^N exchange was determined qualitatively from TOCSY spectra, paramagnetic Mn^{2+} ions were added to the solution, and NOEs between SDS and Novispirin were investigated.

The H^N exchange data (Figure 8) revealed that not a single backbone H^N showed exchange with the bulk solvent. In a control experiment under identical conditions but without SDS, strong exchange peaks could be seen. Protection from exchange can signify a very stable hydrogen bond brought about by regular secondary structure or isolation from the bulk solvent. The two short helical stretches observed here are, however, unlikely to provide enough structural stability to explain the absence of H^N exchange by the existence of very stable hydrogen bonds. It is more likely that the backbone H^N atoms are situated inside the micelle, away from the bulk solvent. Only labile side-chain protons from arginine could be found to exchange with the solvent. This is indeed expected, since the positive charges in the vicinity of these atoms are supposed to be situated at the surface of the SDS micelle, where they can interact with the anionic sulfate headgroup. No lysine H^{ζ} could be observed in any of the spectra.

Additional evidence for a micelle-embedded conformation comes from NOESY spectra with nondeuterated SDS. As summarized in Table 5, cross-peaks could be detected from Novispirin hydrogen atoms to SDS hydrogen atoms. No NOEs could be detected from backbone H^N atoms to SDS atoms. However, nearly all visible side-chain atoms of Novispirin with a chemical shift bigger than 5 ppm (R5,6,8 H^{ϵ}, H12 $H^{\delta 2}$, $H^{\epsilon 1}$, Y17 $H^{\delta 1,2}$, $H^{\epsilon 1,2}$) showed cross-peaks to SDS. Cross-peaks to the aliphatic side chains could not be detected due to severe spectral distortion by the strong SDS signals. Therefore, neither the absence nor presence of such NOEs can be confirmed. Most NOEs show to the overlapping CH_2-group signals from CH_2-4−11 of SDS. Only weak interactions with 2-CH_2 and 3-CH_2 groups could be established. This could be due to the fact that the first group of signals yields a stronger cross-peak owing to the high amount of hydrogen atoms contributing to this peak, while signals observed from only one group are not strong enough. In a mobile ensemble, cross-peaks to several different atoms can be expected that do not necessarily point at short distances that have to be fulfilled simultaneously. No cross-peaks could be seen to SDS−CH_3 group. This could point at the fact that Novispirin does not protrude that deeply into the micelle but could also just mean that signals are too weak to be detected.

The visible cross-peaks, however, present strong evidence for a micelle-embedded structure. Under the high-salt concentration used for the NMR experiments, the cmc of SDS (around 0.1 mM) is too low to allow monomeric SDS to cause these cross-peaks.

The addition of paramagnetic Mn^{2+} ions gave another indication as to where in the micelle Novispirin is situated. Mn^{2+} was titrated into the solution until a relative difference in the ratio of remaining-to-original signal intensity could be seen between different peptide atoms. In the case of SDS, this proved to be at 0.5 mM. Probably, the Mn^{2+} ions stick to the surface of the SDS micelle and thus form a much higher local concentration. The data recorded in the presence of Mn^{2+} ions point toward a micelle-embedded structure, with the first helical stretch being buried in the micelle, a surface-exposed hinge around G10 and I11, and thereafter the second helical stretch being oriented in parallel to the surface, showing alternating protection and lack of it. The C-terminal residues are not protected at the backbone level; the presence of a negative charge at the C-terminus would also suggest that the C-terminus points away from the anionic micellar surface. The apparent low protection might also be caused by Mn^{2+} ions interacting with the C-terminus. In either case, the backbone of the C-terminus is exposed to the bulk solution. However, the aromatic side-chain atoms of Y17 are only moderately influenced by the presence of Mn^{2+}, which points at an interaction of the phenyl ring with the micelle. This interaction is also corroborated by NOEs from the aromatic protons of Y17 to SDS protons.

Finally, the diffusion constants obtained on Novispirin in SDS and the SDS micelle in the same sample are equal, which is strongly supporting a firm attachment of Novispirin to the SDS micelle.

In summary, the data point at a conformation where amino acids 2−8 (roughly speaking, the first helix) are buried in the micelle, whereas amino acids 9−18 (the kink and the second helix) are situated on the surface of the micelle.

Novispirin Is Only Loosely Associated with the LTAC Micelle. Similar experiments as those for Novispirin in SDS were also conducted to investigate Novispirin in LTAC micelles. The results, however, pointed in a very different direction.

The H^N exchange was likewise estimated qualitatively from TOCSY spectra. Unlike SDS, several backbone H^N were found to exchange with bulk water in the presence of LTAC micelles. The spectrum shown in Figure 8G,H exhibits a range of exchange peaks. The only backbone H^N atoms, which definitely do not exchange, are from the three hydrophobic residues I6, I11, and I13 and from the three C-terminal residues K16, Y17, and G18. The labile side-chain protons of arginine again showed exchange with the solvent.

In LTAB, 8 times more Mn^{2+} was needed than in SDS to elicit an effect on the peak signals, probably due to repulsion between the cationic LTAC headgroup and Mn^{2+}. Only very few residues were protected against Mn^{2+}, namely, I6, I13, and I14.

A NOESY spectrum of Novispirin in nondeuterated LTAC did not show any cross-peaks from Novispirin to LTAC. As for SDS, neither the presence nor the absence of NOEs from LTAC to aliphatic side-chain atoms could be unambiguously proven due to signal overlap and severe spectral distortions brought about by the high concentration of the detergent.

From the results of the three experiments (exchange, addition of Mn^{2+}, and NOESY), it is doubtful whether Novispirin actually is bound to the LTAC micelle at all. Therefore, diffusion measurements were conducted to investigate whether Novispirin is bound to the LTAC micelle or whether it is free in solution. A number of pulsed-field gradient NMR measurements were conducted to determine the diffusion coefficient of Novispirin in the presence of increasing concentrations of LTAC. At pH 5.7, it was found that the apparent hydrodynamic radius of Novispirin remains

constant up to approximately 600 mM LTAC; hereafter, it increases. This points toward the formation of larger aggregates, most probably peptide−micelle clusters. This is further corroborated by the fact that also apparent micellar hydrodynamic radii increase at this point. However, Novispirin still diffuses faster than the micelle and is thus not tightly bound; otherwise, Novispirin's and the micelle's diffusion coefficients and apparent hydrodynamic radii should be equal. Comparing with the 1D NMR spectra at different LTAC concentrations (Figure 4), it can be seen that a dispersion of NMR signals begins already at lower levels of LTAC. We suggest that there is an equilibrium between a micelle-associated, folded and a free, unfolded form, that gradually is shifted toward the micelle-associated, folded form upon increasing detergent concentrations. This is in agreement with far-UV CD titration experiments in up to 1 M LTAC at pH 5.7 which show that the degree of α-helicity increases in an essentially linear fashion between 0 and 1 M LTAC and has not yet reached a plateau level at 1 M LTAC (Figure 3C).

Combining these pieces of information, it seems likely that Novispirin is weakly associated with the micelle in equilibrium between bound and free form. However, even such a weak association appears sufficient to induce an overall folded structure. The induction of structure is not an artifact of the high concentration of detergent used (e.g., through reduction of water activity or binding of the counterion bromide), since it is also observed at 20−40 mM LTAC at pH 7.5 under CD conditions, that is, much lower peptide concentrations; furthermore, halide ions at molar concentrations do not by themselves induce helical structure in Novispirin (data not shown). The strong increase in binding affinity upon increasing the pH from 5.7 to 7.5, which is accompanied only by the deprotonation of the single histidine residue, also points to very specific interactions between LTAC and Novispirin. The somewhat counterintuitive interactions with a positively charged detergent are of great principal interest. The fact that such interactions can be observed might lead to a reevaluation of the driving forces behind peptide/membrane association. Understanding these driving forces will in turn be rewarded with the ability to design target-specific antimicrobial peptides.

ACKNOWLEDGMENT

We thank Dr. Peter Güntert for help with the energy-minimization of the final structures and Dr. Yiannis Kaznessis for providing his results prior to publication. We thank Professor Norbert Müller for valuable discussions and Henning Sørensen and Tina Johnson for initial experiments with Novispirin in LTAB.

REFERENCES

1. Mygind, P. H., Fischer, R. L., Schnorr, K. M., Hansen, M. T., Sönksen, C. P., Ludvigsen, S., Raventós, D., Buskov, S., Christensen, B., De Maria, L., Taboureau, O., Yaver, D., Elvig-Jørgensen, S. G., Sørensen, M. V., Christensen, B. E., Kjærulff, S., Frimodt-Møller, N., Lehrer, R. I., Zasloff, M., and Kristensen, H.-H. (2005) Plectasin is a peptide antibiotic with therapeutic potential from a saprophytic fungus, *Nature 437*, 975−980.
2. Zasloff, M. (2002) Antimicrobial peptides of multicellular organisms, *Nature 415*, 389−395.
3. Bals, R. (2000) Epithelial antimicrobial peptides in host defense against infection, *Respir. Res. 1*, 141−150.
4. Volles, M. J., and Lansbury, P. T. (2002) Vesicle permeabilization by protofibrillar α-synuclein is sensitive to Parkinson's disease-linked mutations and occurs by a pore-like mechanism, *Biochemistry 41*, 4595−4602.
5. Volles, M. J., and Lansbury, P. T. (2003) Zeroing in on the pathogenic form of α-synuclein and its mechanism of neurotoxicity in Parkinson's disease, *Biochemistry 42*, 7871−7878.
6. Shai, Y. (1999) Mechanism of the binding, insertion and destabilization of phospholipid bilayer membranes by α-helical antimicrobial and cell non-selective membrane-lytic peptides, *Biochim. Biophys. Acta 1462*, 55−70.
7. Matsuzaki, K. (1999) Why and how are peptide-lipid interactions utilized for self-defense? Magainins and tachyplesins as archetypes, *Biochim. Biophys. Acta 1462*, 1−10.
8. Huang, H. W. (2000) Action of antimicrobial peptides: Two-state model, *Biochemistry 39*, 8347−8352.
9. Shai, Y. (2002) Mode of action of membrane active antimicrobial peptides, *Biopolymers 66*, 236−248.
10. Yang, D., Chertov, O., and Oppenheim, J. J. (2001) The role of mammalian antimicrobial peptides and proteins in awakening of innate host defenses and adaptive immunity, *Cell. Mol. Life Sci. 58*, 978−98.
11. Jerala, R., and Porro, M. (2004) Endotoxin neutralizing peptides, *Curr. Top. Med. Chem. 4*, 1173−1184.
12. Chertov, O., Yang, D., Howard, O. M., and Oppenheim, J. J. (2000) Leukocyte granule proteins mobilize innate host defenses and adaptive immune responses, *Immunol. Rev. 177*, 68−78.
13. Park, I. Y., Cho, J. H., Kim, K. S., Kim, Y.-B., Kim, M. S., and Kim, S. C. (2004) Helix stability confers salt resistance upon helical antimicrobial peptides, *J. Biol. Chem. 279*, 13896−13901.
14. Wu, M., Maier, E., Benz, R., and Hancock, R. E. W. (1999) Mechanism of interaction of different classes of cationic antimicrobial peptides with planar bilayers and with the cytoplasmic membrane of *Escherichia coli*, *Biochemistry 38*, 7235−7242.
15. Lee, I. H., Cho, Y., and Lehrer, R. I. (1997) Effects of pH and salinity on the antimicrobial properties of clavanins, *Infect. Immun. 65*, 2898−2903.
16. Lee, M.-T., Chen, F.-Y., and Huang, H. W. (2004) Energetics of pore formation induced by membrane active peptides, *Biochemistry 43*, 3590−3599.
17. Henzler-Wildman, K. A., Martinez, G. V., Brown, M. F., and Ramamoorthy, A. (2004) Perturbation of the hydrophobic core of lipid bilayers by the human antimicrobial peptide LL-37, *Biochemistry 43*, 8459−8469.
18. Heller, W. T., He, K., Ludtke, S. J., Harround, T. A., and Huang, H. W. (1997) Effect of changing the size of lipid headgroup on peptide insertion into membranes, *Biophys. J. 73*, 239−244.
19. Buffy, J. J., Waring, A. J., Lehrer, R. I., and Hong, M. (2003) Immobilization and aggregation of the antimicrobial peptide protegrin-1 in lipid bilayers investigated by solid-state NMR, *Biochemistry 42*, 13725−13734.
20. Hancock, R. E. W., and Rozek, A. (2002) Role of membranes in the activities of antimicrobial cationic peptides, *FEMS Microbiol. Lett. 206*, 143−149.
21. Jing, W., Hunter, H. N., Hagel, J., and Vogel, H. J. (2003) The structure of the antimicrobial peptide Ac-RRWWRF-NH_2 bound to micelles and its interactions with phospholipid bilayers, *J. Pept. Res. 61*, 219−229.
22. Watson, R. M., Woody, R. W., Lewis, R. V., Bohle, D. S., Andreotti, A. H., Ray, B., and Miller, K. W. (2001) Conformational changes in pediocin AcH upon vesicle binding and approximation of the membrane-bound structure in detergent micelles, *Biochemistry 40*, 14037−14046.
23. Montserret, R., McLeish, M. J., Böckmann, A., Geourjon, C., and Penin, F. (2000) Involvement of electrostatic interactions in the mechanism of peptide folding induced by sodium dodecyl sulfate binding, *Biochemistry 39*, 8362−8374.
24. Lewis, R. N., Kiricsi, M., Prenner, E. J., Hodges, R. S., and McElhaney, R. N. (2003) Fourier transform infrared spectroscopic study of the interactions of a strongly antimicrobial but weakly hemolytic analogue of gramicidin S with lipid micelles and lipid bilayer membranes, *Biochemistry 42*, 440−449.
25. Zhong, L., and Johnson, W. C. (1992) Environment affects amino acid preference for secondary structure, *Proc. Natl. Acad. Sci. U.S.A. 89*, 4462−4465.
26. Yonath, A., Podjarny, A., Honig, B., Sielecki, A., and Traub, W. (1977) Crystallographic studies of protein denaturation and renaturation. 2. Sodium dodecyl sulfate induced structural changes in triclinic lysozyme, *Biochemistry 16*, 1418−1424.

27. Pervushin, K. V., Orekhov, V. Y., Popov, A. I., Musina, L. Y., and Arseniev, A. S. (1994) Three-dimensional structure of (1-71)bacterioopsin solubilized in methanol/chloroform and SDS micelles determined by ^{15}N-^{1}H heteronuclear NMR spectroscopy, *Eur. J. Biochem. 219*, 571−583.
28. Keifer, P., Peterkovsky, A., and Wang, G. (2004) Effects of detergent alkyl chain length and chemical structure on the properties of a micelle-bound bacterial membrane targeting peptide, *Anal. Biochem. 331*, 33−39.
29. Travis, S. M., Anderson, N. N., Forsyth, W. R., Espiritu, C., Conway, D., Greenberg, E. P., McCray, P. B. J., Lehrer, R. I., Welsh, M. J., and Tack, B. F. (2000) Bacteriocidal activity of mammalian cathelicidin-derived peptides, *Infect. Immunol. 68*, 2748−2755.
30. Sawai, M. V., Waring, A. J., Kearney, W. R., McCray, P. B. J., Forsyth, W. R., Lehrer, R. I., and Tack, B. F. (2002) Impact of single-residue mutations on the structure and function of ovispirin/novispirin antimicrobial peptides, *Protein Eng. 15*, 225−232.
31. Jasanoff, A., and Fersht, A. R. (1994) Quantitative determination of helical propensities from trifluoroethanol titration curves, *Biochemistry 33*, 2129−2135.
32. Hirota, N., Mizuno, K., and Goto, Y. (1998) Group additive contributions to the alcohol-induced α-helix formation of melittin: Implication for the mechanism of the alcohol effects on proteins, *J. Mol. Biol. 275*, 365−378.
33. Gavin, P., and Better, M. (2000) Production of antifungal recombinant peptides in *Escherichia coli*, *J. Biotechnol. 79*, 127−136.
34. Jauregui-Adell, J., and Marti, J. (1975) Acidic cleavage of the aspartyl-proline band and the limitations of the reaction, *Anal. Biochem. 69*, 468−473.
35. Sambrook, J., Fritsch, E. F., and Maniatis, T. (1989) *Molecular Cloning*, Cold Spring Harbor Laboratory Press, New York.
36. Svendsen, I., and Breddam, K. (1992) Isolation and amino acid sequence of a glutamic acid specific endopeptidase from *Bacillus licheniformis*, *Eur. J. Biochem. 204*, 165−171.
37. Byler, D. M., and Sussi, H. (1986) Examination of the secondary structure of proteins by deconvolved FTIR spectra, *Biopolymers 25*, 469−487.
38. Hwang, T. L., and Shaka, A. J. (1995) Water suppression that works. Excitation sculpting using arbitrary wave-forms and pulsed-field gradients, *J. Magn. Reson. 112*, 275−279.
39. Emsley, L., and Bodenhausen, G. (1992) Optimisation of shaped selective pulses for NMR using a quaternion description of their overall propagators, *J. Magn. Reson. 97*, 135−148.
40. Piotto, M., Saudek, V., and Sklenar, V. (1992) Gradient-tailored excitation for single-quantum NMR spectroscopy of aqueous solutions, *J. Biomol. NMR 2*, 661−666.
41. Griesinger, C., Otting, G., and Wüthrich, K. (1988) Clean TOCSY for 1H spin system identification in macromolecules, *J. Am. Chem. Soc. 110*, 7870−7872.
42. Wüthrich, K. (1986) *NMR of Proteins and Nucleic Acids*, Wiley, New York.
43. Bartels, C., Xia, T.-H., Billeter, M., Günter, P., and Wüthrich, K. (1995) The program XEASY for computer-supported NMR spectral of biological macromolecules, *J. Biomol. NMR 5*, 1−10.
44. Jerschow, A., and Müller, N. (1997) Suppression of convection artifacts in stiumlated-echo diffusion experiments: Double-stimulated-echo experiments, *J. Magn. Reson. 125*, 372−375.
45. Fersht, A. R. (1999) *Structure and Mechanism in Protein Science. A Guide to Enzyme Catalysis and Protein Folding*, Freeman & Co., New York.
46. Keller, R. (2004) *The Computer Aided Resonance Assignment Tutorial*, Cantina Verlag, Goldau.
47. Cornilescu, G., Delagio, F., and Bax, A. (1999) Protein backbone angle restraints from searching a database for chemical shift and sequence homology, *J. Biomol. NMR 13*, 289−302.
48. Güntert, P., Braun, P., and Wüthrich, K. (1991) Efficient computation of three-dimensional protein structures in solution from nuclear magnetic resonance data using the program DIANA and the supporting programs CALIBA, HABAS and GLOMSA, *J. Mol. Biol. 217*, 517−530.
49. Güntert, P., Billeter, M., Ohlenschläger, O., Brown, L. R., and Wüthrich, K. (1998) Conformational analysis of proteins and nucleic acid fragments with the new grid search algorithm FOUND, *J. Biomol. NMR 12*, 543−548.
50. Güntert, P., Mumenthaler, C., and Wüthrich, K. (1997) Torsion angle dynamics for NMR structure calculation with the new program DYANA, *J. Mol. Biol. 273*, 283−298.
51. Cornell, W. D., Cieplak, P., Bayly, C. I., Gould, I. R., Merz, K. M., Ferguson, D. M., Spellmeyer, D. C., Fox, T., Caldwell, J. W., and Kollman, P. A. (1995) A second generation force field for the simulation of proteins, nucleic acids, and organic molecules, *J. Am. Chem. Soc. 117*, 5179−5197.
52. Luginbühl, P., Güntert, P., Billeter, M., and Wüthrich, K. (1996) The new program OPAL for molecular dynamics simulations and energy refinements of biological macromolecules, *J. Biomol. NMR 8*, 136−146.
53. Laskowski, R. A., MacArthur, M. W., Moss, D. S., and Thornton, J. M. (1993) PROCHECK: A program to check the stereochemical quality of protein structures, *J. Appl. Crystallogr. 26*, 283−291.
54. Provencher, S. W., and Glöckner, J. (1981) Estimation of globular protein secondary structure from circular dichroism, *Biochemistry 20*, 33−37.
55. Santos, N. C., Silva, A. C., Castanho, M. A., Martins-Silva, J., and Saldanha, C. (2003) Evaluation of lipopolysaccharide aggregation by light scattering spectroscopy, *ChemBioChem 4*, 96−100.
56. Lindberg, M., Biverståhl, H., Gräslund, A., and Mäler, L. (2003) Structure and positioning comparison of two variants of penetratin in two different membrane mimicking systems by NMR, *Eur. J. Biochem. 270*, 3055−3063.
57. Rosen, M. J. (1988) *Surfactants and Interfacial Phenomena*, Wiley, New York.
58. Tanford, C. (1970) Protein denaturation. Part C. Theoretical models for the mechanism of denaturation, *Adv. Protein Chem. 24*, 1−95.
59. Pertinhez, T. A., Bouchard, M., Smith, R. A. G., Dobson, C. M., and Smith, L. J. (2002) Stimulation and inhibition of fibril formation by a peptide in the presence of different concentrations of SDS, *FEBS Lett. 529*, 193−197.
60. Yamamoto, S., Kasegawa, K., Yamaguchi, I., Tsutsumi, S., Kardos, J., Goto, Y., Gejyo, F., and Naiki, H. (2004) Low concentrations of sodium dodecyl sulfate induces the extension of β_2-microglobulin-related amyloid fibrils at neutral pH, *Biochemistry 43*, 11075−11082.
61. Zhao, H., Tuominen, E. K. J., and Kinnunen, P. K. J. (2004) Formation of amyloid fibers triggered by phosphatidylserine-containing membranes, *Biochemistry 43*, 10302−10307.
62. Sparr, E., Engel, M. F. M., Sakharov, D. V., Sprong, M., Jacobs, J., de Kruijff, B., Höppner, J. W. M., and Killian, J. A. (2004) Islet amyloid polypeptide-induced membrane leakage involves uptake of lipids by forming amyloid fibers, *FEBS Lett. 577*, 117−120.
63. Khandelia, H., and Kaznessis, Y. N. (2005) Molecular dynamics simulations of helical antimicrobial peptides in SDS micelles: What do point mutations achieve? *Peptides 26*, 2037−2049.
64. Koradi, R., Billeter, M., and Wüthrich, K. (1996) MOLMOL: A program for display and analysis of macromolecular structures, *J. Mol. Graphics 14*, 51−55.

BI051876R